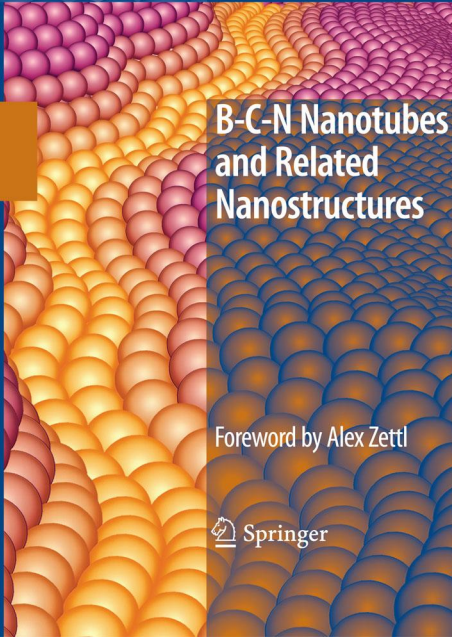


LECTURE NOTES IN  
NANOSCALE SCIENCE AND  
TECHNOLOGY 6

Yoke Khin Yap  
*Editor*



**B-C-N Nanotubes  
and Related  
Nanostructures**

Foreword by Alex Zettl



Springer

# B-C-N Nanotubes and Related Nanostructures

# Lecture Notes in Nanoscale Science and Technology

## Volume 6

### Series Editors:

Zhiming M. Wang

Department of Physics, University of Arkansas, Fayetteville, AR, USA

Andreas Waag

Institut für Halbleitertechnik, TU Braunschweig, Braunschweig, Germany

Gregory Salamo

Department of Physics, University of Arkansas, Fayetteville, AR, USA

Naoki Kishimoto

Quantum Beam Center, National Institute for Materials Science, Tsukuba, Ibaraki, Japan

### Volumes Published in This Series:

*Volume 1: Self-Assembled Quantum Dots*, Wang, Z.M., 2007

*Volume 2: Nanoscale Phenomena: Basic Science to Device Applications*, Tang, Z., and Sheng, P., 2007

*Volume 3: One-Dimensional Nanostructures*, Wang, Z.M., 2008

*Volume 4: Nanoparticles and Nanodevices in Biological Applications: The INFN Lectures - Vol I*, Bellucci, S., 2009

*Volume 5: Toward Functional Nanomaterials* Wang, Z.M., 2009

*Volume 6: B-C-N Nanotubes and Related Nanostructures*, Yap, Y.K., 2009

### Forthcoming Titles:

*Crystallization and Growth of Colloidal Nanocrystals*. Leite, E.R., 2009

*Epitaxial Semiconductor Nanostructures*, Wang, Z.M., and Salamo, G., 2009

*Nanoscale Photonics and Optoelectronics: Science and Technology*, Wang, Z.M., and Neogi, A., 2010

Yoke Khin Yap (Ed.)

# B-C-N Nanotubes and Related Nanostructures

 Springer

*Editor*  
Yoke Khin Yap  
Michigan Technological University  
Department of Physics  
1400 Townsend Drive  
Houghton MI 49931-1291  
USA

ISBN: 978-1-4419-0085-2      e-ISBN: 978-1-4419-0086-9  
DOI: 10.1007/978-1-4419-0086-9  
Springer Dordrecht Heidelberg London New York

Library of Congress Control Number: 2009928899

© Springer Science+Business Media, LLC 2009

All rights reserved. This work may not be translated or copied in whole or in part without the written permission of the publisher (Springer Science+Business Media, LLC, 233 Spring Street, New York, NY 10013, USA), except for brief excerpts in connection with reviews or scholarly analysis. Use in connection with any form of information storage and retrieval, electronic adaptation, computer software, or by similar or dissimilar methodology now known or hereafter developed is forbidden.

The use in this publication of trade names, trademarks, service marks, and similar terms, even if they are not identified as such, is not to be taken as an expression of opinion as to whether or not they are subject to proprietary rights.

Printed on acid-free paper

Springer is part of Springer Science+Business Media ([www.springer.com](http://www.springer.com))

# Foreword

For many, in the 1980s and early 1990s, the accidental discovery of carbon-based fullerenes and nanotubes heralded the beginning of the nanoscience and nanotechnology revolution. These unique materials promised new chemistries, diverse electronic and thermal properties, extreme mechanical behavior, and novel optical response. Today, a number of applications have been commercially realized and the future, especially for carbon nanotubes, looks bright.

What makes these materials so special? One key feature is the  $sp^2$  chemical bond, the strongest in nature. This hybridized bond is what binds together the carbon atoms in planar graphene and it is even stronger than the tetrahedral  $sp^3$  bonds of diamond. This is the basis for the exceptional strength and stiffness of nanotubes. A second key feature is the relatively light mass of carbon, which, when combined with strong bonds, leads to high vibrational frequencies and transport anomalies such as high thermal conductivity. A third feature is the intrinsic low-dimensional nature of the materials. Carbon nanotubes serve as ballistic, one-dimensional quantum wires.

In the periodic table of the elements, carbon is flanked by boron and nitrogen. As it turns out, boron and nitrogen also form exceptionally strong  $sp^2$  bonds, leading to planar BN configurations. Hexagonal BN, structurally similar to naturally occurring graphite, was synthesized in the early nineteenth century. BN-based planar materials are quite diverse. When combined with carbon, a host of different B–C–N configurations are possible. Many B–C–N-based planar compounds were first synthesized by N. Bartlett at the University of California at Berkeley in the 1970s and 1980s. The discovery of carbon nanotubes led researchers to investigate the possibility of nanotubes formed from other materials. In 1994, M. Cohen, a theorist at Berkeley, predicted that various B–C–N-based nanotubes should be stable, including pure BN nanotubes. Shortly thereafter, BN nanotubes were experimentally realized by A. Zettl, again at Berkeley, in 1995. Hence, the discovery of BN nanotubes was not an accident. Other B–C–N-based nanotubes and nanoparticles (such as nanococones) have also been synthesized, including those with  $BC_3$  and  $BC_2N$  stoichiometry. Generally, B–C–N nanomaterials development has been theoretically guided much more strongly than has carbon nanomaterials development.

B–C–N nanotubes and nanoparticles form an exciting materials set with a phenomenally rich set of physical properties. Pure BN nanotubes are uniformly semiconducting with a large bandgap, independent of diameter, chirality, or wall

number (this is in sharp contrast to carbon nanotubes, where the electronic properties are strongly influenced by geometrical subtleties). However, application of transverse electric fields to BN nanotubes, or mechanical deformation, depresses the local bandgap, opening up the possibility of external voltage-tuned optical components or sensitive transducers.  $BC_2N$  nanotubes are predicted to support helical currents.  $BC_3$  nanotubes are predicted to be insulating in isolation but metallic in bundles. Doped BN nanotubes are excellent, stable electron field emission sources. BN nanotubes are useful as hydrogen storage media, with  $H_2$ -binding energies significantly larger than those for carbon nanotubes. BN nanotubes have unusual exciton configurations as well as unique spin states, and have exceptional thermal conductivity properties. They can easily be chemically functionalized and are noncytotoxic to living cells; hence, they have important biological applications. B–C–N materials also typically have extreme resistance to chemical degradation and oxidation; BN nanotubes are extremely stable at high temperatures.

Why then, with all the wonderful characteristics of B–C–N nanomaterials, are they relatively unknown compared with pure carbon nanomaterials? One reason is that B–C–N nanotubes and nanoparticles are harder to synthesize than their carbon counterparts. The synthesis temperatures are typically higher, and boron and nitrogen containing precursor materials are more difficult to work with, than those for carbon. Researchers and industrialists today wishing to study or implement B–C–N nanomaterials have limited options for obtaining these materials from commercial vendors. Another reason for the less popular image of B–C–N nanomaterials is that the relevant scientific literature is scattered amongst many different journals, theses, and lectures. In sharp contrast to carbon-based nanomaterials, for which many reference books exist, none such single volume has existed for B–C–N nanomaterials, and reliable information is hard to find.

Hence, this volume on B–C–N nanotubes and nanostructures, superbly edited by Yoke Khin Yap, serves a critical need. It brings together under one cover the full spectrum of B–C–N-based nanomaterial, from theoretical models to synthesis techniques to characterization and application. Chapter authors are leaders in the field, and they have done a magnificent job of distilling the most exciting and most important topics, and presenting them in clear, tractable fashion. This volume represents the first comprehensive book on B–C–N nanomaterials including pure BN,  $B_xC_yN_z$ , CN, BC, and boron, and will no doubt become a classic reference. The B–C–N field is in its infancy with great science and applications potential; this volume will surely facilitate rapid expansion of the field.

Berkeley, CA

Alex Zettl

# Preface

The arrangement of carbon atoms differentiates a pencil lead from pricey diamonds. New carbon materials such as fullerenes, carbon nanotubes, and graphene have attracted tremendous research interest and have led to a Nobel Prize. Clearly, the change of bond hybridization and molecular packing among carbon atoms can make very exciting new materials. Materials in the boron nitride (BN) system are structurally similar to the carbon solids. However, carbon and BN materials have different properties. For instance, graphite is a conductor while hexagonal-BN is an insulator. Hybridization of the carbon and BN phases (boron carbon-nitride, BCN or  $B_xC_yN_z$ ) was predicted to create another series of novel materials with tunable properties intermediate to that of their precursors.

Materials within the B–C–N triangular zone offer new vistas for materials research. They include nanostructures of carbon, boron, and compounds constructed of multiple elements using B, C, and N atoms, the smallest atoms that can form the strongest covalent bonds in solids. Clearly, the ability to control bond hybridization, molecular packing, and composition of these materials is important in the creation of new materials. Significant research efforts have been invested in the B–C–N area in the past decade. However, there is no comprehensive reference available for the scientific community. Since this research area has been growing significantly in the past few years, a group of experts have come together in the making of this reference book on B–C–N nanotubes and related nanostructures.

This is the first book emphasizing the latest research on B–C–N nanomaterials, which will complement the many volumes devoted to carbon nanotubes. The contents cover all possible materials within the B–C–N triangular zone: Carbon, BN, BCN, carbon nitrides (CN), boron, boron carbide ( $B_xC_y$ ), and doped carbon nanostructures. The first chapter provides fundamental background on all B–C–N materials, which is reviewed in detail in subsequent chapters. The chapter by Wang et al. focuses on multiwalled boron nitride nanotubes (BNNTs). This chapter is followed by a review of single wall BNNTs. The chapter by Arenal and Loiseau also summarizes the latest understanding of single wall nanotubes of BN, CN,  $B_xC_y$ , and  $B_xC_yN_z$ . The chapter by Blasé and Chacham outlines theoretical findings on the electronic properties of BNNTs, nanotubes of  $B_xC_yN_z$  and novel heterojunctions of CNTs and BNNTs. The chapter by Wirtz and Rubio complements the chapters by Wang et al., Arenal and Loiseau, and Blasé and Chacham by reviewing the phonon



and optical properties of BNNTs. The chapter by Oku focuses on interesting BN nanostructures such as nanocages and nanohorns. The chapter by Yu and Wang describes experimental efforts on interesting nanostructures of CN and  $B_xC_yN_z$ , which are different from those discussed in the chapter by Arenal and Loiseau. The chapter by Filho and Terrones summarizes efforts on modified CNTs, an emerging area closely associated with CNTs. Finally, the chapter by Lau et al. reviews both experimental and theoretical efforts on boron and boron carbide materials. All these chapters have been carefully planned to fulfill the goal of providing a comprehensive reference book on B–C–N nanomaterials.

The volume editor acknowledges the superior contributions from all participating authors, which has made the successful and timely completion of this book possible.

Houghton, MI

Yoke Khin Yap

## About the Volume Editor



Professor Yoke Khin Yap received his Ph.D. in 1999 from Osaka University as a “*Monbusho*” scholar. He was a fellow of the *Japan Society for the Promotion of Science (JSPS)* before joining Michigan Tech in 2002. Professor Yap received the National Science Foundation *CAREER* Award in 2005. He has published more than 140 articles including book and encyclopedia chapters, review papers, peer-reviewed articles, and conference proceedings. His research program at Michigan Tech has been supported by the U.S. Department of Army (DOA), National Science Foundation (NSF), Defense Advanced Research Projects Agency (DARPA), the U.S. Department of Energy (DOE), the U.S. Department of Agriculture (USDA), and multiple DOE

Nanoscale Science Research Centers. Professor Yap is also the first elected Chair of the user group of the Center for Nanophase Materials Sciences at Oak Ridge National Laboratory.

# Contents

<b>1 Introduction to B–C–N Materials.....</b>	<b>1</b>
Chee Huei Lee, Vijaya K. Kayastha, Jiesheng Wang and Yoke Khin Yap	
<b>2 Multiwalled Boron Nitride Nanotubes: Growth, Properties and Applications.....</b>	<b>23</b>
Jiesheng Wang, Chee Huei Lee, Yoshio Bando, Dmitri Golberg and Yoke Khin Yap	
<b>3 Heteroatomic Single-Wall Nanotubes Made of Boron, Carbon, and Nitrogen.....</b>	<b>45</b>
Raul Arenal and Annick Loiseau	
<b>4 Electronic Properties of Boron-Nitride and Boron Carbonitride Nanotubes and Related Heterojunctions.....</b>	<b>83</b>
Xavier Blase and Helio Chacham	
<b>5 Optical and Vibrational Properties of Boron Nitride Nanotubes.....</b>	<b>105</b>
Ludger Wirtz and Angel Rubio	
<b>6 Boron Nitride Nanocage Clusters, Nanotubes, Nanohorns, Nanoparticles, and Nanocapsules.....</b>	<b>149</b>
Takeo Oku, Ichihito Narita, Naruhiro Koi, Atsushi Nishiwaki, Katsuaki Sukanuma, Masahiro Inoue, Kenji Hiraga, Toshitsugu Matsuda, Makoto Hirabayashi, Hisato Tokoro, Shigeo Fujii, Makoto Gonda, Masahiko Nishijima, Toshio Hirai, Rodion V. Belosludov, and Yoshiyuki Kawazoe	
<b>7 Carbon Nitride and Boron Carbon Nitride Nanostructures.....</b>	<b>195</b>
Jie Yu and E.G. Wang	

**8 Properties and Applications of Doped Carbon Nanotubes** ..... 223  
Antonio G. Souza Filho and Mauricio Terrones

**9 Boron and Boron Carbide Materials: Nanostructures and Crystalline Solids** ..... 271  
Kah Chun Lau, Yoke Khin Yap, and Ravindra Pandey

**Index** ..... 293

# Contributors

## **Raul Arenal**

Laboratoire d'Etude des Microstructures (LEM), UMR 104 CNRS-ONERA,  
Avenue de la Division Leclerc, 92322 Chatillon, France

## **Yoshio Bando**

World Premier International Center for Materials Nanoarchitectonics  
(MANA), National Institute for Materials Science, Namiki 1-1, Tsukuba,  
Ibaraki 305-0044, Japan

## **Rodion V. Belosludov**

Institute for Materials Research, Tohoku University, Sendai 980-8577, Japan

## **Xavier Blase**

Institut Néel, CNRS and Université Joseph Fourier, BP 166,  
38042 Grenoble Cedex 09, France

## **Helio Chacham**

Departamento de Física, ICEx, Universidade Federal de Minas Gerais,  
CP 702, 30123-970 Belo Horizonte, MG, Brazil

## **Shigeo Fujii**

Advanced Electronics Research Laboratory, Hitachi Metals Co. Ltd.,  
Saitama 360-0843, Japan

## **Dmitri Golberg**

World Premier International Center for Materials Nanoarchitectonics  
(MANA), National Institute for Materials Science, Namiki 1-1, Tsukuba,  
Ibaraki 305-0044, Japan

## **Makoto Gonda**

Life Science Laboratory, Shimadzu Corporation, Kyoto 604-8511, Japan

## **Makoto Hirabayashi**

Institute for Materials Research, Tohoku University, Sendai 980-8577, Japan

## **Kenji Hiraga**

Institute for Materials Research, Tohoku University, Sendai 980-8577, Japan

**Toshio Hirai**

Institute for Materials Research, Tohoku University, Sendai 980-8577, Japan

**Masahiro Inoue**

Institute of Scientific and Industrial Research, Osaka University,  
Osaka 567-0047, Japan

**Yoshiyuki Kawazoe**

Institute for Materials Research, Tohoku University, Sendai 980-8577, Japan

**Vijaya K. Kayastha**

Department of Physics, Michigan Technological University,  
118 Fisher Hall, 1400 Townsend Drive, Houghton, MI 49931, USA

**Naruhiko Koi**

Institute of Scientific and Industrial Research, Osaka University,  
Osaka 567-0047, Japan

**Kah Chun Lau**

Department of Physics, Michigan Technological University,  
118 Fisher Hall, 1400 Townsend Drive, Houghton, MI 49931, USA;  
Department of Chemistry, George Washington University, Washington,  
DC 20052, USA

**Chee Huei Lee**

Department of Physics, Michigan Technological University,  
118 Fisher Hall, 1400 Townsend Drive, Houghton, MI 49931, USA

**Annick Loiseau**

Laboratoire d'Etude des Microstructures (LEM), UMR 104 CNRS-ONERA,  
Avenue de la Division Leclerc, 92322 Chatillon, France

**Toshitsugu Matsuda**

JMC New Materials, Inc., Nihonbashi, Tokyo 103-0013, Japan

**Ichihito Narita**

Institute of Scientific and Industrial Research, Osaka University,  
Osaka 567-0047, Japan

**Masahiko Nishijima**

Institute for Materials Research, Tohoku University, Sendai 980-8577, Japan

**Atsushi Nishiwaki**

Institute of Scientific and Industrial Research, Osaka University,  
Osaka 567-0047, Japan

**Takeo Oku**

Department of Materials Science, The University of Shiga Prefecture,  
Hassaka 2500, Hikone, Shiga 522-8533, Japan;  
Cavendish Laboratory, J J Thomson Ave, Cambridge CB3 0HE, UK

**Ravindra Pandey**

Department of Physics, Michigan Technological University, 118 Fisher Hall  
1400 Townsend Drive, Houghton, MI 49931, USA

**Angel Rubio**

Nano-Bio Spectroscopy Group, Departamento de Física de Materiales,  
European Theoretical Spectroscopy Facility (ETSF), Universidad del País Vasco,  
Edificio Korta, Avda. Tolosa 72, 20018 San Sebastián, Spain

**Antonio G. Souza Filho**

Departamento de Física, Universidade Federal do Ceará, C.P. 6030,  
Fortaleza-CE, Brazil, CEP 60455-900

**Katsuaki Suganuma**

Institute of Scientific and Industrial Research, Osaka University,  
Osaka 567-0047, Japan

**Mauricio Terrones**

Laboratory for Nanoscience and Nanotechnology Research LINAN  
and Advanced Materials Department, IPICYT, Camino a la Presa  
San Jose 2055, C.P. 78216, San Luis Potosi, SLP, Mexico

**Hisato Tokoro**

Advanced Electronics Research Laboratory, Hitachi Metals Co. Ltd.,  
Saitama 360-0843, Japan

**E.G. Wang**

Institute of Physics, Chinese Academy of Sciences, Beijing 100080, China

**Jiesheng Wang**

Department of Physics, Michigan Technological University,  
118 Fisher Hall, 1400 Townsend Drive, Houghton, MI 49931, USA

**Ludger Wirtz**

Dept. ISEN, Institute for Electronics, Microelectronics, and Nanotechnology,  
CNRS-UMR 8520, B.P. 60069, 59652 Villeneuve d'Ascq Cedex, France

**Yoke Khin Yap**

Department of Physics, Michigan Technological University,  
118 Fisher Hall, 1400 Townsend Drive, Houghton, MI 49931, USA

**Jie Yu**

Department of Materials Science and Engineering, Shenzhen Graduate School,  
Harbin Institute of Technology, Shenzhen 518055, China

# Introduction to B–C–N Materials

Chee Huei Lee, Vijaya K. Kayastha, Jiesheng Wang, and Yoke Khin Yap

**Abstract** B–C–N is an emerging material system consisting of novel nanostructures of boron (B), carbon (C), boron nitride (BN), carbon nitride ( $CN_x$ ), boron-carbon nitride ( $B_xC_yN_z$ ), and boron carbide ( $B_xC_y$ ). These B–C–N materials are sometimes called as frontier carbon materials, because of their flexibility in forming materials of various types of hybridizations similar to those in the pure carbon system. This chapter provides a concise introduction on all these materials. Readers are referred to various references and other chapters compiled in this book for further reading.

## 1 Introduction

The arrangement of carbon atoms differentiates a pencil lead from a pricey diamond. Pencil leads consist of graphite where carbon atoms are  $sp^2$  hybridized with three covalent bonds ( $\sigma$ -bond) forming the hexagonal network called graphene. These graphene sheets stack in the *ABABAB*... manner and bonded by the weak van der Waals forces. In diamonds, carbon atoms are  $sp^3$  hybridized for four  $\sigma$ -bonds in a tetrahedral configuration. Graphite is soft, semimetallic, and dark (zero energy band gap), while diamond is super-hard, insulating, and transparent (band gap = 5.4 eV). In the past three decades, new carbon materials such as fullerenes [1] and carbon nanotubes (CNTs) [2] have attracted tremendous research interest and have lead to a Nobel Prize (Robert F. Curl Jr., Sir Harold W. Kroto, and Richard E. Smalley) [3]. Although fullerenes and CNTs are having bonding similar to graphite, they are packed into spherical and cylindrical structures, respectively. Clearly, the change of bond hybridization and molecular packing among carbon atoms can make very exciting new materials.

---

C.H. Lee, V.K. Kayastha, J. Wang, and Y.K. Yap (✉)  
Department of Physics, Michigan Technological University, 118 Fisher Hall,  
1400 Townsend Drive, Houghton, MI 49931, USA  
e-mail: ykyap@mtu.edu



Materials in the boron nitride (BN) system are structurally similar to the carbon solids. We have *hexagonal* phase-BN (*h*-BN), *cubic* phase-BN (*c*-BN), and BN nanotubes (BNNTs), which are analogous to the graphite, diamonds, and CNTs, respectively. For comparison, the bond lengths of carbon and BN materials are listed in Table 1. As shown, C–C and B–N bonds are quite close in bond lengths. However, these carbon and BN materials have different physical properties. For instance, graphite is a conductor, while *h*-BN is an insulator. Hybridization of the carbon and BN phases is predicted to create another series of novel materials called boron carbon-nitride (BCN or  $B_xC_yN_z$ ) with physical properties intermediate to that of their precursors [10]. It is possible to tune the physical properties of these hybrids by controlling their atomic compositions.

Materials within the B–C–N triangular zone offer new vistas for materials research. They include bulks, thin films, nanotubes, and new nanostructures of carbon, boron, or compounds constructed of multiple elements using B, C, and N atoms: the smallest atoms that can form the strongest covalent bonds in solids. These materials are sometimes called as frontier carbon materials because of their flexibility to form various covalent bonds such as those in pure carbon solids [11]. Figure 1 summarizes all possible materials within the B–C–N triangular zone. Clearly, the ability to control bond hybridization, molecular packing, and composition of these materials is important to create new materials. They could possibly be useful for protective coatings, high-power electronics, nanoelectronic, and nanoscale

**Table 1** Bond lengths for  $sp^2$  and  $sp^3$  hybridization carbon and boron nitride (BN) bonds [4-9]

Bonds	Bond lengths/nm		
	$sp^2$	$sp^3$	between two hexagonal plane
C-C	0.142	0.154	0.355
B-N	0.145	0.157	0.334

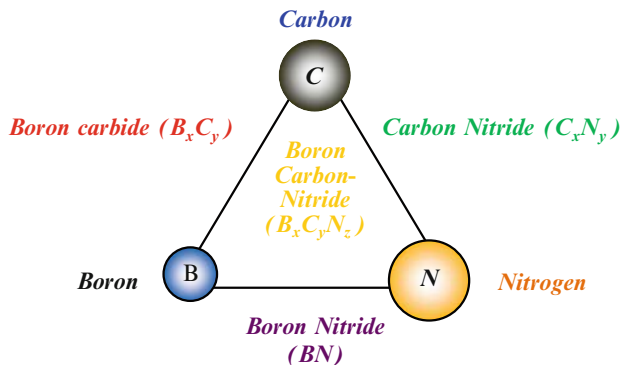


**Fig. 1** The B–C–N ternary material system

sensing devices, which are indispensable materials for nanotechnology and the advancement of science in the twenty-first century.

In this chapter, a brief introduction on carbon, BN, boron, boron carbide, carbon nitride ( $CN_x$ ), and  $B_xC_yN_z$  materials is presented.

## 2 Carbon

Carbon is the sixth element in the periodic table, and is the lightest element in the group IV of the periodic table. A carbon atom has a total of six electrons out of which four are in the valence bands. The electronic configuration of a carbon atom can be written as  $1s^22s^22p^2$ . In carbon, orbital energy difference between  $2s$  and  $2p$  orbitals is small in comparison to the energy released during bond formation. So  $2s$  and  $2p$  orbitals can intermix with each other during the bond formation process. This phenomenon is known as hybridization. If one “ $s$ ” orbital mixes with  $n$  number of “ $p$ ” orbitals, then it is called  $sp^n$  hybridization where  $n = 1, 2, 3$ . These hybridized orbitals possess different geometrical shape. For example,  $sp^1$  hybridized orbital has linear shape,  $sp^2$  possesses trigonal planar shape, and  $sp^3$  possesses tetrahedral symmetry.

Because of the flexibility in forming various type of hybridization, carbon can appear in several allotropes including the well known graphite, diamonds, and amorphous carbon. We will briefly introduce graphite, diamonds,  $C_{60}$ , graphene, and CNTs as examples. In particular, we will discuss a few aspects of CNTs with more details since it is the basis of other form of nanotubes to be discussed in other chapters of this book.

### 2.1 Graphite and Graphene

Graphite is a soft carbon allotrope, which is made of sheets of hexagonal carbon networks. These carbon sheets are known as graphene. As shown in Fig. 2a, graphene sheets in graphite are stacked in a  $ABAB\dots$  sequence or Bernal stacking. In this arrangement, alternate planes are shifted relative to each other. The in-plane distance between two nearest carbon atoms ( $a_{c-c}$ ) is  $1.42 \text{ \AA}$ , and the in-plane lattice constant ( $a_0$ ) is  $2.462 \text{ \AA}$  (in-plane distance between two alternative carbon). The  $C$ -axis lattice constant ( $c_0$ ) is  $6.708 \text{ \AA}$  (out-of-plane distance between two alternative graphene sheets). These graphene sheets are separated by the interlayer spacing of  $c_0/2 = 3.354 \text{ \AA}$ . As we have discussed, carbon atoms within a graphene sheet are  $sp^2$  hybridized. These carbon bonds are stronger than those  $sp^3$  bonds in diamonds. Free carbon atom (C) will have six electrons occupied the  $1s$ ,  $2s$ ,  $2p_x$ , and  $2p_y$  orbitals. The hybridized carbon atom (C\*) in graphite will have their electrons occupied at  $1s$ , three  $sp^2$ , and one  $2p_z$  orbitals. These electronic configurations are shown as follows:

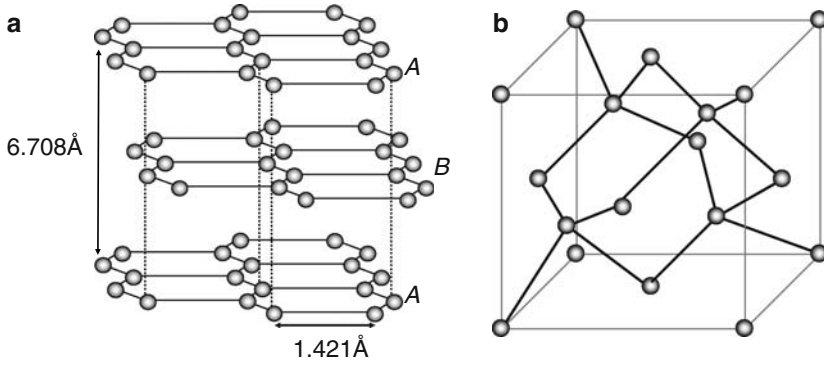
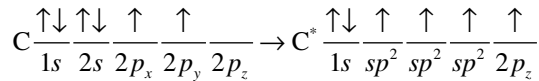


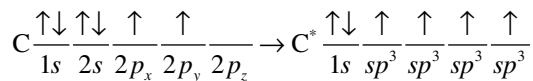
Fig. 2 Crystal structures of (a) graphite and (b) diamonds



The three electrons in the  $sp^2$  orbitals are involved in the strong in-plane  $\sigma$ -bonds with a uniform bond angle ( $120^\circ$ ). The electrons in the  $2p_z$  orbitals will form delocalized  $\pi$ -bonds and are responsible for the electrical conductivity of graphite. Because of the small overlapping of valence and conduction band (0.04 eV), graphite are semi-metals and have fewer charge carriers than metals. The softness of graphite arises from the weak van der Waals forces between adjacent graphene sheets.

## 2.2 Diamond

Diamond is the hardest known material on earth. Carbon atoms in diamonds are bonded with  $sp^3$  hybridization and packed in a face-centered cubic (fcc) lattice. The electronic configuration of ground state carbon (C) and  $sp^3$  hybridized carbon ( $\text{C}^*$ ) are shown as follows:



The hardness of the diamond is attributed to the strength of the interlocking covalent bonds between its constituent carbon atoms. The interatomic spacing in diamond is 1.5445 Å, and the bond angles are all  $109^\circ$  as shown in Fig. 2b. Since all the valence electrons in diamond are involved in the formation of  $\sigma$ -bonds, diamond has very poor electrical conductivity.

### 2.3 $C_{60}$ Fullerene

The  $C_{60}$  molecules, also known as the Buckminsterfullerene, were discovered in 1985 [1]. These molecules are having hollow sphere structures with 60 carbon atoms forming strong  $sp^2$  covalent bonds with each other. Each  $C_{60}$  molecule contains 12 pentagons and 20 hexagons, with carbon atom in each corner as shown in Fig. 3. The van der Waals diameter of a  $C_{60}$  molecule is about 1 nm, while the nucleus to nucleus diameter of a  $C_{60}$  molecule is about 0.7 nm. The  $C_{60}$  molecule has two bond lengths, corresponding to the hexagons and pentagons. Its average bond length is 1.4 Å.

### 2.4 Carbon Nanotubes

The structure of CNTs was revealed in 1991 [2]. CNTs are seamless one-dimensional cylindrical rolls of graphene sheets. Single-wall carbon nanotubes (SWCNTs) are referring to such cylindrical molecules with single layer of graphene sheet. Multiwalled carbon nanotubes (MWCNTs) are coaxial rolls of multiple graphene sheets. MWCNTs were detected in 1991, and SWCNTs were identified two years later [12, 13]. SWCNTs were then found to have the bundling tendency due to the van der Waal forces between nanotubes [14]. Although CNTs are constructed by the conducting graphene sheets, they can be either semimetallic or semiconducting,

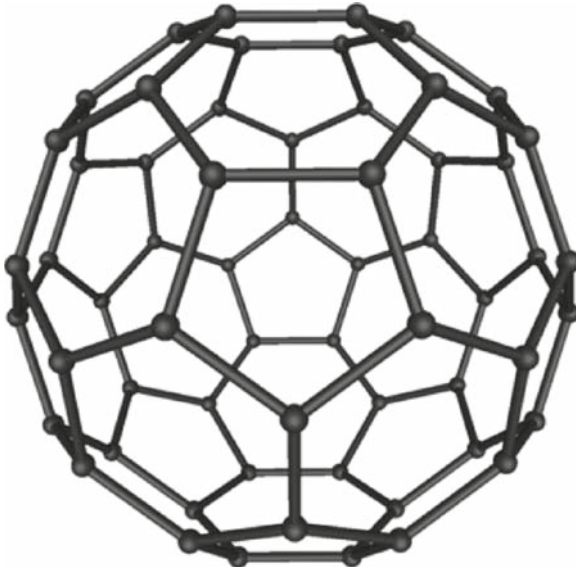


**Fig. 3** Structure of a  $C_{60}$  molecule. This is a file from the Wikimedia Commons

depending upon their structures [15–19]. The typical diameter for SWCNTs is  $\sim 1.4$  nm. However, CNTs with a diameter of 0.4 nm have also been reported [20].

Quantitatively, the structure of a SWCNT can be expressed in terms of a unit cell [15] defined by the chiral vector  $C_h = n\mathbf{a}_1 + m\mathbf{a}_2$ . In this case,  $\mathbf{a}_1$  and  $\mathbf{a}_2$  are unit vectors, and  $n$  and  $m$  are integers often written as  $(n, m)$  to represent the chirality of a SWCNTs as shown in Fig. 4. The magnitude of the circumference is thus given by  $|C_h| = a(n^2 + m^2 + nm)^{1/2}$ , where “ $a$ ” is the length of the unit vectors and is equal to 2.46 Å. For example, on the one hand, SWCNT (10, 0) can be constructed by folding the graphene sheet in Fig. 4 along the direction of  $\mathbf{a}_1$  so that (0, 0) and (10, 0) will join together. In this case,  $C_h$  is parallel to  $\mathbf{a}_1$  and forming a zero chiral angle ( $\theta = 0^\circ$ ). This type of SWCNTs is called zigzag nanotubes, where  $(n, 0)$ . On the other hand, SWCNT (6, 6) can be formed by folding the graphene sheet so that (0, 0) and (6, 6) will join together. In this case, the chiral angle  $\theta = 30^\circ$ . This type of SWCNTs is called armchair nanotubes and can be represented by  $(n, n)$ . SWCNTs with  $0^\circ < \theta < 30^\circ$  are called chiral nanotubes, for example SWCNT (7, 5). For all cases, the diameter of a SWCNT is given by

$$d_t = \frac{C_h}{\pi} = \frac{a(n^2 + m^2 + nm)^{1/2}}{\pi} \text{ and}$$

$$\theta = \sin^{-1} \left( \frac{m\sqrt{3}}{2n+m} \right).$$

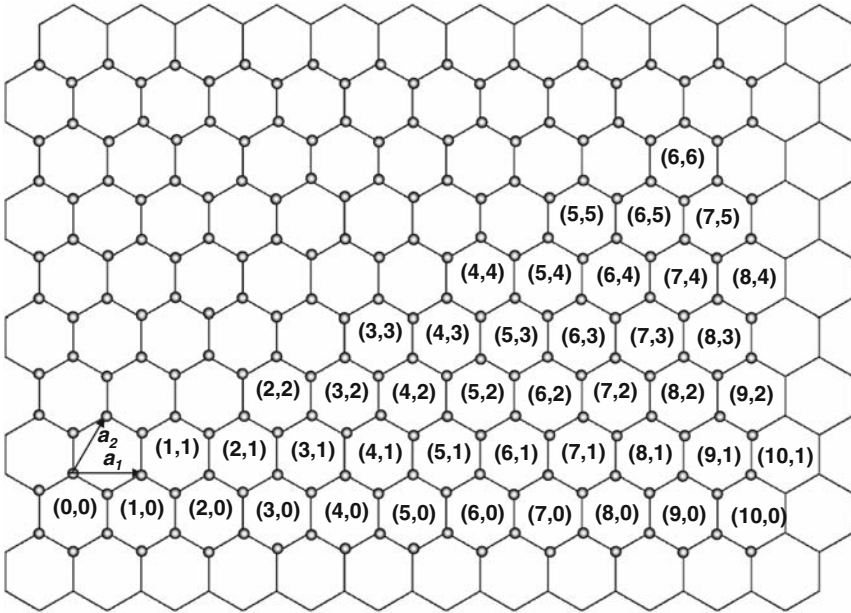
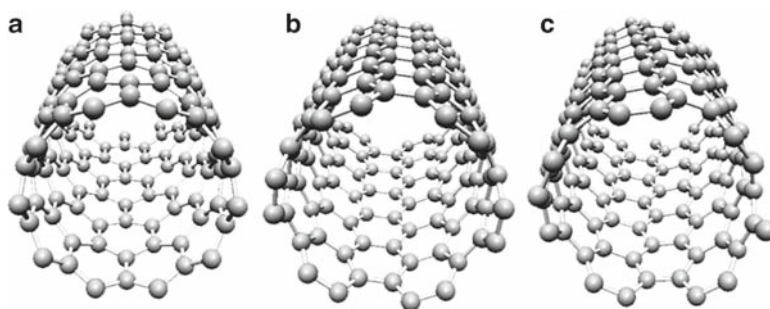


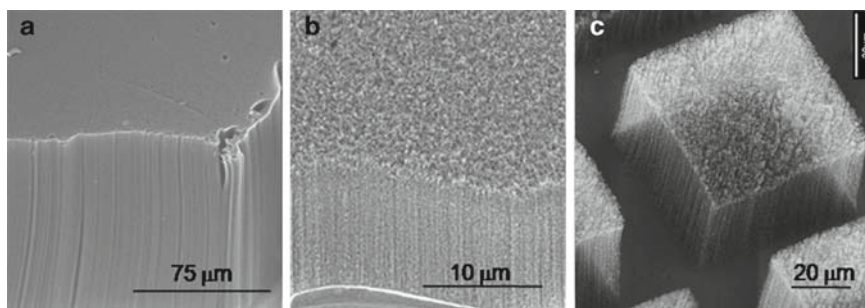
Fig. 4 Vector  $(n, m)$  of SWCNTs on a graphene sheet

Figure 5 illustrates the appearances of (10, 0), (6, 6), and (7, 5) of SWCNTs. It was found that all armchair tubes are semimetallic like graphite. One third (1/3) of zigzag and chiral tubes are semimetallic (when  $n - m = 3p$ ,  $p = \text{integer}$ ) otherwise are semiconducting. As for the case of MWCNTs, they are always semimetallic, irrespective of their diameters and chiralities.

The synthesis techniques for CNTs have been widely investigated. These techniques include arc discharge [2], laser ablation [21], and chemical vapor deposition (CVD). Currently, the most well receiving technique is CVD, which was evolved from the high-temperature approaches ( $\sim 1,000\text{--}1,200^\circ\text{C}$ ) using  $\text{CH}_4$  [22, 23] or  $\text{CO}$  [24] feedstocks to the recent low temperature approaches ( $600\text{--}800^\circ\text{C}$ ). The low temperature approaches prevented aggregation of catalyst nanoparticles and have lead to high-density vertically-aligned grow mode, which requires high density of active catalyst [25, 26]. There are various low-temperature approaches including the use of water vapors [27], oxygen plasma [28], and ethanol [29]. The authors have shown that vertically-aligned single and double-walled CNTs can be grown using  $\text{C}_2\text{H}_2$  source gas without the need of water, plasma, or ethanol as shown in Fig. 6 [30]. This success was obtained by controlling dissociative adsorption of  $\text{C}_2\text{H}_2$  molecules by low flow rates and carrier gases [25, 26].



**Fig. 5** (a) Zigzag (10, 0), (b) Armchair (6, 6), and (c) Chiral (7, 5) CNTs



**Fig. 6** Vertically-aligned (a) single, (b) double, and (c) multiwalled CNTs

As discussed SWCNTs can be semimetallic or semiconducting with various band gaps depending on their chiralities. Thus it is important to characterize their chiralities prior to device fabrication. Raman spectroscopy can be used to estimate the diameters of SWCNTs from the radial breathing mode (RBM) but not the exact  $(n, m)$ . Spectrofluorometry is a powerful tool for identifying the chirality [31]. For spectrofluorometry analysis, a well-dispersed aqueous solution of SWCNTs is prepared, and a light with certain excitation wavelength is incident on the solution. The semiconducting SWNTs undergo absorption and emission transitions, as shown in the Fig. 7a. Since certain fluorescence wavelengths will be emitted with

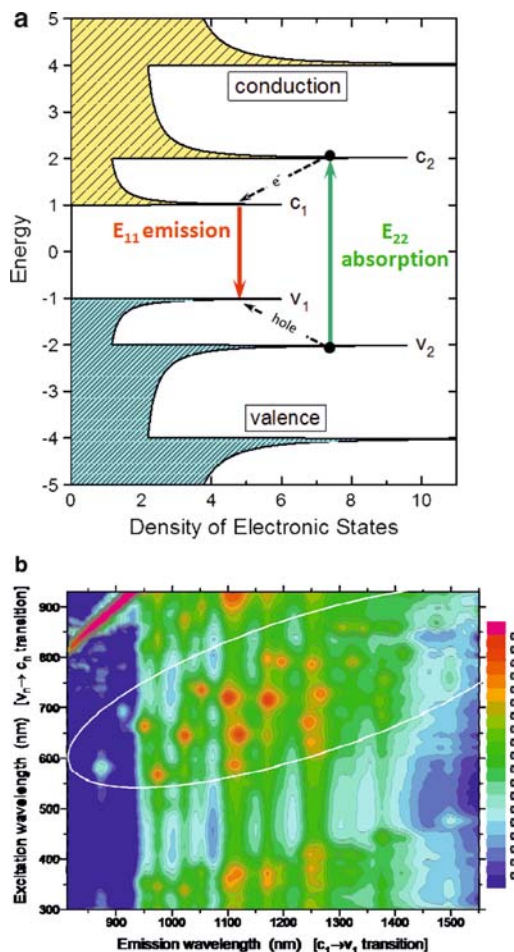
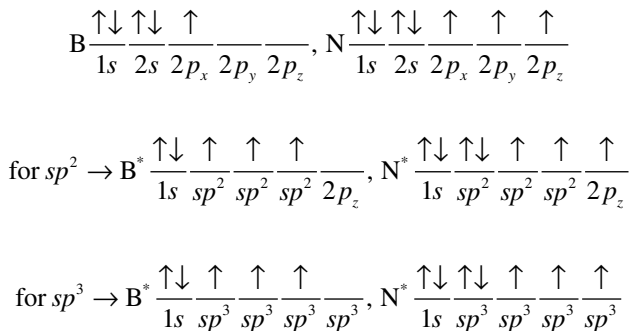


**Fig. 7** (a) Schematic density of electronic states for a single nanotube structure. *Solid arrows* representing the optical excitation and emission transitions. *Dashed arrows* denote nonradiative relaxation of the electron (in the conduction band) and hole (in the valence band) before emission. (b) Contour plot of fluorescence intensity vs. excitation and emission wavelengths for a sample of SWNTs. (Courtesy of R. B. Weisman, Original figure from [31]. Reprinted with permission from AAAS)

particular wavelength of excitation light, the chiral indices ( $n$ ,  $m$ ) can be obtained by referring to the density of states (DOS) of particular SWCNTs. The relation of the excitation and emission wavelengths can be plotted as a fluorescence contour plot as shown in Fig. 7b. The relative intensity of the spectral peaks reveals the relative quantity of each type of semiconducting SWCNTs. However, spectrofluorometry cannot identify the chirality of the semimetallic SWCNTs as they do not produce any fluorescence.

### 3 Boron Nitride

BN is constructed by boron (B) and nitrogen (N) atoms, the group III and V elements next to the group IV carbon (C) in the *Periodic Table of Elements*. Since B–N bonds and C–C bonds are isoelectronic (having the same number of electrons), BN materials are expected to form similar covalent structures to the carbon allotropes. The electronic configuration of ground state B and N atoms and hybridized B–N bonds are shown as follows:



For both  $sp^2$  and  $sp^3$  cases, one can observe that an additional electron is localized at the nitrogen atoms. Although all the electrons in the hybridized orbitals will redistribute to form the desired bonds, these covalent bonds are having some ionic nature, more electronegative at the nitrogen site. In fact, BN can appear in *hexagonal* phase (*h*-BN), *cubic* phase (*c*-BN), *rhombohedral* phase (*r*-BN), and *wurtzite* phase (*w*-BN) as shown in Fig. 8 [32]. These phases are similar to *hexagonal* graphite (*ABAB*.), *cubic* diamonds, *rhombohedral* graphite (*ABCABC*...), and *hexagonal* diamonds (*Lonsdaleite*).

#### 3.1 Phases of Boron Nitride Crystals

*h*-BN are constructed by layers of hexagonal BN networks with lattice constants ( $a_0 = 2.504 \text{ \AA}$ ,  $c_0 = 6.661 \text{ \AA}$ ) comparable to those of graphite ( $a_0 = 2.458 \text{ \AA}$ ,  $c_0 = 6.696 \text{ \AA}$ )



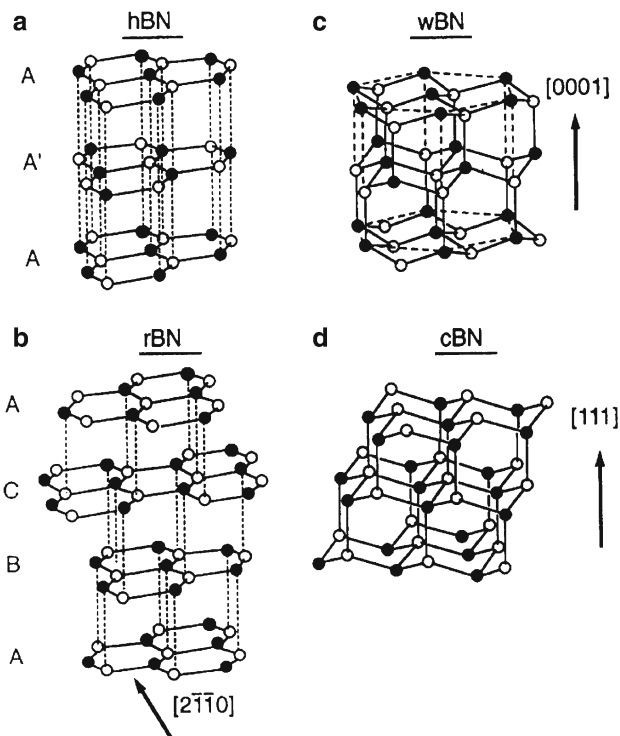


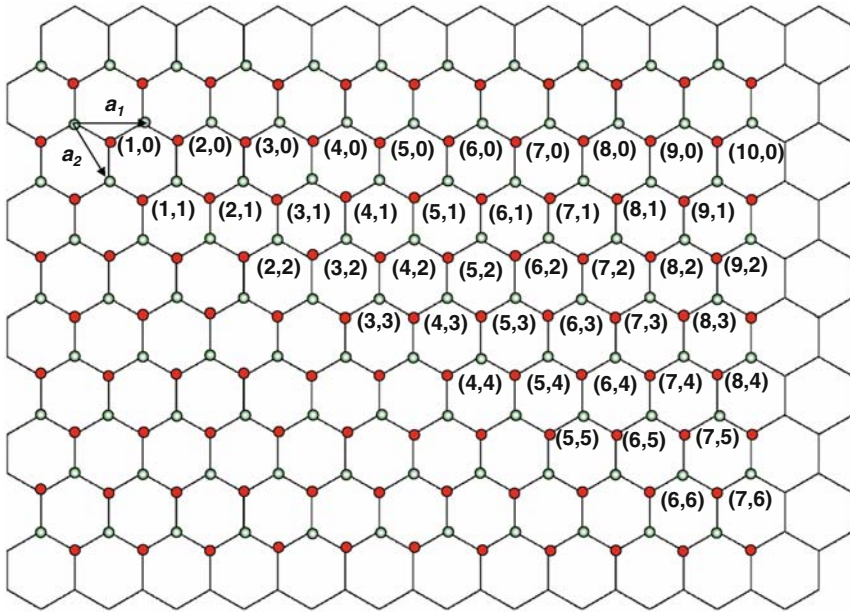
**Fig. 8** Graphical representations of (a) h-BN, (b) r-BN, (c) w-BN, and (d) c-BN phases. (From [32], Reprinted with permission from American Physical Society)

[33, Original data in 1952]. These *h*-BN layers are arranged on top of each other in an AA'AA'... sequence, such that B atoms in one layer are bonded to N atoms in the adjacent layer by electrostatic interaction as shown in Fig. 8a. *Rhombohedral* phase-BN (*r*-BN) is different from *h*-BN mainly in the aspect of stacking sequence as shown in Fig. 8b [34]. The stacking sequence of *r*-BN is threefold (ABCABC...), and hexagonal BN rings are not perfectly overlapped with those in adjacent BN layers.

Both *wurtzite* phase-BN (*w*-BN) and *c*-BN belong to  $sp^3$ -bonded phases. *w*-BN is arranged in a hexagonal unit cell with puckered layers of hexagonal networks as shown in Fig. 8c [35]. The interplanar gap is much smaller than  $sp^2$  phases such as *h*-BN and *r*-BN. *c*-BN [36, 37], another  $sp^3$ -bonded phase, possesses the *Zinc Blende* structure as shown in Fig. 8d. It consists of tetrahedrally-bonded boron and nitrogen atoms with their  $\{111\}$  planes settled in a trilayer (ABCABC...) stacking sequence. The structural parameters of the four BN phases are summarized in Table 2 [38] In addition to these four BN phases, another form of BN is called *turbostatic* phase-BN (*t*-BN) [39], which can be considered as a disordered *h*-BN or *r*-BN phase.

**Table 2** Structural properties of four boron nitride phases

Phase	Hybridization	$a$ (Å)	$b$ (Å)	Space group	Stacking sequence
$h$ -BN	$Sp^2$	2.5043	6.6562	$P6_3/mmc$ (194)	AA'AA'...
$c$ -BN	$Sp^3$	3.6153		$F43m$ (216)	ABCABC...
$r$ -BN	$Sp^2$	2.5042	9.99	$R3m$ (160)	ABCABC...
$w$ -BN	$Sp^3$	2.5505	4.21	$P6_3mc$ (186)	AA'AA'...

**Fig. 9** Vector  $(n, m)$  of SWBNNTs on a  $h$ -BN sheet

### 3.2 Boron Nitride Nanotubes

Seamless nanocylindrical rolls of  $h$ -BN sheets can be formed and are called BNNTs [40, 41]. Depending on the number of  $h$ -BN sheet involved, BNNTs can be single-walled (SW) with only single layer of  $h$ -BN sheet, or multi-walled (MW) that are constructed by several concentric  $h$ -BN sheets. An important difference between BNNTs and CNTs is that the band gap of BNNTs ( $\sim 5$  eV, theoretically) is insensitive to their chirality, number of walls, and diameters. As shown in Fig. 9, the chirality of SWBNNTs can be assigned in identical way as for SWCNTs. The convention of the unit vectors in this figure is chosen in the way consistent to that to be discussed in the chapter by Blasé and Chacham of this book. Again,  $(n, m)$  integers are assigned to represent the structures of SWBNNTs. SWBNNTs  $(n, 0)$  are zig-zag nanotubes, SWBNNTs  $(n, n)$  are armchair nanotubes, and others are chiral nanotubes.

As examples, the atomic arrangements of (a) zigzag  $(10,0)$ , (b) armchair  $(6,6)$ , and (c) chiral  $(7,5)$  SWBNNTs are illustrated in Fig. 10. Images of SWBNNTs, double-walled BNNTs, and MWBNNTs as detected by transmission electron microscopy are shown in Fig. 11 [42]. Further readings on BNNTs and related nanostructures are available in the chapters by Wang et al., Arenal and Loiseau, Blasé and Chacham, Wirtz and Rubio, and Oku et al.

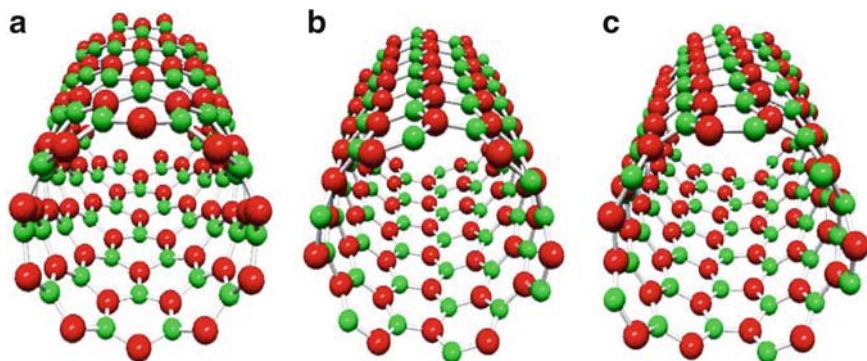


**Fig. 10** (a) Zigzag  $(10,0)$ , (b) Armchair  $(6,6)$ , (c) Chiral  $(7,5)$  BNNTs

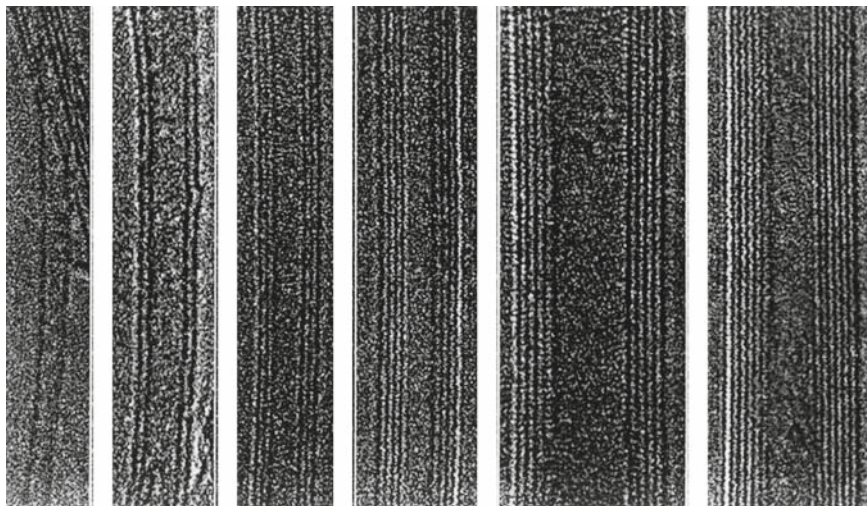


**Fig. 11** Images of transmission electron microscopy of single, to six-walled boron nitride nanotubes (*left to right*). (Courtesy of A. Zettl, Original figure from [42]. Reprinted with permission from American Institute of Physics)

## 4 Boron Carbide

Boron carbide ( $B_4C$ ) is one of the hardest materials known, ranking third behind diamond and *c*-BN described earlier. In fact, ceramic of  $B_4C$  are commercially produced for various applications including those in tank armor and bulletproof vests. The crystal structure of boron carbide has been known to be the rhombohedral unit cell ( $B_{12}C_3$ ), which is composed of the closed-shell  $B_{11}C$  icosahedral subunit clusters as schematically shown in Fig. 12. This unique structure is usually interpreted as follows. There are eight distorted  $B_{11}C$  icosahedra located at the corners of the rhombohedral Bravais lattice. These icosahedra are connected by an atomic linear C–B–C chain within the lattice. However, the locations of the carbon atoms in the icosahedron as well as the composition (not exactly  $B_{11}C$  but  $B_{12-n}C_n$ ) are still debating. In fact, the stability of these boron carbide icosahedra in comparison to the pure boron clusters is still an active research topic [43]. In addition to  $B_4C$ , there have been some interesting investigations on zero, one, and two-dimensional boron carbide nanostructures. These will be discussed further in the chapter by Lau et al.

## 5 Boron

Boron is the smallest and lightest atom that can form solids with high-strength covalent bonds. In fact,  $\beta$ -*rhombohedral boron* is the hardest elementary crystal after diamonds. In addition, boron solids have a series of impressive properties [44]. All forms of boron (allotropes) have very high melting points, from 2,200 to 2,300°C (4,000–4,200°F). They are not reactive to oxygen, water, acids, and alkalis, and thus have high resistance to chemical attacks. Boron can appear in various forms and structures, from amorphous and crystalline phases to nanos-

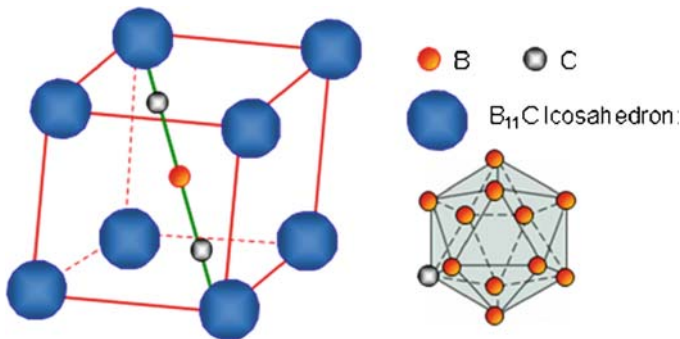


Fig. 12 Unit cell of  $B_4C$  crystals

structures including clusters and nanotubes. Irregular bonding between boron atoms forms amorphous structures and is brown in color. Crystalline phases, however, is in black color and consists of three known structures:  $\alpha$ -*rhombohedra* [45],  $\beta$ -*rhombohedral* [45], and *tetragonal* [46]. The physical and chemical properties of boron solids are expected to be enhanced by forming boron nanotubes (BNTs), boron clusters, and boron fullerenes. These closed-shell nanostructures will eliminate dangling bonds at the surface and thus avoid uncontrollable chemical reactions. In fact, the  $B_{12}$  *icosahedral* unit is well known as the building blocks for all the known boron polymorphs, including the  $\beta$ -*rhombohedral boron*. Detailed description of these boron nanostructures is available in the chapter by Lau et al. of this book.

## 6 Carbon Nitride

The research on carbon nitride had started to gain tremendous attention after the prediction of  $\beta$ - $C_3N_4$  in 1989 [47, 48]. According to the ab initio calculation,  $\beta$ - $C_3N_4$  resembled identical crystal structure as  $\beta$ - $Si_3N_4$  with the carbon atoms substituting the silicon atoms as shown in Fig. 13. The calculated cohesive energy of  $\beta$ - $C_3N_4$  suggested for a metastable carbon nitride compound. More importantly, due to their strong covalent bond, the calculated bulk modulus (4.27 Mbar) was comparable to that of diamond (4.43 Mbar). In addition to  $\beta$ - $C_3N_4$ , other phases of  $C_3N_4$  were also theoretically predicted including  $\alpha$ - $C_3N_4$ , cubic- $C_3N_4$ , pseudocubic- $C_3N_4$ , and graphitic- $C_3N_4$  [49].

There have been many experimental attempts in the synthesis of  $\beta$ - $C_3N_4$  but it was generally accepted that  $\beta$ - $C_3N_4$  may not be realistic materials. The synthesis of  $\beta$ - $C_3N_4$  was attempted by pulse laser deposition in 1993 [50]. Although crystalline structure was claimed, the nitrogen contents in these films was only approximately

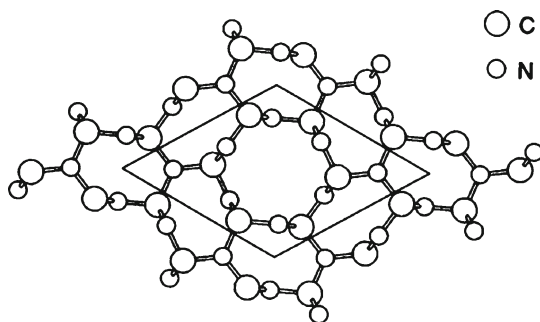


**Fig. 13** Structure of  $\beta$ - $C_3N_4$  in the  $a$ - $b$  plane. The  $c$ -axis is normal to the page. Half the atoms illustrated are located in the  $z = -c/4$  plane, the other half are in the  $z = c/4$  plane. The structure consists of these buckled planes stacked in AAA... sequence. The parallelogram shows the unit cell. (From [47], Reprinted with permission from AAAS)

45%, which was less than that predicted for the  $C_3N_4$  stoichiometry (57%). In the later experiments [51–53], it was found that the carbon atoms in the carbon nitride thin film were transformed from the initial  $sp^3$  hybridization to  $sp^2$ -bonded carbon when the overall nitrogen contents increased. The density of the film was decreased from 3.3 to 2.1 g/cm<sup>3</sup> when the concentration of nitrogen increased from 11–17%. Many other techniques have been used for the synthesis of carbon nitride films including arc discharge [54], RF plasma enhanced pulsed-laser deposition [55–58], RF sputtering [59–63], hot filament plasma sputtering [64], magnetron sputtering [65–69], plasma enhanced CVD (PECVD) [70–73], ion beam sputtering [74–78], other ion or reactive atom beam deposition techniques [79–82], and atmospheric pressure plasma [83]. Most of these attempts were conducted at room temperature, merely the doping of nitrogen into the  $sp^3$  hybridization amorphous diamond-like carbon matrix. High temperature attempt was shown to reverse the  $sp^2C=N$  bonds into  $sp^3C-N$  bonds needed for  $\beta-C_3N_4$  [55–57]. However, the nitrogen contents were below 16 at.%.

Although the attempts in growing for  $C_3N_4$  were not succeeded, nanoscale  $CN_x$  particles or films were found to be promising to be a hard material [84]. Similar to the thin film studies, PECVD [85], plasma sputtering deposition [86], and chemical reaction [87] had been utilized to produce the CN nanoparticles. Apparently, nanoscale carbon nitride compounds appear to be the important area in the future, including the nitrogen-doped CNTs and nanostructures to be discussed in the chapters by Arenal and Loiseau, Yu and Wang, and Filho and Terrones of this book.

## 7 Boron Carbon-Nitride

Since carbon and BN phases are structurally similar, many efforts have been invested in exploring their hybrid phases. These attempts can be classified into three: (1) hexagonal phase boron carbon-nitride ( $h-B_xC_yN_z$ ) that could have intermediate properties between those of graphite and  $h-BN$ , (2) cubic phase boron carbon-nitride ( $c-B_xC_yN_z$ ) that will be superhard like diamonds and  $c-BN$ , and (3) nanohybrids that may have intermediate or modified properties between those of CNTs and BNNTs.

The efforts of producing  $h-B_xC_yN_z$  and  $c-B_xC_yN_z$  bulks and thin films have been initiated since 1980s [88–92], and extended into 1990s [93–100]. In fact, the first report on hybridized  $B_xC_yN_z$  compounds was having grain dimension below 20 nm [88]. These results indicate that  $B_xC_yN_z$  compounds should be considered as nanostructures or nanocrystals instead of macroscopic single crystals as suggested in recent review articles [101, 102]. In fact, the research interest on  $B_xC_yN_z$  hybrids appears to move toward  $B_xC_yN_z$  nanotubes and nanostructures, after the demonstration of CNTs and BNNTs.

### 7.1 Hexagonal Phase Hybrid: $h-B_xC_yN_z$

As discussed, graphite is semimetallic and  $h-BN$  is insulating with a wide band gap  $\geq 5.8$  eV [103, 104]. Since graphite and  $h-BN$  are constructed by layers of carbon and BN honeycombs, respectively, it was anticipated that new  $h-B_xC_yN_z$  hybrid

**Table 3** Bond lengths of various types of bonds in  $h\text{-BC}_2\text{N}$  hybrids [105, 106]

Bonds	Bond lengths/nm
C-C	0.142
B-C	0.155
B-N	0.145
C-N	0.132

These data are also applicable for  $\text{BC}_2\text{N}$  nanotubes

phase would have BCN honeycomb structures. These  $h\text{-B}_x\text{C}_y\text{N}_z$  hybrids may have energy band gap smaller than that of  $h\text{-BN}$ , a new semiconducting materials. Theory on  $h\text{-BC}_2\text{N}$  sheets was then proposed, which consist of various chemical bonds as shown in Table 3.

The attempt of producing  $h\text{-B}_x\text{C}_y\text{N}_z$  was motivated by their attractive physical properties such as controllable band gap by varying their composition and chemical inertness. For example, recent attempts on growing  $\text{B}_x\text{C}_y\text{N}_z$  thin films have involved various approaches including CVD [107, 108], ion beam assisted deposition [109], magnetron sputtering [110, 111], RF plasma enhanced pulsed-laser deposition [112, 113], excimer laser annealing [114], and arc discharge [115]. However, most of these thin films are amorphous phase. In fact, the most challenging obstacle for producing crystalline  $h\text{-B}_x\text{C}_y\text{N}_z$  bulks and thin films is phase separation. Most  $\text{B}_x\text{C}_y\text{N}_z$  compounds are mixtures of pure BN and graphite domains. Recent results shown that hybridized  $h\text{-B}_x\text{C}_y\text{N}_z$  compounds tend to stabilize in nanostructures [116].

## 7.2 Cubic Phase Hybrid: $c\text{-B}_x\text{C}_y\text{N}_z$

The major motivation for the search of cubic phase  $\text{B}_x\text{C}_y\text{N}_z$  ( $c\text{-B}_x\text{C}_y\text{N}_z$ ) compounds is to realize new superhard materials that may be harder than  $c\text{-BN}$ . Although  $c\text{-BN}$  is the second hardest known materials, it has only half the hardness of diamonds. Furthermore, the synthesis of  $c\text{-BN}$  crystals and thin films is much harder than those of diamonds. However,  $c\text{-BN}$  is chemically inert to ferrous metals and more stable than diamond at high temperatures in the presence of oxygen. It was believed that  $c\text{-BC}_2\text{N}$  could be harder than  $c\text{-BN}$  and chemically stable like  $c\text{-BN}$ . Various  $c\text{-BC}_2\text{N}$  structures have been studied by the ab initio pseudopotential density functional method, based on the eight-atom Zinc Blende structured cubic unit cell [117]. All the structures are having positive total energy indicating of their metastable nature. Thus  $c\text{-B}_x\text{C}_y\text{N}_z$  is expected to be formed under high pressure and high temperature (HPHT) condition.

In fact, the growth of  $c\text{-B}_x\text{C}_y\text{N}_z$  hybrid was reported in 1981. This was carried out in a diamond anvil cell at a static pressure of 14 GPa and a temperature of 3,000°C [118]. Polycrystalline  $h\text{-B}_x\text{C}_y\text{N}_z$  powders [88] produced by CVD were used

as the starting materials without any catalyst (which is needed for the growth of *c*-BN and diamonds). The composition of the products was  $(\text{BN})_{0.26}\text{C}_{0.74}$ , similar to that of the starting materials. These *c*- $(\text{BN})_{0.26}\text{C}_{0.74}$  hybrids had lattice constant of  $0.3582 \pm 0.0002$  nm, in between that of diamond ( $0.3570 \pm 0.0001$  nm) and *c*-BN ( $0.3615 \pm 0.0001$  nm). These hybrids were polycrystals, with dimensions of several micrometers. However, transmission electron microscopy (TEM) indicates that the grain size of these cubic hybrids is on the order of nanometers [101]. Similar experiments were then conducted by using a laser-heated diamond cell [119]. The lattice constants of the products [*c*- $\text{B}_{0.35}\text{C}_{0.3}\text{N}_{0.35}$  and *c*- $\text{B}_{0.2}\text{C}_{0.6}\text{N}_{0.2}$ ] were  $0.3613 \pm 0.0003$  nm and  $0.3596 \pm 0.0003$  nm, respectively. The bulk modulus of *c*- $\text{B}_{0.33}\text{C}_{0.33}\text{N}_{0.33}$  was determined as  $355 \pm 19$  GPa, lower than those of diamond (442 GPa) and *c*-BN (369 GPa).

There was also an attempt to transform  $h\text{-B}_x\text{C}_y\text{N}_z$  to *c*- $\text{B}_x\text{C}_y\text{N}_z$  hybrids at HPHT condition using catalyst. Cobalt (Co) was used in these experiments, which were conducted at a pressure of 5.5 GPa and temperature of 1,400–1,600°C [120]. Later experiment was carried out without using any catalyst at 7.7 GPa and 2,000–2,400°C [121, 122]. However, the *c*- $\text{B}_x\text{C}_y\text{N}_z$  product was phase separated into *c*-BCN and diamonds at high temperature. The cubic phase crystals were typically 20–30 nm in diameter. Recently, *c*- $\text{BC}_2\text{N}$  was synthesized from graphite-like  $\text{BC}_2\text{N}$  at pressures above 18 GPa and temperatures higher than 2,200 K [123]. The hardness of *c*- $\text{BC}_2\text{N}$  is higher than that of *c*-BN and slightly less hard than diamond. This is the low-density *c*-BCN structure proposed by the recent theoretical modeling [124].

In addition to the HPHT techniques, other methods such as reactive vapor phase deposition [125] and ball milling [126, 127] have been attempted to synthesize *c*- $\text{B}_x\text{C}_y\text{N}_z$  hybrids. In general, the *c*- $\text{B}_x\text{C}_y\text{N}_z$  tends to phase separate into *c*-BN and diamonds.

### 7.3 $\text{B}_x\text{C}_y\text{N}_z$ Nanostructures

Since 1994,  $\text{BC}_2\text{N}$  nanotubes have been studied theoretically [128] and experimentally [129–131]. Unlike pure CNTs, the electronic structure of  $\text{B}_x\text{C}_y\text{N}_z$  nanotubes is predicted to be prominently influenced by their chemical composition, rather than their geometrical structure [132]. Theoretically, the energy bandgap of  $\text{B}_x\text{C}_y\text{N}_z$  nanotubes are tunable by varying their atomic compositions. They may have potential applications in photoluminescence and photonics applications, as well as nanoelectronic devices or sensors working at high temperature.

In addition to the earlier attempts in growing  $\text{B}_x\text{C}_y\text{N}_z$  nanotubes by arc discharge and laser ablation [129–131], an interesting technique called substitution reaction was also demonstrated. This technique was initially invented to produce BNNTs [133–135]. In short, CNTs was used as the templates and reacted with  $\text{B}_2\text{O}_3$  powder in the presence of  $\text{N}_2$  gas at 1,600°C to form  $\text{B}_x\text{C}_y\text{N}_z$  nanotubes. Further thermal oxidation heating of these products in air at 700°C would convert the  $\text{B}_x\text{C}_y\text{N}_z$  nanotubes into BNNTs with an efficiency of 60%. Later, this substitution method was modified by adding metal oxide promoters in the reaction for the growth of both  $\text{B}_x\text{C}_y\text{N}_z$



nanotubes and BNNTs [136–138]. Results indicate that these  $B_xC_yN_z$  nanotubes were radially phase-separated into BN and carbon shells [139]. The carbon shells formed in the outer or inner layers of the multiwalled structure, rather than being sandwiched between BN shells.

Recently, a significant advancement had been reported to directly synthesize single wall  $B_xC_yN_z$  nanotubes by using bias-assisted hot filament CVD method [140, 141]. In brief,  $CH_4$ ,  $B_2H_6$ , and ethylenediamine vapor were flowed to the growth chamber as the reactant gases. MgO-supported Fe-Mo bimetallic powders were used as the catalyst. The boron and nitrogen contents of these nanotubes are still low. The chapters by Arenal and Loiseau, Blasé and Chacham, and Yu and Wang are devoted to describe current research status on  $B_xC_yN_z$  nanostructures. Readers are encouraged to find more information in previous reviews on  $B_xC_yN_z$  nanostructures [101, 102, 142].

## 8 Doped CNTs

Since the discovery of CNTs, quasi one-dimensional material has become the research of interest. It has been shown theoretically that CNTs doped with exotic elements may alter the band structure and morphological properties of CNTs [143]. There have been some experimental works on boron-doped CNTs [144, 145] and nitrogen-doped CNTs [146, 147] have been demonstrated. For example, nitrogen-doping was shown to enhance electron field emission properties of multiwalled CNTs [148]. The chapter by Filho and Terrones highlights the research on doped CNTs.

**Acknowledgment** Y. K. Yap acknowledges National Science Foundation CAREER Award (DMR 0447555) for supporting the project on frontier carbon materials; the U.S. Department of Energy, Office of Basic Energy Sciences (DE-FG02-06ER46294) for in part supporting the project on boron nitride nanotubes; and the U.S. Department of Army (W911NF-04-1-0029) and the Defense Advanced Research Projects Agency (DAAD17-03-C-0115 through Army Research Laboratory) for supporting his projects on CNTs.

## References

1. H. W. Kroto, J. R. Heath, S. C. O'Brien, R. F. Curl, and R. E. Smalley, *Nature (London)* **318**, 162 (1985).
2. S. Iijima, *Nature (London)* **354**, 56 (1991).
3. [http://nobelprize.org/nobel\\_prizes/chemistry/laureates/1996/](http://nobelprize.org/nobel_prizes/chemistry/laureates/1996/)
4. T. W. Capehart, T. A. Perry, C. B. Beetz, D. N. Belton, G. B. Fisher, C. E. Beall, B. N. Yates, and J. W. Taylor, *Appl. Phys. Lett.* **55**, 957 (1989).
5. R. Saito, G. Dresselhaus, and M. S. Dresselhaus, *Physical Properties of Carbon nanotubes*, Imperial College Press, London (1998).
6. M. S. Dresselhaus and G. Dresselhaus, Eds., *Carbon Nanotubes: Synthesis, Structure, Properties and Applications*, Springer-Verlag, Berlin (2001).
7. M. W. Geis and M. A. Tamor, in *Encyclopedia of Applied Physics*, Vol. 5, Diamond and Diamond-like Carbon, G. L. Trigg, Eds., VCH Publishers, Inc., New York, 1–24 (1993).

8. O. J. Vohler, F. von Sturm, and E. Wege, in *Encyclopedia of Applied Physics*, Vol. 3, Carbon Materials, G. L. Trigg, Eds., VCH Publishers, Inc., New York, 21–40 (1993).
9. M. S. Dresselhaus and G. Dresselhaus, in *Encyclopedia of Applied Physics*, Vol. 7, Graphite, G. L. Trigg, Eds., VCH Publishers, Inc., New York, 289–301 (1993).
10. A. Y. Liu, R. M. Wentzcovitch, and M. L. Cohen, *Phys. Rev. B* **39**, 1760 (1989).
11. <http://www.nsf.gov/awardsearch/showAward.do?AwardNumber=0447555>. Y. K. Yap, National Science Foundation Award # 0447555, “CAREER: Synthesis, Characterization and Discovery of Frontier Carbon Materials.
12. S. Iijima and T. Ichihashi, *Nature (London)* **363**, 603 (1993).
13. D. S. Bethune, C. H. Kiang, M. S. de Vries, G. Gorman, R. Savoy, J. Vazquez, and R. Beyers, *Nature (London)* **363**, 605 (1993).
14. A. Thess, R. Lee, P. Nikolaev, H. Dai, P. Petit, J. Robert, C. Xu, Y. H. Lee, S. G. Kim, A. G. Rinzler, D. T. Colbert, G. E. Scuseria, D. Tomanek, J. E. Fisher, and R. E. Smalley, *Science* **273**, 483 (1996).
15. M. S. Dresselhaus, G. Dresselhaus, and R. Saito, *Phys. Rev. B* **45**, 6234 (1992).
16. J. W. Mintmire, B. I. Dunlap, and C. T. White, *Phys. Rev. Lett.* **68**, 631 (1992).
17. N. Hamada, S. Sawada, A. Oshiyama, *Phys. Rev. Lett.* **68**, 1579 (1992).
18. J. W. G. Wilder, L. C. Venema, A. G. Rinzler, R. E. Smalley, and C. Dekker, *Nature (London)* **391**, 59 (1998).
19. T. W. Odom, J. L. Huang, P. Kim, and C. M. Lieber, *Nature (London)* **391**, 62 (1998).
20. N. Wang, Z. K. Tang, G. D. Li, and J. S. Chen, *Nature* **408**, 50 (2000).
21. T. Guo, P. Nikolaev, A. G. Rinzler, D. Tomanek, D. T. Colbert, and R. E. Smalley, *J. Phys. Chem.* **99**, 10694 (1995).
22. A. Peigney, Ch. Laurent, F. Dobigeon, and A. Rousset, *J. Mater. Res.* **12**, 613 (1997).
23. J. H. Hafner, M. J. Bronikowski, B. R. Azamian, P. Nikolaev, A. G. Rinzler, D. T. Colbert, K. A. Smith, and R. E. Smalley, *Chem. Phys. Lett.* **296**, 195 (1998).
24. H. Dai, A. G. Rinzler, P. Nikolaev, A. Thess, D. T. Colbert, and R. E. Smalley, *Chem. Phys. Lett.* **260**, 471 (1996).
25. V. Kayastha, Y. K. Yap, S. Dimovski, and Y. Gogotsi, *Appl. Phys. Lett.* **85**, 3265 (2004).
26. V. Kayastha, Y. K. Yap, Z. Pan, I. N. Ivanov, A. A. Puzos, and D. B. Geohegan, *Appl. Phys. Lett.* **86**, 253105 (2005).
27. K. Hata, D. N. Futaba, K. Mizuno, T. Namai, M. Yumura, and S. Iijima, *Science* **306**, 1362 (2004).
28. G. Zhang, D. Mann, L. Zhang, A. Javey, Y. Li, E. Yenilmez, Q. Wang, J. P. McVittie, O. Nishi, J. Gibbons, and H. Dai, *PNAS* **102**, 16141 (2005).
29. Y. Murakami, S. Chiashi, Y. Miyauchi, M. Hu, M. Ogura, T. Okubo, and S. Maruyama, *Chem. Phys. Lett.* **385**, 298 (2004).
30. V. K. Kayastha, S. Wu, J. Moscatello, and Y. K. Yap, *J. Phys. Chem. C* **111**, 10158 (2007).
31. S. M. Bachilo, M. S. Strano, C. Kittrell, R. H. Hauge, R. E. Smalley, and R. B. Weisman, *Science* **298**, 2361 (2002).
32. D. L. Medlin, T. A. Friedmann, P. B. Mirkarimi, M. J. Mills, and K. F. McCarty, *Phys. Rev. B.* **50**, 7884 (1994).
33. R. S. Pease, *Acta. Cryst.* **5**, 356 (1952).
34. T. Ishii, T. Sato, Y. Sekikawa, and M. Iwata, *J. Cryst. Growth* **52**, 285 (1981)
35. F. P. Bundy and R. H. Wentorf, Jr, *J. Chem Phys.* **38**, 1144 (1963)
36. R. H. Wentorf, Jr, *J. Chem. Phys.* **34**, 809 (1961)
37. C. B. Samantaray and R. N. Singh, *Int. Mater. Rev.*, **50**, 313 (2005)
38. P. B. Mirkarimi, K. F. McCarty, and D. L. Medlin, *Mat. Sci. Eng. R* **21**, 47 (1997)
39. J. Thomas, N. E. Weston, and T. E. O’Connor, *J. Am. Chem. Soc.* **84**, 4619 (1963)
40. A. Rubio, J. L. Corkill, and M. L. Cohen, *Phys. Rev. B.* **49**, 5081 (1994).
41. X. Blase, A. Rubio, S. G. Louie, and M. L. Cohen, *Euro. Phys. Lett.* **28**, 335 (1994)
42. M. Ishigami, S. Aloni and A. Zettl, *AIP Conf. Proc.* **696**, 94 (2003).
43. D. Ghosh, G. Subhash, C. H. Lee, Y. K. Yap, *Appl. Phys. Letts.* **91**, 061910 (2007).

44. R. Naslain, in *Boron and Refractory Borides*, V. I. Matkovich, Ed., Springer-Verlag, New York, 139 (1977).
45. G. Will and K. Ploog, *Nature* **251**, 406 (1974).
46. A. W. Laubengayer, D. T. Hurd, A. E. Newkirk, and J. L. Hoard, *J. Am. Chem. Soc.* **65**, 1924 (1943).
47. A. Y. Liu and M. L. Cohen, *Science* **245**, 841 (1989).
48. A. Y. Liu and M. L. Cohen, *Phys. Rev. B* **41**, 10727 (1990).
49. D. M. Teter and R. J. Hemley, *Science* **271**, 53 (1996).
50. C. M. Niu, Y. Z. Lu, and C. M. Lieber, *Science* **261**, 334 (1993).
51. C. M. Lieber and Z. J. Zhang, *Chem. Indus.* **22**, 922 (1995).
52. J. T. Hu, P. D. Yang, and C. M. Lieber, *Phys. Rev. B* **57**, R3185 (1998).
53. J. T. Hu, P. D. Yang, and C. M. Lieber, *Appl. Surf. Sci.* **127–129**, 569 (1998).
54. O. Matsumoto, T. Kotaki, H. Shikano, K. Takemura, and S. Tanaka, *J. Electrochem. Soc.* **141**, L16 (1994).
55. Y. K. Yap, S. Kida, T. Aoyama, Y. Mori, and T. Sasaki, *Appl. Phys. Lett.* **73**, 915 (1998).
56. Y. K. Yap, S. Kida, T. Aoyama, Y. Mori, and T. Sasaki, *Diamond Relat. Mater.* **8**, 614 (1999).
57. Y. K. Yap, S. Kida, T. Aoyama, Y. Mori, and T. Sasaki, *Diamond Relat. Mater.* **9**, 1228 (2000).
58. M. Itoh, Y. Suda, M. A. Bratescu, Y. Sakai, and K. Suzuki, *Appl. Phys. A* **79**, 1575 (2004).
59. Y. A. Li, Z. B. Zhang, S. S. Xie, and G. Z. Yang, *Chem. Phys. Lett.* **247**, 253 (1995).
60. Z. B. Zhang, Y. A. Li, S. S. Xie, and G. Z. Yang, *J. Mater. Sci. Lett.* **14**, 1742 (1995).
61. S. Kumar, K. S. A. Butcher, and T. L. Tansley, *J. Vac. Sci. Technol. A* **14**, 2687 (1996).
62. C. Y. Hsu and F. C. N. Hong, *Jpn. J. Appl. Phys.* **37**, L1058 (1998).
63. W. Lu and K. Komvopoulos, *J. Appl. Phys.* **85**, 2642 (1999).
64. J. Peng, P. Zhang, Y. Guo, and G. H. Chen, *Mater. Lett.* **29**, 191 (1996).
65. Y. A. Li, S. Xu, H. S. Li, and W. Y. Luo, *J. Mater. Sci. Lett.* **17**, 31 (1998).
66. L. D. Jiang, A. G. Fitzgerald, and M. J. Rose, *Appl. Surf. Sci.* **158**, 340 (2000).
67. J. Wei, *J. Appl. Phys.* **89**, 4099 (2001).
68. X. C. Wang, P. Wu, Z. Q. Li, E. Y. Jiang, and H. L. Bai, *J. Phys. D: Appl. Phys.* **37**, 2127 (2004).
69. M. Lejeune, O. Durand-Drouhin, S. Charvet, A. Zeinert, and M. Benlahsen, *J. Appl. Phys.* **101**, 123501 (2007).
70. T. Y. Yen and C. P. Chou, *Appl. Phys. Lett.* **67**, 2801 (1995).
71. Y. F. Zhang, Z. H. Zhou, and H. L. Li, *Appl. Phys. Lett.* **68**, 634 (1996).
72. H. K. Woo, Y. F. Zhang, S. T. Lee, C. S. Lee, Y. W. Lam, and K. W. Wong, *Diamond Relat. Mater.* **6**, 635 (1997).
73. J. L. He and W. L. Chang, *Surf. Coat. Technol.* **99**, 184 (1998).
74. J. P. Riviere, D. Texier, J. Delafond, M. Jaouen, E. L. Mathe and J. Chaumont, *Mater. Lett.* **22**, 115 (1995).
75. A. Fernandez, P. Prieto, C. Quiros, J. M. Sanz, J. M. Martin and B. Vacher, *Appl. Phys. Lett.* **69**, 764 (1996).
76. X. W. Su, H. W. Song, F. Z. Cui, W. Z. Li, and H. D. Li, *Surf. Coat. Technol.* **84**, 388 (1996).
77. Z. C. Wu, Y. H. Yu, and X. H. Liu, *Appl. Phys. Lett.* **68**, 1291 (1996).
78. X. M. He, L. Shu, W. Z. Li, and H. D. Li, *J. Mater. Res.* **12**, 1595 (1997).
79. J. Y. Feng, Y. Zheng, and J. Q. Xie, *Mater. Lett.* **27**, 219 (1996).
80. P. N. Wang, Z. Guo, X. T. Ying, J. H. Chen, X. M. Xu, and F. M. Li, *Phys. Rev. B* **59**, 13347 (1999).
81. Y. G. Li, A. T. S. Wee, C. H. A. Huan, W. S. Li, and J. S. Pan, *Surf. Interface Anal.* **28**, 221 (1999).
82. Kazuhiro Yamamoto, *Jpn. J. Appl. Phys.* **44**, 1879 (2005).
83. T. Hidekazu, M. Sougawa, K. Takarabe, S. Sato, and O. Ariyada, *Jpn. J. Appl. Phys.* **46**, 1596 (2007).
84. D. Li, X.-W. Lin, S.-C. Cheng, V. P. Dravid, Y.-W. Chung, M.-S. Wong, and W. D. Sproul, *Appl. Phys. Lett.* **68**, 1211 (1996).
85. J. Pereira, I. G. Grenier, and V. M. Guilbaud, *Thin Solid Films* **482**, 226 (2005).
86. H. Y. Li, Y. C. Shi, and P. X. Feng, *Appl. Phys. Lett.* **89**, 142901 (2006).

87. T. C. Mu, J. Huang, Z. M. Liu, B. X. Han, Z. H. Li, Y. Wang, T. Jiang, and H. X. Gao, *J. Mater. Res.* **19**, 1736 (2004).
88. A.R. Badzian et al. in “*Proceeding of the 3rd International Conference on Chemical Vapor Deposition*” (F.A. Claski, Ed.), pp. 747–753. American Nuclear Society, Hinsdale, IL, 1972.
89. K. Montasser, S. Hattori, and S. Monita, *Thin Solid Films* **117**, 311 (1984).
90. L. Maya, *J. Am. Ceram. Soc.* **71**, 1104 (1988).
91. J. Kouvetaksi, T. Sasaki, C. Shen, R. Hagiwara, M. Lerner, K. M. Krishnan, and N. Bartlett, *Synth. Metals* **34**, 1 (1989).
92. L. Maya and L. A. Harris, *J. Am. Ceram. Soc.* **73**, 1912 (1990).
93. M. Yamada, M. Nakaishi, and K. Sugishima, *J. Electrochem. Soc.* **137**, 2242 (1990).
94. T. M. Besmann, *J. Am. Ceram. Soc.* **73**, 2498 (1990).
95. M. Morita, T. Hanada, H. Tsutsumi, Y. Matsuda, and W. Kawaguchi, *J. Electrochem. Soc.* **139**, 1227 (1992).
96. F. Saugnac, F. Teysandiev, and A. Marchand, *J. Am. Ceram. Soc.* **75**, 161 (1992).
97. N. Kawaguchi and T. Kawashima, *J. Chem. Soc., Chem. Commun.* **14**, 1133 (1993).
98. A. Derré, L. Filipozzi, F. Bouyer, and A. Marchand, *J. Mater. Sci.* **29**, 1589 (1994).
99. M. Hubacek and T. Sato, *J. Solid State Chem.* **114**, 258 (1995).
100. M. O. Watanabe, S. Itoh, K. Mizushima, and T. Sasaki, *Thin Solid Films* **281–282**, 334 (1996).
101. Y. K. Yap, “Boron-Carbon Nitride Nanohybrids,” in *Encyclopedia of Nanoscience and Nanotechnology* (Foreword by R. E. Smalley), H. S. Nalwa, Ed., Volume **1**, 383–394, American Scientific Publishers, (2004).
102. C. H. Lee and Y. K. Yap, “Current Research Status of Boron-Carbon Nitride Bulks, Thin Films, and Nanostructures,” Chapter 10, in *Diamond and Related Materials Research*, Shōta Shimizu Ed., Nova Science Publisher, New York, 277–292 (2008).
103. M. Yano, Y. K. Yap, M. Okamoto, M. Onda, M. Yoshimura, Y. Mori, and T. Sasaki, *Jpn. J. Appl. Phys.* **39**, L300 (2000).
104. Y. Kubota, K. Watanabe, O. Tsuda, and T. Taniguchi, *Science* **317**, 932 (2007).
105. Y. Miyamoto, A. Rubio, M. L. Cohen, and S. G. Louie, *Phys. Rev. B* **50**, 4976 (1994).
106. A. Y. Liu, R. M. Wentzcovitch, and M. L. Cohen, *Phys. Rev. B* **39**, 1760 (1989).
107. T. Yuki, S. Umeda, and T. Sugino, *Diamond Relat. Mater.* **13**, 1130 (2004).
108. J. Yu, E. G. Wang, J. Ahn, S. F. Yoon, Q. Zhang, J. Cui, and M. B. Yu, *J. Appl. Phys.* **87**, 4022 (2000).
109. R. Gago, I. Jiménez, and J. M. Albella, *Thin Solid Films* **373**, 277 (2000).
110. M. K. Lei, Quan Li, Z. F. Zhou, I. Bello, C. S. Lee, and S. T. Lee, *Thin Solid Films* **389**, 194 (2001).
111. D. H. Kim, E. Byon, S. Lee, J.-K. Kim, and H. Ruh, *Thin Solid Films* **447–448**, 192 (2004).
112. Y. Wada, Y. K. Yap, M. Yoshimura, Y. Mori, and T. Sasaki, *Diamond Relat. Mater.* **9**, 620 (2000).
113. Y. K. Yap, Y. Wada, M. Yamaoka, M. Yoshimura, Y. Mori, and T. Sasaki, *Diamond Relat. Mater.* **10**, 1137 (2000).
114. H. Aoki, K. Ohyama, H. Sota, T. Seino, C. Kimura, and T. Sugino, *Appl. Surf. Sci.* **254**, 596 (2007).
115. Pi-Chuen Tsai, *Surf. Coat. Technol.* **201**, 5108 (2007).
116. Y. K. Yap, M. Yoshimura, Y. Mori, and T. Sasaki, *Appl. Phys. Lett.* **80**, 2559 (2002).
117. H. Sun, S.-H. Jhi, D. Roundy, M. L. Cohen, and S. G. Louie, *Phys. Rev. B* **64**, 094108 (2001).
118. A. R. Badzian, *Mat. Res. Bull.* **16**, 1385 (1981).
119. E. Knittle, R. B. Kaner, R. Jeanloz, and M. L. Cohen, *Phys. Rev. B* **51**, 12149 (1995).
120. T. Sasaki, M. Akaishi, S. Yamaoka, Y. Fujiki, and T. Oikawa, *Chem. Mater.* **5**, 695 (1993).
121. S. Nakano, M. Akaishi, T. Sasaki, and S. Yamaoka, *Chem. Mater.* **6**, 2246 (1994).
122. S. Nakano, M. Akaishi, T. Sasaki, and S. Yamaoka, *Mater. Sci. Eng. A* **209**, 26 (1996).
123. Y. Zhao, D. W. He, L. L. Daemen, T. D. Shen, R. B. Schwarz, Y. Zhu, D. L. Bish, J. Huang, J. Zhang, G. Shen, J. Qian, and T. W. Zerda, *J. Mater. Res.* **17**, 3139 (2002).

124. E. Kim, T. Pang, W. Utsumi, V. L. Solozhenko, and Y. Zhao, *Phys. Rev. B* **75**, 184115 (2007).
125. S. Ulrich, H. Ehrhardt, T. Theel, J. Schwan, S. Westermeyr, M. Scheib, P. Becker, H. Oechsner, G. Dollinger, and A. Bergmaier, *Diamond Relat. Mater.* **7**, 839 (1998).
126. Yao, L. Liu and W. H. Su, *J. Mater. Res.* **13**, 1753 (1998).
127. J. Huang, Y. Zhu and H. Mori, *J. Mater. Res.* **16**, 1178 (2001).
128. Y. Miyamoto, A. Rubio, M. L. Cohen, and S. G. Louie, *Phys. Rev. B* **50**, 4976 (1994).
129. Z. W. Sieh, K. Cherrey, N. G. Chopra, X. Blasé, Y. Miyamoto, A. Rubio, M. L. Cohen, S. G. Louie, A. Zettl, and R. Gronsky, *Phys. Rev. B* **51**, 11229 (1995).
130. Y. Zhang, H. Gu, K. Suenaga, and S. Iijima, *Chem. Phys. Lett.* **279**, 264 (1997)
131. M. Terrones, A. M. Benito, C. Manteca-Diego, W. K. Hsu, O. I. Osman, J. P. Hare, D. G. Reid, H. Terrones, A. K. Cheetham, K. Prassides, H. W. Kroto, and D. R. M. Walton, *Chem. Phys. Lett.* **257**, 576 (1996).
132. X. Blasé, J.C. Charlier, A. De Vita, and R. Car, *Appl. Phys. Lett.* **70**, 197 (1997).
133. W. Q. Han, Y. Bando, K. Kurashima, and T. Sato, *Jpn. J. Appl. Phys.* **38**, L755, (1999).
134. W.-Q. Han, J. Cumings, X. Huang, K. Bradley, and A. Zettl, *Chem. Phys. Lett.* **346**, 368 (2001).
135. W.-Q. Han, W. Mickelson, J. Cumings, and A. Zettl, *Appl. Phys. Lett.* **81**, 1110 (2002).
136. M. Terrones, D. Golberg, N. Grobert, T. Seeger, M. R. Reyes, M. Mayne, R. Kamalakaran, P. Dorozhkin, Z.-C. Dong, H. Terrones, M. Ruhle, and Y. Bando, *Adv. Mater.* **15**, 1899 (2003).
137. D. Golberg, P. Dorozhkin, Y. Bando, M. Hasegawa, and Z.-C. Dong, *Chem. Phys. Lett.* **359**, 220 (2002).
138. D. Golberg, Y. Bando, K. Kurashima, and T. Sato, *Solid State Commun.* **116**, 1 (2000).
139. J. Wu, W.-Q. Han, W. Walukiewicz, J. W. AgerIII, W. Shan, E. E. Haller, and A. Zettl, *Nano Lett.* **4**, 647 (2004).
140. C. Y. Zhi, J. D. Guo, X. D. Bai, and E. G. Wang, *J. Appl. Phys.* **91**, 5325 (2002).
141. W. L. Wang, X. D. Bai, K. H. Liu, Z. Xu, D. Golberg, Y. Bando, and E. G. Wang, *J. Am. Chem. Soc.* **128**, 6530 (2006).
142. R. Ma, D. Golberg, Y. Bando, and T. Sasaki, *Phil. Trans. R. Soc. Lond. A*, **362**, 2161 (2004).
143. Y. Miyamoto, M. L. Cohen, and S. G. Louie, *Solid State Commun.* **102**, 605 (1997).
144. W.Q. Han, Y. Bando, K. Kurashima, and T. Sato, *Chem. Phys. Lett.* **299**, 368 (1999).
145. L. S. Panchakarla, A. Govindaraj, and C. N. R. Rao, *ACS Nano* **1**, 494 (2007).
146. R. Czerw, M. Terrones, J.-C. Charlier, X. Blase, B. Foley, R. Kamalakaran, N. Grobert, H. Terrones, D. Tekleab, P. M. Ajayan, W. Blau, M. Rühle, and D. L. Carroll, *Nano Lett.* **1**, 457 (2001).
147. J. Liu, S. Webster, and D. L. Carroll, *Appl. Phys. Lett.* **88**, 213119 (2006)
148. M. Doytcheva, M. Kaiser, M. A. Verheijen, M. Reyes-Reyes, M. Terrones, and N. de Jonge, *Chem. Phys. Lett.* **396**, 126 (2004).

# Multiwalled Boron Nitride Nanotubes: Growth, Properties, and Applications

Jiesheng Wang, Chee Huei Lee, Yoshio Bando,  
Dmitri Golberg and Yoke Khin Yap

**Abstract** This chapter provides a comprehensive review on the current research status of boron nitride nanotubes (BNNTs), especially the multiwalled nanostructures. Experimental and theoretical aspects of the properties, synthesis, and characterization of BNNTs, as well as their potential mechanical, electronic, chemical, and biological applications are compiled here.

## 1 Introduction

Boron nitride nanotubes (BNNTs) were theoretically predicted in 1994 [1, 2] and experimentally realized in the following year [3]. As described in the previous chapter, BNNTs are structurally similar to carbon nanotubes (CNTs). Thus, BNNTs exhibit extraordinary mechanical properties like CNTs [4–6]. Despite these similarities, BNNTs are different from CNTs in other aspects. BNNTs possess nearly uniform electronic properties that are not sensitive to their diameters and chiralities [1, 2]. Theoretically, their band gaps ( $\sim 5$  eV) are tunable and can even be eliminated by transverse electric fields through the giant DC Stark effect [7–9]. Golberg et al. have shown that BNNTs are having high oxidation resistance [10], which was later confirmed by others [11, 12]. Recent result indicates that purified BNNTs are resist to oxidation up to  $1,100^{\circ}\text{C}$  [12]. In addition, BNNTs are predicted to have piezoelectricity [13, 14] and are applicable for room-temperature hydrogen storage [15]. Junctions of CNTs and BNNTs [16] are expected to produce itinerant ferromagnetism and spin polarization [17]. Obviously, these properties make BNNTs very attractive for innovative applications in various branches of science and technology.

---

J. Wang, C.H. Lee and Y.K. Yap (✉)  
Department of Physics, Michigan Technological University, 118 Fisher Hall,  
1400 Townsend Drive, Houghton, MI 49931, USA  
e-mail: ykyap@mtu.edu

Y. Bando and D. Golberg  
World Premier International Center for Materials Nanoarchitectonics (MANA),  
National Institute for Materials Science, Namiki 1-1, Tsukuba, Ibaraki 305-0044, JAPAN

However, the growth of BNNTs is challenging. In the last 10 years, BNNTs were grown by arc discharge [3, 18, 19], laser ablation [20, 21], substitution reactions from CNT<sub>s</sub> [22], ball-milling [23], chemical vapor deposition (CVD) [24], boron oxide CVD (BOCVD)/floating zone method [25, 26], etc. These BNNTs contain impurities including amorphous boron nitride (a-BN) powders and other solid-state by-products. It is also challenging to use these techniques to directly grow BNNTs on substrates. Recently, Yap et al. have acquired for the first time the growth of *pure* BNNTs directly on substrates at significantly low temperature (~600°C) [27]. On the other hand, recent advancement in BOCVD has enabled mass production of BNNTs and the demonstration of a series of potential applications of BNNTs. In view of all these progresses, this chapter is devoted to highlight properties, synthesis, and potential applications of BNNTs.

The remaining of this chapter will provide more description in particular multi-walled (MW) BNNTs. In Sect. 2 of this chapter, various properties of MW-BNNTs will be discussed. Some of the prospective growth techniques of MW-BNNTs are highlighted in Sect. 3. Section 4 describes potential applications of BNNTs for polymer composites, electronic devices, and molecular biological and chemical applications. Readers are encouraged to read more about the experimental aspects of single-wall BNNTs in Chap. 3 and the related theory in Chaps. 4 and 5.

## 2 Properties of BNNTs

### 2.1 Mechanical Properties

The elastic properties of an individual MW-BNNT have been carefully studied by thermal vibration method [28]. The axial Young's modulus for a MW-BNNT with this method was found to be 1.18 TPa, which surpasses that of all other known insulating nanostructures. This experimental value is consistent with theoretical calculations performed by tight-binding (TB) methods [29]. However, recent in situ bending test on individual MW-BNNTs under transmission electron microscopy (TEM) demonstrated lower values of 0.5–0.6 TPa [30]. The lower detected modulus was probably due to the presence of polygonal cross-section morphology of MW-BNNTs. On the other hand, the BNNT could recover amazingly after relieving the load for severe bending.

### 2.2 Thermal Properties

High-density nanoelectronic devices are expected to generate tremendous heat radiation. This has initiated a strong demand of nanomaterials with good thermal conductivity. Various calculation approaches, including tight-binding method, density functional theory, and valence shell model, have been performed in order to address

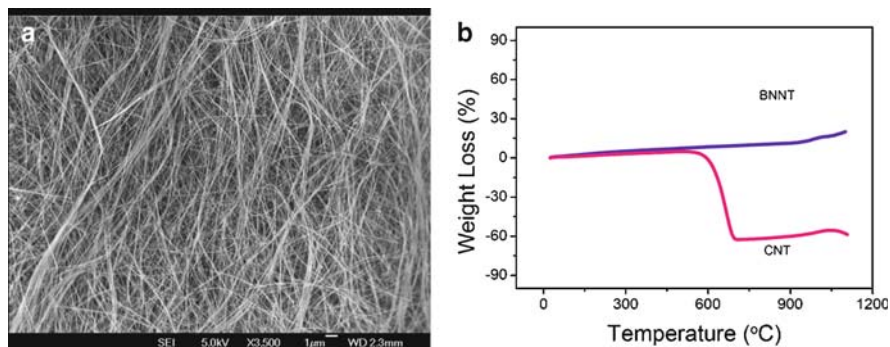


**Fig. 1** (a) Scanning electron microscopy image of purified boron nitride nanotubes grown at 1,500°C, and (b) Comparative thermogravimetric analysis curves of BNNTs and CNTs (reprinted from [12]. © American Chemical Society)

the thermal properties of BNNTs [31–33]. It was shown that BNNTs would have a larger low-temperature thermal conductivity [34] than CNTs given that BNNTs have the same phonon mean free path as CNTs. However, it was demonstrated by experiment that pure and collapsed BNNTs are estimated to have thermal conductivity,  $\kappa$ , of  $\sim 18$  and  $\sim 46$  W/mK, respectively [35]. These values are far lower than the conductivity of the sintered bulk hexagonal BN particles at room temperature ( $>200$  W/mK).

Another noteworthy thermal property of BNNTs is their high resistance to oxidation. A systematic study was first performed by Golberg et al. [10] and 3 years later by Chen et al. [11]. Recent study with purified MW-BNNTs grown at 1,500°C (Fig. 1a) indicated that BNNTs were stable at 1,100°C in air (Fig. 1b) [12]. The oxidation temperature for CNTs was  $\sim 500^\circ\text{C}$  under similar thermogravimetric analysis.

### 2.3 Electronic Properties

BNNTs are theoretically predicted to have merely uniform electronic properties that are hardly modified by their chiralities or diameters [1, 2]. Moreover, zigzag BNNTs with chirality  $(n, 0)$  are expected to have direct band gap. On the other hand, armchair BNNTs with chiral vectors  $(n, n)$  will have indirect band gap [19]. Because of their large band gap of  $\sim 5$  eV, experiments using SW-BNNTs as the conduction channel for field-effect transistors (FETs) showed that BNNTs allowed transport through only the valence band [36].

Another important feature about the band gaps of BNNTs is that they are tunable by doping with carbon [37], radial deformation [38], or by applying a transverse electric field across the BNNTs – the so-called giant Stark effect [7–9]. Theoretical band structure calculations suggested that BNNTs can either be  $p$ -type or  $n$ -type semiconductors by controlling the composition of carbon into BNNTs. Carbon



impurities on the boron sites result in electron carriers while on the nitrogen sites result in hole carriers [37]. On the other hand, the band-gap modification by radial deformation in BNNTs was predicted through first-principles pseudopotential density-functional calculations. In zigzag BN nanotubes, radial deformations due to transverse pressures of about 10 GPa decrease the direct band gap of BNNTs from 5 to 2 eV, allowing for optical applications in the visible range. However, the band gaps of armchair BNNTs are found to be insensitive to radial deformations. Finally, theory indicates that the band gap of BNNTs can be reduced and even completely removed by the application of transverse electric fields. Experimentally, the giant Stark effect has been observed when applying a scanning tunneling microscopy (STM) tip to impose a local transverse electric field onto BNNTs and simultaneously probing the electronic properties [9].

## 2.4 *Piezoelectric Properties*

Another appealing property of BNNTs is piezoelectricity. This phenomenon theoretically originated from the deformation effect due to the rolling of the planar hexagonal BN networks to form tubular structures [13]. Nakhmanson et al. showed that BNNTs could be excellent piezoelectric systems [14]. As an example of calculations, piezoelectric constant for different zigzag BNNTs was found to increase along with the decrease of the radius of BNNTs [14]. It has been also proposed that a (5, 0) BNNT would have the largest piezoelectric constant for all investigated BNNTs.

Experimentally, Bai et al. have shown that under in situ elastic bending deformation at room temperature inside a 300-kV high-resolution transmission electron microscope, a normally electrically insulating MW-BNNT may transform to a semiconductor [39]. The semiconducting parameters of bent MW-BNNTs squeezed between two approaching gold contacts inside the pole piece of the microscope had been retrieved based on the experimentally recorded I–V curves. Remarkably, the nanotubes' electrical transport properties were found to be smoothly tuned from insulating to semiconducting through a bending deformation. Importantly, such unique transition was reversible. This could have been the first experimental sign suggestive of piezoelectric behavior in deformed BNNTs. Since BNNTs possess excellent mechanical properties, the detected deformation-driven tuning of BNNT electrical properties may have many interesting prospective applications in the nanoscale sensors, actuators, and advanced nanoelectromechanical systems (NEMS) with integrated electronic/optical functions.

## 2.5 *Electron Field Emission Properties*

Field emission properties of BNNTs have been tested by Cumings et al. using an in situ manipulation stage inside a TEM system [40]. The turn-on voltages for BNNTs were approximately twice higher than that for CNTs of similar geometries that

were measured with the same setup. The current densities were similar in both cases. In the Fowler-Nordheim plot for BNNTs, a single slope can be observed compared with the case of CNTs where the current often shows saturation at high electric fields or two distinct Fowler-Nordheim slopes are often observed. Besides, BNNTs showed more stable field emission with less noise. However, these results require further confirmation with high-purity BNNTs in the future.

## 2.6 Optical Properties

A local-density approximation (LDA) calculation has pointed out that optical band gap of BNNTs is independent of the chirality [41]. Another interesting point related to their optical properties is the photoelectric effect. According to Kral et al., unpolarized light can induce a shift current in BNNTs, with a direction along the tube axis [42]. These photoelectric effects can lead to new optoelectronic, optomechanical, and magnetic applications.

To understand polarizabilities of BNNTs, Kongsted et al. investigated the polarizability tensors for several types of single-wall BNNTs and compared with corresponding CNTs [43]. Their computations showed that BNNTs had smaller magnitudes of the polarizability tensor components than those of CNTs with the same geometry and number of atoms. Polarizability tensor of BNNTs is shown to depend on the tubule length, chiralities, light frequency, etc.

A comprehensive review on the vibrational and optical properties of BNNTs is compiled in Chap. 5 of this book.

## 3 Synthesis of BNNTs

As described, the synthesis of BNNTs is far more challenging than the growth of CNTs. Some of the growth techniques resembling those for the synthesis of CNTs were shown to work for the growth of BNNTs but some others required very specific growth system and procedures. The details of these approaches are compiled in this section.

### 3.1 Arc Discharge

The arc discharge method that first successfully grew BNNTs was similar to that for growing CNTs [3]. In the case of BNNTs, the anode was built by inserting a h-BN rod into a hollow tungsten electrode and the cathode was a rapidly cooled pure copper electrode. Arc discharge occurred between the tungsten and copper electrodes. The inserted h-BN rod was evaporated indirectly. After the arc discharge,

the gray product was deposited on the copper cathode, which contained some scattered single-wall BNNTs. Other successful attempts to grow BNNTs by arc discharge method were using hafnium diboride ( $\text{HfB}_2$ ) electrodes [19] and arcing hexagonal boron nitride (h-BN) and tantalum in a nitrogen atmosphere [18].

### 3.2 *Laser-Based Methods*

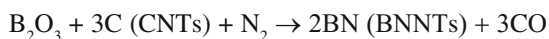
Laser heating is one of the possible methods to synthesize BNNTs as demonstrated by Golberg et al. [44]. Single crystal c-BN specimens were laser heated in a diamond anvil cell under high nitrogen pressures. TEM and other characterization techniques confirmed the product to be BNNTs.

Another laser-based technique was oven-laser ablation method [20]. The target material was prepared by mixing high-purity h-BN and nanosized Ni and Co powders. The target was then placed inside a long quartz tube heated by a tube furnace. An excimer laser with a wavelength of 248 nm was focused on the target to initiate ablation. At optimum laser pulsed energy and oven temperature (1,200°C), the ablated laser plumes were carried by the flowing gas and collected on the water-cooled copper collector. BNNTs with diameters ranging from 1.5 to 8 nm were obtained together with other amorphous by-products. Comparison of the structure of the BNNTs synthesized with different carrier gases revealed an interesting phenomenon. BNNTs obtained in inert argon and helium gases were dominated with single-wall BNNTs. When nitrogen was used as the carrier gas, the BNNTs were dominated with double-wall structures. No BNNTs with more than four walls were observed.

Recently, single-wall BNNTs can be produced in high crystalline quality by Loiseau et al. This technique involves the vaporization of a hexagonal BN target by a continuous wave  $\text{CO}_2$  laser under a nitrogen flow at a pressure of 1 bar. Readers should refer to Chap. 3 for the details.

### 3.3 *Substitution Reaction*

Because of the nearly identical lattice structure between CNTs and BNNTs, the former were used as the templates to prepare BNNTs. This technique is called CNT-substituted reaction, where carbon atoms of CNTs are substituted by boron and nitrogen atoms [22] according to the reaction formula as follows:



The reaction was performed in an induction-heating furnace. In brief,  $\text{B}_2\text{O}_3$  powder was placed in an open sintered graphite crucible and then covered with CNTs.

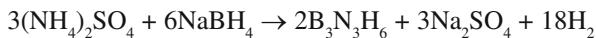
The crucible was kept in a flowing nitrogen atmosphere at 1,500°C for half an hour. Followed by cooling, the starting black CNTs were found to turn into gray color. Different characterization techniques confirmed that BNNTs were grown but were mixed with carbon and other BN phases. To purify the product, oxidation treatment could start to oxidize carbon layers around 550°C and transform these mixed-phase nanotubes into pure BNNTs.

### 3.4 *Ball-Milling Technique*

Ball-milling is a technique that can produce BNNTs at high yield, but it has a disadvantage of low purity [11, 45]. As reported by Chen et al., the ball-milling system has four stainless steel milling vessels with each small vessel loaded with several grams of boron powder and four hardened steel balls. Then, they were filled with ammonia gas at a pressure of 300 kPa prior to milling. With this method, four large vessels could mill powder up to 1 kg. The mechanism behind was the transfer of large amount of mechanical energy into boron powder particles, leading to morphological, structural, and chemical changes. Followed by milling, an isothermal annealing was executed in a tube furnace at 1,200°C for 16 h under nitrogen gas flow. Finally, BNNTs were obtained by converting powder to tubules with the formation yield of 65–85% [45]. It is noted that most of these BNNTs appeared in bamboo-like structures.

### 3.5 *Catalytic CVD*

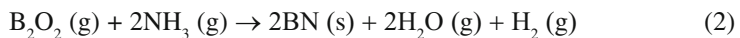
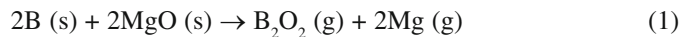
Catalytic CVD (CCVD) is one of the most popular and successful techniques for the synthesis of CNTs and various nanowires. Lourie et al. described the growth of BNNTs by using borazine ( $B_3N_3H_6$ ) as the precursor according to the chemical reaction as follows [24]:



The growth was all successful in trials applying different catalysts such as Co, Ni, NiB, or  $Ni_2B$ . The NiB catalysts were found to be the most effective catalysts. The substrate coated with NiB or  $Ni_2B$  catalysts was placed in the center of the tube-furnace reactor that was heated to 1,000–1,100°C. These were then exposed to the  $B_3N_3H_6$ -containing carrier gas for half an hour. White deposits were observed on the substrate and were identified as MW-BNNTs. Recently, borazine was also used in conjunction with a floating nickelocene catalyst, resulting in the predominant formation of double-walled BNNTs [46].

Instead of using the dangerous borazine, Tang et al. have shown that boron oxide can be an effective precursor for the growth of BNNTs [12, 25, 26]. This was first demonstrated by applying the redox reaction between boron and oxides ( $SiO_2$ ;

Fe<sub>2</sub>O<sub>3</sub>) to generate boron oxide gas (B<sub>2</sub>O<sub>2</sub>) in the reaction area [25]. Therefore, when ammonia was introduced the growth of BNNTs was initiated with Fe<sub>2</sub>O<sub>3</sub> as the possible catalyst as supported on alumina nanopowders. This approach was then improved by using a mixture of boron and magnesium oxide (with molar ratio of 1:1) located in a BN-made reaction tube. The system was heated to 1,300°C using an RF inducting furnace [26]. At this temperature, boron reacted with MgO to form B<sub>2</sub>O<sub>2</sub>, and Mg vapor acted as the floating zone catalyst. The vapors were argon-transported into a reaction chamber while a flow of ammonia was then introduced. BNNTs were synthesized by the simple reaction of B<sub>2</sub>O<sub>2</sub> and ammonia. The chemical reactions are given by (1) and (2):



After fully evaporating the precursor mixture (1.55 g), 310 mg of white product could be collected from the BN wall of the chamber. The conversion rate from boron to boron nitride reached up to 40%. This effective technique is sometimes called BOCVD or floating zone CVD since both the precursors and catalyst are in vapor phase.

### 3.6 Other Synthesis Techniques

A brief description of other growth techniques for BNNTs is provided here.

#### 3.6.1 Liquid Flow of FeB Nanoparticles

The synthesis of BNNTs and BN nanocages from the liquid flow of iron boride (FeB) nanoparticles was reported by the nitrogen plasma treatment of FeB nanoparticles [47]. Si wafers cast by FeB nanoparticles were introduced into a microwave plasma CVD system and then heated to 900°C during plasma treatment. Mixed gases of N<sub>2</sub> and H<sub>2</sub> were used as a gaseous precursor. After the plasma treatment, a whitish-gray product was formed, which included BNNTs. In addition to BNNTs (5–10-nm diameter), other nanostructures consisting of BN nanocages as well as BN hollow microspheres were present.

#### 3.6.2 Electron Beam In Situ Deposition

Bengu et al. demonstrated the use of a low-energy electron cyclotron resonance (ECR) plasma to deposit SW-BNNTs [48]. Tungsten was used as a substrate after being prepared by specific polishing and cleaning. The growth chamber was kept at ultrahigh vacuum. During the growth, the clean substrates experienced a growth

temperature between 300 and 800°C and a pressure around  $10^{-3}$  Pa under a negative DC bias of 300–600 V. To provide B source for BNNTs, a conventional electron-beam evaporation method was applied, while nitrogen ions provided N for BNNTs via a compact ECR source. As confirmed by in situ high-resolution TEM measurements, short SW-BNNTs were synthesized on tungsten substrates.

### 3.6.3 Plasma Jet Method

The reaction chamber for plasma jet method was implemented by a water-cooled plasma torch, target holder, and a powder collector, according to the report by Shimizu et al. [49]. A direct current (DC) arc plasma jet was formed at a power of 8 kW while the chamber pressure was maintained at 100 Torr. A BN sintered disk was used as a target and exposed to a plasma jet for 1 min, giving a temperature of 4,000 K on the sample, which was thus vaporized. BNNTs were found in a vaporized product.

## 3.7 Low-Temperature Growth of BNNTs

As a summary for previous methods, it is noted that most synthesis techniques for BNNTs required high growth temperatures and the products often contained impurities. Moreover, patterned growth at desired locations has not been achieved. Yap et al. showed that *pure* BNNTs could be directly grown on Si substrates at 600°C by a plasma-enhanced pulsed-laser deposition (PE-PLD) technique using Fe film catalyst [27]. Furthermore, these BNNTs were vertically aligned and could be extracted for device fabrication without purification.

Scanning electron microscopy (SEM) indicated the formation of bundled BNNTs (Fig. 2a–c). The growth locations of BNNTs were controllable due to the prepatterned Fe catalyst (Fig. 2d). TEM confirmed that the tubes were long and straight with a nominal diameter of 20–40 nm. The tips of these BNNTs were fully capped and did not contain catalyst particles, which suggested a base-growth mechanism.

The optimum growth of these BNNTs was obtained through an ideal combination of Fe film thickness, the laser energy density, and the substrate DC bias that induced film resputtering, etc. At a too high deposition rate, only BN films were grown on the substrates (Fig. 3a). The thickness of BN films gradually reduced with an increase in the substrate bias (Fig. 3b) until BNNTs started to grow, being balanced by a film deposition rate and a resputtering rate at a higher substrate bias (Fig. 3c). Under decent resputtering, the deposition of BN thin films was suppressed allowing the formation of BNNTs on Fe nanoparticles according to the vapor-liquid-solid (VLS) mechanism. The growth mechanism represents a phase-selective process between BN films and BNNTs. One of the functions of Fe particles was to capture the energetic BN growth species and confine the growth location. By means of scanning probe microscopy, the local density of electronic states (LDOS) of the BNNTs was measured. The band gaps estimated from the LDOS spectra were found to vary from 4.4 to 4.9 eV.

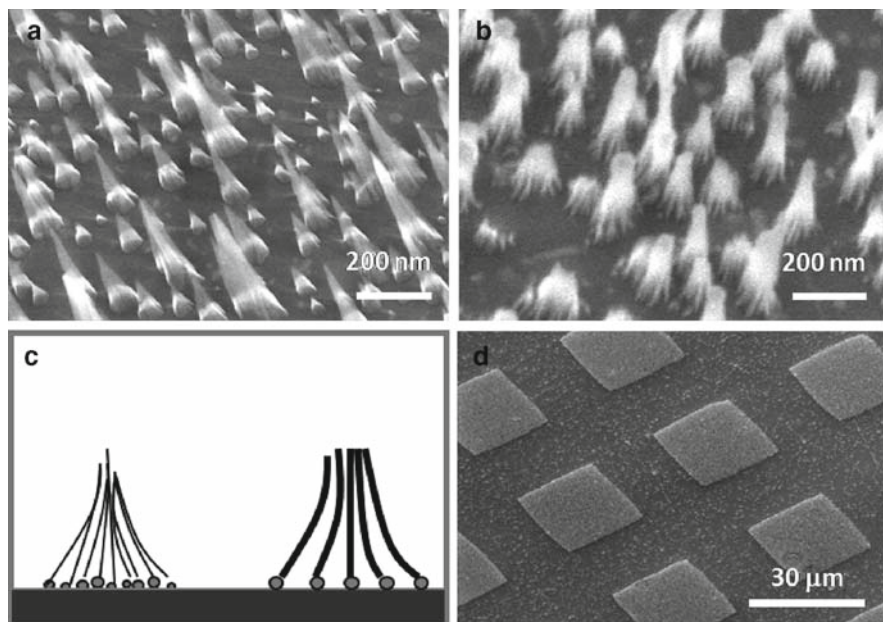


**Fig. 2** SEM images of BNNT bundles with (a) smaller and (b) bigger diameters. Schematic of their corresponding bundling configurations is illustrated in (c). (d) Patterned growth of BNNTs (reprinted from [27]. © American Chemical Society)

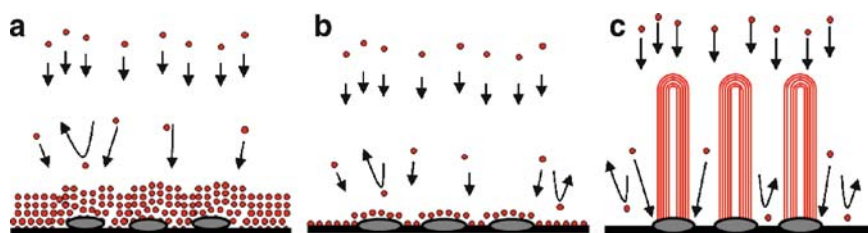


**Fig. 3** Schematic of a phase-selective growth of BNNTs. (a) BN film deposition on Fe nanoparticles at low substrate biases. The film covers the catalysts due to a low resputtering rate of the growth species. (b) The growth rate starts to decrease as the substrate bias increases. (c) Resputtering becomes dominating and enables the growth of BNNTs (reprinted from [27]. © American Chemical Society)

### 3.8 Effective Growth of BNNTs in Horizontal Tube Furnaces

Recently, Yap et al. described a simple route that enables the growth of BNNTs in a conventional horizontal tube furnace [50]. This furnace consists of a quartz tube vacuum chamber, which is commonly used for the growth system of CNTs and

nanowires [51–57]. A mixture of B, MgO, and FeO (or  $\text{Fe}_2\text{O}_3$ ) powders at a 2:1:1 molar ratio was used as a precursor (Fig. 4). These powders were placed in an alumina boat and loaded into a one-end closed quartz tube. The precursor materials were placed near the closed end of this quartz tube and located at the center of the vacuum chamber. Several Si substrates were placed on the top of the alumina boat. The chamber was evacuated to about  $\sim 30$  mTorr before 200 sccm of  $\text{NH}_3$  gas was introduced into the chamber. Subsequently, the precursors were heated up to  $1,200^\circ\text{C}$  for 1 h. Similar to the BOCVD technique using the induction heating method, at a high temperature, reactive  $\text{B}_2\text{O}_2$  vapor was generated and reacted with  $\text{NH}_3$  gas to form BNNTs. White-colored film was uniformly deposited over the whole area of the substrate.

As indicated by SEM, clean and long BNNTs were deposited on the Si substrates (Fig. 5). The tubular structures of these BNNTs can be easily observed with high-resolution SEM (Fig. 5b) and reconfirmed by TEM and electron energy loss spectroscopy (EELS) [50].

Typical Raman and Fourier transformed infrared (FTIR) spectroscopies of these BNNTs are shown in Fig. 6 [50]. A sharp Raman peak at  $\sim 1367\text{ cm}^{-1}$  can be detected (Fig. 6a), which corresponds to the  $E_{2g}$  in-plane vibration of the hexagonal

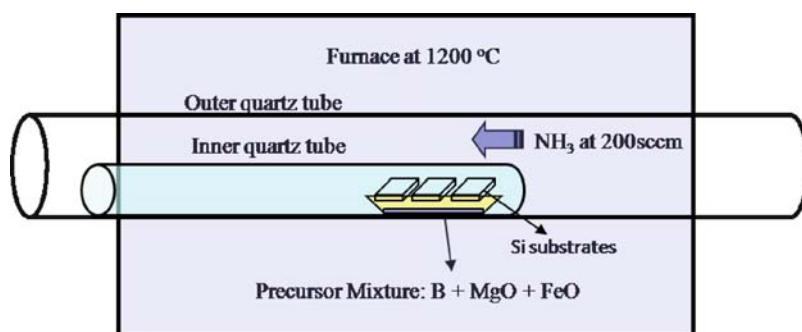


Fig. 4 Experimental setup for the growth of BNNTs by thermal CVD

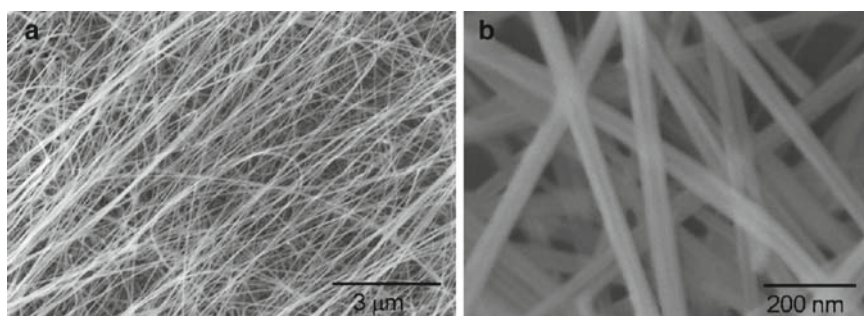
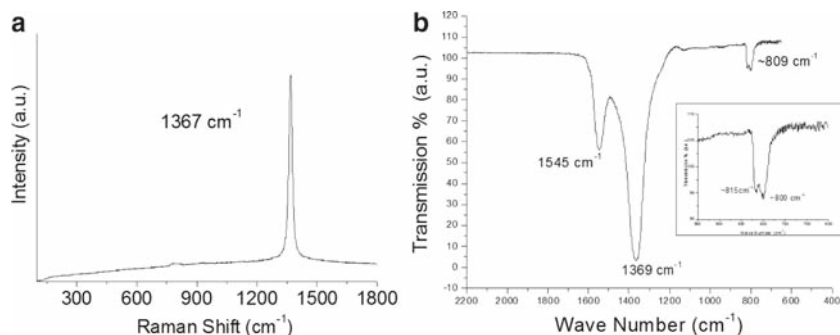


Fig. 5 Scanning electron microscopy images of as-grown BNNTs at (a) low and (b) high resolution





**Fig. 6** Typical (a) Raman and (b) FTIR spectra of the as-grown BNNTs

BN (h-BN) networks. Three IR absorption frequency regimes can be obviously distinguished at  $\sim 809$ ,  $\sim 1,369$ , and  $\sim 1,545$   $\text{cm}^{-1}$  (Fig. 6b). The absorption bands at  $\sim 1,369$  and  $\sim 1,545$   $\text{cm}^{-1}$  are attributed to the in-plane stretching modes of the h-BN networks. This has been explained by the zone-folding method, which considered BNNTs as the seamless cylindrical rolls of h-BN sheets [32]. The  $1,369$   $\text{cm}^{-1}$  band is corresponding to the transverse optical (TO) mode of h-BN sheets that vibrates along the longitudinal (L) or tube axis of a BNNT. The absorption band at  $\sim 1,545$   $\text{cm}^{-1}$  is assigned to the stretching of the h-BN network along the tangential (T) directions of a BNNT. This stretching mode is corresponding to the longitudinal optical (LO) mode of the h-BN sheets, which is Raman inactive. It is also worth noting that this LO mode smears out for h-BN bulks or thin films, and only shows up when the tube curvature induces a strain on the h-BN networks. Thus, it is suggested that only highly crystalline BNNTs would show up this LO mode. In addition, it is noted that the T-mode vibration may shift between  $\sim 1,530$  and  $\sim 1,545$   $\text{cm}^{-1}$ , from samples to samples. This is explained by the change of the average diameter of BNNTs in different samples, attributed to different curvatures of the h-BN sheets in BNNTs and thus the induced lattice strains along the tangential directions of the nanotubes. The absorption at  $\sim 809$   $\text{cm}^{-1}$  is associated to the out-of-plane radial buckling (R) mode where boron and nitrogen atoms are moving radially inward or outward. This interpretation is also identical to the out-of-plane bending mode of h-BN films [58, 59] with a small shift in wavenumber due to the strain developed on the tubular h-BN network in BNNTs. More interestingly, the authors observe a splitting of this R mode vibration at  $\sim 800$  and  $\sim 815$   $\text{cm}^{-1}$ , as highlighted in the inset of Fig. 6b. Tentatively, it is thought that the splitting of the radial buckling vibration is related to the complex interaction of buckling vibration at different h-BN sheets that have different diameters and chiralities. However, the origin of this splitting will require further theoretical and experimental analysis in the future. More theoretical interpretation of these vibrational properties is available in Chap. 5.

UV–Visible absorption spectroscopy was also used to characterize these as-grown BNNTs. This was performed by a suspension of BNNTs in ethanol. Result indicates

that the optical band gap of these BNNTs is as large as  $\sim 5.9$  eV [50]. The optical band gap detected here is larger than that reported for BNNTs (5.5 eV) grown by BOCVD in induction furnaces at higher growth temperatures [60]. The bandgap of our BNNTs is comparable to that of single-wall BNNTs [61] and hexagonal BN single crystals [62].

## 4 Potential Applications

Previous sections summarized experimental works particularly on the growth, properties, and characterization of BNNTs. The discussion on applications of BNNTs is rare in the literature due to present limitations and challenges of mass BNNT productions. However, recent publication especially those from Golberg et al. have indicated some potential applications of BNNTs. Some of these and others are summarized hereafter.

### 4.1 Hydrogen Storage

Hydrogen is regarded as an ideal and nonpolluting energy source that may become an alternative to replace current energy sources. However, hydrogen storage is among the obstacles toward real hydrogen energy technology. Nanomaterials can be more favorable than bulk counterparts with respect to molecular adsorptions due to large specific surface area. CNTs have been the potential materials for hydrogen storage due to their light mass density, high surface to volume ratio, and well-understood chemistry with hydrogen [63]. However, carbon-based materials have weak binding with hydrogen. This significantly restricts possible improvements. Also, experimental results from different groups have not been consistent, especially in regard to single-walled CNTs (SWCNTs) [64]. One possible reason might be due to the fact that SWCNTs can be either semiconducting or metallic, depending upon their diameters and chiralities, and thus have different electronic interactions with guest  $H_2$  molecules and/or H atoms.

BNNTs are always semiconducting with a wide bandgap that is almost independent of the tube diameter and chirality. Moreover, the ionic character of B–N bonds may induce extra dipole moments favorable for stronger adsorption of hydrogen. The binding and diffusion energies of adsorbed hydrogen have recently been computed [65], and BNNTs were found to be suitable for room-temperature hydrogen storage. Also, diffusion through the active sites makes hydrogen penetration toward the inner BNNT surface possible and increases the storage capacity.

On the other hand, metal-doped BNNTs, as investigated by Wu et al., might be even better for hydrogen storage [63], because the presence of defects could enhance the adsorption of hydrogen atoms on BNNTs and reduce the dissociation barrier of the hydrogen molecule on their walls. Baierle et al. also claimed that moderate

substitutional doping in materials with ionic-like bonding, such as carbon-doped BNNTs, could enhance the binding energies of hydrogen, making them optimal for storage [66]. In experiments, Ma et al. showed that MW-BNNTs can absorb 1.8–2.6 wt% hydrogen under ~10 MPa at room temperature [67].

## 4.2 Functionalization

Tremendous research efforts have been made toward chemical functionalization of conventional CNTs since such materials show high potential in many fields of science and technology. It is an essential process to tailor properties of CNTs and make use of them in devices. Some of the motivations include enhancement of CNTs' solubility in solvents, prevention of bundling for better dispersion, production of CNTs composites and biologically compatible CNTs, etc. [68–72]. In particular, the covalent bonding of organic molecules to CNTs may provide a very interesting pathway to new applications in material science, chemistry, and medicine [73–81].

Because of the similarities in geometry it has been proposed that engineering of properties of BNNTs can be carried out along the same way as that of CNTs. Furthermore, a relatively wide band gap of BNNTs restricts their applications primarily to dielectric ones. Thus, it is desirable to control the band structure of BNNTs in order to suit different kinds of applications. The general pathways of functionalization of BNNTs include noncovalent bonding via  $\pi$ – $\pi$  interactions between polymers, covalent attachments of molecules on BNNTs, and doping of BNNTs with exotic atoms.

Several pioneering works on functionalization of BNNTs were reported on covering BNNTs with semiconducting SnO<sub>2</sub> nanoparticles 1–5 nm in size [82, 83]. In fact, the work on functionalization of BNNTs has been hindered due to the challenges of producing pure BNNTs with a high yield. Recently, a significant breakthrough of producing grams of BNNT has been reported by Zhi et al. [84]. Soon after this, intensive functionalization works have been conducted by the same authors.

### 4.2.1 BNNT Composites for Mechanical Applications

Functionalization of BNNTs can be achieved through noncovalent interactions, i.e., wrapping BNNTs with a polymer. Because of the  $sp^2$  hybridized h-BN network, most polymers with a long chain made of benzene rings can interact with the side walls of BNNTs through  $\pi$ – $\pi$  stacking interactions. It had been shown that functionalized BNNTs were perfectly dissolved in many organic solvents [12, 85]. For example, the PmPV-wrapped BNNTs were fully soluble in chloroform, *N,N*-dimethylacetamide, and tetrahydrofuran, but insoluble in water and ethanol. Based on this particular interaction with BNNTs, the functionalization can be implemented to purify BNNTs from big particles and other impurities [86]. Furthermore, it was found that the composites of BNNTs with PmPV possess modified

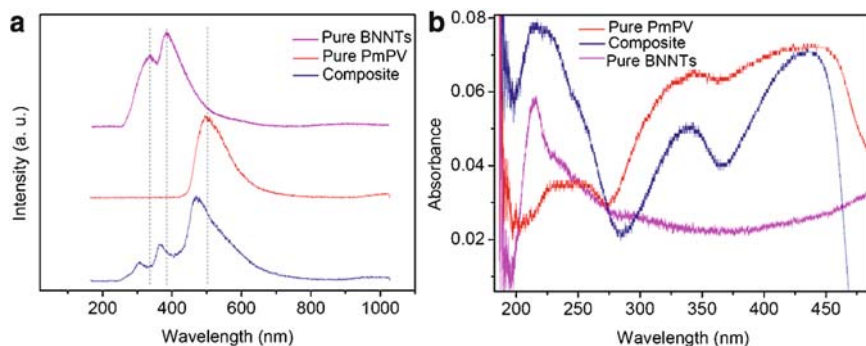


**Fig. 7** (a) Comparative CL spectra and (b) UV-vis absorption spectra of pure BNNTs, pure PmPV, and a composite made of them (courtesy of C. Y. Zhi; reprinted from [12]. © American Chemical Society)

luminescence and absorption properties (Fig. 7), which were different from that of pure PmPV, due to the noncovalent interactions under polymer wrapping [12]. From TEM imaging (Fig. 8a), a layer of polymer (PmPV) can be clearly distinguished from a well-crystallized BNNT's side wall. The functionalized BNNTs are well dispersed on TEM grids as shown in the inset. Because of the remarkable mechanical properties of BNNTs, mixing BNNTs with a polymer may strengthen the polymer matrix for mechanical and reinforcement applications. As shown in Fig. 8b, functionalized BNNTs can be dissolved well in organic solvent while nonfunctionalized BNNTs will be precipitated. These functionalized BNNTs can be used for preparing transparent polystyrene (PS) composite film with 1 and 3 wt% of BNNTs as shown in Fig. 8c.

#### 4.2.2 Bandgap Tuning for Electronic and Chemical Applications

The bandgap of BNNTs can also be modified by attaching molecules on the side walls covalently [87]. Covalent functionalization on the side wall of BNNTs had been performed by synthesizing stearyl chloride-functionalized BNNTs through covalent interaction of  $-\text{COCl}$  groups with amino groups on the tube walls [88]. This particular work was based on the assumption that some of the amino groups remained on side walls of BNNTs during the synthesis process. Theoretical modeling after geometrical relaxation was performed (Fig. 9). It can be seen that a local distortion occurs near the adsorption site, which can be understood by the local  $sp^3$  rehybridization of a N atom at the adsorption site. From the band structure calculations, the HOMO-LUMO (highest occupied molecular orbital and lowest unoccupied molecular orbital) gaps decrease dramatically after functionalization due to new bands introduced into the gap (Fig. 10), which indicates that a charge transfer may take place and functional groups may have a dopant effect on BNNTs. The experimental evidence reveals that the functional groups binding on the side

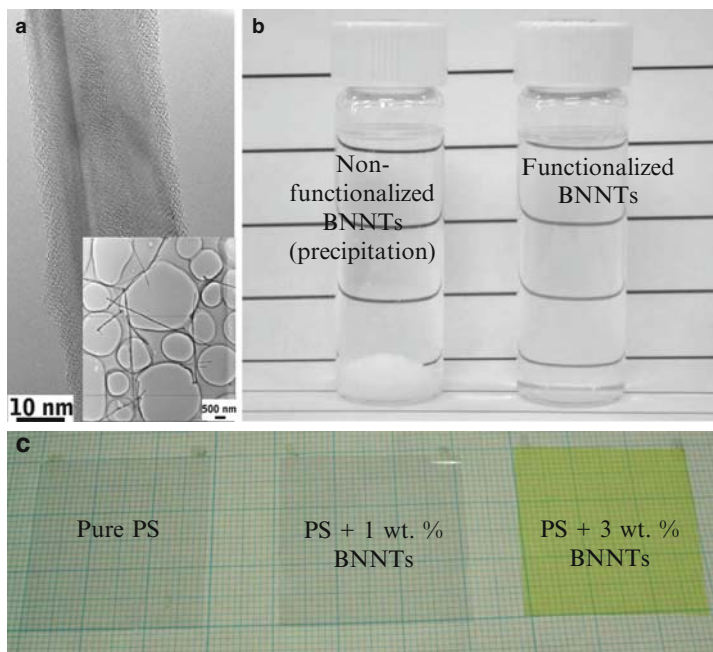


**Fig. 8** (a) HRTEM image of a BNNT coated with PmPV (inset shows the well-dispersed BNNTs on a TEM grid), (b) images of two vials containing BNNTs in chloroform; note that the vial on the left shows BNNT precipitation at the bottom because the tubes were not functionalized with a polymer and are not soluble, whereas the vial on the right does not reveal precipitation because of preliminary BNNT functionalization with polystyrene (PS) or poly(methyl methacrylate) (PMMA), (c) composite films of PS with BNNTs after adding 1 or 3 wt% multiwalled BNNTs; note that the films are still transparent (courtesy of C. Y. Zhi)

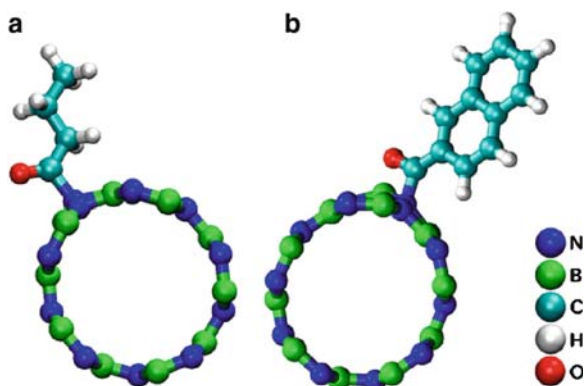


**Fig. 9** The optimized structure of (a)  $\text{CH}_3(\text{CH}_2)_2\text{CO-BNNT}$  and (b)  $\text{C}_{10}\text{H}_7\text{CO-BNNT}$  (courtesy of C. Y. Zhi; reprinted from [87]. © American Physical Society)

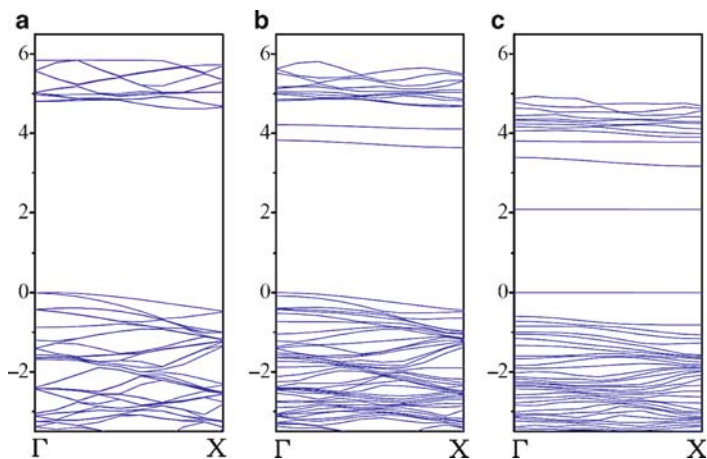


**Fig. 10** Calculated band structure of (a) a (5, 5) BNNT, (b)  $\text{CH}_3(\text{CH}_2)_2\text{CO-BNNT}$ , and (c)  $\text{C}_{10}\text{H}_7\text{CO-BNNT}$  (courtesy of C. Y. Zhi; reprinted from [87]. © American Physical Society)

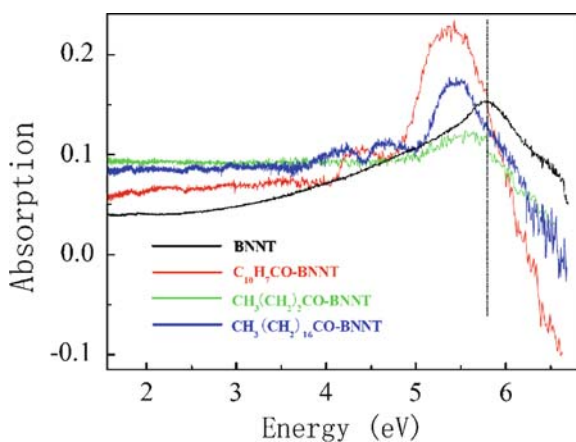


**Fig. 11** Comparative UV-vis absorption spectra of pristine and functionalized BNNTs (courtesy of C. Y. Zhi; reprinted from [87]. © American Physical Society)

wall of BNNTs introduce additional absorption bands (Fig. 11), which reflect the modified band structure. These works have also indicated possible chemical modification of BNNTs for future chemical applications.

### 4.2.3 Functionalization for Molecular Biological Applications

In addition to chemical interactions, the BNNTs have been found to interact with biological molecules such as proteins or single-stranded deoxyribonucleic acid

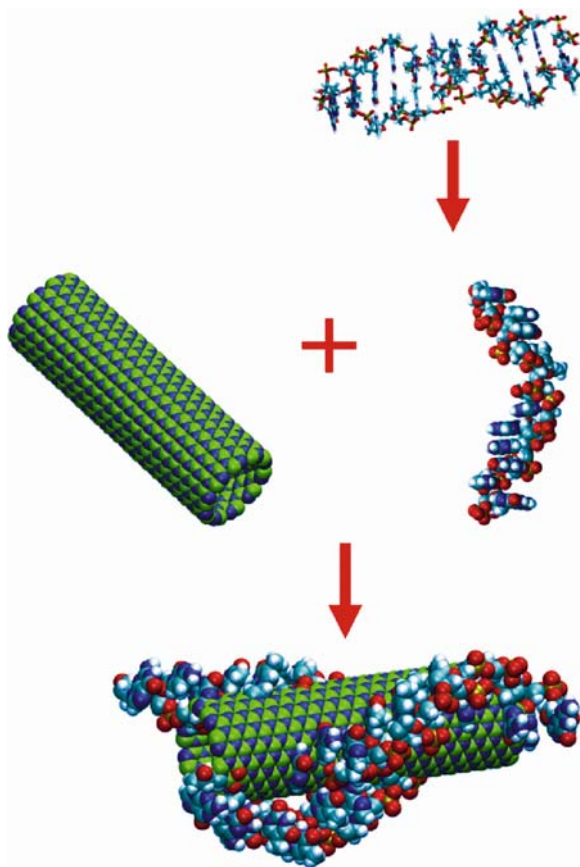


**Fig. 12** The process of fabrication of a DNA–BNNT hybrid (courtesy of C. Y. Zhi; reprinted from [90]. © Wiley-VCH Verlag GmbH & Co. KGaA)

(ss-DNA) via  $\pi$ -stacking interactions with the side walls [89, 90]. Figure 12 illustrates a schematic of the wrapping of an ss-DNA molecule with a BNNT. Experimentally, this has been evidenced as shown by the TEM imaged in Fig. 13a, b. In addition, opened BNNTs can be filled with DNAs as shown in Fig. 13c. DNAs can also be removed by oxidation (annealing at 700°C for 30 min in air). As shown in Fig. 13d, DNAs are oxidized and fully removed to leave a clean BNNT surface. Functionalization of BNNTs with biomaterials opens a new way to incorporate biological molecules on BNNTs for biomedical and sensing applications. Of course, a lot of researches are necessary to be carried out to facilitate BNNTs in real-life applications.

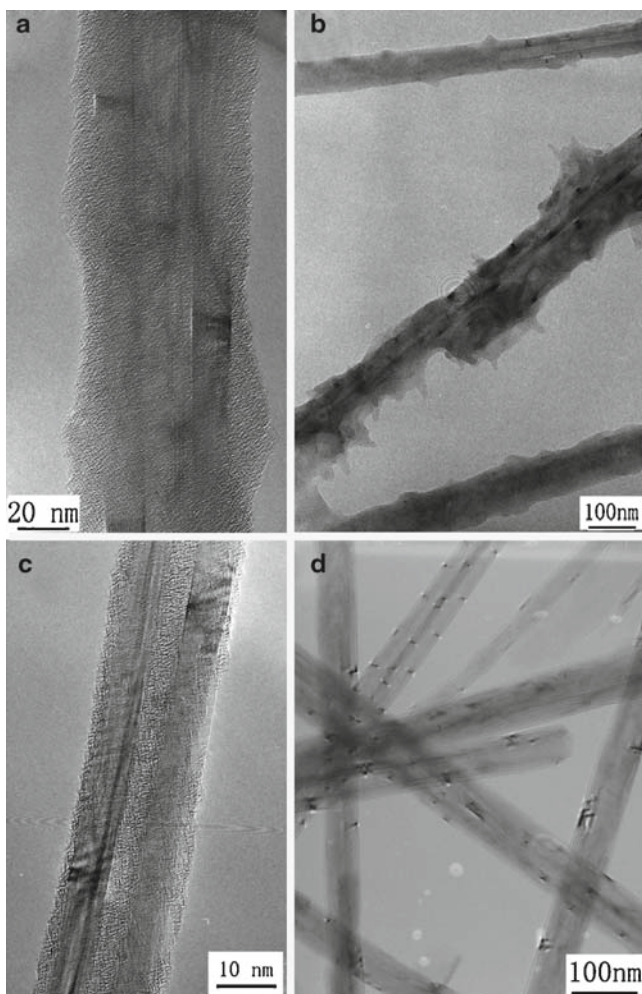


**Fig. 13** (a) and (b) TEM images of BNNTs wrapped with DNA; (c) a DNA-filled BNNT (the *arrow* indicates the core area); (d) a DNA-BNNT sample annealed at 700°C for 30 min in air – the DNA is oxidized and fully removed to leave a clean BNNT surface (courtesy of C. Y. Zhi; reprinted from [90]. © Wiley-VCH Verlag GmbH & Co. KGaA)

## 5 Conclusions

In summary, significant breakthrough in high-yield synthesis of multiwalled BNNTs has been demonstrated by Golberg et al. and more recently by Yap et al. This has stimulated a series of investigations on chemical functionalization of



BNNTs. Promising results have been obtained on tuning the intrinsic properties of BNNTs. However, future research efforts are needed to demonstrate the performance of these functionalized BNNTs in mechanical, electronic, chemical, and biological applications. To date it is still challenging to control placement of BNNTs at desired locations of substrates for device integration. Another key issue will be doping of BNNTs to improve their electrical conductivity, which is required for most electronic devices. We point out here that effective CVD technique for the growth of single-wall BNNTs is still not available. Some of these issues have started to gain attention theoretically and experimentally as reviewed in Chaps. 3, 4, 5, and 7 of this book.

**Acknowledgments** Y.K. Yap acknowledges National Science Foundation CAREER Award (DMR 0447555) for supporting the project on frontier carbon materials and the US Department of Energy, Office of Basic Energy Sciences (DE-FG02-06ER46294) for, in part, supporting the project on boron nitride nanotubes. D. Golberg and Y. Bando acknowledge the WPI Center for Materials Nanoarcitectonics (MANA) of the National Institute for Materials Science (NIMS) for the continuous support of the BNNT-related activities.

## References

1. A. Rubio, J. L. Corkill and M. L. Cohen, *Phys. Rev. B* 49 (1994) 5081.
2. X. Blase, A. Rubio, S. G. Louie and M. L. Cohen, *Europhys. Lett.* 28 (1994) 335.
3. N. G. Chopra, R. J. Luyken, K. Cherrey, V. H. Crespi, M. L. Cohen, S. G. Louie and A. Zettl, *Science* 269 (1995) 966.
4. E. Hernandez, C. Goze, P. Bernier, and A. Rubio, *Phys. Rev. Lett.* 80 (1998) 4502.
5. K. N. Kudin, G. E. Scuseria and B. I. Yakobson, *Phys. Rev. B* 64 (2001) 235406.
6. A. P. Suryavanshi, M.-F. Yu, J. Wen, C. Tang and Y. Bando, *Appl. Phys. Lett.* 84 (2004) 2527.
7. K. H. Khoo, M. S. C. Mazzoni and S. G. Louie, *Phys. Rev. B* 69 (2004) 201401R.
8. C. W. Chen, M. H. Lee and S. J. Clark, *Nanotechnology* 15 (2004) 1837.
9. M. Ishigami, J. D. Sau, S. Aloni, M. L. Cohen and A. Zettl, *Phys. Rev. Lett.* 94 (2005) 56804.
10. D. Golberg, Y. Bando, K. Kurashima and T. Sato, *Scripta Mater.* 44 (2001) 1561.
11. Y. Chen, J. Zou, S. J. Campbell, and G. L. Caer, *Appl. Phys. Lett.* 84 (2004) 2430.
12. C. Y. Zhi, Y. Bando, C. C. Tang, R. G. Xie, T. Sekiguchi and D. Golberg, *J. Am. Chem. Soc.* 127 (2005) 15996.
13. E. J. Mele and P. Kral, *Phys. Rev. Lett.* 88 (2002) 56803.
14. S. M. Nakhmanson, A. Calzolari, V. Meunier, J. Bernholc and M. B. Nardelli, *Phys. Rev. B* 67 (2003) 235406.
15. S. H. Jhi and Y. K. Kwon, *Phys. Rev. B* 69 (2004) 245407.
16. X. Blase, J.-C. Charlier, A. De Vita, and R. Car, *Appl. Phys. Lett.* 70 (1997) 197.
17. J. Choi, Y.-H. Kim, K. J. Chang and D. Tománek, *Phys. Rev. B* 67 (2003) 125421.
18. M. Terrones, W. K. Hsu, H. Terrones, J. P. Zhang, S. Ramos, J. P. Hare, R. Castillo, K. Prassides, A. K. Cheetham, H. W. Kroto and D. R. M. Walton, *Chem. Phys. Lett.* 259 (1996) 568.
19. A. Loiseau, F. Willaime, N. Demoncey, G. Hug and H. Pascard, *Phys. Rev. Lett.* 76 (1996) 4737.
20. D. P. Yu, X. S. Sun, C. S. Lee, I. Bello, S. T. Lee, H. D. Gu, K. M. Leung, G. W. Zhu, Z. F. Dong and Z. Zhang, *Appl. Phys. Lett.* 72 (1988) 1966.
21. R. S. Lee, J. Gavillet, M. L. de le Chapelle, A. Loiseau, J.-L. Cochon, D. Pigache, J. Thibault and F. Willaime, *Phys. Rev. B* 64 (2001) 121405(R).
22. W. Q. Han, Y. Bando, K. Kurashima and T. Sato, *Appl. Phys. Lett.* 73 (1998) 3085.
23. Y. Chen, L. T. Chadderton, J. F. Gerald and J. S. Williams, *Appl. Phys. Lett.* 74 (1999) 2960.

24. O. R. Lourie, C. R. Jones, B. M. Bartlett, P. C. Gibbons, R. S. Ruoff and W. E. Buhro, *Chem. Mater.* 12 (2000) 1808.
25. C. C. Tang, X. X. Ding, X. T. Huang, Z. W. Gan, S. R. Qi, W. Liu and S. S. Fan, *Chem. Phys. Lett.* 456 (2002) 254.
26. C. C. Tang, Y. Bando, T. Sato, and K. Kurashima, *Chem. Commun.* (2002) 1290.
27. J. Wang, V. K. Kayastha, Y. K. Yap, Z. Y. Fan, J. G. Lu, Z. W. Pan, I. N. Ivanov, A. A. Puzos, and D. B. Geohegan, *Nano Lett.* 5 (2005) 2528.
28. N. G. Chopra and A. Zettl, *Solid State Commun.* 105 (1998) 297.
29. E. Hernandez, C. Goze, P. Bernier and A. Rubio, *Phys. Rev. Lett.* 80 (1998) 4502.
30. D. Golberg, P. M. F. J. Costa, O. Lourie, M. Mitome, C. Tang, C. Y. Zhi, K. Kurashima, Y. Bando, *Nano Lett.* 7 (2007) 2146.
31. D. Sanchez-Portal and E. Hernandez, *Phys. Rev. B* 66 (2002) 235415.
32. L. Wirtz, A. Rubio, R. A. de la Concha and A. Loiseau, *Phys. Rev. B* 68 (2003) 045425.
33. V. N. Popov, *Phys. Rev. B* 67 (2003) 85408.
34. Y. Xiao, X. H. Yan, J. X. Cao, J. W. Ding, Y. L. Mao and J. Xiang, *Phys. Rev. B* 69 (2004) 205415.
35. C. C. Tang, Y. Bando, C. H. Liu, S. S. Fan, J. Zhang, X. X. Ding and D. Golberg, *J. Phys. Chem B* 110 (2006) 10354.
36. M. Radosavljevic, J. Appenzeller, V. Derycke, R. Martel, Ph. Avouris, A. Loiseau, J.-L. Cochon and D. Pigache, *Appl. Phys. Lett.* 82 (2003) 4131.
37. Y. Miyamoto, A. Rubio, M. L. Cohen and S. G. Louie, *Phys. Rev. B* 50 (1994) 4976.
38. Y.-H. Kim, K. J. Chang and S. G. Louie, *Phys. Rev. B* 63 (2001) 205408.
39. X. Bai, D. Golberg, Y. Bando, C. Zhi, C. Tang, M. Mitome and K. Kurashima, *Nano Lett.* 7 (1997) 632.
40. J. Cummings and A. Zettl, *Solid State Commun.* 129 (2004) 661.
41. M. F. Ng and R. Q. Zhang, *Phys. Rev. B* 69 (2004) 115417.
42. P. Kral, E. J. Mele and D. Tomanek, *Phys. Rev. Lett.* 85 (2000) 1512.
43. J. Kongsted, A. Osted, L. Jensen, P.-O. Astrand and K. V. Mikkelsen, *J. Phys. Chem. B* 105 (2001) 10243.
44. D. Golberg, Y. Bando, M. Eremets, K. Takemura, K. Kurashima, T. Tamiya, H. Yusa, *Appl. Phys. Lett.* 69 (1996) 2045.
45. Y. Chen, M. Conway, J. S. Williams and J. Zou, *J. Mater. Res.* 17 (2002) 1896.
46. M. J. Kim, S. Chatterjee, S. M. Kim, E. A. Stach, M. G. Bradley, M. J. Pender, L. G. Sneddon and B. Maruyama, *Nano Lett.* 8 (2008) 3298.
47. K. P. Loh, M. Lin, M. Yeadon, C. Boothroyd and Z. Hu, *Chem. Phys. Lett.* 387 (2004) 40.
48. E. Bengu and L. D. Marks, *Phys. Rev. Lett.* 86 (2001) 2385.
49. Y. Shimizu, Y. Moriyoshi, H. Tanaka and S. Komatsu, *Appl. Phys. Lett.* 75 (1999) 929.
50. C. H. Lee, J. Wang, V. K. Kayastha, J. Y. Haung and Y. K. Yap, *Nanotechnology* 19 (2008) 455605.
51. S. L. Mensah, A. Prasad, J. Wang and Y. K. Yap, *J. Nanosci. Nanotechnol.* 8 (2008) 233.
52. J. P. Moscatello, J. Wang, B. Ulmen, S. L. Mensah, M. Xie, S. Wu, A. Pandey, C. H. Lee, A. Prasad, V. K. Kayasha and Y. K. Yap, in *Special Issue on Nanosensors for Defense and Security*, *IEEE Sensor Journal* 8 (2008) 922.
53. S. L. Mensah, V. K. Kayastha, I. N. Ivanov, D. B. Geohegan and Y. K. Yap, *Appl. Phys. Lett.* 90 (2007) 113108.
54. V. K. Kayastha, S. Wu, J. Moscatello and Y. K. Yap, *J. Phys. Chem. C (Letter)* 111 (2007) 10158.
55. S. L. Mensah, V. K. Kayastha and Y. K. Yap, *J. Phys. Chem. C (Letter)* 111 (2007) 16092.
56. V. K. Kayastha, Y. K. Yap, Z. Pan, I. N. Ivanov, A. A. Puzos and D. B. Geohegan, *Appl. Phys. Lett.* 86 (2005) 253105.
57. V. Kayastha, Y. K. Yap, S. Dimovski and Y. Gogotsi, *Appl. Phys. Lett.* 85 (2004) 3265.
58. Y. K. Yap, T. Aoyama, S. Kida, Y. Mori and T. Sasaki, *Diamond Relat. Mater.* 8 (1999) 382.
59. J. Wang and Y. K. Yap, *Diamond Relat. Mater.* 15 (2006) 444.
60. P. Jaffrennou, J. Barjon, J. S. Lauret, A. Maguer, D. Golberg, B. Attal-Trétout, F. Ducastelle and A. Loiseau, *Phys. Status Solidi B* 244 (2007) 4147.

61. R. Arenal, O. Stephan, M. Kociak, D. Taverna, A. Loiseau and C. Colliex, *Phys. Rev. Lett.* 95 (2005) 127601.
62. Y. Kubota, K. Watanabe, O. Tsuda and T. Taniguchi, *Science* 317 (2007) 932.
63. X. J. Wu, J. L. Yang and X. C. Zeng, *J. Chem. Phys.* 125 (2006) 44704.
64. C. Zandonella, *Nature* 410 (2001) 734.
65. S. H. Jhi, *Phys. Rev. B* 74 (2006) 155424.
66. R. J. Baierle, P. Piquini, T. M. Schmid and A. Fazzio, *J. Phys. Chem. B* 110 (2006) 21184.
67. R. Z. Ma, Y. Bando, H. W. Zhu, T. Sato, C. L. Xu and D. H. Wu, *J. Am. Chem. Soc.* 124 (2002) 7672.
68. J. Chen, M. A. Hamon, H. Hui, Y. Chen, A. M. Rao, P. C. Eklund and R. C. Haddon, *Science* 282 (1998) 95.
69. A. Star, J. F. Stoddart, D. Steuerman, M. Diehl, A. Boukai, E. W. Wong, X. Yang, S. W. Chung, H. Choi and J. R. Heath, *Angew. Chem. Int. Ed.* 40 (2001) 1721.
70. J. Chen, H. Liu, W. A. Weimer, M. D. Halls, D. H. Waldeck and G. C. Walker, *J. Am. Chem. Soc.* 124 (2002) 9034.
71. V. Georgakilas, K. Kordatos, M. Proto, D. M. Guldi, M. Holzinger and A. Hirsch, *J. Am. Chem. Soc.* 124 (2002) 760.
72. A. Bianco and M. Prato, *Adv. Mater.* 15 (2003) 1765.
73. K. Jiang, Q. Li and S. Fan, *Nature* 419 (2002) 801.
74. A. A. Mamedov, N. A. Kotov, M. Prato, D. M. Guldi, J. P. Wicksted and A. Hirsch, *Nat. Mater.* 1 (2002) 190.
75. B. R. Azamian, J. J. Davis, K. S. Coleman, C. B. Bagshaw and M. L. Green, *J. Am. Chem. Soc.* 124 (2002) 12664.
76. A. B. Dalton, S. Collins, E. Muñoz, J. M. Razal, V. H. Ebron, J. P. Ferraris, J. N. Coleman, B. G. Kim and R. H. Baughman, *Nature* 423 (2003) 703.
77. Y. Kang and T. A. Taton, *J. Am. Chem. Soc.* 125 (2003) 5650.
78. K. A. Williams, P. T. M. Veenhuizen, B. G. de la Torre, R. Eritjia and C. Dekker, *Nature* 420 (2002) 761.
79. H. Xin and A. T. Woolley, *J. Am. Chem. Soc.* 125 (2003) 8710.
80. J. J. Gooding, R. Wibowo, J. Liu, W. Yang, D. Losic, S. Orbons, F. J. Mearns, J. G. Shapter and D. B. Hibbert, *J. Am. Chem. Soc.* 125 (2003) 9006.
81. R. J. Chen, S. Bangsaruntip, K. A. Drouvalakis, N. W. S. Kam, M. Shim, Y. Li, W. Kim, P. J. Utz, and H. Dai, *Proc. Natl. Acad. Sci. USA* 100 (2003) 4984.
82. W. Q. Han and A. Zettl, *J. Am. Chem. Soc.* 125 (2003) 2062.
83. C. Y. Zhi, Y. Bando, C. Tang and D. Golberg, *J. Phys. Chem. B* 110 (2006) 8548.
84. C. Y. Zhi, Y. Bando, C. Tang and D. Golberg, *Solid State Commun.* 136 (2005) 67.
85. S. Y. Xie, W. Wang, K. A. S. Fernando, X. Wang, Y. Lin and Y. P. Sun, *Chem. Commun.* (2005) 3670.
86. C. Y. Zhi, Y. Bando, C. Tang and D. Golberg, *J. Phys. Chem. B* 110 (2006) 1525.
87. C. Y. Zhi, Y. Bando, C. Tang and D. Golberg, *Phys. Rev. B* 74 (2006) 153413.
88. C. Y. Zhi, Y. Bando, C. Tang, S. Honda, K. Sato, H. Kuwahara and D. Golberg, *Angew. Chem. Int. Ed.* 44 (2005) 7932.
89. C. Y. Zhi, Y. Bando, C. Tang and D. Golberg, *J. Am. Chem. Soc.* 127 (2005) 17144.
90. C. Y. Zhi, Y. Bando, W. Wang, C. Tang, H. Kuwahara and D. Golberg, *Chem. Asaian J.* 2 (2007) 1581.

# Heteroatomic Single-Wall Nanotubes Made of Boron, Carbon, and Nitrogen

Raul Arenal and Annick Loiseau

**Abstract** In this chapter, we review the current status of research on heteroatomic single-walled nanotubes (SWNTs): boron nitride (BN), B–C, C–N, and B–C–N. We present developments in the synthesis, the characterization, and the properties measurements and theoretical studies. These nanotubes have unique properties when compared with that of their carbon counterparts. For instance, BN-SWNTs are chemically inert, resistant to oxidation at high-temperature, and most importantly, possess a uniform electronic structure that is independent of their geometry. In the first part of this chapter, we review the different synthesis methods employed to produce these nanotubes (high and medium-low temperature processes). We then turn to the study of the atomic structure of these nanomaterials by different transmission electron microscopy techniques as well as we review the works concerning the growth mechanism of these nanotubes. Finally, the main physical (electronic, vibrational, optical, mechanical, electromechanical, and thermal) and chemical (functionalization and hydrogen storage) properties of these heteroatomic SWNTs, particularly the case of BN, are outlined, followed by the presentation of the potential applications of these nanoobjects.

## 1 Introduction

In the last two decades, a huge interest in the scientific community has been devoted to the study of nanomaterials. The nanotubes are the most representative example of these nanomaterials leading this research and industrial effort because of their unique physical properties. Although carbon nanotubes (C-NTs) were the first of these objects to be synthesized and remain the most well-known, they are not the unique form of nanotubes. Other heteroatomic nanotubes have been produced, for

---

R. Arenal (✉) and A. Loiseau (✉)  
Laboratoire d'Etude des Microstructures (LEM), UMR 104 CNRS-ONERA,  
Avenue de la Division Leclerc, 92322 Chatillon, France  
e-mails: raul.arenal@onera.fr, loiseau@onera.fr

instance: molybdenum disulfide ( $\text{MoS}_2$ ), tungsten disulfide ( $\text{WS}_2$ ), titanium dioxide ( $\text{TiO}_2$ ), B–C, C–N, B–C–N, and boron nitride (BN). Among all these nanotubes, the latest nanotubes (B–C–, C–N–, B–C–N– and BN–NTs) have generated intense interest because of their novel properties, which make them an attractive alternative to undoped carbon counterparts (C–NTs). BN–NTs were synthesized soon after the discovery of C–NTs by Iijima [1] and became the most interesting heteroatomic NTs. They possess the same hexagonal structure, with boron and nitrogen atoms on alternate lattice sites. The result is a highly polar dielectric material, with a predicted wide band gap larger than 5.5 eV, which is expected to be independent on the tube diameter and helicity [2–4]. These tubes have a potential interest for UV emitters and for high-power high-frequency electronic devices; they also have outstanding mechanical properties, are chemically inert, and can be used as protective cages for nanomaterials [5, 6]. Furthermore, doped C–NTs (C–N, B–C, or B–C–N) that can introduce donor or acceptor states near the Fermi level are thought to be a promising approach for tailoring the electrical and optical properties of C–NTs. Thus, significant efforts have been devoted for finding efficient methods for doping C–NTs, which are reviewed in this chapter and are also discussed in the chapters by Blase and Chacham, Yu and Wang, Filho and Terrones of this book.

As for C–NTs, these heteroatomic (B, N, and BN-doped carbon, and BN) nanotubes can display two different morphologies: multi-walled (MW) or single-walled nanotubes (SWNTs). To date, heteroatomic MWNTs have been more widely studied than SWNTs because of difficulties for synthesizing the latter ones. In this chapter, we will focus on the SWNTs, since they can be considered as the perfect model system for exploring their properties: transport, mechanical, optical, field-emission, etc. In fact, from a heuristic model, a SWNT is structurally equivalent to a sheet of graphene (or hexagonal BN layer) rolled into a tube [7]. Thus, the interpretation and modelisation of their properties are easier and more reliable because interwall interactions as well as the number of layers have not been considered.

This chapter is organized as follows. In the first section, we present the synthesis methods and distinguish between high and medium temperature techniques. In the second section, we examine how the structure and the composition of the tubes can be identified and analyzed by combining different modes of transmission electron microscopy (TEM). In this section, we also discuss how the inspection of the samples by TEM provides clues about their growth mechanism. The third section is devoted to their physical and chemical properties, with a particular emphasis to their transport, optical, and vibrational properties. Finally, in the conclusion, we draw some perspectives and challenges for future research on hetero-atomic tubes.

## 2 Synthesis Methods

In comparison to single-walled C–NTs, there is a significant lack of successful synthesis studies of BN and doped (B, C, or BN) carbon SWNTs. It proves that it is extremely difficult to synthesize those SWNTs using well-established techniques

for the undoped C-SWNT production: chemical vapor deposition (CVD), arc discharge, or laser ablation. However, even if it represents a great challenge, recently several teams have succeeded in producing different kinds of SWNTs. Nevertheless, it is worth noticing that there is not a suitable control of their synthesis yet.

As in the case of undoped C-SWNTs, for doped and heteroatomic SWNTs, it is possible to distinguish between low and high-temperature synthesis methods. All these methods have been inspired from those used for the production of C-SWNTs.

## ***2.1 High Temperature Methods***

These synthesis methods are based on the vaporization of a solid target at temperatures higher than 3,000° C. Two different techniques can be distinguished for achieving the vaporization process: arc discharge and laser vaporization.

### **2.1.1 Arc Discharge**

This method was first employed to produce fullerenes [8]. It consists in establishing a hot plasma between two graphite electrodes, leading to the consumption of the anode and to the formation of a carbon deposit on the cathode. In 1991, Iijima discovered that this deposit contained a variety of graphite-like structures, among these were MWNTs [1]. Shortly afterwards, Ebbesen and Ajayan adapted this method to produce MWNTs in bulk quantities by simply varying the synthesis conditions [9]. Furthermore, C-SWNTs were synthesized for the first time in 1993 via this technique [10] by adding a metal catalyst – such as Ni, Co, Ni–Co – to the graphite powder of the anode. Although this technique can be easily implemented, its main drawbacks are, on one hand, the necessity for the electrodes to be electrically conductive, and on the other hand, the amount of carbon-based by-products and metal particles that cannot be easily removed.

Doped  $CN_x$ -SWNTs have been synthesized using this technique by Droppa et al. [11] and recently by Glerup et al. [12]. In the former case, the synthesis was achieved by vaporizing a rod containing a mixture of graphite and catalyst under a helium–nitrogen atmosphere [11]. It is worth mentioning that in this work, there is no a TEM micrograph showing the presence of these  $CN_x$ -SWNTs. Thus, the production of these SWNTs is only deduced from the interpretation of Raman and X-ray photoemission spectroscopy (XPS) measurements. Hence, as we will discuss later, such kind of bulk measurements are not sufficient to investigate these nano-materials and local probe (atomic resolution) investigation techniques are required. In the second case [12], the synthesis consisted in evaporating composite anodes containing graphite, melamine, and Ni/Y catalyst particles under a helium atmosphere. The presence of  $CN_x$ -SWNTs is attested both by TEM observations and spatially-resolved electron energy loss spectroscopy (SR-EELS) measurements of the N concentration at a nanometer scale within the tubes. The tubes were found to display

the same morphology than their carbon analogs and to contain around 1 at.% of N incorporated into the hexagonal network structure.

As far as we know, even if arc discharge technique has been employed to produce  $B_xC$ -MWNTs [13], this technique has not proved up to now its ability to synthesize  $B_xC$ -SWNTs. However, the very first BN-MWNTs [14] and BN-SWNTs [15] have been synthesized using an adapted arc discharge technique. In this case indeed, the insulating character of the h-BN compound, which is the analog of graphite, prevents one to proceed as for C-NTs that is to arc two h-BN electrodes. This difficulty has been overcome in 1996 by arcing  $HfB_2$  electrodes under a partial pressure of nitrogen gas [15].  $HfB_2$  is a metallic compound with a high melting point and known for its ability to chemically react at high temperature with  $N_2$  in order to form h-BN. With this experimental procedure, a mixture of pure BN-SWNTs and BN-MWNTs made of a few and highly crystalline layers (2–10 maximum) could be produced for the first time but in low yield. Nevertheless, a variant of the conventional arc discharge approach has recently been developed by Lee et al. [16], which is pointed out to be a promising method for a large scale production of BN nanotubes. This method uses the arc jet technique (also known as the plasma torch), which has the advantage to be a continuous process, where the precursor material consists in a mixture of h-BN and catalytic powders (Ni and Y), the forming plasma gas is a mixture of Ar and  $N_2$ , and the temperature is between 5,000 and 20,000 K. The product was shown to be a mixture of highly crystalline BN-SWNTs and BN-MWNTs.

### 2.1.2 Laser Vaporization

Laser vaporization technique is an alternative high temperature route to arc discharge approach to the synthesis of SWNTs. For undoped C-NTs, it consists in the vaporization by a pulsed or a continuous laser of a carbon target, which contains a mixture of catalyst particles under a flow of argon or helium. In the case of heter-atomic and doped SWNTs, one has to adjust the target composition and the other synthesis parameters as gas nature, pressure, and flow depending on the desired nanotube composition.

Lee et al. [17] and Arenal et al. [18, 19] have shown that high yields of BN-SWNTs can be produced with a high crystalline quality. This technique is so far the unique route to synthesize BN-SWNTs in high quantities. The synthesis of these BN-SWNTs consists in the vaporization of a hexagonal BN target via a continuous  $CO_2$  laser under a nitrogen flow at a pressure 1 bar. The temperature at the surface of the target is ranging from 3,200 to 3,500 K. The collected soot consists in a mixture of nanotubes and nanoparticles. Nanotubes are SWNTs, with some (about 20%) multiwall (primarily double-wall) nanotubes. SWNTs are either isolated or organized in small bundles made of 2–10 tubes, as shown in Fig. 1d. The tube length is typically several hundreds of nanometers with few tubes exceeding 1 mm.

Recently, the same laser reactor has been employed to synthesize N-doped C-SWNTs and B–C–N-SWNTs [21–23]. The synthesis conditions were adapted from those used for the synthesis of C-SWNTs [24] and for BN-SWNTs [17, 19].

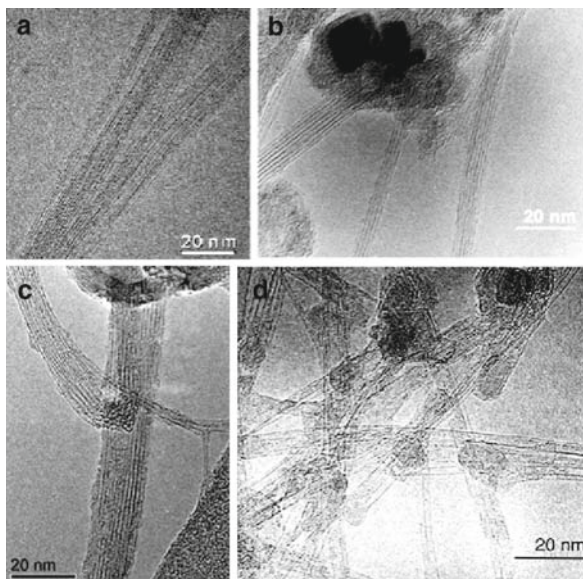


**Fig. 1** (a–c) High-resolution TEM (HRTEM) images of B, N, and BN-doped single-walled carbon nanotubes, as well as pure BN-SWNTs [18]. (a) Reprinted from [20], with permission from Elsevier. (b) Reprinted from [12], with permission from Elsevier. (c) Reprinted from [21], with permission from American Chemical Society

The buffer gas is now not an inert gas (He or Ar) but one of the reactant ( $N_2$ ) as for the synthesis of BN-SWNTs. For N-doped C-SWNTs, the target is made of a graphite powder mixed with catalyst powders (Ni/Y), and the Ni/Y/C proportion is 4.2:1:94.8 at.%, which is proved to be the optimal condition for the synthesis of C-SWNTs [25]. The resulting tubes present structure and morphologies very similar to that of their carbon analogs, whereas the concentration in nitrogen is estimated to be around 1 at.% from electron energy loss spectroscopy (EELS) analysis performed on individual nanotubes [23]. Concerning (B–C–N)-SWNTs, the target employed was a mixture of boron, carbon, and metal catalyst (Co/Ni) [21]. Again, structure and morphologies of these tubes are very similar to their carbon analogs. As detailed in Sect. 3.2, EELS analyses revealed that C, B, and N are not homogeneously distributed along the tube wall but that B and N build small domains embedded into the graphitic network.

Laser vaporization technique has been also employed to synthesize ropes of C-SWNTs and other B–C-nanostructures by Gai et al. [26]. A Nd/YAG laser was employed to ablate a target of Co/Ni/B doped carbon under Ar flow. In this work, the authors demonstrate the difficulty to incorporate a large concentration of B in the carbon network. These results are consistent with the work of Lowell [27] on B-doped graphite.

In summary, laser vaporization technique has shown its ability and its flexibility for the synthesis of different kinds of heteroatomic SWNTs. Furthermore, this approach



is very adequate since it permits a very good control of the different synthesis parameters. Nevertheless, such kind of technique presents two major limiting factors for the large-scale production, the cost, and the impossibility to operate continuously.

## 2.2 Medium-Low Temperature Methods

Medium-low temperature synthesis approaches concern techniques carried out at temperatures lower than 2,000°C, as is the case of CVD and carbo-thermal reaction.

### 2.2.1 Chemical Vapor Deposition

For undoped C-NTs, CVD approach involves the decomposition of gaseous hydrocarbons (methane, carbon monoxide, acetylene, etc.) over metal catalysts (Co, Ni, Fe, Pt, Pd, etc.), using an energy source, usually the heat of a furnace (thermal CVD) assisted or not by a hot filament (HF-CVD) or a plasma generator (PE-CVD). Metal catalysts are deposited on a substrate or spread into the reactor chamber. The energy source is used to *crack*, at the surface of metal catalyst particles, the carbon molecule into reactive atomic carbon. Carbon atoms are assumed to self-organize by diffusing at the surface and in the bulk of the catalytic particles in order to build the nanotube walls at the surface of the particles. In most cases, the diameter of the tubes is directly linked to that of the particles and should therefore be below 5 nm for the growth SWNTs [7]. The temperatures for nanotubes synthesis are generally within the 650–900°C range.

CVD techniques have been widely employed for the synthesis of hetero-atomic nanotubes. However, most of the studies report on multiwall nanotubes. As far as we know, there is no study on synthesis of BN- or B<sub>x</sub>C-SWNTs using CVD techniques. Concerning the other kind of doped C-SWNTs (N and B–C–N), a few teams have succeeded in their synthesis using CVD methods.

Isolated CN<sub>x</sub>-SWNTs were synthesized on bare quartz and SiO<sub>2</sub>/Si substrates by CVD approach in which xylene and acetonitrile were used as carbon and nitrogen sources, respectively [28]. Raman modes were found to be highly sensitive to the nitrogen concentration, indicating a dramatic change in the structure of the tubes. In this context, Villalpando-Paez et al. reported the synthesis of N-doped C-SWNTs using an aerosol-assisted CVD, which consists into the thermal decomposition of ferrocene/ethanol/benzylamine solutions in Ar atmosphere at 950°C [29]. The authors observed that upon increasing nitrogen concentration, there is a clear change in the electronic and structural properties of the NTs. More recently, Ayala et al. synthesized CN<sub>x</sub>-SWNTs by CVD varying the feedstock composition between pure acetonitrile and ethanol/acetonitrile mixtures [30]. These authors pointed out that the morphology of the NTs material (which is a mixture of SWNTs and MWNTs) strongly depends on the composition of the reactive atmosphere. Furthermore, they also noticed that the temperature has a strong influence on the NTs' diameter distribution.

Recently, Wang et al. have reported a large-scale synthesis of (B–C–N)-SWNTs using a bias-assisted hot filament CVD method [31]. These authors employed MgO-supported Fe–Mo bimetallic catalyst, CH<sub>4</sub>, B<sub>2</sub>H<sub>6</sub>, and ethylenediamine vapor as reactant gases to produce this high yield of NTs.

To summarize, the main advantage of CVD technique for the synthesis of heteroatomic SWNTs is that it could easily be scaled up for large-scale production with relative low-cost even if it is not yet the case. Nevertheless, their major drawback is that usually the produced nanotubes using this method have a high density of defects in their structure.

## 2.2.2 Carbothermal Synthesis Approach

The carbothermal process is a modification of one of the most widely used synthesis methods of h-BN, which is known as the “amide” way [32–34]. h-BN is obtained from the reaction of boron oxide (or boric acid) with ammonia at a temperature close to 900°C. Thus the carbothermal approach consists in the carbothermic reduction of boron oxide using pure carbon like reducing agent in the presence of nitrogen at a temperature between 1,000 and 1,450°C [35–37]. Because of its high formation enthalpy, boron oxide is very stable and can be only reduced by carbon at high temperatures (>1,000°C) [38]. One of the possible reactions taking place is:



This synthesis method has been first adapted and successfully employed for the production of BN-MWNTs [39, 40]. Recently, Han et al. [41] used it to synthesize a mixture of SW- and MW-<sup>10</sup>BN-NTs via the reaction of <sup>10</sup>B<sub>2</sub>O<sub>3</sub> and C-NTs, under a flowing nitrogen atmosphere at 1,580°C. Although the diameters of these BN-NTs were smaller than those of the starting C-NTs, their lengths were similar. The authors pointed out that the isotopic ratio of <sup>10</sup>B in BN-NTs depends on the isotopic ratio of the starting B<sub>2</sub>O<sub>3</sub>.

B<sub>x</sub>C-, CN<sub>x</sub>-, and (B–C–N)-SWNTs can also be produced by chemical substitution treatment of undoped C-NTs used as templates [20, 42]. Golberg et al. reported the first studies on the synthesis of high yields of bundles of B<sub>x</sub>C- and CN<sub>x</sub>-SWNTs, using this carbothermal process [42]. The partial substitution is carried out in the presence of boron oxide vapor and nitrogen gas at 1,500–1,700 K. The authors found that almost 100% of the starting C-SWNT bundles were converted in to B and N-doped C-SWNT bundles.

More recently, Borowiak-Palen et al. have reported the production of B-doped C-SWNTs by heating boron oxide in the presence of pure carbon SWNTs and NH<sub>3</sub> at 1,150°C [20]. The raw material was characterized by TEM and EELS as well as by bulk sensitive methods such as optical spectroscopy, X-ray photoemission spectroscopy (XPS), and bulk sensitive high-resolution EELS. Via EELS measurements, the authors found that the local boron concentration within a SWCNT bundle can range between 10 and 20 at.%, which represents a very high content, when

compared with that of previous studies. These authors attributed this high concentration to the use of ammonia instead of nitrogen as carrier gas, since ammonia is chemically more active. It is worth mentioning that such a high concentration is not suitable for standard semiconductor doping level ( $\leq 1\%$ ). Thus, the potential applications of these materials are limited in such field.

To summarize, the substitution technique seems to be a promising and flexible technique for producing different kinds of hetero-atomic tubes. One can expect to be able to produce different spatial distributions of B and N within the walls than those one can obtain from direct synthesis techniques.

### **3 Structural and Composition Analysis via Transmission Electron Microscopy**

To study the properties of these nanomaterials as well as to improve and to control their synthesis, the knowledge of their structural and chemical characteristics are highly required. Hence, the physical properties, in particular the optical and electronic properties, of a nanotube depend on the distribution of its constituent elements. The morphology, composition, and elemental distribution of these nanotubes are dictated by a number of factors, namely the formation mechanism, operating conditions, precursors, gas composition, and catalyst. Thus, a deep knowledge of their chemical composition at the nanometer scale as well as the concentration of the doping elements is needed. TEM has been the key technique throughout the history of research and development on nanostructured materials in particular in the case of nanotubes [7, 43]. Several TEM techniques have been widely employed to investigate the morphology, the atomic structure, and the chemical composition of these nano-objects: conventional TEM imaging, high resolution (HRTEM), electron diffraction (ED), X-rays energy dispersive spectroscopy (EDS), and EELS. Other spectroscopic techniques such as XPS or macroscopic EELS (high resolution EELS) have been used to investigate the doping of C-NTs [20, 30, 44, 45]. Their major drawbacks are that they provide an average bulk measurement and do not discriminate between the nanotubes and the impurities present in the raw sample. In this section, we present a review concerning the works on the characterization and study of the atomic structure and elemental composition of heteroatomic (B, N, and BN-doped carbon, and BN) SWNTs using a set of these TEM techniques.

#### ***3.1 Transmission Electron Microscopy: HRTEM and Electron Diffraction***

It is well-known that HRTEM imaging mode gives access to the crystallographic structure, at the atomic scale, of a sample [46]. That is the reason why it is an invaluable tool to study nanoscale properties of materials. It is a matter of fact that C-NTs have been identified 17 years ago using this technique which still remains the

most widely employed approach to study both their morphology and structure. Moreover, because C-NT can be considered as a weak phase object (it is the ideal example where this approximation applies), great simplifications can be made in the electron imaging theory (dynamical diffraction effects and nonlinear imaging process can be neglected to some extent), which makes easier the imaging interpretation.

Via HRTEM it is possible to obtain, under particular imaging conditions, a direct image of the atomic arrangement in a nanotube and then, as we shall see later, to determine the diameter and the helicity of the nanotubes [7, 43]. It is worth mentioning that the full identification of a nanotube requires to know the chiral indices ( $n, m$ ), which are related to these two parameters (diameter and chiral angle), and see the chapter by Lee, Wang, Kayastha, and Yap. As a general feature, definition of the appropriate imaging conditions and their analysis are supported by image simulations within the dynamical theory [7, 17, 18].

In standard HRTEM (HRTEM microscopes are considered to provide a point resolution around 0.2 nm) image of an individual SWNT observed in longitudinal projection, the tube is imaged by a set of two parallel dark fringes, which correspond to the projected maximum atomic density [7]. Providing to use Scherzer focus conditions, the tube diameter can be directly measured from the fringe spacing with an accuracy of  $\pm 0.5$  nm. In the case of bundles of SWNTs, the diameter of a particular individual NT cannot be measured directly. In fact, the bundle lattice distance, only, can be measured from a HRTEM image of a bundle observed in a longitudinal projection. The image, indeed, consists in a set of lattice fringes, the spacing of which depends on the orientation of the electron beam with respect to the bundle lattice ((11) or (20), in 2D notation). Thus, the mean diameter of the nanotubes can be determined by measuring this lattice distance, knowing the van der Waals distance between the NTs in the bundle [7]. Whatever nanotubes are observed individually or assembled in bundles, the image contrasts described earlier are not sensitive to the presence of atoms in substitution to carbon such as boron or nitrogen, since they behave as weak phase objects as well, and display a phase contrast very close to that of carbon. As a result, Figs. 1 and 2 correspond to a set of typical

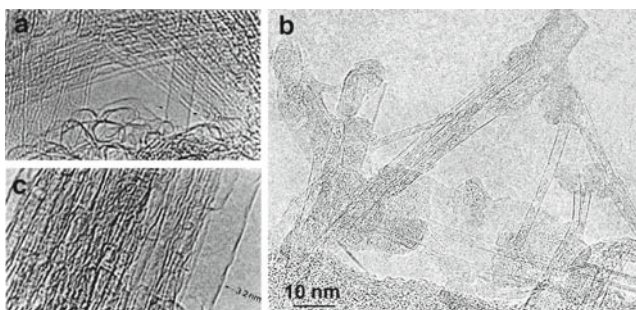


**Fig. 2** (a, c) HRTEM images of B- and N-doped C-SWNTs. Reprinted from [42], with permission from Elsevier. (b) HRTEM micrograph corresponding to different objects present in a BN-NTs sample: BN-NTs (single-walled (individual or organized in small bundles) and multiwalled (mostly double-walled)), cages and other kinds of nanoparticles [18]

electron micrographs showing different samples of boron (Fig. 1a from [20] and Fig. 2a from [42]), nitrogen (Fig. 1b from [12] and Fig. 2c from [42]), and BN (Fig. 1c from [21]) doped carbon SWNTs observed individually or in bundles, as well as pure BN-SWNTs (Fig. 1d [18] and Fig. 2b from [18]). In all these cases, one cannot discriminate the nature of the elements present in the tubes but can only determine the tube morphology. The tube diameter and length obviously depend on the synthesis technique. On the one hand, heteroatomic tubes produced by the laser vaporization technique have been found to display the same diameter around 1.4 nm as their carbon analogs [22, 23]. On the other hand, Golberg et al. pointed out a drastic change in the diameter of the tubes after the carbothermic reaction performed on C-SWNTs [42].

The graphitic lattice can be imaged when the point resolution of the HRTEM used for the observations is below 0.22 nm [7]. In this case, it is possible to determine the helicity of the tube in addition to its diameter. Such an example observed for a sample of BN-SWNTs is displayed in Fig. 3a, where Fig. 3b is an enlarged image of the wall fragment of the nanotube of Fig. 3a. A periodic array of black dots is observed, located at the edge on part of the tube and along its axis, in place of the dark fringe seen in the previous micrographs. The dots and fringe periodicity is equal to 0.21 nm and corresponds to the periodicity of the lattice planes normal to the  $[10\bar{1}0]$  direction of h-BN [7, 17, 18]. Imaging simulations using the EMS code [17, 18, 47] have shown that this periodic contrast can only be observed for tubes having the zigzag configuration (helicity angle =  $0^\circ$ ). The image simulation calculated for a zigzag tube shown in Fig. 3c attests its reliability with the experimental contrast. It has to be mentioned that the observation of such a contrast is very rare in C nanotubes (both MWNT and SWNT) especially when they are produced using a high temperature technique such as laser ablation or electric arc [7]. Its frequent observation in BN-SWNT indicates that BN-NTs present a preferential zigzag atomic configuration, in contrast to the carbon

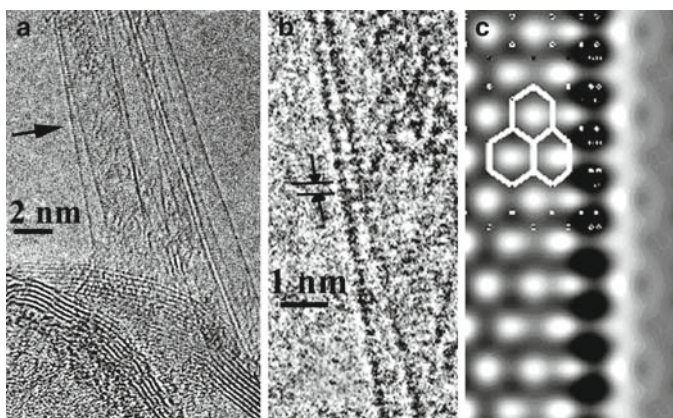


**Fig. 3** (a) HRTEM of a BN-SWNT. (b) Enlargement of the contrast observed in the area indicated by an *arrow* in (a). (c) Image simulation of a BN-SWNT having the zigzag configuration. The hexagonal network of the tube is drawn in *white lines*. Figures from Arenal et al. [18]

case. Similar observations have been reported for BN-MWNTS synthesized by various techniques. They confirmed this preferential zigzag arrangement of BN-NTs, which is independent of their synthesis method and then of their morphology [48, 49]. In the case of (B–C–N)-SWNTs, Golberg et al. showed that in these doped SWNTs there was not a dominant atomic arrangement since zigzag and armchair (chiral angle =  $30^\circ$ ) configurations can be indistinctly observed [42]. To our knowledge, this kind of studies had not been performed on  $CN_x$ - or  $CB_x$ -SWNTs.

The example of Fig. 3 attests that HRTEM is a powerful technique to investigate the nanotubes atomic structure. Structural defects can also be studied by this technique. Recently, Zobelli et al. studied the defects and irradiation effects on BN-SWNTs combining HRTEM images and theoretical calculations [50]. They showed that the point defects formed under electronic irradiation were mainly divacancies, see Fig. 4, and concluded that under irradiation the electronic and optical properties of BN-SWNTs can be dramatically modified.

Recent HRTEM microscopes equipped with an objective  $C_s$  corrector make possible to get direct images of the atoms building the graphitic lattice [51] and therefore to determine not only the helicity but also the defects present in the tube wall such as pentagons. With this new generation of microscopes, the location of heteroatomic atoms might possible in a near future. By this way, it would be possible to know whether doping atoms such as B or N are simply substituted to a C atom in the graphitic network or adopt another atomic configuration involving vacancies or pentagons, or implying a local deformation of the network.

In any case, whatever the instrumental capability of the microscope, the measurement of the nanotube helicity via HRTEM is difficult for three main reasons. First, HRTEM image features are very sensitive to the orientation of the tube with respect to the electron beam and a careful control of the tube orientation cannot always be achieved. Second, the contrast of the image is very low. The contrast related to the zigzag configuration shown in Fig. 3 is a very peculiar situation since it is particularly strong and can easily be detected. This is not the case for chiral and

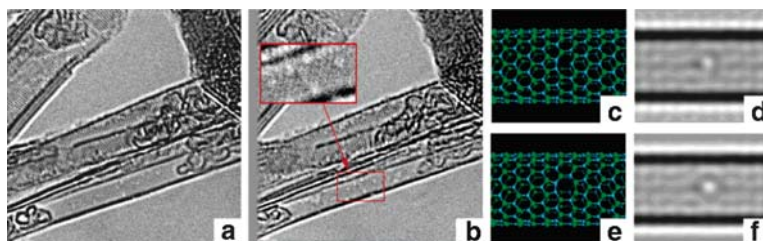


**Fig. 4** (a, b) Two HRTEM images of a bundle of boron nitride nanotubes taken after irradiation times of  $t = 0$  s and  $t = 20$  s. (b) This shows the appearance of single bright spots on the lower tube of the bundle associated with a small decrease in the tube diameter. As already shown in the case of carbon, such bright spots can be interpreted as the signature of point defects such as single vacancies. (c, e) Relaxed structures corresponding to single boron vacancy (c) and BN divacancy (e) for a (14,0) tube. (d, f) Corresponding HRTEM simulated images. Reprinted from [50], with permission from the American Chemical Society

armchair configurations. Finally, even if technically possible, the complete determination of the structure via HRTEM is restricted to individual tubes. In this context, ED provides an alternative to perform such kind of studies. In fact, ED is the most direct and powerful approach for determining the atomic structure geometrically characterized by two parameters (diameter and chirality) and the  $(n, m)$  indices of a given tube, whatever its chirality, as we shall see later. It is worth mentioning, as shown by Lambin et al., that BN and C nanotubes exhibit the same diffraction patterns, except for possible small variations in the diffraction intensities [52]. That is also the case for any heteroatomic nanotube as far as it is formed by a hexagonal-graphitic network.

Two different TEM techniques are available for recording an ED pattern (EDP): selected area electron diffraction (SAED or SAD) and parallel nanobeam electron diffraction (NB-ED). The main advantage of NB-ED is to reduce the specimen area illuminated by the electron beam below 50 nm, which is very useful (even necessary) for analyzing individual nanotubes. This latter technique was used for studying BN-SWNTs. As an example, Fig. 5a shows the bright field image of a BN-SWNT acquired under nanoprobe illumination and Fig. 5b shows the corresponding ED pattern. In this pattern, the intensity is discretely distributed on lines known as “layer-lines” [52]. Both tube diameter and chiral angle can be extracted from such pattern. First, the central line called the “equatorial line” consists in a series of intensity maxima whose spacing is directly equal to the inverse of the tube diameter. Second, spacing between other layers lines provides with an accurate determination of the chiral angle of the tube [53]. In the case of individual SWNTs, their chiral  $(n, m)$  indices are determined as the best value fitting experimental EDPs and simulated EDPs calculated using kinematical electron theory [49]. In the case of the BN-SWNT of Fig. 5, chiral angle is found to be equal to  $2.01^\circ$  and the tube diameter ( $d$ ) equal to 2.36 nm. The corresponding EDPs were simulated with these parameters, and the chiral indices were determined as the best fit between experimental and simulated EDPs. The BN-SWNT of Fig. 5 is thus unambiguously identified as a  $(29, 1)$  configuration.

The most complete diffraction study performed so far on heteroatomic nanotubes concern BN-SWNTs synthesized by laser vaporization [49]. As a result of the analysis

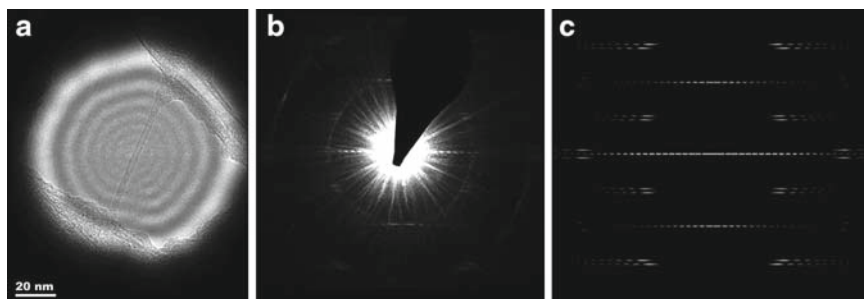


**Fig. 5** (a) Bright field image of a BN-SWNT taken under nano-beam illumination. (b) and (c) experimental and simulated EDPs of this BN-SWNT, respectively. These EDPs are assigned unambiguously to a  $(29,1)$  NT

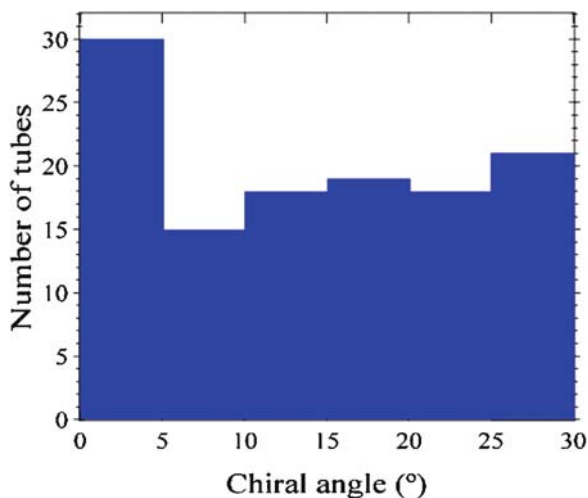


**Fig. 6** Number of boron nitride nanotubes as a function of the chiral angle, deduced from the analysis of the EDP. Reprinted from [49], with permission from the American Institute of Physics

of more than 100 NTs [49, 54], Arenal et al. found that 25% of BN-NTs have helicities between  $0^\circ$  and  $5^\circ$ , among which 12% are strictly zigzag, see Fig. 6. This result is well consistent with HRTEM observations and explains why zigzag or nearly zigzag configurations are easily observed in contrast to C-SWNTs [17, 18]. Concerning other kinds of heteroatomic tubes, the only available study of nanotubes' helicity distribution is, to our knowledge, that performed by Golberg et al. on (B–C–N)-SWNTs produced via carbothermal reaction. As for carbon analogs, they have not found any preferential atomic configuration [42]. We would like to notice that the impact of the presence of N or B atoms on the helicity of the tubes has not yet been studied.

As mentioned earlier, the knowledge of the atomic structure of nanotubes, in particular their helicity, is crucial. Thus we point out that the influence or the role that the heteroatoms (B, N or BN) could play on the helicity of the tubes is still an open question. As we will show later (in the section concerning physical properties), some Raman spectroscopy measurements and optical properties studies seems to indicate, for instance, that boron mediates the growth of smaller-diameter zigzag or near-zigzag nanotubes [55, 56].

### 3.2 *Transmission Electron Microscopy: Electron Energy Loss Spectroscopy*

EELS in a TEM is an essential and powerful technique to perform structural and chemical composition studies at the nanometer scale, making therefore possible the inspection of individual nanostructures. Two kinds of information can be basically



extracted from EEL spectra depending on the investigated energy loss range: core loss region gives access to the chemical and electronic structure of the material whereas low loss region ( $\leq 50$  eV) provides information on its electronic structure [57]. In this section, we shall discuss only the results coming from the exploitation of the core loss region. Analysis of the low-loss region will be presented in the next section and illustrated by the case of BN-SWNTs.

Basically EELS consists in the measure the energy losses of electrons resulting from the specific inelastic interactions of the electron beam with the specimen. Characteristic elemental edges of the core loss region correspond to the excitation in the material of an electronic transition from a core shell. These edges contain near edge fine structures with chemical information similar than those of X-ray absorption edges. Thus EELS in the core loss region provides informations on the chemical species present in the samples, on their concentration, and spatial distribution at a nanometer scale. Furthermore, nature of the chemical environment and chemical bonding can be extracted at least qualitatively from the fine structures near absorption edges (ELNES). As far as B–C–N nanotubes are concerned, these different informations require inspecting C-, N-, and B-K edges and their fine structures.

Spatially resolved (SR) spectroscopic information can be recorded using a scanning TEM (STEM) under a particular acquisition mode called spectrum-imaging (SPIM) or spectrum-line (SPLI) [58]. These modes consist in the acquisition of one EEL spectrum for each position of the probe scanning over a 2D region (SPIM) or a line (SPLI) at the surface of the nanotubes and nanoparticles. The spatial resolution of this technique is mainly limited by the size of the probe and in the case of a dedicated STEM instrument the size probe is namely around 0.5 nm. From the collection of spectra recorded in a SPIM (SPLI), one can extract 2D elemental maps (1D elemental profile) corresponding to the different elements present in the sample with a perfect spatial correlation. However, it is worth mentioning that such measurements must be done under particular illumination conditions to avoid any tube damage. In fact, the structure of heteroatomic C-NTs is in general very sensitive to the electron beam, and can be modified and get amorphous.

Energy-filtered TEM (EFTEM) mode is an alternative method for recording elemental maps, based on EELS. For both techniques (EFTEM and SPIM), the energy-loss processes are identical; the only difference between them is how the information is acquired. In EFTEM an elemental map is directly recording by selecting with an energy window, an energy range corresponding to a given core edge. If different elements are present in the sample, elemental maps should be captured serially.

All these capabilities have been extensively used as they are the only way to investigate locally the chemical structure of heteroatomic nanotubes and then to get some clues about their formation mechanism. The first demonstrative example is provided by BN-SWNTs. The use of a dedicated STEM, allowing to develop SR-EELS studies, was crucial to establish/proof that BN-NTs, synthesized by the laser vaporization technique, corresponded to a  $sp^2$ -bonded BN structure where boron and nitrogen were uniformly distributed in the tube wall according to a ratio equal to unity [18, 19]. These results are illustrated in Fig. 7. This figure shows a SPLI recorded across a BN-SWNT (bright field image in the inset of Fig. 7a) and

one EEL spectrum extracted from this SPLI where the fine structures of the boron and the nitrogen K edges are visible (Fig. 7b). Furthermore, the chemical composition of the various nanostructures accompanying the nanotubes in the samples has been examined in the same way [18, 19, 59, 60]. As boron was found to be present under various states, – namely B,  $B_2O_3$ , and h-BN – in these nanostructures, Arenal et al. developed a statistical analysis technique to extract, from EELS-SPIM, the spatial distribution of this element according to the nature of its chemical bonding. As a result, two kinds of boron-based nanoparticles could thus be identified: pure boron particle encapsulated at the tip of the nanotube and boron particles covered by a thin  $B_2O_3$  layer and encapsulated into a h-BN cage. The former case (particle encapsulated at the tip of the nanotube) is displayed in Fig. 8 where the chemical bonding maps of boron (boron pure (c) and BN ((d) and (e)) at the nanometer scale have been obtained [19, 60]. We shall see in the next section that these features were very valuable for understanding the growth mechanism of BN-SWNTs.

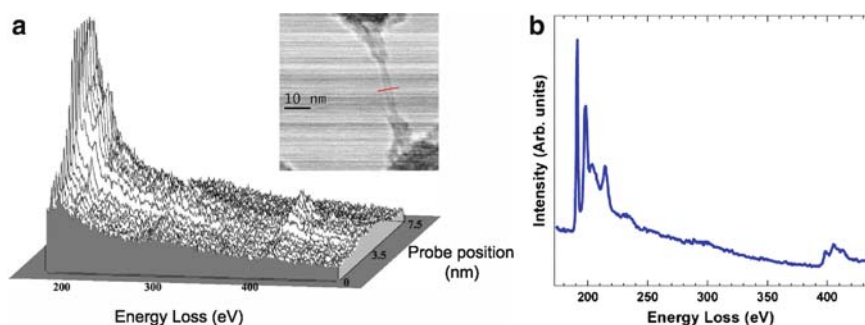


**Fig. 7** (a) Spectrum-line recorded across the BN-SWNT shown in the bright field image (inset). (b) EEL spectrum extracted from (a) showing the boron and nitrogen K edges. Figures from Arenal et al. [18]

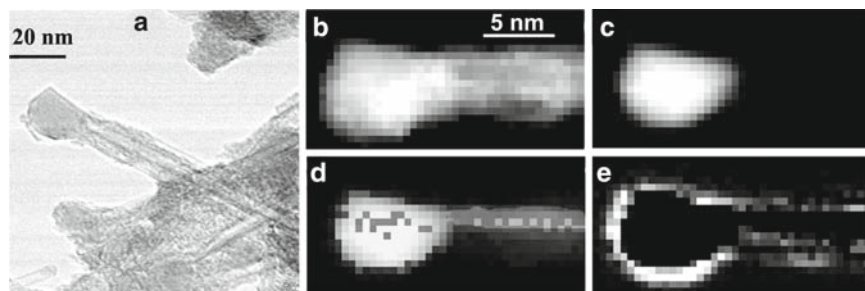


**Fig. 8** (a, b) Bright and HAADF images of a bundle composed by 2 BN-SWNTs, respectively. (c–e) NNLS maps of boron and boron nitride (d, e) for the two extreme orientations (electron beam perpendicular and parallel to the **c** axis), respectively. It can clearly be seen that the core boron particle surrounded by the boron nitride network. This figure is modified from Fig. 6 in Arenal et al. [19]

Furthermore, since h-BN is an anisotropic material, the fine structure of the B-K and N-K edges strongly depend on the orientation of momentum transfer ( $q$ ) with respect to the lattice [60, 61]. Thus the chemical bonding maps of the  $sp^2$  BN lattice of the two extreme orientations (the electron beam parallel and perpendicular to the anisotropic axis ( $c$ )), shown in Fig. 8d, e, provide an additional proff that BN-NTs consist in a  $sp^2$  bounded structure.

Determining the composition of doping element such as boron or nitrogen, its distribution in the carbon network and its atomic configuration is a very delicate and crucial question, especially in single-wall nanotubes, where the recorded EELS signals are always very low. Several studies have been performed on  $CN_x$ -MWNTs. Depending on the local N concentration which can vary from a 1–2 at.% to 30 at.% according to the synthesis technique, N is found to be simply substituted in the graphitic network or to display different local bonding environments reminding that of N in the pyridine and pyrrolic molecules [44]. Investigations of N-doped SWNTs synthesized by electric arc [12] and by laser vaporization [21, 23] have been both performed using SR-EELS on a STEM machine. For each tube inspected, the electron beam was probing a fragment of about 5 nm in length of the tubes. Figure 9 shows

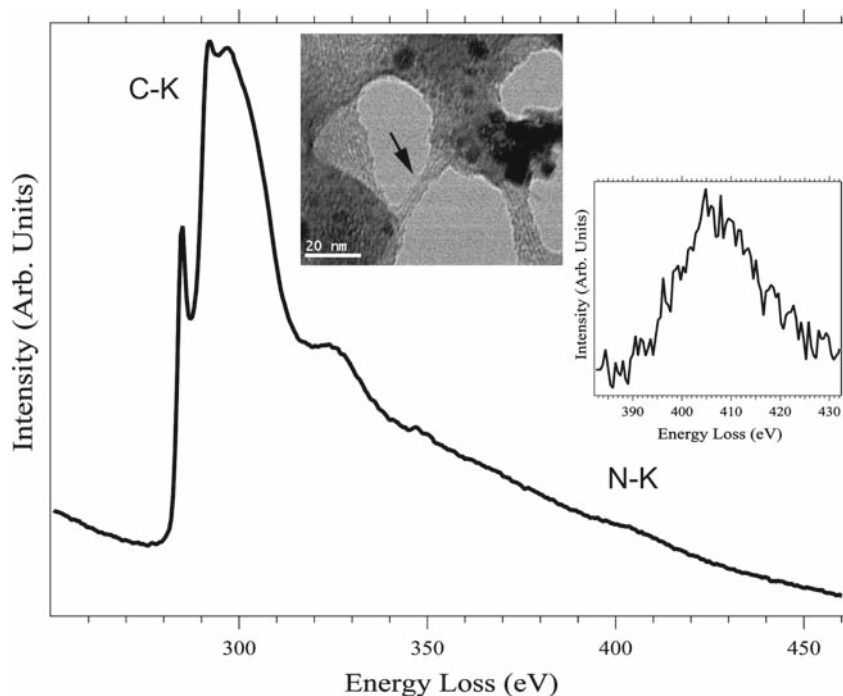


**Fig. 9** Electron energy loss spectrum recorded on the  $CN_x$ -SWNTs bundle shows in the bright field image (marked by an *arrow*). The EEL spectrum displays the C-K and N-K edges. The N-K edge is emphasized in the inset. The nitrogen content in these nanotubes is close to 1 at.%. This figure is modified from Fig. 2 in Hong et al. [23]

typical C-K and N-K edges recorded under these conditions on the NT bundle shown in the bright field image. Both kinds of tubes display remarkable structural similarities. From the intensity of N-K edge recorded on a statistical number of tubes, the nitrogen content was quantified to be around 1 at.%. From the C-K edge, it can be deduced that the nanotubes consist of a typical graphitic network with the typical  $sp^2$ -type bonding and that the tubes are very well graphitized [62]. The fine structure of the N-K edge is emphasized in inset of Fig. 9. It displays a triangular  $\sigma^*$  band at  $\sim 405$  eV, which is characteristic of  $CN_x$  materials. Two other weak features can be observed at  $\sim 398$  and  $\sim 402$  eV, respectively. They could be attributed to the  $\pi^*$  states of the pyridine-like and graphitic-like configuration, respectively, as commonly reported in the literature for  $CN_x$ -MWNTs [12]. It should be emphasized that the same features are observed on XPS spectra [45]. However, the detailed identification of N local environment is far from being complete. The correlation commonly made with pyridine-like and graphitic-like configurations is only indicative of the fact that N displays two kinds of chemical bonding when embedded into a carbon wall. For a more quantitative description of the N-C chemical bonding, it would be necessary to correlate experimental data with accurate theoretical calculations, which is a complex piece of work and has not been achieved yet.

In contrast to  $CN_x$  SWNTs, there is a very few data concerning B doped C-SWNTs. Gai et al. used SR-EELS to study B-doped carbon nanomaterials samples synthesized by laser ablation [26]. The authors pointed out the absence of B in the bundles of C-SWNTs for samples produced from targets containing from 1.5 to 10% of boron. Nevertheless, they detected an unexpected presence of N in a sample synthesized from a target containing 2.5% of B, as well as nanoparticles of  $B_4C$  in a sample synthesized from a target containing 10% of B.

We finally consider single-wall nanotubes made of C, B, and N. Via the combination of HRTEM and SR-EELS on a STEM analysis, Enouz et al. [21] showed that B-C-N nanotubes, synthesized by the laser vaporization technique, were well made of carbon, boron, and nitrogen located at the vertices of a honeycomb lattice. Nevertheless, these authors also demonstrated that the distribution of these elements was not uniform. Chemical maps extracted from EELS spectra (Fig. 10a, b) reveal that boron and nitrogen segregated from carbon to form small BN domains (1–2 nm long) embedded in the carbon network. Furthermore, existence of BN  $sp^2$  bonds is confirmed by the fine structure of B-K and N-K edges (Fig. 10c), which are very similar to those encountered in pure BN tubes (Fig. 7). The BN-entities are a few nanometer square and replace not more than 10 at.% of C locally and 5 at.% in average within a given rope, as attested by a close comparison of intensities of C-K edges in pure carbon parts of the tube and in BN-containing parts (Fig. 10). This particular microstructure is expected to result from the phase separation existing at equilibrium in bulk systems between h-BN and graphite. Furthermore, N was found to be in excess with respect to B, as a fingerprint of the fact that C-B bond is energetically less favorable than C-N bond. Therefore, BN domains are expected to be surrounded by a nitrogen shell to minimize C-B bonds [21]. This property of the bulk B-N-C system explains why the BN-C segregation is not restricted to the tubes obtained by the laser vaporization technique but has been also found in several (B-C-N)-MWNTs

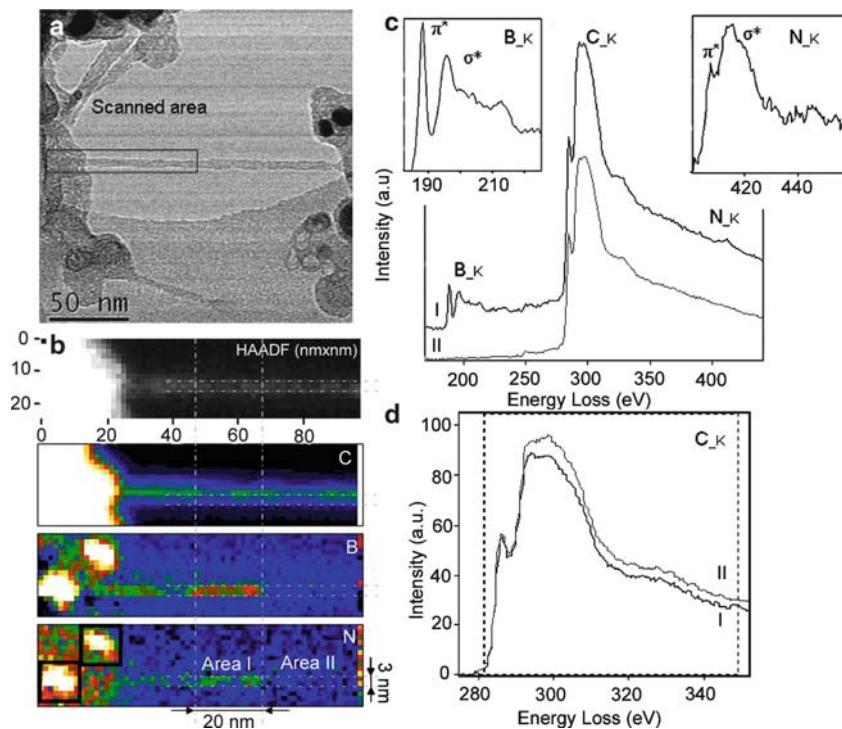


**Fig. 10** (a) Bright-field image of nanotubes rope of 4–5 nm large. The rectangle shows the region analyzed by EELS. (b) HAADF image of the scanned area of  $98 \times 24 \text{ nm}^2$  and the relative intensity chemical maps of C, B, and N elements. The intensity of the signal varies from *dark/blue* (poor signal) to *white/red* (high signal) colors. (c) EEL spectra I and II are defined as the sum of Areas I and II, respectively. Near edge-fine structures of B and N–K edges are shown in the inset. (d) Background subtracted CK-edges of I and II areas. Reprinted from [21], with permission from the American Chemical Society

synthesized by different techniques (for a review see Enouz et al. [63]). It has also been observed in B–C–N SWNTs issued from a carbothermal treatment of C–SWNTs by Golberg et al. [42]. Nevertheless, it seems to be not observed in B–C–N tubes synthesized by HF-CVD by Wang et al. [31]. In fact, these authors reported that in all the (B–C–N)-SWNT bundles that they investigated, boron, carbon, and nitrogen elements were homogeneously distributed within the nanotube shells. This is observed in Fig. 11 where EFTEM images of (B–C–N)-SWNT bundles reported by Wang et al. are displayed [31]. It should be, however, pointed out that conclusions in this study are not based on spatially resolved EELS but on EFTEM. Therefore, one cannot exclude the existence of segregation at a nanometer scale as that found in the laser-made tubes [21]. This example enlightens the difficulty of a faithful identification of heteroatomic tube structure.

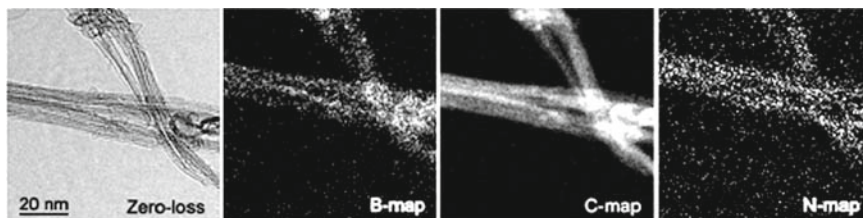


**Fig. 11** (a) Zero-Loss image of bundles of (B–C–N)-SWNTs. Elemental maps of boron (b), carbon (c), and nitrogen (d) obtained using EFTEM from the bundles displayed in (a). Reprinted from Wang et al. [31], with permission from the American Chemical Society

### 3.3 Growth Mechanism of BN- and (B–C–N)-SWNTs

Even if for undoped C-NTs the way in which they are formed is not exactly known, and their growth mechanism is still a subject of controversy (there are different models to explain the formation of these C-NTs [7]), in comparison with those C-SWNTs, relatively little is known about the growth of heteroatomics SWNTs. The main factor limiting these studies is obviously the lack of samples.

Blase et al. studied the growth mechanism of  $CB_x$ -SWNTs via first-principles static calculations and dynamical simulations [64]. These authors reported that zigzag or near-zigzag nanotubes are preferentially grown upon boron incorporation. In fact, they showed that the energy for boron staying at the growth edge of a zigzag nanotube is lower than that at an armchair tube. They established that for the zigzag configuration, boron atoms act as a surfactant during growth, preventing for tube closure.

For BN-SWNTs, Lee et al. [17] and more recently Arenal et al. [19] have proposed a phenomenological model to explain their formation and growth. Arenal et al. [19] combined the HRTEM, ED, and SR-EELS studies with the analysis of the synthesis conditions and of the phase diagram to identify the fundamental factors determining the nanotube growth mechanism [18, 19, 49, 59, 60]. These experiments strongly support a root-growth model, which involves the presence of a droplet of boron. This phenomenological model considers the solubility, solidification, and segregation phenomena of the elements present in this boron droplet. In this model, sketched in Fig. 12, the authors distinguish three different steps as a function of the temperature: (1) formation of the liquid boron droplet from the decomposition of different boron compounds existing in the hexagonal BN target, (2) reaction of these boron droplets with nitrogen gas present in the vaporization chamber and recombination of these elements to form BN, and (3) incorporation of the nitrogen atoms at the root of the boron particle at active reacting sites that achieves the growth of the tube. Moreover, the authors pointed out that the oxygen is a poison of the growth of BN-SWNTs as it has been also confirmed by recent works developed by Dorval et al. [65]. Using first-principles molecular dynamics simulations, Blase et al. [66] showed that armchair BN-SWNTs can develop an ordered metastable edge, and thus may grow uncatalyzed.

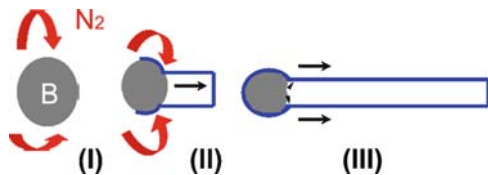


**Fig. 12** Sketches showing the phenomenological model for the formation of the tubes. The model is as follows: (i) formation of boron drops from the decomposition of h-BN and from the boron oxide of the target; (ii) reaction of these drops of boron with the nitrogen injected into the reaction chamber and with nitrogen coming from the h-BN target. Recombination of the boron and nitrogen to form boron nitride; (iii) incorporation of the nitrogen atoms at the root of the boron particle that achieves the growth of the tube. This figure is modified from Fig. 8 in Arenal et al. [19]

On the contrary, zigzag BN-SWNTs rapidly evolve into an amorphous-like tip, preventing further growth. These authors found that this difference originates in the  $\approx 1.6$  eV average frustration energy associated with N–N or B–B bonds when compared with B–N bonds. These results seem to be in agreement with the experimental ones developed by Arenal et al., described earlier, where these authors found that (1) BN-SWNTs produced by laser vaporization were mainly zigzag [49] and (2) that a boron particle is involved in the synthesis of these NTs [19]. This B particle plays a double role of growth support and reactant. Furthermore, from these theoretical and experimental studies, we can deduce that this boron particle could be the origin of the stabilization of zigzag BN-SWNTs.

Concerning (B–C–N)-SWNTs synthesized by the laser vaporization approach, Enouz et al. have proposed a phenomenological model for their growth mechanism already mentioned in the previous section [21]. They considered that the formation of these patterned tubes is a direct consequence of the segregation phase existing at equilibrium between graphite and h-BN. Their TEM observations support a growth mediated by a liquid-like phase as in the V-L-S model invoked in the formation of C-SWNTs. Furthermore, the sequence of BN domains alternating with long C segments along the tube axis results from a phase separation at the solidification front. The structure of these (B–C–N)-SWNTs appears to be governed by thermodynamical properties of the C–B–N system, although its formation is due to particular kinetic conditions.

## 4 Physical and Chemical Properties

### 4.1 Electronic Properties, Electronic Transport

The electronic properties of these heteroatomic NTs are widely discussed in the chapter by Blase and Chacham. Here we present some of the most significant studies done on these tubes to enlighten the properties of these heteroatomic SWNTs and

their potential applications. It is worth mentioning that, as we pointed out in other sections of this chapter, to date, there are only very limited studies on the electronic properties/transport of doped/heteroatomic SWNTs. Thus, further studies are very necessary in this field for improving their knowledge.

The substitution of carbon atoms in the hexagonal network of a C-NT by boron and nitrogen modifies the density of states (DOS) of the carbon nanotube by introducing additional electron states [67]. Whether these will be electron-donor states, electron-acceptor states, or neither of these two, depends crucially on the local bonding arrangements of the hetero atoms as shown for instance by Latil et al. [68]. These authors performed tight-binding and ab-initio calculations on B and N-doped C-NTs and reported that the mean free path of charge carriers decreases (increases) linearly with dopant concentration (tube diameter) at low doping levels [68]. These authors also show that the electron conduction could also be enhanced if for small amount of dopants  $\leq 0.5\%$ .

We would like to point out that from a theoretical point of view, most of the studies carried out only consider graphite-like substitution of boron and nitrogen atoms into the carbon in the honeycomb lattice of a C-SWNT [68]. Thus we consider that further works considering other configurations, for instance pyridine-like or pyrrole-like in the case of  $CN_x$ -SWNTs must be developed to investigate all these systems, which are also found in experimental studies [23]. In this way, the studies of Blase et al. are an exception to this assessment [69, 70]. In fact, these authors, using tight-binding and ab-initio calculations, have demonstrated that pyridine-like N structures in N-doped C-NTs are responsible for introducing donor states close to the Fermi level ( $\sim 0.2$  eV) [69, 70].

For  $CN_x$ -SWNTs, on the one hand, Villalpando et al. studied their transport properties via electrical conductivity measurements [29]. They concluded that nitrogen (at low concentrations) enhances the density of states at energies close to the conduction band edge. On the other hand, Krstic et al. have investigated the charge transport properties of individual nitrogen doped C-SWNTs synthesized by arc discharge [71]. These authors have demonstrated that n-type conduction can be achieved by nitrogen doping. They showed that between the two most probable atomic configurations of N in C-NTs (graphite-like and pyridine-like) only  $CN_x$ -SWNTs with sufficiently high concentration of graphite-like nitrogen bonding configuration can be n-type conductors. Moreover, Krstic et al. also suggested that pyridine-type nitrogen bonding configuration in the honeycomb lattice is the main contributor to the electric dipole scattering process observed in the charge transport [71].

Superconductivity has been observed experimentally in C-SWNTs (individual or forming bundles) and C-MWNTs via low-temperature (below 15 K) transport measurements [72–75]. Very recently, Murata et al. have reported the observation of the Meissner effect at  $T_c = 12$  K in thin films of  $CB_x$ -SWNTs synthesized via laser vaporization technique [76]. These authors pointed out that the Meissner effect was very sensitive to the degree of uniformity of the thin film and that optimizing the control of the deposition of the films higher  $T_c$  values (between 30 and 40 K) could be reached.

Concerning BN-NTs, as we mentioned earlier, Blase and Rubio et al. performed first principles calculations demonstrating that these NTs are insulating and that



this gap is nearly independent of tube diameter, chirality, and number of tube walls [2–4]. More precisely, calculations of the band structure, done within the density Functional Theory (DFT) in the GW quasiparticle approximation, predicts an indirect gap equal to 5.95 eV and a direct one equal to 6.47 eV [4]. Experimentally, transport measurements have been performed by Radosavljevic et al. on BN-SWNTs, which could confirm the existence of a large band gap [77]. Nevertheless, to date, no faithful experiment has been performed to get direct or indirect information on their electronic structure as we shall see in the next sections. In particular, the large gap and huge Stark effects have been shown to prevent one to measure the local density of state and the gap by scanning tunneling spectroscopy [78, 79].

## 4.2 *Optical Properties*

Nanotubes are promising candidates for nanoscale light-emitters and many other optical applications [7]. In the case of pure C-NTs, these applications are especially focused in the infrared (IR) wavelength region having an interest for, for instance, optical communication. In this wavelength region, C-NTs exhibit indeed a saturable absorption effect. For doped N-SWNTs and B-SWNTs, we should mention the lack of studies of their optical properties, even if these nanotubes are expected to be also remarkable as Lim et al. pointed out [80]. These authors showed that  $CN_x$ -NTs can be used in saturable optical absorber devices.

Optical absorption spectroscopy is a widely employed technique for the characterization of C-NTs. It provides indeed with the optical transitions occurring between van Hove singularities of the valence and conduction bands in the density of states, which closely depend on their metallic or semiconducting character and on their diameter [7]. For doped C-nanotubes, it is therefore a rapid and easy way to probe a doping effect on their electronic structure. Borowiak et al. carried out optical absorption measurements on B highly doped C-SWNTs [81] produced by substitutional process from undoped C-SWNTs. Their results suggest that the substitution process leads to preferential boron substitution of the semiconducting NTs. Furthermore, these authors also found that the formation of a new acceptor band in the semiconducting NTs.

More recently, Li et al. [56] have reported optical measurements on  $CN_x$ -SWNTs and on (B–C–N)-SWNTs. These authors have demonstrated that the incorporation of B and N in the network of C-SWNTs have an influence in their emission properties as well as in their structure (they observed modifications in the helicity and the diameter distribution of the NTs, see also later the description of their Raman results on these SWNTs [55]). In fact, the presence of nitrogen significantly affects the emission properties of these nanotubes, causing a shift in the dominant emission to lower energies. The authors consider that this shift could be due to changes in the bundling structure of the nanotubes in solution since for individual NTs, they observed very small changes.

For BN-NTs, their wide band gap implies to undertake optical measurements in the UV range. Lauret et al. have performed the very first optical absorption experiments

on partially purified films of BN-SWNTs and have shown the existence of electronic transitions between 4.4 and 6.2 eV [82]. These transitions not only confirmed the existence of a large band gap in these structures but also were suggested to be associated to excitonic effects. Although far from being understood from this experiment, this result has stimulated an intense theoretical and experimental research effort within the last three years.

From the theoretical point of view, as discussed in detail in the chapter by Blase and Chacham and the chapter by Wirtz and Rubio, strong excitonic effects are expected to occur in insulating structures such as BN. Very recent *ab-initio* calculations of the dielectric function have been performed by solving a Bethe-Salpeter equation for taking into account Coulomb electron-hole interactions. They have shown the existence of excitons of large binding energy in both bulk h-BN and nanotubes [83–87]. According to these calculations, the first mode of the imaginary part of the dielectric function, which is the quantity measured in an optical absorption experiment, corresponds to a Frenkel exciton in both materials with a binding energy equal to 0.72 eV for h-BN and to 2 eV for a (8,0) BN-SWNT [83–87]. As a result, localized excitons (Frenkel type) are predicted to occur in h-BN at energies equal to 5.78, 5.82, and 5.85 eV. Both the existence of these excitonic emissions and their energies have been very recently confirmed by photoluminescence and cathodoluminescence experiments in h-BN [88, 89]. Same luminescence behavior has also been found to occur in large (with a diameter ranging from 20 to 50 nm) BN-MWNTs [89, 90]. Unfortunately, due to instrumental difficulties, such measurements could not be performed yet on BN-SWNTs.

The unique optical experiment done, to date, on individual and isolated BN-SWNTs is the study of their dielectric response in EELS. As we mentioned earlier, the study of the EELS low-loss region provides direct access to the dielectric properties of a material as it corresponds to the excitation of electronic states close to the Fermi level of the material. The physical phenomenon of EELS in this energy region involves excitations of valence electrons (collective plasma oscillations and/or interband transitions), which defines the structure of band gap for the case of semiconductors or insulating materials. Recently, Arenal et al. [91, 92] studied the electronic structure of isolated and bundles of BN-SWNTs (synthesized via laser vaporization technique [18, 19]) using such approach. The experiments were performed on a STEM dedicated EELS microscope displaying simultaneously a high spatial and a good spectral resolutions. The spectra were recorded employing SPLI acquisition mode [58]: 40–60 spectra were acquired for each probe position following a line across the tube. To disentangle the inelastic signal at low energy from the tail of the ZLP, a deconvolution procedure was applied in combination with a subtraction operation of the zero loss peak (ZLP) [93]. All these results were interpreted using the classical continuum dielectric theory [94]. This model is based in a strong hypothesis: locally the dielectric properties of a nanoobject can be described by the macroscopic dielectric tensor of the related anisotropic bulk material (h-BN in the case of BN-NTs). Figure 13a shows a bright field image of a BN-SWNT, and Fig. 13b displays an EEL spectrum recorded on this tube. This spectrum displays two groups of modes, a first one in the 6–9 eV range and a second one centered at

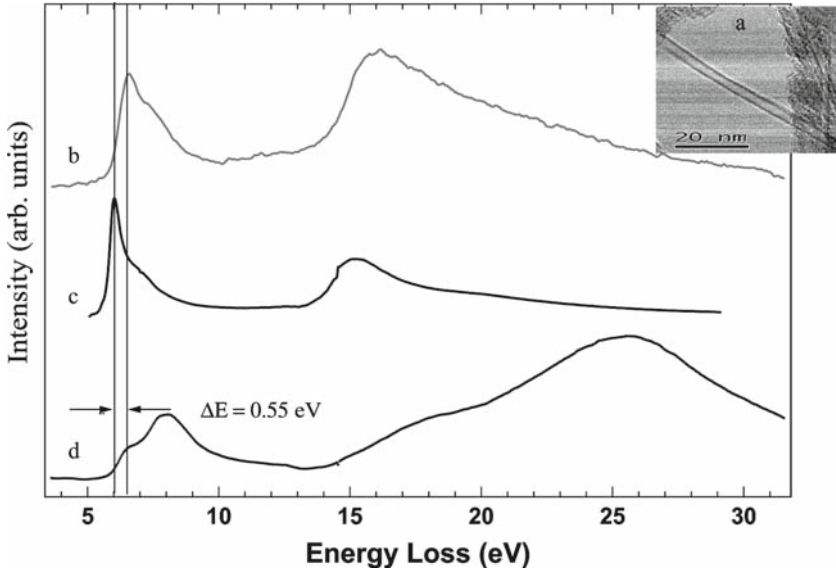


**Fig. 13** (a) Bright field image of a BN-SWNT. (b) Experimental EEL deconvoluted spectrum for the BN-SWNT of (a). (c) Imaginary part of the dielectric constant (in the plane component) of h-BN extracted from the bulk loss spectrum (d). Low-loss spectra recorded by Arenal et al. [18, 91]

16 eV. Figure 13c shows the imaginary part of the dielectric constant of h-BN for an orientation where the momentum transfer is perpendicular to the  $c$ -axis ( $\text{Im}(\epsilon_{\perp}(\omega))$ ). This was obtained after a Kramers–Kronig analysis of an EEL spectrum acquired in a highly purity thin foil of h-BN, Fig. 13d, and it is in agreement with the experimental dielectric constants published in [95, 96]. The high similarity between the spectra corresponding to the NTs and this curve indicates that the different modes of the NT's spectra can mainly be attributed to the  $\text{Im}(\epsilon_{\perp}(\omega))$  contribution. Figure 14 displays a series of deconvoluted spectra recorded scanning the probe from the vacuum to a BN-SWNT. Such spectra contain the signature of surface modes excited in a near-field geometry where the electron beam is focused at an aloof geometry of the NT and does not intersect with it. In this geometry and for a SWNT, it has been shown [97, 98] that the energy loss suffered by the incident electron is proportional to the imaginary part of the polarisability and can be written as a function of  $\text{Im}\left(\epsilon_{\perp}(\omega) - \frac{1}{\epsilon_{\parallel}(\omega)}\right)$  where  $\epsilon_{\perp}(\omega)$  and  $\epsilon_{\parallel}(\omega)$  are the in-plane and out-of-plane components of the dielectric tensor of a planar h-BN sheet, respectively. As the onset of the spectrum mainly reflects the contribution of  $\text{Im}(\epsilon_{\perp}(\omega))$ , the value of the optical gap of BN-NTs can be deduced, as shown in Fig. 14b. This value is found to be equal to  $5.8 \pm 0.2$  eV for BN-SWNTs with different diameters ranging from 1.5 to 3 nm as well as for BN-MWNTs containing between 2 and 4 layers present together with BN-SWNTs in the samples [91, 92].

The interpretation of this result is not straightforward. According to the recent theoretical calculations and luminescence experiments, optical excitations are dominated

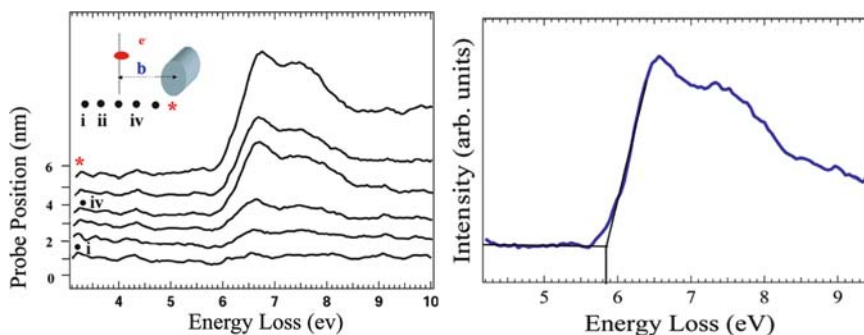


**Fig. 14** (a) Spectrum-line of a BN-SWNT. (b) Measurement of the optical gap of a BN-NT from one of the spectra extracted of (a). Low-loss spectra recorded by Arenal et al. [18, 91]

by excitonic recombinations in BN structures and the optical gap deduced from EELS spectra is related to these excitonic effects. Its value is obviously found to be very close to that found in h-BN and apparently does not reflect confinement effects expected in SWNT with respect to the bulk material. Furthermore, the binding energy of the excitons should depend on the radii and number of walls in a tube. It could be anticipated that the optical band gap should vary with respect of these quantities, which is not the case in low-loss EELS experiments. The reason behind this apparent discrepancy is that the enhanced Coulomb interaction between the electrons and the holes responsible for the large binding energy is also responsible for the increasing of the electron–electron correlation, which thus increases the value of the quasiparticle energy gap. These two effects compensate each other (the quasiparticle energy gap increases roughly in the same amount when the size of the object diminishes as the negative exciton binding energy), leading to an experimental value of the optical gap that remains roughly constant whatever the geometry of the tubes, and almost equal to that of the bulk h-BN. Luminescence experiments on individual SWNTs would be very necessary to study in detail their excitonic response.

All these results show that BN-NTs are wide band gap semiconductors with optical transitions in the UV range above 5.5 eV, which makes them a very promising material in optic applications as blue light and UV emitters.

### 4.3 Vibrational Properties

In the case of NTs, the study of lattice dynamics via Raman spectroscopy is widely employed, because it is a quick and nondestructive tool and because structural and electronic properties can be also probed [99, 100]. In fact, Raman spectroscopy on C-NTs is carried out under resonant conditions (the excitation wavelength must correspond to electronic transition of the investigated NTs that leads to resonance enhancement in the corresponding Raman cross section [101]). These conditions depend on the metallic semiconducting character of the tubes and on their diameter [99, 100].

Recently, several groups have investigated the lattice dynamics of B–C and C–N nanotubes. Although interpretation of these data is not straightforward and suffer from a lack of theoretical calculations, results indicate that tangential modes are sensitive to a substitutional doping. McGuire et al. recorded Raman spectra on  $\text{CB}_x$ -SWNTs, see Fig. 15, synthesized by laser ablation from targets containing boron concentrations ranging from 0.5 to 10% [102]. These authors found different effects in the Raman spectra due to the boron doping: (1) an increasing of the intensity of the D band upon increasing of boron dopant concentration. The D peak is an  $A_{1g}$  breathing mode of a sixfold aromatic ring, which is activated by disorder [101]. This observation is consistent with TEM observations where doped tubes are generally found to display corrugated layers. (2) A systematic downshift in the  $G'$ -band (this  $G'$ -band corresponds to a second order Raman feature and is composed by 2D-band phonons) frequency is observed whereas no change is observed for both the RBM (this mode is unique to SWNTs and corresponds to a mode where all the atoms constituting the NT vibrate in phase in the radial direction mode) modes and G-band (this band corresponds to a bond-stretching vibration of a pair of  $sp^2$  sites). This redshift is attributed to the weakness of C–B bond compared with C–C bond. (3) A nonlinear variation in the RBM and  $G'$ -band intensities is attributed to shifts in resonance conditions in the doped tubes.

Borowiak et al. measured vibrational properties of B doped C-SWNTs by IR absorption spectroscopy [20]. As shown in Fig. 16, they observed three different bands at  $807\text{ cm}^{-1}$ , a broad shoulder at  $1,050\text{ cm}^{-1}$ , and a stronger peak at  $1,385\text{ cm}^{-1}$ . The broad mode at  $1,050\text{ cm}^{-1}$  corresponds to typical boron carbide related phonons. The two other modes are shifted to lower energy with respect to the corresponding peaks in their carbon analogs, the redshift being again attributed to the weakness of B–C bonds.

Raman results obtained by Villalpando-Paez et al. on N-doped C-SWNTs produced by an aerosol-assisted CVD method [29] are qualitatively similar to B doped C-SWNTs. These authors found that upon increasing the N content, the growth of large diameter tubes is inhibited. Furthermore, from the intensity ratio of D and G peaks, they also concluded that the amount of point defects present in the sample increases approximately linearly as a function of nitrogen precursor concentration. Raman spectroscopy measurements carried out by Wiltshire et al. on  $\text{CN}_x$ -SWNTs and (B–C–N)-SWNTs seems to indicate that boron mediates the growth of smaller-diameter zigzag or near-zigzag nanotubes [55].

A complete section of the chapter by Wirtz and Rubio is devoted to the compilation of the theoretical description of the lattice dynamics of BN-NTs. Here, we will briefly present the main results of these calculations and discuss the only few works developed in this field. The phonon frequencies of BN-NTs were calculated by Sanchez-Portal and Hernandez [103] using tight-binding calculations and Wirtz et al. [104] by first principles calculations. Both groups found good agreement between a zone-folding approximation (within zone folding the G point vibrations of a nanotube originate from non-G point vibrations of h-BN) and a full calculation for several BN nanotubes; similar conclusions were drawn from a valence shell model from the calculations done by Popov [105]. Thus to model and understand the properties of BN

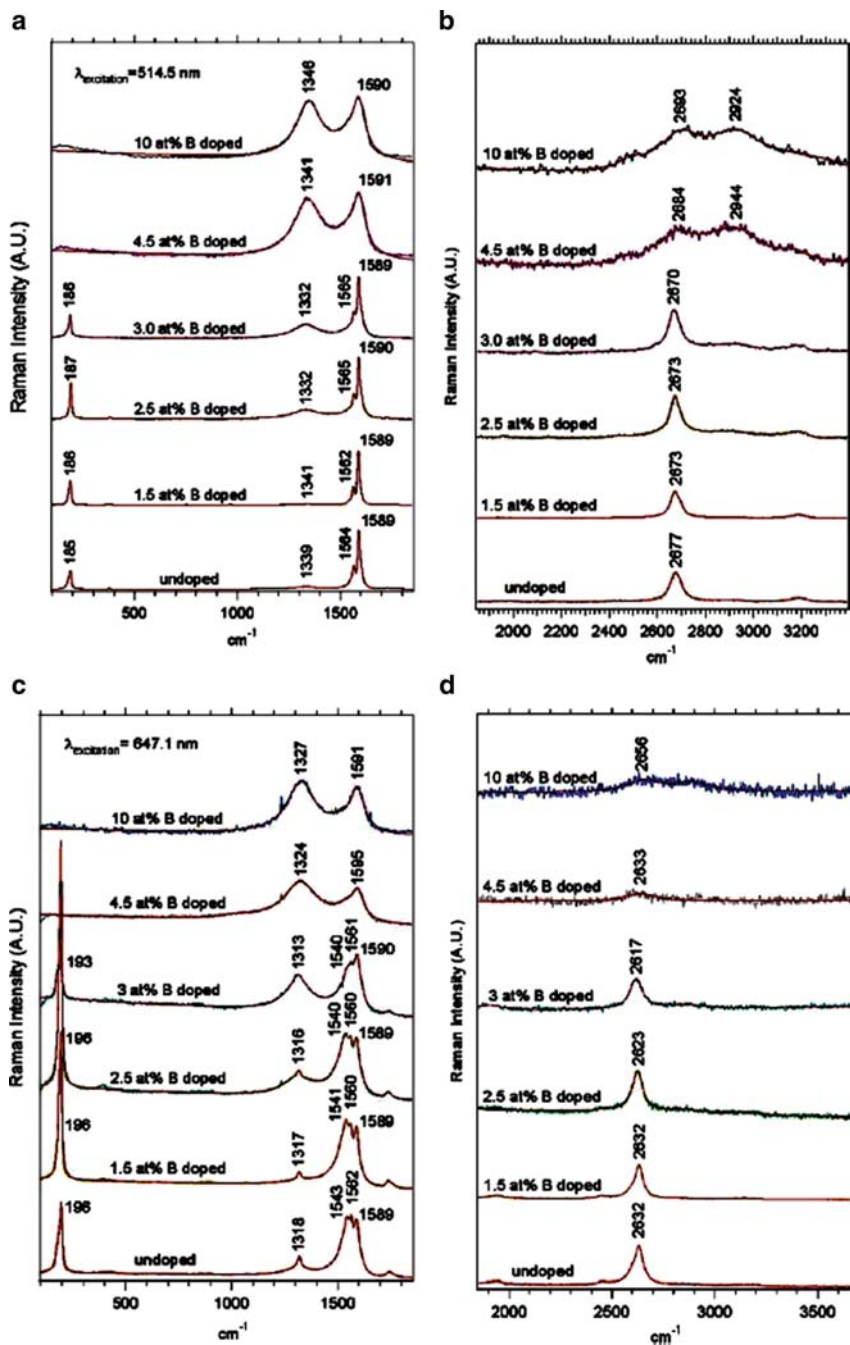
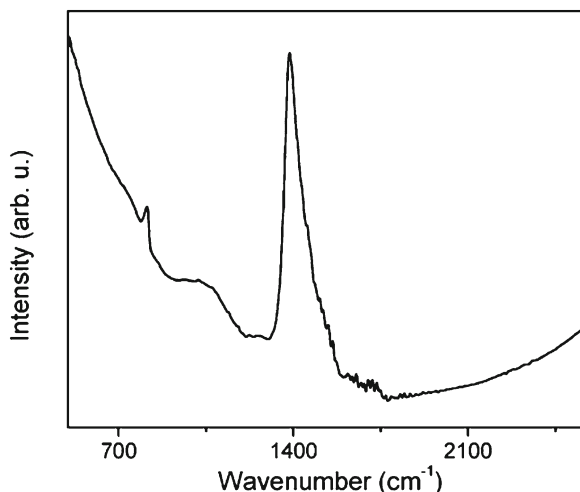


Fig. 15 (a, c) First-order and (b, d) second-order room temperature Raman spectra of products generated from targets with indicated boron concentrations. All Raman spectra were excited using the 514.5 nm (a, b) and 647.1 nm (c, d) excitation energies. Each spectrum in the figure was normalized to the tangential G<sup>+</sup> band intensity. Reprinted from [102], with permission from Carbon



**Fig. 16** Infrared spectrum recorded on B-doped carbon nanotubes sample. Reprinted from [20], with permission from Chemical Physics Letters

nanotubes, a better knowledge of the phonon dispersion of hexagonal BN is highly desirable. In this sense, very recently, Serrano et al. compared the results of the phonon dispersion relation of bulk h-BN, measured by inelastic X-ray scattering and obtained from ab-initio calculations [106]. These studies showed an excellent agreement between the experimental data and the calculations.

Experimentally, lattice dynamics of BNs are mainly investigated by IR spectroscopy, since it is very sensitive to the polar BN bonds [107]. However, this technique has limitations. The substrate supporting the sample has to be either transparent or not highly reflective. Raman spectroscopy is rarely used for BN because of its lower sensitivity, as shown by Reich et al. [108]. Arenal et al. have demonstrated that, as for C-SWNTs, no Raman signal can be detected for BN-SWNTs if excitation conditions are far from resonance with respect to electronic transitions [109]. Knowing that the electronic gap is about 6 eV, this requires to perform Raman spectroscopy in the UV range with excitation wavelengths as close as possible as 200 nm. Arenal et al. succeeded in performing micro UV-Raman measurements at excitation wavelength equal to 229 nm (5.41 eV) on BN-SWNTs [109]. It is worth mentioning that low frequencies radial breathing modes of BN-NTs, which are the only unique and reliable signature of SWNTs, cannot be detected in these UV Raman measurements because the notch filters employed in these spectrometers have a cut off frequency of  $500\text{ cm}^{-1}$ . The Raman spectra, shown in Fig. 17, have been recorded on specific areas well characterized by TEM and marked on the grid prior to the Raman measurements. Figure 17 displays the UV Raman spectra measured at the same power, on two different areas of the TEM grid (Fig. 17a, b), respectively, and on a h-BN reference sample (Fig. 17c). Inset of Fig. 17 displays TEM micrographs in two different areas: the first one (Fig. 17a) contains a high density of SWNTs, whereas the second one (Fig. 17b) is a platelet of h-BN of micrometer size, expelled

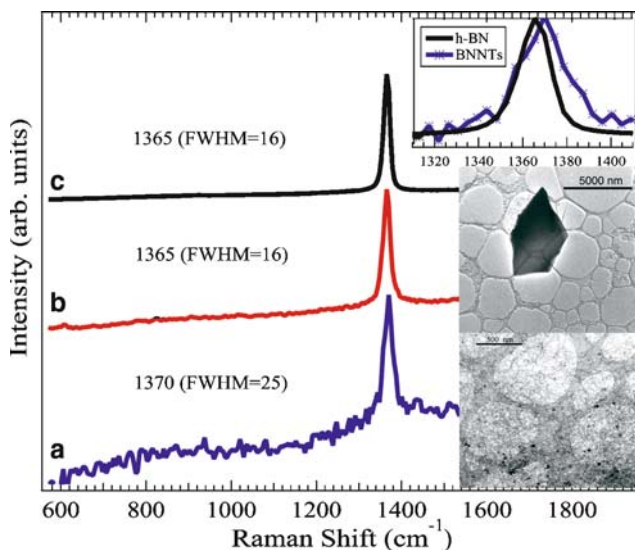


**Fig. 17** Raman spectra excited at 229 nm on (a) a BN-NTs rich area in a standard TEM carbon grid, (b) a particle of h-BN on the same grid [see insets] and (c) highly crystalline powder h-BN. This figure is modified from Fig. 3 in Arenal et al. [109]

from the target during the laser vaporization synthesis. Only one peak at around  $1,365\text{ cm}^{-1}$  is visible in all the UV-Raman spectra. For h-BN, this mode is the  $E_{2g}$  mode at  $1,365\text{ cm}^{-1}$ . The recorded spectrum on the NTs area (Fig. 17a) also displays a peak in this frequency range, but the band differs from h-BN in two ways as emphasized in the inset of Fig. 17. First, the peak is shifted to higher frequencies by  $5\text{ cm}^{-1}$ , second, it is broadened. This behavior is intrinsic of the NTs-containing areas. The peak at  $1,370\text{ cm}^{-1}$  corresponds to the  $A_1$  tangential mode of the NTs. According to ab-initio calculations (see the chapter by Wirtz and Rubio), the increase in phonon frequency compared with that of bulk hexagonal BN is attributed to a hardening of the  $sp^2$  bonds in the BN tubes, the difference being due to the inter-plane interaction in h-BN. Finally, these experiments attested that Raman scattering in the UV at 229 nm excitation provides preresonant conditions, confirming that the electronic gap of BN-SWNTs is larger than 5.5 eV.

#### 4.4 Mechanical Properties

It is now well established that carbon undoped nanotubes are unique nanostructures with remarkable mechanical properties. Single-walled C-NTs are very strong and resist to fracture under extension, having high elastic moduli [7]. Another advantage of nanotubes is their behavior under compression. Unlike carbon fibers, which are brittle under compression, C-NTs form kink-like ridges that can elastically relax



when the stress is released. Thus, it is very interesting to prove these potential and very attractive properties. However, as far as we know there is none experimental study on these properties in heteroatomic SWNTs.

Theoretically, Hernandez et al. [110] calculated, using a tight-binding model, the Young modulus of C and BN-NTs. These authors found that the Young modulus of BN-NTs is lower than that of the C-NTs and that its value depends on the NTs' diameter. In the case of BN-NTs, this value varies between 0.837 and 0.912 TPa, which was about 0.8 times that of C-NTs, for diameters ranging from 0.81 to 2.08 nm.

Nanotube axial stiffness, bending, and torsion dynamics of C- and BN-SWNTs have been studied by Vaccarini et al. [111]. They found that chiral tubes exhibit an interesting asymmetric torsional behavior with respect to left and right twist that is absent in armchair or zigzag tubes. Moreover, topological defects have been seen to modify slightly the mechanical response of the carbon network under an applied strain.

Dumitrica et al. [112], using a molecular dynamics model and ab-initio calculations in the DFT approximation, studied the dislocations that can be formed in BN-NTs under high tensions. In the same way, they noticed that BN-NTs possess a thermodynamic yield limit (critical strain and critical tension) higher than that of C-NTs. It confirms the results of their previous works [113], where Bettinger et al. had shown that BN-NTs have greater yield resistance than C-NTs.

Such exceptional mechanical properties of NTs are desirable for applications as for manipulating other nanoscale structures.

#### **4.5 *Electro-Mechanical Properties***

The existence of piezoelectricity in BN-NTs was predicted by Kral and Mele. This property is due to the polar nature of the B–N chemical bond and the geometric phase involving quantum confinement effect [114, 115]. The work by Nakhmanson et al. [116] confirmed these results via ab-initio calculations. Nakhmanson et al. showed that BN-NTs are excellent nonpolar piezoelectrics exhibiting higher strain response than polar polymers. Moreover, they showed that ideal noninteracting nanotubes are effectively nonpolar because of their intrinsic chiral symmetry, which leads to a total cancellation between the ionic and electronic polarizations. Breaking of this symmetry, as the case of interacting nanotubes in a bundle or by the effect of elastic distortions in a NT, induces spontaneous polarization fields that are comparable to those of wurtzite semiconductors (as zinc oxide (w-ZnO)). Thus BN-NTs have a great potential to be unique electromechanical components in micro and nanosystems.

#### **4.6 *Chemical Reactivity***

Compared with a graphene sheet, the chemical reactivity of a C-NT is enhanced as a direct result of the curvature of the C-NT surface. Carbon nanotube reactivity is directly related to the  $\pi$ -orbital mismatch caused by an increased curvature. Therefore,

a distinction must be made between the sidewall and the end caps of a nanotube. For the same reason, a smaller nanotube diameter results in increased reactivity. Covalent chemical modification of either sidewalls or end caps has shown to be possible. In this way, due to the presence of the heteroatoms in the hexagonal network of doped C-SWNTs, these NTs are expected to be more reactive than the undoped counterparts. Thus, doped C-SWNTs are very good candidates for functionalization and the formation of polymer composites.

Using first principles calculations, Baierle et al. have investigated the electronic and structural properties of CO and NO molecules adsorbed on BN-NTs and carbon-doped BN-NTs [117]. Their results indicated that for nondefective nanotubes, small binding energies (around 150 meV) are obtained. When a carbon substitution impurity is present in the BN-NT, the binding energies were substantially increased and a chemical adsorption was observed. From the calculated band structures, Baierle et al. showed that the defect electronic levels inside the band gap were sensitive to the presence of the adsorbed molecules. The authors pointed out that this increasing of the functionalization capacity of the tubes due to carbon doping is an important mechanism to open up new possibilities for nanodevices applications [117].

Functionalization of BN nanotubes has been theoretically investigated [118] but it is only recently that a few chemical methods have been reported for MW BN nanotubes solubilization [119–121]. These functionalization methods are based on Lewis acid/base interaction between the functionalizing molecule and the nanotubes. Very recent experiments done by Maguer et al. have shown that they do not apply to BN-SWNTs, produced by the laser vaporization technique, because the acid/base interaction is not strong enough [122]. However, these authors have developed a versatile process, based on the strong affinity of nitrogen atoms of quinuclidine molecules for boron atoms of the nanotube network, which is able to solubilize both multi and SWNTs in different media.

## ***4.7 Hydrogen Storage***

Nanostructural materials, and particularly the nanotubes, are good candidates for hydrogen storage because of their cylindrical and hollow geometry and their nanometerscale diameters, having therefore large specific surfaces and a highly porous structure. These characteristics allow the storage of a liquid or of a gas in the inner cores through a capillary effect. Works developed on C-SWNTs showed that probably the semiconductor NTs are better for hydrogen adsorption. Considering the difficulties to develop the NTs sorting between semiconductors and metallic CNTs, the use of BN-NTs (all being insulators showing a large chemical and thermal stability) appears very promising. Experimentally, there are only recent promising works developed on hydrogen adsorption by BN-MWNTs synthesized by CVD by Ma et al. [123]. Jhi et al. [124] showed, using ab-initio calculations, that the binding energies of hydrogen on BN-NTs are 40% higher than CNTs, because of the polarity

of the B–N bond. This therefore suggests that BN-NTs could adsorb higher amount of hydrogen than C-NTs. More recently, Wu et al. [125] studied, via ab-initio calculations (under DFT approximation), the influence of a radial distortion of zigzag BN-NTs on the chemical adsorption of hydrogen. They observed that if this distortion is weak, H prefers to adsorb on the boron atom, which creates an acceptor state in the gap; nevertheless, if the deformation is large enough, H preferentially interacts with the nitrogen atom in the high curvature region of the radially deformed BN-NT and creates a donor state.

More recently, Zhou et al. have studied the atomic and molecular adsorption of hydrogen on B and N doped C-SWNTs by DFT calculations [126]. The authors found that the B-doping increases the hydrogen atomic adsorption energies both in zigzag and armchair nanotubes. However, the N-doping decreases the hydrogen atomic adsorption energies. In case of hydrogen molecular adsorption, both B and N-doping decrease the adsorption energies in SWNTs.

Zhang et al. have studied in detail the mechanisms for hydrogen dissociative adsorption and diffusion on N-doped (8, 0) C-NTs by carrying out DFT calculations [127]. These authors found that nitrogen doping considerably alters the catalytic effects of the carbon nanotube for hydrogen dissociative adsorption. This adsorption of hydrogen on the carbon nanotube is greatly enhanced, with the barrier substantially reduced to  $\approx 0.9$  eV. The differences in the barrier heights are explained by changes in the tube electronic structure.

Li et al. investigated hydrogen-decorated structures of C-doped (9, 0) BN-SWNTs using also DFT calculations [128]. They found that the doping effect of C-doped BN-NTs can be compensated by adsorption of H atom on the C sites. The adsorption energies for hydrogen atoms on different adsorption sites on BN-NTs and C-doped BN-NTs indicate that the most favorable configuration of the adsorption structures is a hydrogen atom adsorbed on the C site.

## 5 Summary and Conclusions

In this chapter, we have discussed the synthesis, atomic, and composition structures of heteroatomic (B-, N- and BN-doped carbon, and BN) SWNTs, as well as their physical and chemical properties. Almost incomplete, the present knowledge that we have from these different tubes, attests their interest for a wide range of properties and applications. In fact, these nanotubes are complementary, even more adequate for some potential applications, to their carbon counterparts. For instance, BN-NTs have a high potential for the applications in optics in the UV range, novel nanoscale sensors, actuators, and advanced nano-electro-mechanical systems (NEMS) with integrated electronic/optoelectronic functions as well as high-power, high-frequency, and high-temperature applications (generators, amplifiers, etc.). In the case of doped ( $B_xC$ ,  $CN_x$ , and B–C–N) SWNTs, their interest stems from the fact that they represent an efficient method for tuning the electronic properties offering very attractive possibilities in the field of nanoelectronics. Furthermore, these kinds of

NTs possess very significant mechanical properties, which can be combined with their optoelectronic properties, making them very promising structures for micro/nano-electro-mechanical system (M/NEMS) applications as actuators, sensors, etc.

Finally, the presence of heteroatoms in the carbon hexagonal network enhances the surface reactivity, which can be an advantage for gas sensors applications.

To summarize, the state-of-the-art regarding the research on a laboratory scale, synthesis of B–C–N heteroatomic SWNTs, most tubes, including BN, both N- and B-doped C-SWNT have been produced only with high temperature physical methods. As we mentioned in Sect. 2, the key aspect that must be considered in this research field will be improving the production techniques of these SWNTs, including increased production efficiency, higher purity, and the development of new techniques. Thus, it is clear that the understanding of NTs formation and growth is necessary to improve their synthesis in both quality and quantity. This progress is crucial to better know and measure their properties and forecast their applications.

**Acknowledgments** Some of the work shown here was supported by the European Community research and training network COMELCAN (HPRN-CT-2000-00128), by the European Commission under the 6 Framework Programme (STREP project BNC Tubes, contract number NMP4-CT-2006-03350), by the “Agence Nationale de la Recherche” – France (A.N.R.) and done within the framework of the GDR-I ‘Nano-I’ (N 2756) of the CNRS. Part of the results presented in this chapter are issued from very fruitful collaborations and discussions with B. Attal-Tretout, X. Blase, L. Bresson, J.L. Cochon, C. Colliex, N. Dorval, F. Ducastelle, S. Enouz-Vedrenne, A.C. Ferrari, M. Glerup, A. Gloter, P. Jaffrennou, M. Kociak, S. Lefrant, H. Lin, A. Maguer, J.Y. Mevellec, D. Pigache, S. Reich, A. Rubio, J. Serrano, O. Stephan, D. Taverna, M. Tence, L. Wirtz, and A. Zobelli.

## References

1. S. Iijima, *Nature* **354**, 56 (1991).
2. X. Blase, A. Rubio, S.G. Louie, M.L. Cohen, *Europhys. Lett.* **28**, 335 (1994).
3. A. Rubio, J.L. Corkill, M.L. Cohen, *Phys. Rev. B* **49**, 5081 (1994).
4. X. Blase, A. Rubio, S.G. Louie, M.L. Cohen, *Phys. Rev. B* **51**, 6868 (1995).
5. D. Golberg, Y. Bando, C. Tang, C.Y. Zhi, *Adv. Mat.* **19**, 2413 (2007).
6. R. Arenal, X. Blase, A. Loiseau, *Adv. Phys.* (in press).
7. A. Loiseau, P. Launois, P. Petit, S. Roche, J.-P. Salvetat (Eds.), *Understanding Carbon Nanotubes from Basics to Applications*, Series: Lecture Notes in Physics, **677**, Springer, Berlin (2006).
8. W. Kratschmer, L.D. Lamb, K. Fostiropoulos, D.R. Huffman, *Nature* **347**, 354 (1990).
9. T.W. Ebbesen, P.M. Ajayan, *Nature* **358**, 220 (1992).
10. S. Iijima, T. Ichihashi, *Nature* **363**, 603 (1993).
11. R. Droppa, Jr. P. Hammer, A.C.M. Carvalho, M.C. dos Santos, F. Alvarez, J. Non-Crystalline Solids **299**, 874 (2002).
12. M. Glerup, J. teinmetz, D. Samaille, O. Stphan, S. Enouz, A. Loiseau, S. Roth, P. Bernier, *Chem. Phys. Lett.* **387**, 193 (2004).
13. J.-C. Charlier, M. Terrones, M. Baxendale, V. Meunier, T. Zacharia, N.L. Rupesinghe, W.K. Hsu, N. Grobert, H. Terrones, G.A.J. Amaratunga, *Nano Lett.* **2**, 1191 (2002).
14. N.G. Chopra, R.J. Luyken, K. Cherrey, V.H. Crespi, M.L. Cohen, S.G. Louie, *Science* **269**, 966 (1995) money, G. Hug, H. Pascard, *Phys. Rev. Lett.* **76**, 4737 (1996).
15. A. Loiseau, F. Willaime, N. Demoncey, G. Hug, H. Pascard, *Phys. Rev. Lett.* **76**, 4737 (1996).

16. C.M. Lee, S.I. Choi, S.S. Choi, S.H. Hong, *Curr. Appl. Phys.* 6, 166 (2006).
17. R.S. Lee, J. Gavillet, M. Lamy de la Chapelle, A. Loiseau, J.-L. Cochon, D. Pigache, J. Thibault, F. Willaime, *Phys. Rev. B* 64, 121405(R) (2001).
18. R. Arenal, PhD Thesis Université Paris XI - Orsay, (2005).
19. R. Arenal, O. Stéphan, J.L. Cochon, A. Loiseau, *J. Am. Chem. Soc.* 129, 16183 (2007).
20. E. Borowiak-Palen, T. Pichler, G.G. Fuentes, A. Graff, R.J. Kalenczuk, M. Knupfer, J. Fink, *Chem. Phys. Lett.* 378, 516 (2003).
21. S. Enouz, O. Stephan, J.L. Cochon, C. Colliex, A. Loiseau, *Nano Lett.* 7, 1856 (2007).
22. S. Enouz, PhD Thesis Université Montpellier II (2007).
23. H. Lin, J. Lagoute, C. Chacon, R. Arenal, O. Stephan, V. Repain, Y. Girard, S. Enouz, L. Bresson, S. Rousset, A. Loiseau, *Phys. Status Solidi B* doi: 10.1002/pspb.200879634 (2008).
24. M. Castignolles, PhD Thesis Université Montpellier II (2004).
25. J. Gavillet, A. Loiseau, C. Journet, F. Willaime, F. Ducastelle, J.-C. Charlier, *Phys. Rev. Lett.* 87, 275504 (2001).
26. P.L. Gai, O. Stephan, K. McGuire, A.M. Rao, M.S. Dresselhaus, G. Dresselhaus, C. Colliex, *J. Mater. Chem.* 14, 669 (2004).
27. C.E. Lowell, *J. of American Chem. Soc.* 50, 142 (1967).
28. G. Keskar, R. Rao, J. Luo, J. Hudson, J. Chen, A.M. Rao, *Chem. Phys. Lett.* 412, 269 (2005).
29. F. Villalpando-Paez, A. Zamudio, A.L. Elias, H. Son, E.B. Barros, S.G. Chou, Y.A. Kim, H. Muramatsu, T. Hayashi, J. Kong, H. Terrones, G. Dresselhaus, M. Endo, M. Terrones, M.S. Dresselhaus, *Chem. Phys. Lett.* 424, 345 (2006).
30. P. Ayala, A. Grneis, C. Kramberger, M.H. Rmmeli, I.G. Solrzano, F.L. Freire, T. Pichler, *J. Chem. Phys.* 127, 184709 (2007).
31. W.L. Wang, X.D. Bai, K.H. Liu, Z. Xu, D. Golberg, Y. Bando, E.G. Wang, *J. Am. Chem. Soc.* 128, 6530 (2006).
32. J. Thomas, N.E. Weston, T.E. O'Connor, *J. Am. Chem. Soc.* 84, 4619 (1963).
33. J. Economy, R.Y. Lin, in *Boron Nitride Fibers in Boron, Refractory Borides*, V.I. Matkovich (Ed.), Springer, Berlin (1977).
34. E.L. Muettterties (Ed.), *The Chemistry of Boron, its Compounds*, Wiley, New York (1967).
35. M. Hubacek, M. Ueki, T. Sato, V. Broiek, *Thermochim. Acta* 282/283, 359 (1996).
36. A. Aydogdu, N. Sevin, *J. Eur. Ceram. Soc.* 23, 3153 (2003).
37. D.-F. Lii, J.-L. Huang, L.-J. Tsui, S.-M. Lee, *Surf. Coat. Technol.* 150, 269 (2002).
38. L. Hackspill, J. Besson, A. Hrold, *Chimie minérale*, Volume II, Presses Universitaires de France, Paris (1968).
39. W. Han, Y. Bando, K. Kurashima, T. Sato, *Appl. Phys. Lett.* 73, 3085 (1998).
40. T.S.M. Bartnitskaya, G.S. Oleinik, A.V. Pokropivnyi, V.V. Pokropivnyi, *JETP Lett.* 69, 163 (1999).
41. W.Q. Han, P. Todd, M. Strongin, *Appl. Phys. Lett.* 89, 173103 (2006).
42. D. Golberg, Y. Bando, L. Bourgeois, K. Kurashima, T. Sato, *Carbon* 38, 2017 (2000).
43. Zhong-lin Wang Chun Hui, *Electron Microscopy of Nanotubes*, Springer, Berlin (2003).
44. C.P. Ewels, M. Glerup, *J. Nanosci. Nanotechnol.* 5, 1345 (2005).
45. S. Enouz, J.L. Bantignies, M.R. Babaa, L. Alvarez, P. Parent, F. Le Normand, O. Stephan, P. Poncharal, A. Loiseau, B. Doyle, *J. Nanosci. Nanotechnol.* 7, 1 (2007).
46. M. De Graef, *Introduction to Conventional Transmission Electron Microscopy*, Cambridge University Press, Cambridge (London/New York) (2003).
47. P. Stadelmann, *Ultramicroscopy* 21, 131 (1987).
48. B.G. Demczyk, J. Cumings, A. Zettl, R.O. Ritchie, *Appl. Phys. Lett.* 78, 2772 (2001).
49. R. Arenal, M. Kociak, A. Loiseau, D.J. Miller, *Appl. Phys. Lett.* 89, 073104 (2006).
50. A. Zobelli, C.P. Ewels, A. Gloter, G. Seifert, O. Stephan, S. Csillag, C. Colliex, *Nano Lett.* 6, 1955 (2006).
51. K. Suenaga, H. Wakabayashi, M. Koshino, Y. Sato, K. Urita, S. Iijima, *Nat. Nanotechnol.*, 2, 358 (2007).
52. P. Lambin, A. Lucas, *Phys. Rev. B* 56, 3571 (1997).

53. M. Gao, J. M. Zuo, R. Twesten, I. Petrov, *Appl. Phys. Lett.* 82, 2703 (2003).
54. R. Arenal, M. Kociak, A. Loiseau, D.J. Miller, *Microsc. Microanal.* 12, 578 (2006).
55. J.G. Wiltshire, L.-J. Li, L.M. Herz, R.J. Nicholas, M. Glerup, J.-L. Sauvajol, A.N. Khlobystov, *Phys. Rev. B* 72, 205431 (2005).
56. L.-J. Li, M. Glerup, A.N. Khlobystov, J.G. Wiltshire, J.-L. Sauvajol, Taylor, R.J. Nicholas, *Carbon* 44, 2752 (2006).
57. R.F. Egerton, *Electron Energy-Loss Spectroscopy in the Electron Microscope*, Plenum Press, New York, (1996).
58. C. Jeanguillaume, C. Colliex, *Ultramicroscopy* 28, 252 (1989).
59. R. Arenal, O. Stephan, A. Loiseau, C. Colliex, *Microsc. Microanal.* 13, 1240 (2007).
60. R. Arenal, F. De la Pena, O. Stephan, M. Walls, M. Tence, A. Loiseau, C. Colliex, *Ultramicroscopy* 109, 32 (2008).
61. R. Arenal, M. Kociak, N.J. Zaluzec, *Appl. Phys. Lett.* 90, 204105 (2007).
62. O. Stephan, P.M. Ajayan, C. Colliex, F. CyrotLackmann, E. Sandre, *Phys. Rev. B* 53, 13824 (1996).
63. S. Enouz-Vedrenne, O. Stephan, M. Glerup, J.-L. Cochon, C. Colliex, A. Loiseau, *J. Phys. Chem. C* 112, 16422 (2008).
64. X. Blase, J.C. Charlier, A. De Vita, R. Car, Ph. Redlich, M. Terrones, W.K. Hsu, H. Terrones, D.L. Carroll, P.M. Ajayan, *Phys. Rev. Lett.* 83, 5078 (1999).
65. M. Cau, N. Dorval, B. Attal-Tirtout, J.L. Cochon, B. Cao, L. Bresson, P. Jaffrennou, M. Silly, A. Loiseau, *J. Nanosci. Nanotech.* (in press).
66. X. Blase, A. De Vita, J.C. Charlier, R. Car, *Phys. Rev. Lett.* 80, 1666 (1998).
67. M. Terrones, J.M. Romo-Herrera, E. Cruz-Silva, F. Lopez-Urias, E. Munoz-Sandoval, J.J. Velazquez-Salazar, H. Terrones, Y. Bando, D. Golberg, *Mat. Today* 10, 30 (2007).
68. S. Latil, S. Roche, D. Mayou, J.C. Charlier, *Phys. Rev. Lett.* 92, 256805 (2004).
69. R. Czerw, M. Terrones, J.C. Charlier, X. Blase, B. Foley, R. Kamalakaran, N. Grobert, D. Tekleab, P.M. Ajayan, W. Blau, M. Ruhle, D.L. Carroll, *Nano Lett.* 1, 457 (2001).
70. M. Terrones, P.M. Ajayan, F. Banhart, X. Blase, D.L. Carroll, J.C. Charlier, R. Czerw, B. Foley, N. Grobert, R. Kamalakaran, P. Kohler-Redlich, M. Ruhle, T. seeger, H. Terrones, *Appl. Phys. A* 74, 355 (2002).
71. V. Krstic, G.L.J.A. Rikken, P. Bernier, S. Roth, M. Glerup, *Eur. Phys. Lett.* 77, 37001 (2007).
72. A. Yu Kasumov, R. Deblock, M. Kociak, B. Reulet, H. Bouchiat, I. Khodos, Yu.B. Gorbatov, V.T. Volko, C. Journet, M. Burghard, *Science* 284, 1508 (1999).
73. A.Y. Kasumov, M. Kociak, M. Ferrier, R. Deblock, S. Gueron, B. Reulet, I. Khodos, O. Stephan, H. Bouchiat, *Phys. Rev. B* 68, 214521 (2003).
74. M. Kociak, A.Y. Kasumov, S. Gueron, B. Reulet, I.I. Khodos, Yu.B. Gorbatov, V.T. Volkov, L. Vaccarini, H. Bouchiat, *Phys. Rev. Lett.* 86, 2416 (2001).
75. I. Takesue, J. Haruyama, N. Kobayashi, S. Chiashi, S. Maruyama, T. Sugai, H. Shinohara, *Phys. Rev. Lett.* 96, 057001 (2006).
76. N. Murata, J. Haruyama, J. Reppert, A.M. Rao, T. Koretsune, S. Saito, M. Matsudaira, Y. Yagi, *Phys. Rev. Lett.* 100, 27002 (2008).
77. M. Radosavljevic, J. Appenzeller, V. Derycke, R. Martel, P. Avouris, A. Loiseau, J.-L. Cochon, D. Pigache, *Appl. Phys. Lett.* 82, 4131 (2003).
78. K.H. Khoo, M.S.C. Mazzoni, S.G. Louie, *Phys. Rev. B* 69, 201401 (2004).
79. M. Ishigami, J. Sau, S. Aloni, M. Cohen, A. Zettl, *Phys. Rev. Lett.* 94, 056804 (2005).
80. S.H. Lim, H.I. Elim, X.Y. Gao, A.T.S. Wee, W. Ji, J.Y. Lee, J. Lin, *Phys. Rev. B* 73, 045402 (2006).
81. E. Borowiak-Palen, T. Pichler, A. Graff, R.J. Kalenczuk, M. Knupfer, J. Fink, *Carbon* 42 1123 (2004).
82. J.S. Lauret, R. Arenal, F. Ducastelle, A. Loiseau, M. Cau, B. Attal-Tretout, E. Rosencher, L. Goux-Capes, *Phys. Rev. Lett.* 94, 037405 (2005).
83. L. Wirtz, A. Marini, M. Gruning, A. Rubio, *Cond-Mat* 0508421 (2005).
84. L. Wirtz, A. Marini, A. Rubio, *Phys. Rev. Lett.* 96, 126104 (2006).

85. A.G. Marinopoulos, L. Wirtz, A. Marini, V. Olevano, A. Rubio, L. Reining, Appl. Phys. A 78, 1157 (2004).
86. C.-H. Park, C.D. Spataru, S.G. Louie, Phys. Rev. Lett. 96, 126105 (2006).
87. B. Arnaud, S. Lebegue, P. Rabiller, M. Alouani, Phys. Rev. Lett. 96, 026402 (2006).
88. M.G. Silly, P. Jaffrennou, J. Barjon, J.-S. Lauret, F. Ducastelle, A. Loiseau, E. Obraztsova, B. Attal-Tretout, E. Rosencher, Phys. Rev. B 75, 085205 (2007).
89. P. Jaffrennou, J. Barjon, T. Schmid, L. Museur, A. Kanaev, J.-S. Lauret, C.Y. Zhi, C. Tang, Y. Bando, D. Golberg, B. Attal-Tretout, F. Ducastelle, A. Loiseau, Phys. Rev. B 77, 235422 (2008).
90. P. Jaffrennou, F. Donatini, J. Barjon, J.-S. Lauret, B. Attal-Tretout, H. Mariette, F. Ducastelle, A. Loiseau, Chem. Phys. Lett. 442, 372 (2007).
91. R. Arenal, O. Stephan, M. Kociak, D. Taverna, A. Loiseau, C. Colliex, Phys. Rev. Lett. 95, 127601 (2005).
92. R. Arenal, O. Stephan, M. Kociak, D. Taverna, A. Loiseau, C. Colliex, Microsc. Microanal. 14, 274 (2008).
93. A. Gloter, A. Douiri, M. Tencé, C. Colliex, Ultramicroscopy 96, 385 (2002).
94. A.A. Lucas, L. Henrard, Ph. Lambin, Phys. Rev. B 49, 2888 (1994).
95. R. Vilanove, C.R. Acad. Sc. Paris 272, 1066 (1971).
96. C. Tarrio, S.E. Schnatterly, Phys. Rev. B 40, 7852 (1989).
97. L. Henrard, F. Malengreau, P. Rudolf, K. Hevesi, R. Caudano, Ph. Lambin, Th. Cabioch, Phys. Rev. B 59, 5832 (1999).
98. O. Stéphan, M. Kociak, D. Taverna, K. Suenaga, L. Henrard, C. Colliex, Phys. Rev. B 66, 155422 (2002).
99. M.S. Dresselhaus, G. Dresselhaus, and Ph. Avouris (Eds.), *Carbon Nanotubes: Synthesis, Structure, Properties, and Applications*, Springer-Verlag, Berlin, 2001.
100. S. Reich, C. Thomsen, J. Maultzsch, *Carbon Nanotubes: Basic Concepts and Physical Properties*, Wiley-VCH, Berlin, 2004.
101. A.C. Ferrari, J. Robertson, Phys. Rev. B 61, 14095 (2000).
102. K. McGuire, N. Gothard, P.L. Gai, M.S. Dresselhaus, G. Sumanasekera, A.M. Rao, Carbon 43, 219 (2005).
103. D. Sanchez-Portal, E. Hernandez, Phys. Rev. B 66, 235415 (2002).
104. L. Wirtz, A. Rubio, R. Arenal, A. Loiseau, Phys. Rev. B 68, 045425 (2003).
105. V.N. Popov, Phys. Rev. B 67, 085408 (2003).
106. J. Serrano, A. Bosak, R. Arenal, M. Krisch, K. Watanabe, T. Taniguchi, H. Kanda, A. Rubio, L. Wirtz, Phys. Rev. Lett. 98, 095503 (2007).
107. R. Geick, C.H. Perry, G. Rupprecht, Phys. Rev. 146, 543 (1966).
108. S. Reich, A.C. Ferrari, R. Arenal, A. Loiseau, I. Bello, J. Robertson, Phys. Rev. B 71, 205201 (2005).
109. R. Arenal, A.C. Ferrari, S. Reich, L. Wirtz, J.-Y. Mevellec, S. Lefrant, A. Rubio, A. Loiseau, Nano Lett. 6, 1812 (2006).
110. E. Hernandez, C. Goze, P. Bernier, A. Rubio, Phys. Rev. Lett. 80, 4502 (1998).
111. L. Vaccarini, C. Goze, L. Henrard, E. Hernandez, P. Bernier, A. Rubio, Carbon 38 1681 (2000).
112. T. Dumitrica, H. Bettinger, G.E. Scuseria, B. Yakobson, Phys. Rev. B 68, 085412 (2003).
113. H. Bettinger, T. Dumitrica, G.E. Scuseria, B. Yakobson, Phys. Rev. B 58, 041406 (2002).
114. P. Kral, E.J. Mele, D. Tomanek, Phys. Rev. Lett. 85, 1512 (2000).
115. E.J. Mele, P. Kral, Phys. Rev. Lett. 88, 056803 (2002).
116. S.M. Nakhmanson, A. Calzolari, V. Meunier, J. Bernholc, M. Buongiorno Nardelli, Phys. Rev. B 67, 235406 (2003).
117. R.J. Baierle, T.M. Schmidt, A. Fazzio, Sol. State Comm. 142, 49 (2007).
118. X.J. Wu, W. An, X.C. Zheng, J. Am. Chem. Soc. 128, 12001 (2006).
119. C. Zhi, Y. Bando, C. Tang, R. Xie, T. Sekiguchi, D. Golberg, J. Am. Chem. Soc. 127, 15996 (2005).

120. S.Y. Xie, W. Wang, K.A. Shiral Fernando, X. Wang, Y. Lin, Y.P. Sun, *Chem. Commun.*, 3670 (2005).
121. S. Pal, S. R. C. Vivechand, A. Govindaraj, C. N. R. Rao, *J. Mater. Chem.* 17, 450 (2007).
122. A. Maguer, E. Leroy, Lionel Bresson, E. Doris, A. Loiseau, C. Mioskowski, *J. Mater. Chem.* 19, 1271 (2008).
123. R. Ma, Y. Bando, H. Zhu, T. Sato, C. Xu, D. Wu, *J. Amer. Chem. Soc.* 124, 7672 (2002).
124. S.-H. Jhi, Y.-K. Kwon", *Phys. Rev. B* 69, 245407 (2004).
125. X. Wu, J. Yang, J.G. Hou, Q. Zhu, *Phys. Rev. B* 69, 153411 (2004).
126. Z. Zhou, X. Gao, J. Yan, D. Song, *Carbon* 44, 939 (2006).
127. Z.Y. Zhang, K. Cho, *Phys. Rev. B* 75, 75420 (2007).
128. F. Li, Y. Xia, M. Zhao, X. Liu, B. Huang, Y. Ji, C. Song, *Phys. Lett. A* 357, 369 (2006).



# Electronic Properties of Boron-Nitride and Boron Carbonitride Nanotubes and Related Heterojunctions

Xavier Blase and Helio Chacham

**Abstract** We review in the present chapter the electronic and optical properties of hexagonal boron-nitride and hexagonal composite boron carbonitride planar and nanotubular structures. We focus mainly on theoretical aspects, but illustrate in all situations the link with existing experimental findings. In a first part, the insulating nature, and the band gap stability, of boron-nitride nanotubes are shown to be related to the ionicity character of the boron-nitrogen bond. Specific emphasis is given to the optical properties and the related excitonic effects. In a second part, the evolution of the stability and band gap of boron carbonitride systems as a function of the degree of segregation in pure carbon or boron-nitride domains is illustrated and their potential in terms of rectifying hetero-junctions, quantum dots, or visible-light optoelectronics devices is emphasized.

## 1 Boron-Nitride Nanotubes

On the basis of the structural similarities between the graphite and the hexagonal form of boron-nitride (*h*-BN), the idea that boron-nitride nanotubes (BNTs) could be synthesized was suggested theoretically as early as 1994 [1, 2]. Using accurate *ab-initio* calculations [1], it was demonstrated in particular that the elastic energy of folding an isolated BN sheet onto a nanotube was equivalent, and even smaller, than folding a graphene sheet onto a tube of the same radius (Fig. 1). These predictions, even though certainly not providing the experimental pathways to synthesis, were strong indications that such novel forms of tubes could be synthesized.

Together with these preliminary studies on structural stability, the electronic properties of BNTs were predicted at the theoretical level [1, 2]. It was shown in particu-

---

X. Blase (✉)

Institut Néel, CNRS and Université Joseph Fourier, BP 166, 38042, Grenoble Cedex 09, France  
e-mail: xavier.blase@grenoble.cnrs.fr

H. Chacham

Departamento de Física, ICEx, Universidade Federal de Minas Gerais, C.P.  
702, 30123970 Belo Horizonte, MG, Brazil

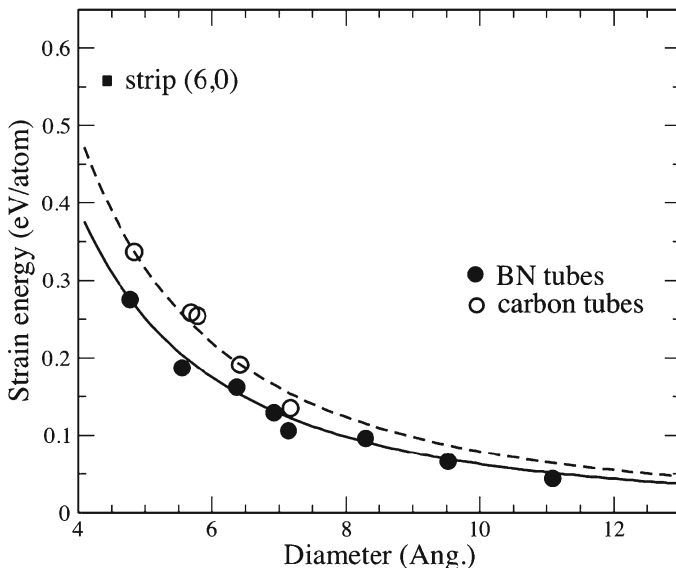


**Fig. 1** Total energy of nanotubes in eV/atom as a function of tube diameter. The *black (opened) circles* represent the BN (C) nanotube energies above the energy of an isolated BN (graphene) sheet. The *solid and dashed lines* are  $1/R^2$  fits as a guide to the eyes (Adapted from [1])

lar that, due to the ionic character of the BN bond, boron-nitride tubes were insulating systems with a band gap largely independent of the radius and helicity, in great contrast with the carbon case. The difficulties in performing experimental measurements of the electronic properties of nano-sized objects, either through STM or optical experiments, certainly explains that it took several years for achieving an experimental verification of these predictions. This is reminiscent of the carbon nanotubes case for which the first STS measurements of the density of states of diameter-selected tubes [3, 4] came in 1998, that is, 6 years after the first theoretical predictions of the now well-known radius and chirality dependence of CNTs band gap [5–7].

Rapidly following these theoretical predictions, pure BNTs were synthesized in 1995–1996, 4 years after the synthesis of their carbon analogues, using at first high-temperature experiments such as arc-discharge [8–10] or laser ablation [11] techniques. Since then, numerous groups have performed the synthesis of single-wall (SW) or multiwall (MW) BN nanotubes on the basis of a variety of high and low-temperature techniques, and large amounts of samples are now routinely available.

As a matter of fact, before the synthesis of pure BNTs, and in an attempt to synthesize boron and nitrogen-doped CNTs, the so-called composite BCN tubes, mixing in various percentage boron, carbon, and nitrogen atoms, were synthesized and characterized as early as 1994 [12]. Using electron energy loss spectroscopy analysis, it was shown in particular that while the B to N ratio was always close to one, the BCN tubes were composed either of single-phase  $C_yB_xN_x$  sections or well separated nano-domains of BN in the carbon network. This ability of composite BCN tubes to form

either segregated carbon and BN domains, or homogeneous BCN structures, is the main issue in discussing the electronic properties of such systems, which are affiliated both to metallic, or small gap, CNTs and insulating BN tubes.

We present here an extensive review of the work devoted to BN and composite BCN tubes since their first synthesis. Although most experimental aspects of the physics of BN and BCN tubes have been reviewed in a previous book [13] or recent online articles [14, 15], a large emphasis on theoretical aspects is provided in the present pages.

### 1.1 Structure and Stability

The most studied crystallographic structure of hexagonal boron-nitride (*h*-BN) belongs to the  $D_{6h}^4$  point group with an ABAB stacking type. In such a structure, and in contrast with graphite, where one carbon atom out of two is located at the vertical of a hexagon center, B(N) atoms are located at the vertical of neighboring layers N(B) atoms. Such a stacking geometry may be tentatively assigned to the strong ionic character of the B–N bond. Other hexagonal stacking geometry have been proposed [16] and shown, on the basis of ab-initio calculations, to be very close in energy, or as stable, as the above-mentioned structure. The existence of several stacking allotrops may explain some of the inconsistencies between theory and experiment as far as electronic properties are discussed (see later and [16]).

The B–N bond length is larger than the C–C one in graphite ( $a_{\text{BN}} \approx 1.45 \text{ \AA}$  instead of  $a_{\text{CC}} \approx 1.42 \text{ \AA}$ ). The crystal structure, lattice vectors, and reciprocal lattice vectors for a single *h*-BN or graphene sheet are summarized in Fig. 2. The unit cell contains two atoms (one boron and one nitrogen in the case of *h*-BN). The lattice vectors

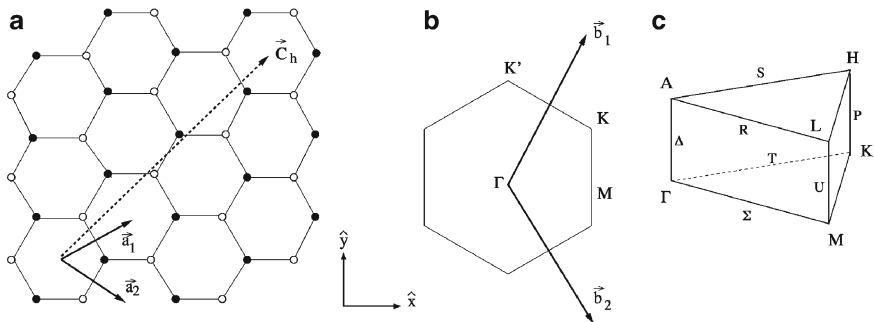


**Fig. 2** (a) Isolated *h*-BN sheet lattice structure. The two nonequivalent atoms in the unit cell are represented in *black* and *white*, respectively, together with the in-plane lattice vectors ( $\mathbf{a}_1, \mathbf{a}_2$ ). The  $\mathbf{C}_h$  vector represented here is the chiral vector for a  $(4, -1)$  BN tube. (b) The reciprocal space Brillouin zone and lattice vectors ( $\mathbf{b}_1, \mathbf{b}_2$ ) for the 2D isolated sheet. (c) The irreducible Brillouin zone for the stacked 3D material

$(\mathbf{a}_1, \mathbf{a}_2)$  have been chosen here to form an angle of  $60^\circ$  so that the reciprocal lattice vectors  $(\mathbf{b}_1, \mathbf{b}_2)$  form an angle of  $120^\circ$ .

Relying on the structural similarity between graphite and *h*-BN, the existence of BN nanotubes was first postulated [1, 2] at the theoretical level in 1994, that is, a few months before the actual synthesis. On the basis of ab-initio calculations [1], it was shown in particular that the folding of an isolated *h*-BN sheet onto a nanotubular shape was slightly more favorable than the folding of a graphene sheet onto a cylinder of the same radius. Namely, the elastic energy associated with bending a sheet onto a tube was reduced in the case of *h*-BN. An interesting property of *h*-BN tubes is that N atoms are located closer to the tube axis (inward relaxation) so as to come closer to the center of the triangle formed by its three boron nearest neighbors. This so-called “buckling” effect was first noticed by Blase and coworkers [1] and then studied in details by Wirtz et al. [17], who showed that this buckling energy scales as  $1/R$  ( $R$ , the tube radius) (Fig. 3).

The argument of elastic folding energy was subsequently used in particular in the case of “multilayered” sheets, such as  $\text{WS}_2$ ,  $\text{MoS}_2$  planar compounds (formed of a metal sheet sandwiched in between two sulfur sheets) [18–22] or GaSe [23] and  $\text{B}_2\text{O}$  or  $\text{BeB}_2$  [24] systems, to predict the average radius of the resulting tubes. Further, as indicated in Fig. 1, even in the limit of very small diameters, the energy of dangling bonds associated with “opened” BN strips is so large that it is energetically more favorable to preserve the cylindrical tube geometry, despite the increasing curvature energy upon decreasing radius.

As in the carbon case, BN nanotubes can be labeled with two indices  $(n, m)$  that define uniquely the so-called chiral vector  $\mathbf{C}_h = n\mathbf{a}_1 + m\mathbf{a}_2$ , which is perpendicular to the tube axis direction and defines the tube folding direction. The tube diameter  $d_t$ , chiral angle  $T$ , translational vector  $\mathbf{T}$ , and number  $N_c$  of atoms per unit cell are summarized in Table 1.

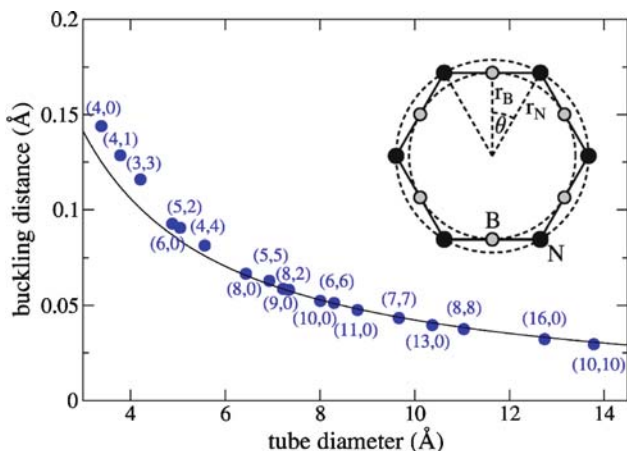


**Fig. 3** Buckling distance in BN nanotubes as a function of diameter (Reprinted with permission from [17], Copyright by the American Physical Society)

**Table 1** Summary of the properties of BN nanotubes as a function of the chiral indices ( $n, m$ )

Symbol	Name	Formula	Value
$A$	Lattice constant	$a = \sqrt{3}a_{\text{BN}}$	$a_{\text{BN}} = 1.45 \text{ \AA}$
$(\mathbf{a}_1, \mathbf{a}_2)$	Basis vectors	$a \left\{ \frac{\sqrt{3}}{2}, \pm \frac{1}{2} \right\}$	(x, y) cartesian
$(\mathbf{b}_1, \mathbf{b}_2)$	Reciprocal lattice vectors	$\left\{ \frac{1}{\sqrt{3}}, \pm 1 \right\} \frac{2\pi}{a}$	(x, y) cartesian
$\mathbf{C}_h$	Chiral vector	$\mathbf{C}_h = n\mathbf{a}_1 + m\mathbf{a}_2 = (n, m)$	$(0 \leq  m  < n)$
$d_t$	Tube diameter	$d_t = \frac{ \mathbf{C}_h }{\pi} = \frac{a}{\pi} \sqrt{n^2 + nm + m^2}$	
$\Theta$	Chiral angle	$\sin(\theta) = \frac{m\sqrt{3}}{2\sqrt{n^2 + nm + m^2}}$ $\cos(\theta) = \frac{2n + m}{2\sqrt{n^2 + nm + m^2}}$	$(0 \leq  \theta  \leq \pi / 6)$
$\mathbf{T}$	Translational vector	$\mathbf{T} = t_1\mathbf{a}_1 + t_2\mathbf{a}_2 = (t_1, t_2)$ $t_1 = \frac{2m + n}{N_R}, t_2 = -\frac{2n + m}{N_R}$	$\text{gcd}(t_1, t_2) = 1$ $N_R = \text{gcd}(2m + n, 2n + m)$
$N_c$	Number of atoms in unit cell	$N_c = \frac{4(n^2 + nm + m^2)}{N_R}$	

gcd stands for "greatest common divisor." Adapted from [25], Copyright@ American Physical Society.

## 1.2 Electronic Properties

Despite a rather large number of experimental studies [26], the nature (direct or not) and magnitude of the band gap remains difficult to assess experimentally. This is certainly due to the difficulty in obtaining high purity samples and to the large value of the band gap. In such situations, accurate theoretical studies may help in interpreting and discussing the properties of this material and its related forms, namely BN nanotubes.

### 1.2.1 A Large Ionicity Band Gap Insulator with Stable Electronic Properties

The most important difference between  $h$ -BN and graphite is the strong ionic character of the B–N bond related to the largest electronic affinity of nitrogen when compared with that of boron. A Bader analysis [27, 28] of the charge density reveals a charge transfer of  $\sim 2.2$  valence electrons from boron to nitrogen. Although the graphene sheet is semimetallic [25], the ionic character of  $h$ -BN results in a

large band gap opening. The formation of this “ionic band gap” can be simply understood from the standard  $\pi$ - $\pi^*$  tight-binding model widely used for the graphene sheet. In such a model, valid around the Fermi level, we consider only one  $p_z$  orbital per atom ( $z$ -direction perpendicular to the sheet) with an  $E_{A(B)}$  onsite energy for the A(B) atoms in the unit cell and an overlap energy between first nearest neighbors orbitals labeled  $\gamma$  ( $\sim -2.9$  eV). With such a basis, the electronic eigenstates are linear combination of the two possible Bloch basis states, namely:

$$\phi_k(r) = c_A p_k^A(r) + c_B p_k^B(r), \text{ with } p_k^{A/B} = \frac{1}{\sqrt{N}} \sum_R e^{ik \cdot R} p_z(r - \tau_{A/B} - R),$$

where  $\tau_{A/B}$  are the positions of the A/B atoms in the unit cell and  $R$  is the lattice vectors. In such a basis, the secular equation leads to the following energy dispersion

$$E(k) = \pm \gamma \sqrt{(\Delta / 4\gamma)^2 + \alpha(k)^2}, \text{ with: } \Delta = E_A - E_B \text{ and}$$

$$\alpha(k) = \gamma \sqrt{1 + 4 \cos\left(\frac{k_x a \sqrt{3}}{2}\right) \cos\left(\frac{k_y a}{2}\right) + 4 \cos^2\left(\frac{k_y a}{2}\right)}.$$

It can be shown that  $\alpha(k)$  cancels for  $k = K = (2\mathbf{a}_1 + \mathbf{a}_2)/3$ . In the case of graphene, the A and B atoms are both carbon atoms so that  $E_A = E_B$  and  $\Delta = 0$ . This explains the semimetallic character of the graphene sheet with a band gap closing at the Brillouin zone corners. However, in the case of  $h$ -BN, since the A and B atoms are no longer equivalent,  $\Delta$  is nonzero and at  $k = \mathbf{K}$ , the band gap does not close and takes a value of  $E_{BN}(k = \mathbf{K}) = 2\Delta$ . This band gap is independent of the  $\alpha(k)$  factor, which depends on the crystallographic structure and hopping strength  $\gamma$ , so that the band gap of BN compounds can be expected to be first-order independent of the details of the atomic structure. This explains the so-called “stability” of the band gap in  $h$ -BN nanotubes, which indeed hardly depends on curvature and helicity [1], except in the limit of very small diameters.

### 1.2.2 Quasiparticle Band Structure of $h$ -BN and Related Nanotubes

The simple  $\pi$ - $\pi^*$  model is not as useful in the case of  $h$ -BN as it is for graphene. Indeed, the large band gap opening between bonding  $\pi$  and antibonding  $\pi^*$  states is such that the clear decoupling of energy between  $\pi$  and  $\pi^*$  and  $\sigma$ - $\sigma^*$  excitation energies in graphite is not verified in the case of  $h$ -BN. As such, full calculations including all valence electrons are needed to provide a reliable description of the electronic properties of  $h$ -BN. A more accurate tight-binding parametrization along that line has been worked out by Robertson [29]. However, since experimental results yield very scattered results, for example, with band gaps ranging from 3.2 to 5.97 eV, the parametrization of the one-site and hopping terms turns out to be a difficult problem and parameter-free first-principles approaches are desirable.

Ab-initio calculations of the band structure of *h*-BN within the density functional theory (DFT) [16, 30–32] or Hartree-Fock (HF) [33] came as early as the mid-eighties. However, the well-known large underestimation (overestimation) of the band gap values of insulators within DFT (HF) does not allow to fully rationalize the electronic properties of *h*-BN systems. Fortunately, more accurate many-body techniques, such as the quasiparticle GW approach [34], have been used to predict a much better accuracy of the band structure of *h*-BN bulk and nanotubes [1, 35–39]. In the case of bulk *h*-BN, the most recent GW calculations [37] predict an indirect band gap of 5.95 eV between the top of the valence bands at the  $T_1$  point (close to  $K$  along  $\Gamma K$ ) and the conduction band minimum at  $M$ . Such a value is 1.93 eV larger than the corresponding DFT value (4.02 eV). The smallest direct band gap is located at the  $H$  point and takes a value of 6.47 eV. Such values are consistent with an earlier GW calculations [36] with an indirect and direct band gap of 6.04 and 6.66 eV, respectively. Similarly, the earliest GW calculations on *h*-BN [35], based on an extrapolation of the self-energy correction calculated at a few high-symmetry points, confirmed the indirect nature of the band gap between  $T_1$  and  $M$ , but with a smaller 5.4 eV value. We compare in Fig. 4 the latest DFT and GW band *h*-BN structures for bulk *h*-BN.

Similar GW calculations have been performed on isolated *h*-BN sheet [1, 35, 36, 38, 39] and small diameter SW BN nanotubes [38, 39], with even larger differences between DFT and GW calculations. In the case of the BN (8, 0) tube, the GW quasiparticle correction to the DFT value was found to be as large as 3.25 eV, yielding a direct GW quasiparticle band gap at zone-center of  $\sim 6.5$  eV.

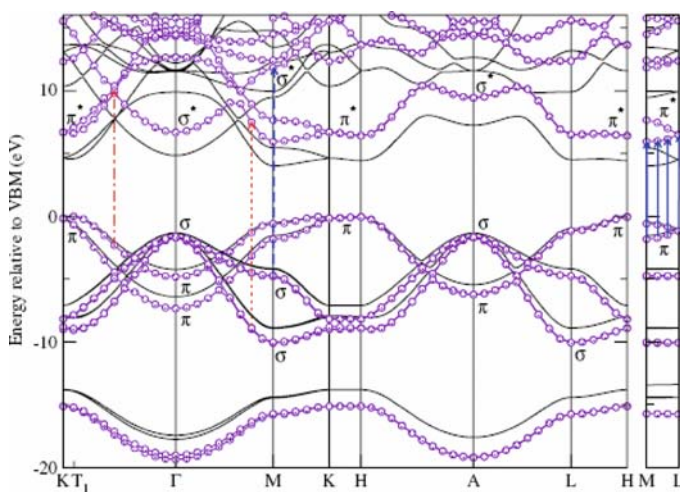


**Fig. 4** Quasiparticle band structure for bulk *h*-BN. The *solid lines* are the result of DFT-LDA calculations. *Open circles* represent the GW calculations. The two band structures have been aligned at the valence bands maximum ( $T_1$  point near  $K$  along the  $\Gamma$ - $K$  direction). The *vertical arrows* indicate optical transitions contributing to the main optical absorption spectrum features (Reprinted with permission from [37], Copyright by the American Physical Society)

### 1.2.3 The Interlayer State

An interesting property of *h*-BN and BNTs is related to the electronic state controlling the bottom of the conduction bands at  $\Gamma$ . This state has been studied by several groups on the basis of first-principles approaches [30, 35, 40], an interest that stems from its potential role in n-type doped *h*-BN systems and, in particular, its interplay with intercalants as shown recently in the case of the analogous interlayer state in graphite [41].

Because of the large band gap of *h*-BN compounds, the states at the bottom of the conduction bands are located close, or above, the vacuum level. As such, their energy is dominated by their kinetic component, and they are weakly bound to the BN sheets.

This feature can be clearly seen when representing the charge density associated with the state at the bottom of the conduction bands at  $\Gamma$  in a plane perpendicular to the BN layers (Fig. 5d). Clearly, the charge density cannot be described as a linear combination of boron or nitrogen  $p_z$  orbitals (as for the states represented in Fig. 5a–c) since the charge density extends much further into the interlayer region.

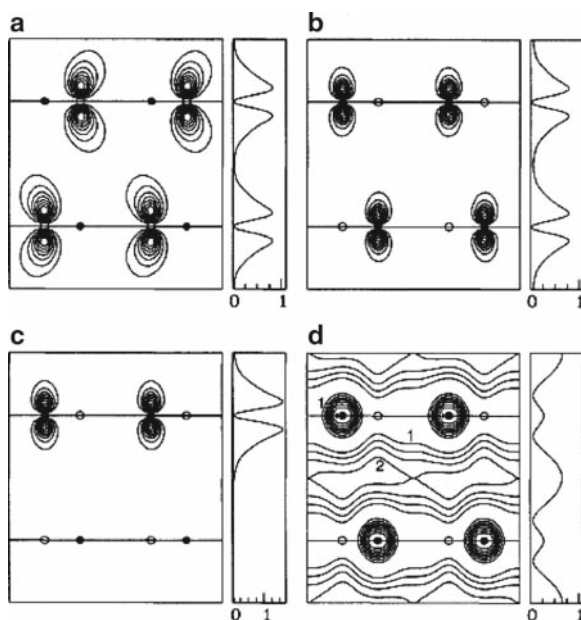


**Fig. 5** Contour plots in a plane perpendicular to the BN layers of the charge density of selected states for bulk hexagonal BN. BN layers are indicated by *horizontal lines*. N atoms are represented with *filled circles* and B atoms with *empty circles*. The charge densities are averaged over planes parallel to the BN layers and normalized to unity in the unit cell. (a) LUMO state at  $M$ , (b) HOMO state at  $K$ , (c) HOMO state at  $H$ , and (d) LUMO state at  $\Gamma$ . In (d), contours labeled 1 and 2 corresponds to a charge density of, respectively,  $0.16 \times 10^{-4}$  and  $0.63 \times 10^{-4}$  electron/a.u.<sup>3</sup>. The maximum charge density is  $1.26 \times 10^{-4}$  electron/a.u.<sup>3</sup> on the nitrogen atom. (Adapted from [35], Copyright by the American Physical Society)



Such a state, localized mainly in between the atomic layers, is therefore labeled a “nearly-free-electron-state” (NFE).

### 1.3 Optical Properties and Excitons

The band structure and band gap discussed earlier correspond to photoemission spectroscopy experiments where electrons are brought to (or from) infinity, creating thus a charged excitation of the system. In an optical experiment, excited (hot) electrons are not removed from the system. They are promoted from the valence to the conduction bands, leaving a hole behind. Optical experiments thus probe neutral excitations where electrons and hole can interact through the screened Coulomb potential. In particular, the optical “band gap” (absorption threshold) is usually smaller than the quasiparticle band gap, the difference being related to the electron-hole interaction energy, the so-called excitonic binding energy.

As a preliminary remark to the physics of optical absorption in BN nanotubes, we recall that in the case of carbon tubes, it was shown theoretically [42–44] and experimentally [45] that the absorption is dominated by the component of the electric field parallel to the tube axis. For perpendicular components, the depolarization fields are important and reduce considerably the absorption at low energy. Simple considerations lead to the following expression for the perpendicular polarizability [42]:

$$\alpha_{\text{perp}}(\omega) = \frac{\alpha_{0,\text{perp}}(\omega)}{1 + 2\alpha_{0,\text{perp}}(\omega) / R^2},$$

where  $R$  is the tube radius and  $\alpha_{0,\text{perp}}$  is the independent-electron perpendicular polarizability. On the contrary, when the electric field component is parallel to the tube axis,  $\alpha_{\text{para}}$  and  $\alpha_{0,\text{para}}$  do not differ much. Similar effects were evidenced in the case of small BN nanotubes using *ab initio* time-dependant density functional theory (TD-DFT) calculations [46].

The above-mentioned TDDFT calculations fail, however, in providing an accurate description of the electron–hole interactions, a drawback related in particular to the absence of long-range interactions in the so-called exchange–correlation kernel (for a review, see Onida et al. [47]). We will not deal here with the general theory of excitons in semiconducting materials and refer the reader to elementary textbooks on the subject [48]. Let us briefly remind that it is traditional to distinguish between extended Mott–Wannier excitons [49], where hole and the electrons are separated by a rather large number of unit cells, and the so-called Frenkel excitons where the electron–hole pair is spatially confined over a few atoms. Frenkel excitons form in molecular systems and strongly ionic crystals where the charged ions can trap the excited electrons and holes.

In the standard Mott–Wannier approach [49], the electron–hole system is treated as an effective “hydrogenoid” problem with an electron (hole) effective mass

( $m_e^* m_h^*$ ) related to the curvature of the bands at the bottom (top) of the conduction (valence) bands, and a Coulomb interaction screened by the macroscopic dielectric constant  $\epsilon_M$ . One thus obtains a renormalized Rydberg series with excitonic binding energies obtained through:

$$E = -\left(\frac{1}{n^2}\right)\left(\frac{\mu^*}{\epsilon_M^2 m_e^*}\right) \text{Ry with } \frac{1}{\mu^*} = \frac{1}{m_e^*} + \frac{1}{m_h^*}.$$

This model assumes “extended” excitons for which the hole and the electrons are separated by a rather large number of unit cells. This is indeed the condition, for example, for using the long range macroscopic dielectric constant  $\epsilon_M$  for reducing the electron–hole interaction.

Excitonic effects in strictly 1D systems have been shown to exhibit specific signatures related to the divergency of the Coulomb integrals on a line. In particular, Loudon [50] showed that in principle the excitonic binding energy should diverge within a 1D generalization of the Mott-Wannier model. Further, it was demonstrated that the so-called Sommerfeld factors [51, 52] should be quenched and compensated for the van Hove singularities in the valence to conduction convoluted density of states. Such results are valid for strictly 1D systems but are expected to affect the physics of nanotubes, especially in the small diameter limit, with an enhanced excitonic binding energy, for example, when compared with bulk systems.

It is difficult to assess a priori the validity of such simplified models in the case of low-dimensionality systems such as nanotubes. For example, the notion of macroscopic dielectric constant is certainly difficult to handle. As such, a few groups have performed fully ab-initio calculations within the so-called Bethe-Salpeter approach [47] to explore the optical properties of *h*-BN systems, including bulk, isolated sheet and small diameter nanotubes [37–39]. Such an approach can be viewed as a generalization of the Mott–Wannier model with excitonic wavefunctions built from an extended combination of valence  $|v\mathbf{k}\rangle$  and conduction bands  $|c\mathbf{k}\rangle$  products (noted  $|vc\mathbf{k}\rangle$  below) and with the electron-hole interaction being screened by the full microscopic dielectric function  $\epsilon(\mathbf{r}, \mathbf{r}')$  (not only its long-wavelength limit  $\epsilon_M$ ). Technically, the electron-hole two-body eigenvalue problem reads:

$$H^{e-h} |\Psi^\lambda\rangle = E^\lambda |\Psi^\lambda\rangle \text{ with } |\Psi^\lambda\rangle = \sum_{vc\mathbf{k}} A^{vc\mathbf{k}\lambda} |vc\mathbf{k}\rangle,$$

$$H_{vc\mathbf{k}, v'c'\mathbf{k}'}^{e-h} = D_{vc\mathbf{k}, v'c'\mathbf{k}'} + V_{vc\mathbf{k}, v'c'\mathbf{k}'}^{\text{direct}} + \delta_{S,0} V_{vc\mathbf{k}, v'c'\mathbf{k}'}^{\text{exch}}.$$

with the electron-hole Bethe-Salpeter Hamiltonian  $H^{e-h}$  which decomposes as:

$$D_{vc\mathbf{k}, v'c'\mathbf{k}'} = (\epsilon_{c\mathbf{k}}^{\text{QP}} - \epsilon_{v\mathbf{k}}^{\text{QP}}) \delta_{vv'} \delta_{cc'} \delta_{\mathbf{k}\mathbf{k}'},$$

$$V_{vc\mathbf{k}, v'c'\mathbf{k}'}^{\text{direct}} = -\int d\mathbf{r} d\mathbf{r}' \phi_{v\mathbf{k}}(r) \phi_{c\mathbf{k}}^*(r') W(r, r', \omega = 0) \phi_{v'\mathbf{k}'}^*(r) \phi_{c'\mathbf{k}'}(r),$$

$$V_{vc\mathbf{k}, v'c'\mathbf{k}'}^{\text{exch}} = \int d\mathbf{r} d\mathbf{r}' \phi_{v\mathbf{k}}(r) \phi_{c\mathbf{k}}^*(r) \bar{V}_C(r, r') \phi_{v'\mathbf{k}'}^*(r') \phi_{c'\mathbf{k}'}(r).$$

The  $\varepsilon_{\nu\mathbf{k}}^{\text{QP}}$  and  $\varepsilon_{\mathbf{c}\mathbf{k}}^{\text{QP}}$  energies are the quasiparticle (GW) eigenvalues in the absence of electron–hole interaction as described previously. The term  $V_{\nu\mathbf{k},\nu'\mathbf{k}'}^{\text{direct}}$  accounts for the direct screened Coulomb interaction between the hole and the electron. The statically screened Coulomb interaction  $W(r,r')$  is built from the full microscopic dielectric function  $\varepsilon(r,r')$ , which allows to properly describe the reduction of screening at short distances. This contrasts with the Mott-Wannier model where the screening is introduced by using only the macroscopic dielectric constant  $\varepsilon_{\text{M}}$ , a concept valid only whenever the hole and the electron are spatially well separated, a condition that is not verified in the case of *h*-BN systems as shown later (Fig. 6).

The exchange term  $V_{\nu\mathbf{k},\nu'\mathbf{k}'}^{\text{exch}}$  accounts for the splitting between the singlet ( $S = 0$ ) and the triplet states ( $S = 1$ ).  $S$  refers here to the total value of the spin. In particular, due to this exchange term, the first excited state with ( $S = 1$ ) is lower in energy than the ( $S = 0$ ) first excited state, an energy ordering reminiscent of the so-called Hund’s rules in atomic physics. This is an important consideration since an excited electron, promoted from the ( $S = 0$ ) ground state to the ( $S = 0$ ) first excited state may relax onto the lower energy ( $S = 1$ ) level. In the ( $S = 1$ ) energy level, the photoelectron cannot relax onto the ( $S = 0$ ) ground state, which is orthogonal in spin space. Excitons with ( $S = 1$ ) are labeled as dark excitons since recombination

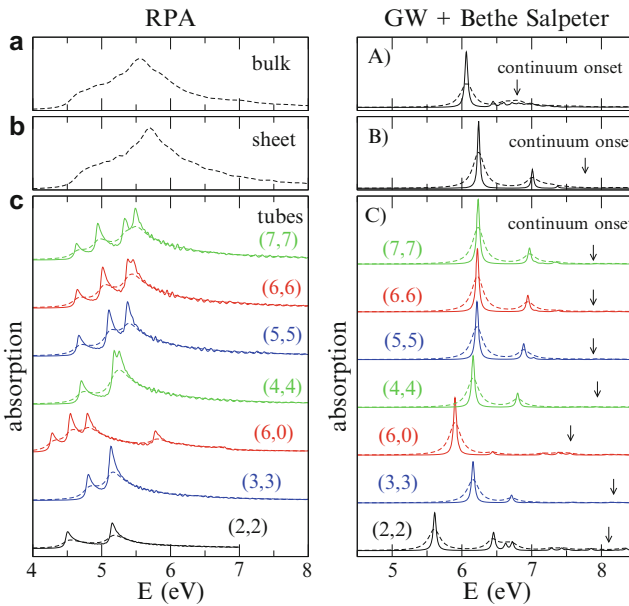


**Fig. 6** Optical absorption spectra of (a) bulk *h*-BN, (b) a BN sheet, and (c) six BN tubes with increasing diameter  $d$ . The GW+Bethe-Salpeter results (including e–h interactions) are compared with those resulting from the random-phase approximation (RPA or time-dependent Hartree, not including e–h interactions). The light polarization is parallel to the tube axis/plane [except for the dotted line in the (6, 6) case where it is perpendicular to the tube axis] (Reprinted with permission from [38], Copyright by the American Physical Society)

with photon emission is not allowed by symmetry. This selection rule can be broken if spin-orbit coupling is strong enough (a condition not verified for first row elements) or if an applied magnetic field can mix spin components.

These calculations point out to dramatic excitonic effects with binding energies ranging from  $\sim 0.7$  eV in the case of bulk *h*-BN [37] up to  $\sim 3$  eV in small diameter BN nanotubes [38, 39]. Such values are consistent with the 2.3 eV binding energy for the low lying bright exciton in the BN (6, 0) tube found by Park and coworkers [39]. This evolution of the binding energy shows a strong dimensionality effect, which can be understood by the reduction of screening in 1D systems.

When compared with carbon systems, the excitonic binding energies are found to be much larger and the excitons much more localized. For example, the root-mean-square of the exciton radius is found to be  $\sim 3.7$  and  $\sim 8.59$  Å in the (8, 0) BN and C tubes, respectively, while the binding energies are enhanced from  $\sim 1.0$  eV in carbon to  $\sim 2.3$  eV in the BN case [39]. Such an evolution can be associated with the strong ionic character of the BN network, which enhances the “Frenkel” nature of the excitons (Fig. 7).

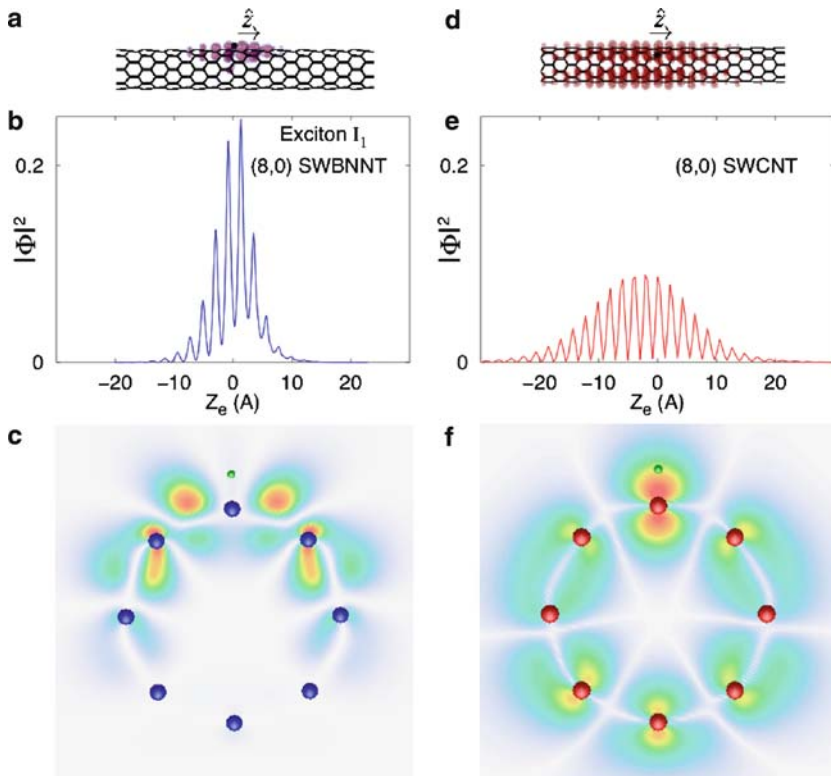


**Fig. 7** Excitonic wavefunction extent in (a–c) the (8, 0) BN tube, and (d–f) the (8, 0) carbon tube. In such a representation, the hole is fixed at the origin and one plots the electron wavefunction (Reprinted with permission from [39], Copyright by the American Physical Society)

### 1.4 Polarization Effects in BN Nanotubes

Theoretical calculations suggested the existence of a nonzero ground-state polarization in BN ( $n, m$ ) nanotubes such that  $(n - m)$  is not a multiple of three [53, 54]. This is a nontrivial quantum effect. The existence of a nonzero ground-state polarization induces a photo-current upon photon absorption even if the light is nonpolarized. Finally, it has been shown on the basis of ab-initio calculations that the band gap of BN tubes can be dramatically reduced upon application of a transverse static electric field, a phenomena labeled “giant dc Stark effect” [55]. The latter effect has been experimentally confirmed [56], while the sooner still has not.

### 1.5 Insights from the Physics of BN Fullerenes

In a similar way as carbon nanostructures, BN nanostructures can be synthesized in either nanotube or fullerene forms. The first experimental evidence of BN fullerenes was obtained by Stephan et al. [57], who observed nested BN concentric cages with a square-like shape in electron-irradiated BN samples. Following that, Golberg et al. [58] observed single-layered BN fullerenes that clearly revealed octahedral shapes, which could be modeled by fullerenes with 4 and 6-membered rings. More recently, Oku et al. [59, 60] have produced BN fullerenes by an arc melting technique, in quantities large enough to allow their characterization by mass spectroscopy. This revealed the existence of  $B_{24}N_{24}$  and several other BN fullerenes.

From the theoretical point of view, it has been predicted, before the experimental evidence, that stoichiometric BN cages should be composed of even-membered rings, which prevents the formation of homopolar B–B or N–N bonds [61, 62]. However, the specific types of rings in the cage seem to depend on the fullerene size: for instance, recent ab-initio calculations [63–65] indicate a stable tubular structure with 6, 4, and 8-membered rings for  $B_{24}N_{24}$ , while an octahedral cage with 4 and 6-membered rings for  $B_{36}N_{36}$  [66] accounts for transmission electron microscopy images observed by Golberg et al. [58] Selected tubular and octahedral BN structures, optimized from ab-initio calculations [65], are shown in Fig. 8. The figure also shows hypothetical icosahedral BN structures, where the 5-membered rings lead to the formation of line defects consisting of homopolar bonds.

The above-mentioned even-membered-rings rule for stable BN nanostructures does not always apply. For instance, in the case of nonstoichiometric  $B_mN_n$  cages, calculations indicate that fullerenes with adjoining pairs of fivefold membered rings can be stable [67, 68]. Also, in the case of BN nanocones, calculations indicate [69] that cones with a fivefold ring at the tip can be more stable than those with fourfold rings at the tip. The BN nanocones terminated with fivefold rings at the tip necessarily contain an antiphase boundary, a line defect with a sequence of N–N or B–B bonds. These line defects can be further stabilized by carbon doping, and lead to electronic states deep into the BN band gap region [69, 70], which might lead to optical and electronic properties useful for device applications.

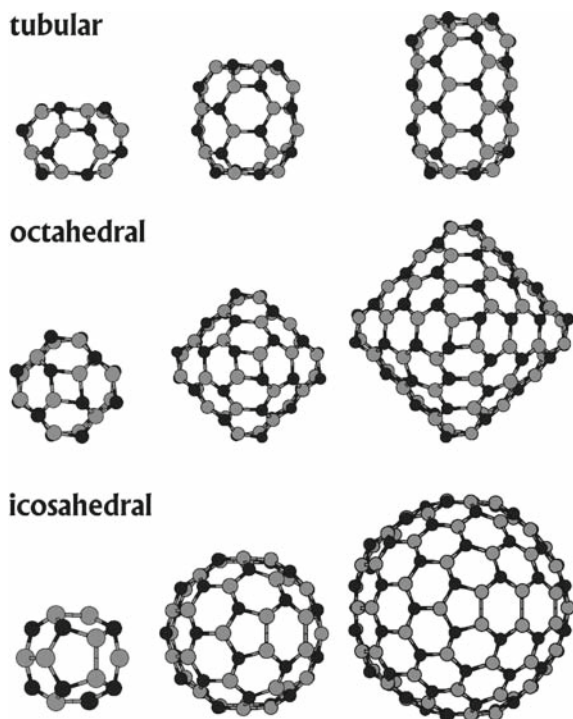


**Fig. 8** Selected tubular and octahedral BN fullerenes, optimized from ab-initio calculations. We also show hypothetical icosahedral BN structures, where the 5-membered rings lead to the formation of line defects consisting of homopolar B–B bonds. Nitrogen atoms are indicated by *black circles*, and boron atoms by *grey circles*. The atoms in the back part of the structures were omitted for visualization purposes (Adapted from [65], Copyright by Elsevier)

## 2 Composite Boron-Carbonitride Nanotubes

The synthesis of carbon and BN nanotubes, and the similarities between the two structures, was a strong motivation to attempt to synthesize composite  $B_xC_yN_z$  nanotubes with various carbon, boron, and nitrogen content. As a matter of fact, the characterization of pure carbon tubes containing “domains” of *h*-BN was reported in 1994 [12], that is before the synthesis of pure BN tubes in 1995. The goal was then to obtain doped carbon tubes, not composite structures, but this experiment, combined with early reports on planar hexagonal phases with the  $BC_2N$  stoichiometry [71], was a clear suggestion that homogeneous BCN tubes could be synthesized. The optical properties of BCN planar hexagonal phases, photoluminescent in the visible range [72, 73], provides further a strong incentive, in terms of applications, to study such systems.

## 2.1 Structure and Properties of $h\text{-BC}_2\text{N}$ Phases

An early model for the structure of  $h\text{-BC}_2\text{N}$  systems was obtained by minimizing the energy with respect to atomic positions of an 8-atoms hexagonal cell, corresponding to a  $(2 \times 2)$  graphene cell, where one half of the atoms are substituted by boron and nitrogen in equal content [74]. This scheme leads to the geometry represented in Fig. 9a with chains of C–C bonds intercalated by chains of B–N bonds. An analysis of this topology reveals that it is actually the structure that maximizes the number of C–C and B–N bond within this geometry constraint.

This early model for  $h\text{-BC}_2\text{N}$  structures was exploited by Miyamoto and coworkers [76] to predict the occurrence of chiral currents in  $h\text{-BC}_2\text{N}$  tubes, since the conductivity along the C–C chains is much larger than that perpendicular to the insulating B–N chains.

The recipe that one should maximize the number of C–C or B–N bonds to obtain the most stable structures with the  $\text{BC}_2\text{N}$  stoichiometry leads to the conclusion that, in the thermodynamic limit, such systems are driven toward segregation, or demixion, in pure carbon and  $h\text{-BN}$  domains. As a simple model for such a segregation, it was shown on the basis of ab-initio calculations [75, 77] that increasing the width of the intercalated C and BN strips, generalizing the early Liu et al. model (see Fig. 9b, c), would significantly stabilize the system as shown in Fig. 10a. This segregation in

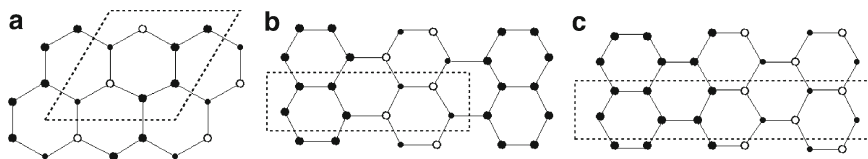


**Fig. 9** (a) Original Liu et al. model (labeled as well type-II  $h\text{-BC}_2\text{N}$ ). (b, c) Generalized  $h\text{-C}_n(\text{BN})_n$  strip models with  $n = 2$  and  $n = 3$  (Adapted from [75], Copyright by Springer)

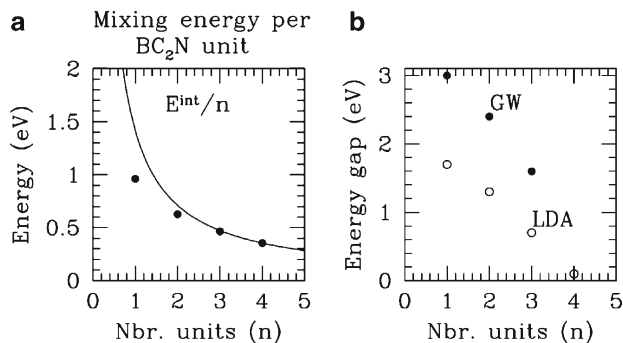


**Fig. 10** (a) Stability of  $h\text{-(C}_2)_n(\text{BN})_n$  structures taking as a reference fully segregated  $h\text{-BN}$  and graphene sheets, and (b) corresponding evolution of the band gap with DFT-LDA and GW approaches (Adapted [75], Copyright by Springer)

strips of pure  $h$ -BN or graphene can be generalized to segregation in pure domains of various shapes, a possibility studied theoretically by means of semiempirical approaches [78].

Experimentally, the segregation into domains requires the diffusion of atoms over long distances. As diffusion is activated by temperature, such phenomena is likely to be observed in high-temperature synthesis techniques such as arc discharge or laser ablation. As a matter of fact, in the arc discharge synthesis of MW composite BCN tubes, a complete segregation was observed leading to concentric shells of pure carbon and pure BN walls [79], a phenomenon for which a theoretical kinetic model was proposed [80]. However, using low temperature CVD synthesis, or substitution techniques on preformed carbon tubes, homogeneous samples can be obtained. The existence of  $h$ -BC<sub>2</sub>N systems with a band gap in the visible range [72, 73] requires indeed the synthesis of rather homogeneous BCN samples as discussed now.

## 2.2 *Electronic Properties of $h$ -BC<sub>2</sub>N Systems*

The metallic, or small gap semiconductor, behavior of carbon nanotubes, and the large gap insulator character of BN tubes, suggest that  $h$ -BC<sub>2</sub>N planar or tubular forms should display intermediate electronic properties. The photoluminescent character of planar  $h$ -BC<sub>2</sub>N phases with an absorption threshold in the visible range proves indeed that the corresponding band gap can enter the 1.8–3.2 eV range. Further, resonant Raman scattering [81] or transport [82] experiments clearly confirmed such values for boron carbonitride nanotubes. These results are also consistent with ab initio simulations both within the density functional theory (DFT) and, beyond, within an accurate quasiparticle many-body (GW) approach [75, 77] for various planar  $h$ -BC<sub>2</sub>N systems with increasing segregation character (Fig. 10b). Clearly, low segregation (small index  $n$ ), that is structures with a significant number of C–B or C–N bonds, is needed to obtain a band gap in the visible range. Such a control of the band gap by atomic structure was clearly demonstrated experimentally yielding “adjustable” band gap nanotubes [83]. Further, several synthesis techniques to enhance the number of B–C bonds, with respect to pure B–N bonds, or tailor the B/C/N ratio, have been explored [84, 85]. We will come back to that point below in the case of nonstoichiometric  $h$ -C <sub>$x$</sub> (BN) <sub>$y$</sub>  structures.

## 2.3 *Nanotube C/BN Hetero-Junctions and Properties of C/BN Edges*

In the limit of moderate segregation, one may expect the realization of carbon graphene flakes or cylindrical sections quantum dots surrounded by an insulating BN matrix, leading thus to C/BN hetero-structures. In the limit of complete segregation



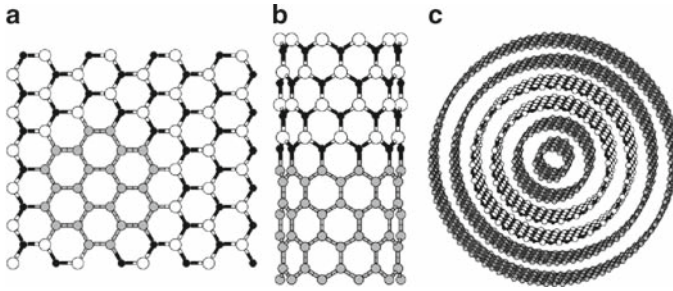


**Fig. 11** Symbolic representation of (a) graphene island in *h*-BN matrix quantum dot, (b) C/BN hetero-junction, and (c) concentric C/BN/C nanotubes

within a same nanotube wall (high-temperature synthesis), one obtains metal/insulator (Schottky) or semiconductor/insulator C/BN rectifying hetero-junctions (see Fig. 11b) that were first suggested and studied [86]. C–BN patterned single-walled nanotubes have been recently synthesized together with a growth model that allows to understand how one might control the observed C/BN self-organisation [87].

Interesting effects related to C/BN interface states have been proposed on the basis of *ab initio* simulations. At the C/BN interface, metal-induced gap states, exponentially decaying in the BN section, have been shown to exist both using *ab initio* calculations on finite size sections, or recursive tight-binding approaches allowing to study connected semiinfinite BN and carbon tubes [86]. It was shown in particular that C–N bonds at the junction would yield in-gap states close to the BN conduction band edge (donor character), while C–B bonds would yield on the contrary acceptor states. Interestingly enough, upon switching of spin polarization using local spin density approaches, it was predicted that such edge states would be spin polarized [88]. As a result, isolated C/BN junctions could be used to polarize incoming electrons, while ordered C/BN hetero-structures may display ferromagnetic order. Similar effects of spontaneous spin polarization, related to the presence of nondispersive edge states, were discussed in the case of BNC ribbons [89].

## 2.4 Nonstoichiometric $h\text{-B}_x\text{C}_y\text{N}_z$ structures

Beyond the *h*-BC<sub>2</sub>N structures, where C–C and B–N dimers are in equal number, more general B<sub>*x*</sub>C<sub>*y*</sub>N<sub>*z*</sub> systems can be expected to be found in experimental samples. This possibility was explored by Mazzoni and coworkers [90] in first-principles calculations for B<sub>*x*</sub>C<sub>*y*</sub>N<sub>*z*</sub> layers. The authors considered 20 distinct eight-atom-cell structures with four possible stoichiometries, namely BC<sub>2</sub>N, BCN<sub>2</sub>, B<sub>2</sub>CN, and B<sub>3</sub>C<sub>2</sub>N<sub>3</sub>. Given that the number of each atom species is not conserved among the structures, the energetic stability has to be obtained from the formation energies  $E_f = E - n_B\mu_B - n_C\mu_C - n_N\mu_N$ , where  $n_i$  and  $\mu_i$  are the number and the chemical potentials of species *i* in a given structure, respectively, and *E* is the total energy of that

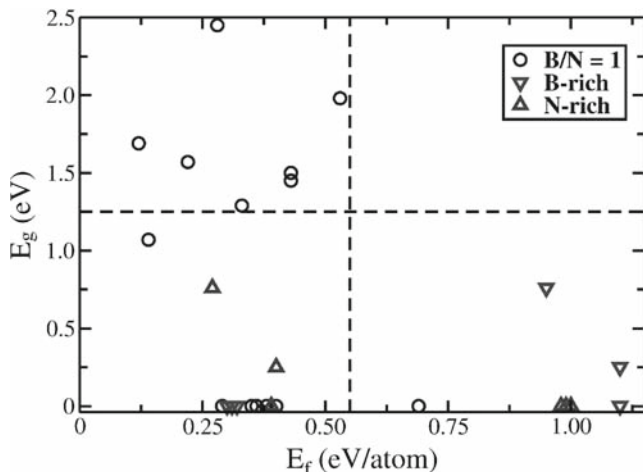


**Fig. 12** Calculated bandgaps of several types of  $B_xC_yN_z$  layers (within the DFT-GGA approach) vs. their formation energies. The stoichiometric structures (B/N ratio of one) are indicated by *open circles*. For the nonstoichiometric structures, indicated by *triangles*, the formation energies are calculated in both B-rich and N-rich environment conditions (Reprinted with permission from [90], Copyright by the American Physical Society)

structure. The  $\mu_i$  are constrained so as to result in  $E_f = 0$  for complete segregation into graphene and planar BN, and stability criteria can be derived from  $E_f$  in the limits of either boron-rich or nitrogen-rich environments [68]. Surprisingly, the most stable structure, among the considered ones, was not one with  $BC_2N$  stoichiometry, but a  $B_3C_2N_3$  structure instead. The authors also found that the structures with a B/N ratio of 1 tend to have simultaneously large band gap values and small formation energies. This is shown in Fig. 12, where the calculated bandgaps of several types of  $B_xC_yN_z$  layers (within the DFT-GGA approach) are plotted vs. their formation energies. It is also interesting to notice that the nonstoichiometric structures (B/N ratio different than one) have either small or null bandgaps.

Another interesting prediction regarding nonstoichiometric structures, from Okada and Oshiyama, reveals on the basis of *ab initio* simulations that specific stoichiometry should lead to a flat-band-related ferromagnetic order [91], as a generalization of Lieb's theorem on nonstoichiometric bipartite systems [92], even in the absence of edge states such as in the case of C/BN heterojunctions or BN and BCN strips. Such a prediction is still to be verified experimentally.

### 3 Conclusions

Despite tremendous progress in the synthesis techniques and the quality of the produced nanotubes, the physics of BCN tubes is still in its infancy when compared, e.g., with their carbon analogs that are currently incorporated in devices such as transistors or

nano-electro-mechanical systems (NEMS). For example, the electronic and optical properties of *h*-BN nanotubes, displaying a priori the most simple structure, have been only very recently characterized experimentally, and there is still much controversies about their absorption spectrum and the contribution of defect assisted emission lines.

The case of BCN structures is even more challenging. Even though bearing much potentiality in terms of applications, with a band gap that can be tuned in the visible range, the versatility of the possible atomic structures, driven by a competition between kinetics and thermodynamics, remains as a challenge to the physicists aiming at synthesizing tubes with a well-controlled stoichiometry, geometry, and electronic properties. From visible-range light-harvesting materials, to C/BN rectifying junctions and quantum dots or BN-sheated (that is protected) carbon nanotubes, the expectations associated with such systems are extremely large, provided that a better understanding of the growth mechanisms be achieved.

**Acknowledgments** X.B. acknowledges support from the French CNRS and National Agency for Research (ANR) under contract PNANO-ACCENT n° ANR-06-NANO-069-02. H.C. acknowledges support from the Brazilian agencies CNPq and FAPEMIG, and from the project Instituto do Milênio de Nanotecnologia/MCT.

## References

1. X. Blase, A. Rubio, M.L. Cohen, S.G. Louis, *Europhys. Lett.* **28**, 335 (1994).
2. A. Rubio, J. Corkill, M.L. Cohen, *Phys. Rev. B* **49**, 5081 (1994).
3. J.W.G. Wildöer, L.C. Venema, A.G. Rinzler, R.E. Smalley, C. Dekker, *Nature (London)* **91**, 19 (1998).
4. T.W. Odom, J.L. Huang, P. Kim, C.M. Lieber, *Nature (London)* **91**, 62 (1998).
5. N. Hamada, S. Sawada, A. Oshiyama, *Phys. Rev. Lett.* **68**, 1579 (1992).
6. R. Saito, M. Fujita, G. Dresselhaus, M. S. Dresselhaus, *Appl. Phys. Lett.* **60**, 2204 (1992).
7. J.W. Mintmire, B.I. Dunlap, C.T. White, *Phys. Rev. Lett.* **68**, 631 (1992).
8. N.G. Chopra et al., *Science* **269**, 966 (1995).
9. A. Loiseau et al., *Phys. Rev. Lett.* **76**, 4737 (1996).
10. M. Terrones et al., *Chem. Phys. Lett.* **259**, 568 (1996).
11. D. Golberg et al., *Appl. Phys. Lett.* **69**, 2045 (1996).
12. O. Stephan, P.M. Ajayan, C. Colliex, P. Redlich, J.M. Lambert, P. Bernier, P. Lefin, *Science* **266**, 1683 (1994).
13. Loiseau, A., P. Launois, P. Petit, S. Roche, J.-P. Salvetat, *Understanding Carbon Nanotubes from Basics to Applications*. Lecture Notes in Physics 677, Springer-Verlag, Berlin (2006).
14. M. Terrones et al., *Mat. Today* **10**, 30–38 (2007).
15. D. Golberg, Y. Bando, C.C. Tang, C.Y. Zhi, *Adv. Mater.* **19**, 2413–2432 (2007).
16. L. Liu, Y.P. Fezng, Z.X. Shen, *Phys. Rev. B* **68**, 104102 (2003).
17. L. Wirtz, R. Arenal de la Concha, A. Loiseau, A. Rubio, *Phys. Rev. B* **68**, 045425 (2003).
18. R. Tenne et al., *Nature* **360**, 444 (1992).
19. L. Margulis et al., *Nature* **365**, 113 (1993).
20. R. Tenne et al., *Chem. Mater.* **10**, 3225 (1998).
21. L. Rapoport et al., *Nature* **387**, 791 (1997).
22. G. Seifert et al., *Phys. Rev. Lett.* **85**, 146 (2000).
23. M. Côté et al., *Phys. Rev. B* **58**, R4277 (1998).

24. P. Zhang and V.H. Crespi, *Phys. Rev. Lett.* **89**, 056403 (2002).
25. J.-C. Charlier, X. Blase, S. Roche, *Rev. Mod. Phys.* **79**, 667 (2007).
26. K. Watanabe, T. Taniguchi, H. Kanda, *Nat. Mater.* **3**, 404 (2004).
27. R.F.W. Bader, *Atoms in Molecules: A Quantum Theory*, International Series of Monographs in Chemistry, Clarendon Press, Oxford (1990).
28. C. Katan, P. Rabiller, C. Lecomte, M. Guezo, V. Oison, M. Souhassou, *J. Appl. Cryst.* **36**, 65 (2003).
29. J. Robertson, *Phys. Rev. B* **29**, 2131 (1984).
30. A. Catellani, M. Posternak, A. Balderschi, A.J. Freeman, *Phys. Rev. B* **36**, 6105 (1997).
31. J. Furthmüller, J. Hafner, G. Kresse, *Phys. Rev. B* **50**, 15606 (1994).
32. Y.N. Xu, W.Y. Ching, *Phys. Rev. B* **44**, 7787 (1991).
33. R. Dovesi, C. Pisani, C. Roetti, *Int. J. Quantum Chem.* **17**, 517–529 (1980).
34. L. Hedin and S. Lundquist, in *Solid State Physics*, Vol. 23, edited by H. Ehrenreich, F. Sietz, and D. Turnbull, Academic, New York, (1969), p. 1.
35. X. Blase, A. Rubio, M.L. Cohen, S.G. Louie, *Phys. Rev. B* **51**, 6868 (1995).
36. G. Cappellini, G. Satta, M. Palumbo, G. Onida, *Phys. Rev. B* **64**, 035104 (2001).
37. B. Arnaud, S. Lebègue, P. Rabiller, M. Alouani, *Phys. Rev. Lett.* **96**, 026402 (2006).
38. L. Wirtz, A. Marini, A. Rubio, *Phys. Rev. Lett.* **96**, 126104 (2006).
39. C.-H. Park, C.D. Spataru, S.G. Louie, *Phys. Rev. Lett.* **96**, 126105 (2006).
40. K.T. Park, K. Terakura, N. Hamada, *J. Phys. C: Solid State Phys.* **20**, 1241–1251 (1987).
41. E.R. Margine and H. Vincent, *Crespi*, *Phys. Rev. Lett.* **96**, 196803 (2006).
42. L.X. Benedict, S.G. Louie, M.L. Cohen, *Phys. Rev. B* **52**, 8541 (1995).
43. S. Tasaki, K. Maekawa, T. Yamabe, *Phys. Rev. B* **57**, 9301 (1998).
44. A.G. Marinopoulos, L. Reining, A. Rubio, N. Vast, *Phys. Rev. Lett.* **91**, 046402 (2003).
45. N. Wang, Z.K. Tang, G.D. Li, and J.S. Chen, *Nature* (London) **408**, 50 (2000).
46. A.G. Marinopoulos, L. Wirtz, A. Marini, V. Olevano, A. Rubio, L. Reining, *Appl. Phys. A* **78**, 1157–1167 (2004).
47. G. Onida, L. Reining, A. Rubio, *Rev. Mod. Phys.* **74**, 601 (2002).
48. C.F. Klingshim, *Semiconductor Optics*, Springer-Verlag, Berlin (1995).
49. R.J. Elliott, *Phys. Rev.* **108**, 1384 (1957).
50. R. Loudon, *Am. J. Phys.* **27**, 649 (1959).
51. Ogawa and Takagahara, *Phys. Rev. B* **43**, 14325 (1991).
52. Ogawa and Takagahara, *Phys. Rev. B* **44**, 8138 (1991).
53. P. Král et al., *Phys. Rev. Lett.* **85**, 1512 (2000).
54. E.J. Mele and P. Král, *Phys. Rev. Lett.* **88**, 056803 (2002).
55. K. H. Khoo, M.S.C. Mazzoni, Steven G. Louie, *Phys. Rev. B* **69**, 201401 (2004).
56. M. Ishigami et al., *Phys. Rev. Lett.* **94**, 056804 (2005).
57. O. Stephan et al., *Appl. Phys. A Mater. Sci. Process* **67**, 107 (1998).
58. D. Golberg, Y. Bando, O. Stephan, K. Kurashima, *Appl. Phys. Lett.* **73**, 2441 (1998).
59. T. Oku, A. Nishiwaki, I. Narita, M. Gonda, *Chem. Phys. Lett.* **380**, 620 (2003).
60. T. Oku, A. Nishiwaki, I. Narita, *J. Phys. Chem. Solids* **65**, 369 (2004).
61. F. Jensen and H. Toftlund, *Chem. Phys. Lett.* **201**, 89 (1993).
62. X. Blase, A. De Vita, J.-C. Charlier, R. Car, *Phys. Rev. Lett.* **80**, 166 (1998).
63. H. S. Wu, X. H. Xu, H. Jiao, *Chem. Phys. Lett.* **386**, 369 (2004).
64. R.R. Zope, T. Baruah, M.R. Pederson, B.I. Dunlap, *Chem. Phys. Lett.* **393**, 300 (2004).
65. R.J.C. Batista, M.S.C. Mazzoni, H. Chacham, *Chem. Phys. Lett.* **421**, 246 (2004).
66. S.S. Alexandre, M.S.C. Mazzoni, H. Chacham, *Appl. Phys. Lett.* **73**, 61 (1999).
67. P.W. Fowler, K.M. Rogers, G. Seifert, M. Terrones, H. Terrones, *Chem. Phys. Lett.* **209**, 359 (1994).
68. S.S. Alexandre, H. Chacham, R.W. Nunes, *Phys. Rev. B* **63**, 045402 (2001).
69. S. Azevedo, M.S.C. Mazzoni, R.W. Nunes, H. Chacham, *Phys. Rev. B* **70**, 205412 (2004).
70. S. Azevedo, M.S.C. Mazzoni, H. Chacham, R.W. Nunes, *Appl. Phys. Lett.* **82**, 2323 (2003).
71. J. Kouvetakakis, R.B. Kaner, M.L. Sattler, N. Bartlett, *J. Chem. Soc., Chem. Commun.* (24), 1785 (1986).

72. M.O. Watanabe, S. Itoh, T. Sasaki, K. Mizushima, *Phys. Rev. Lett.* **77**, 187 (1996); Erratum, *Phys. Rev. Lett.* **77**, 2846 (1996).
73. Y. Chen, J.C. Barnard, R.E. Palmer, M.O. Watanabe, T. Sasaki, *Phys. Rev. Lett.* **83**, 2406 (1999).
74. A.Y. Liu et al., *Phys. Rev. B* **39**, 1760 (1989).
75. X. Blase, J.-C. Charlier, A. De Vita, R. Car, *Appl. Phys. A* **68**, 293–300 (1999).
76. Y. Miyamoto, S.G. Louie, M.L. Cohen, *Phys. Rev. Lett.* **76**, 2121–2124 (1996).
77. X. Blase, *Comp. Matt. Sci.* **17**, 107 (2000).
78. H. Nozaki and S. Itoh, *J. Phys. Chem. Solids* **57**, 41–49 (1996).
79. K. Suenaga, C. Colliex, N. Demoncy et al., *Science* **278** 653–655 (1997).
80. O.A. Louchev, Y. Sato, H. Kanda, Y. Bando, *Appl. Phys. Lett.* **77**, 1446–1448 (2000).
81. C.Y. Zhi, X.D. Bai, E.G. Wang, *Appl. Phys. Lett.* **84**, 1549–1551 (2004).
82. D. Goldberg, P. Dorozhkin, Y. Bando, M. Hasegawa, Z.C. Dong, *Chem. Phys. Lett.* **359**, 220–228 (2002).
83. C.Y. Zhi, J.D. Guo, X.D. Bai, E.G. Wang, *J. Appl. Phys.* **91**, 5325–5333 (2002).
84. Y.K. Yap, Y. Wada, M. Yamaoka, M. Yoshimura, Y. Mori, T. Sasaki, *Diam. Rel. Mater.* **10**, 1137–1141 (2001).
85. Y. Wada, Y.K. Yap, M. Yoshimura, Y. Mori, T. Sasaki, *Diam. Rel. Mater.* **9**, 620–624 (2000).
86. X. Blase, J.-C. Charlier, A. De Vita, R. Car, *Appl. Phys. Lett.* **70**, 197 (1997).
87. S. Enouz, O. Stephan, J.-L. Cochon, C. Colliex, A. Loiseau, *Nano Lett.* **7**, 1856 (2007).
88. J. Choi, Y.-H. Kim, K.J. Chang, D. Tománek, *Phys. Rev. B* **67**, 125421 (2003).
89. J. Nakamura, T. Nitta, A. Natori, *Phys. Rev. B* **72**, 205429 (2005).
90. M.S.C. Mazzoni, R.W. Nunes, S. Azevedo et al., *Phys. Rev. B* **73**, 073108 (2006).
91. S. Okada, A. Oshiyama, *Phys. Rev. Lett.* **87**, 146803 (2001).
92. E.H. Lieb, *Phys. Rev. Lett.* **62**, 1201 (1989).

# Optical and Vibrational Properties of Boron Nitride Nanotubes

Ludger Wirtz and Angel Rubio

**Abstract** As for carbon nanotubes, optical and vibrational spectroscopy – in particular Raman and luminescence spectroscopy – play an important role for the characterization of BN nanotubes. In this chapter we review, from a theoretical view point, the different spectroscopic techniques that are currently used for BN nanotubes and make a close link with available experimental data. We summarize experimental and theoretical data on optical absorption spectroscopy, luminescence spectroscopy, electron-energy loss spectroscopy, Raman spectroscopy, and infrared (IR) absorption spectroscopy. The combination of all those methods allows for a fairly complete characterization of the electronic structure and the vibrational properties of BN tubes. Possible applications in optoelectronic devices are briefly discussed.

## 1 Introduction

Boron nitride (BN) is isoelectronic to carbon and displays, among others, a graphite-like hexagonal phase (h-BN). The elastic constants are very similar (although smaller), but the polar nature of the BN bond leads to significant changes in the electronic structure of h-BN as compared to graphite. While graphite is a semimetal (zero bandgap in the single sheet), h-BN has a large bandgap (above 6 eV). Furthermore, its high thermal stability and relative chemical inertness distinguishes it from its carbon counterpart. Together with graphite and BN, the lesser known  $BC_3$ ,  $BC_2N$ , and CN ( $C_3N_4$ ) also crystallize into graphitic-sheet like structures. Whereas the single BN sheet is a wide bandgap semiconductor the less ionic  $BC_3$

---

L. Wirtz

Institute for Electronics, Microelectronics, and Nanotechnology (IEMN),  
CNSR-UMR 8520, B.P. 60069, 59652 Villeneuve d'Ascq Cedex, France

A. Rubio (✉)

European Theoretical Spectroscopy Facility (ETSF), Departamento de Física de Materiales,  
Universidad del País Vasco, Edificio Korta, Avda, Tolosa 72, 20018 San Sebastián, Spain  
e-mail: angel.rubio@ehu.es

and  $\text{BC}_2\text{N}$  are small and medium gap semiconductors, respectively, with envisaged potential new applications.

Briefly after the discovery of carbon nanotubes and based on the similarities among graphite and other  $sp^2$ -like bonded materials, the existence of boron nitride [1] and boron–carbon–nitrogen nanotubes was predicted [2–5]. Specific synthesis of these nanotubes was achieved afterward: boron nitride in [6], and  $\text{BC}_2\text{N}$  and  $\text{BC}_3$  in [7, 8] as well as other inorganic tubular forms. The growth of the composite nanotubes is still an open question and deserves more theoretical as well as experimental studies. The predicted properties of these tubules are quite different from those of carbon with numerous possible technological applications in the fields of catalysis, lubrication, and electronic and photonic devices.

In contrast to C nanotubes which can be either semiconducting or metallic, depending on the chirality of the tube, BN nanotubes are always semiconducting with a large bandgap, that is nearly independent of the tube diameter, chirality, and whether the nanotube is single-walled, multiwalled, or packed in bundles [1, 2]. A structural difference between BN and C tubes is that for tubes with small diameter, the BN system buckles with the B atoms moving inward and the N atoms outward [2]. This results in a dipolar double cylinder shell structure. The uniform electronic properties and the dipolar barrier suggest that BN nanotubes may have significant advantages for applications in electronic and mechanical devices. Furthermore, the bottom of the conduction band is a nearly free electron like-state (NFE). This state remains the bottom of the conduction band even in the multiwall case and, in the case of n-type doping, will play an important role for potential applications in field emission devices and molecular transport.

Several spectroscopic methods are commonly used for the identification and characterization of BN nanotube samples. High-resolution transmission electron microscopy (HRTEM) allows for a quick view at the scene with almost atomic resolution. Scanning tunneling microscopy/spectroscopy (STM/STS) allow to get atomic resolution and to map the electronic structure to the underlying nanotube geometry. In optical spectroscopy, using laser light, the spatial resolution is lost. However, alternative information about the band structure and the vibrational properties of the constituents can be gained. Optical absorption spectroscopy probes the electronic band structure by direct excitation of an electron from the valence to the conduction band. Since BN tubes have a wide bandgap, either multiphoton processes or ultraviolet (UV) light are necessary for this process to occur in BN nanotubes. The detailed knowledge of the optical properties of BN tubes is indispensable for their characterization and may help to guide their use as nanoelectronic devices: for example, BN nanotubes have been used to build a field effect transistor [9] and the observed high yield of UV luminescence [10] of bulk hexagonal BN suggest to use of BN nanotubes as UV light sources. Therefore, it is important to know about possible excitonic states whose importance has been shown for the optoelectronic properties of carbon nanotubes.

At lower energy, IR absorption probes the direct excitation of phonons. Raman spectroscopy probes the excitation of phonons by measuring the frequency shift in elastically scattered laser light. In contrast to carbon nanotubes, in BN tubes the Raman scattering is nonresonant due to the large bandgap of the tubes. The resulting

spectra are, therefore, weaker in intensity and must be carefully separated from a possible overlap by resonant Raman scattering from contaminants. On the other hand, the efficiency of IR-absorption is enhanced by the polarity of the material and gives rise to a much more pronounced IR spectrum than in the case of carbon tubes where the IR spectra have very little structure and can hardly be distinguished from the IR spectrum of graphite. It is then expected that a combination of optical, Raman, and IR spectroscopy will be important for the characterization of BN tubes such as it is already in the case of C tubes.

For the interpretation of such spectra, an accurate knowledge of the phonon frequencies as a function of tube diameter and chirality together with the corresponding photoabsorption cross section is indispensable. Therefore, we present in detail the calculations of phonons in BN nanotubes and their symmetry analysis. For zigzag and chiral nanotubes, the set of IR-active modes is a subset of the Raman-active modes. In particular, the radial breathing mode (RBM) is not only Raman but also IR active. However, for armchair tubes, the sets of IR- and Raman-active modes are disjoint.

This chapter is organized as follows. First, we provide a detailed description of the absorption spectra of bulk hexagonal BN and the tubes, making a connection between the two and highlighting the relevance of many-body correlations (quasi-particle and excitonic corrections). Then, we will address some important issues related to the high-yield luminescence in BN samples and how it can be externally controlled and modified by the presence of intrinsic defects in the samples. Furthermore we will discuss the excitation of plasmons in electron-energy loss spectroscopy (EELS). The second part of the chapter will be devoted to the phonons and the IR and Raman spectroscopy of BN tubes.

## 2 Optical Absorption Spectra of BN Nanotubes

Due to the large bandgap of h-BN ( $>6$  eV), optical absorption only starts in the UV regime. Thus, optical absorption spectra of BN tubes are difficult to measure and may not be the method of choice for the characterization of tubes. However, their understanding on a theoretical level is of utmost importance as a first step toward the understanding of luminescence in BN tubes. Furthermore, we will see that the absorption spectra are conceptually interesting because they are dominated by one strongly bound exciton.

### 2.1 Absorption Spectra in the Independent-Particle Picture

The absorption cross section of an isolated nanotube is given by the imaginary part of its polarizability (per unit length). To first order, absorption of a photon of energy  $\hbar\omega$  is commonly explained through the vertical excitation of an electron from a state  $|n_v, k\rangle$  with energy  $E_v$  in the valence-band to a conduction-band state  $|n_c, k\rangle$  of energy  $E_c$ :



$$\text{Im}[\alpha(\omega)] \propto \int dk \sum_{n_v, n_c} \left| \langle n_v, k | D | n_c, k \rangle \right|^2 \delta(E_c - E_v - \hbar\omega). \quad (1)$$

The matrix element of the dipole operator  $D$  “selects” only certain “allowed” transitions. Since the photon carries vanishing momentum, both valence and conduction band states must have the same wave vector  $k$ . Equation (1) corresponds to the so-called random-phase approximation (RPA). It is also called the “one-electron” or “independent-particle” picture of absorption. The latter name stems from the assumption that the Coulomb potential in which the active electron is moving and which is caused by the charge density of all other electrons is static and independent of the state of the active electron. While this assumption is reasonable for many materials, we will see below that it has serious deficiencies for h-BN and BN nanotubes. Nevertheless, it is instructive to start the exploration of the absorption spectra of BN nanotubes in the independent-particle picture.

The electronic structure of BN nanotubes can be constructed from the electronic structure of the single sheet via the zone-folding procedure (see below). Therefore, we present in Fig. 1 the band structure of an h-BN sheet and of a (6,6) armchair BN nanotube. The band structure of the sheet is characterized by the large direct gap at the  $K$ -point.<sup>1</sup> According to the zone-folding procedure, the band structure of the tube can be obtained by cutting the band dispersion of the sheet along certain parallel lines in the reciprocal space (vertical lines in the gray-shaded area of Fig. 1c). The distance of the lines is determined by the quantization of the wave-vector component  $K_\perp$  along the tube circumference. The different lines correspond to different angular momenta (quantum number  $m$ ) along the axis of the tube. Comparing the band structure of the sheet to that of the tube, we see that the highest valence band and the lowest conduction band of the tube can be directly obtained from the  $\pi$  and  $\pi^*$  bands of the sheet along the line  $M \rightarrow K$  and beyond. The wavefunctions of the  $\pi$  and  $\pi^*$  bands are predominantly composed of atomic  $p_z$  orbitals (i.e.,  $p$  orbitals with an orientation perpendicular to the plane). We show in Fig. 2 the corresponding wavefunctions for the sheet at the point  $K$ . The  $\pi$ -band wavefunction is predominantly located at the nitrogen atoms and the  $\pi^*$ -band wavefunction is mostly located at the boron atoms. This is due to the higher electronegativity of nitrogen. It is the strong difference in electronegativity between B and N that leads to the large bandgap. (In a graphene sheet, where both atoms in the unit cell are equivalent, the  $\pi$  and  $\pi^*$  bands are degenerate at  $K$ , leading to the linear crossing of the two bands.)

In order to understand how an absorption spectrum is constructed via (1), we look in the following at the RPA-spectrum of a single sheet of h-BN and of the (6,6) nanotube. Figure 3 shows the RPA-absorption spectrum of the sheet. In the low

---

<sup>1</sup>Much can be written about the exact value of the gap. For the dispersion in Fig. 1, we have used DFT and LDA for the exchange-correlation functional. This yields a gap of 4.5 eV. The exact value of the bandgap is discussed further in the text.

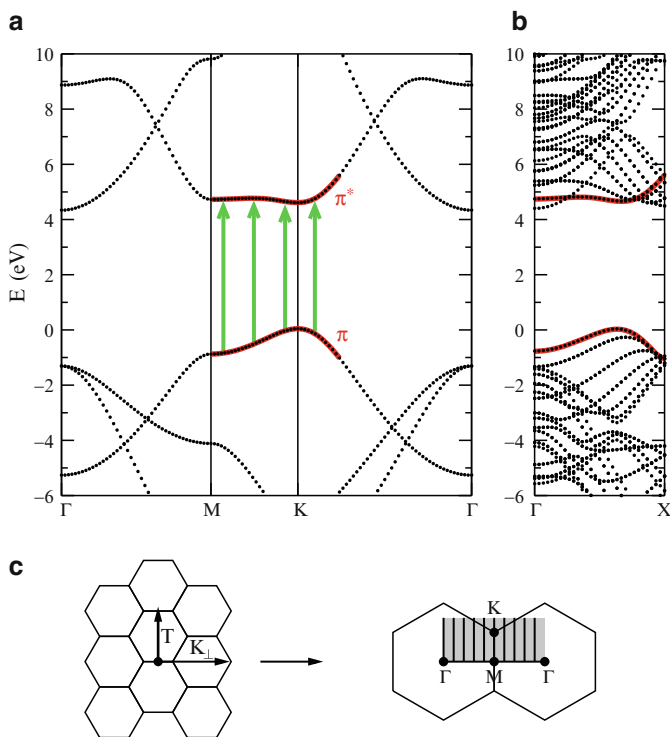


**Fig. 1** Band structure (calculated with DFT-LDA) for the single sheet of h-BN **(a)** and for the (6,6) BN nanotube **(b)**; **(c)** demonstrates how the band structure of the tube can be obtained by cutting the band structure of the sheet along certain lines (zone folding): The *left panel* shows a piece of a h-BN sheet that is rolled up along the vector  $K_{\perp}$ , thus forming an armchair tube. The *right panel* shows the corresponding reciprocal space with quantized values of the momentum in circumferential direction

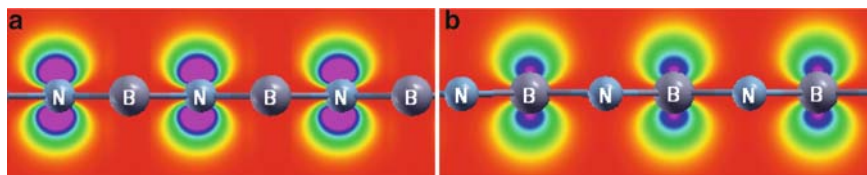


**Fig. 2** Wavefunctions in the single BN sheet of **(a)** the  $\pi$  (N-based) and **(b)** the  $\pi^*$  (B-based) band at  $K$

energy regime ( $<10$  eV) and for light-polarization parallel to the sheet (panel a), the dipole-matrix element in (1) only selects transition from the  $\pi$  to the  $\pi^*$  band (arrows in Fig. 1). The onset of the spectrum is at 4.5 eV which corresponds to the

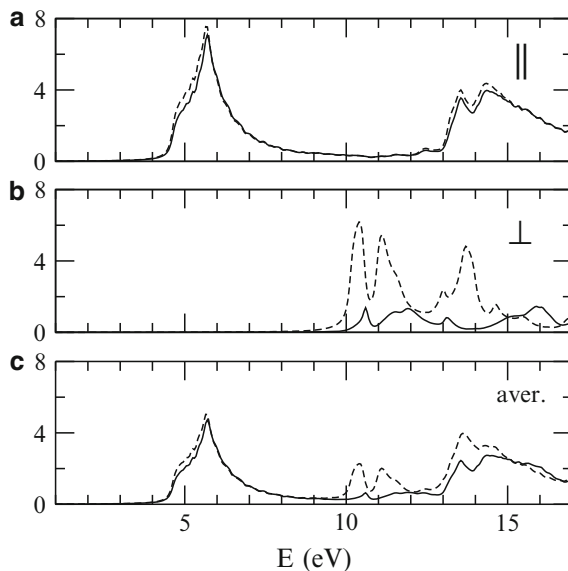


**Fig. 3** RPA-absorption spectrum of a single BN sheet with (*solid lines*) and without (*dashed lines*) depolarization effects: (a) light-polarization parallel to the plane, (b) polarization perpendicular to the plane, (c) averaged spectrum

direct gap of the sheet at  $K$ . The peak at 5.7 eV stems from the  $M$ -point where the  $\pi$  and  $\pi^*$  bands display saddle-points and the joint density of states has a maximum. If the light is polarized perpendicularly to the sheet (Fig. 3b), the  $\pi$ - $\pi^*$  transitions are dipole-forbidden. Optical absorption is due to  $\sigma$ - $\pi^*$  and  $\pi$ - $\sigma^*$  transitions and the onset of the RPA-spectrum is only at about 10 eV. Figure 3 also demonstrates the effect of depolarization. The dashed line shows the spectrum calculated with (1). The external field polarizes the charge distribution of the sheet, creating a layer of dipoles. This dipole layer, in turn, leads to an induced electric field that is directed opposite to the external field. The absorption spectrum must therefore be calculated self-consistently. (Mathematically, this corresponds to taking into account off-diagonal elements of the dielectric tensor in reciprocal space.) The resulting spectrum (solid line in Fig. 3) is strongly reduced in oscillator strength in the energy range below 15 eV. For the parallel polarization (Fig. 3a), the depolarization effects have only a minor influence. The direction-averaged spectra (Fig. 3c) is dominated by the contribution from the parallel polarization.

In Fig. 4a, we present the RPA spectra of bulk h-BN, of the single-sheet of h-BN and of different BN nanotubes with diameters ranging from 2.8 Å (for the purely hypothetical BN (2,2) tube) to 9.7 Å (for the BN (7,7) tube), which is at the lower border of the range of experimentally produced tubes. The light polarization is set parallel to the planes or tube-axis, respectively, because, as discussed above, depolarization effects strongly suppress the absorption in the perpendicular direction. For the

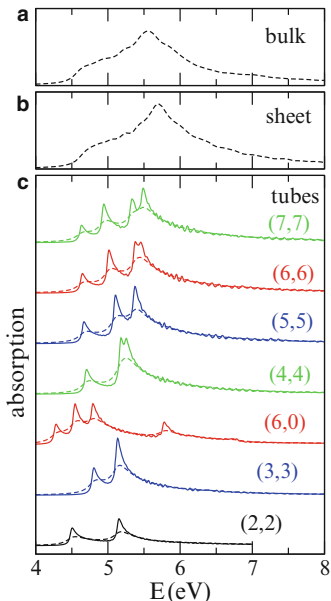


**Fig. 4** RPA-absorption spectra of (a) bulk hexagonal BN, (b) a single sheet of hexagonal BN, (c) six different BN tubes with increasing diameter  $d$ . *Solid lines* are calculated with a Lorentzian broadening of 0.025 eV, *dashed lines* with a broadening of 0.1 eV (reprinted with permission from [11], copyright (2006) by the American Physical Society)

bulk and for the single-sheet, the spectra are almost indistinguishable. This is due to the relatively weak interaction between neighboring sheets in the bulk phase.

Since the bands of the tubes can be constructed from the sheet via the zone-folding procedure, the RPA spectra of the tubes display transitions at the same energies as in the sheet. With increasing diameter, the shape of the tube spectra converges rapidly toward the sheet spectrum, in particular if plotted with a Lorentzian broadening of 0.1 eV (corresponding roughly to usual experimental broadening). A calculation with a fine broadening of 0.025 eV (and a correspondingly fine sampling with 200  $\mathbf{k}$ -points in the first Brillouin zone) reveals additional fine-structure below 5.5 eV. This structure is due to the van-Hove singularities in the 1D density of states. For tubes with larger radii, the density of the fine-structure peaks increases and the RPA spectrum approaches that of the 2D sheet. The onset of absorption is constantly at  $4.7 \pm 0.1$  eV for all tubes except for the (2,2) and the (6,0) tube (and other small diameter zigzag tubes) where the gap is lowered due to curvature effects [1, 12]. A very detailed discussion of the RPA absorption spectra can be found in [12]. We would like to emphasize however, that for BN materials, the RPA-absorption spectra are of purely academic interest. We will discuss below that correlation effects strongly modify the shape of the spectra (i.e., position and strength of the main peak-structure and onset of the continuum).

## 2.2 *Influence of Correlation Effects on the Absorption Spectra*

What is the practical meaning of “correlation effects” in the context of optical absorption? A photon is absorbed by exciting an electron from the valence band to the conduction band. For a quantitative prediction of the spectrum, we thus need to know the exact size of the bandgap. Furthermore, we have to take into account that the excited electron may interact with the hole that is left behind in the valence band. These studies are done using many-body perturbation theory with a self-energy formalism in which electron-correlations are treated on the level of the GW approximation while the electron–hole attraction is dealt with by means of a static Bethe–Salpeter equation.

### 2.2.1 **The Bandgap Problem**

The bandgap is defined as the energy difference between the lowest unoccupied molecular orbital (LUMO) and the highest occupied molecular orbital (HOMO). The energy of the HOMO is the energy that it would take to extract an electron from that orbital. Experimentally, the HOMO energy can be directly measured by photoemission spectroscopy. The energy of the LUMO is the energy that one gains (or loses) by adding an electron to the neutral cluster. Experimentally, the LUMO energy can be measured by inverse photoemission (an electron beam is directed at a surface and the energy of the emitted photons is measured). For strongly insulating materials both photoemission and inverse photoemission are very difficult to perform (the accuracy in direct photoemission, reaching meV resolution, is at present much larger than for inverse photoemission). Hence, for bulk h-BN (and equally for the single-sheet and for the tubes), no direct experimental data for the bandgap exists and we have to rely on theoretical predictions.

The situation for theorists is similarly difficult. We discuss here briefly the performance of the two most frequently used methods for band-structure calculations: the Hartree–Fock approximation (HFA) and density functional theory (DFT). Let us assume that in both approximations, the HOMO energy is described properly. The problem lies then in the LUMO energy. If an additional electron is attached to the material, it interacts with the other electrons through the dielectrically screened electron–electron repulsion which leads to a polarization of the environment. This is a correlation effect and lowers the energy of the LUMO with respect to an imaginary system where correlation effects are absent. In the HFA, correlation effects are not included (the electron density is the static charge density of the neutral ground-state). Therefore, in general, the HFA severely overestimates the bandgap. DFT in the local-density approximation (LDA) or in the generalized-gradient approximation (GGA) [13] tends to overestimate the screening of additional electrons. This results, in general, in an underestimation of the bandgap. In this way, we obtain for the single sheet of h-BN a gap of 4.5 eV in LDA, 4.6 eV in GGA, and 14 eV within the HFA! The real bandgap must lie within these limiting values. Using more sophisticated exchange–correlation functionals in DFT, one can get closer to the

exact bandgap. With the B3LYP hybrid functional [14], we obtain 6.4 eV. Baumeier et al. [15] report a value of 6.3 eV, using a self-interaction corrected DFT approach. A reliable calculation of the gap can only be achieved taking electron–electron correlation explicitly into account. This is achieved in the so-called GW approximation which will be briefly discussed below. In the GW approximation, the bandgap of the single h-BN sheet is 8.1 eV [11].

The only exact way to calculate the bandgap of a material consists in the use of the methods of many-body perturbation theory. Starting from either HFA or DFT wavefunctions and energies, the first step is the calculation of the inverse dielectric function  $\epsilon^{-1}$  on the level of the RPA. The dielectric function describes how the bare Coulomb-potential  $V_c$  between two electrons is screened by the other charges in the material. Within the GW approximation [16–19], the quasiparticle energies (single-particle excitation energies),  $\epsilon_{nk}$ , are calculated by solving the quasiparticle equation (atomic units are used all through this chapter unless otherwise stated)

$$\left[ -\frac{\nabla^2}{2} + V_{\text{ext}} + V_{\text{Hartree}} + \Sigma(E_{nk}) \right] \Psi_{nk} = E_{nk} \Psi_{nk}. \quad (2)$$

The self-energy  $\Sigma = i\text{GW}$  is nonlocal and energy dependent. It is approximated as the product of the one-particle Green’s function  $G$  and the dynamically screened Coulomb interaction  $W = \epsilon^{-1} V_c$ . The resulting energy levels are “true” electron-removal and electron-addition energies, i.e., they include the effect of dynamic screening upon removing an electron from the valence band or adding one to the conduction band, respectively.

In Fig. 5, we show the effect of the GW approximation on the band structure of bulk h-BN [20, 21]. Note that with respect to the band structure of the single-sheet

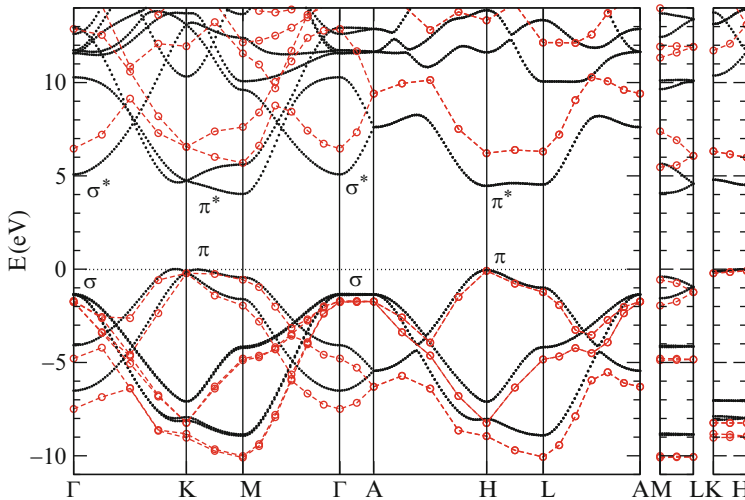


**Fig. 5** Band structure of bulk h-BN: LDA (dotted line), GW approximation (circles and dashed lines)

(see Fig. 1), in bulk h-BN, the  $\pi$  and  $\pi^*$  bands are split into two bands each. (This is a consequence of the AA'-stacking of the layers in the bulk.) The minimum direct gap of 4.47 eV in LDA is shifted to 6.26 eV in the GW approximation. The large shift points to a strong electron–electron interaction which can be associated with the layered structure of h-BN: electrons are mostly confined to 2D sheets, hopping between the layers is weak. For the single-sheet, the gap opening is even stronger: from 4.5 eV in LDA to 8.1 eV in the GW approximation! This huge GW shift is due to (1) the fact that electrons are strictly confined to a 2D sheet and (2) due to the much weaker screening in the isolated sheet as compared to the bulk crystal.

### 2.2.2 Excitonic Effects

In addition to electron–electron (e–e) interaction, the electron–hole (e–h) interaction can play an important role for the quantitative description of absorption spectra. The excited electron in the conduction band and the hole left behind in the valence band interact through an attractive Coulomb potential. As in the case of e–e interaction, the attractive e–h potential is screened through the inverse dielectric function. In many large bandgap materials, the e–h attraction leads to the formation of bound excitons, i.e., discrete states in the bandgap. On a qualitative level, bound excitons can be compared with bound states of the hydrogen atom. In analogy to the hydrogen atom, the Hamiltonian of the exciton can be written as

$$H^{\text{exc}}(r) = \frac{p^2}{2\mu^*} - \frac{e^2}{2r}, \quad (3)$$

where  $r$  is the electron–hole distance and  $\mu^*$  is the reduced effective mass which is the average of the electron and hole effective masses

$$\mu^* = \frac{(m_c^* m_h^*)}{(m_c^* + m_h^*)}.$$

As in the case of hydrogen, the eigenvalues form a Rydberg series of bound states with energies

$$E_n^{\text{exc}} = E_c - \frac{1}{2n^2} \frac{\mu^* e^4}{2\epsilon \hbar^2}, \quad (4)$$

where  $E_c$  is the minimum of the conduction band. The “Bohr radius” of the lowest bound exciton is

$$a_0^{\text{exc}} = \frac{\hbar^2 \epsilon^2}{\mu^* e^2}. \quad (5)$$

For typical semiconductors, the dielectric constant is of the order of 10 and the reduced effective mass is smaller than half the free electron mass. This leads to typical

excitonic binding energies of several tens of meV and to Bohr radii that are large compared to the interatomic distance in the lattice. In the excitonic state, the electron is on the average quite far from the hole from where it was excited. This justifies the use of the average dielectric constant in (3). If the dielectric constant is small ( $\epsilon \rightarrow 1$ ), i.e., if dielectric screening is weak, the excitonic radius shrinks to the order of the lattice constant and the binding energy can attain several hundred meV. In this case, however, the use of the simple excitonic Hamiltonian (3) is no longer justified.

A precise calculation of the exciton energies has to take into account the band structure of the material [going beyond the simple effective mass approach of (3)]. Furthermore, the nonlocality of the screening has to be taken into account. This is achieved by the Bethe–Salpeter equation [18, 22, 23]:

$$(E_{c\mathbf{k}} - E_{v\mathbf{k}})A_{v\mathbf{k}}^S + \sum_{\mathbf{k}'v'c'} \langle v\mathbf{c}\mathbf{k} | K_{eh} | v'\mathbf{c}'\mathbf{k}' \rangle A_{v'\mathbf{c}'\mathbf{k}'}^S = \Omega^S A_{v\mathbf{k}}^S. \quad (6)$$

Here, the excitons are expressed in the basis of electron–hole pairs (i.e., vertical excitations at a given  $\mathbf{k}$ -point from a state in the valence band with quasiparticle energy  $E_{v\mathbf{k}}$  to a conduction-band state with energy  $E_{c\mathbf{k}}$ ). The  $A_{v\mathbf{k}}^S$  are the expansion coefficients of the excitons in the electron–hole basis and the  $\Omega^S$  are the eigenenergies (corresponding to the possible excitation energies of the system). If the interaction kernel  $K_{eh}$  is absent, (6) simply yields  $\Omega^S = (E_{c\mathbf{k}} - E_{v\mathbf{k}})$ , i.e., the excitations of the system correspond to independent electron–hole pairs. The interaction kernel  $K_{eh}$  “mixes” different electron transitions from valence band states  $v, v'$  to conduction band states  $c, c'$  leading to modified transition energies  $\Omega^S$ . It is defined by

$$\begin{aligned} \langle v'\mathbf{c}\mathbf{k} | K_{eh} | v\mathbf{c}'\mathbf{k}' \rangle = & \int d\mathbf{r} \int d\mathbf{r}' d\mathbf{r}'' \phi_{c\mathbf{k}}^*(\mathbf{r}) \phi_{v\mathbf{k}}(\mathbf{r}) \frac{2}{|\mathbf{r} - \mathbf{r}'|} \phi_{c'\mathbf{k}'}(\mathbf{r}') \phi_{v'\mathbf{k}'}^*(\mathbf{r}') \\ & - \int d\mathbf{r} \int d\mathbf{r}' d\mathbf{r}'' \phi_{c\mathbf{k}}^*(\mathbf{r}) \phi_{c'\mathbf{k}'}(\mathbf{r}') \int d\mathbf{r}_1 e^{-1}(\mathbf{r}, \mathbf{r}_1) \frac{1}{|\mathbf{r}_1 - \mathbf{r}'|} \phi_{v\mathbf{k}}(\mathbf{r}'') \phi_{v'\mathbf{k}'}^*(\mathbf{r}''). \end{aligned} \quad (7)$$

The second term on the RHS of (7) represents the screened Coulomb interaction between electrons and holes. The first term is the (unscreened) exchange interaction. The overall effect of the interaction kernel on the optical absorption spectrum is a redistribution of oscillator strength as well as the appearance of bound excitons within the bandgap.

### 2.3 Absorption Spectrum of Bulk h-BN

Before we discuss the influence of e–e and e–h interaction onto the spectra of the tubes, we turn our attention to the absorption spectrum of bulk h-BN for two reasons: (1) bulk h-BN is the precursor material for the fabrication of BN nanotubes and



spectroscopic methods should thus be able to distinguish tubes and bulk; (2) for bulk h-BN, sufficient experimental data exists to judge the validity of the combined approach of GW for the e–e interaction and the Bethe–Salpeter Equation for the e–h correlation (in the following abbreviated by GW + BS).

Results for the energy-dependent dielectric function of h-BN (light polarization parallel to the layers) are shown in Fig. 6a and compared with the experimental data from EELS [24] (in panel b). The dash-dotted line shows the RPA absorption spectrum which is in agreement with earlier RPA calculations [12, 25–27]. The broad peak with a maximum at 5.6 eV is entirely due to the continuum of interband transitions between the  $\pi$  and  $\pi^*$  bands (see Fig. 5). The calculated GW + BS absorption spectrum displays a double peak structure with the main peak at 5.7 eV and a second peak at 6.4 eV. The shape of the spectrum is entirely different from the RPA spectrum: the first peak is due to a strongly bound exciton [21], and the second peak contains contributions from higher excitons and from the onset of the continuum of interband transitions (see below). The similarity between the RPA and GW + BS spectra stems exclusively from the strong broadening employed in the calculation. The main peaks in the two spectra are at about the same position because of an almost-cancellation between the bandgap widening due to the GW approximation and the red-shift of oscillator strength due to excitonic effects. Comparison with Fig. 6b shows that the shape of the GW + BS spectrum is in much better agreement with experiment than the RPA spectrum. This underlines the importance of excitonic effects in h-BN. The influence of excitonic effects becomes even more pronounced when we compare the real part of  $\epsilon$ . Only the GW + BS calculation can reproduce qualitatively the shape of the experimental  $\epsilon_1$ .

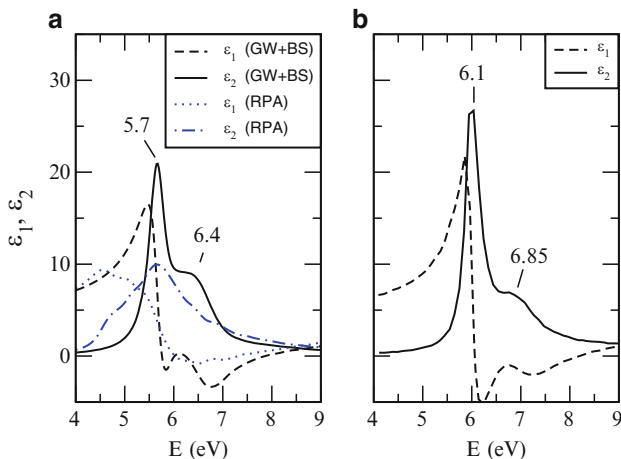


**Fig. 6** (a) Real ( $\epsilon_1$ ) and imaginary ( $\epsilon_2$ ) parts of the dielectric function of h-BN calculated in the GW + BSE approach and in RPA. (b) Experimental data from EELS [24], where  $\epsilon_1$  and  $\epsilon_2$  are calculated from the loss function via a Kramers–Kronig transform. The calculations include a Lorentzian broadening of 0.2 eV (full-width at half-maximum) in order to mimic the estimated experimental broadening. The light-polarization is parallel to the BN layers

The excitonic nature of the absorption spectrum becomes clear if plotted with a very small broadening as in Fig. 7. The dominant first peak at 5.7 eV in the theoretical absorption spectrum is clearly a discrete bound exciton. Its huge binding energy of 0.7 eV was explained by Arnaud et al. [21] as due to the fact that the excitonic wavefunction is mostly confined within one layer. In the pure 2D limit, the binding energy of a hydrogenic system is increased by a factor of four compared to the 3D case [29, 30]. Even if the exciton confinement to one layer in bulk h-BN is not perfect, it leads to a considerable enhancement of the exciton binding energy with respect to nonlayered materials. In the inset (c) of Fig. 7, we show an image of the excitonic wavefunction [28]. Since only the relative position between electron and hole can be shown, we choose the position of the hole at a small distance above one of the nitrogen atoms. (The hole is localized there with a high likelihood, because the HOMO stems from a superposition of nitrogen  $p_z$  orbitals, as shown in Fig. 2.) The wavefunction plot thus represents the probability density to find the excited electron if the hole is at a given position. Clearly, the probability is enhanced around the boron atoms (the LUMO being a superposition of boron  $p_z$  orbitals). Furthermore, the probability density is confined to within a few atomic distances. According to the hydrogenic exciton model [(4) and (5)], the strong confinement of the exciton is linked to a strong binding energy.

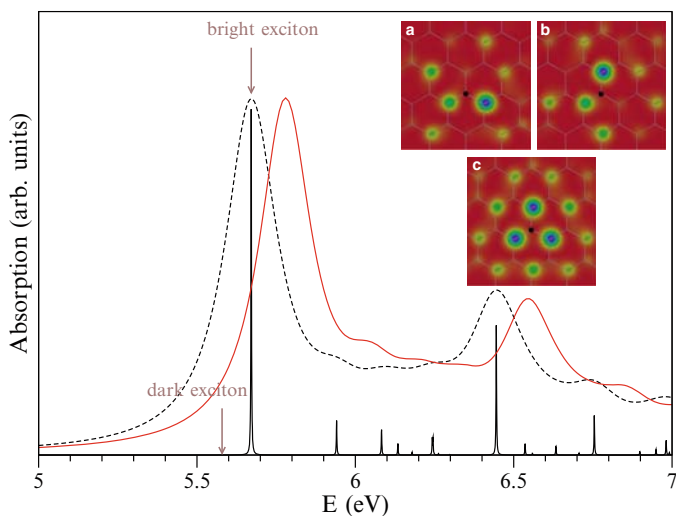


**Fig. 7** Optical absorption spectrum of h-BN with a broadening of 0.001 eV (*black solid line*) and with an estimated experimental broadening of 0.1 eV calculated with Yambo (*black dashed line*) and with VASP (*red solid line*). Inset: 2D projections of the probability density  $|\Psi^{\lambda}(r_h, r_e)|^2$  of the degenerate exciton states with (a)  $\lambda = 3$  and (b)  $\lambda = 4$ . The hole is located 0.4 a.u. above the nitrogen atom in the center (*black circle*). Summing the two densities [panel (c)] restores the three-fold rotation symmetry (reprinted with permission from [28], copyright (2008) by the American Physical Society)

Not all excited states that are obtained with the Bethe–Salpeter equation are optically active. We indicate in Fig. 7 that about 90 meV below the dominant excitonic peak, there is a “dark” bound exciton. This exciton cannot be directly excited through absorption of a photon, but it may play a role in luminescence. Both the dark and the bright exciton are doubly degenerate states. The electron densities of each of the two states that contribute to the bright exciton are not rotationally symmetric (Fig. 7a, b), but adding the densities of the two states, we recover the expected threefold rotation symmetry (Fig. 7c). If the symmetry of the perfect crystal is broken, the degeneracy of the excitons is lifted and the dark exciton acquires some oscillator strength [28, 31].

Figure 7 shows calculations with two different GW + BS codes. Small differences in the absolute position of the spectra (of the order of 0.1 eV) stem probably from the different pseudopotentials used which play a role for the GW correction to the bandgap.<sup>2</sup> Both spectra have in common that they are about 0.3 eV too low in comparison with the various experimental data [24, 36, 37]. One reason for this (small) mismatch may be that the GW approximation is only the first-order correction to the bandgap. Higher-order corrections may enlarge the theoretical bandgap even further and thus blue-shift the spectrum. Another explanation is the effect of phonon renormalization on the absorption spectrum. Theoretical calculations are usually performed at zero temperature. Only recently, the first ab initio calculations of excitonic effects including the exciton–phonon coupling were achieved [38]. This allowed to calculate absorption spectra at finite temperature. For bulk h-BN at room temperature the dominant excitonic peak has been shown to be at 5.98 eV, in excellent agreement with the experimental data [24, 36, 37].

## 2.4 Absorption Spectrum of BN Tubes

After the discovery of carbon nanotubes in 1991, for several years, the optical spectra were only discussed in the independent-particle picture. In 1997, the presence of excitons in carbon tubes was predicted by Ando [39]. Since GW + BS calculations are quite expensive and since the unit cell of nanotubes comprises more than 20 atoms, it was only in 2004 that the first ab initio excitonic spectra of carbon tubes were published [40–42]. The excitonic nature of the spectra was confirmed in numerous experiments [43–45].

Since BNNTs have a much larger bandgap than semiconducting CNTs, it can be expected that excitonic effects are even more pronounced than in CNTs. This has been indeed confirmed by GW + BS calculations [11, 46]. Due to the lower dimensionality (and due to lower screening of the e–e interaction), both in the single-sheet and in isolated BN nanotubes, the GW-bandgap correction (with respect to the DFT-LDA band structure) is strongly enhanced compared to bulk h-BN: 3.6 eV for

---

<sup>2</sup>The code Yambo [32] that was used for the black curve in Fig. 7 uses norm-conserving pseudo-potentials, while VASP [33, 34] (red curve in Fig. 7) uses the projector-augmented-wave (PAW) method [35]. PAW was also used in [21].

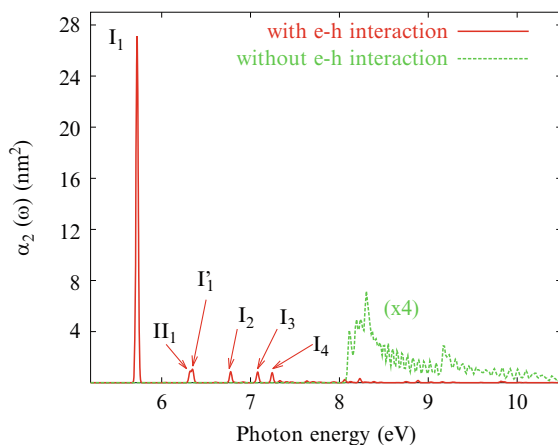


**Fig. 8** Absorption spectra of the (8,0) SWBNNTs. The imaginary part of the polarizability per unit of tube length,  $\alpha_2(\omega)$ , is given in unit of  $\text{nm}^2$ . The spectra are broadened with a Gaussian of 0.0125 eV (reprinted with permission from [46], copyright (2006) by the American Physical Society)

the single sheet [11] and 3.25 eV for the (8,0) tube [46] as compared to 1.8 eV for the bulk h-BN.

Figure 8 shows the absorption spectrum of the BN (8,0) tube with and without e–h interaction (in both cases, GW corrections to the bandgap are included). Without e–h interaction, the continuum of band-to-band transitions would start above 8 eV. A strong excitonic binding energy of 2.3 eV leads, however, to a first absorption peak at 5.72 eV. As in the case of bulk h-BN, the first absorption peak comprises most of the oscillator strength of the entire absorption spectrum.

The wavefunction of the 5.72-eV exciton is displayed in Fig. 9a–c and compared to the wavefunction of the lowest bright exciton in an (8,0) carbon nanotube (panels d–f). The hole is located above a chosen N (C) atom on one side of the tube. While the exciton in the carbon tube is nevertheless delocalized around the whole tube circumference, the exciton in the BN tube is localized on the side where the hole is located. Also along the tube axis, the exciton in the BN tube is much more localized than the one in the carbon tube. This is in line with the much higher excitonic binding energy in BN tubes than in C tubes.

Figure 10 presents the excitonic absorption spectra for the same series of BN nanotubes as in Fig. 4. We compare with the spectra of the single sheet and of bulk h-BN. With increasing diameter, the shape of the tube spectra converges rapidly toward the sheet spectrum which in turn is not very different from the spectrum of the bulk. The rapid convergence as a function of tube diameter toward the sheet spectrum can be understood from Fig. 9. Since the exciton is not delocalized around the circumference but localized within a few nearest neighbors’ distance, it “sees” a locally flat environment and behaves thus as an exciton in the flat sheet. We note that there is a chirality dependence of the optical spectra but it is only visible for

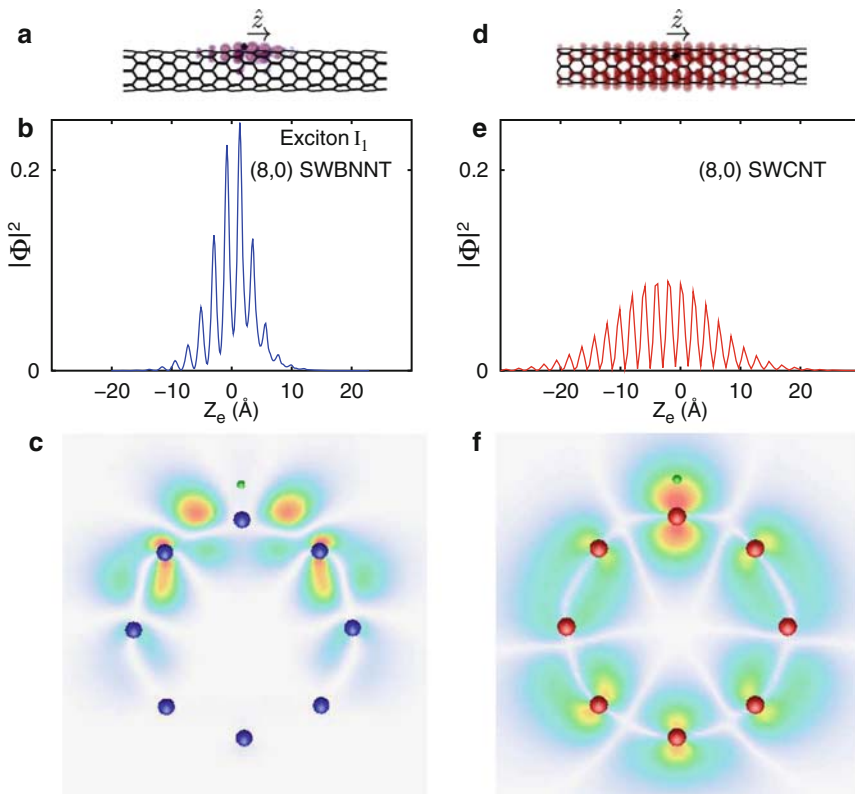


**Fig. 9** (a–c) Wavefunction of the lowest energy bright exciton of the (8,0) BNNT. (a) Isosurface plot of electron probability distribution  $|\Phi(\mathbf{r}_e, \mathbf{r}_h)|^2$  with the hole fixed at the position indicated by *black star*. (b)  $|\Phi(\mathbf{r}_e, \mathbf{r}_h)|^2$  along the tube axis, averaged over the tube cross section. The hole position is set at zero. (c)  $|\Phi(\mathbf{r}_e, \mathbf{r}_h)|^2$  evaluated on a cross-sectional plane of the tube. (d–f) Wavefunction of the lowest energy bright exciton of the (8,0) SWCNT. Plotted quantities are similar to those in (a–c) (reprinted with permission from [46], copyright (2006) by the American Physical Society)

the smallest diameter tubes. The spectra of the armchair tubes converge much faster to the 2D case than the ones of the zigzag tubes.

Many-body effects in carbon nanotubes have been found to be quite different [40, 42]: binding energies and quasiparticle shifts are much smaller, and the extension of the excitonic wavefunction (several nm) is larger than the typical tube circumference. Thus, excitonic binding energies strongly vary with the diameter. Excitons in carbon nanotubes are 1D objects, i.e., squeezed in the circumferential direction.

The strongly localized nature of the exciton in BN structures makes the appearance of 1D confinement effects very restricted to small diameter tubes, i.e., tubes for which the extension of the excitonic wavefunction is comparable to the nanotube

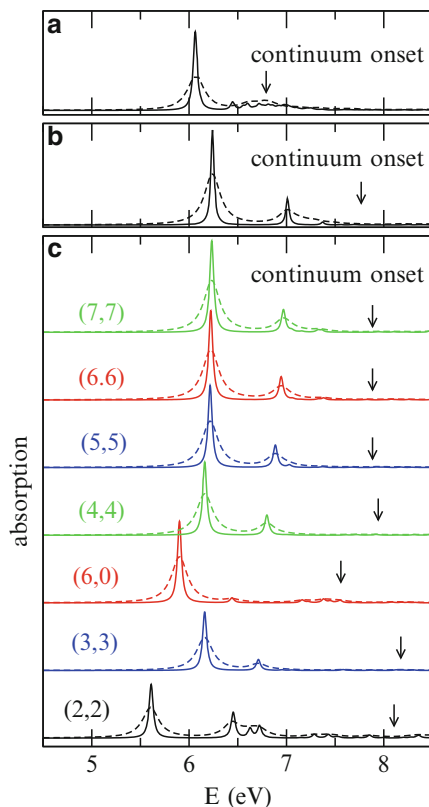


**Fig. 10** Absorption spectra (including electron–electron and electron–hole correlation effects of (a) bulk hexagonal BN, (b) a single sheet of hexagonal BN, (c) six different BN tubes with increasing diameter  $d$ . *Solid lines* are calculated with a Lorentzian broadening of 0.025 eV, *dashed lines* with a broadening of 0.1 eV (reprinted with permission from [11], copyright (2006) by the American Physical Society)

circumference. As the experimental tubes have diameters around 1.4 nm, the 1D nature of the tubes cannot be observed and only the 2D nature of the local exciton environment (tube surface) controls the optical activity.

We remark that dimensionality effects in the electronic properties of BN nanostructures would be more visible in other spectroscopic measurements such as photoemission spectroscopy, where we mainly map the quasiparticle spectra, and this (as the exciton binding itself) is sensitive to the change in screening going from the tube to the sheet to bulk hexagonal BN. In particular the *quasiparticle bandgap* will vary strongly with dimensionality (opening as dimensionality reduces) as well as the onset of continuum excitations that also increases with dimensionality, and for the case of BN tubes it approaches the value for a sheet as the tube diameter increases from above (see Fig. 10).

### 3 Luminescence Spectroscopy

Recently, the observed high luminescence yield in bulk h-BN crystals [10, 47] has raised the interest in BN compounds as potential candidates for UV light-emitting materials. The main luminescence peak (for very pure h-BN crystals) was measured at 215 nm (5.77 eV) [10]. It is ascribed to the radiative decay of the lowest lying exciton. In the electronic structure community, this exciton is called a “bound exciton” because it corresponds to an electron that is “bound” to a hole in the valence band. Thus the energy of this state lies below the range of “free” conduction band electrons (see the discussion on optical absorption above). In contrast, the luminescence spectroscopy community tends to call this exciton a “free exciton” because it is independent of structural defects of the material. For the remainder of this section, we will use the notation of the luminescence spectroscopy.

In comparison to the main absorption peak which is located between 6 and 6.1 eV [24, 36, 37], the luminescence peak experiences a strong Stokes shift toward lower energy. We note, however, that recent photoluminescence excitation (PLE) spectra (i.e., measuring the luminescence intensity as a function of the exciting laser energy) locate the absorption peak corresponding to the “free” exciton rather at 5.81 eV [48]. This yields only a very small Stokes shift of the luminescence peak (5.77 eV).

At low temperature (<100 K), additional luminescence peaks at 220 nm (5.64 eV) and 227 nm (5.46 eV) have been observed [10, 49] (see Fig. 11). Jaffrennou et al. found that luminescence at the latter two wavelengths occurs at the grain boundaries and around dislocations. They ascribed the two peaks to excitons

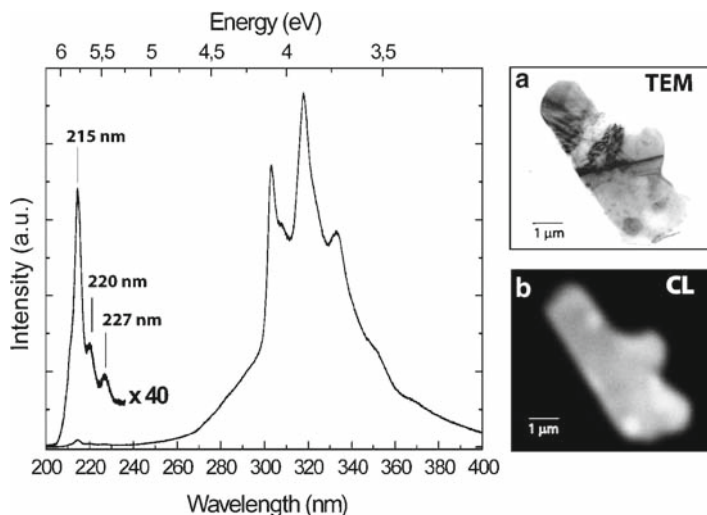


**Fig. 11** Cathodoluminescence spectrum of h-BN crystallite at  $T = 100$  K. (a) TEM image of the h-BN crystallite and (b) polychromatic CL image (reprinted with permission from [49], copyright (2007) by the American Institute of Physics)

that are bound to structural defects and thus have a higher binding energy than the free exciton (and thus a lower position in the luminescence spectrum). At very low temperature (8 K), Museur and Kanaev [48] found an additional “bound” exciton line at 5.56 eV and a line at 5.3 eV that they ascribed to a transition between filled acceptor and donor states.

Luminescence peaks in h-BN have also been observed in the energy region of 4 eV [48–52] (see Fig. 11). They have a much lower intensity than the high energy peaks and are explained by the presence of deep level impurities, probably due to Carbon or Oxygen atoms. Indeed, when h-BN crystals were grown under ultraclean conditions, the 4-eV energy band disappeared from the luminescence spectra [53]. The main peak displays several phonon replica on the low energy side. The proof that those peaks are really due to electron–phonon coupling was given by Han et al. [52] who showed that the splitting between the peaks, i.e., the vibrational frequency, changes as a function of the Boron isotope. The nature of the deep level impurity is not clear. However, calculations indicate the stability of Oxygen in substitution for Nitrogen atoms [52]. Vacancies and other impurities such as Carbon could give rise to deep levels as well. The assignment of all the defect-related peaks observed in luminescence requires more detailed theoretical work. However, it seems that all luminescence features observed below the main absorption peak are defect-mediated excitations, i.e., excitons bound to structural defects or transitions from/to acceptor/donor levels.

Luminescence on multiwalled BNNT samples was observed by several groups. Wu et al. [54] performed photoluminescence (PL) on multiwall BN tubes. They only detected the deep-level impurity peaks around 4 eV. The zero-phonon line at 4.02 eV was falsely ascribed to the direct bandgap. Other groups also detected the excitonic bands in the luminescence of multiwalled BNNTs [52, 55–57]. Bound excitonic peaks were observed at 5.49 and 5.34 eV [57], i.e., at somewhat lower energy than in bulk h-BN (5.77 eV). This difference was tentatively explained in [56, 57]: trapping of excitons on crystalline defects appears to be a major phenomenon. In the tubes, dislocations and stacking faults along the walls may lead to a stronger trapping of excitons than in h-BN and to an absence of the “free-exciton line” at 5.77 eV. The stronger trapping leads to slight red-shift of the bound excitonic lines with respect to the corresponding lines in the PL spectra of bulk h-BN.

From this discussion, it is a logical next step trying to build lasing or optoelectronic devices with BN nanotubes. In this respect, it is interesting to know if the optical properties can be tuned in a controlled way. It has been shown theoretically [58–60] that the bandgap of BNNTs can be reduced by applying an electric field perpendicular to the tube axis. This decrease of the gap is due to the Stark Effect, i.e., the charge densities of the top of the valence band and bottom of the conduction band become spatially separated on opposite sides of the tube. Even though the gap is reduced considerably, the effect of an electric field on the optical absorption spectrum was found to be less pronounced [60] (for light polarization parallel to the tube axis which gives the dominant contribution to the averaged light-scattering cross section). This situation may, however, change for luminescence spectra. Peaks around 4 eV in the luminescence spectra are related to defect levels (possible candidates discussed



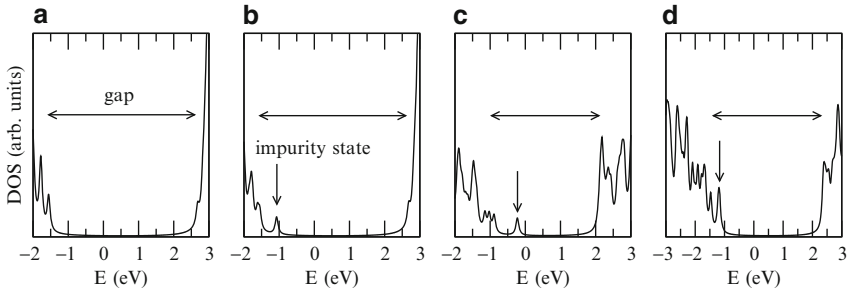


**Fig. 12** Density of states of (a) a pure (9,9) BN nanotube, (b) a tube with a Carbon impurity atom, (c) with a C atom and a perpendicular E-field of  $0.2 \text{ V/\AA}$ , (d) with a C atom on the opposite side and an E-field of  $0.2 \text{ V/\AA}$ . The light-polarization is parallel to the tube axis

above are vacancies, oxygen substitutions, or carbon substitutions). As an example, we have calculated the influence of the electric field on the acceptor level that is due to the replacement of a nitrogen atom by a carbon atom. (The calculations have been performed in a large supercell [60].) In Fig. 12, we show the density of states of the pure (9,9) BNNT calculated within DFT-LDA. Adding the carbon impurity in panel (b) introduces an impurity level at about  $0.5 \text{ eV}$  above the valence band edge. Depending on the orientation of the carbon impurity with respect to the direction of the electric field, this impurity level can move up or down with respect to the valence and conduction band edges (Fig. 12c, d). Photoluminescence may involve transitions from the conduction band to the impurity level and from the impurity level to the valence band. Defect-mediated luminescence spectra may thus be more sensitive to the influence of an electric field than the spectra of pure BNNTs [60].

## 4 Plasmons and Electron-Energy Loss Spectroscopy

The loss function is calculated as the imaginary part of the inverse dielectric function,  $\text{Im}\{-1/\epsilon(\omega, q)\}$ . The loss function of bulk h-BN with wave vector  $q$  parallel to the layers has been measured with EELS by Tarrío and Schnatterly [24]. The spectrum for  $q \rightarrow 0$  displays two peaks, the so-called “ $\pi$  plasmon” at  $8.7 \text{ eV}$  and the “ $\pi+\sigma$  plasmon” at  $26.5 \text{ eV}$ . The names indicate that the latter plasmon represents the collective excitation mode of all the valence electrons in h-BN while the first one is a collective oscillation of the  $\pi$  electrons alone. The loss function of bulk h-BN is quite well reproduced if  $\epsilon(\omega, q)$  is calculated on the level of the RPA [12, 27].

The measured loss-function of bundled multiwall BNNTs in the limit  $q \rightarrow 0$  displays the same two plasmonic peaks as bulk h-BN; however, red-shifted by  $0.6 \text{ eV}$  [61]. The similarity of the two spectra is expected, since the inner-radius of the multiwall tubes was quite large ( $3.1 \text{ nm}$ ). The origin of the  $0.6\text{-eV}$  shift, was tentatively

assigned [61] to the curvature of the inner tubes. Indeed, calculations for small diameter BN tubes have demonstrated a downshift of the “ $\pi$ ” plasmon [12, 27]. Fuentes et al. [61] also presented data on the  $q$  dispersion of the  $\pi$  plasmon which is similar to the dispersion in bulk h-BN. For a detailed discussion of the  $\pi$ -plasmon dispersion in single-walled BN tubes (using a simple two-band tight-binding model), we refer the reader to [62].

The experiments of Fuentes et al. were performed on “bulk-like” samples of tubes. This allowed for a momentum ( $q$ ) resolution of the loss spectra. The opposite limit was reached in the spatially resolved EELS measurements on *isolated* BN tubes [63]. For isolated tubes, the “dielectric constant”  $\epsilon$  (which is a bulk quantity) loses its meaning. Indeed, when a fast electron beam passes (near or through) a nanotube, the EELS spectrum is proportional to a weighted sum of multipolar polarizabilities  $\alpha_m(q)$  with weights decreasing rapidly as a function of the azimuthal momentum  $m$  [64]. To a good approximation, the EELS spectra of isolated BN nanotubes are proportional to  $\text{Im}(\alpha_0(q \rightarrow 0))$ , i.e., to the optical polarizability. In the “continuum dielectric theory” [65],

$$\alpha_0(\omega) \propto \text{Im} \left\{ -\frac{1}{\epsilon_{\perp}(\omega, q \rightarrow 0)} + \epsilon_{\parallel}(\omega, q \rightarrow 0) \right\}, \quad (8)$$

where  $\epsilon_{\perp}$  and  $\epsilon_{\parallel}$  are, respectively, the components of the dielectric tensor perpendicular and parallel to the layers. Since  $\epsilon_{\perp}$  is strongly reduced through depolarization effects, the main contribution to the spatially resolved EELS of isolated BN tubes is thus given by  $\{\epsilon_{\parallel}(\omega, q \rightarrow 0)\}$ . Therefore, one can access the direct optical gap in EELS experiments, in contrast to bulk materials where one needs to perform a Kramers–Kronig analysis of the experimental data to extract the dielectric constant.

Indeed, the EELS data (see Fig. 14 in Chapter “Heteroatomic Single-Wall Nanotubes made of Boron, Carbon and Nitrogen”) displays a lot of similarity with the measured  $\epsilon_{\parallel}(\omega)$  from optical absorption. Most importantly, the “optical gap” was shown to remain almost constant as a function of tube diameter and as a function of the number of tube walls [63]. Furthermore, it was measured to be almost the same as in bulk h-BN. This behavior can be understood from the calculations of  $\epsilon_{\parallel}(\omega)$  presented above in Fig. 10. While the quasiparticle bandgap of the tubes is strongly increased with respect to bulk h-BN, the optical gap displays only minor changes. This is because the increased binding energy of the dominant excitonic peaks almost cancels the increase in the quasiparticle gap as one passes from bulk BN via the 2D single sheet to the 1D tubes.

## 5 Phonons and Vibrational Spectroscopy

Raman and IR spectroscopy in which phonons are excited by inelastic scattering of light or light absorption, respectively, are convenient tools to investigate the composition of macroscopic samples of nanotubes. Carbon nanotubes have been investigated

extensively through vibrational spectroscopy. Early Raman [66] and IR [67] investigations were performed on samples of multiwall carbon nanotubes (MWNTs) and showed signatures close to those of graphite. However, after the production of single-wall nanotubes (SWNTs) in large quantities, resonant Raman spectroscopy turned into a very precise, highly diameter selective identification tool [68]. Especially the low frequency Raman modes such as the RBM strongly depend on the tube diameter and thus facilitate the characterization of tubes. The high frequency modes are only weakly diameter dependent, but their intensity in the resonant Raman spectra strongly depends on the diameter through the electronic excitation energy [69]. IR spectroscopy on single-wall carbon nanotubes [70] shows only small differences when compared to IR data of graphite.

For BN nanotubes, the situation is quite different: The Raman intensities in the visible light frequencies are weaker than for C nanotubes, since the Raman scattering (for lasers in the visible light regime) is nonresonant due to the wide bandgap. On the other hand, BN nanotubes are a polar material and show a much higher IR absorbance than C nanotubes [71]. It is expected, that the combination of Raman and IR spectroscopy will develop into a standard characterization tool for BN tubes such as it is already in the case of C tubes. At this stage, it is very important to have a detailed knowledge of phonon frequencies in BN nanotubes and to understand the dependence on diameter and chirality, in order to guide future experiments. We will give in the following a short description on how phonons are calculated. The phonons of bulk h-BN and BN nanotubes are presented and Raman- and IR-active modes are analyzed. We present the calculation of nonresonant Raman intensities and give an overview on the experimental results as compared to the theoretical predictions.

## 5.1 Phonon Calculations

The phonons are obtained from the change in total energy as the atoms are displaced from their equilibrium position. Mathematically, the phonon frequencies  $\omega$  as a function of the phonon wave vector  $\mathbf{q}$  are obtained as the solution of the secular equation

$$\det \left| \frac{1}{\sqrt{M_s M_t}} C_{st}^{\alpha\beta}(\mathbf{q}) - \omega^2(\mathbf{q}) \right| = 0. \quad (9)$$

$M_s$  and  $M_t$  denote the atomic masses of atoms  $s$  and  $t$  and the dynamical matrix is defined as

$$C_{st}^{\alpha\beta}(\mathbf{q}) = \frac{\partial^2 E}{\partial \mathbf{u}_s^{\alpha}(\mathbf{q}) \partial \mathbf{u}_t^{\beta}(\mathbf{q})}, \quad (10)$$

where  $\mathbf{u}_{st}^{\alpha\beta}$  denotes the displacement of atom  $s$  in direction  $\alpha$ . The second derivative of the energy in (10) corresponds to the change of the force acting on atom  $t$  in direction  $\beta$  with respect to a displacement of atom  $s$  in direction  $\alpha$

$$C_{st}^{\alpha\beta}(\mathbf{q}) = \frac{\partial}{\partial u_s^{\alpha}(\mathbf{q})} F_t^{\beta}(\mathbf{q}). \quad (11)$$

Note the  $\mathbf{q}$  dependence of the dynamical matrix and the displacements. In an explicit calculation of the dynamical matrix by displacing each of the atoms of the unit cell into all three directions, a periodic supercell has to be used which is commensurate with the phonon wavelength  $2\pi/q$ . Fourier transform of the  $\mathbf{q}$ -dependent dynamical matrix leads to the real space force constant matrix  $C_{st}^{\alpha\beta}(\mathbf{R})$  where  $\mathbf{R}$  denotes a vector connecting different unit cells.

A phonon calculation starts thus with the determination of the dynamical matrix in real space or reciprocal space. For h-BN and BN tubes, three different approaches have been used. (1) In the force constant approach [72, 73], a reduced set of  $C_{st}^{\alpha\beta}(\mathbf{R})$  was fitted in order to reproduce the experimental phonon dispersion [74]; (2) The force constants were obtained from total-energy calculations using a semiempirical tight-binding approach [75]; and (3) Force constants were obtained from ab initio total energy calculations [76, 77]. We will first discuss the equilibrium geometry of nanotubes following from ab initio calculations and afterward the resulting phonon dispersion and the Raman- and IR-active modes.

## 5.2 Equilibrium Geometry

In the isolated sheet of h-BN, ab initio calculations on the level of DFT-LDA yield a B–N bond length of 1.44 Å which is close to the literature value of 1.45 Å for bulk h-BN [78]. In the tubes, the boron–nitrogen bonds display a buckling [2, 15, 76] with the Nitrogen atoms moving slightly outward and the Boron atoms moving slightly inward (see inset of Fig. 13). This leads to the formation of a negative outer N-cylinder and a positive inner B-cylinder. Figure 13 shows that the buckling distance between these two cylinders is to a very good approximation inversely proportional to the tube diameter (except for the tubes with very small diameters where the decrease is faster). The threefold coordinated (and slightly positively charged) Boron atoms have the tendency to keep the planar  $sp^2$  bonding geometry with bond angles of  $120^\circ$  while the (slightly negatively charged) Nitrogen atoms are more susceptible to an admixture of  $sp^3$  hybridization leading to smaller bond angles [2]. With this hypothesis, a very simple explanation of the  $1/r$  dependence can be given. The inset of Fig. 13 shows a 2D projection of the buckled geometry for a  $(n, 0)$  zigzag tube. The nitrogen atoms are located at the corners of the polygon with distance  $r_N$  from the center. The boron atoms are accordingly placed at the midpoints of the sides of the polygon. The angle  $\theta$  is inversely proportional to  $n$  and thereby to the tube radius  $r$ . Therefore, also the buckling distance is inversely proportional to the radius

$$r_N - r_B = r - r \cos\theta \approx r - r \left(1 - \frac{1}{2}\theta^2\right) \propto 1/r$$

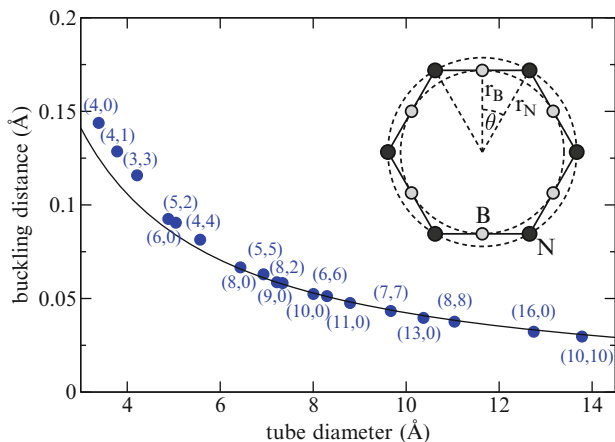


**Fig. 13** Buckling distance in BN single-wall nanotubes as a function of tube diameter (reprinted with permission from [76], copyright (2003) by the American Physical Society)

For smaller tube diameters ( $D < 7 \text{ \AA}$ ), the strain energy due to the curvature of the tube [2] becomes so large that the boron atoms no longer keep their planar bonding geometry but also acquire an admixture of  $sp^3$  hybridization.

### 5.3 Phonon Dispersion Relations

#### 5.3.1 Bulk h-BN

Detailed information on the phonons in BN tubes is up to date only available from theoretical calculations. In order to check the predictive power of these, we compare first the results of ab initio calculations of the phonon dispersion relation of bulk h-BN [79–81] with available experimental data [81–84].

Hexagonal BN has a crystal structure with four atoms in the unit cell and space group  $P6_3/mmc$ . Hence, the phonon dispersion relations show 12 different branches that can be divided into the  $2E_{1u} + 2A_{2u} + 2E_{2g} + 2B_{1g}$  irreducible representations at the center of the Brillouin zone ( $\Gamma$ -point). The branches are usually classified in the following terms: longitudinal optical (LO) and transverse optical (TO) denote the high frequency in plane optical modes with vibration amplitude parallel/perpendicular to the phonon wave vector, respectively. Analogous terms are used for the in-plane acoustic (LA and TA) modes. ZA/ZO denote the out-of-plane acoustic/optical modes. At the ( $\Gamma$ -point), the  $E_{1u}$  (LO/TO) and  $A_{2u}$  (ZO) modes are IR active, the  $E_{2g}$  (TO/LO) are Raman active. The  $B_{1g}$  (ZA and ZO) modes cannot be observed, neither with Raman nor with IR spectroscopy.

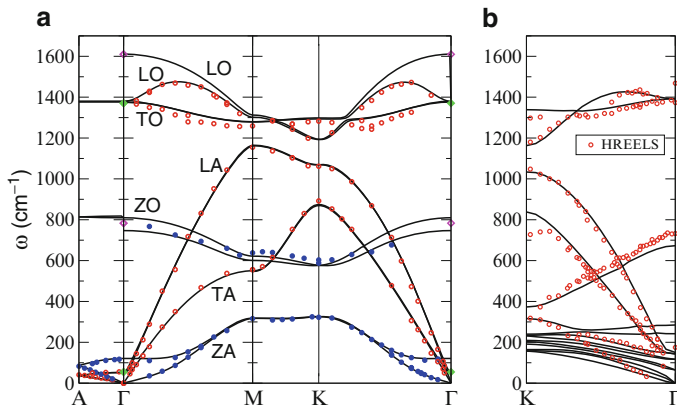


**Fig. 14** (a) Phonon dispersion relations of h-BN along the main symmetry directions. The *open (red) circles* display modes polarized in the hexagonal plane whereas the *solid (blue) circles* correspond to modes polarized along the *c*-axis. The *solid curves* represent the calculated phonon dispersion and infrared [82] and Raman [83, 84] data are displayed at the  $\Gamma$ -point by *open (magenta) and solid (green) diamonds*. (b) Calculated phonon dispersions of a monolayer of h-BN deposited on three layers of Ni (*solid lines*) compared to the EELS data from [74] (*red open circles*). Note that in the experiment only vibrational modes involving boron or nitrogen atoms were detected while in the calculations also the vibrational modes of the Ni substrate are included (reprinted with permission from [81], copyright (2007) by the American Physical Society)

Figure 14 shows the phonon dispersion, measured by inelastic X-ray scattering [81] along with the Raman and IR data at  $\Gamma$  and compared with *ab initio* calculations. The agreement is very good and confirms the validity of *ab initio* calculations for the phonons in h-BN systems. BN is a polar material. In the optical modes, the positive ions vibrate in opposition to the negative ions which leads to a local time-dependent dipole moment. The resulting crystal field gives rise to a splitting between the LO  $E_{1u}$  and the TO  $E_{1u}$  modes (Lyddane–Sachs–Teller relation [85]). In contrast, the  $E_{2g}$  modes are doubly degenerate at  $\Gamma$  and the LO  $E_{2g}$  mode displays a strong overbending close to  $\Gamma$ .

The gap between the ZA and ZO modes at the K point, predicted by the theoretical models, is well reproduced by the IXS data. Contrary to this, in the EELS measurements of Rokuta et al. [74] on a monolayer of h-BN deposited on a Ni(111) substrate, an almost-degeneracy of ZA and ZO was found at K. This is caused by the influence of the interlayer interaction with the substrate. The influence of the binding to the Ni substrate has been demonstrated by *ab initio* calculations of the phonon dispersion of a BN sheet on a Nickel surface. The calculated dispersion [81] and the EELS data are in excellent agreement, as displayed in Fig. 14b. The differences between the EELS and IXS dispersions can therefore be attributed to the binding between the h-BN monolayer and the Ni substrate.

We remark that although modes related to interlayer vibrations should be very much sensitive to errors in the correlation functional (as the typical variations in the

correlation energy that has to be resolved are up to two orders of magnitude smaller for interlayer phonons than for structural characterization), a description of exchange-correlation effects beyond the LDA do not modify the phonon dispersion relations shown in Fig. 14 [86], indicating the robustness and accuracy of the present DFT-based approach to describe the ion dynamics in polar nanostructures.

### 5.3.2 Single Sheet of h-BN

The calculated phonon dispersion of the single hexagonal BN sheet is presented in Fig. 15 together with the one of a single graphene sheet. In general, the phonons of the BN sheet are softer than the phonons of the graphene sheet: the purely covalent bonds of graphene are stronger than the (mostly covalent, but partially ionic) bonds of BN. Furthermore, the degeneracy at K of the out-of-plane acoustic and optical (ZA and ZO) modes and the degeneracy of the longitudinal acoustic and optical (LA and LO) modes in graphene is lifted in BN due to the different masses of B and N. Figure 16 presents sketches of the optical phonons of the BN sheet at  $\Gamma$ .

The phonon dispersion relation of the sheet follows very closely the ab initio calculated dispersion relation of bulk hexagonal BN when one subtracts the phonon branches that are influenced by the interplane interaction. This is analogous to the comparison of phonon dispersion relations in the graphene sheet [87] and in bulk graphite [88–90] and due to the fact that the interlayer interaction is much weaker than the interaction between atoms within one layer. The effect of LO–TO splitting is absent in a 2D single sheet [75, 91]. However, the LO mode displays an overbending close to  $\Gamma$  that is more pronounced than the overbending in the corresponding bulk LO mode. The phonon dispersion of the sheet will be used below in order to derive the phonon dispersion and the diameter dependence of phonons of the tubes via the zone-folding procedure.

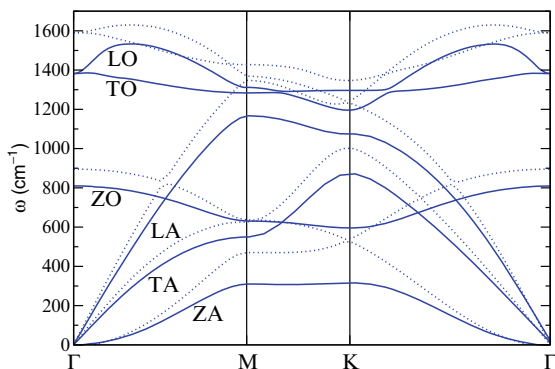


**Fig. 15** Calculated phonon dispersion relation of the single hexagonal BN sheet (*solid lines*) in comparison with graphene (*dotted lines*) (reprinted with permission from [76], copyright (2003) by the American Physical Society)

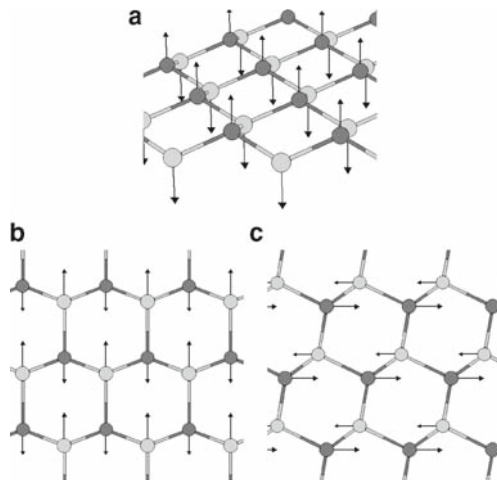


**Fig. 16** Sketch of the optical phonon modes at  $\Gamma$  in the hexagonal BN sheet: (a) out-of-plane mode, (b) transverse optical (TO) mode, and (c) longitudinal optical (LO) mode. For the assignment of “transverse” and “longitudinal,” the phonon wave-vector points in horizontal direction with  $q \rightarrow 0$  (reprinted with permission from [76], copyright (2003) by the American Physical Society)

### 5.3.3 Tubes

In Fig. 17, we compare the *ab initio* phonon dispersion relation of a (6,6) BN nanotube with the corresponding zone-folding dispersion relation. The zone-folding method works equally good as in the case of carbon nanotubes [87]. Here and there, the major difference lies in the low frequency part of the spectrum and is due to the coupling of in-plane and out-of-plane modes of the sheet upon rolling into a tube. This leads to a stiffening of the low-frequency tube modes with respect to the zone-folding model. In general, the zone-folding method does not only reproduce quite well the dispersion relation, but also yields a good estimate of the total phonon density of states (right panel of Fig. 17).

## 5.4 Symmetry Analysis

In Raman and IR spectroscopy, only phonons at (or close to) the  $\Gamma$ -point of the 1D Brillouin zone can be excited (as long as we restrict our discussion to first-order processes). Furthermore, in Raman spectroscopy, only modes that transform under symmetry operations as a quadratic form are active; in IR spectroscopy, only modes that transform as a vector are active [92]. For (infinitely extended) systems with translational symmetry, the “point group in the space group” determines through the selection rules which modes are active and which are not. In quasi-1D systems with



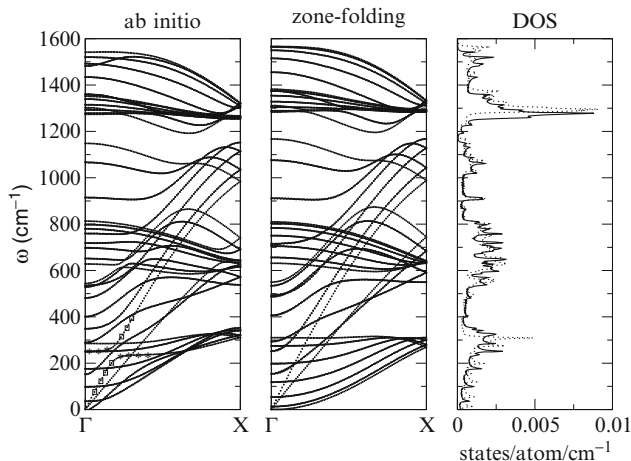


**Fig. 17** Calculated phonon dispersion relation and density of states (DOS) in the (6, 6) armchair BN nanotube. We compare the results of ab initio calculations with the zone-folding method (see text for details). In the *right panel* the *solid line* is the ab initio DOS and the *dotted line* is the zone-folding DOS. The *symbols* in the *left panel* indicate the avoided crossing between the RBM (*asterisks*) and the longitudinal acoustic  $A_1$  mode (*boxes*) (reprinted with permission from [76], copyright (2003) by the American Physical Society)

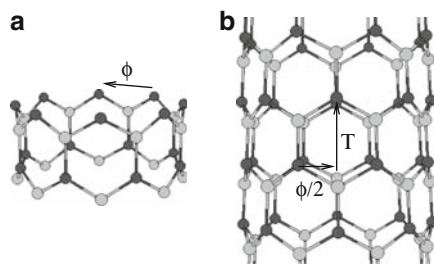


**Fig. 18** Comparison of the point-group symmetry of the unit cell with the space-group symmetry of zigzag BN tubes (reprinted with permission from [76], copyright (2003) by the American Physical Society)

translational symmetry, it is accordingly the “point group in the rod group” that has to be evaluated [93–95]. Figure 18 summarizes the findings for BN tubes: It can be easily seen that the unit cell of a  $(n, 0)$  zigzag tube possesses an  $n$ -fold rotation axis (with rotation angle  $\varphi = 2\pi/n$ ). In addition,  $n$  (indeed, even  $2n$ ) vertical reflection-symmetry planes (containing the tube axis) can be found. Thus the unit cell of a zigzag tube transforms under the  $C_{nv}$  symmetry group. In the infinitely extended tube, the operations of the  $C_{nv}$  point group are valid as well, but – in addition – a rotation by  $\varphi/2$  with subsequent translation by  $T/2$  also maps the system onto itself. This leads to the conclusion that for the infinitely extended system, the  $C_{2nv}$  symmetry

group is the relevant one for symmetry analysis of Raman- and IR-active modes. Analogously, for  $(n, n)$  armchair tubes, the symmetry group of the unit cell is  $C_{nh}$  and the symmetry group of the infinitely extended tube is  $C_{2nh}$ . Finally, for chiral  $(n, m)$  tubes, the unit cell has the low point-group symmetry  $C_d$ , where  $d$  is the greatest common divisor of  $n$  and  $m$ . However, the infinitely extended tube is described by the  $C_N$  symmetry group, where  $N$  is the number of hexagons (= two times the number of atoms) per unit cell which is, in general, much larger than  $d$ .

The number of active modes is found by determining how often each irreducible representation appears in the (reducible) representation of the symmetry group ( $C_{2m}$ ,  $C_{2nh}$ , or  $C_N$ , respectively) which is given by the  $12n$  vibrational degrees of freedom of the unit cell. For zigzag tubes this leads to 14 Raman-active modes [94] (3 with  $A_1$  symmetry, 5 with  $E_1$  symmetry, and 6 with  $E_2$  symmetry, where the  $E_1$  and the  $A_1$  modes with vanishing frequency have already been subtracted). Out of these modes, 8 modes ( $3A_1$  and  $5E_1$ ) are also IR active. In the case of chiral tubes, there are 15 Raman-active modes ( $4A$ ,  $5E_1$ , and  $6E_2$ ) out of which 9 modes ( $4A$  and  $5E_1$ ) are also IR active. The small difference in the number of active modes between zigzag and chiral tubes stems from the fact that the additional vertical reflection symmetry of the zigzag tube causes a distinction between Raman + IR active  $A_1$  modes and nonactive  $A_2$  modes. The sets of Raman- and IR-active modes for BN armchair tubes are disjoint: 9 modes are Raman active (3 with  $A_g$  symmetry, 2 with  $E_{1g}$  symmetry and 4 with  $E_{2g}$  symmetry) and 4 modes are IR active (1 with  $A_u$  symmetry and 3 with  $E_{1u}$  symmetry).<sup>3</sup> In the next section, it will be explained how these modes can be constructed from the modes at or close to the  $\Gamma$ -point in the BN sheet.

## 5.5 Zone-Folding Method

Here, we review the zone-folding method which has been frequently used for the calculation of electronic band structure and phonons in C nanotubes [97] and demonstrate how the different Raman- and IR-active modes can be deduced from it in the case of BN nanotubes. Thus, the symmetry analysis of Sect. 5.4 can be understood in a pictorial way. Figure 19a demonstrates the scenario for  $(n, 0)$  zigzag nanotubes. The sheet is rolled up such that the tube-axis is parallel to the translation vector  $\vec{T}$  whose lengths corresponds to the lengths of the 1D unit cell of the tube. The component  $K_\perp$  of the phonon wave vector  $\vec{K}$  which points into the circumferential direction of the tube is quantized. For zigzag nanotubes, this means that in reciprocal space,  $K_\perp$

<sup>3</sup>The fact that for zigzag and chiral tubes, the IR-active modes are a subset of the Raman-active modes is different in BN tubes and C tubes and is due to the reduced symmetry (= less strict selection rules) for BN tubes. In carbon tubes, only the set of IR-active modes of chiral tubes partially overlaps with the set of Raman-active modes [96]. For zigzag and armchair C tubes, the sets of Raman- and IR-active modes are disjoint.

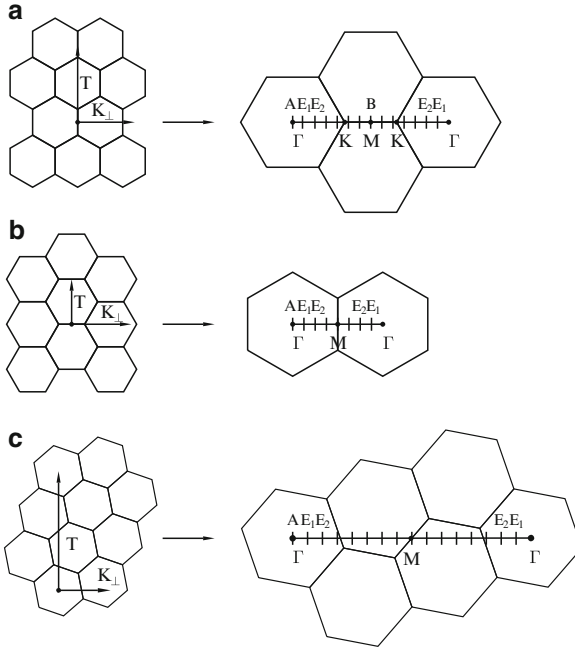


**Fig. 19** Sketch of the zone-folding method **(a)** for  $(n, 0)$  zigzag nanotubes, **(b)** for  $(n, n)$  armchair nanotubes, and **(c)** for  $(4n, n)$  chiral nanotubes. *Left side:* A hexagonal BN sheet is rolled in perpendicular direction to the primitive translation vector  $\vec{T}$ . The component  $K_{\perp}$  of the phonon wave vector in circumferential direction is quantized. *Right side:* For zigzag nanotubes, the quantization of the circumferential momentum corresponds to  $2n$  steps along the line  $\Gamma \rightarrow K \rightarrow \Gamma$  in the 2D Brillouin zone of the sheet  $\rightarrow K \rightarrow \Gamma$ . In armchair nanotubes,  $2n$  discrete steps are taken along the line  $\Gamma \rightarrow M \rightarrow \Gamma$ , while in chiral tubes the discretization proceeds along a line connecting more distant  $\Gamma$ -points. The points at and close to  $\Gamma$  give rise to the Raman- and IR-active  $A$ ,  $E_1$ , and  $E_2$  modes (reprinted with permission from [76], copyright (2003) by the American Physical Society)

can assume  $2n$  discrete values ( $\mu = 0, \dots, 2n-1$ ) along the line  $\Gamma \rightarrow K \rightarrow M \rightarrow \Gamma \rightarrow \Gamma$ . The parallel component  $K_{\parallel}$  is unrestricted. However, the Raman- and IR-active modes are modes at the  $\Gamma$ -point of the 1D Brillouin zone of the tube and correspond thus to  $K_{\parallel} = 0$ . Since the points at  $\mu$  and  $2n-\mu$  are equivalent in reciprocal space, all modes of the tube are doubly degenerate, except for the mode that corresponds to  $\mu = 0$  (the  $\Gamma$ -point of the sheet) and the mode that corresponds to  $\mu = n$  (the  $M$ -point of the sheet). If one applies the strict selection rules according to the  $C_{2nv}$  symmetry group, the modes of the sheet at  $\Gamma$  map onto tube modes with  $A$  symmetry, the modes at  $M$  map onto modes of  $B$  symmetry and the modes at  $\mu = 1, \dots, n-1$  map onto modes of symmetry  $E_1, \dots, E_{n-1}$ [1]. Since there are six different phonon branches in the sheet, there are six different phonon modes in the tube for each of the above symmetries. Each of the six phonon branches leads to  $(n+1)$  different phonon modes in the tube,  $(n-1)$   $E$  modes, one  $A$  mode, and one  $B$  mode.

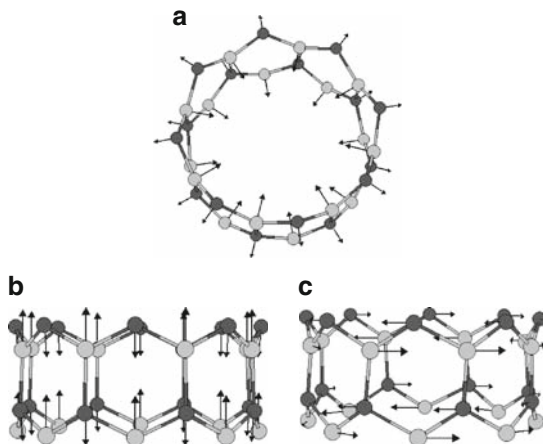


**Fig. 20** Sketch of high frequency  $A$  modes in a BN zigzag tube: (a) radial buckling (R) mode, (b) bond-stretching or longitudinal (L) mode, (c) bond-bending or tangential (T) mode (reprinted with permission from [76], copyright (2003) by the American Physical Society)

Since the  $E$  modes are doubly degenerate, this sums up to  $12n$  phonon modes corresponding to the  $4n$  atoms in the unit cell of a zigzag tube.

Figures 16 and 20 demonstrate the mapping of the three optical modes of the sheet at  $\Gamma$  onto the corresponding  $A$  modes of the tube. The out-of-plane optical (ZO) modes of the sheet lead to radial (R) “buckling” modes of the tube where all Boron atoms move inward/outward at the same time and all Nitrogen atoms move outward/inward, giving rise to an oscillation of the buckling amplitude in the tube. The transverse optical (TO) mode of the sheet maps onto a longitudinal (L) mode of the tube and, accordingly, the longitudinal optical (LO) mode of the sheet maps onto a transverse or tangential (T) mode of the tube. In the  $A$  modes, all atoms along the circumference move in phase (corresponding to  $K_{\perp} = 0$ ). In the modes of  $E_i$  symmetry, there are  $2i$  nodes along the circumference ( $i$  nodal planes containing the symmetry axis of the tube). The  $B$  modes contain  $2n$  nodes along the circumference which means that a rotation by  $\varphi/2$  (with the proper translation along the tube axis) maps the mode onto its negative. In other words, for the  $B$  modes, neighboring “columns” of atoms oscillate with a phase difference of  $\pi$ .

The points in the Brillouin zone of the sheet that give rise to the Raman and IR active  $A$ ,  $E_1$ , and  $E_2$  modes are denoted in Fig. 19. They are the points at and close to  $\Gamma$ . With larger tube diameter (increasing  $n$ ), the points giving rise to the  $E_1$  and  $E_2$  modes converge toward the  $\Gamma$ -point of the BN sheet. Therefore, as a first check on the frequencies of active modes of larger diameter tubes, it is sufficient to look at the frequencies at the  $\Gamma$ -point of the sheet. The frequencies of modes that correspond to the acoustic branches of the sheet converge accordingly to zero for large diameters. Note that not all of the  $A$ ,  $E_1$ , and  $E_2$  modes may be Raman active, because one still has to distinguish between the different “subsymmetries.” For example, the TO mode of the sheet at  $\Gamma$  (see Fig. 16b) folds into a tube mode of  $A_1$

symmetry (see Fig. 20b) and is thus Raman active, whereas the LO mode of the sheet at  $\Gamma$  (see Fig. 16c) folds into a mode of  $A_2$  symmetry (see Fig. 20c) which changes sign under reflection at a plane that contains the symmetry axis of the tube.

The zone folding for armchair tubes works in an analogous way to the zone folding for zigzag tubes (see Fig. 19b). The only difference is that the active modes of the tube correspond to a discrete set of modes along the line  $\Gamma \rightarrow M \rightarrow \Gamma$  in the reciprocal space of the sheet.

Finally, Fig. 19c illustrates the zone folding for a general chiral nanotube. In the example, we have chosen a  $(4n, n)$  tube with a relatively short primitive translation vector  $\vec{T}$ . As in the case of armchair and zigzag tubes, the quantization of the circumferential phonon wave vector corresponds in the reciprocal space of the sheet to a discrete set of modes along a line  $\Gamma \rightarrow M \rightarrow \Gamma$ . However, the line does not connect nearest or next-nearest  $\Gamma$ -points but connects  $\Gamma$ -points further apart (with the distance depending on the chirality of the tube).

## 5.6 Diameter Dependence of Raman- and IR-Active Modes

In this section, we present the results of ab initio calculations of selected zigzag, chiral, and armchair tubes [76] and compare with the results obtained by zone folding the ab initio dispersion relation of the single sheet. Figure 21 displays the frequencies of the Raman- and IR-active modes of the three types of tubes as a

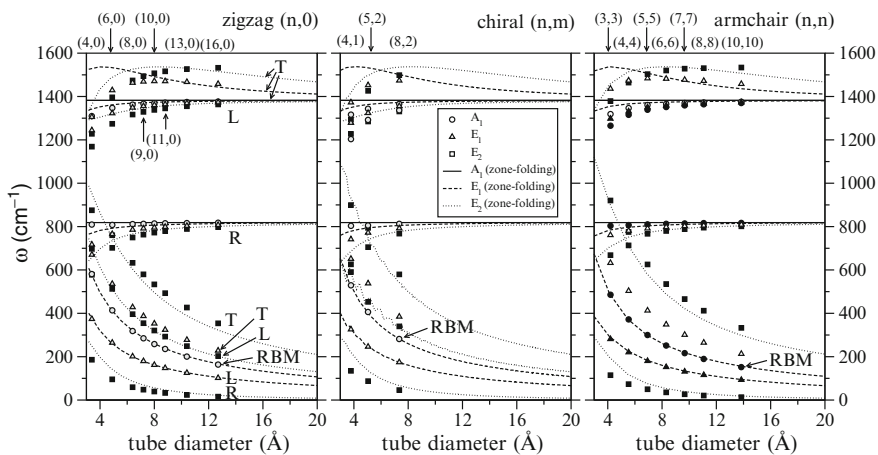


**Fig. 21** Frequencies of Raman- and IR-active modes in BN nanotubes as a function of tube diameter: comparison of ab initio values (symbols) with zone-folding method (lines). The shape of the symbols denotes the symmetry of the modes (see legend). *Black filling* marks modes which are Raman active only. *White filling* stands for IR active only. *Gray filling* stands for modes which are both Raman and IR active. R, L, T marks the radial, longitudinal, and tangential high-frequency modes (as in Fig. 20) (reprinted with permission from [76], copyright (2003) by the American Physical Society)

function of the tube diameter  $D$ . The ab initio values are plotted as symbols, while the zone-folding values are connected by lines in order to guide the eye and extrapolate to larger tube diameters. Three frequency regimes are easily distinguishable:

1. The low frequency modes whose frequencies approach zero for  $D \rightarrow \infty$  are the modes that are derived from the acoustic branches of the sheet.
2. The three modes that approach  $\omega \approx 818 \text{ cm}^{-1}$  for  $D \rightarrow \infty$  are radial (R) modes (see Fig. 20a) which are related to the optical out-of-plane (ZO) modes (Fig. 16a) in the dispersion relation of the sheet (Fig. 15).
3. The high frequency regime above  $1,200 \text{ cm}^{-1}$  consists of longitudinal (L) and transverse (T) modes (Fig. 20b, c) which are zone-folded TO and LO modes of the sheet (Fig. 16b, c).

We discuss at first the three different frequency regimes separately in the case of the zigzag tubes (left panel of Fig. 21). Afterward, we extend the discussion to the chiral and armchair tubes.

Figure 22 is a double-logarithmic plot of the low frequency modes in the zigzag nanotubes. For the RBM (marked by asterisks), we have also included the values of chiral and armchair tubes. From phonon calculations in C nanotubes, it is well known that the RBM is inversely proportional to the tube diameter [98]:  $\omega_{RBM} \propto 1/D$ . The same holds for BN nanotubes. In fact, not only the RBM, but also most of the low frequency modes display the same  $1/D$  scaling. This can be easily understood from the phonon dispersion of the sheet (Fig. 15) in combination with the zone-folding procedure in Fig. 19: The LA and TA branches of the sheet have a linear slope at the  $\Gamma$ -point. The distance between the  $\Gamma$ -point and the points that map onto

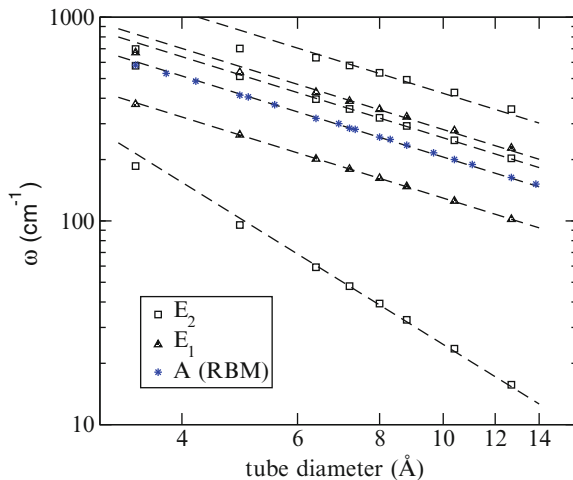


**Fig. 22** Double-logarithmic plot of the low phonon frequencies in the BN zigzag tubes. The dashed lines are least square fits to the form  $A/D^2$  for the lowest  $E_2$  mode and to the form  $A/D$  for all other modes. The fit has been performed on the diameter interval between 6 and 14 Å (reprinted with permission from [76], copyright (2003) by the American Physical Society)

the  $E_1$  and  $E_2$  modes in Fig. 19 is proportional to  $1/N$  (with  $N$  being the number of hexagons in the tube unit cell) and hence proportional to  $1/D$ . Hence, all the low frequency modes in the tubes that are folded from the LA and TA branches of the sheet exhibit the  $1/D$  scaling. Only the frequency of the lowest  $E_2$  mode in Fig. 22 displays a  $1/D^2$  proportionality[87]. This is because it is folded from the ZA mode of the sheet which does not increase linearly but quadratically around the  $\Gamma$ -point [97]. For small diameter, the phonon modes deviate from the functional form  $A/D$  or  $A/D^2$ , because the linear/quadratic behavior in the acoustic branches of the sheet ceases to be valid further away from the  $\Gamma$ -point. Only the RBM follows the functional behavior  $A/D$  down to very low radius. While the RBM cannot be obtained from zone folding of an *infinite* sheet, it is related to the in-plane stretching mode of a sheet of *finite* width [76] and the functional  $A/D$  behavior can be proven analytically [98].

The power law fit of the RBM scaling in Fig. 22 yields a scaling constant  $A = 2,060 \pm 2 \text{ cm}^{-1} \text{ \AA}$  and may be used for the diameter determination in Raman characterization of BN tubes. As is the general trend of phonons in BN as compared to carbon, this value is considerably lower than the corresponding ab initio value  $A_c = 2,288 \text{ cm}^{-1} \text{ \AA}$  for the RBM in carbon nanotubes [87, 99]. Since the other low frequencies modes with the  $1/D$  scaling may be used as well for the radius determination, we list in Table 1 the corresponding scaling constants.

We discuss now the radial phonon modes in the intermediate frequency regime around  $800 \text{ cm}^{-1}$  [see, e.g., panel (a) of Fig. 21]. According to the zone-folding picture, the  $A$  mode should be diameter independent and have the constant frequency of  $\approx 818 \text{ cm}^{-1}$ . Indeed, the ab initio values lie almost exactly on this line. The  $E_1$  branch is the nearest neighbor in frequency of the  $A$  mode and the  $E_2$  branch is the next nearest neighbor, because in the zone-folding picture (Fig. 19), the  $E_1$  and  $E_2$  modes derive from the points close to the  $\Gamma$ -point of the sheet. Since in the dispersion relation of the BN sheet (Fig. 15), the ZO branch approaches the  $\Gamma$ -point from below, the radial  $E_1$  and  $E_2$  modes both have lower frequencies than the corresponding  $A$  mode. At small diameters, the ab initio values lie below the zone-folding curves due to bond weakening introduced by curvature effects.

The L and T modes of the high-frequency branch converge toward the asymptotic value  $\omega = 1,380 \text{ cm}^{-1}$  for  $D \rightarrow \infty$ . In the zone-folding picture, the  $E_1$  and  $E_2$  L modes approach this value from below since in the dispersion relation of the sheet (Fig. 15), the corresponding TO branch from which these modes are derived

**Table 1** First principle determination of scaling constants for the  $A/D$  dependence of the low-frequency modes as a function of the tube diameter  $D$

Mode symmetry	$A \text{ (cm}^{-1} \text{ \AA)}$
$E_1$ (L)	1,296
$A$ (RBM)	2,060
$E_2$ (L)	2,560
$E_1$ (T)	2,808
$E_2$ (T)	4,232

approach the  $\Gamma$ -point from below. The LO branch, in contrast, displays a strong over-bending which leads to the nonmonotonic diameter scaling of the  $E_1$  (T) and  $E_2$  (T) modes in Fig. 21. The ab initio values follow the general trend of the zone-folding curves. However, all high-frequency T and L modes, even the A modes which should be diameter independent, experience a strong down-shift for small diameter. This general trend is also observed for the C nanotubes [87] and can be attributed to curvature effects. The  $E_1$  (T) mode displays the nonmonotonic behavior which is predicted by zone folding, but due to the curvature-induced softening at small radius, it reaches the maximum at a larger diameter than the zone-folding curve. The  $E_2$  (T) mode displays a similar behavior. It reaches its maximum at a larger diameter than the  $E_1$  (T) mode and ultimately converges toward the asymptotic value of  $1,380 \text{ cm}^{-1}$ .

The scaling of the phonon frequencies with the tube diameter is very similar for zigzag, chiral, and armchair tubes as can be seen from comparing the three panels of Fig. 21. In the case of the chiral tubes, the zone-folding lines of the low-frequency L modes and – to a lesser extent – the ones of the low-frequency T modes display a zigzag pattern. We have calculated all chiral nanotubes in the diameter range between 3 and 20 Å and connected the discrete points by lines in order to guide the eye. For large diameter, the frequencies of the low frequency modes follow the same scaling as given in Table 1 for the zigzag tubes. This is because the slope of the acoustic branches of the sheet at  $\Gamma$  is independent of the direction in the Brillouin zone (corresponding to an isotropic sound velocity in all directions). Only at smaller diameter, corresponding to larger distance from the  $\Gamma$ -point in the dispersion relation of the sheet where the LA and TA modes deviate from the linear behavior, the frequency clearly depends on the chiral angle. The slopes of the zigzag and of the armchair curves are the limiting cases. For example, the zone-folding curve of the  $E_2$  (T) mode reaches a value of  $1,000 \text{ cm}^{-1}$  at  $D = 3 \text{ Å}$  for the zigzag tubes and a value of  $1,100 \text{ cm}^{-1}$  for the armchair tubes.

In Fig. 21, only Raman- or IR-active modes are shown. This leads to a different number of displayed values in the three different panels. The fact that for zigzag and chiral tubes, the IR-active modes are a subset of the Raman-active modes while for armchair tubes the two sets are disjoint, should help in the experimental identification of the ratio of different chiralities in a macroscopic tube sample. In particular, the RBM can be detected both by Raman and IR spectroscopy in zigzag and chiral tubes, while in the case of armchair tubes, it should only appear in the Raman spectrum. Of course, an exact theoretical calculation of the chirality dependence of IR and Raman *intensities* is desirable for this purpose.

## 5.7 Raman Intensities

So far, we have discussed only the position of the peaks in the Raman spectra. The positions are given by the frequencies  $\omega_\nu$  of the Raman-active modes  $\nu$  with null wave vector. Raman scattering in BNNTs takes place in the nonresonant regime,



because the optical-gap of BNNTs exceeds the photon energies of lasers in the visible and near UV-range. The intensities for nonresonant Raman scattering,  $I^v$ , can be written within the Placzek approximation [100] as

$$I^v \propto |\mathbf{e}_i \cdot \mathbf{A}^v \cdot \mathbf{e}_s|^2 \frac{1}{\omega_v} (n_v + 1). \quad (12)$$

Here  $\mathbf{e}_i$  ( $\mathbf{e}_s$ ) is the polarization of the incident (scattered) light and  $n_v = [\exp(\hbar\omega_v / k_B T) - 1]^{-1}$  with  $T$  being the temperature. The Raman tensor  $\mathbf{A}^v$  is

$$A_{ij}^v = \sum_{\gamma} B_{ij}^{k\gamma} \frac{w_{k\gamma}^v}{\sqrt{M_{\gamma}}}, \quad (13)$$

where  $w_{k\gamma}^v$  is the  $k$ th Cartesian component of atom  $\gamma$  of the  $v$ th orthonormal vibrational eigenvector and  $M_{\gamma}$  is the atomic mass.

$$B_{ij}^{k\gamma} = \frac{\partial^3 \varepsilon}{\partial E_i \partial E_j \partial u_{k\gamma}} = \frac{\partial \alpha_{ij}}{\partial u_{k\gamma}}, \quad (14)$$

where  $\varepsilon$  is the total energy of the unit cell,  $\mathbf{E}$  is a uniform electric field, and  $u_{k\gamma}$  are atomic displacements. This is equivalent to the change of the electronic polarizability of a unit cell,  $\alpha_{ij} = \Omega \chi_{ij}$ , (where  $\Omega$  is the unit cell volume and  $\chi_{ij}$  the electric susceptibility) upon the displacement  $u_{k\gamma}$ . The derivative tensor  $B_{ij}^{k\gamma}$  can either be calculated approximately from a bond-polarizability model [72, 101] or can be calculated ab initio with an extension of density-functional perturbation theory [102].

We show in the following the ab initio Raman spectra [101] for the (9,0), (13,0), and (16,0) zigzag BN nanotubes and for the (10,10) armchair tube (Fig. 23). The latter two have diameters (12.8 Å and 13.8 Å) in the range of experimentally produced BN tubes. The dominant peak (besides the low frequency  $E_2$  (R) which is close to zero and thus hardly measurable) is the  $A_1$  peak at about 1,370  $\text{cm}^{-1}$ . Note that for zigzag tubes this mode corresponds to a transverse (T) vibration of the atoms while for armchair tubes it corresponds to a longitudinal (L) vibration. Depending on the chirality of the tube, the dominant peak can have a side peak on the lower frequency side. With increasing diameter, this side-peak rapidly merges into the main-peak but remains visible as a shoulder. About 120  $\text{cm}^{-1}$  above the main peak, The  $E_1$  (T) mode gives a small contribution to the spectrum. For chiral tubes, its intensity is reduced and becomes zero for armchair tubes. If Raman spectra of isolated single-walled BN tubes ever become available (due to the nonresonant character of the spectra, the intensity is very low), the intensity of this peak with respect to the intensity of the main peak can be taken as a measure of the tube chirality. The  $A_1$  mode at 810  $\text{cm}^{-1}$  is the radial buckling mode. Its intensity decreases with increasing diameter. Therefore, it is not clear if it is detectable. In the low frequency regime, the RBM plays the dominant role and is a good measure for the radius of the tube (just as in the case of carbon nanotubes).

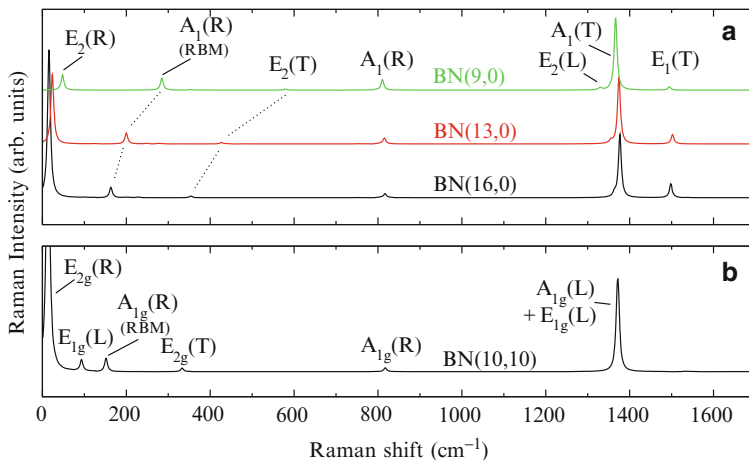


**Fig. 23** Calculated Raman intensities for (a) three different zigzag BNNTs and (b) the (10,10) armchair BNNT. The spectra are plotted with a full-width at half-maximum (FWHM) of  $10 \text{ cm}^{-1}$ . Modified from [101], copyright (2005) by the American Physical Society

## 5.8 Experimental Results on Raman and IR Spectroscopy

### 5.8.1 Experimental Raman Spectra

The essential test on the performance of Raman spectroscopy for the characterization of BN nanotubes is the comparison of the spectra of nanotube samples with the spectra of crystalline h-BN. At high frequency, bulk h-BN displays a single Raman line due to the  $E_{2g}$  LO/TO mode. (This mode does not display an LO–TO splitting, contrary to the IR active  $E_{1u}$  mode which has almost the same frequency). Originally, its frequency was measured at  $1,370 \text{ cm}^{-1}$  [82]. However, later Nemanich et al. [83] showed that this mode depends sensitively on the domain size in polycrystalline samples: the finite domain size leads to an uncertainty for the phonon wave vector  $q$ . This leads to a superposition of the bulk  $E_{2g}$  mode with  $q$  averaged over a region in the first Brillouin zone around  $\Gamma$ . Since the  $E_{2g}$  LO mode displays a strong over-bending, the resulting Raman peak not only broadened but also shifted toward higher frequency [83]. Nemanich et al. extrapolated the value of the infinite crystal as  $1,366 \text{ cm}^{-1}$ . Recently, the  $E_{2g}$  LO/TO mode was measured at  $1,364 \text{ cm}^{-1}$  [84]. The domain-size dependence of the Raman spectra needs to be taken into account when one analyzes the Raman spectra of nanotube raw-products that may contain both nanotubes and microcrystallites of h-BN at the same time.

Before we discuss the measured Raman spectra of multi- and single-walled BN nanotubes, we would like to point out a further important detail in the theoretical calculations of frequencies of the  $E_{2g}$  mode in bulk h-BN and of the  $E_{2g}$  mode in the sheet: The value for the bulk is  $3.8 \text{ cm}^{-1}$  lower than the value for the sheet [103].

This lower frequency is related to an increase of the calculated in-plane lattice constant which is 4.718 a.u. for bulk h-BN and 4.714 a.u. for the single sheet. The difference stems from the – small but nonnegligible – interaction of neighboring sheets in bulk h-BN. The interaction leads to a small elongation of the B–N bondlength and consequently a softening of the phonons.

The Raman spectra of multiwall tubes (with 2–8 walls and an average outer diameter of 8 nm) were measured by Wu et al. [54]. They measured the bulk  $E_{2g}$  peak at  $1,366\text{ cm}^{-1}$  (corresponding to the limit of infinite size crystallites) and found an upshift of  $2.1\text{ cm}^{-1}$  with respect to this value for the BNNT sample. [Note that IR spectra on multiwalled tubes have also displayed an upshift of the  $E_{1u}$  mode with respect to the bulk value [71] (see below).] Wu et al. took the tube diameter as a measure for the “crystal size” and used the theory of Nemanich et al. [83] to explain the upshift of the Raman peak. It is not clear if this argument is admissible, since the phonon calculations for (single-wall) nanotubes shows unanimously a softening of the dominant Raman peak with respect to the phonon value of the infinite sheet [72, 75, 76]. An alternative explanation may be given by the increased interlayer distance and the noncommensurate stacking in multiwall tubes. Both effects reduce the interlayer interaction and may explain why the  $E_{2g}$  mode in multiwalled tubes displays a similar upshift as the isolated sheet.

For single-walled nanotubes (with an average diameter of 2 nm), an upshift of  $5\text{ cm}^{-1}$  with respect to the bulk  $E_{2g}$  frequency has been measured [103] (see Fig. 17 in Chapter Heteroatomic Single-Wall Nanotubes made of Boron, Carbon and Nitrogen). To understand this upshift, we compare with ab initio calculations of the phonon frequencies of nanotubes and bulk h-BN. Figure 24 shows the convergence of the  $A_1$  mode in zigzag nanotubes toward the  $E_{2g}$  mode of the single sheet. A fit

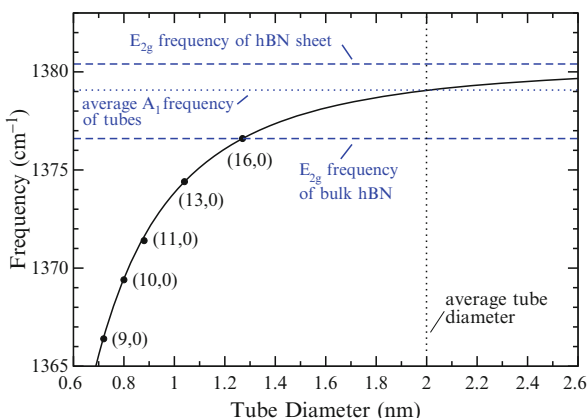


**Fig. 24** Calculated frequencies of the Raman-active optical  $A_1$  mode for different  $(n, 0)$  zigzag BN nanotubes (symbols). The solid line is a fit (see text) that describes the convergence of the mode frequency with increasing tube diameter toward the value for the isolated sheet (reprinted with permission from [103], copyright (2006) by the American Chemical Society)

of the calculated tube frequencies as a function of the diameter  $d$  yields  $\omega(d) = \omega_{E_{2g}}^{\text{sheet}} - 1,268.3 / d^{2.29} \text{ cm}^{-1}$  with  $d$  given in  $\text{\AA}$  [72]. This functional form is also displayed in Fig. 24. For the tubes with average diameter of 2 nm, the  $A_1$  mode frequency is just  $1.3 \text{ cm}^{-1}$  below the value for the sheet and thus  $2.5 \text{ cm}^{-1}$  above the value of the bulk. While ab initio calculations using DFT cannot reproduce properly the van der Waals part of the interactions between the layers, they nevertheless give a qualitative indication of the origin of the Raman peak shift in single- and multi-wall tube samples (as already proven for the case of interlayer modes in hexagonal BN including exchange-correlation effects on the level of GW which includes the description of van der Waals interactions [86]).

### 5.8.2 IR Spectra

IR spectroscopy on bulk h-BN [82] yielded the TO  $E_{1u}$  mode at  $1,367 \text{ cm}^{-1}$  and the LO  $E_{1u}$  mode at  $1,610 \text{ cm}^{-1}$ . The latter one is shifted due to the coupling with the electric field of the laser. Furthermore, the ZO  $A_{2u}$  mode (which also couples to the electric field) was measured at  $783 \text{ cm}^{-1}$ .

Relatively little is known on the IR spectra of BN tubes. IR measurements of single-wall BN tubes have so far be impeded by the presence of boric acid in the sample which dominated the IR absorption spectrum [103]. Experimental IR data is available, however, for samples of multiwalled BN tubes (2–10 walls, diameter:  $30 \pm 10 \text{ \AA}$ ) [71]: Absorption peaks were measured at  $800$  and at  $1,372 \text{ cm}^{-1}$  with a shoulder at  $1,540 \text{ cm}^{-1}$ . At the same time, for polycrystalline h-BN, they measured peaks at  $811 \text{ cm}^{-1}$  and at  $1,377 \text{ cm}^{-1}$  with a shoulder at  $1,514 \text{ cm}^{-1}$ . The interpretation of both results is not straightforward, because in finite-size samples of polar materials, the induced electric field depends not only on the direction of light propagation but also on the boundary conditions at the surface of the sample [104], i.e., the sample geometry. Furthermore, the dielectric properties of the surrounding medium (KBr pellets) can play a role. Both effects strongly influence the position of the  $A_{2u}$  mode and the LO  $E_{1u}$  mode. The upshift of the TO  $E_{1u}$  mode in the polycrystalline sample with respect to the bulk sample is due to the finite size of the crystal domains [83]. The upshift by  $5 \text{ cm}^{-1}$  of the TO  $E_{1u}$  mode in the multiwall tubes with respect to the bulk stems probably from the increased interwall distance in multiwall tubes as compared to the bulk phase [71]. This upshift corresponds to a similar upshift (of  $2.1 \text{ cm}^{-1}$ ) in the Raman spectra of BN multiwall nanotubes [54] (see above).

## 6 Summary and Conclusions

In this chapter, we have reviewed the spectroscopic properties of BN nanotubes covering the basic principles of electronic and vibrational excitations from the theoretical view point. Comparing the electronic properties of BN and C nanotubes, the

most striking difference between the two classes of tubes is the constancy of the quasiparticle gap for BN tubes. The bandgap constancy may be of importance for technological applications because samples containing many different sizes could be grown with predictable electronic properties. Applications as field-emission devices have been envisioned and a first prototype field-effect transistor has been constructed [9].

The optical spectra of BN nanotubes – as well as the spectrum of bulk h-BN and of a single sheet of BN – are dominated by a strongly bound exciton that collects most of the oscillator strength in the spectrum. The binding energy of this exciton increases strongly as the dimensionality is reduced from the 3D bulk over the 2D sheet to the 1D tubes. At the same time, however, the quasiparticle gap increases and the resulting spectra thus display an almost constant “optical gap.” Due to the similarity in the spectra of the tubes and bulk BN, we expect the tubes to exhibit strong UV lasing behavior as already observed for bulk BN [10]. The fact that this luminescence response would be rather insensitive to tube diameter and chirality makes the BN tubes ideal candidates for optical devices in the UV regime as the carbon nanotubes are in the IR regime [105]. The photoluminescence quantum yield of BN tubes should surpass the efficiency of carbon. Furthermore we have shown how defects control the luminescence and the impact of an external electric field perpendicular to the tube axis: While the gap decreases as a function of the electric field strength, the optical spectra of BN nanotubes are quite robust to the application of external fields. On the contrary, an external field affects the defect energy levels due to impurities. These defects give rise to strong luminescence within the gap, in particular in the visible region, as well as modification of the shape of the main absorption peak. Therefore, an external electric field can be used as tool to discriminate the photoemission due to exciton recombination in pure systems with respect to the one due to defects. BN nanotubes may thus be very good candidates for tunable nanoscale optoelectronic devices in the UV regime and below.

The flexibility of composite nanotubes during bending in a wide range of practical conditions shows substantial promise for structural, fiber applications (the “ultimate” lightweight-high-strength flexible and quite inert fiber) and nanotube-reinforced materials. This is due to the remarkable flexibility of the hexagonal network, which resists bond breaking and bond switching up to very high strain values. The lattice dynamics of BN tubes is similar to that of carbon nanotubes. The most important difference is the polarity of the system which leads to softer bonds and lower phonon frequencies. Furthermore, the lower symmetry of BN tubes gives rise to a higher number of Raman- and IR-active modes than in C tubes. As in the case of carbon nanotubes, the lattice dynamics of BN nanotubes can be explained to a large extent by the zone-folding method. The strong overbending of the LO branch of the single sheet is responsible for the strongly nonmonotonic diameter scaling of the transverse high-frequency modes in the tubes. Combined study of BN tubes by Raman and IR spectroscopy can serve to distinguish armchair tubes, where IR- and Raman-active modes are disjoint, from chiral and zigzag tubes, where the IR-active modes are a subset of the Raman-active modes. In particular, the RBM is

both Raman and IR active for chiral and zigzag tubes but only Raman active for armchair nanotubes.

Improvements in the synthesis of BN nanotubes and their unique electronic properties (luminescence, inertness, piezoelectricity, field emission, robustness, etc.) make them ideal candidates to confront – together with carbon nanotubes – the future of real active components in nanoelectronic devices.

**Acknowledgments** We acknowledge funding by Spanish MEC (FIS2007-65702-C02-01), Grupos Consolidados UPV/EHU of the Basque Country Government (IT-319-07), and European Community through e-I3 ETSF project (INFRA-211956); NoE Nanoquanta (NMP4-CT-2004-500198) and SANES (NMP4-CT-2006-017310). All this work started as an activity of the European research and training network COMELCAN and benefited a lot from fruitful collaborations and discussions with A. Marini, M. Grüning, C. Attaccalite, F. Mauri, M. Lazzeri, R. Arenal, P. Jaffrennou, and A. Loiseau. A.R. acknowledge Profs. S.G. Louie, M.L. Cohen, and A. Zettl for fundamental collaborations and support while we started the field of BN nanotubes that now is the scope of the present book chapter.

## References

1. A. Rubio, J.L. Corkill, and M.L. Cohen, *Phys. Rev. B* 49, 5081(R) (1994).
2. X. Blase, A. Rubio, S.G. Louie, and M.L. Cohen, *Europhys. Lett.* 28, 335 (1994).
3. Y. Miyamoto, A. Rubio, S.G. Louie, and M.L. Cohen, *Phys. Rev. B* 50, 18360 (1994).
4. Y. Miyamoto, A. Rubio, S.G. Louie, and M.L. Cohen, *Phys. Rev. B* 50, 4976 (1994).
5. Y. Miyamoto, A. Rubio, S.G. Louie, and M.L. Cohen, *Phys. Rev. Lett.* 76, 2121 (1996).
6. N.G. Chopra, R.J. Luyken, K. Cherrey, V.H. Crespi, M.L. Cohen, S.G. Louie, and A. Zettl, *Science* 269, 966 (1995).
7. Z. Weng-Sieh, K. Cherrey, N.G. Chopra, X. Blase, Y. Miyamoto, A. Rubio, M.L. Cohen, S.G. Louie, A. Zettl, and R. Gronsky, *Phys. Rev. B* 51, 11229 (1995).
8. O. Stephan, P.M. Ajayan, C. Colliex, Ph. Redlich, J.M. Lambert, P. Bernier, and P. Lefin, *Science* 266, 1683 (1994).
9. M. Radosavljević, J. Appenzeller, V. Derycke, R. Martel, P. Avouris, A. Loiseau, J.-L. Cochon, D. Pigache, *Appl. Phys. Lett.* 82, 4131 (2003).
10. K. Watanabe, T. Taniguchi and H. Kanda, *Nat. Mater.* 3, 404 (2004).
11. L. Wirtz, A. Marini, and A. Rubio, *Phys. Rev. Lett.* 96, 126104 (2006).
12. G.Y. Guo and J.C. Lin, *Phys. Rev. B* 71, 165402 (2005).
13. J.P. Perdew, K. Burke, and M. Ernzerhof, *Phys. Rev. Lett.* 77, 3865 (1996).
14. A.D. Becke, *J. Chem. Phys.* 98, 5648 (1993).
15. B. Baumeier, P. Krüger, and J. Pollmann, *Phys. Rev. B* 76, 085407 (2007).
16. M.S. Hybertsen and S.G. Louie, *Phys. Rev. B* 34, 5390 (1986).
17. W.G. Aulbur, L. Jönsson, and J.W. Wilkins, *Quasiparticle calculations in solids in Solid State Physics*, edited by H. Ehrenreich and F. Spaepen (Academic, New York, 2000), Vol. 54, p. 1.
18. G. Onida, L. Reining, and A. Rubio, *Rev. Mod. Phys.* 74, 601 (2002).
19. C. Friedrich and A. Schindlmayr, in *Computational Nanoscience: Do It Yourself!* (NIC Series), edited by J. Grotendorst, S. Blügel, and D. Marx (John von Neumann Institute for Computing, Jülich, 2006), Vol. 31, p. 335.
20. X. Blase, A. Rubio, S.G. Louie and M.L. Cohen, *Phys. Rev. B* 51, 6868 (1995).
21. B. Arnaud, S. Lebègue, P. Rabiller, and M. Alouani, *Phys. Rev. Lett.* 96, 026402 (2006).
22. G. Strinati, *Phys. Rev. B* 29, 5718 (1984).
23. M. Rohlfing and S.G. Louie, *Phys. Rev. Lett.* 81, 2312 (1998).

24. C. Tarrío and S.E. Schnatterly, *Phys. Rev. B* 40, 7852 (1989).
25. Y.N. Xu and W.Y. Ching, *Phys. Rev. B* 44, 7787 (1991).
26. G. Cappellini, G. Satta, M. Palummo, and G. Onida, *Phys. Rev. B* 64, 035104 (2001).
27. A.G. Marinopoulos, L. Wirtz, A. Marini, V. Olevano, A. Rubio, and L. Reining, *Appl. Phys. A* 78, 1157 (2004).
28. L. Wirtz, A. Marini, M. Grüning, C. Attaccalite, G. Kresse, and A. Rubio, *Phys. Rev. Lett.* 100, 189701 (2008).
29. M. Shinada and S. Sugano, *J. Phys. Soc. Jpn* 21, 1936 (1966).
30. T.G. Pedersen, *Phys. Rev. B* 67, 073401 (2003).
31. B. Arnaud, S. Lebègue, P. Rabiller, and M. Alouani, *Phys. Rev. Lett.* 100, 189702 (2008).
32. A. Marini, C. Hogan, M. Grüning, D. Varsano, *Comp. Phys. Comm.* (2009), doi:10.1016/j.cpc.2009.02.003.
33. G. Kresse and J. Furthmüller, *Phys. Rev. B* 54, 11169 (1996).
34. M. Shishkin and G. Kresse, *Phys. Rev. B* 74, 035101 (2006).
35. P.E. Blöchl, *Phys. Rev. B* 50, 17953 (1994).
36. R. Mamy, J. Thomas, G. Jezequel, and J.C. Lemonnier, *J. Phys. (Paris) Lett.* 42, 473 (1981).
37. J.S. Lauret, R. Arenal, F. Ducastelle, A. Loiseau, M. Cau, B. Attal-Trétout, and E. Rosencher, *Phys. Rev. Lett.* 94, 037405 (2005).
38. A. Marini, *Phys. Rev. Lett.* 101, 106405 (2008).
39. T. Ando, *J. Phys. Soc. Jpn* 66, 1066 (1997).
40. C.D. Spataru, S. Ismail-Beigi, L.X. Benedict, and S.G. Louie, *Phys. Rev. Lett.* 92, 077402 (2004).
41. C.D. Spataru, S. Ismail-Beigi, L.X. Benedict, and S.G. Louie, *Appl. Phys. A* 78, 1129 (2004).
42. E. Chang, G. Bussi, A. Ruini, and E. Molinari, *Phys. Rev. Lett.* 92, 196401 (2004).
43. F. Wang, G. Dukovic, L.E. Brus, and T.F. Heinz, *Science* 308, 838 (2005).
44. Y.-Z. Ma, S.L. Dexheimer, L. Valkunas, S.M. Bachilo, and G.R. Fleming, *Phys. Rev. Lett.* 94, 157402 (2005).
45. Y.-Z. Ma, L. Valkunas, S.M. Bachilo, and G.R. Fleming, *J. Phys. Chem. B* 109, 15671 (2005).
46. C.-H. Park, C.D. Spataru, S.G. Louie, *Phys. Rev. Lett.* 96, 126105 (2006).
47. Y. Kubota, K. Watanabe, O. Tsuda, and T. Taniguchi, *Science* 317, 932 (2007).
48. L. Museur and A. Kanaev, *J. Appl. Phys.* 103, 103520 (2008).
49. P. Jaffrennou, J. Barjon, J.-S. Lauret, B. Attal-Trétout, F. Ducastelle, and A. Loiseau, *J. Appl. Phys.* 102, 116102 (2007).
50. C.A. Taylor II, S.W. Brown, V. Subramaniam, S. Kidner, S.C. Rand, and R. Clark, *Appl. Phys. Lett.* 65, 1251 (1994).
51. M.G. Silly, P. Jaffrennou, J. Barjon, J.-S. Lauret, F. Ducastelle, A. Loiseau, E. Obraztsova, B. Attal-Trétout, and E. Rosencher, *Phys. Rev. B* 75, 085205 (2007).
52. W.-Q. Han, H.-G. Yu, C. Zhi, J. Wang, Z. Liu, T. Sekiguchi, and Y. Bando, *Nano Lett.* 8, 491 (2008).
53. T. Taniguchi and K. Watanabe, *J. Cryst. Growth* 303, 525 (2007).
54. J. Wu, W.-Q. Han, W. Walukiewicz, J.W. Ager III, W. Shan, E.E. Haller, A. Zettl, *Nano Lett.* 4(4), 647 (2004).
55. P. Jaffrennou, F. Donatini, J. Barjon, J.-S. Lauret, A. Maguer, B. Attal-Trétout, F. Ducastelle, and A. Loiseau, *Chem. Phys. Lett.* 442, 372 (2007).
56. P. Jaffrennou, J. Barjon, J.-S. Lauret, A. Maguer, D. Goldberg, B. Attal-Trétout, F. Ducastelle, and A. Loiseau, *Phys. Status Solidi B* 244, 4147 (2007).
57. P. Jaffrennou, J. Barjon, T. Schmid, L. Museur, A. Kanaev, J.-S. Lauret, C.Y. Zhi, C. Tang, Y. Bando, D. Goldberg, B. Attal-Trétout, F. Ducastelle, and A. Loiseau, *Phys. Rev. B* 77, 235422 (2008).
58. K.H. Koo, M.S.C. Mazzoni, and S.G. Louie, *Phys. Rev. B* 69, 201401(R) (2004).
59. C.-W. Chen, M.-H. Lee, and S.J. Clark, *Nanotechnology* 15, 1837 (2004).
60. C. Attaccalite, L. Wirtz, A. Marini, and A. Rubio, *Phys. Status Solidi B* 244, 4288 (2007).

61. G.G. Fuentes, E. Borowiak-Palen, T. Pichler, X. Liu, A. Graff, G. Behr, R.J. Kalenczuk, M. Knupfer, and J. Fink, *Phys. Rev. B* 67, 035429 (2003).
62. V.I.A. Margulis, E.E. Muryumin, and E.A. Gaiduk, *Phys. Rev. B* 77, 035425 (2008).
63. R. Arenal, O. Stéphan, M. Kociak, D. Taverna, A. Loiseau, and C. Colliex, *Phys. Rev. Lett.* 95, 127601 (2005).
64. D. Taverna, M. Kociak, V. Charbois, and L. Henrard, *Phys. Rev. B* 66, 235419 (2002).
65. L. Henrard and P. Lambin, *J. Phys. B* 29, 5127 (1996).
66. P.C. Eklund, J.M. Holden, R.A. Jishi, *Carbon* 33, 959 (1995).
67. J. Kastner, T. Pichler, H. Kuzmany, S. Curran, W. Blau, D.N. Weldon, M. Delamesiere, S. Draper, and H. Zandbergen, *Chem. Phys. Lett.* 221, 53 (1994).
68. A.M. Rao, E. Richter, S. Bandow, B. Chase, P.C. Eklund, K.A. Williams, S. Fang, K.R. Subbaswamy, M. Menon, A. Thess, R.E. Smalley, G. Dresselhaus, and M.S. Dresselhaus, *Science* 275, 187 (1997).
69. R. Saito, T. Takeya, T. Kimura, G. Dresselhaus, and M.S. Dresselhaus, *Phys. Rev. B* 57, 4145 (1998).
70. U. Kuhlmann, H. Jontoljak, N. Pfänder, P. Bernier, C. Journet, and C. Thomsen, *Chem. Phys. Lett.* 294, 237 (1998).
71. E. Borowiak-Palen, T. Pichler, G.G. Fuentes, B. Bendjemil, X. Liu, A. Graff, G. Behr, R.J. Kalenczuk, M. Knupfer, and J. Fink, *Chem. Commun.* 1, 82 (2003).
72. V. N. Popov, *Phys. Rev. B* 67, 085408 (2003).
73. P. Saxena, Pand S.P. Sanyal, *Phys. E* 24, 244 (2004).
74. E. Rokuta, Y. Hasegawa, K. Suzuki, Y. Gamou, C. Oshima, and A. Nagashima, *Phys. Rev. Lett.* 79, 4609 (1997).
75. D. Sánchez-Portal and E. Hernández, *Phys. Rev. B* 66, 235415 (2002).
76. L. Wirtz, R. Arenal de la Concha, A. Loiseau, and A. Rubio, *Phys. Rev. B* 68, 045425 (2003).
77. L. Wirtz and A. Rubio, *IEEE Trans. Nanotechnol.* 2, 341 (2003).
78. O. Madelung (Ed.), *Semiconductors – Basic Data* (Springer, Berlin, 1996).
79. G. Kern, G. Kresse, and J. Hafner, *Phys. Rev. B* 59, 8551 (1999).
80. W.J. Yu, W.M. Lau, S.P. Chan, Z.F. Liu, and Q.Q. Zheng, *Phys. Rev. B* 67, 014108 (2003).
81. J. Serrano, A. Bosak, R. Arenal, M. Krisch, K. Watanabe, T. Taniguchi, H. Kanda, A. Rubio, and L. Wirtz, *Phys. Rev. Lett.* 98, 095503 (2007).
82. R. Geick, C.H. Perry, and G. Rupprecht, *Phys. Rev.* 146, 543 (1966).
83. R.J. Nemanich, S.A. Solin, and R.M. Martin, *Phys. Rev. B* 23, 6348 (1981).
84. S. Reich, A.C. Ferrari, R. Arenal, A. Loiseau, I. Bello, and J. Robertson, *Phys. Rev. B* 71, 205201 (2005).
85. N.W. Ashcroft, N.D. Mermin, *Solid State Physics* (Saunders College Publishing, Orlando, 1976).
86. A. Marini, P. García-Gonzalez, and A. Rubio, *Phys. Rev. Lett.* 96, 136404 (2006).
87. O. Dubay and G. Kresse, *Phys. Rev. B* 67, 035401 (2003).
88. G. Kresse, J. Furthmüller, and J. Hafner, *Europhys. Lett.* 32, 729 (1995).
89. P. Pavone, R. Bauer, K. Karch, O. Schütt, S. Vent, W. Windl, D. Strauch, S. Baroni, and S. de Gironcoli, *Phys. B* 219 & 220, 439 (1996).
90. L. Wirtz and A. Rubio, *Solid State Commun.* 131, 141 (2004).
91. E.J. Mele and P. Kral, *Phys. Rev. Lett.* 88, 056803 (2002).
92. The selection rules for Raman and IR spectroscopy are discussed in many textbooks. E.g., a nice introduction can be found in: D.C. Harris and M.D. Bertolucci, *Symmetry and Spectroscopy: An Introduction to Vibrational and Electronic Spectroscopy* (Dover, New York, 1989).
93. M. Damnjanović, T. Vuković, I. Milošević, and B. Nikolić, *Act Cryst.* A57, 304 (2001).
94. O.E. Alon, *Phys. Rev. B* 64, 153408 (2001).
95. O.E. Alon, *J. Phys.: Condens. Mat.* 15, S2489 (2003).
96. O.E. Alon, *Phys. Rev. B* 63, 201403 (2001).



97. R. Saito, G. Dresselhaus, and M.S. Dresselhaus, *Physical Properties of Carbon Nanotubes* (Imperial College Press, London, 1998).
98. R.A. Jishi, L. Venkataraman, M.S. Dresselhaus, and G. Dresselhaus, *Chem. Phys. Lett.* 209, 77–82 (1993).
99. J. Kürti, G. Kresse, and H. Kuzmany, *Phys. Rev. B* 58, R8869 (1998).
100. H. Vogt, in *Light Scattering in Solids II*, edited by M. Cardona and G. Güntherodt (Springer, Berlin, 1982).
101. L. Wirtz, M. Lazzeri, F. Mauri, and A. Rubio, *Phys. Rev. B* 71, 241402(R) (2005).
102. M. Lazzeri and F. Mauri, *Phys. Rev. Lett.* 90, 036401 (2003).
103. R. Arenal, A.C. Ferrari, S. Reich, L. Wirtz, J.-Y. Mevellec, S. Lefrant, A. Rubio, and A. Loiseau, *Nano Lett.* 6, 1812 (2006).
104. E. Balan, A.M. Saitta, F. Mauri, and G. Calas, *Am Mineral* 86, 1321 (2001).
105. J.A. Misewich et al., *Science* 300, 783 (2003).

# Boron Nitride Nanocage Clusters, Nanotubes, Nanohorns, Nanoparticles, and Nanocapsules

Takeo Oku, Ichihito Narita, Naruhiro Koi, Atsushi Nishiwaki, Katsuaki Suganuma, Masahiro Inoue, Kenji Hiraga, Toshitsugu Matsuda, Makoto Hirabayashi, Hisato Tokoro, Shigeo Fujii, Makoto Gonda, Masahiko Nishijima, Toshio Hirai, Rodion V. Belosludov, and Yoshiyuki Kawazoe

**Abstract** Various types of boron nitride (BN) nanostructured materials such as nanocage clusters, nanotubes, nanohorns, nanoparticles, and nanocapsules were synthesized by arc melting, thermal annealing, and chemical vapor deposition methods, which were characterized by high-resolution electron microscopy and molecular orbital calculations, and their properties were discussed. The BN clusters consisted of 4-, 6-, 8- and 10-membered BN rings satisfying the isolated tetragonal rule, which was optimized by molecular orbital calculations. Total energy calculation showed that some elements stabilize and expand the  $B_{36}N_{36}$  structure. Bandgap energies of the  $B_{36}N_{36}$  clusters were found to be reduced by introducing a metal atom inside the cluster, which indicates controllability of the energy gap. Chiralities of BN nanotubes with zigzag- and armchair-type structures were directly determined from high-resolution images, and structure models are proposed. Total energies of BN nanotubes with a zigzag-type structure were lower than those of armchair-type structure, and these results agreed well with the experimental data. Cup-stacked BN nanotubes and Fe-filled BN nanotubes were also produced, and the atomic structures, structural stability, and electronic property were investigated and discussed. BN nanohorns were synthesized, and multiwalled BN nanohorns would be stabilized by stacking of BN nanohorns. Formation and structures of multiply twinned nanoparticles with fivefold symmetry in chemical vapor-deposited BN were also investigated. A new process for Fe or Co nanoparticles coated with BN layers in large quantity was developed, and they exhibited a soft magnetic characteristic and good oxidation resistances. These unique structures would be suitable materials for nanoelectronics devices, magnetic recording media, and biological sensors with excellent protection against oxidation and wear. Possibility of hydrogen gas storage in BN clusters was also investigated by molecular orbital calculations, which indicated possibility of hydrogen storage of ~5 wt%. The new BN nanostructured materials would be expected as future nanocage devices.

---

T. Oku

Department of Materials Science, The University of Shiga Prefecture, Hassaka 2500, Hikone, Shiga 522-8533, Japan  
e-mail: oku@mat.usp.ac.jp

## 1 Introduction

Since the development of boron nitride (BN) nanotubes [1], various types of BN nanostructured materials have been reported because of the great potential for using materials with low dimensions in an isolated environment. Many studies have been reported on BN nanomaterials and single crystals such as nanotubes [2–11], bundled tubes [12, 13], nanocorns [14–16], nanohorns [17–21], nanocapsules [7, 22–28], nanoparticles [29, 30], BN clusters [7, 18, 32–35], and BN metallofullerenes [18, 21, 36, 37], which are expected to be useful as electronic devices [38], field-effect transistors [39], high heat-resistant semiconductors, insulator lubricants, nanowires [40, 41], magnetic nanoparticles [42, 43], gas storage materials [44–47], and optoelectronic applications including ultraviolet light emitters [48, 49]. Theoretical calculations on BN nanomaterials such as nanotubes [50–55], cluster-included nanotubes [56–59], BN clusters [60–76], BN metallofullerenes [77–79], cluster solids [80–82], nanohorns [83, 84], and hydrogen storage [85–89] have also been carried out for prediction of the properties. By controlling the size, layer numbers, helicity, compositions, and included clusters, these cluster-included BN nanocage structures with bandgap energy of  $\sim 6$  eV [48, 49] and nonmagnetism are expected to show various electronic, optical, and magnetic properties as shown in Fig. 1. The differences between BN and carbon nanomaterials [90, 91] are summarized as shown in Table 1.

The present review shows BN nanocage clusters, nanotubes, nanohorns, nanoparticles, and nanocapsules synthesized by arc melting, thermal annealing, and

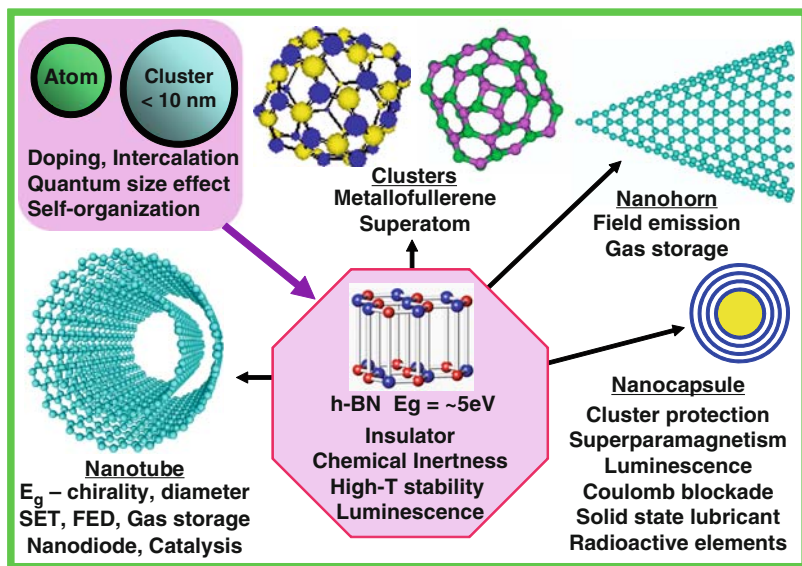


Fig. 1 Structures and properties of BN nanostructured materials

**Table 1** Differences between BN and carbon (C) nanomaterials

	C	BN
Structure	5-, 6-, 7-membered rings	4-, 6-, 8-membered rings
Oxidation resistance	~600°C	~900°C
Electronic property (Eg)	Metal-semiconductor (0~1.7 eV)	Insulator (~6 eV)
Band structure	Indirect transition	Direct transition

chemical vapor deposition methods. They were characterized by high-resolution electron microscopy (HREM), and their properties were investigated and discussed. In order to confirm the atomic structures and to investigate stabilities, electronic states, and hydrogen storage, total energy calculations were carried out by molecular mechanics and molecular orbital calculations. These studies will give us a guideline for the synthesis of the BN fullerene materials, which are expected for the future nanoscale devices.

## 2 BN Clusters

In order to prepare BN nanocage clusters, an arc-melting method was selected. An yttrium (Y) element was selected as catalysis for the BN cluster formation. Yttrium had been reported to show excellent catalytic properties for producing single-walled carbon nanotubes [92]. The  $YB_6$  powder was used for the formation of BN clusters [93]. BN nanotubes were also synthesized from  $YB_6$  with Ni powder [94, 95]. The  $YB_6$  and Ni powders with the atomic ratio of 1:1 were set on a copper mold in an electric-arc furnace, which was evacuated down to  $1 \times 10^{-3}$  Pa. After introducing a mixed gas of Ar and  $N_2$ , arc melting was applied to the samples at an accelerating voltage of 200 V and an arc current of 125 A for 10 s. Arc melting was performed with a vacuum arc-melting furnace, and gray to white powder were obtained around the copper mold.

An AXIMA-CFR (Shimadzu/Kratos, Manchester, UK) instrument was used to obtain laser desorption time-of-flight (LD-TOF) mass spectra [96]. The operating conditions were as follows: nitrogen laser (337 nm); linear mode; accelerating voltage at 20 kV; and detection of positive ions. The sample powder (50 mg) was suspended in pyridine ( $C_5H_5N$ , 200 ml) with ultrasonication. The aliquot (1-2 ml) was spotted on the sample plate and dried at room temperature. The mass spectra were corrected by using  $C_{60}$  and  $C_{70}$  clusters [97].

Figure 2a shows a mass spectrum for BN clusters in pyridine solution, and demonstrates the existence of (BN) $n$  ( $n = 12-60$ ) clusters [32, 93]. In addition, (BN) $n$  ( $n \sim 80$ ) clusters were detected in the present work. Further, endohedral BN clusters [ $Y_x@(BN)_n$ ] with yttrium atoms encapsulated inside the BN clusters were detected. A mass spectrum for pyridine solution, which was used for matrix in LD-TOF mass spectrometry, is also shown for reference in Fig. 2b. The mass

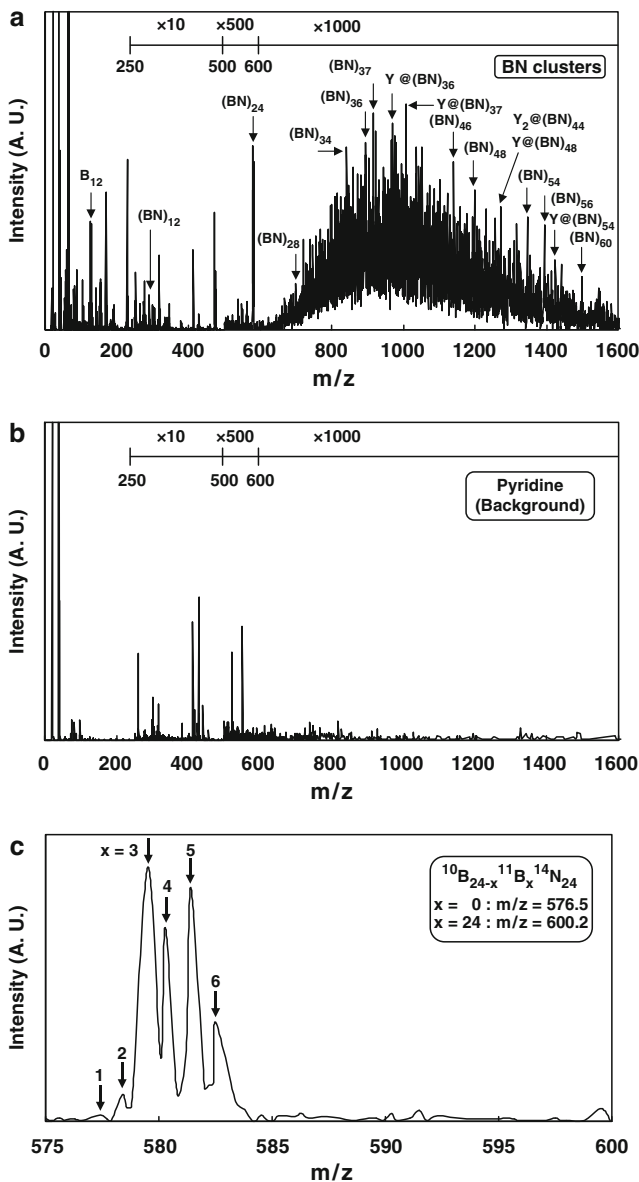


**Fig. 2** LD-TOF mass spectrum for (a) BN clusters and (b) pyridine (background). (c) Enlarged LD-TOF mass spectra for  $B_{24}N_{24}$  cluster

spectrum peaks have a somewhat broad distribution because of the two isotopes of  $^{10}B$  and  $^{11}B$ . For localized structures of BN clusters, it should be noted that the isotopic ratio of boron atoms might be different from the natural averaged ratio because of minimization of the clusters' structural energy. Mass spectrum peaks for

(BN) $_n$  clusters are observed in the range of  $m/z = 600$ -1,600, and the distribution peak is around  $n \sim 40$ , which supports previously reported  $B_{36}N_{36}$  clusters with high symmetry [7, 18, 65]. Figure 2c shows an enlarged mass spectrum for  $B_{24}N_{24}$  clusters, and demonstrates the existence of  $^{10}B_{24-x}^{11}B_x^{14}N_{24}$  ( $x = 1-6$ ) clusters. The mass spectrum peaks have a somewhat broad distribution because of the two isotopes of  $^{10}B$  and  $^{11}B$ . Peaks of the cluster distribution are observed around  $x$  values of 3-5. For localized structures of BN clusters, it should be noted that the isotopic ratio of boron atoms might be different from the natural averaged ratio ( $^{10}B:^{11}B = 19.9:80.1$ ) because of the minimization of the clusters structural energy.

Although fullerenes satisfy the isolated pentagon rule, the present BN cage clusters satisfy the isolated tetragonal rule, as proposed for structural models of (BN) $_n$  ( $n = 12, 24, 28, 36, 48, \text{ and } 60$ ) in Fig. 3. All BN clusters have tetragonal BN rings

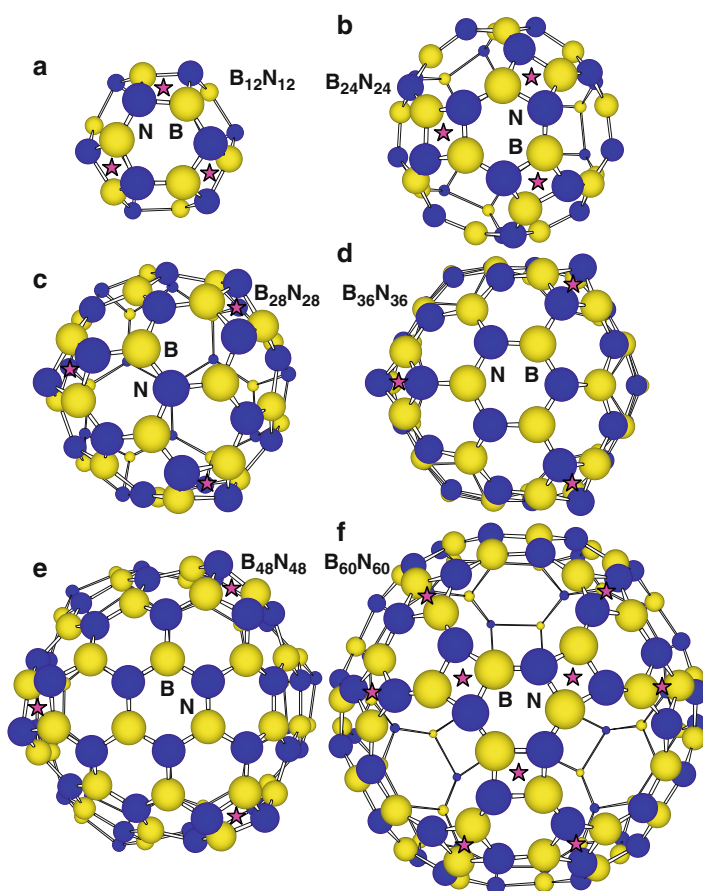


**Fig. 3** Atomic structure models of (a)  $B_{12}N_{12}$ , (b)  $B_{24}N_{24}$ , (c)  $B_{28}N_{28}$ , (d)  $B_{36}N_{36}$ , (e)  $B_{48}N_{48}$ , and (f)  $B_{60}N_{60}$  clusters viewed along hexagonal BN rings. Tetragonal BN rings are indicated by *star marks*

isolated by hexagonal-BN (h-BN) rings. In addition to the tetragonal and hexagonal rings, octagonal and decagonal BN rings [80] were introduced for  $B_{24}N_{24}$  and  $B_{60}N_{60}$  clusters in the present work.

In order to confirm the structure of the BN clusters, HREM observations were carried out. Hollow BN clusters were often observed on and inside the BN nanotubes, and the BN fullerene clusters had a single BN sheet, as shown in Fig. 4a. Sizes of the BN clusters were in the range of 0.7-1.0 nm, which corresponds to the size of  $B_{36}N_{36}$  clusters [36, 93]. The  $B_{36}N_{36}$  cluster consists of 6 four-membered rings and 32 six-membered rings as shown in Fig. 4d. In addition to the empty BN cage clusters, BN clusters containing doped atoms were also observed in HREM images. A typical HREM image of the BN clusters is shown in Fig. 4b, c, and a ring

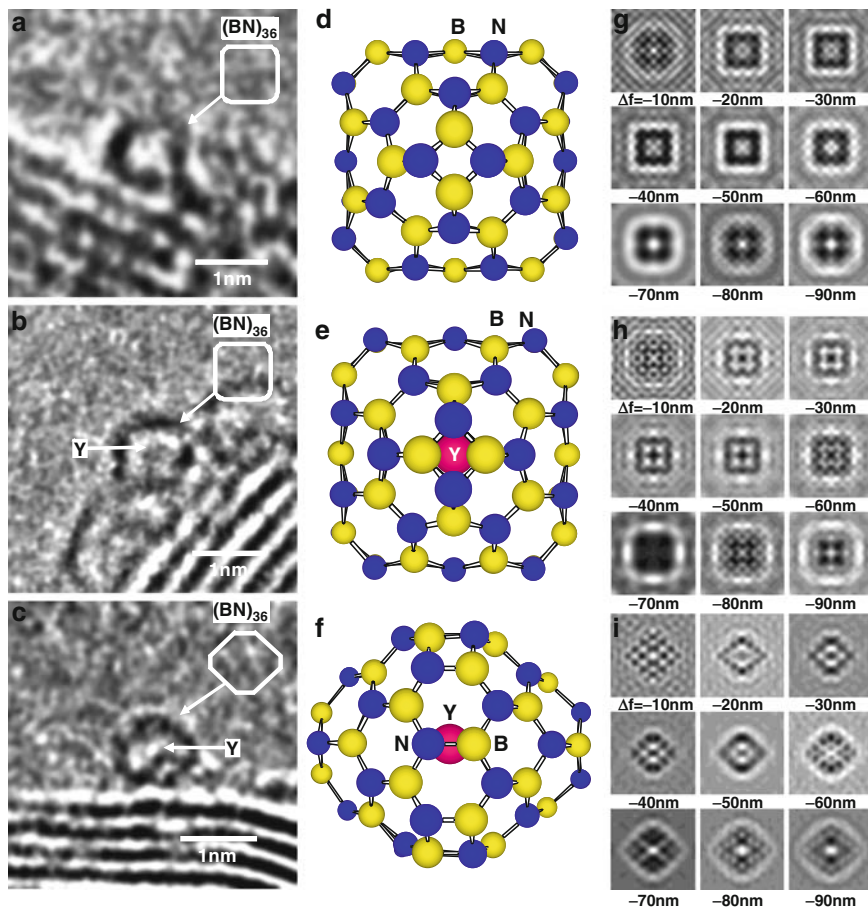


**Fig. 4** HREM images of (a)  $B_{36}N_{36}$  and (b, c)  $Y@B_{36}N_{36}$  clusters. Structure models of (d)  $B_{36}N_{36}$  and (e, f)  $Y@B_{36}N_{36}$  clusters corresponding to (a) and (b, c), respectively. The structure model (e) is viewed perpendicular to (f). Calculated HREM images of (g)  $B_{36}N_{36}$  and (h, i)  $Y@B_{36}N_{36}$  clusters as a function of defocus values along the same directions of (d-f), respectively

contrast indicates  $B_{36}N_{36}$  cluster. A dark contrast is observed inside the BN clusters, which indicates the existence of an yttrium atom inside the  $B_{36}N_{36}$  clusters. During arc melting of  $YB_6$  powder, yttrium atoms could be introduced inside the  $B_{36}N_{36}$  clusters [93]. Structure models for  $Y@B_{36}N_{36}$  metallofullerene are proposed as shown in Fig. 4e, f. The structures are optimized by molecular mechanics calculations (MM2), and the yttrium atom is closed to the center of the  $B_{36}N_{36}$  cluster. Dark contrast is also observed outside of the BN cluster, which would be due to the quantum noise of electrons. However, inside the BN cluster, the contrast is strongly dependent on the diffraction conditions [36, 98, 99]. Therefore, the dark contrast inside the BN clusters is believed to be due to the existence of an yttrium atom.

To compare observed images with calculated ones, HREM images were calculated by the multislice method using the MacTempas software (Total Resolution, CA, USA). The parameters used in the calculations are as follows: accelerating voltage = 300 kV, radius of the objective aperture =  $5.9 \text{ nm}^{-1}$ , spherical aberration  $C_s = 0.6 \text{ mm}$ , spread of focus  $\Delta = 8 \text{ nm}$ , semiangle of divergence  $a = 0.55 \text{ mrad}$ , under defocus values  $\Delta f = -10$  to  $90 \text{ nm}$ , unit cell (one cluster) =  $2 \times 2 \times 2 \text{ nm}$ , crystal thickness (unit-cell thickness, 7 slices)  $t = 2 \text{ nm}$  and  $5 \text{ nm}$ , respectively, space group  $PI$ , and assumed temperature factors [100, 101]  $0.02 \text{ nm}^2$  (B and N) and  $0.14 \text{ nm}^2$  (Y).

Based on the projected structure models of Fig. 4d-f, image calculations on the  $B_{36}N_{36}$  and  $Y@B_{36}N_{36}$  clusters were carried out to investigate the cluster structures. HREM images of the  $B_{36}N_{36}$  and  $Y@B_{36}N_{36}$  clusters calculated along the [100] direction of the projected unit cell as a function of defocus values are shown in Fig. 4g-i. The experimental images of Fig. 4a-c agree with calculated HREM images (Fig. 4g-i), especially at defocus value of  $-40 \text{ nm}$ , which is nearly Scherzer defocus ( $\Delta f_s = -41.2 \text{ nm}$ ). This indicates the yttrium atom is included inside the BN cluster. The dark contrast corresponding to the yttrium atom inside the  $B_{36}N_{36}$  cluster is smeared a little compared to the simulated image, which would be due to the vibration of the yttrium atom by electron beam irradiation. The formation of BN endohedral fullerene clusters including lanthanum and iron atoms has been previously reported [36]. For the present data, the endohedral BN metallofullerenes of  $Y@B_nN_n$  ( $n = 36, 37, \text{ and } 48$ ) were produced and characterized from HREM and LD-TOF mass spectrometry. Various lanthanide elements could be introduced into the BN clusters, as reported in the carbon-based metallofullerenes [102].

Densities of states (DOS) for  $B_{24}N_{24}$ ,  $B_{36}N_{36}$ , and  $B_{60}N_{60}$  clusters are calculated and shown in Fig. 5a-c, respectively. The energy levels and density of states were calculated by the first principles calculation with discrete variational (DV)-Xa method. Strong effects of B-2p and N-2p orbitals on the DOS are observed. The structural optimization and electronic structures of the BN clusters performed by molecular orbital calculations (PM5) are summarized in Table 2. The  $B_{36}N_{36}$  cluster shows the largest energy gap of  $5.367 \text{ eV}$  between the highest occupied molecular orbital (HOMO) and the lowest unoccupied molecular orbital (LUMO), and the  $B_{24}N_{24}$  and  $B_{60}N_{60}$  clusters with octagonal and decagonal BN rings shows the smallest energy gap of  $4.9 \text{ eV}$ . The  $B_{36}N_{36}$  and  $B_{48}N_{48}$  clusters show the lowest total energies per atom as listed in Table 2, which agreed with the results of LD-TOF mass spectroscopy in the range of  $m/z = 600\text{--}1,600$ .



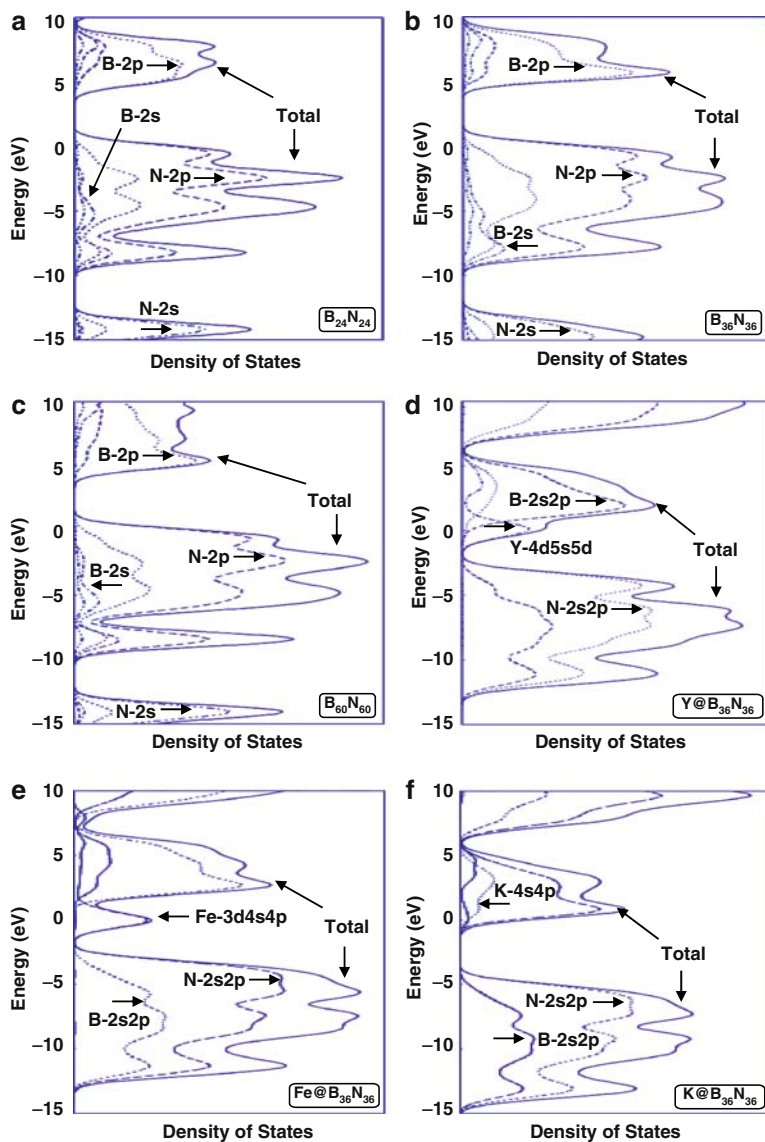


**Fig. 5** Densities of states for (a)  $B_{24}N_{24}$ , (b)  $B_{36}N_{36}$ , (c)  $B_{60}N_{60}$ , (d)  $Y@B_{36}N_{36}$ , (e)  $Fe@B_{36}N_{36}$ , and (f)  $K@B_{36}N_{36}$  clusters

Figure 6 shows heat of formation (total energies) per atom of  $B_{36}N_{36}$  clusters with doping element M ( $M@B_{36}N_{36}$ ) clusters presented in periodic table [18, 78]. A total energy of  $B_{36}N_{36}$  was calculated to be  $-19.68$  kcal/atom mol. Comparing this value with the other total energies in Fig. 6, energies of  $K@B_{36}N_{36}$  and  $Ga@B_{36}N_{36}$  show lower energies than that of  $B_{36}N_{36}$  clusters. This indicates that potassium

**Table 2** Calculated values for  $B_nN_n$  ( $n = 12-60$ ) clusters

	$B_{12}N_{12}$	$B_{24}N_{24}$	$B_{28}N_{28}$	$B_{36}N_{36}$	$B_{48}N_{48}$	$B_{60}N_{60}$
Heat of formation (kcal/mol)	-298.3	-832.4	-1162.6	-1597.8	-2312.3	-2311.1
Heat of formation (kcal/mol-atom)	-12.4	-17.3	-20.8	-22.2	-24.1	-19.3
Tetragonal BN rings	6	12	6	6	6	30
Hexagonal BN rings	8	8	24	32	52	20
Octagonal BN rings	0	6	0	0	0	0
Decagonal BN rings	0	0	0	0	0	12
$BN_{10-6}$ (nm)	-	-	-	-	-	0.1399
$BN_{10-4}$ (nm)	-	-	-	-	-	0.1492
$BN_{8-6}$ (nm)	-	0.1425	-	-	-	-
$BN_{8-4}$ (nm)	-	0.1503	-	-	-	-
$BN_{6-4}$ (nm)	0.1527	0.1529	0.1512	0.1509	0.1511	0.1532
$BN_{6-6}$ (nm)	0.1462	-	0.1493	0.1487	0.1472	-
$d_{max}$ (nm)	0.488	0.683	0.780	0.743	1.063	1.102
$d_{min}$ (nm)	0.488	0.682	0.647	0.882	0.862	1.102
$e_{HOMO}$ (eV)	-3.123	-3.127	-2.993	-3.051	-2.983	-2.966
$e_{LUMO}$ (eV)	1.957	1.818	2.230	2.316	2.221	1.944
Energy gap $E_g$ (eV)	5.080	4.945	5.222	5.367	5.205	4.910

-, Data were not available

and gallium elements introduced inside the BN cluster stabilize the  $B_{36}N_{36}$  structure, and the  $B_{36}N_{36}$  clusters were found to be expanded by an atomic doping. Several other elements also have higher energies than that of  $B_{36}N_{36}$  clusters. As indicated by asterisks, when molybdenum and barium elements were introduced, the structures of  $B_{36}N_{36}$  were highly distorted or broken.

Electronic structures of  $Y@B_{36}N_{36}$ ,  $Fe@B_{36}N_{36}$  and  $K@B_{36}N_{36}$  clusters were investigated as shown in Fig. 5d-f, respectively. DOS of endohedral  $M@B_{36}N_{36}$  clusters show effect of doping elements in BN clusters. Energy gaps of  $B_{36}N_{36}$ ,  $Y@B_{36}N_{36}$ ,  $Fe@B_{36}N_{36}$ , and  $K@B_{36}N_{36}$  clusters were calculated to be 5.367, 0.114, 0.107, and 0.522 eV, respectively. Reduction of bandgap energies for  $Y@B_{36}N_{36}$ ,  $Fe@B_{36}N_{36}$ , and  $K@B_{36}N_{36}$  are due to the Y4d, Fe3d, and K4s orbitals. The present results indicate that the energy gap  $E_g$  of the  $B_{36}N_{36}$  can be controlled by introducing an atom inside the  $B_{36}N_{36}$  cluster, and that some atoms such as potassium or gallium in the  $B_{36}N_{36}$  cluster might stabilize the BN clusters by doping [78].

The BN cluster is a molecule with polarity because of a positive charge at boron atom positions and a negative charge at nitrogen atom positions; so an electrophilic or nucleophilic reagent would work as a solution for BN clusters. Since  $C_{60}$  fullerene clusters have no polarity and are soluble in nonpolar solvents such as toluene [103] and benzene, they have difficulty in dissolving in a polar solvent. In the present work, pyridine ( $C_5H_5N$ ) did work well for the extraction of BN clusters because of an electrophilic reaction; pyrrole ( $C_4H_4NH$ ) would also work as a nucleophilic reagent. In order to investigate these BN nanocage clusters further, separation technique using high performance liquid chromatography should also be developed.

	1/I	2/II	3	4	5	6	7	8	9	10	11	12	13/III	14/IV	15/V	16/VI	17/VII	18/VIII	
1	H -18.7																		He
2	Li -18.8	Be 16.38											B -17.5	C -16.4	N	O	F		Ne
3	Na -19.4	Mg -19.7											Al -18.5	Si -17.5	P -17.8	S -18.7	Cl -19.0		Ar
4	K -20.3	Ca -11.6	Sc	Ti	V	Cr	Mn	Fe -16.7	Co	Ni	Cu -17.9	Zn -17.8	Ga -19.7	Ge -19	As -18.5	Se -19.0	Br		Kr
5	Rb	Sr	Y	Zr	Nb	Mo *	Tc	Ru	Rh	Pd -18.8	Ag -17.8	Cd -17.4	In	Sn	Sb	Te	I		Xe
6	Cs	Ba *	La-Lu	Hf	Ta	W	Re	Os	Ir	Pt -15.2	Au	Hg -17.8	Tl	Pb -18	Bi	Po	At		Rn
7	Fr	Ra	Ac-Lr	Rf	Db	Sg	Bh	Hs	Mt										

**Fig. 6** Heat of formation (kcal/mol) of endohedral  $M@B_{36}N_{36}$  clusters with doping element M. Total Energy of  $B_{36}N_{36}$  per atom is  $-19.68$  kcal/atom. *Asterisks* indicate  $B_{36}N_{36}$  structure was highly distorted or broken

### 3 BN Nanotubes

A low magnification image of BN nanotubes produced from  $YB_6/Ni$  powder is shown in Fig. 7a. The lengths and diameters of BN nanotubes are  $\sim 5$   $\mu$ m and 3–50 nm, respectively. A HREM image of a  $B_{36}N_{36}$  cluster inside a BN nanotube is shown in Fig. 7b [18]. The BN nanotube has a multiwalled structure, and a diameter of the most inner tube is 1.75 nm. An atomic structure model of the center of Fig. 7b is shown in Fig. 7c. Diameter and chirality of the BN nanotube are 1.747 nm and (22, 0), respectively. This kind of peapod-type self-organized structure would be useful for the nanoscale devices [104]. Another HREM image of BN nanotubes with a bundled structure is shown in Fig. 7d, and an atomic structure model observed from three different directions is shown in Fig. 7e. There are some spaces among the BN nanotubes, and the space would be useful for gas storage such as hydrogen.

Figure 8a is a HREM image of a quadruple-walled BN nanotube. In the present work, all HREM images were taken close to the Scherzer defocus ( $\Delta f_s = -41.2$  nm), which is an optimum defocus value of electron microscope, in order to investigate the atomic structures in detail. HREM observations and electron diffraction analysis on BN nanotubes have been reported [105–108], and direct observations of nanotube chirality were tried in the present work. An enlarged HREM image is shown in Fig. 8b, which indicates lattice fringes in the BN nanotubes [109, 110]. A filtered Fourier transform of Fig. 8b showed that this nanotube had a zigzag-type structure as shown in Fig. 8c. A HREM image with clear contrast processed after Fourier noise filtering is shown in Fig. 8d. The intervals of the bright and dark dots are 0.14 nm, which corresponds to the structure of h-BN rings, as shown in Fig. 8e. Layer intervals of each tube are 0.35 nm, as shown in Fig. 8f. Diameters of each nanotube are 2.8, 3.5, 4.2, and 4.9 nm from the inside to outside.

Another HREM image of BN nanotube produced from  $YB_6$  powder is shown in Fig. 9a. Width of the multiwalled BN nanotube is 8.5 nm. The BN nanotube consists of nine layers and has asymmetry layer arrangements. Layer distances are

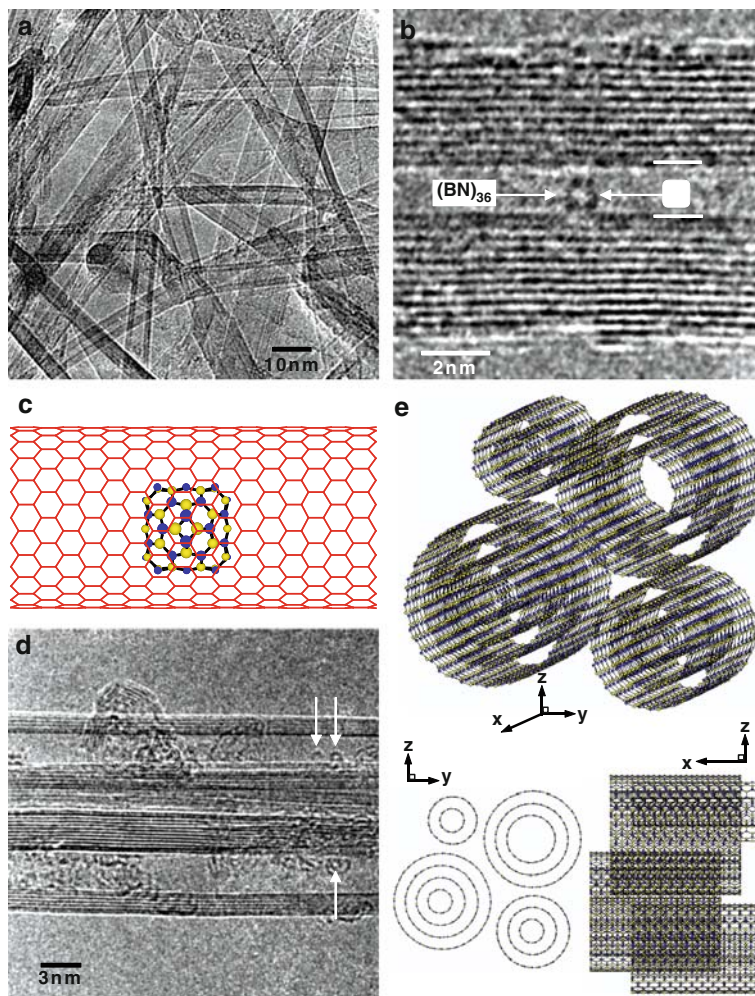


**Fig. 7** (a) Low magnification image of BN nanotubes. (b) HREM image of  $B_{36}N_{36}$  cluster in BN nanotube. (c) Structure model of the center of (b). (d) HREM image of bundled BN nanotubes. BN clusters are indicated by *arrows*. (e) Atomic structure model from three different directions for bundled BN nanotubes

in the range of 0.34–0.51 nm, which is larger than that of {002} of ordinary h-BN (0.34 nm). Diameters of the first and second internal nanotubes are 1.7 nm and 2.6 nm, respectively. Hexagonal net planes of BN nanotube are observed in an enlarged image of Fig. 9b. Figure 9c is a filtered Fourier transform of Fig. 9b, which indicates 002 and 100 reflections of BN structure. Inverse Fourier transform of Fig. 9c is shown in Fig. 9d, which indicates the lattice fringes of hexagonal networks clearly. A h-BN ring is shown in Fig. 9d, and the BN has an armchair-type structure.

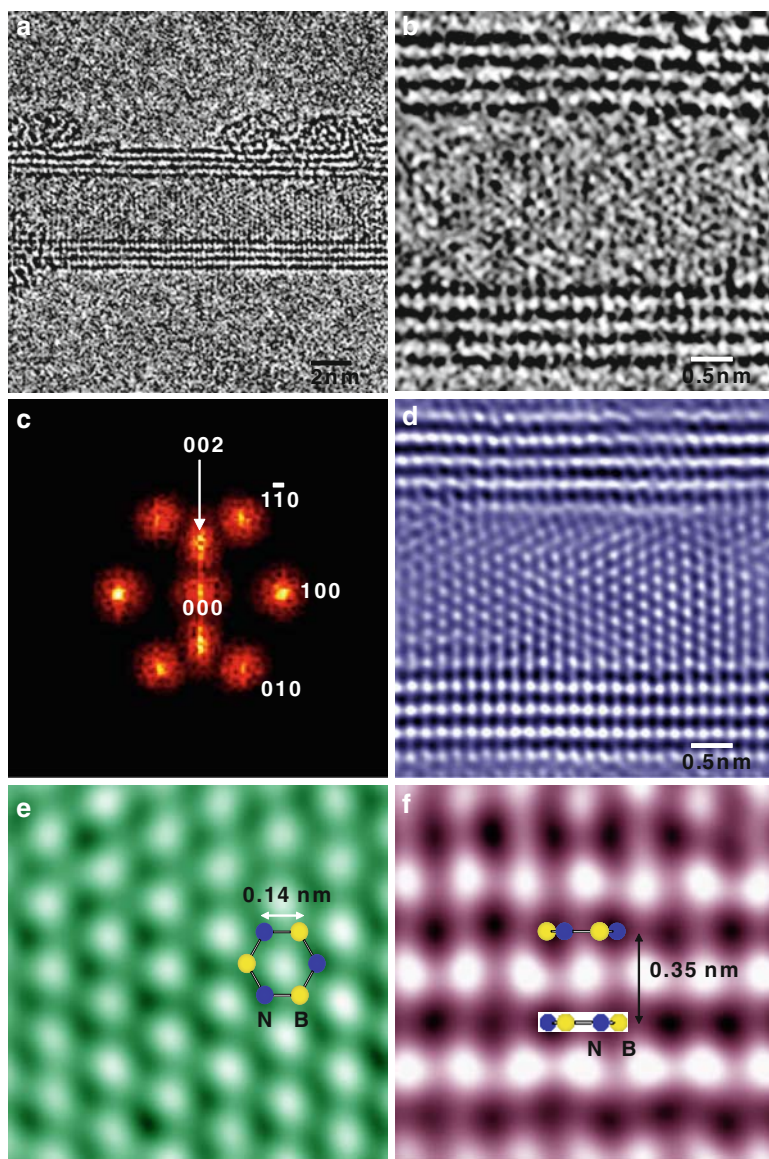


**Fig. 8** (a) HREM image of zigzag-type BN nanotube. (b) Enlarged HREM image of (a). (c) Filtered Fourier transform of (b). (d) Inverse Fourier transform of (c). Enlarged images of center (e) and edge (f) of the BN nanotube in (d)

Atomic structure models were proposed from observed diameters of BN nanotubes, which were based on layer intervals of 0.34–0.35 nm. The chirality of  $(n, m)$  is derived from the equation

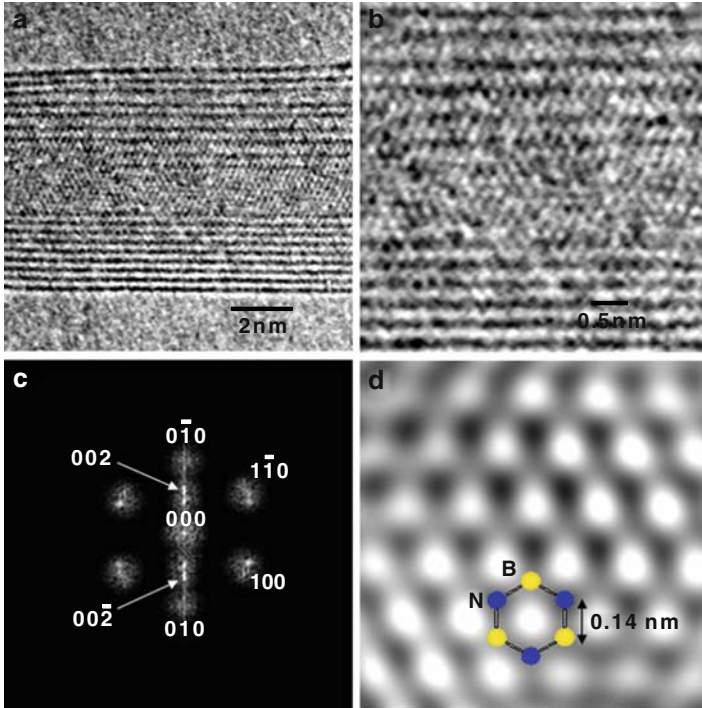


**Fig. 9** (a) HREM image of armchair-type BN nanotube. (b) Enlarged HREM image of (a). (c) Filtered Fourier transform of (b). (d) Inverse Fourier transform of (c)

$$d_t = \frac{\sqrt{3}a_{B-N}\sqrt{n^2 + nm + m^2}}{\pi} \tag{1}$$

The  $d_t$  means a diameter of BN nanotube with nm scale, and the  $a_{B-N}$  corresponds to the nearest distance of boron and nitrogen atoms. For the BN nanotubes, the value of  $a_{B-N}$  is 0.144 nm. When a BN nanotube has a zigzag structure, the value of  $m$  is zero.

Figure 10a shows a proposed structure model of the quadruple-walled BN nanotube. Chiralities of each zigzag BN nanotube are (35, 0), (44, 0), (53, 0), and (62, 0) from the inside to outside. These chiralities were derived from (1). The arrangement of boron and nitrogen atoms was reversed at each layer, as boron atoms exist just above the nitrogen atoms while maintaining the layer intervals of 0.35 nm. Calculated images of the proposed model as a function of defocus values are shown in Fig. 10b. Contrast of hexagonal rings was clearly imaged at the defocus values in the range of -40 to -50 nm, and these simulated images agree well with the observed HREM image of Fig. 8d.

A proposed structure model of double-walled BN nanotube corresponding to Fig. 9 is shown in Fig. 10c. Chiralities of the BN nanotube are (13, 13) and (19, 19)

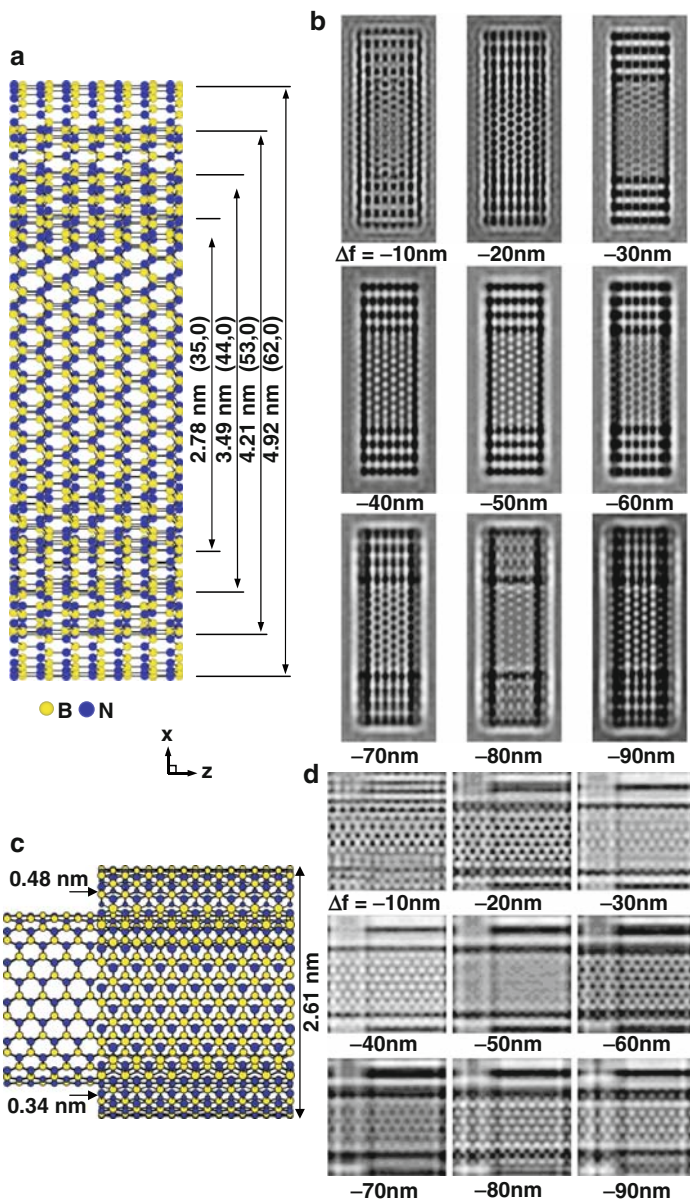


**Fig. 10** (a) Proposed structure model of quadruple-walled BN nanotube. Chiralities of zigzag BN nanotubes are (35, 0), (44, 0), (53, 0), and (62, 0) from inside to outside. (b) Calculated images of the proposed model (a) as a function of defocus values. (c) Proposed structure model of double-walled BN nanotube. Chiral vectors of nanotube are (13, 13) and (19, 19) for the first and second layers, respectively. (d) Calculated images of the proposed model (c)

for the first and second layers, respectively. Layer intervals of lattice fringes of {002} planes are accorded with observed ones in Fig. 9a. Based on the projected structure model, image calculations were carried out for various defocus values, as shown in Fig. 10d and a HREM image calculated at  $-40$  nm agrees well with the experimental data of Fig. 9d.

When the zigzag-type BN nanotubes are characterized using HREM, the BN atom pairs at sides of the nanotubes are sometimes imaged as dots, as observed in Fig. 8f. Taking such dot contrast would be difficult for armchair-type BN nanotubes because of high density distribution of atoms along nanotube axis, and the HREM image contrast would show straight lines at the sides of nanotubes. Multihelix BN nanotubes would also show unclear dot contrast at the side of the nanotube, which indicates that the contrast of side edges of BN nanotubes would also give us useful information on the chirality. If clear dot contrast is observed at the sides of BN nanotubes, possibility of zigzag-type BN nanotube is high. Image contrast also could be changed by rotation of nanotubes, and the further study on the rotation of BN nanotubes has been presented [110].

Structural stabilities of BN nanotubes were investigated and summarized as reported [111]. Since an effect of nanotube edges should be considered, nanotubes with short and long lengths were investigated. Total energies of zigzag-type structures showed lower values than those of armchair-type structures, which indicates that the zigzag-type is more stable compared to the armchair-type structures. This also agreed with distorted nanotube structures in experimental data [110]. A similar experimental result was also reported [112], and the present calculations also confirmed the stability of the zigzag-type BN nanotubes. Encapsulation of a BN cluster in a BN nanotube showed reduction of total energy, which indicates that the encapsulation of the BN cluster in BN nanotube would stabilize the BN cluster [18, 59].

## 4 BN Nanotubes with Cup-Stacked Structures

Although the arc-melting method is a good technique for producing BN nanocage materials, the amount is not so much, and a method for mass production should be developed. There are several methods for it [113, 114], and one of the methods is described here [115]. Solubilization of BN nanotubes were also reported [116, 117].

$\text{Fe}_4\text{N}$  (99%, Kojundo Chemical Laboratory (KCL) Co. Ltd., Saitama, Japan) and boron (B) powders (99%, KCL) were used as raw materials [118, 119]. Their particle sizes were about 50 and 45 nm, respectively. After the  $\text{Fe}_4\text{N}$  and B (weight ratio  $\text{WR} = 1:1$ ) were mixed by a triturator, the samples were set on an alumina boat and annealed in the furnace. The furnace was programmed to heat at  $6^\circ\text{C}/\text{min}$  from ambient to  $1,000^\circ\text{C}$  and hold for 1 h and then cooled at  $3^\circ\text{C}/\text{min}$  to ambient temperature. Nitrogen pressure was 0.10 MPa, and its gas flow was 100 sccm (standard cubic centimeter per minute).



As-produced soot synthesized from  $\text{Fe}_4\text{N/B}$  via the above method was purified by the following steps. The as-produced soot were poured in 4 M HCl solution and stirred for 4 h at a room temperature. The green color of the solution provides an indication of the dissolution of Fe ions. After HCl treatment, the samples were poured in 1 M  $\text{HNO}_3$  solution and stirred for 30 h at  $50^\circ\text{C}$ . The yellow color of the solution provides an indication of the dissolution of boron. After both acid treatment, the solution was filtered and rinsed with deionized water until the pH of the filtrate became neutral and dried. Then, the samples were poured in pyridine to eliminate bulk BN, and high purity BN nanotubes with a cup-stacked structure were obtained by collecting supernatant.

X-ray diffraction patterns in a purification process are shown in Fig. 11a. Diffraction peaks of h-BN, boron, and a-Fe are observed for the sample annealed at  $1,000^\circ\text{C}$  for 1 h as shown in Fig. 11a. It is found that Fe was removed after HCl treatment, and boron was removed after  $\text{HNO}_3$  treatment. After pyridine treatment, a strong peak of BN was obtained.

Figure 11b, c shows TEM image of BN nanotubes with a cup-stacked structure after purification process. Diameters and lengths of the BN nanotubes are in the range of 40-100 nm and 5-10  $\mu\text{m}$ , respectively. Fe nanoparticles and bulk BN was eliminated during the process. An enlarged image of one of the BN nanotubes is shown in Fig. 11d, which shows a cup-stacked structure as indicated by lines of BN {002}. Figure 11e is an electron diffraction pattern of Fig. 11d. 002 reflections of BN are splitting in Fig. 11e, which indicates that the BN nanotube has a cup-stacked structure and the cone angle between the BN layers at both nanotube walls is  $\sim 20^\circ$ . Most of BN nanotubes ( $\sim 90\%$ ) have this cup-stacked structure with cone angle of  $\sim 20^\circ$ , and normal structures with a cone angle of  $0^\circ$  were sometimes observed ( $\sim 10\%$ ). An optical absorption spectrum of BN nanotubes is shown in Fig. 11f. In Fig. 11f, a strong peak is observed at 4.8 eV, which would correspond to the energy gap of BN nanotubes. A broad, weak peak is also observed around 3.4 eV, which is considered to be impurity level (oxygen or hydrogen) of the BN layers as reported previously [36]. Comparable data (4.5-5.8 eV) were reported for other optical measurements [120–122].

A HREM image of edge of the nanotube side wall in Fig. 11d is shown in Fig. 12a, and a cup-stacked structure was observed. Edge structures are observed as indicated by arrows, and the BN {002} planes are inclined compared to nanotube axis ( $z$ -axis). Figure 12b is a processed HREM image after Fourier filtering of nanotube center of Fig. 12a, and hexagonal arrangements of white dots are observed, which would correspond to BN six-membered rings. From these observations, a structure model for BN cup-structure was proposed, which consists only of h-BN rings, as shown in Fig. 12c, d.

In order to investigate the stability of the cup-stacked structure, four types of nanotubes are considered, as shown in Fig. 13 [123]. Atomic structure models of double-walled BN nanotubes with zigzag-type and armchair-type structures, respectively, are shown in Fig. 13a, b. Atomic structure models of four-layered, cup-stacked BN nanotubes with different cone angles are shown in Fig. 13c, d. The values of these structures were summarized as in Tables 3 and 4. Total energies of

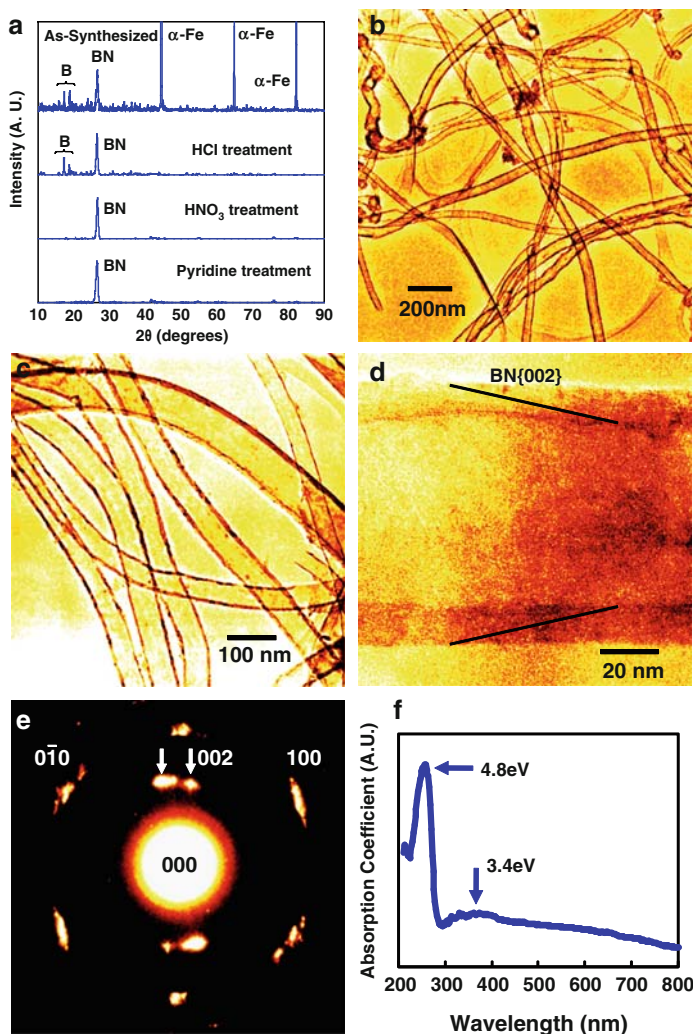


**Fig. 11** (a) X-ray diffraction patterns of samples after synthesis, HCl treatment, HNO<sub>3</sub> treatment, and pyridine treatment. (b) TEM and (c) enlarged image of the sample after pyridine treatment. (d) Enlarged image of BN nanotube with cup-stacked structure. (e) Electron diffraction pattern of (d). (f) Optical absorption spectrum of BN nanotubes

these four-type structures indicates that BN multilayered nanotubes with and without a cup-stacked structure would be stabilized by stacking h-BN networks. Distance between BN layers of nanotubes with a cup-stacked structure in a HREM image was found to be  $\sim 0.35$  nm, and the basic structure model was constructed based on this observation. Geometry optimizations at molecular mechanics level result in the interlayer distances of  $\sim 0.38$  nm. Comparing the empirical total energies of all the considered structures, a cup-stacked structure ( $B_{2240}N_{2240}$ ) with cone

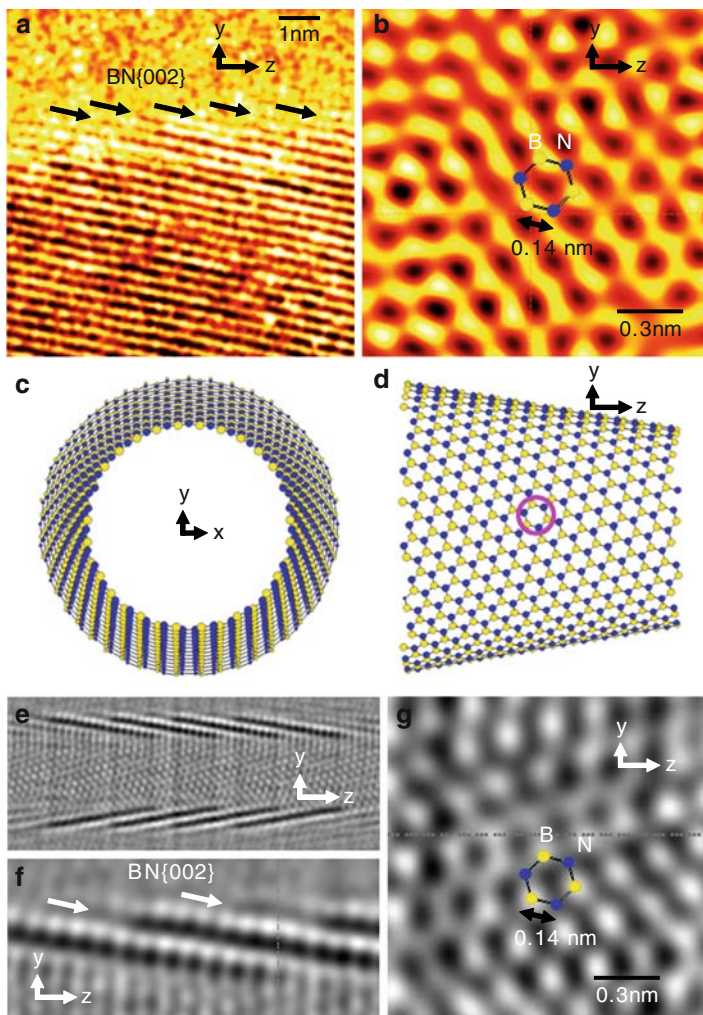


**Fig. 12** (a) HREM image of edge of the BN nanotube wall in Fig. 11d. (b) Processed HREM image after Fourier filtering of the nanotube center of Fig. 11d. Proposed model of the BN cup structure projected along (c) the  $z$ -axis (nanotube axis) and (d) the  $x$ -axis. (e) Calculated HREM image of four-layered, cup-stacked BN nanotube at defocus values of  $-40$  nm. Enlarged image of (f) edge and (g) center of BN nanotube in (e)

angle of  $20^\circ$  was found to be the lowest in energy, which indicates the high stability of this structure.

Based on the structure model of a four-layered cup-stacked  $B_{2240}N_{2240}$  nanotube, an image calculation was carried out as shown in Fig. 12e. Enlarged calculated HREM images of the edge and the center of the BN nanotube in Fig. 12e are shown in Fig. 12f, g, respectively. These calculated images agree with the experimental data of Fig. 12a, b, respectively.

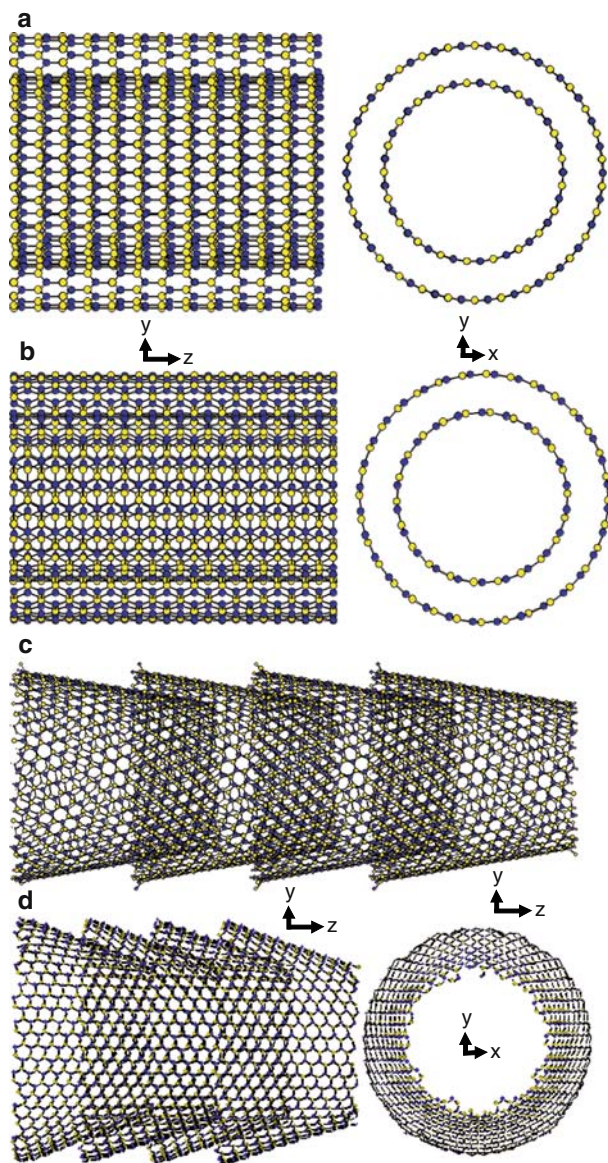


**Fig. 13** Atomic structure models of double-walled BN nanotubes with (a) zigzag-type and (b) armchair-type structures. Atomic structure models of four-layered, cup-stacked BN nanotubes with cone angles of (c) 20° and (d) 36°

Cup-stacked carbon nanotubes with Pt nanoparticles in inner surface of the hollow core had been reported [124]. The BN nanotubes with cup-stacked structures in the present work would also be one of the candidates for atomic and gas storage, as well as carbon nanotubes. Cone angles of BN cup-stacks were measured

**Table 3** Calculated values for various BN nanotubes

Structure type	Zigzag type			Armchair type		
	$B_{273}N_{273}$	$B_{390}N_{390}$	$B_{273}N_{273} @ B_{390}N_{390}$	$B_{264}N_{264}$	$B_{384}N_{384}$	$B_{264}N_{264} @ B_{384}N_{384}$
Outer diameter (nm)		2.3	2.3		2.2	2.2
Inner diameter (nm)	1.6		1.6	1.5		1.5
Number of layers	1	1	2	1	1	2
Total energy (kcal/mol)	459.2	701.5	556.0	466.6	693.2	779.3
Total energy (kcal/mol atom)	0.841	0.899	0.419	0.883	0.902	0.601

**Table 4** Calculated values for various BN nanotubes with a cup-stacked structure

	$B_{560}N_{560}$	$B_{1120}N_{1120}$	$B_{2240}N_{2240}$	$B_{494}N_{494}$	$B_{988}N_{988}$	$B_{1976}N_{1976}$
Corn angle (°)	20			36		
Outer diameter (nm)	3.4			4.2		
Inner diameter (nm)	2.4			2.4		
Number of layers	1	2	4	1	2	4
Total energy (kcal/mol)	31.456	-287.924	-936.415	895.1	1,269	2,062
Total energy (kcal/mol atom)	0.028	-0.129	-0.209	0.906	0.642	0.522

to be  $\sim 20^\circ$ , which agreed well with that of the model in Fig. 13c. Although atomic structure models for BN nanotubes with a cup-stacked structure have been proposed from HREM observation and molecular mechanics calculations [95], the cone angles were  $\sim 36^\circ$ , and they had bamboo-type structures. In the present work, there is no bamboo-type structure, which was removed during purification process, and the more stable cup-stacked structure with cone angle of  $20^\circ$  was formed.

Cone angles of carbon nanotubes with a cup-stacked structure were reported to be in the range of  $45\text{--}80^\circ$  [124]. The cause of the different cone angles of the present cup-stacked BN nanotubes would be due to the different stacking of BN layers along *c*-axis (B–N–B–N...) from carbon layers [123].

Although the network structure of carbon nanotubes has already been observed by scanning tunneling microscopy (STM), only few works on the STM observation of the hexagonal plane of BN nanotubes have been reported because of the insulating behavior. The STM image of BN nanotubes on highly oriented, pyrolytic graphite (HOPG) is shown in Fig. 14a [125]. Three BN nanotubes are observed in the image, and the smallest one is selected for enlarged observation and electronic measurements. The nanotube axis is indicated as the *z*-axis. An enlarged image of the surface of the BN nanotube is shown in Fig. 14b. The surface of the BN nanotubes is indicated by arrows. A lattice image of the BN nanotubes is observed, and an enlarged STM image of the BN nanotubes is shown in Fig. 14c. Hexagonal arrangements of dark dots are observed, which correspond to the size of the six-membered rings of BN. Current-voltage (*I*-*V*) measurements were also carried out for the BN nanotubes, as shown in Fig. 14d. The *I*-*V* curve indicates an onset

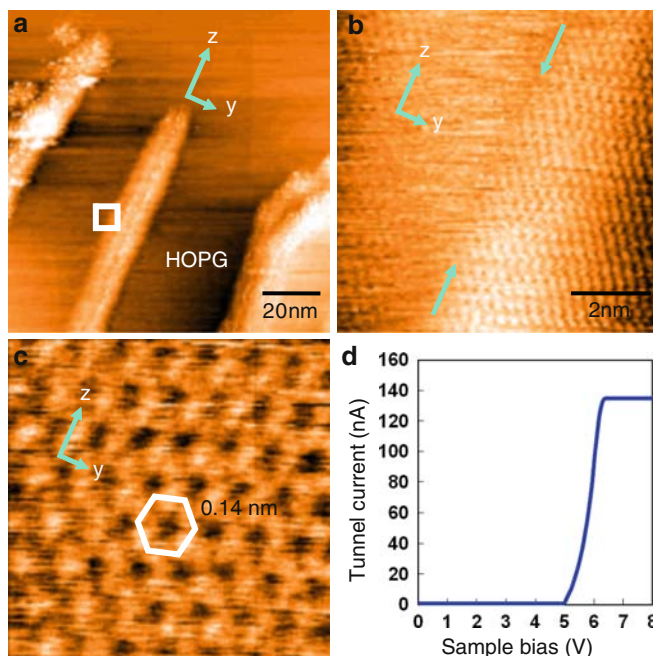


**Fig. 14** (a) STM image of BN nanotubes on HOPG. (b) Enlarged image of the surface of the BN nanotube indicated by a *square* in (a). (c) Enlarged STM image of the BN nanotube. (d) *I-V* characteristic of the single BN nanotube

voltage at 5.0 V, which agreed with optical measurement of Fig. 11f, and is almost comparable to the energy gap of BN nanomaterials [18]. Comparable data were also reported for other STM measurements [126–129].

## 5 BN Nanotubes Encaging Fe Nanowires

Figure 15a, b shows TEM and high-angle annular dark-field scanning transmission electron microscopy (HAADF-STEM) images of Fe-filled BN nanotubes (weight ratio, WR = 9:1), which were remaining sediment after centrifugation [130, 131]. Similar structures were reported in [132]. The contrast in the TEM image is weak and direct observation of Fe-filled BN nanotubes is difficult. The same area imaged by HAADF-STEM shows excellent contrast and the morphology of Fe-filled BN nanotubes can be observed in detail. A great number of Fe-filled BN nanotubes were observed by HAADF-STEM. High WR of  $\text{Fe}_4\text{N}$  would be necessary for synthesis of Fe nanowires. TEM image of one of the Fe-filled BN nanotubes is shown in Fig. 15c. Figure 15d is an EDX spectrum of the Fe-filled BN nanotube. In Fig. 15d, two peaks of boron and nitrogen are observed. This shows the atomic ratio of B:N = 46.5:53.5, which indicates the formation of BN. A strong peak of Fe (0.70 keV) is also observed, while a Cu peak arises from the HREM grid.

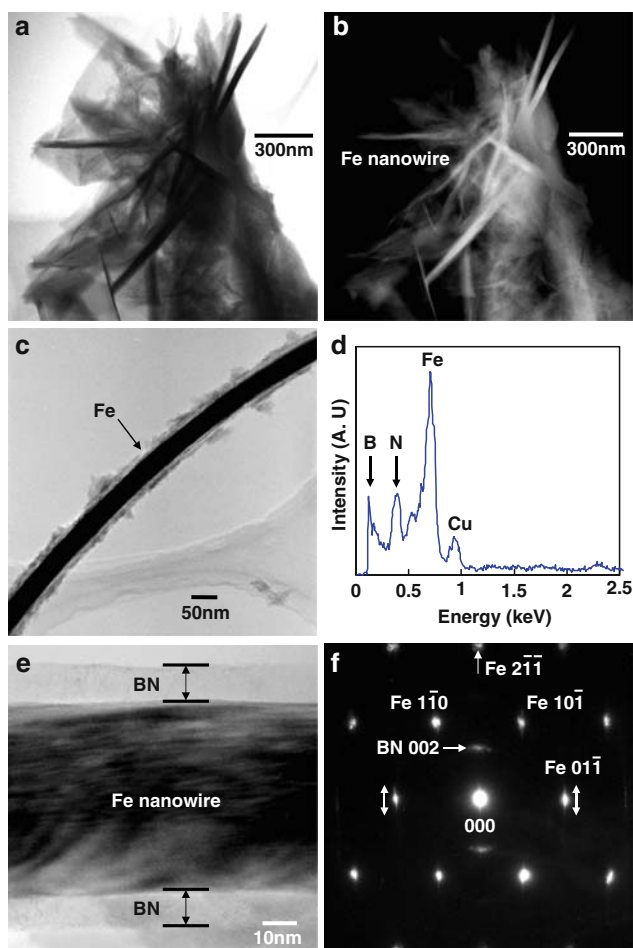


**Fig. 15** (a) TEM and (b) HAADF images of Fe-filled BN nanotubes. (c) TEM image of Fe-filled BN nanotube. (d) EDX spectrum of Fe-filled BN nanotube. (e) Enlarged image of (c). (f) Electron-diffraction pattern obtained from (e)

Figure 15e is an enlarged image of Fig. 15c. Figure 15f is an electron diffraction pattern of the Fe-filled BN nanotube. Strong peaks of BN nanotubes correspond to the planes of (002) of BN. Strong peaks are also indexed as metallic Fe with a bcc structure, and the incident beam is parallel to the [111] zone axis of  $\alpha$ -Fe.

Figure 16a is an enlarged HREM image of Fig. 15e, and Fig. 16b is filtered Fourier transform of Fig. 16a [131]. Figure 16c is inverse Fourier transform of Fig. 16b, and Fig. 16d is an enlarged image of Fig. 16c. Figure 16d shows a lattice image of the bcc Fe-filled BN nanotube. The nanotube axis is parallel to the [110] direction of Fe, which indicates the bcc Fe is epitaxially grown to the [110] zone axis. The tubular layers around the nanowire have an average interlayer spacing of 0.34 nm, which corresponds to the (002) spacing of BN.

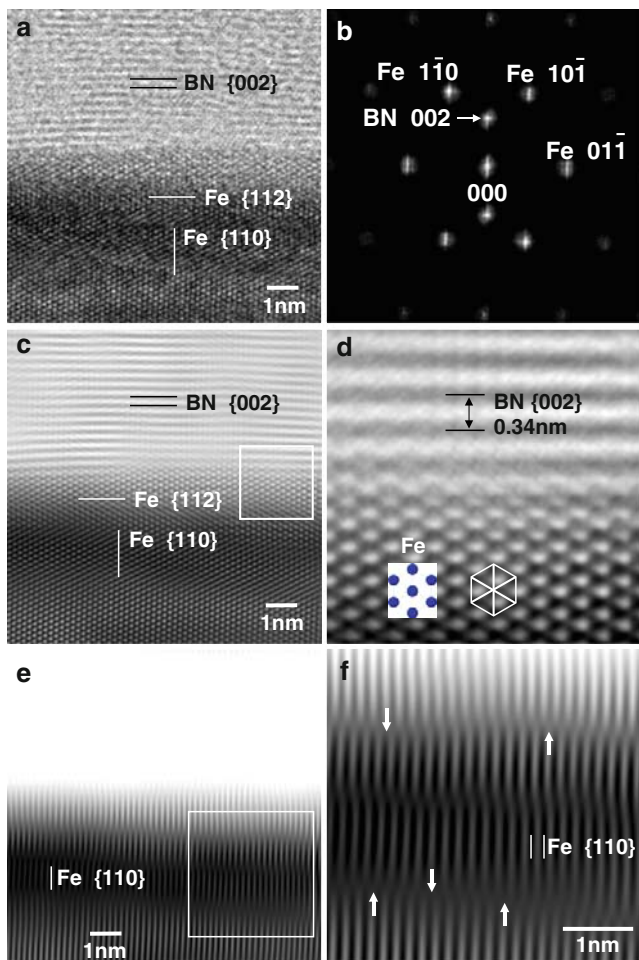
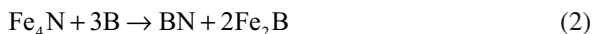


**Fig. 16** (a) HREM image of Fe-filled BN nanotube. (b) Filtered Fourier transform of (a). (c) Inverse Fourier transform of (b). (d) Enlarge image of *square* in (c). (e) Inverse Fourier transform of (b) using 000, Fe 01-1 and Fe 0-11 reflections. (f) Enlarged image of *square* in (e)

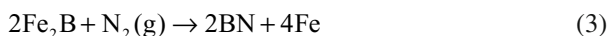
Figure 16e is inverse Fourier transform of Fig. 16b using 000, Fe (01-1 and 0-11) reflections, and Fig. 16f is an enlarged image of Fig. 16e. Several edge-on dislocations are observed as indicated by arrows, which would be due to lattice distortion produced during Fe-filled nanotube growth. This lattice distortion is also observed as expansion in the electron diffraction pattern of Fig. 16f, as indicated by arrows.

A small amount of nanocrystalline  $\text{Fe}_2\text{B}$  compounds were observed at the tip of the BN nanotubes [133]. Chemical formulas that  $\text{Fe}_4\text{N}$  reacts with B, and generates Fe and BN in the experiments can be proposed as follows:





$\text{Fe}_2\text{B}$  and dissolution of boron were obtained, and BN was produced in the reaction expressed as (2) because  $\text{Fe}_2\text{B}$  is thermodynamically more stable than  $\text{Fe}_4\text{N}$ . Although the  $\text{Fe}_2\text{B}$  is stable up to  $1,389^\circ\text{C}$ , the Gibbs-Thompson effect shows that the melting occurs at a significantly lower temperature compared to values in the standard phase diagram. Therefore, fluid-like  $\text{Fe}_2\text{B}$  can be attained more easily. In the next process, the reaction expressed as (3) would take place.



Boron in liquid-like  $\text{Fe}_2\text{B}$  started to segregate on the surface of the particle. The boron would react with  $\text{N}_2$  gas, and BN was produced.  $\alpha\text{-Fe}$  in liquid-like  $\text{Fe}_2\text{B}$  is epitaxially grown to the [110] direction, and Fe nanowires were produced in the reaction of (3). In addition, high WR would be mandatory for the formation of Fe-filled BN nanotubes. As a result of these reactions, the [110] of Fe is parallel to the BN nanotube axis.

Gibb's energy on each formula is calculated as  $-89.4$  and  $-23.2$  kcal for the formulas (2) and (3) at  $1,000^\circ\text{C}$ , respectively. These negative values would stand for correctness of the proposed formulas. It is considered that formation of Fe–B compounds might play an important role for growth of the BN nanotubes, and that amorphous boron might change to BN and  $\text{Fe}_2\text{B}$  on the surface of the  $\text{Fe}_4\text{N}$  nanoparticles.

When magnetic materials are used as catalysis metals for BN nanotube formation, the magnetic nanoparticles would move around by magnetic field of a coil heater during the reaction process. Then, segments of BN {002} layers were produced in the tubes, which results in the formation of bamboo structures. The interval of the BN layer segments might be related to the amount of iron nanoparticles, and further studies are expected on the control of the bamboo structure.

## 6 BN Nanohorns

HREM images of BN nanohorns with various tip structures, which were synthesized by an arc-melting method, are shown in Fig. 17a–e. The BN nanohorns have a hollow structure, and tip angles of BN nanohorns were  $22^\circ$ ,  $35^\circ$ ,  $60^\circ$ ,  $90^\circ$ , and  $102^\circ$ , respectively [17,21,134,135]. {002} layers of BN are clearly observed in these images. Since the distortion of apexes of BN nanohorns is very large, the structure may not be completely perfect, which results in the vague contrast at the apexes. Figure 17f is a HREM image of a BN nanohorn with an amorphous phase at the tip axis of the horn, as indicated by a star mark. As observed in the HREM images, the number of BN layers are in the range of 2–8.

EDX spectra of BN nanohorns with a hollow and an amorphous phase are shown in Fig. 18a, b, respectively. Both graphs are normalized by nitrogen peaks. Figure 18a shows boron and nitrogen peaks, and Fig. 18b shows a peak of yttrium in addition

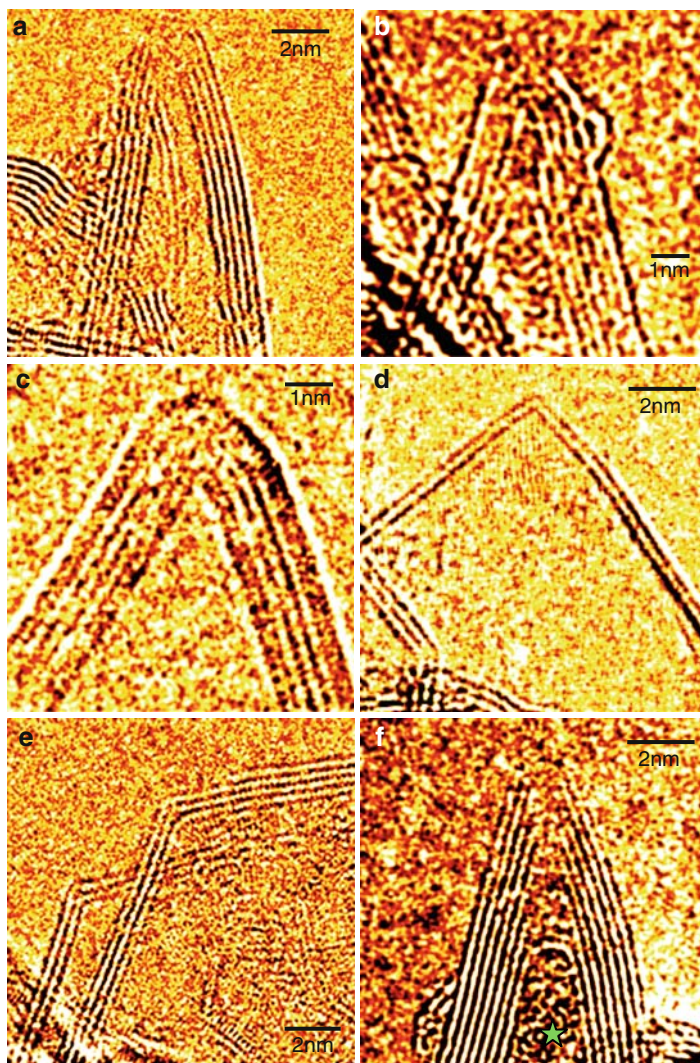


**Fig. 17** HREM images of (a–e) BN nanohorns with hollow structures and (f) BN nanohorn with amorphous phase

to peaks of boron, nitrogen, and oxygen. The composition ratio of B:N in Fig. 18a, b is calculated to be 45.8:54.2 and 49.2:50.8, respectively. Since the composition ratios of B:N in Fig. 18 are almost  $\sim 1.0$ , these B and N peaks are believed to be detected from BN layers. If the composition ratio of BN in Fig. 18b is assumed to be 1.0, composition of the amorphous phases is calculated as Y:O = 42.6:57.4, which indicates that the amorphous phase might be  $Y_2O_3$  phase. Amorphous phases observed at the root of BN nanohorns would be starting points of BN growth.

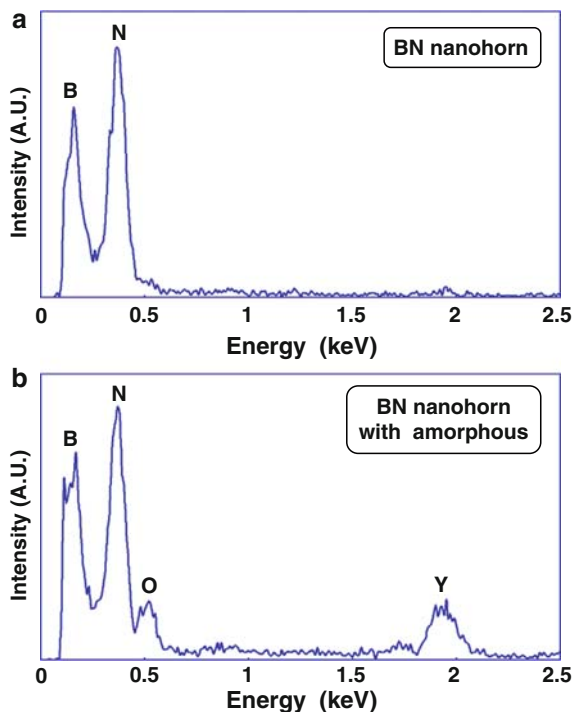


**Fig. 18** EDX spectrum of BN nanohorns with (a) a hollow structure and (b) amorphous phase

Figure 19a–e are atomic structure models of triple-walled  $B_{1638}N_{1563}$ ,  $B_{1635}N_{1635}$ ,  $B_{1671}N_{1623}$ ,  $B_{1605}N_{1605}$ , and  $B_{1608}N_{1575}$  nanohorns with tip angles of  $20^\circ$ ,  $40^\circ$ ,  $60^\circ$ ,  $84^\circ$ , and  $112^\circ$ , respectively, which agree with the HREM image in Fig. 17. Some different tip angles were also observed, which would be due to the lattice defects. Two and one tetragonal BN rings are introduced for the models in Fig. 19b,d, respectively. Since a trigonal BN ring is introduced for structure models in Fig. 19a, c, they have some B–B single bonds [21]. Pentagonal BN rings are introduced for the model of Fig. 19e, which is different from the model of Fig. 19a with trigonal BN rings. Total energies of the BN nanohorns calculated by molecular mechanics calculation are listed in Table 5. Distance between BN layers of nanohorn in HREM images were measured to be  $\sim 0.35$  nm, and the basic structure models were constructed based on them. After molecular mechanics calculation, the layer distances were optimized as  $\sim 0.37$  nm.

Figure 20a, b shows HREM images of triple- and double-walled BN nanohorns synthesized by the present method, respectively [136]. The minimum number of BN layers in nanohorns synthesized by the present work is two, which would be due to stacking stability with two elements of boron and nitrogen. Tip angles of both BN nanohorns are  $\sim 60^\circ$ . In Fig. 20b, a dark contrast is observed inside the double-walled BN nanohorn, and this would be due to the existence of a BN

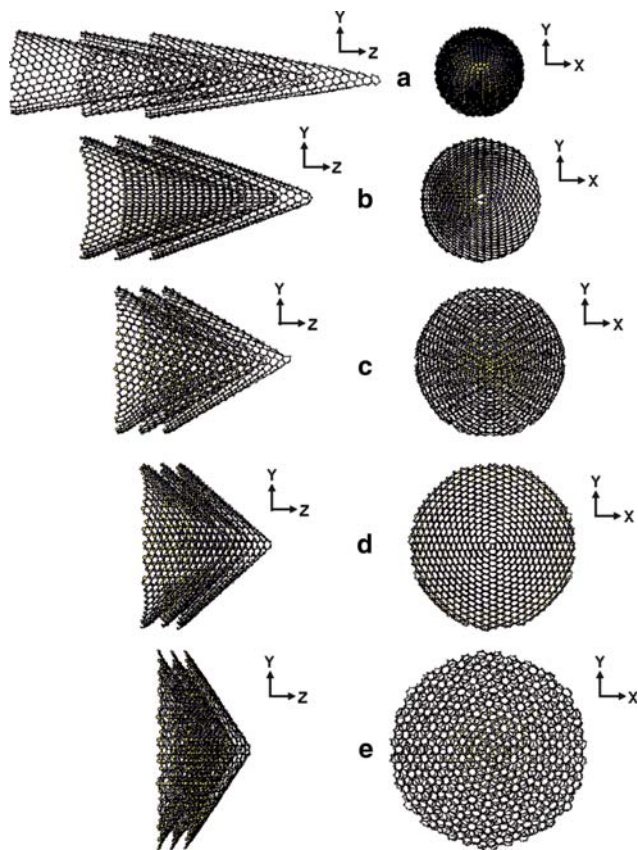


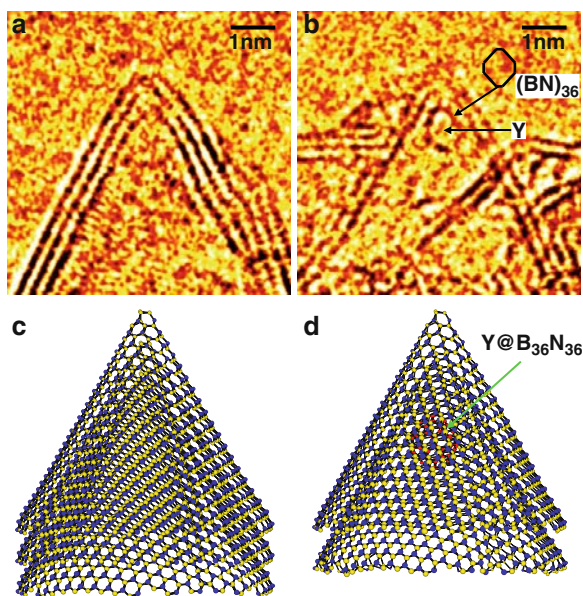
**Fig. 19** Structure models for triple-walled BN nanohorns with tip angles of (a) 20°, (b) 40°, (c) 60°, (d) 84°, and (e) 112°, respectively

cluster with metal atom. Since  $Y@B_{36}N_{36}$  clusters had already been detected by mass spectroscopy [18,39], it is believed that the dark contrast would correspond to a  $Y@B_{36}N_{36}$  cluster. Atomic structure models for triple-walled BN nanohorn ( $B_{1671}N_{1623}$ ) and double-walled BN nanohorn ( $B_{1114}N_{1082}$ ) encaging  $Y@B_{36}N_{36}$  are proposed as shown in Fig. 20c, d, respectively. Since a trigonal BN ring is introduced for a model at the top in both models, the structure models have some B–B bonds.

Energy level diagrams of BN nanohorns show narrow energy gaps between the highest occupied molecular orbital (HOMO) and the lowest unoccupied molecular (LUMO), as shown in Table 5. The energy level diagram for BN nanohorn ( $B_{24}N_{21}$ ) with a tip angle of 40° is shown in Fig. 21a. DOS of  $B_{39}N_{31}$ ,  $B_{31}N_{31}$ ,  $B_{27}N_{21}$ ,  $B_{32}N_{32}$ , and  $B_{24}N_{21}$  nanohorns were calculated, as shown in Fig. 21b–f, respectively. The HOMO-LUMO gaps of  $B_{39}N_{31}$ ,  $B_{31}N_{31}$ ,  $B_{27}N_{21}$ ,  $B_{32}N_{32}$ , and  $B_{24}N_{21}$  were calculated to be 0.29, 0.80, 0.20, 0.85, and 0.22 eV, respectively [21].

**Table 5** Total energies and energy gaps of BN nanohorns by molecular mechanics/orbital calculations

	$B_{547}N_{520}$		$B_{545}N_{545}$		$B_{557}N_{541}$		$B_{535}N_{535}$		$B_{536}N_{525}$	
Nanohorn angle	20°		40°		60°		84°		112°	
Number of layers	1	3	1	3	1	3	1	3	1	3
Total energy (kcal/mol atom)	1.03	0.64	0.98	0.47	1.08	0.53	0.99	0.38	0.03	-0.44
Energy gap (eV)	0.29 ( $B_{39}N_{31}$ )		0.80 ( $B_{31}N_{31}$ )		0.20 ( $B_{27}N_{21}$ )		0.85 ( $B_{32}N_{32}$ )		0.22 ( $B_{24}N_{21}$ )	

**Fig. 20** HREM images of (a) triple-walled BN nanohorn with tip angle of 60° and (b) double-walled BN nanohorn including  $Y@B_{36}N_{36}$ . Atomic structure models for (a) triple-walled BN nanohorn ( $B_{1671}N_{1623}$ ) and (b) double-walled BN nanohorn ( $B_{1114}N_{1082}$ ) encaging  $Y@B_{36}N_{36}$ 

Energy gaps calculated based on the atomic structure models show lower values (0.2-0.85 eV) compared to those of BN nanotubes or BN fullerenes (~6 eV). The low energy gaps would be due to trigonal and pentagonal BN rings and nanohorn structures. The bandgaps of BN nanohorns were reduced, and various new applicable fields are expected by combining the BN nanohorns with BN nanotubes or BN fullerenes. Total energies of BN nanohorns were reduced by stacking of BN nanohorns, and it is believed that the structure of BN multiwalled nanohorns would be stabilized by multiplying h-BN ring networks.

BN nanohorns with various tip angles were synthesized by the present arc-melting method. The total energy of BN nanohorns with tip angles of 84° is

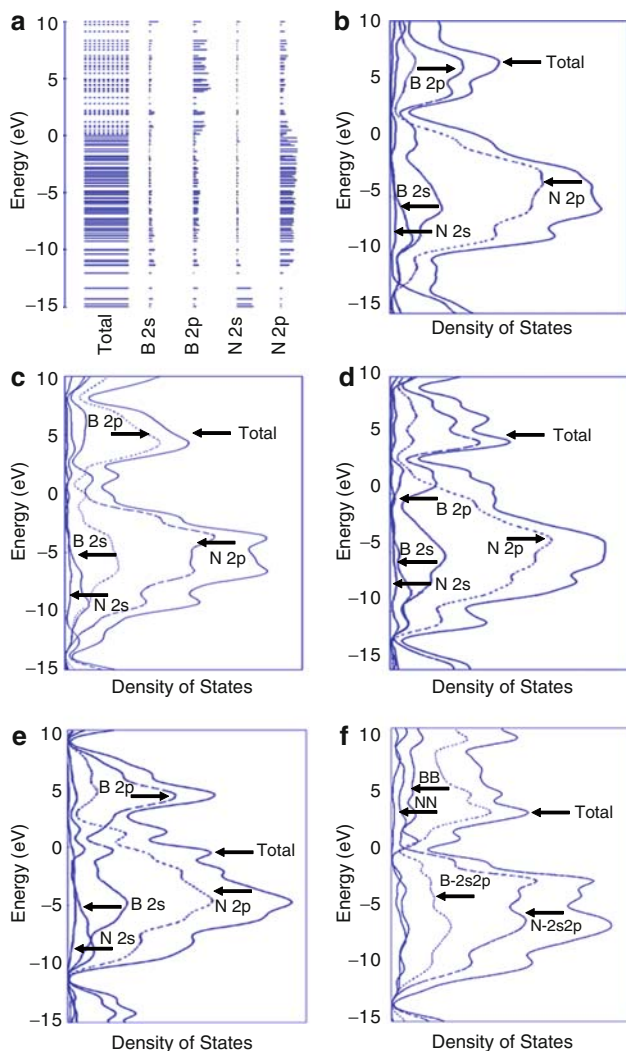


**Fig. 21** (a) Energy level diagram for BN nanohorn with tip angle of  $40^\circ$ . Density of states for BN nanohorns with tip angles of (b)  $20^\circ$ , (c)  $40^\circ$ , (d)  $60^\circ$ , (e)  $84^\circ$ , and (f)  $112^\circ$ , respectively

fairly low in the present work as listed in Table 5, which agree well with the experimental observation. The lowest total energy of BN nanohorns with tip angles of  $112^\circ$  would be strongly related with the nanoparticle growth of this structure up to 300 nm [29], as described in Sect. 7.

In the present work, yttrium worked as a good catalytic element to produce BN nanotubes. Catalytic metals for the formation of BN nanotubes, nanocapsules, and nanocages, which were confirmed by experiments on arc method, are summarized in Fig. 22a as periodic table. It has been reported that Zr, Hf, Ta, W, Nb, and La can be good catalytic metals for synthesis of BN nanotubes [2–13, 95]. On the other

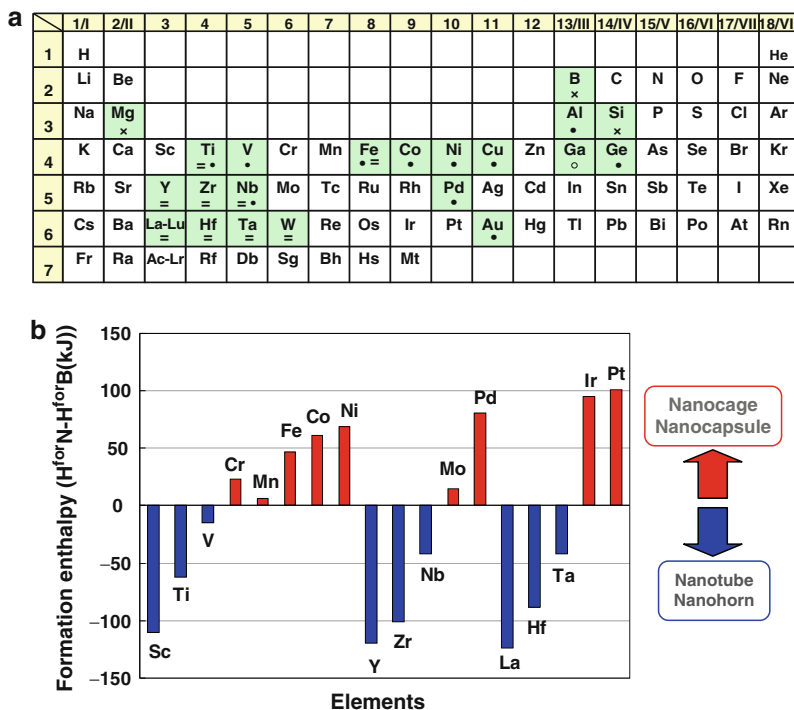


**Fig. 22** (a) Catalysis metals for BN fullerene nanomaterials confirmed by experiments on arc method (*equals*, BN nanotube; *filled circle*, BN nanocapsule; *open circle*, BN nanocage; *cross*, non BN fullerene nanomaterials). (b) Difference formation enthalpy ( $H^{\text{forN}} - H^{\text{forB}}$ ) of nitrides and borides

hand, other metals could not form BN nanotubes, although BN nanocapsules or nanocages were formed. The relationship between catalytic metals and structures of BN fullerene materials would be summarized by formation enthalpy with nitrogen and boron. About some metals, formation enthalpies with boron ( $H^{\text{forB}}$ ) and nitrogen ( $H^{\text{forN}}$ ) were theoretically calculated [95]. Difference of formation enthalpy ( $H^{\text{forN}} - H^{\text{forB}}$ ) is also shown in Fig. 22b. From our previous results [18,95], BN nanotubes and BN nanocapsules (or nanocages) were formed when  $H^{\text{forN}} - H^{\text{forB}}$  was negative and positive, respectively. From Fig. 22b, BN nanotubes are formed when rare earth metals are used as catalytic metals. Y, Zr, Nb, La, Hf, Ta, Sc, Ti, and V, would work as good catalytic elements, which agreed well with the experimental results.

In the case of  $YB_6$ /Ni powder, the yttrium and nickel worked as good catalytic elements to produce bundled BN nanotubes. From the results of only  $YB_6$  powder, yttrium atoms would work as core element to produce BN nanotubes, and Ni atoms would have a role for combination of each BN nanotube. Therefore, existence of nickel atoms would have an effect on formation of bundled BN nanotubes, and the

nickel atoms might exist among BN nanotubes. Further studies will be needed to understand the role of nickel atoms in bundled BN nanotubes.

## 7 BN Nanoparticles

Chemically vapor deposited boron nitride (CVD-BN) nanoparticles were synthesized from  $B_3N_3H_6$  and  $BCl_3-NH_3-H_2$  gas systems at temperatures of 1,400-2,000°C and total gas pressures of 0.2-30 Torr on graphite substrates [137,138]. A scanning electron microscopy (SEM) image of the CVD-BN nanoparticles, synthesized from a  $BCl_3-NH_3-H_2$  gas system at deposition temperatures 2,000°C, is shown in Fig. 23a, which shows a surface structure of pyramidal pentagonal facets [29]. The twin boundaries are indicated by solid lines, and the *c*-direction of the h-BN is indicated by arrows.

TEM images of CVD-BN nanoparticles, synthesized from a  $BCl_3-NH_3-H_2$  gas system at deposition temperatures of 2,000°C and 1,800°C and synthesized from  $B_3N_3H_6$  gas at 2,000°C, are shown in Fig. 23b-d, respectively [139]. In Fig. 23b-d, a number of particles are visible with the structures of pentagons, stars, and maple leaf shapes, respectively. It should be noted that only those particles which satisfy certain diffraction conditions are visible in the images. A considerable number of particles are contained in the samples, as confirmed by tilting. An electron diffraction pattern of Fig. 23b is shown in Fig. 23e. The electron diffraction pattern was taken from a wide area (1 mm) and shows many diffraction spots attributed to the nanocrystalline particles and also the Debye-Scherrer rings from the turbostratic-BN (t-BN) matrix. The rings are indexed as 002, 100, 102, 110, and 112 of h-BN [31].

An enlarged image of BN nanoparticles in Fig. 23c is shown in Fig. 24a. Five twin boundaries are observed in the particle, and the strain contrast results from some defects in the particles. Figure 24b is a filtered HREM image of the center of the BN nanoparticle. Twin boundaries are indicated by arrows. In the image, two-dimensional lattice fringes are visible with separations of 0.18 and 0.22 nm, which correspond to the lattice spacings of {102} and {100}, respectively. The image clearly shows that the five parts have twin relations at their boundaries. The center of the fivefold axis indicates some distortion.

Figure 24c is an electron diffraction pattern of the fivefold multiply twinned h-BN in Fig. 23b. All diffraction spots in the pattern in Fig. 24c can be interpreted by the superposition of five twin-related electron diffraction patterns. A selected area electron diffraction pattern of one of the five parts can be indexed by the h-BN structure with lattice constants as 0.25044 nm and  $c = 0.66562$  nm [140]. The twin boundaries are {112}, and the fivefold axis (equal to incident beam direction) is [2 0 -1].

A projection of the atomic arrangement of the fivefold multiply twinned h-BN nanoparticle is illustrated schematically in Fig. 24d, where open circles correspond to rows of an alternate sequence of boron and nitrogen atoms lying parallel to the



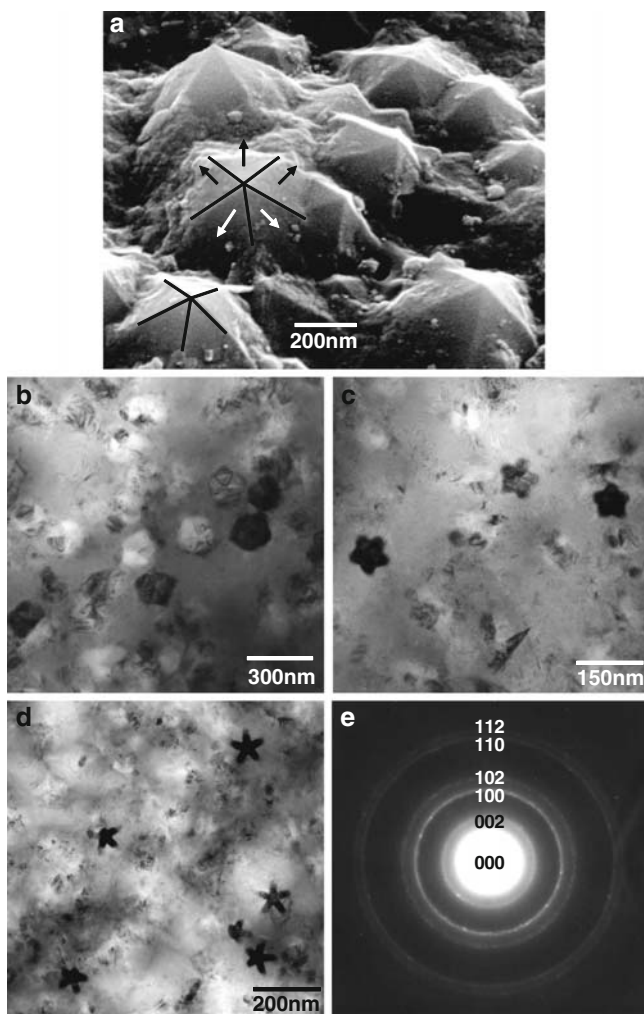


**Fig. 23** (a) SEM image of BN nanoparticles. TEM images of CVD-BN nanoparticles, synthesized from a  $\text{BCl}_3\text{-NH}_3\text{-H}_2$  gas system at deposition temperatures of (b)  $2,000^\circ\text{C}$  and (c)  $1,800^\circ\text{C}$ , and synthesized from (d)  $\text{B}_3\text{N}_3\text{H}_6$  gas at  $2,000^\circ\text{C}$ . (e) Electron diffraction pattern of (b)

fivefold symmetry axis  $[2\ 0\ -1]$ . The twin planes  $\{112\}$  are indicated by broken lines, and the h-BN cell is shown by solid lines. The fivefold axis, normal to the figure at the star mark, is tilted  $37^\circ$  from the  $c$ -axis of the hexagonal cells. Taking account of the lattice parameters of h-BN [140], the misfit of the multiply twinned h-BN particle is 1.68, which is much smaller than the  $7^\circ 20'$  of multiply twinned fcc nanoparticles. This small amount of misfit allows the growth of relatively large sized particles with little inner distortion. The atomic cluster at the center of the particle consists of  $\text{B}_{24}\text{N}_{21}$ , and the structure was optimized by molecular orbital calculation, to give a calculative total energy of  $-11.8$  kcal mol [141]. BN clusters such as  $\text{B}_{24}\text{N}_{24}$  and  $\text{B}_{36}\text{N}_{36}$  have been reported to have cage structures [39]. However,

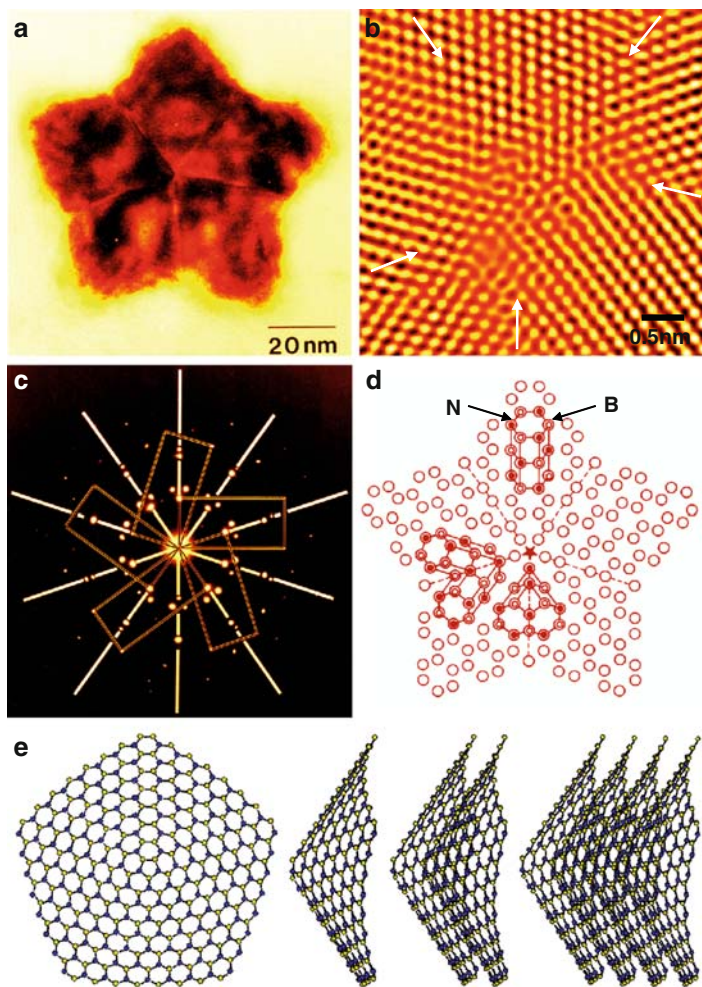


**Fig. 24** (a) TEM image of BN nanoparticle. (b) Filtered HREM image of the center of the BN nanoparticle. (c) Electron diffraction pattern of the BN nanoparticle. (d) Atomic structure model. (e) Atomic structure models of  $B_{164}N_{156}$ ,  $B_{328}N_{312}$ , and  $B_{656}N_{624}$

the BN nanoparticles have a layered structure with fivefold symmetry. The heat of formation of  $B_{24}N_{24}$  cluster was calculated to be 17.3 kcal/mol atom, which is a little smaller than that of the present  $B_{24}N_{21}$  cluster with fivefold symmetry. This result may indicate that the growth kinetics cause a change in the structure of BN clusters into decagonal shapes from octahedral shapes during cluster growth.

Atomic structure models of  $B_{164}N_{156}$ ,  $B_{328}N_{312}$ , and  $B_{656}N_{624}$  clusters with stacking structures are shown in Fig. 24e. Total energies per atom-mol of BN clusters were reduced by stacking of BN layers, and it is believed that the electrons below and above h-BN networks would have a role of van der Waals bonding between stacking layers, and the structure of BN nanoparticles with fivefold symmetry would be stabilized by multiplying h-BN ring networks.

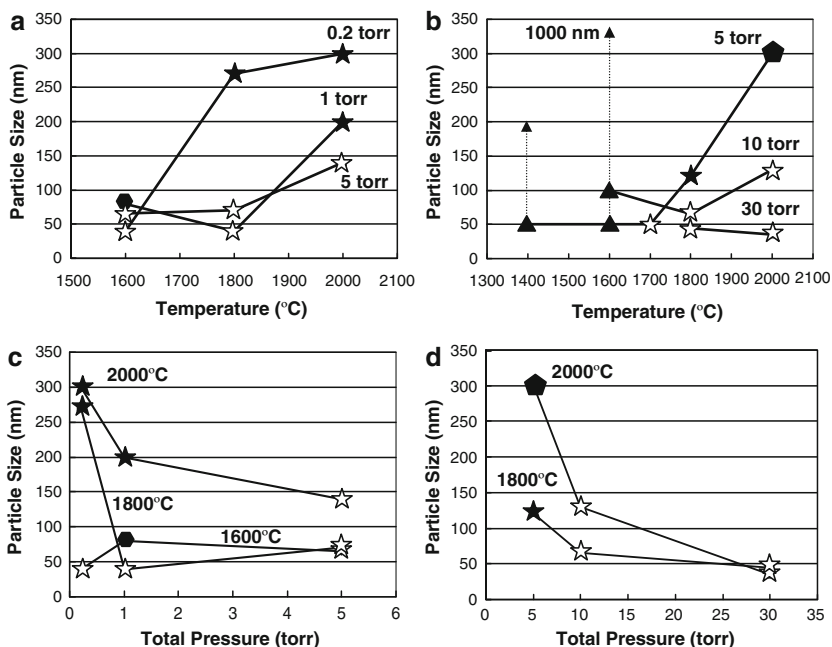


**Fig. 25** (a, b) Particle sizes in CVD-BN synthesized from  $B_3N_3H_6$  and  $BCl_3-NH_3-H_2$  gas systems, respectively, as a function of deposition temperatures. (c, d) Particle sizes in CVD-BN synthesized from  $B_3N_3H_6$  system and  $BCl_3-NH_3-H_2$  gas systems, respectively, as a function of total gas pressures. *Filled circle*, pentagonal particle; *filled star*, star-shaped particle; *open star*, a few star-shaped particle; *filled triangle*, rhombohedral-BN; *filled square*, hexagonal-BN

The particle size dependences on deposition temperature for CVD-BN synthesized from the  $B_3N_3H_6$  and  $BCl_3-NH_3-H_2$  gas system are shown in Fig. 25a, b, respectively [139]. The sizes for both systems increase as the deposition temperature increases. Figure 25c, d shows the particle size dependences on the total gas pressures for CVD-BN synthesized from the  $B_3N_3H_6$  and  $BCl_3-NH_3-H_2$  gas systems, respectively. The particle sizes for both systems decrease as the total gas pressure increases. It is believed that high temperature and low gas pressure are effective for the formation of fivefold BN nanoparticles, which would be due to the growth rate of h-BN on the graphite substrates. Thermodynamic calculations of the Gibbs free energies for BN synthesis at 2,000°C are as follows:  $B_3N_3H_6(g) = 3BN + 3H_2(g) - 152$  (kcal);  $BCl_3(g) + NH_3(g) = BN + 3HCl(g) - 72$  (kcal).

## 8 BN Nanocapsules

Nanosized particles have been extensively studied not only for their fundamental interests but also for their unique magnetic and electronic transport properties, and they have many potential for the future applications [142, 143]. Especially,

metal nanoparticles of Fe, Co, and some Fe-based alloys have an advantage of showing high magnetization. However, oxidation- and wear-resistances of the surface are weak points of these nanoparticles. In addition, most of the magnetic materials are accompanied by exothermic heat due to an eddy current loss in high frequency. As a solution, it is well known that increasing of the resistance by using insulators is good.

BN nanomaterials provide excellent protection against oxidation and wear, and its electrical conductance is insulator ( $\sim 5$  eV). Therefore, magnetic nanoparticles coated with BN layers would have significant advantages for technological applications. Fe and Co nanocapsules coated with BN layers have been synthesized by an arc-discharge and thermal annealing method [37, 24, 144]. However, the arc-discharge method is not suitable for mass production because of the limitation of the plasma area, and it is difficult to control the particle size and the number of BN layers. Fe nanocapsules coated with BN layers have been synthesized by annealing of boron and  $\alpha$ -Fe<sub>2</sub>O<sub>3</sub> powders [45, 145]. Since they contained oxygen in the starting materials, a high annealing temperature was needed to remove the oxygen. Hu et al. also reported that nanocrystalline boron nitride had been synthesized with a whisker-like morphology by a reaction of KBH<sub>4</sub> and NH<sub>4</sub>Cl at a temperature of 650°C and a pressure of about 22 MPa [146]. This synthesis method does not contain oxides in the starting materials.

The purpose is to synthesize magnetic nanoparticles coated with BN layers, and to investigate the nanostructures and magnetic properties. An Ellingham diagram of nitride metals for N<sub>2</sub> gas per mol was calculated by HSC software as shown in Fig. 26. Fe<sub>4</sub>N particles would be reduced to  $\alpha$ -Fe completely by annealing with boron, because boron reacted with nitrogen more easily compared to Fe. Similarly, several nitrides would be reduced to pure metals by reaction with boron. In the present work, Fe and Co were selected for the magnetic nanoparticles, and mixture powders of Fe<sub>4</sub>N/B and Co(NH<sub>3</sub>)<sub>6</sub>Cl<sub>3</sub>/KBH<sub>4</sub> were used for the synthesis, respectively [119].

X-ray diffraction patterns of annealed samples of Fe<sub>4</sub>N/B with various WR of Fe<sub>4</sub>N:B annealed at 1,000°C are shown in Fig. 27a. Peaks of h-BN and  $\alpha$ -Fe were confirmed for all samples, and no peak of Fe<sub>4</sub>N and B was observed. Average diameters of Fe particles are summarized in Table 6, which were calculated from half-widths of  $\alpha$ -Fe (110) by using the Scherrer equation. The sizes of Fe nanoparticles are below  $\sim 30$  nm.

Figure 27b shows X-ray diffraction patterns of Co(NH<sub>3</sub>)<sub>6</sub>Cl<sub>3</sub>/KBH<sub>4</sub> samples annealed at 700–1,000°C for 2 h. Although BN nanocapsules were formed, boron did not react with nitrogen perfectly yet for a sample annealed at 700°C. Diffraction peaks of h-BN and fcc-cobalt were confirmed for samples annealed at 1,000°C. Average particle sizes were calculated from half-widths of fcc-Co (111) by using Scherrer equation as listed in Table 7. The particle size depends on annealing temperatures rather than a flowing rate of N<sub>2</sub> gas.

Figure 28a is a TEM image of Fe nanocapsules coated with BN layers produced by annealing a powder of Fe<sub>4</sub>N/B (1:1) at 1,000°C for 1 h. Bamboo-type BN nanotubes with interval cells of 30 nm were also produced by annealing the mixture at

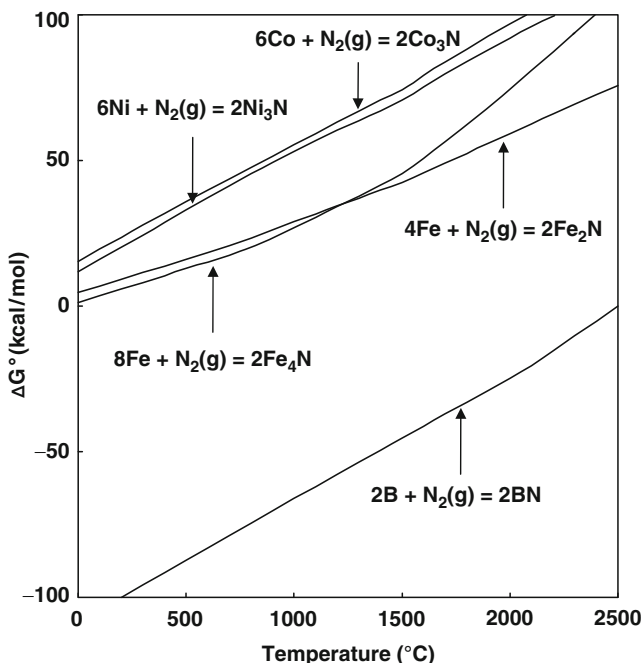


**Fig. 26** Ellingham diagram of Fe, Ni, and Co nitrides for a  $N_2$  molecule

1,000°C for 5 h as shown in Fig. 28b. Length and width of bamboo-type BN nanotubes are approximately 10  $\mu$ m and 40 nm, respectively. Fe nanoparticles were often observed at tips of bamboo-type BN nanotubes. Figure 28c shows a TEM image of fcc-Co nanoparticles coated with BN layers produced by annealing a mixture powder of  $Co(NH_3)_6Cl_3/KBH_4$  at 1,000°C for 2 h with flowing 100 sccm  $N_2$  gas. An enlarged image of BN nanocapsules encaging fcc-Co nanoparticles is shown in Fig. 28d. Numbers of BN layers covering fcc-Co nanoparticles are in the range of 15–30 layers, and they increased more compared to sample annealed at 700°C (5–10 layers).

A magnetic hysteresis loop of BN nanocapsules encaging Fe nanoparticles is shown in Fig. 29a, which was produced from  $Fe_4N/B$  (9:1) sample annealed at 1,000°C for 1 h with flowing 100 sccm  $N_2$  gas. The sample exhibits a soft magnetic characteristic, and saturation magnetization ( $M_s$ ) and coercivity values ( $H_c$ ) were 174.9 emu/g and 19.0 Oe, and the  $M_s$  and  $H_c$  values are 80% and 88% of bulk Fe (217.6 emu/g and 21.5 Oe), respectively. Results of VSM measurements are summarized in Table 6. Fe powders with only oxidized surface gives  $M_s$  value of 130 emu/g, and  $M_s$  value of magnetite ( $Fe_3O_4$ ) is 92 emu/g. For the present Fe nanoparticles coated with BN layers, the  $M_s$  values were reduced due to the weight loss of BN layers, and are as high as pure Fe metal.

Figure 29b is a magnetic hysteresis loop of BN nanocapsules encaging Co nanoparticles synthesized at 1,000°C with flowing 100 sccm  $N_2$  gas for 2 h.  $M_s$  and  $H_c$

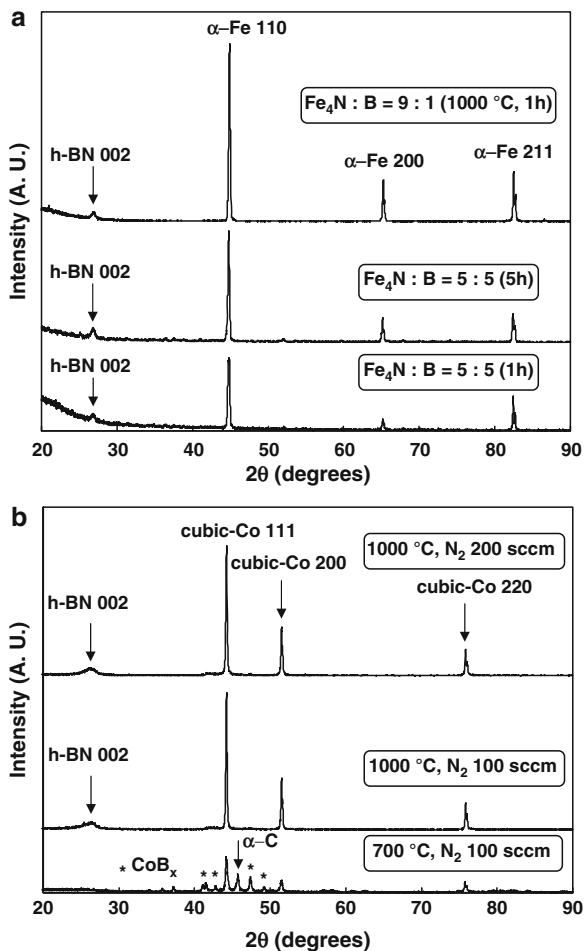


**Fig. 27** X-ray diffraction patterns of (a)  $\text{Fe}_4\text{N}/\text{B}$  samples annealed at  $1,000^\circ\text{C}$  and (b)  $\text{Co}(\text{NH}_3)_6\text{Cl}_3/\text{KBH}_4$  samples annealed at  $700$ – $1,000^\circ\text{C}$  for 2 h

**Table 6** Average diameters of Fe nanoparticles, and results of VSM measurements of Fe nanoparticles coated with BN layers at room temperature

Composition of $\text{Fe}_4\text{N}:\text{B}$	Annealing time at $1000^\circ\text{C}$	Particle diameter (nm)	$M_s$ (emu/g)	$H_c$ (Oe)	$M_s^*$ (emu/g)	$H_c^*$ (Oe)	Degauss coefficient (%)
5:5	1 h	24	95.0	24.4	78.3	42.5	-17.6
5:5	5 h	28	92.6	22.5	78.9	39.8	-14.8
7:3	1 h	-	134.2	20.9	117.4	33.8	-12.5
9:1	1 h	30	174.9	19.0	149.9	37.5	-14.3

Saturation magnetization ( $M_s^*$ ) and coercivity ( $H_c^*$ ) values of Fe nanoparticles coated with BN layers were measured after PC tests ( $120^\circ\text{C} \times 12$  h, humidity 100%, 1 atm.). Values of Degauss coefficient were calculated according to the following equation:  $(M_s^* - M_s)/M_s \times 100\%$

**Table 7** Average diameters of Co nanoparticles, and VSM measurement of Co@BN cage nano-materials at room temperature

Temperature (°C)	Flow rate (sccm)	Particle diameter (nm)			$M_s^*$ (emu/g)	$H_c^*$ (Oe)	Degauss coefficient (%)
			$M_s$ (emu/g)	$H_c$ (Oe)			
700	100	27	48.6	342.9	22.1	396.1	-54.6
1000	100	40	74.5	88.0	54.0	106.9	-27.5
1000	200	37	72.3	134.1	61.7	143.2	-14.7

$M_s^*$  and  $H_c^*$  after PC tests. Values of Degauss coefficient were calculated according to the following equation:  $(M_s^* - M_s)/M_s \times 100\%$

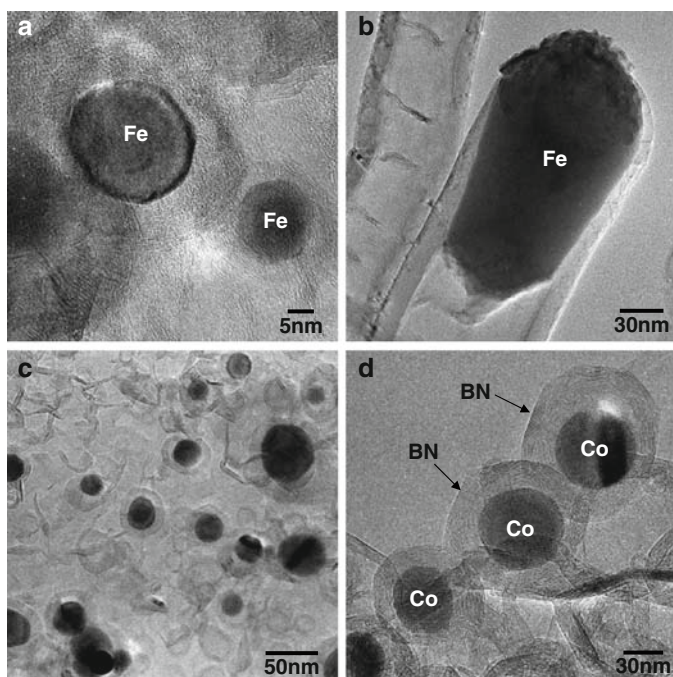


**Fig. 28** TEM images of (a) Fe nanocapsules coated with BN layers, (b) bamboo-type BN nanotubes with Fe nanoparticles, (c) BN nanocapsules encaging fcc-Co nanoparticles, and (d) enlarged image of the BN nanocapsules with Co

values of the sample were 74.5 emu/g and 88 Oe, respectively, as summarized in Table 7.  $M_s$  values of samples annealed at 1,000°C are larger than that of 700°C. On the other hand,  $H_c$  values decreased at elevated temperatures, which would be due to an effect of particle size. Herzer showed that  $H_c$  of soft magnetic metal particles depended on the particle size, and that the  $M_s$  values were inversely proportional to variance of the  $H_c$  values. Therefore, decrease of the  $H_c$  values of the present samples annealed at 1,000°C would be due to large particle sizes.

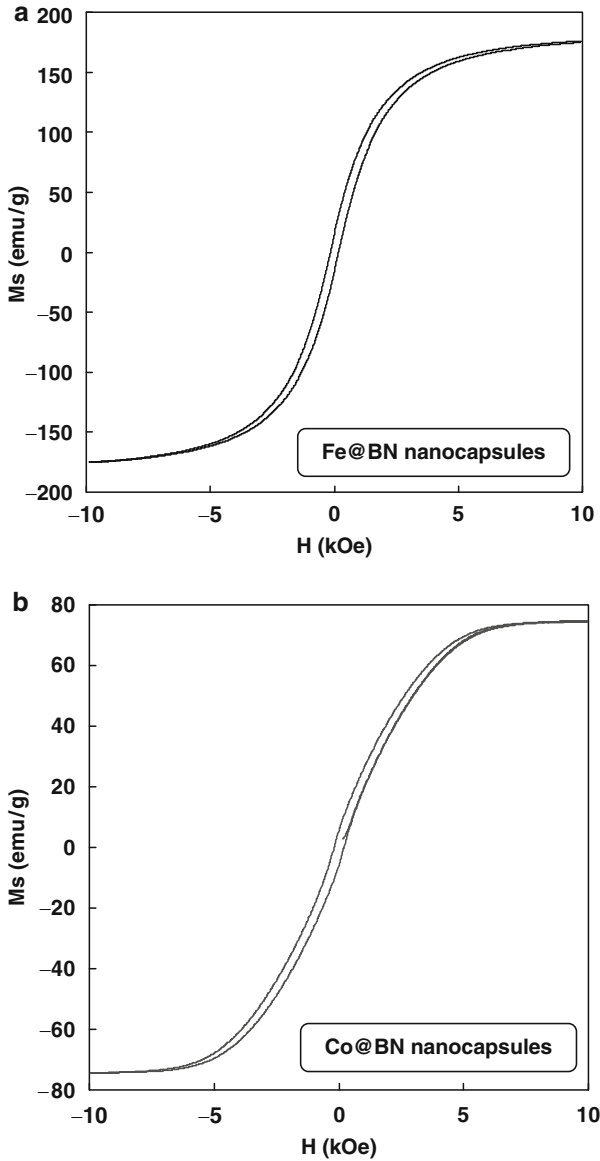


**Fig. 29** Hysteresis loops of BN nanocapsules encaging (a) Fe and (b) Co nanoparticles

In order to investigate oxidation- and wear-resistances,  $M_s^*$  and  $H_c^*$  values of samples were measured by VSM after PCT, and the results are summarized in Tables 6 and 7. Values of Degauss coefficient were calculated according to the following equation:  $(M_s^* - M_s)/M_s \times 100\%$ . A sample of  $Fe_4N/B$  (7:3) was more



stable for oxidation- and wear-resistances than other samples for the BN nanocapsules encaging Fe nanoparticles. Although  $M_s$  value increased as increase of  $\text{Fe}_4\text{N}$  powder in the composition, appropriate amount of B powder is needed to keep the  $M_s$  value high for oxidation- and wear-resistances by covering the Fe nanoparticles with BN layers. BN nanocapsules with Co nanoparticles synthesized at  $1,000^\circ\text{C}$  were more stable than that of  $700^\circ\text{C}$ , which would be due to that strong connection of boron and nitrogen atoms for the samples annealed at  $1,000^\circ\text{C}$ .

## 9 Hydrogen Storage in BN and C Clusters

Many works have been reported on hydrogen storage ability of carbon (C) nanotubes, fullerenes, and nanomaterials, as 1–4 wt%. These results indicate the excellent storage ability of carbon nanotubes although the evaluation of hydrogen storage measurements is necessary. Recently, several studies on  $\text{H}_2$  gas storage of 1–4 wt % in boron nitride (BN) nanomaterials have also been reported [147]. BN nanomaterials are expected in prospective application because BN nanomaterials provide good stability at high temperatures with high electronic insulation in air. In the present work,  $\text{H}_2$  gas storage ability was investigated for C/BN fullerene-like materials by theoretical calculations. Although huge amount of calculation is required to calculate nanotubes, it is considered that  $\text{H}_2$  molecules enter from the cap of nanotubes. Barrier energy of ring structures, energy of chemisorption, and stable hydrogen position inside the clusters were investigated in the minimum structure of nanotubes. Theoretical calculations for structural stability of the clusters and hydrogen storage were carried out by molecular orbital calculations (Hamiltonian: Parameterized Model Revision 5) and Gaussian 98.

$\text{C}_{60}$ ,  $\text{B}_{24}\text{N}_{24}$ , and  $\text{B}_{36}\text{N}_{36}$  clusters have energy barriers for  $\text{H}_2$  molecules to pass through 4-, 5-, 6-, and 8-membered rings. Figure 30a is a structural model of a  $\text{H}_2$  molecule passing from the hexagonal rings of clusters. Single point energies for  $\text{C}_{60}$ ,  $\text{B}_{24}\text{N}_{24}$ , and  $\text{B}_{36}\text{N}_{36}$  clusters were calculated [147]. When  $\text{H}_2$  molecules are set at the center and outside of the cage, the single point energy is equal.  $E$  is regarded as the energy barrier for  $\text{H}_2$  molecules to pass through 4-, 5-, 6-, and 8-membered rings.  $E$  of  $\text{B}_{24}\text{N}_{24}$  octagonal rings showed the smallest value in the present calculation. This result was reached because the octagonal rings of  $\text{B}_{24}\text{N}_{24}$  have a large curvature and ring size. Since single point energy is equal when  $\text{H}_2$  molecules are set at the center and outside of the cage, the energy for  $\text{H}_2$  discharge from fullerene-like materials is similar to that of  $\text{H}_2$  storage.

Energies for hydrogen chemisorption on each position are summarized in Table 8. Figure 30b is the schematic illustration for hydrogen chemisorption on  $\text{B}_{36}\text{N}_{36}$ . Hydrogen bonding with nitrogen is more stable than that with boron. In addition, hydrogen bonding on tetragonal ring is more stable than that of hexagonal ring. Chemisorption of hydrogen with  $\text{C}_{60}$  reduced the energy. When two hydrogen atoms were chemisorbed on carbon clusters, energies of carbon clusters increased.

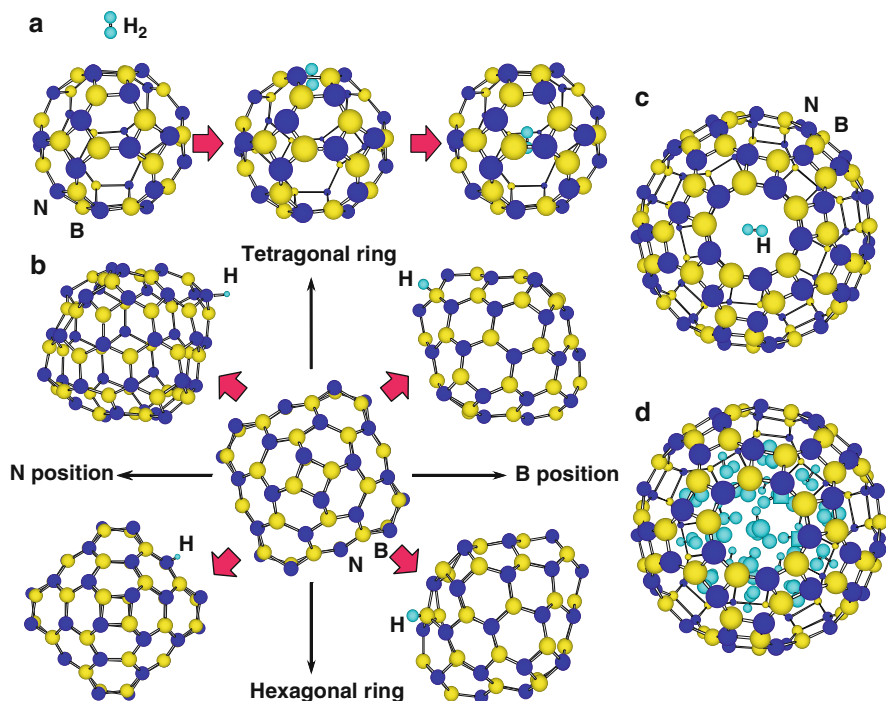


**Fig. 30** (a) Structural model of  $H_2$  molecule passing from a hexagonal ring of  $B_{24}N_{24}$ . (b) Structure models for hydrogen chemisorption on  $B_{36}N_{36}$ . Optimized structural models of (c) one and (d)  $38H_2$  molecules in  $B_{60}N_{60}$  clusters

**Table 8** Chemisorption energy of hydrogen atoms on  $C_{60}$  and  $B_{24}N_{24}$

		Heat of formation [eV/mol-atom]				$^a\Delta E$ (eV/mol-atom)				
		Before addition	Additional position of hydrogen							
			C		B	N	C		B	N
			H	2H			H	2H		
$C_{60}$		35.21	35.03	35.81			-0.18	0.60		
$B_{24}N_{24}$		-36.12			-34.66	-35.67			1.46	0.45
$B_{36}N_{36}$	Tetragon	-69.33			-67.83	-69.16			1.50	0.17
	Hexagon				-67.51	-68.83			1.83	0.51

$^a\Delta E = (\text{Heat of formation after hydrogen addition}) - (\text{Heat of formation before hydrogen addition})$

To investigate the stability of a  $H_2$  molecule in clusters, energies were calculated for a  $H_2$  molecule introduced inside the clusters. One of the structural models for  $B_{60}N_{60}$  is shown in Fig. 30c. Energies of  $C_{60}$ ,  $B_{24}N_{24}$ ,  $B_{36}N_{36}$ , and  $B_{60}N_{60}$  clusters with a  $H_2$  molecule were calculated to be 0.58, -0.71, -0.93, and -0.82 eV/mol atom, respectively. This result indicates that  $B_{24}N_{24}$ ,  $B_{36}N_{36}$ , and  $B_{60}N_{60}$  with a  $H_2$  molecule are more stable than  $C_{60}$  with  $H_2$  molecule, and that  $B_{36}N_{36}$  is the most stable in BN clusters.

**Table 9** Energy of clusters with hydrogen

	Introduced H <sub>2</sub>	Heat of formation (eV/mol atom)	Chemisorbed H inside cluster	Hydrogen storage (wt.%)
C <sub>60</sub>	0	35.21	0	5.8-6.5
	22	143.01	0	
	25	164.87	4	
	26	169.63	8 <sup>a</sup>	
B <sub>24</sub> N <sub>24</sub>	0	-36.12	0	2.9
	9	-9.44	0	
B <sub>36</sub> N <sub>36</sub>	0	-69.33	0	4.3
	20	-6.66	0	
B <sub>60</sub> N <sub>60</sub>	0	-100.28	0	4.9
	38	-61.74	0	

<sup>a</sup>A C–C bond was broken

Energies of H<sub>2</sub> absorption on B<sub>36</sub>N<sub>36</sub> cluster were calculated, and structural models for B<sub>60</sub>N<sub>60</sub> with 38 H<sub>2</sub> molecules are shown in Fig. 30d. When more than 22 H<sub>2</sub> molecules were introduced in C<sub>60</sub>, hydrogen atoms chemisorbed inside the cluster. When more than 26 H<sub>2</sub> molecules were introduced in the C<sub>60</sub> clusters, 22 H<sub>2</sub> molecules were remained in the cluster and 8 hydrogen atoms chemisorbed inside the clusters, and a C–C bond was broken. Absorption of such large amount of hydrogen indicates rather unstable energy state. Maximum storages are 9, 20, and 38 H<sub>2</sub> molecules for B<sub>24</sub>N<sub>24</sub>, B<sub>36</sub>N<sub>36</sub>, and B<sub>60</sub>N<sub>60</sub>, as summarized in Table 9. From Table 9, stability of H<sub>2</sub> molecules in B<sub>24</sub>N<sub>24</sub>, B<sub>36</sub>N<sub>36</sub>, and B<sub>60</sub>N<sub>60</sub> seem to be higher than that of C<sub>60</sub>. C and BN cluster showed possibility of hydrogen storage of ~6.5 and ~4.9 wt %, respectively [147]. Effects of metal atoms were also investigated [148].

Carbon nanotubes are oxidized at 600°C in air. On the other hand, BN are stable up to 900°C in air [92], which indicates BN fullerenes have higher thermal and chemical stability than those of carbon fullerenes. BN fullerenes with good thermal and chemical stability can store H<sub>2</sub> molecules with less energy, and they have the same chemisorption energy and higher stability, compared to carbon clusters. BN fullerene materials would be better candidates for H<sub>2</sub> storage materials.

## 10 Conclusion

BN nanocage clusters, nanotubes, nanohorns, nanoparticles, and nanocapsules, developed in our work, were reviewed in the present paper. These BN nanomaterials which have some superior properties and unique structures compared to carbon nanomaterials can be expected to have applications in a wide variety of future nanodevices such as nanoelectronics, magnetic recording media, and biological sensors, in combination with carbon-based fullerenes and nanotubes.

## References

1. N.G. Chopra, R.J. Luyken, K. Cherrey, V.H. Crespi, M.L. Cohen, S.G. Louie and A. Zettl, *Science* 269, 966 (1995).
2. A. Loiseau, F. Willaime, N. Demoncey, G. Hug and H. Pascard, *Phys. Rev. Lett.* 76, 4737 (1996).
3. M. Terrones, W.K. Hsu, H. Terrones, J.P. Zhang, S. Ramos, J.P. Hare, R. Castillo, K. Prassides, A.K. Cheetham, H.W. Kroto and D.R.M. Walton, *Chem. Phys. Lett.* 259, 568 (1996).
4. A. Loiseau, F. Willaime, N. Demoncey, N. Schramchenko, G. Hug, C. Colliex and H. Pascard, *Carbon* 36, 743 (1998).
5. D. Golberg, Y. Bando, K. Kurashima and T. Sato, *Chem. Phys. Lett.* 323, 185 (2000).
6. J. Cumings and A. Zettl, *Chem. Phys. Lett.* 316, 211 (2000).
7. T. Oku, T. Hirano, M. Kuno, T. Kusunose, K. Niihara and K. Suganuma, *Mater. Sci. Eng. B* 74, 206 (2000).
8. C.C. Tang, M.L. de la Chapell, P. Li, Y.M. Liu, H.Y. Dang and S.S. Fan, *Chem. Phys. Lett.* 342, 492 (2001).
9. C. Tang, Y. Bando and T. Sato, *Chem. Phys. Lett.* 362, 185 (2002).
10. D. Goldberg, F.-F. Xu and Y. Bando, *Appl. Phys. A* 76, 479 (2003).
11. W. Mickelson, S. Aloni, W.-Q. Han, J. Cumings and A. Zettl, *Science* 300, 467 (2003).
12. D. Goldberg, Y. Bando, M. Mitome, K. Kurashima, T. Sato, N. Grobert, M. Reyes-Reyes, H. Terrones and M. Terrones, *Phys. B* 323, 60 (2002).
13. T. Oku, I. Narita and A. Nishiwaki, *Mater. Manuf. Process.* 19, 1215 (2004).
14. L. Bourgeois, Y. Bando, W.Q. Han and T. Sato, *Phys. Rev. B* 61, 7686 (2000).
15. M. Terauchi, M. Tanaka, K. Suzuki, A. Ogino and K. Kimura, *Chem. Phys. Lett.* 324, 359 (2000).
16. M. Machado, R. Mota, and P. Piquini, Electronic properties of BN nanocones under electric fields, *Microelectron. J.* 34, 545 (2003).
17. A. Nishiwaki, T. Oku and I. Narita, *Sci. Technol. Adv. Mater.* 5, 629 (2004).
18. T. Oku, I. Narita, A. Nishiwaki, N. Koi, *Defects Diffus. Forum* 226-228, 113 (2004).
19. C. Zhi, Y. Bando, C. Tang and D. Golberg, *Phys. Rev. B* 72, 245419 (2005).
20. C. Zhi, Y. Bando, C. Tang, D. Golberg, R. Xie and T. Sekiguchi, *Appl. Phys. Lett.* 87, 063107 (2005).
21. A. Nishiwaki and T. Oku, *Diam. Relat. Mater.* 14, 1183 (2005).
22. T. Oku, T. Kusunose, K. Niihara and K. Suganuma, *J. Mater. Chem.* 10, 255 (2000).
23. J.F. Li, L.Z. Yao, C.H. Ye, C.M. Mo, W.L. Cai, Y. Zhang and L.D. Zhang, *J. Cryst. Growth* 223, 535 (2001).
24. H. Kitahara, T. Oku, T. Hirano and K. Suganuma, *Diam. Relat. Mater.* 10, 1210 (2001).
25. I. Narita and T. Oku, *Diam. Relat. Mater.* 11, 949 (2002).
26. G. Xing, G. Chen, X. Song, X. Yuan, W. Yao and H. Yan, *Microelectron. Eng.* 66, 70 (2003).
27. Y.-C. Zhu, Y. Bando, L.-W. Yin and D. Golberg, *Chem. Eur. J.* 10, 3667 (2004).
28. E. Borowiak-Palen, M.H. Rummeli, M. Knupfer, G. Behr, K. Biedermann, T. Gemming, R.J. Kalenczuk, T. Pichler, *Carbon* 43, 615 (2005).
29. T. Oku and K. Hiraga, *Diam. Relat. Mater.* 10, 1398 (2001).
30. T. Oku, K. Hiraga, T. Matsuda, T. Hirai and M. Hirabayashi, *Diam. Relat. Mater.* 12, 1138 (2003).
31. F. Banhart, M. Zwanger and H.-J. Muhr, *Chem. Phys. Lett.* 231, 98 (1994).
32. T. Oku, A. Nishiwaki, I. Narita and M. Gonda, *Chem. Phys. Lett.* 380, 620 (2003).
33. T. Oku, A. Nishiwaki and I. Narita, *Sci. Technol. Adv. Mater.* 5, 635 (2004).
34. D. Golberg, Y. Bando, O. Stéphan, and K. Kurashima, *Appl. Phys. Lett.* 73, 2441 (1998).
35. O. Stéphan, Y. Bando, A. Loiseau, F. Willaime, N. Schramchenko, T. Tamiya and T. Sato, *Appl. Phys. A* 67, 107 (1998).
36. T. Oku, M. Kuno, H. Kitahara and I. Narita, *Int. J. Inorg. Mater.* 3, 597 (2001).

37. T. Oku, M. Kuno and I. Narita, *Diam. Relat. Mater.* 11, 940 (2002).
38. S. Kokado and K. Harigaya, *Synthetic Met.* 135-136,745 (2003).
39. M. Radosavljević, J. Appenzeller, V. Derycke, R. Martel, Ph. Avouris, A. Loiseau, J.-L. Cochon and D. Pigache, *Appl. Phys. Lett.* 82, 4131 (2003).
40. Y. Bando, K. Ogawa and D. Golberg, *Chem. Phys. Lett.* 347, 349 (2001).
41. C.C. Tang, Y. Bando and T. Sato, *Appl. Phys. A* 75, 681 (2002).
42. H. Tokoro, S. Fujii and T. Oku, *IEEE Trans. Mag.* 39, 2761 (2003).
43. H. Tokoro, S. Fujii and T. Oku, *J. Mater. Chem.* 14, 253 (2004).
44. R. Ma, Y. Bando, H. Zhu, T. Sato, C. Xu and D. Wu, *J. Am. Chem. Soc.* 124, 7672 (2002).
45. T. Oku, M. Kuno and I. Narita, *J. Phys. Chem. Solids* 65, 549 (2004).
46. X. Chen, X.P. Gao, H. Zhang, Z. Zhou, W.K. Hu, G.L. Pan, H.Y. Zhu, T.Y. Yan, and D.Y. Song, *J. Phys. Chem. B* 109, 11525 (2005).
47. S.H. Lim, J. Luo, W. Ji and J. Lin, *Catal. Today* 120, 346 (2007).
48. K. Watanabe, T. Taniguchi, H. Kanda, *Nat. Mater.* 3, 404 (2004).
49. Y. Kubota, K. Watanabe, O. Tsuda and T. Taniguchi, *Science* 317, 932 (2007).
50. A. Rubio, J.L. Corkill and M.L. Cohen, *Phys. Rev. B* 49, 5081 (1994).
51. J.-Ch. Charlier, X. Blase, A. De Vita and R. Car, *Appl. Phys. A* 68, 267 (1999).
52. Y.-H. Kim, K.J. Chang and S.G. Louie, *Phys. Rev. B* 63, 205408 (2001).
53. Ş. Erkoç, *J. Mol. Struct. (Theochem)* 542, 89 (2001).
54. S. Okada, S. Saito and A. Oshiyama, *Phys. B* 323, 224 (2002).
55. Z. Peralta-Ingá, P. Lane, J.S. Murray, S. Boyd, M.E. Grice, C.J. O'Connor and P. Politzer, *Nano Lett.* 3, 21 (2003).
56. V.V. Ivanovskaya, A.A. Sofronov and A.L. Ivanovskii, *Phys. Lett. A* 297, 436 (2002).
57. W. Song, M. Ni, J. Lu, Z. Gao, S. Nagase, D. Yu, H. Ye, X. Zhang, *J. Mol. Struct. (Theochem)* 730, 121 (2005).
58. X. Li, W. Yang and B. Liu, *Nano Lett.* 7, 3709 (2007).
59. N. Thamwattana and J.M. Hill, *J. Phys. Condens. Matter* 19, 406209 (2007).
60. F. Jensen and H. Toflund, *Chem. Phys. Lett.* 201, 89 (1993).
61. M.E. Zandler, E.C. Behrman, M.B. Arrasmith, J.R. Myers and T.V. Smith, *J. Mol. Struct. (Theochem)* 362, 215 (1996).
62. G. Seifert, R.W. Fowler, D. Mitchell, D. Porezag and Th. Frauenheim, *Chem. Phys. Lett.* 268, 352 (1997).
63. Z. Slanina, M.-L. Sun and S.-L. Lee, *Nanostruct. Mater.* 8, 623 (1997).
64. H.-Y. Zhu, T.G. Schmalz and D.J. Klein, *Int. J. Quant. Chem.* 63, 393 (1997).
65. S.S. Alexandre, M.S.C. Mazzoni and H. Chacham, *Appl. Phys. Lett.* 75, 61 (1999).
66. P.W. Fowler, K.M. Rogers, G. Seifert, M. Terrones and H. Terrones, *Chem. Phys. Lett.* 299, 359 (1999).
67. K.M. Rogers, P.W. Fowler and G. Seifert, *Chem. Phys. Lett.* 332, 43 (2000).
68. G. Will and P.G. Perkins, *Diam. Relat. Mater.* 10, 2010 (2001).
69. S.S. Alexandre, H. Chacham and R.W. Nunes, *Phys. Rev. B* 63, 085406 (2001).
70. H.-S. Wu and H. Jiao, *Chem. Phys. Lett.* 386, 369 (2004).
71. R.R. Zope, B.I. Dunlap, *Chem. Phys. Lett.* 386, 403 (2004).
72. R.R. Zope, T. Baruah, M.R. Pederson and B.I. Dunlap, *Phys. Rev. A* 71, 025201 (2005).
73. V.V. Pokropivny and V.L. Bekenev, *Semiconductors* 40, 636 (2006).
74. V. Barone, A. Koller and G.E. Scuseria, *J. Phys. Chem. A* 110, 10844 (2006).
75. H.-S. Wu, and H. Jiao, *J. Mol. Model* 12, 537 (2006).
76. L. Koponen, L. Tunturivuori, M.J. Puska and Risto M. Nieminen, *J. Chem. Phys.* 126, 214306 (2007).
77. Q. Wang, Q. Sun, T. Oku and Y. Kawazoe, *Phys. B* 339, 105 (2003).
78. A. Nishiwaki, T. Oku and K. Suganuma, *Phys. B* 349, 254 (2004).
79. R.J.C. Batista, M.S.C. Mazzoni and H. Chacham, *Phys. Rev. B* 75, 035417 (2007).
80. V.V. Pokropivny, V.V. Skorokhod, G.S. Oleinik, A.V. Kurdyumov, T.S. Bartnitskaya, A.V. Pokropivny, A.G. Sisonyuk, D.M. Sheichenko, *J. Solid State Chem.* 154, 214 (2000).
81. D.L. Strout, *J. Phys. Chem. A* 104, 3364 (2000).

82. S.S. Alexandre, R.W. Nunes and H. Chacham, *Phys. Rev. B* 66, 085406 (2002).
83. S. Azevedo, M.S.C. Mazzoni, R.W. Nunes and H. Chacham, *Phys. Rev. B* 70, 205412 (2004).
84. W. An, X. Wu and X.C. Zeng, *J. Phys. Chem. B* 110, 16346 (2006).
85. T. Oku and I. Narita, *Phys. B* 323, 216 (2002).
86. I. Narita and T. Oku, *Diam. Relat. Mater.* 11, 945 (2002).
87. S.S. Han, J. Ku Kang, H.M. Lee, A.C.T. van Duin and W.A. Goddard III, *J. Phys. Chem.* 123, 114703 (2005).
88. S.-H. Jhi, *Phys. Rev. B* 74, 155424 (2006).
89. G. Mpourmpakis, G.E. Froudakis, *Catal. Today* 120, 341 (2007).
90. Y. Chen, J. Zou, S.J. Campbell, G. Le Caer, *Appl. Phys. Lett.* 84, 2430 (2004).
91. T. Oku, I. Narita, A. Nishiwaki, N. Koi, K. Suganuma, R. Hatakeyama, T. Hirata, H. Tokoro, S. Fujii, *Top. Appl. Phys.* 100, 187 (2006).
92. Y. Saito, M. Okuda, M. Tomita and T. Hayashi, *Chem. Phys. Lett.* 236, 419 (1995).
93. T. Oku, A. Nishiwaki and I. Narita, *Phys. B* 351, 184 (2004).
94. I. Narita and T. Oku, *Solid State Commun.* 122, 465 (2002).
95. I. Narita and T. Oku, *Diam. Relat. Mater.* 12, 1146 (2003).
96. K. Tanaka, H. Waki, Y. Ido, S. Akita, Y. Yoshida and T. Yoshida, *Rapid Commun. Mass Spectrom.* 2, 151 (1988).
97. H. Ajje, M.M. Alvarez, S.J. Anz, R.D. Beck, F. Diederich, K. Fostiropoulos, D.R. Huffman, W. Krätschmer, Y. Rubin, K.E. Schriver, D. Sensharma and R.L. Whetten, *J. Phys. Chem.* 94, 8630 (1990).
98. T. Oku, A. Carlsson, L.R. Wallenberg, J.-O. Malm, J.-O. Bovin, I. Higashi, T. Tanaka and Y. Ishizawa, *J. Solid State Chem.* 135, 182 (1998).
99. T. Oku, *J. Ceram. Soc. Jpn* 109, S17 (2001).
100. P.W. Stephens, G. Bortel, G. Faigel, M. Tegze, A. Jánossy, S. Pekker, G. Oszlanyi and L. Forró, *Nature* 370, 636 (1994).
101. M. Takata, B. Umeda, E. Nishibori, M. Sakata, Y. Saito, M. Ohno and H. Shinohara, *Nature* 377, 46 (1995).
102. H. Shinohara, *Rep. Prog. Phys.* 63, 843 (2000).
103. W. Krätschmer, L.D. Lamb, K. Fostiropoulos and D.R. Huffman, *Nature* 347, 354 (1990).
104. E. Bengu and L.D. Marks, *Phys. Rev. Lett.* 86, 2385 (2001).
105. D. Golberg, Y. Bando, L. Bourgeois, K. Kurashima and T. Sato, *Appl. Phys. Lett.* 77, 1979 (2000).
106. B.G. Demczyk, J. Cumings, A. Zettl and R.O. Ritchie, *Appl. Phys. Lett.* 78, 2772 (2001).
107. A. Celik-Aktas, J.M. Zuo, J.F. Stubbins, C. Tang and Y. Bando, *Appl. Phys. Lett.* 86, 133110 (2005).
108. R. Arenal, M. Kociak, A. Loiseau, D.-J. Miller, *Appl. Phys. Lett.* 89, 073104 (2006).
109. I. Narita and T. Oku, *Chem. Phys. Lett.* 377, 354 (2003).
110. I. Narita and T. Oku, *Solid State Commun.* 129, 415 (2004).
111. T. Oku and I. Narita, *Diam. Relat. Mater.* 13, 1254 (2004).
112. D. Golberg, Y. Bando, K. Kurashima and T. Sato, *Solid State Commun.* 116, 1 (2000).
113. C. Zhi, Y. Bando, C. Tang, S. Honda, K. Sato, H. Kuwahara and D. Golberg, *J. Phys. Chem. B* 110, 1525 (2006).
114. H. Chen, Y. Chen, J. Yu and J.S. Williams, *Chem. Phys. Lett.* 425, 315 (2006).
115. N. Koi, T. Oku, M. Inoue and K. Suganuma, *J. Mater. Sci.* 43, 2961 (2008).
116. C. Zhi, Y. Bando, C. Tang, R. Xie, T. Sekiguchi and D. Golberg, *J. Am. Chem. Soc.* 127, 15996 (2005).
117. S.-Y. Xie, W. Wang, K.A.S. Fernando, X. Wang, Y. Lin and Y.-P. Sun, *Chem. Commun.* 3670 (2006).
118. I. Narita, T. Oku, H. Tokoro and K. Suganuma, *J. Electron Microsc.* 55, 123 (2006).
119. T. Oku, I. Narita and H. Tokoro, *J. Phys. Chem. Solids* 67, 1152 (2006).
120. J.S. Lauret, R. Arenal, F. Ducastelle, A. Loiseau, M. Cau, B. Attal-Tretout, and E. Rosencher, L. Goux-Capes, *Phys. Rev. Lett.* 94, 037405 (2005).

121. R. Arenal, O. Stéphan, M. Kociak, D. Taverna, A. Loiseau and C. Colliex, *Phys. Rev. Lett.* 95, 127601 (2005).
122. H. Chen, Y. Chen, Y. Liu, C.-N. Xu, J.S. Williams, *Opt. Mater.* 29, 1295 (2007).
123. T. Oku, N. Koi, K. Suganuma, R.V. Belosludov and Y. Kawazoe, *Solid State Commun.* 143, 331 (2007).
124. M. Endo, Y.A. Kim, T. Hayashi, T. Yanagisawa, H. Muramatsu, M. Ezaka, H. Terrones, M. Terrones and M.S. Dresselhaus, *Carbon* 41, 1941 (2003).
125. T. Oku, N. Koi and K. Suganuma, *J. Phys. Chem. Solids* 69, 1228 (2008).
126. M. Ishigami, J.D. Sau, S. Aloni, M.L. Cohen and A. Zettl, *Phys. Rev. Lett.* 94, 056804 (2005)
127. M. Ishigami, J.D. Sau, S. Aloni, M.L. Cohen and A. Zettl, *Phys. Rev. Lett.* 97, 176804 (2006).
128. J. Wang, V.K. Kayastha, Y.K. Yap, Z. Fan, J.G. Lu, Z. Pan, I.N. Ivanov, A.A. Puretzky, D.B. Geohegan, *Nano Lett.* 5, 2528 (2005)
129. X. Bai, D. Golberg, Y. Bando, C. Zhi, C. Tang, M. Mitome and K. Kurashima, *Nano Lett.* 7, 632 (2007).
130. N. Koi, T. Oku and M. Nishijima, *Solid State Commun.* 136, 342 (2005).
131. T. Oku, N. Koi, I. Narita, K. Suganuma and M. Nishijima, *Mater. Trans.* 48, 722 (2007).
132. K.P. Loh, M.L.M. Yeadon, C. Boothroyd and Z. Hu, *Chem. Phys. Lett.* 387, 40 (2004).
133. T. Oku, I. Narita and A. Nishiwaki, *J. Eur. Ceram. Soc.* 26, 443 (2006).
134. A. Nishiwaki and T. Oku, *J. Electron Microsc.* 54, i9 (2005).
135. A. Nishiwaki and T. Oku, *J. Eur. Ceram. Soc.* 26, 435 (2006).
136. T. Oku and A. Nishiwaki, *Phys. E* 29, 712 (2005).
137. T. Matsuda, N. Uno, H. Nakae, T. Hirai, *J. Mater. Sci.* 21, 649 (1986).
138. T. Matsuda, H. Nakae, T. Hirai, *J. Mater. Sci.* 23, 509 (1988).
139. T. Oku, K. Hiraga, T. Matsuda, T. Hirai and M. Hirabayashi, *Diam. Relat. Mater.* 12, 1918 (2003).
140. Joint Committee on Powder Diffraction Standards (1984) 34-421.
141. T. Oku, N. Koi and A. Nishiwaki, *Diam. Relat. Mater.* 14, 1193 (2005).
142. F.E. Kruis, H. Fissan, A. Peled, *J. Aerosol Sci.* 29, 511 (1998).
143. S. Sun, C.B. Murray, D. Weller, L. Folks, A. Moser, *Science* 287, 1989 (2000).
144. M. Kuno, T. Oku, and K. Suganuma, *Scripta Mater.* 44, 1583 (2001).
145. H. Tokoro, S. Fujii, T. Oku, *Solid State Commun.* 133, 681 (2005).
146. J.Q. Hu, Q.Y. Lu, K.B. Tang, S.H. Yu, Y.T. Qian, G.E. Zhou, X.M. Liu, J.X. Wu, *J. Solid State Chem.* 148, 325 (1999).
147. N. Koi and T. Oku, *Sci. Technol. Adv. Mater.* 5, 625 (2004).
148. N. Koi, T. Oku, K. Suganuma, *Phys. E* 29, 541 (2005).

# Carbon Nitride and Boron Carbon Nitride Nanostructures

Jie Yu and E.G. Wang

**Abstract** This chapter is devoted to carbon nitride and boron carbon nitride nanostructures, an important and indispensable member in the family of nanomaterials for various applications, especially in nanoelectronics. It covers all the main aspects of the current research on the carbon nitride and boron carbon nitride nanostructures. The attention is mainly focused on the one-dimensional carbon nitride and boron carbon nitride nanotubes. The most critical issues were addressed from the perspectives of synthesis, composition, structure, property, and application. Due to the presence of multielements in graphite-like layers, the carbon nitride and boron carbon nitride nanotubes display much richer diversities than their carbon counterparts in structure and property. The carbon nitride nanotubes behave always as metallic wires, and the boron carbon nitride nanotubes exhibit semiconducting properties tailorable in a large range depending only on compositions. The properties of electrical conducting, electron field emission, photoluminescence, hydrogen storage, and lithium storage are also presented in this chapter based on the current knowledge.

## 1 Introduction

The elemental and compound materials by the light elements, such as boron, carbon, and nitride, have long been attracting interest due to their versatile and unique properties. It is known that graphite is semimetallic and hexagonal boron nitride (hBN) is semiconducting with a bandgap of over 5 eV [1–4]. Interestingly, the ternary boron carbonitride (BCN) compound has adjustable bandgaps between graphite and hBN depending mainly on composition [5–7]. Single-phase superhard materials are exclusively found in this system. Diamond, tetrahedral amorphous carbon (t-aC), and cubic boron nitride (cBN) can now be synthesized by thin film growth or high pressure – high temperature techniques, and are widely used as superhard materials. Carbon nitride (CN) was predicted to have hardness comparable

---

J. Yu and E.G. Wang (✉)

Institute of Physics, Chinese Academy of Sciences, Beijing, 100080, China



to diamond [8–10]. Cubic  $\text{BC}_2\text{N}$  was reported to have hardness higher than cBN [11, 12]. Besides the hardness, these materials possess many other extreme properties, such as high thermal conductivity, wide bandgap, and high melting point, which make them very attractive for applications such as high-temperature, high-power, and high-frequency microelectronic devices. Conventionally, the materials in the boron–carbon–nitrogen (B–C–N) system include diamond, graphite, t-aC, cBN, hBN, boron carbide, and the recently developed carbon nitride and BCN in the form of bulk and thin film [13].

Since the discovery of carbon nanotubes (CNTs) [14], various new tubular members with unique structures and properties have been found in the B–C–N family. They are CNTs, BN nanotubes (BN-NTs) [15–18], carbon nitride nanotubes (CN-NTs) [19–22], boron carbonitride nanotubes (BCN-NTs) [23–26], carbon and carbon nitride nanobells (CNBs and CN-NBs) [27, 28], and tubular graphitic cones [29]. Due to the nanometer size and unique structure, these new B–C–N nanomaterials are expected to exhibit novel properties different from their bulk counterparts [30].

Both theoretical and experimental results show that a CNT can behave either as a semiconductor or a metal depending on its radius and chirality [31–33], which displays a fascinating future for nanodevice application. Even a large amount of efforts have been made so far, it is still a big challenge to control the chirality and diameter of the CNTs technologically. On the contrary, the nanomaterials from the B–C–N system offer a large variety of mutually complementary electronic properties. The bandgap of all BN-NTs is remarkably stable around 5.5 eV, independent of their radius, chirality, and wall–wall interactions [15, 33–37]. The BCN-NT possesses a tunable bandgap intermediate between those of BN-NTs and CNTs, which can be easily controlled by changing their atomic compositions. Theoretical studies have predicted that tubular forms of  $\text{C}_3\text{N}_4$  are insulating while that of CN are metallic independent of diameter and chirality [38]. Due to the tailorable electronic properties, the BCN-related nanostructures are expected to play an important role in future nanoelectronics. Excellent electron field emission properties were observed for the BCN-related nanomaterials and full color displays were fabricated based on CNT electron sources [39]. A reproducible hydrogen storage capacity up to 8 wt% and good Li storage properties with a reversible specific capacity of 480 mA h/g were achieved for the CN nanobells/nanotubes [40, 41].

In this chapter, we will discuss the current research on the CN and BCN nanostructures. Our main attention will be focused on the review of processing, structure, composition, property, and potential application of these light element nanomaterials.

## 2 Carbon Nitride Nanostructures

Theoretical calculations have predicted that carbon nitrides behave as superhard materials for the phases of cubic  $\text{C}_3\text{N}_4$  and planar hexagonal  $\text{C}_3\text{N}_4$  [42, 43] or as metallic nanowires for CN-NTs [38]. The doping of graphite-like C structures with N will considerably improve their electron-conducting properties due to the presence

of additional lone pairs of electrons that act as donors with respect to the delocalized  $\pi$ -system of the hexagonal framework [19]. Similar to pure carbon nanostructures, the carbon nitride (CN) nanostructures are also consisted of graphitic layers containing nitrogen more or less. But the CN nanostructures bear different structural features from the carbon nanostructures due to the introduction of nitrogen atoms.

Various types of CN nanostructures have been fabricated successfully, which include single-walled CN-NTs (CN-SWNTs), double-walled CN-NTs (CN-DWNTs), multiwalled CN-NTs (CN-MWNTs), bamboo-like or corrugated CN-NTs, CN nanobells, and CN nanospheres. Because the structural variation is mainly induced by the presence of the nitrogen atoms, the structural features of the CN nanostructures are strongly dependent on the nitrogen concentration. Usually, the crystallinity of the CN nanostructures decreases with increasing the nitrogen concentration and it is difficult to generate highly ordered structures in which high concentrations of N are incorporated within the carbon network. Many growth techniques, such as chemical vapor deposition (CVD), arc-discharge, physical vapor deposition (PVD), and hydrothermal, have been used to grow the CN nanostructures by changing the precursor; and the core issue in these studies is to control their nitrogen concentration.

## ***2.1 Structure and Composition***

### **2.1.1 Bamboo-Like and Polymerized Nanobell Structures**

The synthesis of CN-NTs was first reported by Terrones et al. and Sen et al. [44, 45] using pyrolysis of organic precursor over cobalt catalysts, and by Ma et al. [27] using plasma-assisted CVD from a gas system. Different from the CNTs, the CN-NTs are consisted of stacked cones or nanobells and present a bamboo-like or corrugated morphology as shown in Fig. 1. The individual cones or nanobells are formed by the nested-type stacking of graphene sheets. Generally, there are two types of bamboo-like structures for the CN-NTs: one of which is formed by periodically stacking the regular cones as shown in Fig. 1a, b [22, 27, 42] and the other has irregularly compartmentalized morphology by randomly distorted transverse graphitic layers as shown in Fig. 1c, d [20]. The former morphology was usually observed in thin CN-NTs and the later observed in some thick ones although the detailed formation mechanism is not clear yet [27]. The regular cones building the CN-NTs have been denominated as nanobells and the bamboo-like CN-NTs with the periodically stacked cones are called as polymerized nanobells. The CN-NTs with irregularly compartmentalized morphology is most frequently observed in experiments. The graphitic layers forming the cones are often buckled and not perfectly flat. The layers are generally tilted in respect to the axial direction of the nanotube with apparently opened edges on the surface. The morphology of the CN-NTs is strongly dependent on the nitrogen concentration and the stacked cones become more prominent as the nitrogen concentration increases [45].

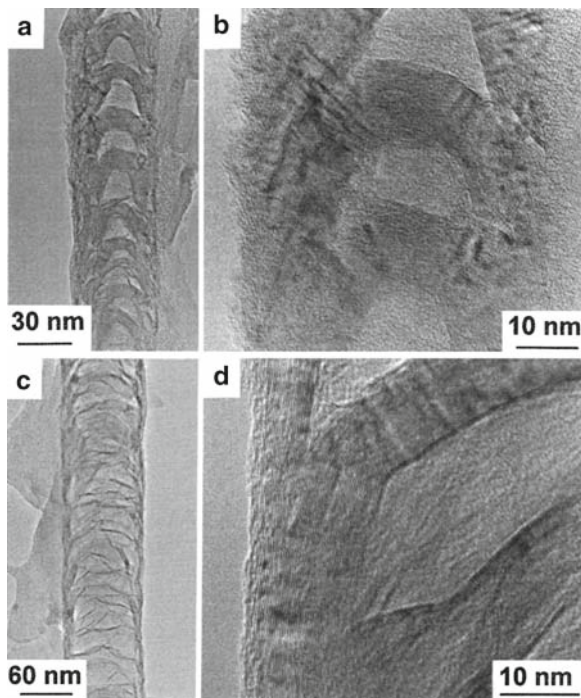


**Fig. 1** HRTEM images. (a) A single fiber of the nitrogen-containing polymerized carbon nanobells with a small diameter of  $\sim 50$  nm obtained at low magnification. (b) An enlarged image of (a) showing detailed connection of the nanobells. (c) A single fiber of the nitrogen-containing polymerized carbon nanobells with a large diameter of  $\sim 100$  nm, (d) An enlarged part of (c) showing the atomic structure inside the nanofiber (reprinted with permission from [27], copyright by the American Institute of Physics)

### 2.1.2 Separation of Individual Nanobells

The most interesting results are the length control of the polymerization of the nanobells, especially separation of the individual carbon nanobells from the stem of the CN-NTs. Very short nanotubes containing only a few nanobells and even individual nanobells have been produced from the as-grown CN-NTs by two methods, the  $H_2$  plasma treatment, followed by grinding, and the oxidation with acidified potassium permanganate [28]. Figure 2a shows the typical morphology of the shortened CN-NTs obtained by  $H_2$  plasma treatment and grinding. It is found that many tubes consist of several nanobells, and also that discrete individual nanobells are distributed in the samples (shown by the hollow arrow). These individual nanobells, such as in Fig. 2b, have similar diameters and lengths and readily aggregate, indicated by the hollow arrows. By using the grinding method, the long nanotubes can be cut into short ones with length determined by the grinding

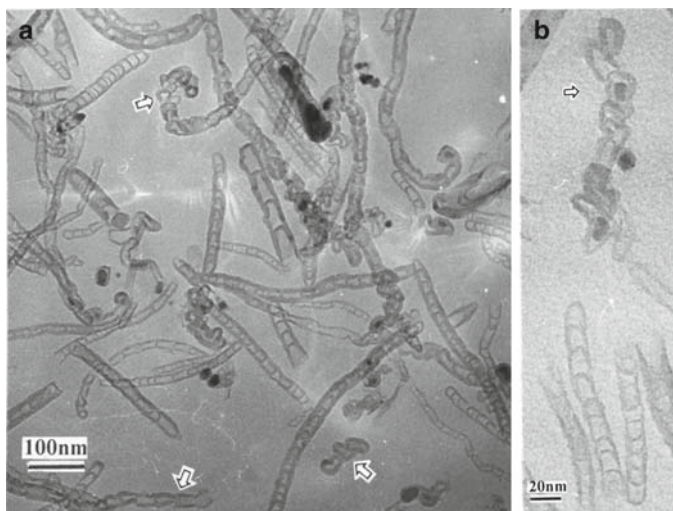


**Fig. 2** (a) TEM images of the shortened CN nanotubes with polymerized nanobell structures and the individual nanobells. (b) Many individual nanobells gathered together (marked by *arrow*) and several short nanofibers containing only a few nanobells (modified from [28], copyright by the American Institute of Physics)

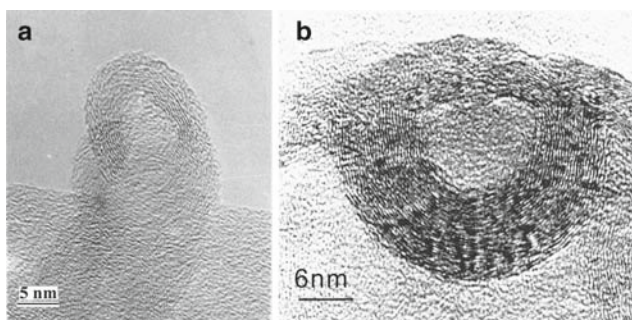


**Fig. 3** (a) HRTEM image of an individual nanobell obtained by grinding. The diameter and length of this nanobell are 14 and 16 nm, respectively. (b) HRTEM image of a single nanobell with an inner diameter of 14 nm and wall thickness of 7.6 nm. The sample was obtained by reacting with potassium permanganate for 96 h; in which the scale bar is 6 nm (modified from [28], copyright by the American Institute of Physics)

conditions. Figure 3a is a typical high resolution transmission electron microscopy (HRTEM) image of a single nanobell obtained by grinding, which has a diameter and length of 14 nm and 16 nm, respectively. Figure 3b shows a nanobell obtained by oxidation with acidified potassium permanganate. The nanobells are of great interest in application due to their unique structure.

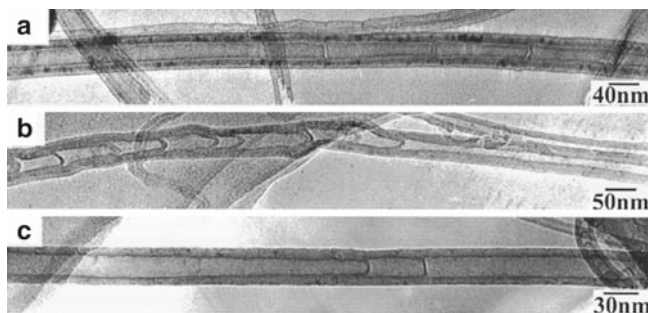


**Fig. 4** TEM images of heterojunctions between a CN-NT and a pure carbon nanotube. (a) Heterojunction of CNT/CN-NT, (b) heterojunction of CN-NT/CNT, and (c) biheterojunction of CNT/CN-NT/CNT (reprinted with permission from [46], copyright by the American Institute of Physics)

### 2.1.3 Heterojunction

Fabrication of heterojunction is one of the core issues for the application of the nanotubes in nanoelectronics. The heterojunctions consisted of the CNTs and CN-NTs have been obtained by using a simple process, as shown in Fig. 4 [46, 47]. The production of the CNT part is by using  $\text{CH}_4$  and  $\text{H}_2$  as reactive gases, and the CN-NT part is by using  $\text{CH}_4$  and  $\text{N}_2$ . By switching the reactive gases between  $\text{H}_2$  and  $\text{N}_2$  continuously without interrupting the growth process, the heterojunctions of CNTs and CN-NTs can be obtained. Depending on the sequence of introducing  $\text{H}_2$  and  $\text{N}_2$ , the heterojunctions of CNT/CN-NT and CN-NT/CNT, as well as biheterojunction of CNT/CN-NT/CNT were all fabricated successfully, as shown in Fig. 4a–c, respectively. These heterojunctions are expected to act as building blocks in nanoscale electronic devices, for examples of nanodiode [48] and Schottky junction [49].

### 2.1.4 Formation Mechanism

The formation of the bamboo-like CN-NT structure is closely related to the behavior of the catalyst particles during growth. The morphology of the carbon cones or nanobells maybe inherits the shape of the catalyst particles. Some models were proposed to explain the growth mechanism; however, no sufficient and systematic experimental evidence supports these assumptions. In addition, a little attention was paid to the role of nitrogen during the formation of this structure in these models.

A model describing the growth process of the CN-NTs composed of the nanobells was proposed by considering the role of nitrogen [46]. This model includes three sequential steps (a) formation of the catalyst particles on the substrate surface; (b) precipitation of the initial graphite sheets and stretching the quasispherical catalyst particles into bell shapes; and (c) the growth of nanobells. The schematic pictures are given in Fig. 5, which clearly describes the formation mechanism of the polymerized

CN-NTs. Initially, at appropriately high temperature, the catalyst particles melt and forms quasispherical shape. Subsequently, active carbon and nitrogen species dissolve into the catalyst particles. When the surface of the catalyst particles is supersaturated with carbon, the first graphite sheet begins to precipitate on the surface of the catalyst particle, and once the graphite sheets cover the surface of the catalyst particle, the following carbon atoms can only be supplied from the root of the catalyst particles (Fig. 5b). From the shape of the catalyst particles embedded at the end of the CN-NTs observed by TEM, it is inferred that catalyst particles must have undergone stretching from a quasispherical shape to a bell-like shape, which results in the shape of the nanobells. Due to the relatively long diffusion distance, the supply rate of carbon atoms to the top surface will be slower than those to the side surface. A nanobell forms when the carbon atoms cease to precipitate on the top surface of the bell-like catalysts due to scarcity of the carbon atoms in this area. The growth of the next nanobells starts again once supersaturation of carbon atoms on the top surface of the catalyst particles resumes. In this way, the polymerized carbon nanobells were obtained. Different from a CNT, the outside surface of the CN-NT leaves many open-edged graphite sheets (shown in Fig. 5d–f).

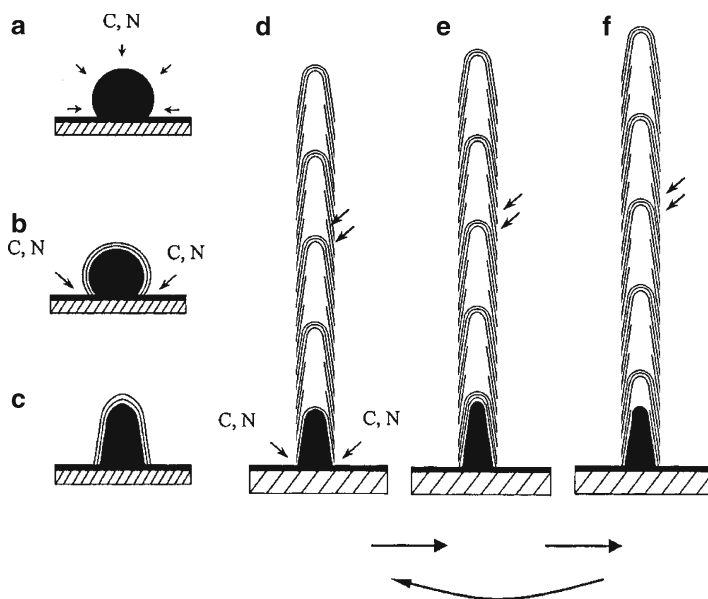


**Fig. 5** Schematic of the growth process of carbon nitride nanobells. (a) Forming a quasispherical catalyst particle, (b) beginning to precipitate graphite sheets, (c) stretching the catalyst particle into a bell-like shape, (d) precipitating the first graphite layer of a nanobell when the top curvature of the catalyst is supersaturated with carbon, (e) stopping to growth at the top curvature of the catalyst particle, and (f) beginning to precipitate graphite sheets on the side surface of the catalyst particle (reprinted with permission from [46], copyright by the American Institute of Physics)

### 2.1.5 Other CN Nanostructures

Apart from the bamboo-like CN-NTs, several other types of CN nanostructures were also observed. Single-walled CN-NTs were obtained by arc-discharge process [50]. A maximum nitrogen concentration of 1 at.% was found despite the nitrogen content in precursors. High-purity double-walled CN-NTs with diameter in the range of 1.5–2 nm were synthesized by CVD [51]. The N content in the inner wall is 3 at.%, which is higher than that in the outer wall. The graphite-like and pyridine-like N exist with about 1:1 ratio. Interestingly, a new type of CN nanostructure, CN sphere, with diameter as small as 30 nm was prepared by template-directed solid-state or solution reaction of cyanuric chloride or fluoride with lithium nitride [52]. These hollow spheres show multiwalled nanostructure, built by disorderly stacked  $C_3N_4$  curved layers assembled from triazine rings and nitrogen bridges of pyramidal structure. The closed spherical shape of this kind of CN nanostructure suggests its application in lubricants, catalyst supports, gas storage, drug delivery, and a precursor for the high pressure – high temperature synthesis of superhard materials.

### 2.1.6 Nitrogen Concentration and Chemical Bonding

Most of the results show that the structural features and properties of the CN nanostructures are vitally related to the nitrogen content. Although high nitrogen concentration up to 57.1 at.% was reported by hydrothermal method [53, 54], the CN nanostructures obtained by other methods, such as CVD, are usually below 10 at.%. Because both graphitic carbon and nitrogen molecule are much more stable, it is difficult to prepare the CN nanostructures with high nitrogen concentration in equilibrium state. The nitrogen concentration generally decreases with increasing the synthesis temperature [45, 55, 56]. For example, the N contents were around 5, 3.5, and 3 at.% in the CN nanostructures prepared by the pyrolysis of pyridine at 700, 850, and 1,000°C, respectively, and up to 1 at.% remained when the pyrolysis is carried out at 1,100°C [45, 55]. Low growth temperature leads to a high N/C atomic ratio. The CN-NTs with high N concentration of 50% (CN) and 57.1% ( $C_3N_4$ ) have been obtained by hydrothermal method at 230°C and 220°C, respectively [53, 54]. However, this structure should be in a nonequilibrium state and the nitrogen component may be liberated at high temperature.

Theoretical calculations have suggested that there exist three possible ways to incorporate nitrogen, denoted graphite-like, pyridine-like, and pyrrole-like [57, 58], which can be detected by electron energy loss spectroscopy (EELS) and X-ray photoelectron spectroscopy (XPS). The pyridine-like N is that bonded with two carbon atoms inside the graphitic layers by forming cavities or located at the edges of the layers. The graphite-like N is that bonded with three C atoms by substituting a C atom in the graphitic lattice. It is found that, when the overall N content increases for the CN-NTs, the number of graphitic walls within these structures decreases and the proportion of pyridine-like N increases with the number of

graphite-like N atoms almost constant. It is thus deduced that the pyridine-like N “cavities” or “edges” within the predominantly graphitic framework should be responsible for the interlinked morphologies in the N-doped structures [59].

The graphite-like and pyridine-like nitrogen were frequently observed [20, 45, 51, 59, 60], and the relative content of the two types of N is strongly dependent on growth temperature. The annealing experimental studies on both CN nanotubes and films have indicated that the graphite-like nitrogen is more stable than the pyridine-like nitrogen [61, 62]. The pyridine-like N exists in the products of low temperature and decreases gradually with increasing the reaction temperature. Experimental results show that the pyridine-like N disappears when the growth temperature exceeds 1,000°C [45, 56]. It seems that there exists a limit concentration of N atoms incorporated into the graphitic layers, above which the CN nanostructures are not stable. It is difficult to generate highly ordered structures, where high concentration of nitrogen is incorporated within the carbon network.

The overall morphology and structure are strongly dependent on the N concentration in the CN nanostructures. For examples, the degree of perfection and linearity of the structure decreases as the N content increases [20]. The alignment of the lattice fringes is gradually lost as the amount of nitrogen increases and the roughness of the tube surface starts to increase drastically when a small amount of nitrogen is incorporated in the graphitic structure [63]. It is the incorporating nitrogen atoms that induce the buckled layers. This is the reason why the CN tubules by sputtering show more heavily buckled structure and higher nitrogen concentration [64] than the CN tubes obtained by CVD. The single-walled CN-NTs contain N at a concentration of 1 at.% [50]. When the N content increases further but below 10 at.% bamboo-like CN-NTs are always observed, while the amorphous carbon nitride can accommodate larger amounts of nitrogen up to 80 at.% [65]. This clearly indicates the effects of the N concentration on the crystallinity of the CN nanostructures.

High-resolution spatial EELS (HREELS) line scanning across the hollow part of the CN-NTs shows that the C elemental profile reflects the tubular geometry and the N profile follows the shape of the C profile, thus implying that N and C are always homogeneously distributed in the hexagonal framework [20, 66, 67]. However, the N/C atomic concentration ratio was typically found to be slightly higher in curved region of transverse layers with 10% N than in straight region with 6% N [66]. In addition, the N content of the inner wall is higher than that of the outer wall for the double-walled CN-NTs [51]. Theoretical calculation [51] shows that the N-doping of the inner wall is more favorable than that of the outer wall for both graphite-like and pyridine-like N. The formation of the N-binding structure would release the strains of curved graphite layers, more efficiently for the inner wall than for the outer wall. It is also indicated that a substitutional level of nitrogen in a curved graphite sheet strongly favors the formation of pentagons and heptagons, which are required for forming curvature and fullerene-like structures [68]. The tendency that the N atoms prefer to incorporate into the graphitic layers with high curvature may account for the formation mechanism of the bamboo-like CN-NTs.



## 2.2 Properties and Applications

### 2.2.1 Conductance and Field Emission

All CN-NTs are metallic with the conductance higher than that of the CNTs [19, 69]. The average gap obtained from the normalized conductance  $[(d \ln I)/(d \ln V) \text{ vs. } V]$  curves, is  $\sim 0.60$  eV and  $\sim 0.65$  eV for the multiwalled and singlewalled CNTs, respectively, while it is only  $\sim 0.4$  eV for the CN-NTs [19]. The electrical resistance measured for single CN-NT ropes is  $20 \text{ k}\Omega$  or less, much lower than those of CNTs [67]. The metallic conductance of the CN-NTs makes them good candidates as the conducting wires in nanoscale electronic device. The heterojunctions of CNT/CN-NT may exhibit metal–metal or metal–semiconductor contact behaviors and act as building blocks for future nanodevices.

One of the interesting topics for the nanotube research is electron field emission property due to their unique shape and structure. The CN-NTs exhibit field emission properties even superior to the CNTs in some aspects probably because of the increased conductance and the existence of the open edges on the surface. The current density of  $200 \text{ mA/cm}^2$  at a low field of  $6 \text{ V}/\mu\text{m}$  [27] and the highest density of  $0.4 \text{ A/cm}^2$  [67] were reported for the CN-NTs, which is much higher than the required current density of at least  $1 \text{ mA/cm}^2$  for display application. Figure 6 is a typical current–field characteristic of a CN-NT film and its Fowler–Nordheim (FN) plot (inset). The FN plot follows straight lines both under high and low fields, which

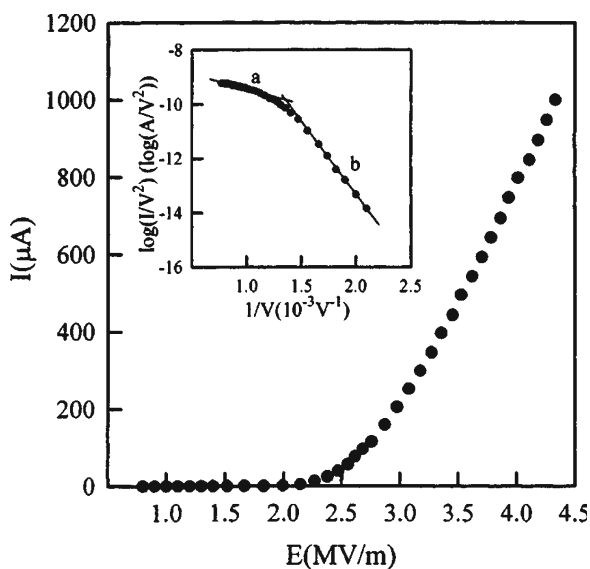


**Fig. 6** Current–field characteristic of a CN-NT film and its Fowler–Nordheim (FN) plot (inset) (reprinted with permission from [27], copyright by the American Institute of Physics)

indicates that the emission follows the conventional FN mechanism. The emission was observed not only from the tip but also from the surface, which is resulted from the presence of opened edges on the tube surface [27].

The emission characteristics are stable with little fluctuation. For example, it was observed from a specimen at a current density of  $150 \text{ mA/cm}^2$  that the relative fluctuation is 1.3% during a test period of 200 s. No significant degradation of the current density was observed over 100 h, similar to the recent results from well-organized pure CNTs [27, 67]. It is demonstrated that the CN-NTs are excellent and highly stable field emitters up to very high current [67].

### 2.2.2 Hydrogen Storage

Due to the formation of the open edges on the surface, which provides easy channels for Li-ion insertion and active sites for hydrogen adsorption, the CN-NTs are expected to be important candidates for hydrogen and lithium storage. Recently, the CN-NTs with 0.6-nm pores were produced. Experimental and theoretical investigations indicated that these 0.6-nm pores may provide the route for reversible hydrogen storage [70]. A hydrogen storage capacity up to 8 wt% was achieved reproducibly under ambient pressure and at temperature of  $300^\circ\text{C}$  [40]. Figure 7 shows a typical thermogravimetric analysis (TGA) curve, which shows that very little of hydrogen released at the temperatures below  $140^\circ\text{C}$ , a significant amount of hydrogen released at about  $230^\circ\text{C}$ , and then the adsorbed hydrogen in C–N nanobells completely released at  $360^\circ\text{C}$ . A hydrogen rechargeability of the CN nanobells was also tested.

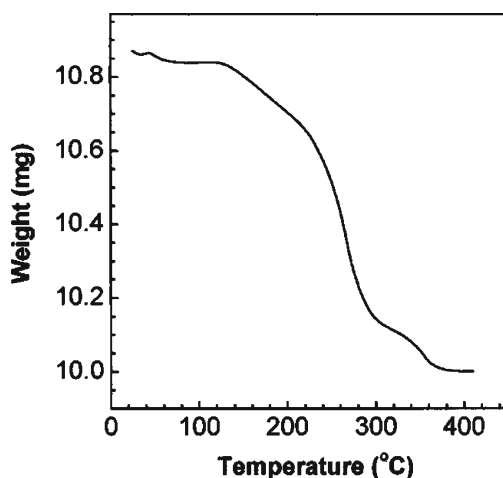


**Fig. 7** A typical TGA curve for the nanobells stored hydrogen is presented showing the hydrogen adsorption process with heating temperature (reprinted with permission from [40], copyright by the American Institute of Physics)

After ten cycles of adsorption, the hydrogen uptake capacity was reduced by less than 15%. The simple and effective storage method, as well as the controllable CN nanobell structures suggests that the C–N nanobells are an interesting and important candidate as hydrogen storage material. In addition, the  $N_2$  molecules have been introduced and encapsulated in the hollow cavities of the CN-NTs by the CVD processes [71, 72]. These results demonstrate that the CN-NTs could be used as nanoscale gas containers due to the presence of the closed compartments, which ensure the encapsulation of gases.

### 2.2.3 Lithium Storage

The intercalation behavior of the Li-ions into the CN-NTs has also been investigated [41]. Compared to the CNTs with an integrated hollow cylindrical structure, the CN-NTs is assumed to be beneficial to Lithium storage, for the reason that Li ions are easily intercalated from the opened edges of the graphene layers on the outside surfaces. At the first discharge process, the capacity of Li ions is 860 mA h/g, which is much larger than the theoretical capacity of graphite, 372 mA h/g. It decreases to about 480 mA h/g at the first charge process and kept invariable in the following cycles. Figure 8 shows the voltage profiles at the ninth discharge–charge cycle and the inset displays a relationship between the cycle number and the Li intercalation capacity. It is indicated that the reversible capacity almost keeps the same during more than 30 cycles, and the CN-NTs have a good cyclic performance.

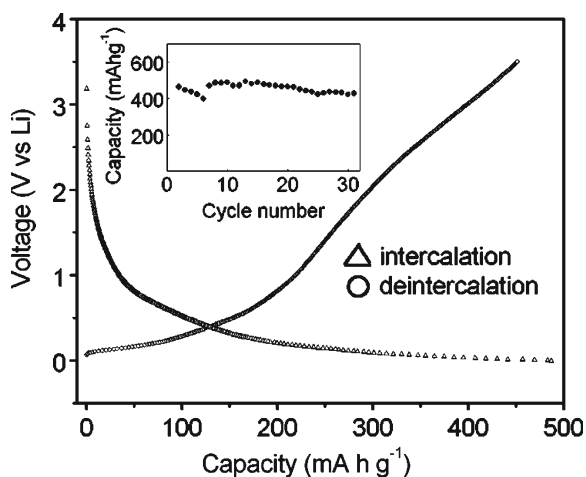


**Fig. 8** Discharge–charge curve (ninth cycle) of CN-NTs recorded at a current density of 0.1 mA/cm<sup>2</sup>. The *inset* shows a relationship between the cycle number and Li intercalation capacity (reprinted with permission from [41], copyright by the American Institute of Physics)

### 3 Boron Carbonitride Nanostructures

The BCN materials with graphitic-layered structure were first synthesized by Bartlett and his coworkers [73, 74] in 1986 after the pyrolysis of  $C_2H_2$ ,  $BCl_3$ , and  $NH_3$ . The compositions of the products prepared at  $400^\circ C$  and  $700^\circ C$  were  $B_{0.485}C_{0.02}N_{0.485}$  and  $B_{0.35}C_{0.30}N_{0.35}$ , respectively. In 1996, Watanabe et al. studied the electronic properties of layered  $BC_2N$  materials by using scanning tunneling spectroscopy and determined a semiconducting behavior with an energy gap of 2 eV, which is in agreement with the previous theoretical calculations of homogeneous BCN layers [75].

The main purpose in attempting to synthesize the BCN compounds is to pursue their tunable electronic properties intermediate between those of graphite and hBN. The BCN nanostructures are expected to exhibit semiconducting properties similar to their bulk counterparts, which will be of great importance in nanoelectronics. The main member of the BCN nanostructures is BCN-NTs, including single-walled (BCN-SWNTs), multi-walled (BCN-MWNTs), bamboo-like, cable-like, and hetero-juncted BCN-NTs. Up to now, the BCN-NTs have been synthesized in a large composition range. The BCN-NTs can be synthesized by CVD and arc-discharge from various precursors and substitutional reaction by using templates. The structural features and their formation mechanism, photoluminescence properties, and electron field emission properties have been investigated in detail. Very recently, a direct synthesis of BCN-SWNTs was reported by Wang's group using hot-filament CVD [76].

#### 3.1 Structure and Composition

##### 3.1.1 Bamboo-Like Structure

Three types of BCN-NTs were observed from the standpoint of microstructure, i.e., hollow tubular (without transverse layers), bamboo-like (with transverse layers), and cactus-like nanotubes. From the research results so far reported, the structural features are closely related to the synthesis methods. Almost all the BCN-NTs with hollow tubular structure are obtained by substitutional reaction using the CNTs or CN-NTs with low nitrogen concentration as templates [77–81]. There is an exception that BCN-SWNTs were successfully synthesized by bias-assisted hot filament CVD [76]. Usually, most directly synthesized BCN-NTs by CVD [82–86] and laser ablation [87] exhibit bamboo-like or cactus-like structure.

Similar to the CN-NTs, the bamboo-like BCN-NTs are composed of stacked cones, but these cones seem to be more irregular than those observed in the CN-NTs and sometimes appear as randomly oriented transverse layers. The structure of the BCN-NTs is closely related to the concentration of the incorporated B and N atoms. Figure 9 indicates the effects of the composition on the structure of BCN-NTs [88]. Different from the pure CNTs, the BCN-NTs contain some transverse layers in the

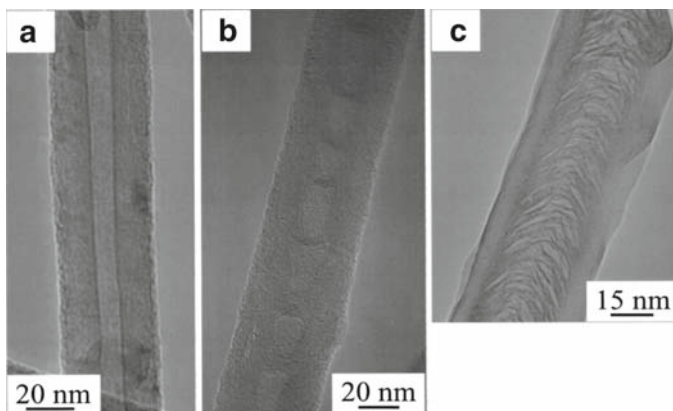


**Fig. 9** TEM images of BCN nanotubes with different compositions: (a) a pure CNT, (b) a  $B_{0.08}C_{0.76}N_{0.16}$  nanotube, and (c) a  $B_{0.45}C_{0.29}N_{0.26}$  nanotube (reprinted with permission from [88], copyright by the American Institute of Physics)

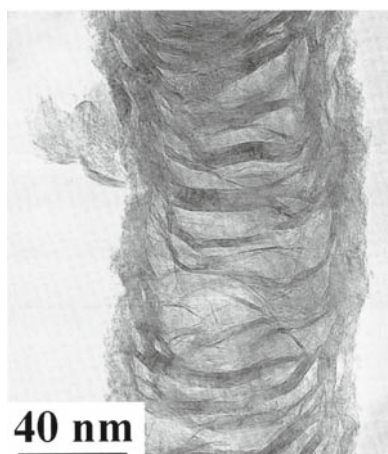


**Fig. 10** Typical structure of the bamboo-like BCN-NTs (reprinted with permission from [91], copyright by the American Institute of Physics)

central hollow [88, 89]. The formation of this kind of structure is because of the incorporation of B and N atoms in the graphitic layers. It is known that the odd-number rings appear in the perfect graphite layers if other light element atoms are introduced, which tend to bend the graphite layers for reducing the system energy [90]. So in the BCN-NTs, the curve of the graphite layers determines the shape of the transverse layers. The distances between two adjacent transverse layers are related to the B and N atomic concentrations. The density of the transverse layers increases with increasing the B and N concentration in the nanotubes. Figure 10

shows the typical structure of the bamboo-like BCN-NTs, where the transverse layers are clearly observed [91].

### 3.1.2 Cactus-Like Structure

Sometimes the BCN-NTs exhibit a unique surface structure, where there are many small graphitic spines standing on the outside surface of the nanotubes, making the tubes cactus-like as shown in Fig. 11 [89]. HRTEM observation reveals that the spines are highly graphitized cones or columns with caps. The graphite layers near the spines are contorted unparallel to the wall of the nanotubes. Besides the incorporation of the B and N atoms in the nanotubes, the cactus-like morphology is most likely induced by the ion bombardment.

### 3.1.3 Phase Separation

The composition distribution is generally heterogeneous for the BCN-NTs, both along the radial and axial directions. It has been found that the C concentration increases gradually toward the core layer along the radial direction and the BCN layers tend to form in the outer part of the BCN-NTs [84, 87, 92]. The boron is rich in transverse layers [92], but the composition varies for the layers from one to

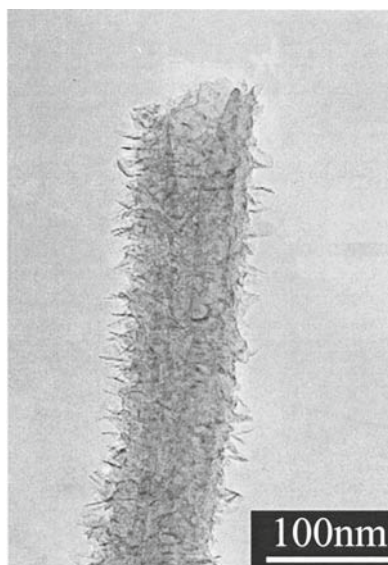


**Fig. 11** Cactus-like B–C–N nanostructure (reprinted with permission from [89], copyright by the American Institute of Physics)

another [86]. Phase separation and sandwich-like structures were also observed for the BCN-NTs. For example, for the products prepared by pyrolyzing  $\text{CH}_3\text{CN}\text{-BCl}_3$  over Co at  $1,000^\circ\text{C}$ , B, C, and N are not homogeneously distributed within the nanostructures but are separated into pure C and BN domains. Pure h-BN layers are always sandwiched between graphite-like shells [83]. The high concentrations of B up to 45% and N up to 26% were obtained for the bamboo-like BCN-NTs [19, 25, 26, 83–87, 89]. But the chemical states and distribution of the B and N atoms are very complicated. The B and N atoms prefer to incorporate into the network of the nanotubes in the ratio of unity, implying that the incorporation of the two atoms are correlated and phase separation of pure C and hBN may exist [25, 83, 86]. The deviation of the B/N ratio from unity was also frequently observed, indicating the existence of some B or N atoms doped into graphite layer and bonded only with carbon atoms [87].

The detailed mechanism accounting for the concentration distribution is not clear so far although some models were proposed. But it can be affirmed that the chemical distribution in the BCN-NTs is caused by the growth kinetics, including the growth parameters, such as reaction temperature, mass transfer rate of the reactive species, and growth and diffusion rates of constituting atoms arising therefrom.

### 3.1.4 Heterojunction

Nanometric heterojunctions of BCN-NTs were also controllably fabricated by bias-assisted hot filament CVD [88]. Tailored composition saltation across the nanotube junction is obtained by simply varying the gas composition in a two-step growth process. In the first step, BCN-NTs are prepared at a certain  $\text{B}_2\text{H}_6$  concentration. Then, the growth is paused with both the filament and the dc discharge power supply shut down and the deposition chamber evacuated. After that, the second stage is started with introducing the precursor again but at a varied  $\text{B}_2\text{H}_6$  flow rate. Figure 12 shows the TEM images of the nanometric heterojunction. The junction can be observed clearly from the different structure of the two sections. This type of nanojunctions may be a candidate for potential application in future nanoelectronics.

### 3.1.5 Single-Walled BCN Nanotubes

One of the important developments in the processing of the BCN-NTs is the successful direct synthesis of the BCN-SWNTs [76]. Conventionally, the BCN-NTs are corrugated and have a lot of defects because of the introduction of dissimilar atoms into the graphitic lattice. As a consequence, it is difficult to synthesize the BCN-SWNTs. However, in 2006, Wang and his coworkers achieved the synthesis of the BCN-SWNTs by bias-assisted hot filament CVD over the powdery MgO-supported Fe–Mo bimetallic catalyst from a gas mixture of  $\text{CH}_4$ ,  $\text{B}_2\text{H}_6$ , and ethylenediamine vapor [76]. TEM observation revealed that the as-grown SWNTs have clean and smooth surfaces with diameters in the range of 0.8–2.5 nm. Sometimes

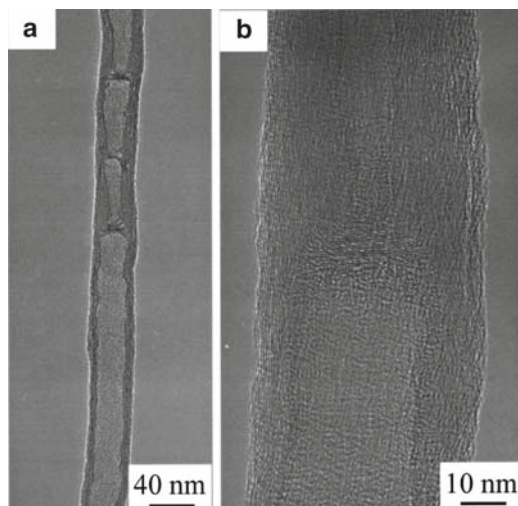


**Fig. 12** A C/BCN nanometric heterojunction: (a) TEM image and (b) HRTEM image at the junction (reprinted with permission from [88], copyright by the American Institute of Physics)

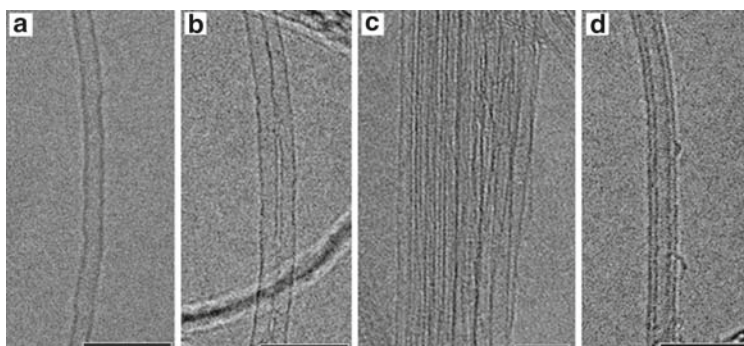


**Fig. 13** Typical HRTEM images of (a) an individual BCN-SWNT; (b) a thin SWNT bundle; (c) a thick SWNT bundle; and (d) an individual DWNT. Scale bar = 5 nm (reprinted with permission from [76], copyright by the American Chemical Society)

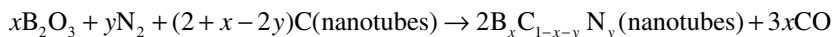
DWNTs with slightly larger outer diameter can also be found to coexist with the SWNTs, but their amount is not dominating.

As shown in Fig. 13a-d, the BCN-SWNTs normally have the straight cylindrical tube walls, a morphological feature similar to that of the pristine C-SWNTs. This is in contrast to the defective, bamboo-like structures of BCN-NTs. It is likely that the B and/or N incorporation will introduce topological defects in the graphite shell, but not necessarily result in the defective, bamboo-like structural features. The BCN-DWNTs coexisting with the SWNTs also exhibit similar nonbuckled



hollow tube structure (Fig. 13d). The EELS and XPS measurements indicate that the B and N atoms are built into the graphite network by substitutional doping, rather than gathered in the bundle intratube tunnels. The B contents usually vary in the range of 2–4 at.%, whereas the N concentration often range from 3 to 8 at.% and can, on occasion, reach as high as ~16 at.%. The energy-filtered elemental maps shows that all constituting B, C, and N elements are homogeneously distributed within the SWNT tube shells.

Another effective and widely adopted method for preparing the BCN-NTs is substitutional reaction by using pure CNTs or CN-NTs as templates to react with B and N containing precursors, mainly  $B_2O_3$  vapor and  $NH_3$  or  $N_2$  at high temperature, by which the BCN-SWNTs and BCN-MWNTs with well-defined concentric cylinder layers and hollow cores were obtained, following the original structure of the template nanotubes. For the products obtained by this method, there is a trend to a phase separation between BN-rich and C-rich domains most frequently. The structure feature and composition distribution vary depending mainly on the reaction conditions, e.g., temperature, reaction time, and the nature of the templates. Starting from the MWCNT templates, both sandwich-like structure and pure BN-NTs were obtained [93, 94]. The sandwich-like BCN-NTs were synthesized at the temperature below 1,700°C, where the BN-rich domains constitute the tube innermost and outermost parts, whereas the C-based layers compose the intermediate shells. With increasing the reaction temperature to 1,700°C or higher, the C templates were converted to pure BN-NTs completely. The following chemical reaction was proposed for the formation of the BCN-NTs from CNTs [77]:



This reaction proceeds when the  $B_2O_3$  vapor and  $N_2$  gas come into contact with the CNT surface. For the uncapped CNT templates the conversion processes of inside-out and outside-in lead to the formation of BN-rich layers on the innermost and outermost tubular surfaces first. With increase in the synthesis temperature (1,700°C or above) the tubes become more and more BN-rich, while the C species are continuously burned out from the nanostructure until pure BN-NTs form. In contrast, in the case of using CN-NTs as templates, the C-based layers are enriched close to the tube cores and the external layers are rich in B and N atoms [79, 93]. This is because the access of gases to the internal cores is restricted due to the existence of transverse layers between the innermost shells, typically observed in pyrolytically grown CN-NTs. We believe that the CN-NTs can also be converted into pure BN-NTs if increasing the temperature to high enough or prolonging the reaction time.

From the theoretical standpoint, it is indicated that the phase diagram of BCN system favors a phase separation between graphite and hBN without intermediate phases. However, the BCN-SWNTs [77] and BCN-MWNTs [80] with homogeneous distribution of B, C, and N were synthesized successfully. By using C-SWNTs as starting materials, the BCN-SWNTs with diameters of 2.1–3.2 nm were readily synthesized by the above substitutional reaction process under moderate conditions [77].

The B concentration up to 10 at.% and N up to 2 at.% were achieved in the graphitic layers for the BCN-SWNTs. Furthermore, the pure  $BC_xN$  ( $1 \leq x \leq 5$ ) nanotubes with uniformly distributed concentrations of B, C, and N were produced by reacting the CN-MWNTs with  $B_2O_3$  and CuO in a  $N_2$  atmosphere at about  $1,800^\circ C$  [80]. The authors attributed this novel result to the use of CNTs and a careful selection of the reaction temperature. The reaction temperature and the way the materials are heated are crucial factors to obtain homogeneous  $BC_xN$  shells. Higher or lower temperatures may also result in inhomogeneous and segregated B, C, and N cylinders. Considering the high temperature used for producing the materials ( $\sim 1,800^\circ C$ ), these novel BCN-NTs are promising semiconductors.

## 3.2 Properties and Applications

### 3.2.1 Semiconducting Property and Blue Photoluminescence

The BCN-NTs are expected to behave as semiconductor with electronic properties tunable in a large range, which has been validated both theoretically and experimentally. Liu et al. [95] predicted a 2.0-eV bandgap for a  $BC_2N$  stoichiometric sheet, while Zhu et al. [96] calculated a 0.2-eV gap for a BCN layered network. Transport measurements on individual ropes composed of tens of nanotubes with composition of  $BCN_x$  ( $x < 0.1$ ) reveal that the resistance is in the range of 50–300 M $\Omega$  and a bandgap of about  $\sim 1.5$  eV [67], but perplexingly, measurements on the  $BC_xN$  ( $1 \leq x \leq 5$ ) nanotube ropes show the same values of resistance and bandgap with  $BCN_x$  ( $x < 0.1$ ) nanotubes [67], while measurement on a bundle containing over ten nanotubes with composition of  $B_{0.79}C_{0.48}N$  gave a bandgap of 1 eV [78]. For the BCN-NT ropes composed of BN-shielded BCN-NT, the resistance through the BN outer layer was found to be  $\sim 1$  G $\Omega$ , sometimes exceeding 10 G $\Omega$ , demonstrating that the BN-rich outer layers act as an almost perfect insulator [79]. Considering the complicated structure and composition distribution it is very difficult to explain the semiconducting behavior of the BCN-NTs precisely based on the very limited experimental results.

The electronic structure of the BCN-NTs is investigated by photoluminescence (PL) both at room temperature and low temperature [26, 85, 89]. Figure 14a shows the PL spectra of the BCN-NTs with different compositions taken at room temperature excited by Ar+ laser with 488-nm wavelength. By decreasing the C concentration from 87 to 57%, the emission peak shifts from 2.13 to 2.34 eV as shown in Fig. 14b. In addition, the BCN-NTs emit blue-violet light when excited using a He–Cd laser with 325-nm wavelength. The peak positions range from 2.55 to 3.14 eV for the BCN-NTs with different compositions. These emission bands are most probably originated from the defect states because of the large amount of defects in the BCN-NTs. The corresponding bandgap energy should be larger or much larger than the above emission energy.

It is demonstrated that the electronic structure of the BCN-NTs can be controlled by their compositions. However, the observed energy range of the emission peaks

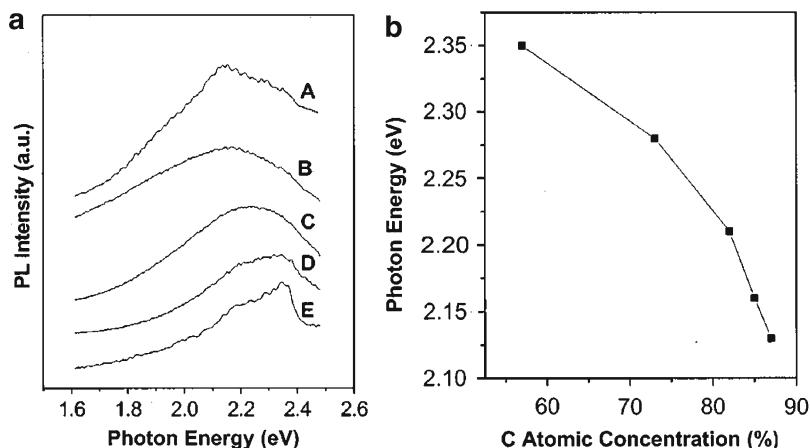


**Fig. 14** (a) Room-temperature PL spectra (excited by Ar laser at 488 nm) grown at different B<sub>2</sub>H<sub>6</sub> concentration: (a) 1.0%, (b) 1.5%, (c) 2.0%, (d) 2.5%, and (e) 3.0%, respectively, (b) The emission energy vs. C concentrations in the nanotubes (reprinted with permission from [89], copyright by the American Institute of Physics)

is too narrow compared with the very wide range of the bandgap energy from semimetallic graphite to insulating hBN. The emissions from the narrow bandgap close to graphite and the wide gap close to hBN are not observed yet. The continuous emission between the graphite and hBN from the BCN-NTs has not been realized also. One reason is that the synthesis of the defect-free BCN-NTs is very difficult, which makes the interband emission very difficult. In addition, the synthesis of graphite-based BCN-NTs with traces of B and N atoms and the hBN-based BCN-NTs with traces of C atoms is underway, which will make low energy emission near graphite and high energy emission near hBN is possible. In one previous study, a sharp emission peak at about 1.0 eV was observed for the BCN-NTs with the composition of B<sub>0.34</sub>C<sub>0.42</sub>N<sub>0.24</sub> at 4.2 K as shown in Fig. 15 [26]. Ultraviolet emission centered at 3.89 eV was revealed for the BCN-NTs with the BCN stoichiometry [97]. The luminescence properties are greatly influenced by the defects and composition distribution in the BCN-NTs; far more work than the presently existing is needed for understanding the luminescence properties of the BCN-NTs.

### 3.2.2 Field Emission

Nanotubes are unavoidably related to electron field emitters ever since their discovery because of their special shapes. Recent developments have demonstrated that the nanotubes have good prospects as electron field emitters for flat-panel displays. The field emission (FE) properties of the BCN-NTs were investigated as a function of the composition [89]. The threshold field at an emission current of 1 nA varies

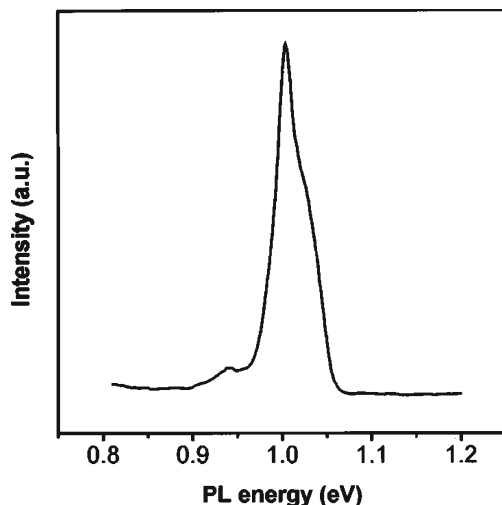


**Fig. 15** PL spectrum at 4.2 K for the BCN nanotubes with the formula of  $B_{0.34}C_{0.42}N_{0.24}$  (reprinted with permission from [26], copyright by the American Institute of Physics)

from 4 to 16 V/ $\mu\text{m}$  when the  $B_2H_6$  flux ratio is changed from 1.0 to 3.0% in the gas mixture. The emission capability of the BCN-NTs depends on their compositions and can be optimized by adjusting the growth parameters. For a sample grown with a  $B_2H_6$  flux ratio of 1.0%, the threshold field is 4 V/ $\mu\text{m}$  and the current density reaches 1 mA/ $\text{cm}^2$  at an electrical field of 6 V/ $\mu\text{m}$ .

Excellent FE properties were observed for the cactus-like structure [84], where a high emission current density of about 20–80 mA/ $\text{cm}^2$  was achieved at an electrical field of 5–6 V/ $\mu\text{m}$ , eligible for the technological application of flat-panel displays, which generally require 10 mA/ $\text{cm}^2$ . The high current density of field emission from the cactus-like BCN nanostructures is due to the distinctive surface structure of the BCN-NTs. However, the field emission stability from the BCN-NTs is inferior to the CN-NTs at high current densities [67]. At lower current densities of  $\sim 0.2$ – $0.4$  mA/ $\text{cm}^2$ , both CN-NTs and BCN-NTs emit rather steadily over tens of minutes, whereas after increasing the current density to 0.2–0.4 A/ $\text{cm}^2$  (at significantly shortened anode-film distances of several tens of  $\mu\text{m}$ ), the electron emission from BNC-NTs becomes highly unstable, accompanied with clearly visible sparkling, followed by the complete current degradation within several tens of seconds [67]. It is considered that in the case of not necessarily requiring very high field-emitting densities (a few  $\sim$ mA/ $\text{cm}^2$  or less), BCN-NTs may have a significant advantage over their pure C counterparts due to superior chemical and thermal stability.

Considering the tunable semiconducting properties and chemical stability, the BCN nanostructures may be used as photoluminescent devices, high temperature nanotransistors, lightweight electrical conductors, or high temperature lubricants. It is worth noting that due to the significant fraction of B/N presence in

the semiconducting BCN bundles they are presumed to have higher oxidation resistance and thermal stability than semiconducting pure CNTs [78]. This is of prime importance for applications.

## 4 Concluding Remarks

The carbon nitride and BCN nanostructures are important, sometimes indispensable members in the family of nanomaterials for various applications, especially in nanoelectronics. Due to the presence of multielements in graphitic layers, the CN and BCN nanotubes display much more diversities than their C counterparts in structure and electronic properties. The CNTs, CN-NTs, and BCN-NTs are mutually complementary in electronic properties, where the CNT can be metallic or semiconducting depending on its radius and chirality, CN-NTs behave always as metallic wires, and the BCN-NTs exhibit semiconducting properties tailorable in a large range depending only on compositions. CN-NTs and most directly synthesized BCN-NTs exhibit bamboo-like morphology due to the incorporation of N and B atoms into the graphitic layers, while the BCN-NTs converted from the CNT and CN-NT templates can be tubular hollow by replicating the original structure of the templates.

A great many of CN and BCN nanostructures have been successfully prepared, including single-walled CN- and BCN-NTs, double-walled CN- and BCN-NTs, multiwalled CN- and BCN-NTs, bamboo-like CN- and BCN-NTs, CN nanobells, CN nanospheres, heterojunctions of CNT/CN-NT and CNT/BCN-NT, and cable-like and sandwich-like BCN-NTs, etc. The B and N concentrations play crucial roles in controlling the structure and properties of the CN-NTs and BCN-NTs. For the CN-NTs, outstanding field emission properties with current density as high as  $0.2 \text{ A/cm}^2$  at a low field of  $6 \text{ V}/\mu\text{m}$ , high hydrogen storage capacity up to 8 wt%, and stable Li storage capacity of 480 mA h/g have been reported. While for the BCN-NTs, the light emission up to 3.89 eV and excellent field emission properties have been also realized. These results indicate the potential applications of the CN and BCN nanostructures in the related fields.

Even if great progress has been made in recent years; the research on the CN and BCN nanostructures still faces serious challenges both scientifically and technologically. They are the definition of the chemical states of the B and N atoms in the nanotubes, element distribution, thermal stability, the relationship between structure and properties, the device behavior of the heterojunctions, the precise control of the composition and structure, and so on. We believe that the CN and BCN nanostructures will contribute to the future nanoelectronics and nanomaterials greatly with the deepening of understanding these problems.

**Acknowledgments** The work was partly supported by NSFC, MOST, and CAS of China. We also thank Xuedong Bai, Xucun Ma, Dingyong Zhong, Chunyi Zhi, Wenlong Wang, Zhi Xu, Kaihui Liu, and Guangyu Zhang for their contribution, and W. Zhou at St. Andrews, Ningsheng Xu at Zhongshan University, Hongjie Dai at Stanford, Zhonglin Wang at GIT, D. Golberg and Y. Bando at NIMS for helpful discussion during the course.

## References

1. A. Catellani, M. Posternak, and A. Baldereschi, Bulk and surface electronic structure of hexagonal boron nitride, *Phys. Rev. B* **36**, 6105–6111 (1987).
2. C. Tarrío and S. E. Schnatterly, Interband transitions, plasmons, and dispersion in hexagonal boron nitride, *Phys. Rev. B* **40**, 7852–7859 (1989).
3. C. A. Taylor II, S. W. Brown, V. Subramaniam, S. Kidner, S. C. Rand, and R. Clarke, Observation of near-band-gap luminescence from boron nitride films, *Appl. Phys. Lett.* **65**, 1251–1253 (1994).
4. K. Watanabe, T. Taniguchi, and H. Kanada, Direct-bandgap properties and evidence for ultra-violet lasing of hexagonal boron nitride single crystal, *Nat. Mater.* **3**, 404–409 (2004).
5. Y. Miyamoto, A. Rubio, M. L. Cohen, and S. G. Louie, Chiral tubules of hexagonal  $BC_2N$ , *Phys. Rev. B* **50**, 4976–4979 (1994).
6. A. Ribio, J. L. Corkill, and M. L. Cohen, Theory of graphitic boron nitride nanotubes, *Phys. Rev. B* **49**, 5081–5084 (1994).
7. Y. H. Kim, K. J. Chang, and S. G. Louie, Electronic structure of radially deformed BN and  $BC_3$  nanotubes, *Phys. Rev. B* **63**, 205408–1-5 (2001).
8. M. L. Cohen, Calculation of bulk moduli of diamond and zinc blende solids, *Phys. Rev. B* **32**, 7988–7991 (1985).
9. E. G. Wang, Research on carbon nitrides, *Prog. Mater. Sci.* **41**, 24–298 (1997).
10. E. G. Wang, New development in covalently bonded carbon-nitride and related materials, *Adv. Mater.* **11**, 1129–1133 (1999).
11. V. L. Solozhenko, D. Andrault, G. Fiquet, M. Mezouar, and D. C. Rubie, Synthesis of superhard cubic  $BC_2N$ , *Appl. Phys. Lett.* **78**, 1385–1387 (2001).
12. V. L. Solozhenko, S. N. Dub, and N. V. Novikov, Mechanical properties of cubic  $BC_2N$ , a new superhard phase, *Diam. Relat. Mater.* **10**, 2228–2231 (2001).
13. E.G. Wang, Nitride-related nanomaterials by chemical vapor deposition: Structure and property, *J. Am. Ceram. Soc.* **85**, 105–108 (2002).
14. S. Iijima, Helical microtubules of graphitic carbon, *Nature* **354**, 56–58 (1991).
15. N. G. Chopra, R. J. Luyken, K. Cherrey, V. H. Crespi, M. L. Cohen, S. G. Louie, and A. Zettl, Boron-nitride nanotubes, *Science* **269**, 966–967 (1995).
16. W. Han, Y. Bando, K. Kurashima, and T. Sato, Synthesis of boron nitride nanotubes from carbon nanotubes by a substitution reaction, *Appl. Phys. Lett.* **73**, 3085–3087 (1998).
17. T. Laude, Y. Matsui, A. Marraud, and B. Jouffrey, Long ropes of boron nitride nanotubes grown by a continuous laser heating, *Appl. Phys. Lett.* **76**, 3239–3241 (2000).
18. O. R. Lourie, C. R. Jones, B. M. Bartlett, P. C. Gibbons, R. S. Ruoff, and W. E. Buhro, CVD growth of boron nitride nanotubes, *Chem. Mater.* **12**, 1808–1810 (2000).
19. R. Sen, B. C. Satishkumar, A. Govindaraj, K. R. Harikumar, G. Raina, J. P Zhang, A. K. Cheetham, and C. N. R. Rao, B–C–N, C–N and B–N nanotubes produced by the pyrolysis of precursor molecules over Co catalysts, *Chem. Phys. Lett.* **287**, 671–676 (1998).
20. M. Terrones, P. Redlich, N. Grobert, S. Trasobares, W. K. Hsu, H. Terrones, Y. Q. Zhu, J. P. Hare, C. L. Reeves, A. K. Cheetham, M. Ruhle, H. W. Kroto, and D. R. M. Walton, Carbon nitride nanocomposites: Formation of aligned  $C_xN_y$  nanofibers, *Adv. Mater.* **11**, 655–658 (1999).
21. S. L. Sung, S. H. Tsai, C. H. Tseng, F. K. Chiang, X. W. Liu, and H. C. Shih, Well-aligned carbon nitride nanotubes synthesized in anodic alumina by electron cyclotron resonance chemical vapor deposition, *Appl. Phys. Lett.* **74**, 197–199 (1999).
22. D. Y. Zhong, S. Liu, G. Y. Zhang, and E. G. Wang, Large-scale well aligned carbon nitride nanotube films: Low temperature growth and electron field emission, *J. Appl. Phys.* **89**, 5939–5943 (2001).
23. O. Stephan, P. M. Ajayan, C. Colliex, P. Redlich, J. M. Lambert, P. Bernier, P. Lefin, Doping graphitic and carbon nanotube structures with boron and nitrogen, *Science* **266**, 1683–1685 (1994).
24. Z. Weng-Sieh, K. Cherry, N. G. Chopra, X. Blase, Y. Miyamoto, A. Rubio, M. L. Cohen, S. G. Louie, A. Zettl, and R. Gronsky, Synthesis of  $B_xC_yN_z$  nanotubules, *Phys. Rev. B* **51**, 11229–11232 (1995).

25. P. Redlich, J. Loeffler, P. M. Ajayan, J. Bill, F. Aldinger, M. Ruhle, B–C–N nanotubes and boron doping of carbon nanotubes, *Chem. Phys. Lett.* **260**, 465–470 (1996).
26. J. Yu, J. Ahn, S. F. Yoon, Q. Zhang, Rusli, B. Gan, K. Chew, M. B. Yu, X. D. Bai, and E. G. Wang, Semiconducting boron carbonitride nanostructures: Nanotubes and nanofibers, *Appl. Phys. Lett.* **77**, 1949–1951 (2000).
27. X. C. Ma and E. G. Wang, Polymerized carbon nanobells and their field-emission properties, *Appl. Phys. Lett.* **75**, 3105–3107 (1999).
28. X. Ma, E. G. Wang, R. D. Tilley, D. A. Jefferson, and W. Zhou, Size-controlled short nanobells: Growth and formation mechanism, *Appl. Phys. Lett.* **77**, 4136–4138 (2000).
29. G. Y. Zhang, X. Jiang, and E. G. Wang, Tubular graphite cones, *Science* **300**, 472–474 (2003).
30. E. G. Wang, Nitrogen-induced carbon nanobells and their properties, *J. Mater. Res.* **21**, 2726–2773 (2006).
31. N. Hamada, S. Sawada, and A. Oshiyama, New one-dimensional conductors: Graphitic microtubules, *Phys. Rev. Lett.* **68**, 1579–1581 (1992).
32. A. Hassaniien, M. Tokumoto, Y. Humazawa, H. Kataura, Y. Maniwa, S. Suzuki, and Y. Achiba, Atomic structure and electronic properties of single-wall carbon nanotubes probed by scanning tunneling microscope at room temperature, *Appl. Phys. Lett.* **73**, 3839–3841 (1998).
33. A. Hassaniien, M. Tokumoto, S. Ohshima, Y. Kuriki, F. Ikazaki, K. Uchida, and M. Yumura, Geometrical structure and electronic properties of atomically resolved multiwall carbon nanotubes, *Appl. Phys. Lett.* **75**, 2755–2757 (1999).
34. A. Loiseau, F. Willaime, N. Demoncy, G. Hug, and H. Pascard, Boron nitride nanotubes with reduced numbers of layers synthesized by arc discharge, *Phys. Rev. Lett.* **76**, 4737–4740 (1996).
35. M. Terrones, W. K. Hsu, H. Terrones, J. P. Zhang, S. Ramos, J. P. Hare, R. Castillo, K. Prassides, A. K. Cheetham, H. W. Kroto, and D. R. M. Walton, Metal particle catalysed production of nanoscale BN structures, *Chem. Phys. Lett.* **259**, 568–573 (1996).
36. X. Blase, A. Rubio, S. G. Louie, and M. L. Cohen, Stability and band-gap constancy of boron-nitride nanotubes, *Europhys. Lett.* **28**, 335–340 (1994).
37. X. Blase, A. Rubio, S. G. Louie, and M. L. Cohen, Quasiparticle band structure of bulk hexagonal boron nitride and related systems, *Phys. Rev. B* **51**, 6868–6875 (1995).
38. Y. Miyamoto, M. L. Cohen, and S. G. Louie, Theoretical investigation of graphitic carbon nitride and possible tubule forms, *Solid State Commun.* **102**, 605–608 (1997).
39. W. B. Choi, D. S. Chung, J. H. Kang, H. Y. Kim, Y. W. Jin, I. T. Han, Y. H. Lee, J. E. Jung, N. S. Lee, G. S. Park, and J. M. Kim, Fully sealed, high-brightness carbon-nanotube field-emission display, *Appl. Phys. Lett.* **75**, 3129–3131 (1999).
40. X. D. Bai, D. Y. Zhong, G. Y. Zhang, X. C. Ma, S. Liu, E. G. Wang, Y. Chen, and D. T. Shaw, Hydrogen storage in carbon nitride nanobells, *Appl. Phys. Lett.* **79**, 1552–1554 (2001).
41. D. Y. Zhong, G. Y. Zhang, S. Liu, E. G. Wang, Q. Wang, H. Li, and X. J. Huang, Lithium storage in polymerized carbon nitride nanobells, *Appl. Phys. Lett.* **79**, 3500–3502 (2001).
42. A. Y. Liu and M. L. Cohen, *Science* **245**, 841–842 (1989).
43. D. M. Teter and R. J. Hemley, Low-compressibility carbon nitrides, *Science* **271**, 53–55 (1996).
44. M. Terrones, N. Grobert, J. Olivares, J. P. Zhang, H. Terrones, K. Kordatos, W. K. Hsu, J. P. Hare, P. D. Townsend, K. Prassides, A. K. Cheetham, H. W. Kroto, and D. R. M. Walton, Controlled production of aligned-nanotube bundles, *Nature* **388**, 52–55 (1997).
45. R. Sen, B. C. Satishkumar, A. Govindaraj, K. R. Harikumar, M. K. Renganathan, and C. N. R. Rao, Nitrogen-containing carbon nanotubes, *J. Mater. Chem.* **7**, 2335–2337 (1997).
46. G. Y. Zhang, X. C. Ma, D. Y. Zhong, and E. G. Wang, Polymerized carbon nitride nanobells, *J. Appl. Phys.* **91**, 9324–9332 (2002).
47. X. C. Ma and E. G. Wang, CN<sub>x</sub>/carbon nanotube junctions synthesized by microwave chemical vapor deposition, *Appl. Phys. Lett.* **78**, 978–980 (2001).
48. Y. Chai, X. L. Zhou, P. J. Li, W. J. Zhang, Q. F. Zhang, and J. L. Wu, Nanodiode based on a multiwall CN<sub>x</sub>/carbon nanotube intramolecular junction, *Nanotechnology* **16**, 2134–2137 (2005).
49. K. Xiao, Y. Q. Liu, P. A. Hu, G. Yu, W. P. Hu, D. B. Zhu, X. Y. Liu, H. M. Liu, and D. X. Wu, *Appl. Phys. A* **83**, 53–56 (2006).

50. M. Glerup, J. Steinmetz, D. Samaille, O. Stephan, S. Enouz, A. Loiseau, S. Roth, and P. Bernier, Synthesis of N-doped SWNT using the arc-discharge procedure, *Chem. Phys. Lett.* **387**, 193–197 (2004).
51. S. Y. Kim, J. Y. Lee, C. W. Na, J. Park, K. Seo, and B. Kim, N-doped double-walled carbon nanotubes synthesized by chemical vapor deposition, *Chem. Phys. Lett.* **413**, 300–305 (2005).
52. J. L. Zimmerman, R. Williams, V. N. Khabashesku, and J. L. Margrave, Synthesis of spherical carbon nitride nanostructures, *Nano Lett.* **1**, 731–734 (2001).
53. C. H. Cao, F. L. Huang, C. T. Cao, J. Li, and H. Zhu, Synthesis of carbon nitride nanotubes via a catalytic-assembly solvothermal route, *Chem. Mater.* **16**, 5213–5215 (2004).
54. Q. X. Guo, Y. Xie, X. J. Wang, S. Y. Zhang, T. Hou, and S. C. Lv, Synthesis of carbon nitride nanotubes with the  $C_3N_4$  stoichiometry via a benzene-thermal process at low temperatures, *Chem. Commun.* **1**, 26–27 (2004).
55. K. Suenaga, M. Yudasak, C. Colliex, and S. Iijima, Radially modulated nitrogen distribution in CN nanotubular structures prepared by CVD using Ni phthalocyanine, *Chem. Phys. Lett.* **316**, 365–372 (2000).
56. H. Chen, Y. Yang, Z. Hu, K. F. Huo, Y. W. Ma, Y. Chen, X. S. Wang, and Y. O. Lu, Synergism of  $C_5N$  six-membered ring and vapor–liquid–solid growth of  $CN_x$  nanotubes with pyridine precursor, *J. Phys. Chem. B* **110**, 16422–16427 (2006).
57. J. Casanovas, J. M. Ricart, J. Rubio, F. Illas, and J. M. Jimenez-Mateos, Origin of the large N 1s binding energy in X-ray photoelectron spectra of calcined carbonaceous materials, *J. Am. Chem. Soc.* **118**, 8071–8076 (1996).
58. I. Shimoyama, G. H. Wu, T. Sekiguchi, and Y. Baba, Evidence for the existence of nitrogen-substituted graphite structure by polarization dependence of near-edge x-ray-absorption fine structure, *Phys. Rev. B* **62**, R6053–R6056 (2000).
59. M. Terrones, P. M. Ajayan, F. Banhart, X. Blase, D. L. Carroll, J. C. Charlier, R. Czerw, B. Foley, N. Grobert, R. Kamalakaran, P. Kohler-Redlich, M. Ruhle, T. Seeger, and H. Terrones, N-doping and coalescence of carbon nanotubes: Synthesis and electronic properties, *Appl. Phys. A* **74**, 355–361 (2002).
60. M. Nath, B. C. Satishkumar, A. Govindaraj, C. P. Vinod, and C. N. R. Rao, Production of bundles of aligned carbon and carbon–nitrogen nanotubes by the pyrolysis of precursors on silica-supported iron and cobalt catalysts, *Chem. Phys. Lett.* **322**, 333–340 (2000).
61. H. C. Choi, S. Y. Bae, W. S. Jang, J. Park, H. J. Song, H. J. Shin, H. Jung, and J. P. Ahn, Release of N-2 from the carbon nanotubes via high-temperature annealing, *J. Phys. Chem. B* **109**, 1683–1688 (2005).
62. I. Shimoyama, G. Wu, T. Sekiguchi, and Y. Baba, Study of electronic structure of graphite-like carbon nitride, *J. Electron Spectrosc.* **114**, 841–848 (2001).
63. R. Kurt and A. Karimi, Influence of nitrogen on the growth mechanism of decorated C:N nanotubes, *ChemPhysChem* **6**, 388–392 (2001).
64. K. Suenaga, M. P. Johansson, N. Hellgren, E. Broitman, L. R. Wallenberg, C. Colliex, J.E. Sundgren, and L. Hultman, Carbon nitride nanotubulite - densely-packed and well-aligned tubular nanostructures, *Chem. Phys. Lett.* **300**, 695–700 (1999).
65. N. Takada, K. Arai, S. Nitta, and S. Nonomura, Preparation and properties of reactive-sputtered amorphous  $CN_x$  films, *Appl. Surf. Sci.* **114**, 274–277 (1997).
66. W. Q. Han, P. Kohler-Redlich, T. Seeger, F. Ernst, M. Ruhle, N. Grobert, W. K. Hsu, B. H. Chang, Y. Q. Zhu, H. W. Kroto, D. R. M. Walton, M. Terrones, and H. Terrones, Aligned  $CN_x$  nanotubes by pyrolysis of ferrocene/ $C_{60}$  under  $NH_3$  atmosphere, *Appl. Phys. Lett.* **77**, 1807–1809 (2000).
67. D. Golberg, P. S. Ddorozhkin, Y. Bando, Z.C. Dong, C. C. Tang, Y. Uemura, N. Grobert, M. Reyes-reyes, H. Terrones, and M. Terrones, Structure, transport, and field-emission properties of compound nanotubes:  $CN_x$  vs.  $BNC_x$  ( $x < 0.1$ ), *Appl. Phys. A* **76**, 499–507 (2003).
68. S. Stafstrom, Reactivity of curved and planar carbon-nitride structures, *Appl. Phys. Lett.* **77**, 3941–3943 (2000).



69. R. Czerw, M. Terrones, J.C. Charlier, X. Blase, B. Foley, R. Kamalakaran, N. Grobert, H. Terrones, D. Tekleab, P. M. Ajayan, W. Blau, M. Ruhle, and D. L. Carroll, Identification of electron donor states in N-doped carbon nanotubes, *Nano Lett.* **1**, 457–460 (2001).
70. S. Y. Kim, H. S. Kim, S. Augustine, and J. K. Kang, Nanopores in carbon nitride nanotubes: Reversible hydrogen storage sites, *Appl. Phys. Lett.* **89**, 253119-1-3 (2006).
71. M. Terrones, R. Kamalakaran, T. Seeger, and M. Rühle, Novel nanoscale gas containers: Encapsulation of N<sub>2</sub> in CN<sub>x</sub> nanotubes, *Chem. Commun.* **23**, 2335–2336 (2000).
72. J. H. Yang, D. H. Lee, M. H. Yum, Y. S. Shin, E. J. Kim, C. Park, M. H. Kwon, C. W. Yang, J. B. Yoo, H. J. Song, H. J. Shin, Y. W. Jin, J. M. Kim, Encapsulation mechanism of N<sub>2</sub> molecules into the central hollow of carbon nitride multiwalled nanofibers, *Carbon* **44**, 2219–2223 (2006).
73. J. Kouvetakis, R. B. Kaner, M. L. Sattler, and N. Bartlett, A novel graphite-like material of composition BC<sub>3</sub> and nitrogen–carbon graphites. *J. Chem. Soc. Chem. Commun.* 1758–1759 (1986).
74. R.B. Kaner, J. Kouvetakis, C. E. Warble, M. L. Sattler, and N. Bartlett, Boron–carbon–nitrogen materials of graphite-like structure, *Mat. Res. Bull.* **22**, 399–404 (1987)
75. M. O. Watanabe, S. Itoh, T. Sasaki, and K. Mizushima, Visible-light-emitting layered BCN semiconductor, *Phys. Rev. Lett.* **77**, 187–190 (1996).
76. W. L. Wang, X. D. Bai, K. H. Liu, Z. Xu, D. Golberg, Y. Bando, and E. G. Wang, Direct synthesis of B–C–N single-walled nanotubes by bias-assisted hot filament chemical vapor deposition, *J. Am. Chem. Soc.* **128**, 6530–6531 (2006).
77. D. Golberg, Y. Bando, W. Han, K. Kurashima, and T. Sato, Single-walled B-doped carbon, B/N-doped carbon and BN nanotubes synthesized from single-walled carbon nanotubes through a substitution reaction, *Chem. Phys. Lett.* **308**, 337–342 (1999).
78. D. Golberg, Y. Bando, L. Bourgeois, and T. Sato, Large-scale synthesis and HRTEM analysis of single-walled B- and N-doped carbon nanotube bundles, *Carbon* **38**, 2017–2027 (2000).
79. D. Golberg, P. Dorozhkin, Y. Bando, M. Hasegawa, and Z.C. Dong, Semiconducting B–C–N nanotubes with few layers, *Chem. Phys. Lett.* **359**, 220–228 (2002).
80. D. Golberg, P. S. Dorozhkin, Y. Bando, and Z.C. Dong, Cables of BN-insulated B–C–N nanotubes, *Appl. Phys. Lett.* **82**, 1275–1277 (2003).
81. M. Terrones, D. Golberg, N. Grobert, T. Seeger, M. Reyes-Reyes, M. Mayne, R. Kamalakarn, P. Dorozhkin, Z. C. Dong, H. Terrones, M. Ruhle, and Y. Bando, Production and state-of-the-art characterization of aligned nanotubes with homogeneous BC<sub>x</sub>N<sub>1-x</sub> (1 ≤ x ≤ 5) compositions, *Adv. Mater.* **15**, 1899–1903 (2003).
82. M. Terrones, A. M. Benito, C. Manteca-Diego, W. K. Hsu, O. I. Osman, J. P. Hare, D. G. Reid, H. Terrones, A. K. Cheetham, K. Prassides, H. W. Kroto, and D. R. M. Walton, Pyrolytically grown B<sub>x</sub>C<sub>y</sub>N<sub>z</sub> nanomaterials: Nanofibres and nanotubes, *Chem. Phys. Lett.* **257**, 576–82 (1996).
83. P. Köhler-Redlich, M. Terrones, C. Manteca-Diego, W. K. Hsu, H. Terrones, M. Ruhle, H. W. Kroto, and D.R.M. Walton, Stable B<sub>x</sub>C<sub>y</sub>N<sub>z</sub> nanostructures: Low-temperature production of segregated C/BN layered materials, *Chem. Phys. Lett.* **310**, 459–465 (1999).
84. X. D. Bai, J. D. Guo, J. Yu, E. G. Wang, J. Yuan, and W. Z. Zhou, Synthesis and field-emission behavior of highly oriented boron carbonitride nanofibers, *Appl. Phys. Lett.* **76**, 2624–2626 (2000).
85. X. D. Bai, E. G. Wang, and J. Yu, Blue-violet photoluminescence from large-scale highly aligned boron carbonitride nanofibers, *Appl. Phys. Lett.* **77**, 67–69 (2000).
86. W. Q. Han, J. Cumings, and A. Zettl, Pyrolytically grown arrays of highly aligned B<sub>x</sub>C<sub>y</sub>N<sub>z</sub> nanotubes, *Appl. Phys. Lett.* **78**, 2769–2771 (2001).
87. Y. Zhang, H. Gu, K. Suenaga, and S. Iijima, Heterogeneous growth of B–C–N nanotubes by laser ablation. *Chem. Phys. Lett.* **279**, 264–269 (1997).
88. J. D. Guo, C. Y. Zhi, X. D. Bai, and E. G. Wang, Boron carbonitride nanojunctions, *Appl. Phys. Lett.* **80**, 124–126 (2002).
89. C. Y. Zhi, J. D. Guo, X. D. Bai, and E. G. Wang, Adjustable boron carbonitride nanotubes, *J. Appl. Phys.* **91**, 5325–5333 (2002).
90. H. Sjöstrom, S. Stafstrom, M. Boman, and J. E. Sundergren, Superhard and elastic carbon nitride thin-films having fullerene-like microstructure, *Phys. Rev. Lett.* **75**, 1336–1339 (1995).

91. C. Y. Zhi, X. D. Bai, and E. G. Wang, Raman characterization of boron carbonitride nanotubes, *Appl. Phys. Lett.* **80**, 3590–3592 (2002).
92. R. M. Wang and H. Z. Zhang, Analytical TEM investigations on boron carbonitride nanotubes grown via chemical vapour deposition, *New J. Phys.* **6**, 78 (2004)
93. D. Golberg, Y. Bando, M. Mitome, K. Kurashima, T. Sato, N. Grobert, M. Reyes-Reyes, H. Terrones, M. Terrones, Preparation of aligned multi-walled BN and B/C/N nanotubular arrays and their characterization using HRTEM, EELS and energy-filtered TEM, *Phys. B* **323**, 60–66 (2002).
94. D. Golberg, P. S. Dorozhkin, Y. Bando, M. Mitome, C. C. Tang, Discrimination of B–C–N nanotubes through energy-filtering electron microscopy, *Diam. Relat. Mater.* **14**, 1857–1866 (2005).
95. A. Y. Liu, R. M. Wetzcovitch, and M. L. Cohen, Atomic arrangement and electronic structure of  $BC_2N$ , *Phys. Rev. B* **39**, 1760–1765 (1988).
96. H.Y. Zhu, D. J. Klein, N. H. March, and A. Rubio, Small band-gap graphitic CBN layers, *J. Phys. Chem. Sol.* **59**, 1303–1308 (1998).
97. L.W. Yin, Y. Bando, D. Golberg, A. Gloter, M. S. Li, X. L. Yuan, and T. Sekiguchi, Porous BCN nanotubular fibers: Growth and spatially resolved cathodoluminescence, *J. Am. Chem. Soc.* **127**, 16354–16355 (2005).

# Properties and Applications of Doped Carbon Nanotubes

Antonio G. Souza Filho and Mauricio Terrones

**Abstract** Carbon nanotubes are very stable systems having a considerable chemical inertness due to the strong  $sp^2$  hybridized covalent carbon bonds on their surface. However, various applications of carbon nanotubes require their doping or chemical modification through the addition of atoms and/or molecules (covalently or noncovalently) in order to alter their physicochemical properties. In this chapter we review the importance of different types of doping in carbon nanotubes (single, double, and multiwalled). Regarding the location of the dopant species within the nanotubes, it is possible to classify the doping process as being exohedral (intercalation), endohedral (filling), and in-plane (replacing carbon atoms). The effects of doping on the electronic, vibrational, chemical, magnetic, and mechanical properties are discussed by analyzing the experimental results obtained with different spectroscopic techniques such as resonant Raman, X-ray photoelectron (XP), electron energy loss, and others. Applications of doped-carbon nanotubes are also summarized.

## 1 Introduction

Carbon nanostructures such as graphene, nanoribbons, fullerenes, and nanotubes exhibit different physicochemical properties that could result in the development of novel nanotechnology products. In particular, carbon nanotubes possess fascinating electronic, optical, and mechanical properties depending on their geometry (diameter and chirality) [1, 2]. These carbon nanostructures are relatively stable and exhibit

---

A.G.S. Filho  
Departamento de Física, Universidade Federal do Ceará, C.P. 6030,  
Fortaleza-CE, Brazil, CEP 60455-900  
e-mail: agsf@fisica.ufc.br

M. Terrones (✉)  
Laboratory for Nanoscience and Nanotechnology Research LINAN  
and Advanced Materials Department, IPICYT,  
Camino a la Presa San Jose 2055, C.P. 78216, San Luis Potosi, SLP, Mexico  
e-mail: mterreres@titan.ipicyt.edu.mx

chemical surface inertness, which could be improved by replacing carbon atoms (from parts per million to small weight percentages) into their crystalline lattice. This process called doping opens up the opportunity for tailoring their electronic, vibrational, chemical, and mechanical properties.

In this chapter we review different ways of doping carbon nanotubes and other carbon nanostructures. There are three main doping categories: (a) exohedral doping or intercalation, (b) endohedral doping or encapsulation, and (c) in-plane or substitutional doping. By definition, in-plane doping is a covalent functionalization whereas the endohedral and exohedral kind of doping can be either covalent or noncovalent functionalization (see Fig. 1). Because of the curvature it is expected that exohedral covalent functionalization is more favorable than the endohedral counterpart because the outer surface (convex) is more reactive than the inner surface (concave). Using surface science terminology, covalent and noncovalent functionalization are also termed as chemisorption and physisorption, respectively.

We will also show in this chapter that the doped nanotubes possess outstanding properties when compared with pure carbon nanotubes, and it is foreseen that these systems will develop further nanotube science and will eventually transform the potential applications of carbon nanotubes into real-world technology.

This chapter is organized as follows. In Sect. 2, we describe general concepts behind the main doping-process types. In Sect. 3, we focus on the properties of

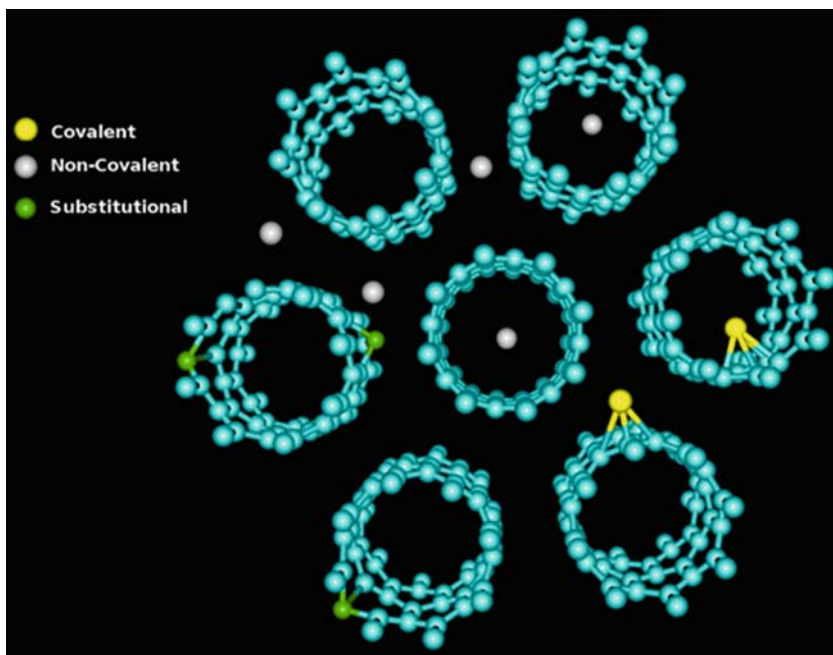


**Fig. 1** Schematic illustrating the possible sites and different functionalization processes in carbon nanotubes

substitutional doping processes discussing the synthesis methods as well as the main physical properties of these systems. Section 4 discusses the characterization of different doped-carbon nanotubes using resonant Raman spectroscopy, which is a very powerful technique for obtaining information regarding electronic, structural, and vibrational properties of the doped nanotubes. Some of the applications of doped carbon nanotubes are described in Sect. 5. The chapter finally summarizes the perspectives in this field.

## 2 Different Types of Doping

The possibility of filling the core (*endohedral doping*) of these 1D structures with carbon is attractive for scientists because both storage and transport of molecular species at the nanoscale is of great interest, especially in biology as drug deliverers and models for biochemical processes. This field started with the theoretical work of Pederson and Broughton [3] claiming the nanocapilarity of carbon nanotubes. From the experimental standpoint, Ajayan et al. [4] were the first to report the filling of MWNTs with lead or lead oxide by heating the tubes in air together with metallic lead (Fig. 2a, b). There is an extensive work related to the filling of carbon nanotubes that has been reviewed elsewhere [5, 7–9] (Fig. 2c, d).

The filling of carbon nanotubes has been of historical importance in nanotube science. It was the attempt to fill the core of MWNTs with pure transition metals such as Ni, Co, and Fe that resulted in the production of SWNTs using the arc discharge technique [10, 11]. Five years later, the first reports related to the successful filling of SWNTs with  $C_{60}$  molecules were presented by Smith et al. [12] and Sloan et al. [13]. The remarkable properties for those endohedrally doped systems lead to a fast development in using the 1D structure of SWNTs to prepare a large variety of filled-nanotube systems (Figs. 2 and 3). The natural attempt was to use the unique 1D tubular morphology as the template for preparing a new generation of very small diameter wires or to prepare quasi-1D superconductors using alkali metals as fillers. Heavy metals such as Ru, Bi, Au, Pt, Pd, and Ag have also been inserted in the nanotube cavity [13–16]. Different compounds such as halides and oxides have also been introduced into SWNTs (Fig. 2c, d) [6, 17, 18].

The discovery of  $C_{60}$ @SWNTs (also called fullerene peapods) is another very important advance in carbon nanotube science. The control and high yield of  $C_{60}$  filling could lead to double-walled carbon nanotubes (DWNTs) after heat treatments (Fig. 3). Furthermore, this system allowed the observation in real time using an electronic microscope of nanoscale phenomena such as dimerization, diffusion, and coalescence [19, 20]. Subsequently, 1D crystals have been synthesized using the encapsulation of metallofullerenes [21].

The bundles of as-prepared carbon nanotubes (SWNTs, DWNTs, or MWNTs) can serve as a host lattice for different chemical moieties. The electronic properties can be tailored by doping with electron-donating or electron-accepting guest atoms and small molecules, which reside in the interstitial channels. Chemical doping is expected to

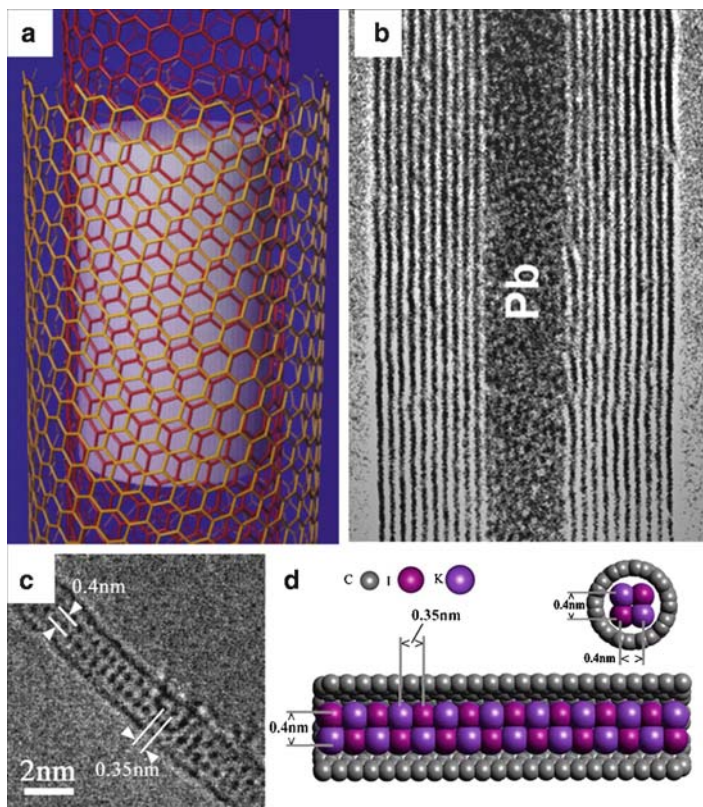


**Fig. 2** (a) Molecular model representing a double-walled carbon nanotube (DWNT) filled with a solid material; (b) HRTEM images of a Pb-filled MWNT (courtesy of P.M. Ajayan) (reprinted with permission from [5]); (c) HRTEM image of a  $2 \times 2$  KI crystal inside a 1.4-nm diameter SWNT; (d) Structural representation of (c) (inset: end-on view – courtesy of J. Sloan) (reprinted with permission from [6], copyright American Chemical Society)

substantially increase the density of free charge carriers (electrons or holes) and thereby enhance the electrical and thermal conductivity in the SWNT bundles.

The intercalated alkali metal atoms (*exohedral doping*) act as an electron donor and this charge transfer weakens the C–C bonds in the SWNTs, as electrons have been known to soften the C–C bond in all  $sp^2$  bonded carbon materials [22, 23]. The acceptor halogens (e.g.,  $\text{Br}_2$ ) were found to stiffen the C–C bonds. This kind of doping is noncovalent, and the carbon nanotube samples can be easily undoped by heat treatments at high temperatures. The atomic structure of the nanotubes is not affected in this process (Fig. 4) but as we will show in next sections the electronic structure is strongly affected.

The exohedral doping can also be covalent, which can modify the nanotube wall to a great extent depending on the concentration of dopant molecules. There are several routes for covalently attaching moieties in the carbon nanotube surface

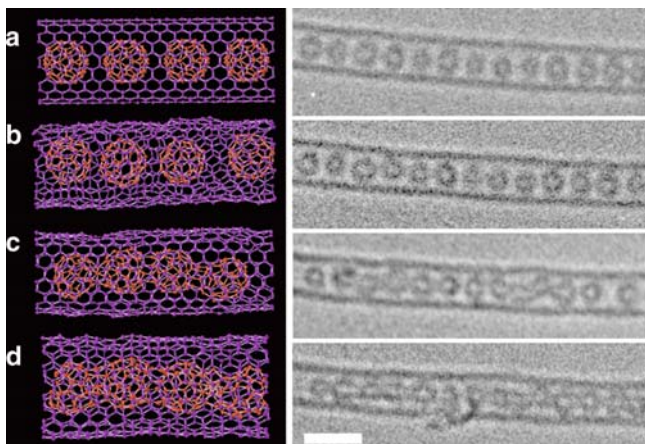


**Fig. 3** Left column: Molecular models obtained during molecular tight binding calculations of C<sub>60</sub>-filled SWNT (also known as fullerene peapods). The simulations show the annealing process of the fullerene molecules. Note that as the molecules merge a DWNT begins to be formed. Right column corresponds to the experimentally observed sequence of a fullerene peapod under electron irradiation at room temperature (scale bar is 2 nm) [20]

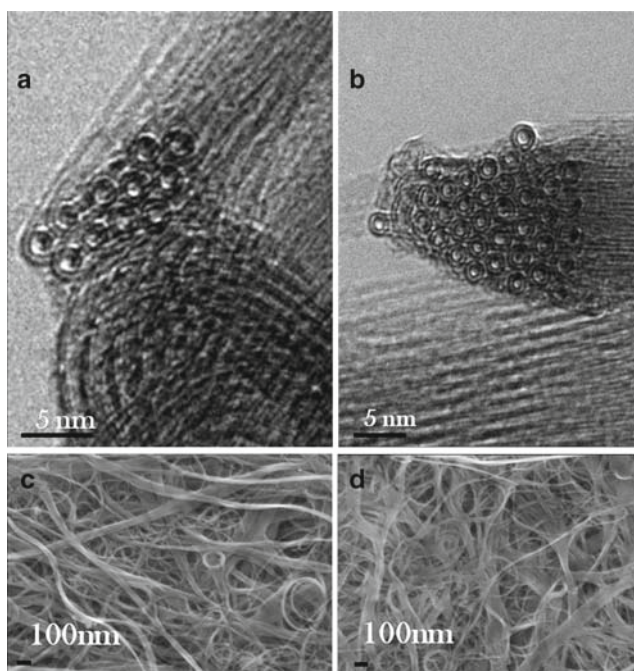


**Fig. 4** High-resolution transmission electron microscope (HRTEM) images of pristine double-wall carbon nanotubes (a) before and (b) after Br<sub>2</sub> adsorption. (c) and (d) show, respectively, scanning electron microscope (SEM) images, for both pristine and Br<sub>2</sub>-doped DWNTs (reprinted with permission from [24], copyright American Physical Society)

but one of the most simple covalent functionalization is the carboxylation of the nanotubes (Fig. 5). The charge plots for the local densities of states coming from the half-occupied levels indicate that charges are mainly located around the functional groups (Fig. 5b) [25]. The carboxylic acid group (COOH) is considered the prototype chemical group for achieving the covalent functionalization of carbon nanotube because the carbon atom is covalently bonded to the tube and the  $-OH$  group can be exchanged by other chemical groups using standard chemical reactions via a coupling agent. This approach allows one to attach more complex molecules such as aminoacids and DNA, and other groups such as amine and amide [26].

Optical absorption spectra of doped SWNT thin films can provide insight into which electronic states are primarily influenced by charge transfer interaction with the dopants. Kazaoui et al. [27] have separately monitored the doping behavior of semiconducting and metallic SWNTs in a combined optical absorption and DC resistance measurement study. Both electron acceptors ( $Br_2$ ,  $I_2$ ) and donors (K, Cs) were used as dopants with controlled stoichiometry. Disappearance of absorption bands at 0.68 and 1.2 eV (assigned to semiconductor SWNTs) and at 1.8 eV (assigned to metallic SWNTs) in pristine SWNTs with a concomitant decrease in the electrical resistance upon doping has been attributed to electron depletion from, or filling to specific bands in semiconducting or metallic SWNTs.

Both structural and electronic properties of the nanotubes are highly affected by substitutional (*in-plane*) doping. In this process one or more heteroatoms are added to the nanotube lattice, thus breaking the translational symmetry of the lattice. Both the number of electrons and the size of the heteroatom play an important role in determining the physical properties (structure, morphology, and electronic) of the doped structures. In the next section we discuss in detail this doping process focusing mainly on B, N, BN, and PN-doped carbon nanotubes.

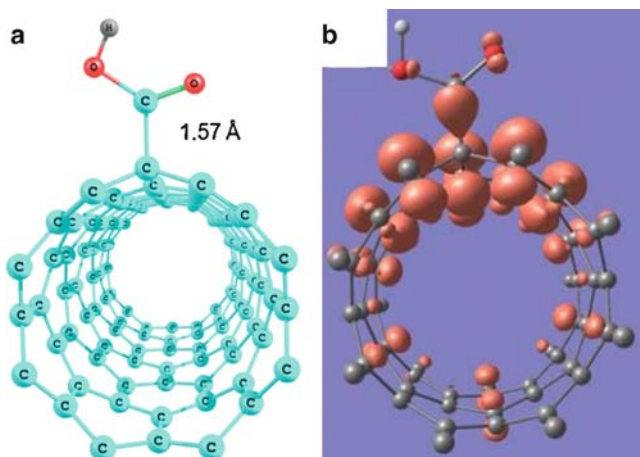


**Fig. 5** (a) Structural configurations and (b) local density of electronic states of the covalent functionalization of carbon nanotube with carboxyl COOH groups [25] (reprinted with permission from [25], copyright Elsevier)



### 3 Boron- and Nitrogen-Doped Carbon Nanotubes

By analogy with graphite, it is possible to replace the atoms from the carbon nanotube walls with elements such as boron, nitrogen, and others [28–36]. The most studied systems are B- and N-doped carbon nanotubes ( $CN_x$  and  $CB_x$ ), as well as the more complex  $B_xC_yN_z$  ternary systems [37].

Because of the quantum confinement and curvature of the carbon cylinders, it is expected that by doping carbon nanotubes novel electronic, mechanical, and chemical properties will result, which should be also different from their undoped counterparts. In particular, substitutional doping of B and N within nanotube lattice will introduce strongly localized electronic features in the valence or conduction bands, respectively, and this will enhance the number of electronic states at the Fermi level ( $E_f$ ) depending on the location and concentration of dopants (Fig. 6a).

The changes in the electronic structure of B-doped carbon nanotubes are basically derived from the fact that Boron has one electron less than C, and its incorporation into the carbon lattice generates sharp localized states below the Fermi level (valence band) (Fig. 6a). These states are caused by the presence of holes in the structure leading the tube to behave as a p-type material. This charge localization suggests that this doped structure would be more likely able to react with donor-type molecules.

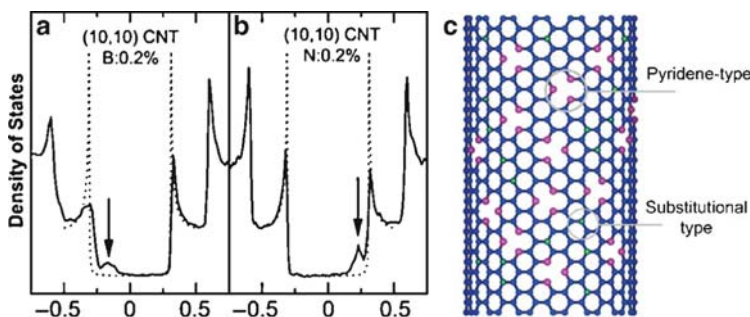


**Fig. 6** Calculated densities of states (DOS) using tight-binding parameters fitted with ab-initio calculation approaches (see [38]) for: (a) an armchair (10, 10) B-doped carbon nanotube (B = 0.2 at.%, solid line) exhibiting a clear peak in the valence band (see arrow), and (d) an armchair (10, 10) N-doped carbon nanotube (N = 0.2 at.%, solid line), in which a sharp and localized peak arises in the conduction band (see arrow). Solid lines correspond to the doped materials whereas dotted lines are related to the pure C nanotubes (undoped). Note that for all cases the presence of B introduced states in the valence band (holes), whereas N injects electrons in the conduction band (donors). Because of the quantum confinement within the nanotube, electrons can only propagate along the nanotube axis, and so their wave vectors point in this direction. The spikes shown in the DOS of the tubules are called “van Hove” singularities and are the typical signature of one-dimensional quantum conduction, which is not present in an infinite graphite crystal (calculations performed by S. Latil). The energy scale is written in units of  $\gamma_0 = 2.9$  eV. (c) Molecular model of N-doped carbon nanotubes, exhibiting two types of Nitrogen: (1) Pyridine-type in which each N atoms are bonded to two carbon atoms, responsible for creating cavities and corrugation in the nanotube structure (see marked area), and (2) substitutional N atoms, which are bonded to three carbon atoms (see marked area)

For N-doped SWNTs, two types of C-N bonds could occur in carbon nanotubes (Fig. 6b). A three-coordinated N atom within the  $sp^2$ -hybridized network induces sharp localized states above the Fermi level due to the presence of additional electrons (Fig. 6b). A two-coordinated N is also possible for doping carbon nanotubes in the pyridine-type substitution where an additional carbon atom is removed from the lattice (Fig. 6b), thus generating localized states below and above the Fermi level. Therefore, substitutional N doping in SWNTs should result in n-type conducting behavior, whereas pyridine-type N may produce either a p- or n-type conductor, depending on the level of doping, the number of N atoms, and the number of removed C atoms within the hexagonal sheet.

When performing a mixing, BN-doped carbon nanotubes could result; the electronic band structure is predicted to be between a semiconducting and an insulating behavior. Different from pristine SWNTs where the electronic band gap is primarily controlled by the diameter and chirality in the BN-doped tubes, the gap could be controlled by chemical composition [37, 39].

To observe genuine quantum effects in doped carbon nanotubes, dopants must be present within SWNTs of narrow diameter ( $<1-2$  nm). In addition, we should point out that a low concentration of either B or N should not alter significantly the mechanical properties and may enhance electron conduction if the number of foreign atoms is less than  $<0.5\%$ . Mechanical properties are also affected by doping. Hernández et al. described the mechanical properties of individual  $CN_x$  and  $CB_x$  nanotubes [40, 41], demonstrating that high concentrations of B and/or N within SWNTs lower the Young's modulus. Interestingly, the Young's modulus still remains in the order of 0.5–0.8 TPa. This phenomenon has been experimentally confirmed in pristine and N-doped MWNTs [42]. In this context, the Young's moduli for pure carbon and N-doped MWNTs are 0.8–1 TPa and  $\sim 30$  GPa, respectively. We believe that the low values observed for N-doped nanotubes are due to the relatively high N concentration (e.g., 2–5%) within the carbon tubes, which introduces defects and lowers significantly the mechanical strength. However, if the N concentration is  $<0.5\%$ , one would expect that the mechanical properties will not be substantially altered.

### 3.1 Phosphorous- and Nitrogen-Doped Carbon Nanotubes

The substitutional doping of the carbon lattice with other chemical elements is also possible. For example, arrays of multiwalled carbon nanotubes (MWNTs) doped with phosphorus (P) and nitrogen (N) (the so-called heterodoping process) were synthesized using a solution of ferrocene, triphenylphosphine (TPP), and benzylamine in conjunction with spray pyrolysis [43]. The iron phosphide ( $Fe_3P$ ) nanoparticles act as catalysts during nanotube growth, leading to the formation of novel PN-doped MWNTs. The PN-doped structures reveal important morphology and chemical changes when compared with N-doped nanotubes. These types of hetero-doped nanotubes are predicted to offer many novel opportunities in the fabrication of fast response chemical sensors. By using similar approaches other chemical elements

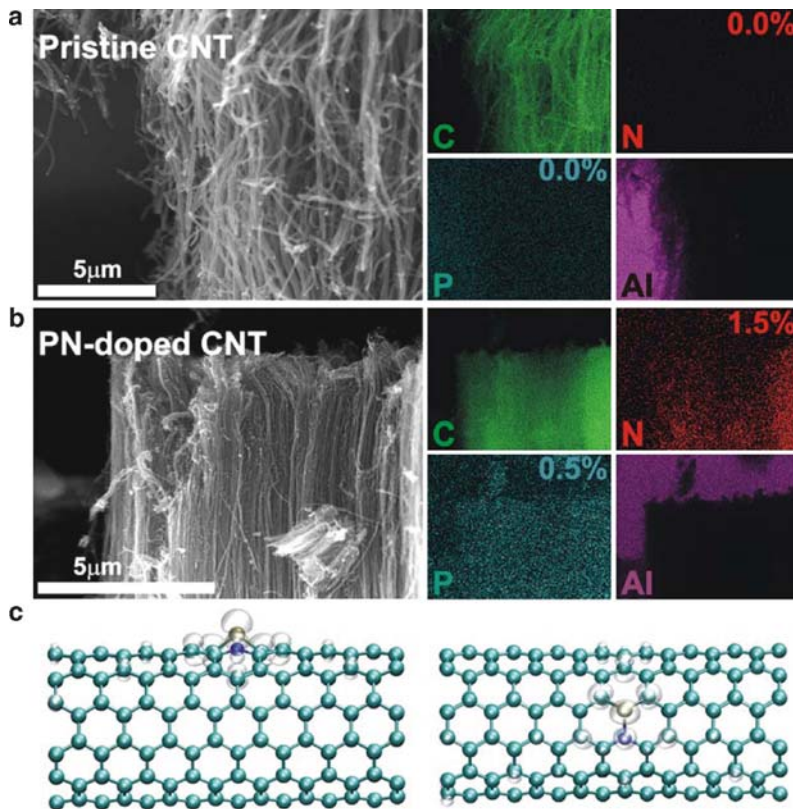


**Fig. 7** (a) EDX elemental mappings for three different types of nanotubes: (a) Pristine pure carbon nanotubes (CNTs) obtained by thermolyzing toluene ( $C_6H_5-CH_3$ ) and ferrocene at  $850^\circ C$  and (b) PN-doped CNTs described in the materials and methods section (see *bottom frame*). Samples were mounted on standard aluminum pins in order to have contrast for the carbon map. It can be clearly observed that the PN samples contain both phosphorus and nitrogen in their structure, thus confirming the successful synthesis of PN heteroatomic doping. (c) Molecular model of a (6,6) PN-doped carbon nanotube in the most stable configuration. Two carbon atoms are removed for accommodating the P–N defect (adapted from reference 43)

can be used for in-plane doping. The PN-doped samples were examined by high-resolution electron microscopy and microanalysis techniques as shown in Fig. 7a, b. Theoretical calculations have pointed out that the most stable structure is to have a P–N defect incorporated into the carbon lattice as shown in Fig. 7c.

### 3.2 Preparation of Substitutionally Doped Carbon Nanotubes

The synthesis of doped carbon nanotubes is performed using processes far from the thermodynamical equilibrium. Basically, there are two approaches used for obtaining doped tubes: the *direct synthesis* and *postsynthesis exchange reactions* methods.

The former process consists of using carbon sources containing the dopants and the second makes use of chemical exchange reactions for replacing carbon atoms with other species in the already formed carbon nanotubes. Later, we briefly describe these methods.

### 3.2.1 Direct Synthesis (Single-Step Processes)

*Arc Discharge Method.* B-doped MWNTs could be produced when arcing either BN/graphite or B/graphite electrodes in an inert atmosphere such as He and N<sub>2</sub>. Large amounts of crystalline and long MWNTs ( $\leq 100 \mu\text{m}$ ) could be obtained. In some cases, ill-formed caps containing B occasionally open or exhibit negative curvature regions [44–46]. In contrast, the production of B-doped SWNTs using this technique is difficult because B appears to frustrate the tubule growth. Arc experiments using pure graphite electrodes in a NH<sub>3</sub> atmosphere indicate that it is also difficult to produce N-doped SWNTs and MWNTs, possibly because N<sub>2</sub> molecules are easily created and do not react with the carbon [47]. Glerup et al. [48] reported the possibility of growing N-doped SWNTs by arcing composite anodes containing graphite, melamine, Ni, and Y. These authors also revealed using EELS that the tubes possess low concentrations of N (<1%), and sometimes the tubes are corrugated due to the presence of N atoms in the hexagonal network. The authors claim that EELS is able to detect low concentrations of dopants (e.g., 0.1%). This is mainly because the spectrometer used is very sensitive and unique. However, additional arc discharge experiments and more detailed characterization should be carried out.

*Laser Ablation.* Zhang et al. [49] were the first to report sandwich-like C-BN nanotubes by laser vaporization of graphite–BN targets. These researchers showed evidence of BC<sub>7</sub>N layers within the MWNTs as well as areas of segregated B and C. Subsequently, Rao and colleagues [50] demonstrated that it is possible to generate B-doped SWNTs using laser vaporization of B–graphite–Co–Ni targets. The authors characterized the samples using HRTEM and EELS and found SWNTs in the products when the B content in the target material was less than 3 at.%. For higher B concentrations in the graphite target (e.g., >3.5 at.%), graphite and metal encapsulated particles were mainly generated and only low quantities of SWNTs were obtained under these conditions. It may be possible that more energetic lasers (e.g., CO<sub>2</sub> lasers, femtosecond lasers, etc.) should also be tested to generate either N- or B-doped SWNTs using this technique.

*Chemical Vapor Deposition.* The thermal decomposition of N-containing hydrocarbons over metal particles (e.g., Fe, Co, Ni) results in the formation of N-doped MWNTs or CN<sub>x</sub> nanotubes. The first report on the formation of aligned arrays of N-doped MWNTs (<1–2%) involved the pyrolysis of aminodichlorotriazine over laser-etched Co thin films at 1,050°C [51]. Subsequently, the use of melamine (triaminotriazine) as a CN precursor resulted in an increased nitrogen content (<7%) within “corrugated” carbon tubular structures [52]. These results indicated that it is very difficult to produce crystalline and highly ordered structures containing large concentrations of N within the hexagonal carbon lattice. CN<sub>x</sub> nanotubes with

low nitrogen concentrations were subsequently generated via pyrolysis of pyridine and methylpyrimidine [53]. Unfortunately, these  $CN_x$  MWNTs are easily oxidized (e.g., combustion sets in at ca. 450°C in air, whereas pure carbon tubes do not burn in air below ca. 700°C) [53]. The degree of perfection within graphene sheets is highly dependent upon the nitrogen concentration (i.e., the lower the nitrogen content, the more “graphitic” and the straighter the nanotubes become). It is also important to note that the morphology of N-doped MWNTs exhibits a bamboo-type.

Keskar et al. have prepared isolated N-doped SWNTs from a thermal decomposition of xylene-acetonitrile mixture over nanosized Fe catalyst particles [54]. The N-dopant concentration is controlled by the amount of acetonitrile in the mixture [54]. Very recently, long strands of N-doped SWNT bundles (Figs. 8 and 9) were successfully produced by pyrolyzing ferrocene/ethanol solutions containing small weight ratios of benzylamine (e.g., from 1 to 22 wt% in ethanol) at 950°C in an Ar atmosphere [55]. These authors demonstrated that the electron conduction of the

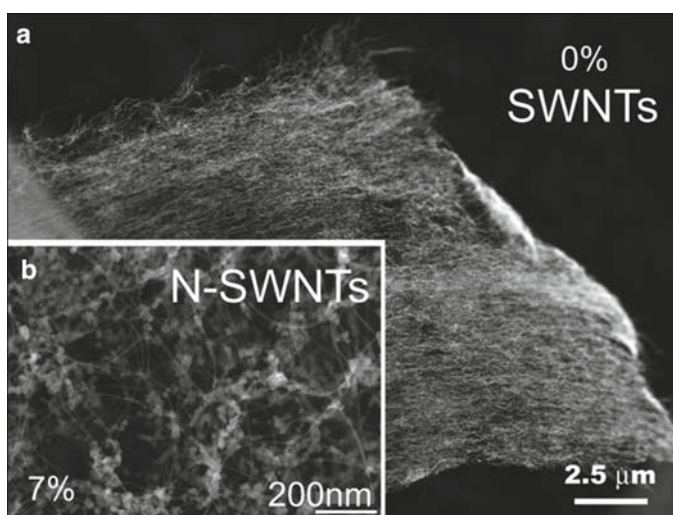


**Fig. 8** Scanning electron micrographs of SWNT strands synthesized with (a) 0 wt% and (b) 7 wt% nitrogen precursor (benzylamine) in the ferrocene:ethanol:benzylamine (FEB) solution (adapted from reference 55)

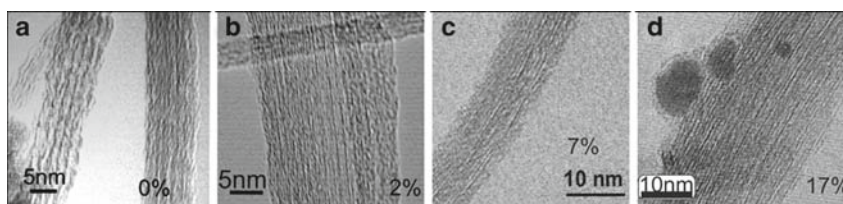


**Fig. 9** Transmission electron micrographs of samples with (a) 0%, (b) 2%, (c) 7, and (d) 17% nitrogen precursor (benzylamine) in the FEB solution (adapted from reference 55)

N-doped SWNT ropes is very different from that of pure carbon SWNTs, especially at temperatures lower than 20 K [55]. It is important to note that N-doped SWNTs do not usually exhibit the bamboo-type morphology, and it is believed that either B- and N-doped SWNTs contain mainly substitutional-type doping, and in lower concentration when compared with MWNTs. The latter is because the single-shell cylinders would collapse (would not grow) if a large amount of foreign atoms are being introduced into the hexagonal carbon lattice.

From HRTEM, Raman spectroscopy, and TGA analysis, common features that arise when doping SWNTs with N are: (a) As the N content increases, the diameter of SWNTs decreases and only narrow diameter tubes are formed (Fig. 10), (b) the tubes oxidize faster than the pure C counterparts, (c) corrugation within the tube walls is sometimes observed (in this case not damaged by the electron beam) and fullerene-like structures are formed inside the cores of the N-doped SWNTs (Fig. 10d), (d) on rare occasions, bamboo-like SWNTs could be observed (see arrows in Fig. 10e). The tube bundles appear to be more easily dispersed following sonication treatments when compared with pure C SWNTs (e.g., N-doped SWNTs dispersed faster than pure C SWNTs with 2-propanol as a solvent; the latter required twice as long to be dispersed. This is also true for MWNT), and (f) the entanglement of the nanotube strands is reduced as the N content is increased.

To understand the role of N atoms during nanotube growth at the synthesis temperatures, first-principles molecular dynamics have been performed [56].

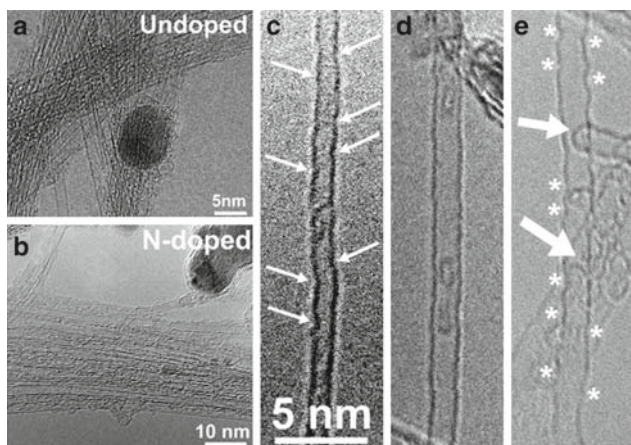


**Fig. 10** HRTEM images of N-doped SWNTs produced by the pyrolysis at 950°C of a ferrocene:benzylamine:ethanol solution with a composition ratio of 1.25:7.5:91.25 by weight: (a–b) SWNT bundles showing that N-doped tubes exhibit more compacted bundles of narrow diameter tubes. (c) N-doped SWNT of narrow diameter (ca. 1 nm) exhibiting some degree of corrugation. (d) N-doped SWNT of 1.4 nm in diameter exhibiting fullerene-like structures in its core (possibly N-doped fullerenes that resulted from the frustrated growth of the inner tubules; see *arrows*); and (e) highly corrugated N-doped SWNT of large diameter (1.7 nm) exhibiting internal bamboo-like closures (see *arrows*) as well as a symmetric tubule cap (see *arrows*) (adapted from reference 43)

The results showed the rapid formation of pentagons (pentagons form within 1 ps, notable in the decreased diameter, and persist throughout the entire simulation) at the growing rim, which results in the subsequent inward bending of the edge structure, leading to a defected graphitic dome and partial closure of the tubule. Figure 11 depicts snapshots of the dynamics and the time dependence of the average tube rim diameter when N atoms are substituted at the two-coordinated sites of the tube rim. After 4 ps of dynamics at 2,500 K, no stable pentagons have formed at the edge and those that did form during the simulation as a result of an atomic N–N bridge across the tube end ( $t = 0.163$  ps) were relatively short-lived ( $<0.1$  ps). Also, it clearly causes a decrease in the local diameter. This suggests that the N atoms remain included in the nanotube lattice of narrow diameter tubes.

With this experimental information at hand together with first-principles statics and dynamics calculations, Sumpter et al. [56] demonstrated that nitrogen mediates the growth of SWNTs by acting as a surfactant and leads to narrow diameter doped tubules. The authors also showed that the tube closures, which includes N atoms embedded in the carbon lattice, are also preferred, thereby suggesting that the presence of morphologies such as bamboo structures can be triggered by the presence of N dopants. The inclusion of N inside the tube lattice leads to weaker tube–tube interactions as well as providing sites where encapsulated or intercalated N can undergo chemical reaction, which may form smaller fullerene structures that become encapsulated within the compartment. Metallic tubes were found to be

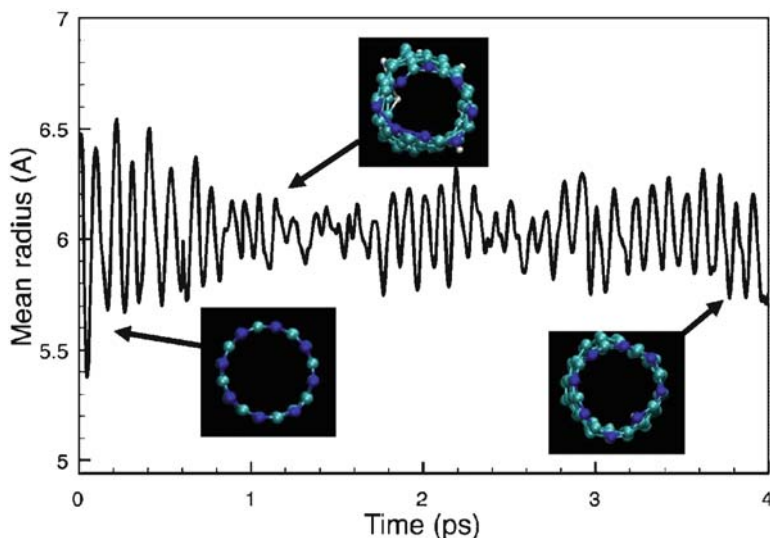


**Fig. 11** Time dependence of the diameter for a N-doped (8,0) SWNT (*top*) (N atoms on the rim at the two coordinated sites). The results are taken from the first-principles MD simulation at 2,500 K. The inserts show snapshots of the structure for the N-doped (8,0) SWNT at  $T = 0$ , 0.163, and 4 ps taken from the quantum molecular dynamics simulations [56]

somewhat more energetically stable for N-doping, a behavior that has the potential to favor sample enrichment.

Although some work has been carried out for producing N-doped SWNTs, further research on the synthesis of substitutionally doped SWNTs using this CVD technique needs to be carried out.

It is expected that by using B-containing organic precursors (e.g., boranes, boric acid, etc.) in conjunction with hydrocarbons and metal catalysts (e.g., Fe, Co, Ni), MWNTs doped with B could be produced. However, there is still an enormous amount of experimental work to be carried out to enable control of the B or N content or both BN as well as the nanotube structure using the CVD approaches.

*Spray-pyrolysis technique.* PN-doped carbon nanotubes were prepared using as precursor a solution composed of benzylamine  $C_6H_5-CH_2-NH_2$  (Sigma 99%) as carbon and nitrogen sources, ferrocene  $Fe(C_5H_5)_2$  (Sigma, 98%) as catalyst, and triphenylphosphine  $P(C_6H_5)_3$  (Sigma, 99%) as the phosphorus source. The precursor was atomized using an aerosol generator and carried by an inert gas flow (argon) inside a quartz tube with an inner diameter of ca. 24 mm, which was placed inside a two-stage furnace system. This spray pyrolysis technique is similar to that described by Pinault et al. [57] and Kamalakaran et al. [58]. The nanotubes were collected from the soot deposited on the surface of the quartz tube in the region located inside the furnace. The scanning electron microscopy (SEM) of PN-doped samples is shown in Fig. 12. It was observed that for a given synthesis temperature, and by increasing the phosphorus content in the solution, a considerable reduction in the yield of carbon nanotubes was observed [43].

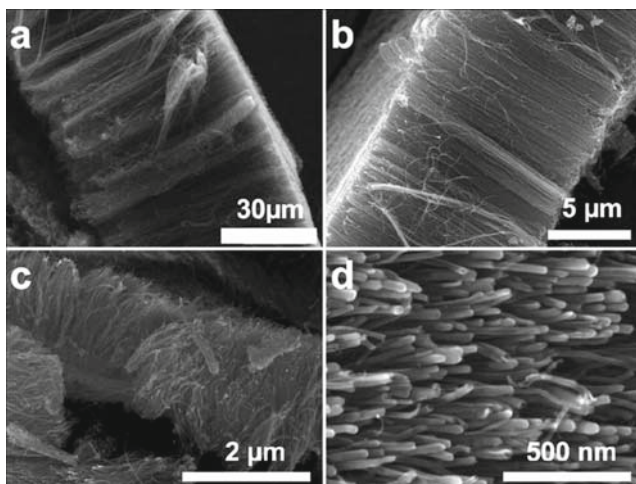


**Fig. 12** Scanning electron micrographs of PN-doped carbon nanotube (CNT) arrays, synthesized at optimum temperature and carrier gas flow rate and different TPP concentrations. (a) Pristine N-doped CNTs (sample A); (b) 2.5 wt% TPP (sample B); (c) 3.3 wt% TPP (sample C); (d) Substrate side of a PN-CNT mat (sample B; adapted from reference 43)



*Plasma-assisted CVD.* The microwave plasma-enhanced chemical vapor (PECVD) deposition technique has been used to produce large areas of aligned N-doped MWNTs [59–61]. These experiments involve catalytic particles of Fe and/or Ni dispersed on silica substrates. During growth at 500°C, acetylene or CH<sub>4</sub> and N<sub>2</sub> or NH<sub>3</sub> can be used. For producing B- or BN-doped MWNTs, other gases such as B<sub>2</sub>H<sub>6</sub> in conjunction with H<sub>2</sub>, and CH<sub>4</sub> could be used as a reacting gas in the PECVD process [62]. However, these methods have not yet been exploited to produce substitutionally doped SWNTs.

### 3.2.2 Postsynthesis Methods

*B and N exchange reactions.* B- and N-doped SWNTs can also be produced using partial substitution in the presence of B<sub>2</sub>O<sub>3</sub> vapor and N<sub>2</sub> at 1,500–1,700 K [63]. In these experiments, B-doped tubes exhibited a B/C ratio of <0.1. However, lower amounts of N (N/C < 0.01) were also incorporated within the hexagonal framework. In contrast to B-doped MWNTs, SWNTs do not exhibit preferred chiralities, possibly because the dopants only substitute individual C atoms within the framework, thus preserving the tubule chirality. It is noteworthy that either B- or N-doped SWNTs have a corrugated surface, which could be attributed to defects created on the C surface or to electron irradiation effects (Fig. 13).

Borowiak-Palen et al. have also published the synthesis of B-doped SWNTs with high concentrations of B [64], in which 15% of the C atoms are replaced by B. These experiments were carried out by heating B<sub>2</sub>O<sub>3</sub> in the presence of pure C SWNTs and NH<sub>3</sub> at 1,150°C. However, additional experiments and further studies on these and similar samples should be conducted because the reported amount of B seems to be high when compared with the solubility of B found in graphite and MWNTs (<2 wt% B).

The synthesis of B-doped DWNTs was also done by annealing powders together with pure DWNTs at different temperatures (ranging from 1,200 to 2,600°C;

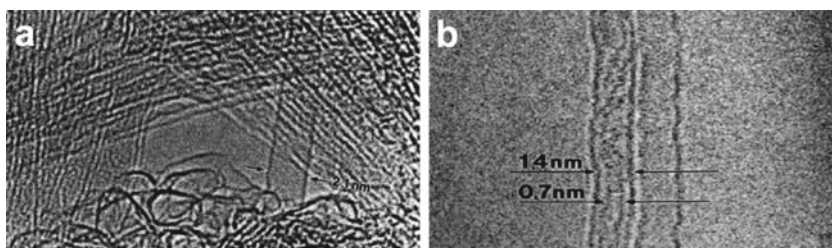


**Fig. 13** (a) HRTEM image of a N-doped SWNT bundle synthesized at 1,533 K over 240 min by reacting N<sub>2</sub>, B<sub>2</sub>O<sub>3</sub> with SWNT bundles of 1.4-nm diameter. Note the isolated SWNT exhibiting a diameter of 2.1 nm, and (b) HRTEM image of a two-tube B-doped bundle synthesized at 1,503 K over 240 min by reacting N<sub>2</sub>, B<sub>2</sub>O<sub>3</sub> with SWNT bundles. The left-hand tube exhibits a SWNT with an inner shell ( $d = 0.7$  nm) formed inside the outer shell ( $d = 1.4$  nm) (courtesy of D. Golberg)

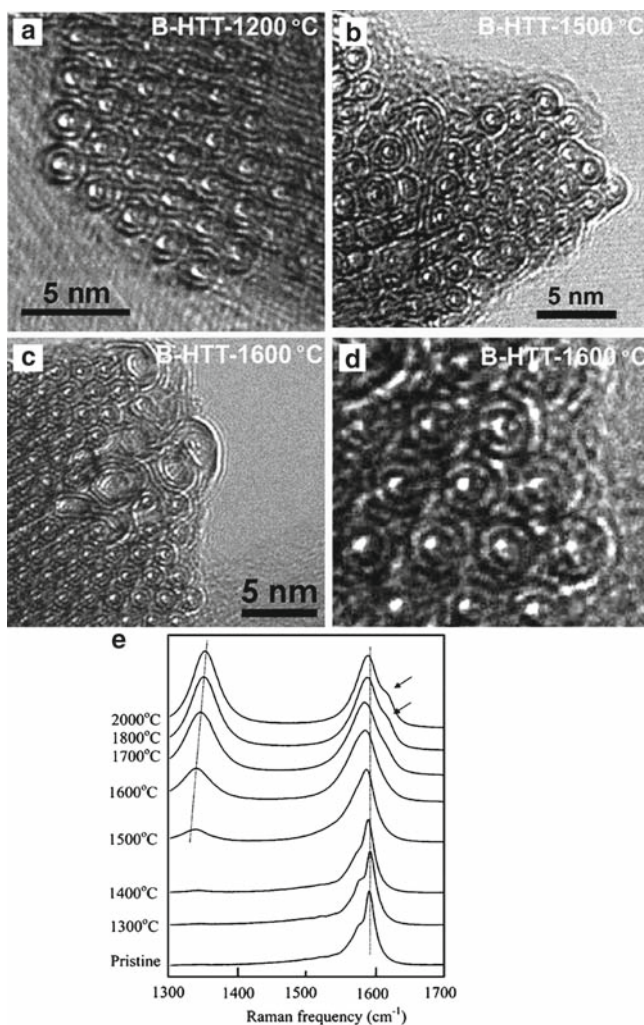


**Fig. 14** High-resolution TEM image of DWNT bundles annealed together with B powder at (a) 1,200°C, (b) 1,500°C, and (c–d) 1,600°C. Note that a coalescence reaction between the adjacent two or three DWNTs starts at 1,500°C with the help of elemental boron addition, which acts as an atomic welder. (e) High-frequency Raman spectra of B-doped DWNTs heat-treated at temperatures ranging from 1,300 to 2,000°C. When B gets incorporated in the tube wall the D-band increases in intensity (adapted from reference 65)

Fig. 14) [65]. After 1,600°C, B gets incorporated into the carbon lattice as can be clearly seen on the rising of the defect-induced D mode in the Raman spectra as shown in Fig. 14e. B served as an efficient trigger for coalescing nanotubes under thermal treatment. Theoretical work showed that interstitial B atoms function as atomic welders and eventually get incorporated into the tube lattice.

## 4 Properties and Applications of Doped Carbon Nanotubes

### 4.1 Structural Properties

The most useful techniques to study the structure and morphology of MWNTs, DWNTs, and SWNTs are as follows: (a) high-resolution transmission electron microscopy (HRTEM), (b) SEM, and (c) scanning tunneling microscopy (STM). To determine the overall crystalline structure of bundles of carbon nanotubes, X-ray powder diffraction (XRD) becomes a powerful route. Electron diffraction (ED) has also proven useful in determining the chirality of tubes (the orientation of the hexagonal rings along the tube axis: zigzag, armchair, or chiral).

To estimate the dopant concentration within SWNTs, DWNTs, and MWNTs, analytical techniques associated with HRTEM can be used. In this context, electron energy loss spectroscopy (EELS) becomes a useful and powerful tool to determine the stoichiometry of elements in individual nanotubes, as well as the nature of the chemical bond. Similarly, X-ray photoelectron spectroscopy (XPS) could be used to determine stoichiometries of elements and their corresponding binding energies. However, these techniques are generally only accurate and sensitive to elements, when concentrations are above 1 at.%. Therefore, Raman spectroscopy, which is sensitive to the incorporation of foreign elements, may provide an efficient route to determine dopant concentrations lower than 0.1 at.% in SWNTs and MWNTs (see later). The technique may require significantly more development before a quantitative evaluation of the dopant concentration can be determined accurately.

The  $CN_x$  tubular structures produced using the CVD process present unusual stacked-cone or compartmentalized morphologies (bamboo-type), and the degree of tubular perfection decreases as a result of the N incorporation into the carbon lattice. The EEL data indicated two bonding types between N and C, within the hexagonal network: (1) *highly coordinated N atoms* replacing C atoms within the graphene sheets (ca. 401–403 eV), and to *pyridinic-type nitrogen* (ca. 399 eV; Fig. 6). It has been found that as the *overall* N content increases within these structures, the number of graphitic walls within the nanofibers decreases and the proportion of pyridine-like N increases (remaining almost constant with the three-coordinated N atoms). From EEL and XP spectra, it has been estimated that the N content within the tubes is ca.  $\leq 10\%$ , commensurate with  $C_9N_x$  ( $x \leq 1$ ) stoichiometries.

More recently, Koziol et al. [66] reported an astonishing result, which consists in the production of highly crystalline thick MWNTs with three-dimensional order (the concentric cylinders adopt the crystal structure of perfect graphite). These tubes were produced using a CVD process involving the thermolysis of toluene/1,4-diazine ( $C_7H_8/C_4H_4N_2$ ) solutions containing 2 wt% ferrocene ( $FeCp_2$ ) under an Ar atmosphere at 760°C. Interestingly, the tubes contain 3% nitrogen, but very differently to previous N-doped nanotubes they exhibit an extremely high crystallinity, which is very similar to that of 3-D graphite. Subsequent studies confirmed that these samples were indeed highly crystalline [67], and N, which seems to be responsible for the dramatic structural order, was found to segregate preferentially

within the core of the nanotubes. Therefore, researchers should try to test these novel 3D ordered MWNTs and demonstrate that they are capable of exhibiting enhanced performance when compared with conventional corrugated N-doped MWNTs. We still need to understand nanotube growth but doping appears to be an alternative route to enhance graphitization at relatively low temperatures using CVD approaches.

*Atomic structure of B-doped MWNTs.* These tubes are mainly produced using the arc discharge method because in CVD technique, the B precursors tend to frustrate the nanotube growth at temperatures below 900°C. As mentioned earlier, the arc-produced B-doped MWNTs are extremely long (<100  $\mu\text{m}$ ) and usually exhibit open or ill-formed caps. These caps appear to contain higher B concentrations (as revealed by EELS analyses), thus suggesting that B acts as a catalyst in the formation of long tubules. Although it has been difficult to determine the correct binding energy for B using either EELS or XPS on these systems, it is likely that substitutional B (three-coordinated) is incorporated in the hexagonal C lattice. In this context, careful EELS studies (using first and second derivative spectra) have shown that minute B traces (<1%) are present within the body of tubules [68]. Electron diffraction studies have shown that these long B-doped CNTs exhibit a preferred *zigzag* or *near zigzag* chirality (e.g.,  $\text{zigzag} \pm 3^\circ$ ) [69, 70]. Static and dynamic *ab initio* and *tight binding* calculations carried out by Blase et al. and Hernández et al., respectively [69, 71], demonstrated that B atoms act as a surfactant during the growth of long tubes and inhibit tube closure during its formation. Therefore, in-plane doping during nanotube growth may well control the tube chirality.

Bulk XRD studies on B-doped MWNTs reveal the presence of highly ordered three-dimensional graphite crystals, attributed to *ABA...* stacking. This observation has never been observed in conventional pure carbon MWNTs and nanoparticles. From the (00l) reflections (caused by the presence of parallel layers), two different *average* interlayer spacings were observed in these samples (Fig. 15). It was proposed that one family of these spacings correspond to standard CNTs/nanoparticles (ca. 3.4 Å) and the other type of spacing to AB-stacked graphite (ca. 3.35 Å). The AB stacking observed in nanotubes could arise from concentric B-doped *zigzag* tubes exhibiting *ABA...* stacking or flattened tube domains (also confirmed by the interlayer spacing irregularities) [37].

*Atomic structure of doped SWNTs.* The structure of SWNT bundles doped with B and N has been recently reported [50, 55, 72]. However, it was difficult to observe clear morphological changes on the doped tubules when compared with their undoped counterparts. For B-doped SWNTs, continuous tubules were also produced, and B coordinated to three carbon atoms are expected [72].

TEM observations of N-doped SWNTs revealed tube diameters around 1.6 nm, a result that is also consistent with the Raman measurements [55]. Interestingly, as the N-containing precursor (benzylamine) was added in the CVD solution, the resulting tubes exhibited narrower diameters (e.g., 0.8 nm). It is also important to mention that in these materials, it was difficult to detect traces of N using EELS or XPS. This is because levels below 1–2% of N are below the detection limit of these instruments. For this reason, it is very important to conduct Raman spectroscopy

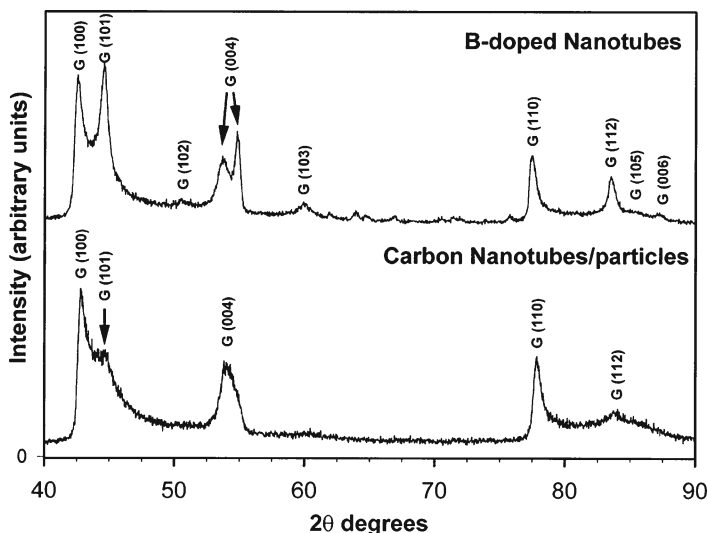


**Fig. 15** XRD patterns from the inner core deposits obtained from the BN/graphite arc discharge experiments compared with pure MWNTs and nanoparticles produced using the arc discharge technique. The pattern from 40–90  $2\theta$  degrees clearly shows the high degree of crystallinity of the B-doped sample [note the (101), (103), and (112) reflections, which denote a three-dimensional order and a ABAB stacking of the layers]. Also note that the (00l) reflection exhibits two peaks corresponding to 3.35 and 3.42 Å, thus confirming the presence of two different “graphitic” structures (graphite-like ABAB... possibly from faceted areas of polygonized nanotubes and turbostratic graphite arising from concentric graphene cylinders – MWNTs; adapted from reference 37)

measurements, TGA analysis, and four-probe electrical conductivity measurements (see later), and in each of these techniques clear changes in the structure as well as differences in the electrical response and reactivity of the N-doped SWNT strands, as a function of the N content, were observed.

For B- and N-doped SWNTs, it was noted that as the B or N content was increased in the laser target or the precursor solution, respectively, the production of SWNTs was inhibited. Therefore, only low concentrations (below 2% wt) of dopants could be embedded in the hexagonal cylinders.

Chirality determination of doped SWNTs and bundles using electron diffraction has been difficult to carry out, and novel techniques to determine the chirality of individual SWNTs are being developed.

## 4.2 Electronic and Transport Characterization

Microwave conductivity studies on bulk B-doped MWNTs (produced using the arc discharge method) reveal that these structures are intrinsically metallic [73], differing from standard pure CNTs, which show thermally-activated transport. Subsequently,

Carroll and coworkers detected for the first time characteristic peaks in the density of states (DOS) using scanning tunneling spectroscopy (STM) on B-doped MWNTs produced using the arc method [74]. The peaks that appeared in the valence band were caused by the introduction of B (which acts as an acceptor) in the carbon lattice. These authors suggested that  $BC_3$  islands, distributed within the tubules, alter significantly the local density of states (LDOS) from a semimetal to an intrinsic metal. The results were confirmed using ab initio calculations, indicating that the changes in the electronic structure are mainly due to the presence of dopant-rich islands and not due to isolated substitutional B atoms.

STM and STS studies have revealed that N-doped MWNTs are metallic and exhibit a characteristic peak in the conduction band DOS. For pure CNTs, the valence and conduction band features appear to be symmetric about the Fermi level, whereas for the N-doped MWNT an additional electronic feature occurs at ca. 0.18 eV. This result is in contrast to the B-doped case [75]. It is noteworthy that the electron donor feature observed in the N-doped material is always seen all along the doped nanotubes. Therefore, both two- and three-coordinated N (substitutional and pyridinic, respectively), randomly distributed within armchair and zigzag CNTs, should lead to these prominent donor peaks close to above the Fermi energy (at ca. 0.18 eV). Careful ab initio calculations are now underway to explain the exact type of C–N bond within the tubes. It has been demonstrated that  $CN_x$  nanotubes exhibit a metallic-like behavior [76].

Electronic transport measurements on individual B-doped MWNTs reveal a metallic behavior above 30 K, due to an enhancement in conduction channels without experiencing strong back scattering [77]. In addition, the  $dI/dV$  vs.  $V$  curves of MWNTs exhibit a small peak close to the Fermi level,  $E_F$ , which is associated with the presence of acceptor states caused by  $BC_3$  islands. At lower temperatures, the resistance starts to increase. The results suggest that B-doping induces a p-type behavior within MWNTs [77].

Four probe measurements carried out in long strands of pure carbon SWNTs and N-doped SWNTs have been reported recently [55]. The undoped SWNT sample (0% N) showed a semiconducting behavior over the whole temperature range; the conductivity decreased exponentially with temperature.

However, for strands of SWNTs containing different nitrogen precursor concentrations (0%, 2%, 13%, and 26%), the relative conductivity ( $r/r_{RT}$ , where  $RT$  refers to room temperature = 300 K) at very low temperatures is higher as the dopant concentration is increased. In contrast to the pristine case, the conductivity of the doped samples did not continue dropping all the way to 0. In addition, and according to the fitting results, the DOS has been comparatively enhanced at similar energy levels.

In this study it was remarkable to observe that below a certain temperature, the nitrogen-doped samples did not continue to show the original decrease in conductivity. In the case of the 23% N sample, the conductivity stopped decreasing as the temperature dropped below 30 K. The authors mentioned that it was unlikely that the mechanical stability of the electrical contacts was the cause for this behavior. However, as the doping level increases, ionized impurity scattering cannot be ignored. In this context, Latil et al. [38] performed calculations on B- and N-doped

nanotubes and reported that the mean free path of charge carrier decreases (increases) linearly with dopant concentration (tube diameter) at low doping levels. These authors also demonstrated that the electron conduction could also be enhanced if the amount of foreign atoms is less than 0.5%. The latter suggested that below 13% of benzylamine in the FEB solution, N-SWNTs with less than 0.5 wt% of N (not detectable by TEM analytical techniques) could be produced. Above 13% of benzylamine in the FEB, the generation of tubes with larger concentrations of N arises, and this creates enhanced quantum interference effects within the tubes, so that the electrical conduction starts to decrease.

In future, additional and careful electron conductivity measurements should be carried out. One should also bear in mind that this method could be very efficient in detecting low-dopant concentrations within nanotubes. However, low-temperature measurements should be conducted to observe any electron conductance enhancement. We believe that the electronic transport of doped DWNTs and SWNTs will be intensively studied in the near future.

Electron spin resonance (ESR) studies have also confirmed the intrinsic metallic behavior of bulk B-doped MWNTs [78]. In particular, a  $g$ -value of 2.002 at room temperature has been observed for B-doped nanotubes whereas the typical value for pure CNTs is 2.0189. Furthermore, superconducting quantum interference device (SQUID) measurements have demonstrated that the bulk material is paramagnetic (standard carbon tubes are strongly diamagnetic), exhibiting a weak temperature dependence of the magnetization commensurate with a metallic response.

Thermoelectric power measurements (TEP) are sensitive to the carrier sign and they have been carried out on mats of B- and N-doped MWNTs [79]. These studies indicate that the TEP of B-doped MWNTs is positive, thus indicating hole-like carriers. In contrast, the N-doped tubes exhibit negative TEP over the same temperature range, suggesting electron-like conduction [79]. These results could be correlated to the DOS for B- and N-doped MWNTs. It is important to note that as-produced *pure carbon* MWNTs exhibit positive TEP, which has been attributed to the presence of oxygen dopants within the tube mats. If the sample is left in vacuum for 94 h, the TEP signal decreases considerably [79]. In this context, it is important to note that TEP studies for SWNTs have been able to indicate clearly alkali metal intercalation [80] and O contamination (or doping) [81]. Recently, Rao and coworkers [72] demonstrated that B-doped SWNTs (produced using the laser technique) display positive TEP values, thus implying the presence of holes (as for B-doped MWNTs). One should emphasize that these clear changes in the TEP occurred for very low B concentrations (e.g., 0.05–0.1 at.% B), too low to be detected with EELS or XPS. Therefore, TEP measurements are extremely sensitive to low doping levels of B (or N) within SWNTs and MWNTs.

It is clear that thermal conductivity measurements on B- and N-doped carbon nanotubes with different dopant concentrations also need to be performed. By changing the doping level, the electronic and thermal properties would vary drastically, since the conductivity of undoped nanotubes is dominated by the lattice. Further studies of B-doped SWNTs and B- (N-) doped DWNTs need to be performed to elucidate the transport characteristics of these doped 1D systems.

Carbon nanotubes are amphoteric [ability to accept (donate) electrons from (to) dopant species] materials as unveiled by Raman scattering [23] and electrical resistivity data [82]. Lee et al. [82] found that room-temperature resistance decreased by several orders of magnitude in potassium-doped SWNT bundles relative to pristine bundles.

### 4.3 *Vibrational Properties (Resonant Raman Spectroscopy)*

Raman spectroscopy is a well-established and widely used technique for characterizing carbon nanotubes, being capable of providing information more than other available techniques. This spectroscopy allows one to readily probe the structural, vibrational, and electronic properties of single-walled, double-walled, or MWNTs [83–87] and is sensitive to the environment in which the nanotube resides – isolated, bundled, or doped forms. The low dimensional (1D) nature of carbon nanotubes lends its distinct Raman features that are significantly different from those exhibited by other forms of carbon. The Raman spectra for SWNTs and DWNTs contain four important Raman features as follows [88]: (1) The radial breathing mode (RBM) in which all carbon atoms vibrate in phase in the radial direction of the nanotube. Its frequency  $\omega_{\text{RBM}}$  is related to the nanotube diameter  $d_t$  as  $\omega_{\text{RBM}} \sim 1/d_t$ . (2) The tangential G-band, which is derived from the in-plane Raman-active mode present in graphite at  $\sim 1,580 \text{ cm}^{-1}$  and its line shape for a semiconducting SWNT, is very distinct from that of a metallic SWNT [89]. Detailed analysis of these line shapes are important for studying doping-induced changes in the vibrational and electronic properties of carbon nanotubes [90]. (3) The disorder-induced D-band that is associated with any defect that breaks translational symmetry, and (4) its second-order harmonic, the G'-band. The bands labeled M and iTOLA are second-order modes originating from double resonance process. Their frequency depends on tube geometry and its physics is clear for isolated tubes. In bundled samples they carry out the averages over many tubes and their relatively weak intensities somewhat prevent their use as a probe for studying carbon-doped systems. The Raman spectra in carbon nanotube is mediated via a resonance process in which the energy of the incident or scattered photon matches interband transition energies  $E_{ii}$  [88].

The dopant-induced interactions (whether it is an inorganic species such as an alkali metal donor or a halogen acceptor, or an organic polymer chain or a DNA strand, or a substitutional atom such as B and N) will perturb the Fermi level of the nanotube through charge-transfer effects. Since electrons and phonons are strongly coupled to each other in resonance Raman spectroscopy, these perturbations will influence the various Raman modes present in carbon nanotubes, similar to what has been observed in the  $sp^2$  hybridized carbon (graphite) intercalation compounds [22]. Doping of carbon nanotubes with electron donors or electron acceptors is a very active field, and much effort has been dedicated for understanding and controlling the electronic properties of SWNTs [91–93]. Next, we discuss some clear examples on how this technique is used for probing modifications of the nanotube surface, such as by the introduction of surface species and the charge-transfer



effects resulting from the doping. Bundles of SWNTs or DWNTs offer at least three different sites where dopant atoms/molecules can reside without substituting the carbon atoms in the nanotube cage with dopant atoms. These sites are schematically shown in Fig. 1. If the end caps of the tubes in a bundle are opened, the dopant may reside inside the tubule cores. These sites are called the endohedral sites. Regardless of the endcaps being opened or closed, the interstitial sites and groove sites are always accessible. In the case of substitutional doping, the dopant atoms substitute for the carbon atoms in the framework of a single SWNT.

### 4.3.1 B and N Doping

For B-doped SWNTs produced using the laser technique that was described earlier [72], the overall effect of the boron incorporation primarily leads to (1) a systematic increase in intensity of the disorder-induced band (D-band) upon boron doping (Fig. 16), with increasing D-band intensity observed for higher doping levels, (2) a systematic downshift in the G'-band frequency due to the relatively weaker C-B bond, and (3) a nonlinear variation in the RBM and G'-band intensities, which is attributed to shifts in resonance conditions in the doped tubes [72]. Resonant Raman spectroscopy thus provides large changes in the intensity of prominent features even when the dopant concentration is below the detectable limit of EELS (0.05–0.1 at.%), although and as mentioned earlier TEP data also provided complementary evidence for the presence of a small boron concentration in the SWNT lattice, which transforms the SWNTs into a permanently p-type material.

The Raman characterization of long-strand N-doped SWNTs has been recently reported and the RBM spectra are shown in Fig. 17a. By observing the RBM evolution it can be concluded that the formation of large-diameter tubes (region A) is prevented by the amount of N precursor. The D-band to G-band ratio increases as the amount of N precursor increases as shown in Fig. 17b. Since it is not possible to separate in the D-band profile the contribution of specific defects, the  $I_D/I_G$  result indicates that the nanotube wall is getting more disordered, and in part this effect should be related to the incorporation of N atoms in the carbon lattice [55]. For in-plane doping extracting the information on charge transfer from the G-band frequency shifts is more complicated than that for intercalated systems. This is because for the substitutional doping, the carbon nanotube atomic structure and electronic bands are affected very much and the phonon frequency is affected also by the lattice distortion because of different chemical nature of the dopant.

The Raman features that are most affected due to the nitrogen doping are as follows: (1) the intensity of RBM, which is much lower in nitrogen-doped SWNTs than in pristine SWNTs. The nitrogen dopant most likely hinders the collective in-and-out movement of the carbon atoms (breathing mode) in the nanotube. (2) The modes associated with defects in the lattice, i.e., D-band and D'-bands become strongly Raman active with increasing nitrogen concentration in the feed. Collectively, the data set in Fig. 17 seems to suggest substitution of nitrogen atoms within the nanotube network. The amount of nitrogen actually incorporated into the

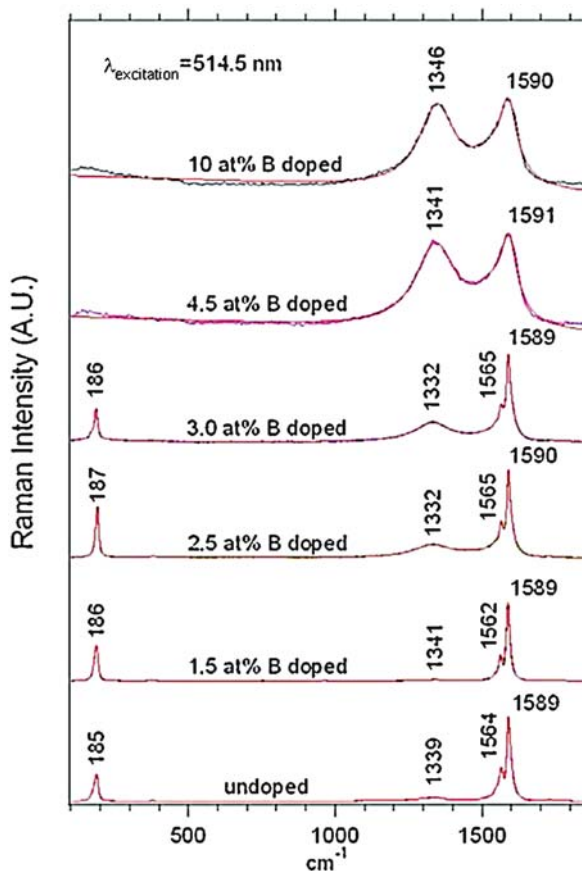


**Fig. 16** Room-temperature Raman spectra of products generated from targets with indicated boron concentrations using the laser technique. All Raman spectra were excited using the 514.5-nm excitation energy. Each spectrum in the figure was normalized to the tangential G<sup>+</sup>-band intensity, and the peak frequencies were determined from a Lorentzian line shape analysis (adapted from reference 72)

tube lattice is unknown but it should be less than <1 wt%. The D/G Raman intensity ratio dependence on N precursor concentration in the FEB solution may provide a means to estimate the N concentration in the sample, after more detailed studies are carried out. Temperature-dependent electrical conductivity indicates that SWNTs are doped with N.

The doped nanotubes are also important for unveiling new features of the Raman spectra of nanocarbon-based systems [94]. When DWNTs are annealed at high temperatures, a very sharp mode is observed at about 1,850  $\text{cm}^{-1}$  (Fig. 18) that has

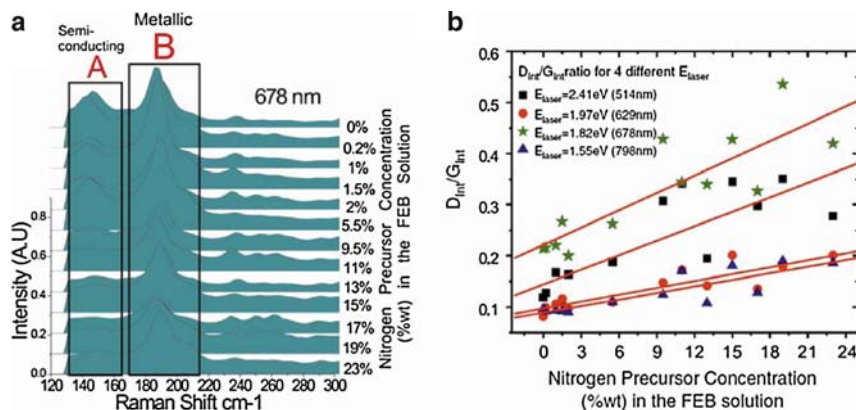


**Fig. 17** (a) RBM spectral region for samples with different initial N precursor (benzylamine) concentrations in the FEB solution. The laser energy is always  $E_{laser} = 1.82$  eV (678 nm). Each spectrum is the result of repeating the same experiment five times at different spots on the sample and averaging the results. Note how the intensity of the low-frequency peak decreases as the initial N precursor concentration increases. (b) Integrated D-band to G-band intensity ratios for four different  $E_{laser}$  as a function of initial nitrogen precursor (benzylamine) concentration (adapted from reference 55)

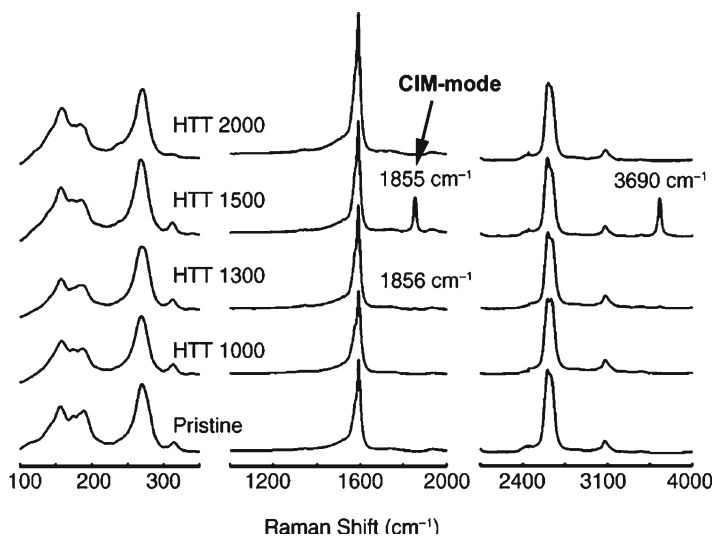


**Fig. 18** Raman spectra taken at 2.33 eV on DWNT samples heated in an inert atmosphere at different temperatures (1,000, 1,300, 1,500, and 2,000°C). At 1,300 and 1,500°C the CIM feature located at  $1855\text{ cm}^{-1}$  and its harmonic at  $3690\text{ cm}^{-1}$  appears (adapted from reference 95)

been called the coalescence-induced mode. The resonance Raman window for this mode has a maximum at about 2.2 eV [95]. By comparing the resonance Raman experimental results with first-principles calculations for the vibrational frequency

and the energy gap, it was proposed that the CIM feature is associated with short carbon chains with an odd number of atoms, interconnecting the nanotube surfaces.

### 4.3.2 Nonsubstitutional Doping

The doping with alkali metals such as K, Rb, and Cs leads to a softening (or downshift) of the G-band frequencies and is accompanied by dramatic changes in its line shape [23, 84]. The downshifts in Raman frequencies provide evidence for charge transfer between the dopants and SWNT bundles, indicating an ionic character for the dopant-SWNT bonds. The intercalation of other metals such as silver (Ag) into SWNT bundles has also been studied and the downshift in the tangential G modes indicates that electrons are transferred from the silver atoms to the SWNTs [96, 97]. The D-band intensity did not change, thus indicating that Ag was not covalent functionalized in the tube wall. Calculations based on ab initio methods support this experimental observation.

An opposite behavior, compared with SWNT/Ag system, was observed for SWNT/CrO<sub>3</sub>. The upshift observed for the G-band indicates an effective stiffening of the C–C bonds due to charge transfer from the SWNT bundles to the well-known oxidizing CrO<sub>3</sub> species. By analyzing the disorder-induced (D-band) mode located at about 1348 cm<sup>-1</sup> for pristine and SWNT/CrO<sub>3</sub> we get further information about the interaction between SWNT and CrO<sub>3</sub>. When the CrO<sub>3</sub> is attached to the SWNT sidewall, the translational symmetry is broken and this contributes to enhancing the D-band intensity and linewidth when compared with the pristine SWNT. The linewidth of all the modes increases, thus indicating that the system becomes disordered due to the CrO<sub>3</sub> attachment to the tube walls. Thus, the carbon atom to which the Cr is bonded exhibits a *sp*<sup>3</sup>-like hybridization, breaking the symmetry and thus enhancing the D-band intensity. From a theoretical standpoint, these results are often discussed within the framework of a rigid band model, whereby it is assumed that there is no modification to the  $E_{ii}$  values of a SWNT through the doping process, but the Fermi level is shifted very significantly by the addition of electrons and holes [23, 98].

We should comment that the effects of doping on the phonon frequencies of carbon nanotubes are similar to graphite only for high doping level. The frequency shifts observed in doped carbon nanotubes as a function of doping level are not as clear as in graphite intercalation compounds [22]. Recent studies showed that for both isolated and bundled SWNTs, there is an anomalous change in the C–C bond length upon doping with alkali metals [99, 100]. Four regimes have been identified in the behavior of the Raman frequencies of SWNT modes as a function of doping concentration [99]. For low-dopant content, the intercalant adsorption mainly occurs on the outside surface of the bundle and the frequencies do not change. In the second regime of dopant concentration, the G-band frequencies increase and the RBM intensity is suppressed. In the third regime, the frequency of the G-band decreases with a continuous loss in intensity. Finally, in the fourth regime,

the G-band frequency remains constant, thus indicating the saturation regime. These results are different from GICs for which the downshift is monotonic and this difference in behavior should be related to curvature effects of nanotubes and to the bundling effect. The C–C bond lengths along nanotube axis and along the circumference are differently affected by the doping and they have a nonlinear behavior, thus exhibiting either contraction or expansion depending on the doping concentration [101]. For small doping levels nonadiabatic effects are very important and the Raman shift of both metallic and semiconducting tubes upon doping behaves anomalously compared with what we discussed earlier [102, 103]. In the regime of high doping level the dominant effect on the Raman shifts comes from the spring constant.

Resonant Raman scattering data of Br<sub>2</sub> adsorbed by high-purity bundled DWNTs (essentially free of catalyst particles and SWNTs) were analyzed by considering the effect of doping on the electronic transitions [24]. The use of different laser lines allowed the study of different configurations of outer/inner tubes separately, such as M/S and S/M [outer/inner metallic (M) and semiconducting (S)] tubes, and to contrast the difference in screening effects for these two cases. Both decreases and increases in the RBM intensity due to bromination are observed and attributed to the shift of electronic transition values  $E_{ii}$ . A joint theoretical and experimental study of exohedral chemically doped double-wall carbon nanotubes demonstrates charge transfer-mediated electronic properties [104]. Both theoretical and experimental findings converge to the existence of a real nanoscale coaxial cable with a semiconducting inner tube screened by a metallic outer shell. These coaxial cables are promising for hybrid electronic and optical devices where the conduction of the outer shell is tuned through doping and the optical properties (such as photoluminescence) of the inner semiconducting tube are preserved as recently shown for fluorinated DWNTs [105].

To support our theoretical predictions, we carried out resonance Raman scattering (RRS) experiments on doped DWNTs with different species (Br<sub>2</sub> and H<sub>2</sub>SO<sub>4</sub>). The experimental results obtained with RRS are suitable for such comparisons since the Raman spectral profiles are very sensitive to charge-transfer effects. Furthermore, by using the diameter-selective resonance Raman effect, it is possible to clearly identify the outer/inner configuration that is being probed for a given laser excitation. It should be pointed out that some of the resonant inner and outer tubes observed do not correspond to the same DWNT, but from the diameter distribution it is very likely that a significant portion of the DWNTs in the bundled sample, both inner and outer tubes from the same DWNTs, answer to the same excitation energy. Future experiments on isolated DWNTs will address this point.

Calculations based on ab initio methods allowed to get a deep understanding of the doping process of the inner and outer shells. In Fig. 19, we display a plot of the electronic charge density difference ( $\rho_{\text{doped}} - \rho_{\text{undoped}}$ ) on a plane perpendicular to the (a) (18,0)@(28,0) and (b) (17,0)@(27,0) nanotube pairs to visualize spatial charge distribution. The plotted charge difference shows the extra holes located in the system after doping. For the (18,0)@(28,0) DWNT, there is a clear delocalization of charges (holes) onto the nanotube systems and a charge redistribution on the

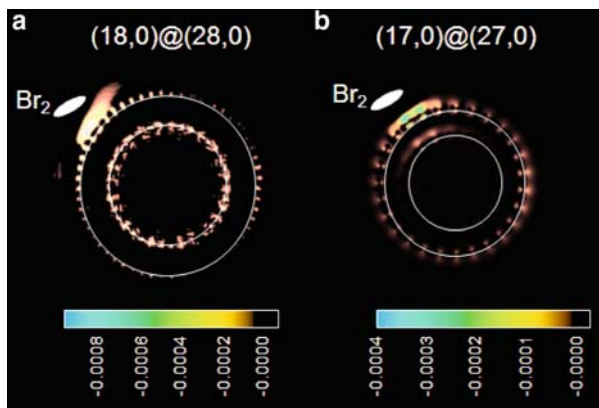


**Fig. 19** The calculated electronic charge density difference ( $\rho_{\text{doped}} - \rho_{\text{undoped}}$ ) of  $\text{Br}_2$ -doped DWNTs. (a) Electronic charge density of  $\text{Br}_2$ -doped (18,0)@(28,0) DWNTs sitting on a plane perpendicular to the DWNT tube axis. (b) Same as in (a) except that the data is for (b) (17,0)@(27,0) DWNT. The charge density at the position close to  $\text{Br}_2$  has been saturated. The white circles refer to the carbon nanotube cross sections and the white ellipse is the position of  $\text{Br}_2$ . The lower panels give the ranges of charge density differences for the two figures (reprinted with permission from [104]. Copyright American Chemical Society)

semiconductor tube. A net transfer of charge occurs primarily on the inner metallic tube. This result is in clear contrast with the charge distribution for the (17,0)@(27,0) pair, as shown in Fig. 19, where there is very little spillover of charge onto the inner tube and most of the charge (holes) is located around the outer metallic shell. This indicates that the inner semiconducting tube for the (17,0)@(27,0) DWNT is weakly affected by the presence of the exohedral doping.

In Fig. 20, we show the experimental G-band Raman spectra for  $\text{Br}_2$ -doped DWNTs excited with different laser lines. The laser lines were selected to probe the metallic outer/semiconducting inner ( $E_{\text{laser}} = 1.58 \text{ eV}$ ) and semiconducting outer/metallic inner ( $E_{\text{laser}} = 2.33 \text{ eV}$ ) configurations, which allows to confirm the theoretical predictions presented earlier. Although both semiconducting and metallic tubes are contributing to the spectra, the G-band of undoped DWNTs shown in Fig. 3a has a complex line shape, but we can identify the contribution of inner and outer tubes because the splitting ( $\Delta\omega = \omega_{\text{G}^+} - \omega_{\text{G}^-}$ ) between the  $\text{G}^+$  and  $\text{G}^-$  modes exhibits a different diameter dependence for metallic ( $\Delta\omega = 79.1/d_1^2$ ) and semiconducting ( $\Delta\omega = 47.7/d_2^2$ ) tubes [106]. The average diameter of both the inner and outer tubes is easily identified in the RBM spectra and the splitting defined earlier is easily tracked experimentally. We can thus observe that for the pristine sample there is a weak and broad Breit-Wigner-Fano (BWF) tail peaked at about  $1,485 \text{ cm}^{-1}$  (dotted line in Fig. 20a). This BWF tail in the Raman line shape is typical of small-diameter metallic tubes and originates from the inner tubes that are metallic [106]. The large splitting  $\Delta\omega = \omega_{\text{G}^+} - \omega_{\text{G}^-} \sim 100 \text{ cm}^{-1}$  is consistent with the average diameter of the inner metallic tubes as measured by their RBM spectra. After  $\text{Br}_2$  doping, the experimental G-band profile is significantly modified. First, we observe a considerable

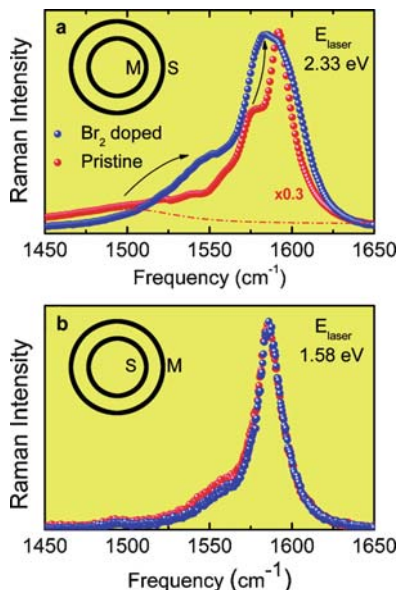


**Fig. 20** Tangential G-band for pristine and Br<sub>2</sub>-doped DWNTs. (a) Experimental G-band Raman profile of pristine (red) and bromine doped (blue) DWNTs for the metallic inner/semiconductor outer configuration. (b) Same profile as in (a) except for the semiconductor inner/metallic outer configuration. The laser excitation energies used to excite the inner and outer tubes for the two cases are indicated (reprinted with permission from [104], copyright American Chemical Society)

line broadening, which suggests that contributions from metallic and semiconducting tubes are affected differently by the doping. It is clear that for the pristine undoped sample, the BWF peak due to the metallic inner tube is identified and it does not overlap with the modes of the outer semiconducting tube because of their very different  $\Delta\omega = \omega_G^+ - \omega_G^-$  discussed earlier. We note that the BWF profile for the inner tube is strongly affected by the Br<sub>2</sub> adsorption. Its frequency exhibits a large upshift from 1,485 to 1,545 cm<sup>-1</sup> (see arrow in Fig. 20a). Strikingly, when the sample is doped with Br<sub>2</sub>, the G<sup>-</sup> component is upshifted in frequency, thus indicating extra holes on the nanotubes. Furthermore, the peak at 1,575 cm<sup>-1</sup> in the undoped sample (attributed to the semiconducting outer tubes) also experiences an upshift in frequency (see arrow in Fig. 20a) indicating that semiconducting outer tubes are also being affected by the doping in agreement with theoretical predictions. These upshifts are related to a direct electron charge-transfer process from the nanotube to the acceptor Br<sub>2</sub> molecules. These results indicate that metallic nanotubes are very sensitive to doping even when they are surrounded by a semiconducting tube. The observed behavior is in full agreement with the theoretical predictions discussed above for the (18,0)@(28,0) DWNT.

Turning to the S@M system, we show a typical G-band Raman spectra in Fig. 20b taken with  $E_{\text{laser}} = 1.58$  eV. The profile is typical of semiconducting nanotubes and after Br<sub>2</sub> doping there are little or no changes in the G-band spectra regarding

frequency and line shape. The absence of frequency shifts is an unambiguous indication that the inner tubes are only weakly affected by the doping when the outer shell is a metallic tube. Again, this observation comes in full agreement with the theoretical prediction made by the *ab initio* calculations for the (17,0)@(27,0) DWNT. A similar screening effect was experimentally observed for  $\text{H}_2\text{SO}_4$ -adsorbed DWNTs [107].

### 4.3.3 Wider Applications of Doped Nanotubes

In this section we briefly review some possible applications of different types of doped carbon nanotubes (MWNTs, SWNTs, or DWNTs). Depending on the application the performance of doped nanotubes is superior to that of their undoped counterparts.

*Purification and separation.* Since the preparation methods are not yet able to selectively produce metallic nanotube the development of efficient purification and separation methods is a very important step in nanotube-based technology at the present time. Several methodologies have been employed aiming to waste remaining catalyst particles and amorphous carbon from the nanotube mat. Much progress has been done in using functionalization with organic molecules as a purification method. The functionalization with azomethine ylides has been used to purify nanotubes. The treated samples were found to be free of amorphous carbon whereas the catalysts content was found to be less than 0.5% in weight [108]. Functionalization with DNA has been employed to disperse and separate metallic from semiconducting nanotubes. There is a large molecular library consisting of single-stranded DNA (ss-DNA). By exposing the aromatic nucleotide bases from the ss-DNA they can interact with the tube wall through  $\pi$ -stacking interaction [109]. The ss-DNA (right- or left-handed) goes warping the tube guided by aromatic rings from nucleotide basis arrangement that tends to be close to the tube surface. The phosphate groups of the DNA negatively charge the nanotube surface that in turn is controlled by the DNA sequence. The charge density on the tube wall is high for semiconducting tubes because in metallic ones an opposite image charge is created. Since the systems are differently charged the ion-exchange liquid chromatography technique can be used for separating metallic from semiconducting tubes. The analysis of the separated fractions on the chromatography column indicates that the samples are either semiconducting or metallic-enriched, thus indicating that the DNA-mediated separation process is efficient. Furthermore, the anionic-exchange process also allows one to separate different tube diameters and lengths because the position in the chromatography column depends on the amount of induced charge in the tube. Raman scattering studies on these fractions have proven the DNA-mediated diameter separation process [110]. These dispersed carbon nanotubes exhibit photoluminescence properties, and these properties have been used for building extremely sensitive sensors able to detect changes in the polymorphism of DNA when exposed to very small concentration of  $\text{Hg}^+$  counter ions [111].

*Field Emission devices.* Carbon nanotubes could easily emit electrons from their ends when a potential is applied between a CNT surface and an anode. In this context,



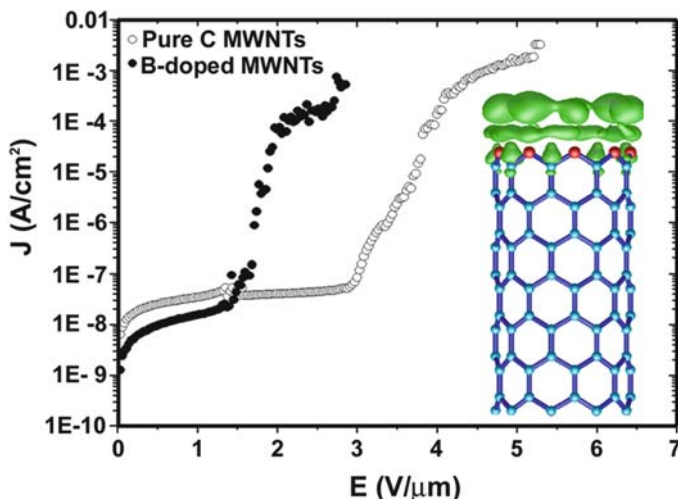


**Fig. 21**  $J$  versus  $E$  emission characteristics measured in parallel plate configuration of the B-doped MWNT films and comparable films of pure carbon arc-produced MWNTs. The plate area was  $0.25 \text{ cm}^2$ . Inset side view of localized states at the edges of a boron saturated zigzag (9,0) carbon nanotube computed using ab-initio calculations. The work function of this tube is 1.7 eV lower than that of the same nanotube made exclusively of carbon atoms (adapted from reference 112)

Charlier et al. [112] demonstrated experimentally and theoretically that B-doped MWNTs exhibit enhanced field emission (turn-on voltages at ca.  $1.4 \text{ V}/\mu\text{m}$ ) when compared with pure carbon MWNTs (turn-on voltages at ca.  $3 \text{ V}/\mu\text{m}$ ) (see Fig. 21). This phenomenon is thought to be due to the presence of B atoms at the nanotube tips, which results in an increased DOS close to the Fermi level. Theoretical tight binding and ab initio calculations demonstrate that the work function of B-doped SWNT is much lower (1.7 eV) than that observed in pure carbon MWNTs. Similarly, it has been demonstrated that bundles of N-doped MWNTs are able to emit electrons at relatively low turn-on voltages ( $2 \text{ V}/\mu\text{m}$ ) and high current densities ( $0.2\text{--}0.4 \text{ A}/\text{cm}^2$ ) [76]. More, recently, individual N-doped MWNTs have also shown excellent field emission properties at 800 K, experimental work functions of 5 eV, and emission currents of ca. 100 nA obtained at  $\pm 10 \text{ V}$  (Fig. 22) [113]. Therefore, additional research on field emission properties of doped nanotubes should be carried out and other types of tubes (either SWNTs or DWNTs) should be tested in this respect.

*Li ion batteries.* Lithium is an alkali metal, which could donate electrons from  $\text{Li}^+$ , and has proved to be extremely important for the fabrication of lightweight and energy-efficient batteries. When using graphite-like materials in Li ion batteries, the ions are intercalated between the graphite layers, so that  $\text{Li}^+$  migrates from a graphitic anode to the cathode (usually  $\text{LiCoO}_2$ ,  $\text{LiNiO}_2$ , and  $\text{LiMn}_2\text{O}_4$ ). The Li storage capacity in graphite is ca.  $372 \text{ mAh/g}$  ( $\text{LiC}_6$ ), and the charge and discharge phenomenon in these batteries is based upon the  $\text{Li}^+$  intercalation and deintercalation [114]. At present, several electronic companies commercialize these batteries in portable

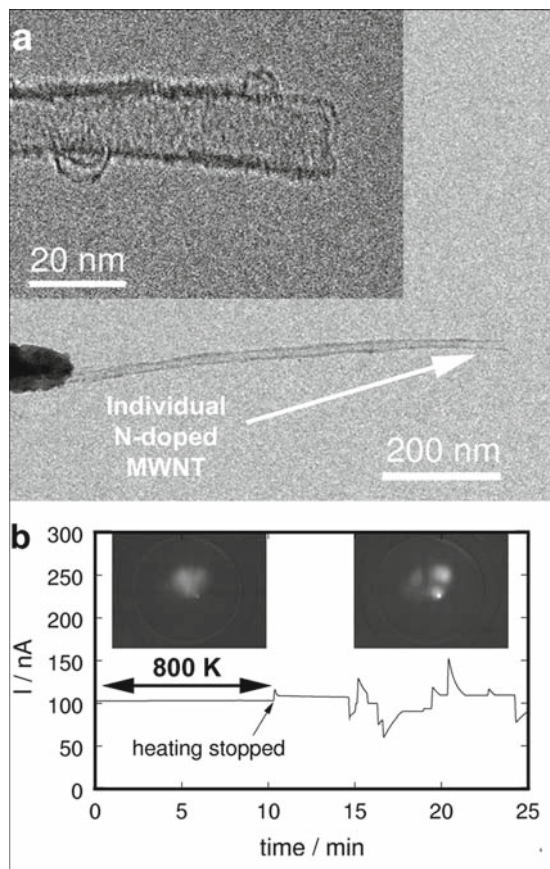


**Fig. 22** TEM image of an individual N-doped MWNT taken after the filed emission measurements; (inset) image of the end cap of the nanotube shown in (a) with a radius of ca. 8 nm. The dark contour connecting the two main walls at the end of the nanotube could indicate a closed cap, and (b) a stable emission profile of the tube shown in (a) obtained at 800 K. Note that the current fluctuations occurred after the heating were stopped as shown in the plot. Here, the extraction voltage was adjusted by maximal  $\pm 10$  V to obtain approximately 100 nA of emitted current. The corresponding emission patterns before and after heating recorded with a microchannel plate and a phosphor screen positioned 1.5 cm in front of the emitter are also depicted (adapted from reference 113)

computers, mobile telephones, digital cameras, etc. Interestingly, Endo et al. [114] demonstrated that B-doped vapor-grown carbon fibers (VGCFs) and carbon nanofibers are by far superior compared with any other carbon source present in the graphitic anode inside Li-ion batteries. This effect could be due to the fact that the population of Li ions has a stronger affinity in the B-doped sites, thus resulting in a higher storage efficiency. N-doped CNTs and nanofibers have also shown efficient reversible Li storage (480 mAh/g), much higher when compared with commercial carbon materials used for Li<sup>+</sup> batteries (330 mAh/g) [115].

*Gas sensors.* Since 1998, it was demonstrated by various groups [116–118] that *pure* carbon SWNTs and MWNTs can be used to detect toxic gases and other species, because small concentrations of these species are capable of producing significant variations in the nanotube conductance, thus shifting the Fermi level to the valence band and generating hole-enhanced conductance [116]. However, N-doped MWNTs appear to be more efficient in this context because they are able to display a fast response (order of milliseconds) when toxic gases and organic solvents are approached [119]. In all cases, an increase in the electrical resistance is caused by the presence of molecules strongly bound to the nitrogenated sites present within the  $CN_x$  nanotubes (Fig. 23). From the theoretical standpoint, a decrease in the DOS at  $E_F$  is observed, which is an indicative of lower conduction and chemisorption. Therefore,  $CN_x$  nanotubes (MWNTs) could potentially be more efficient in detecting quickly gaseous hazardous species due to the presence of reactive

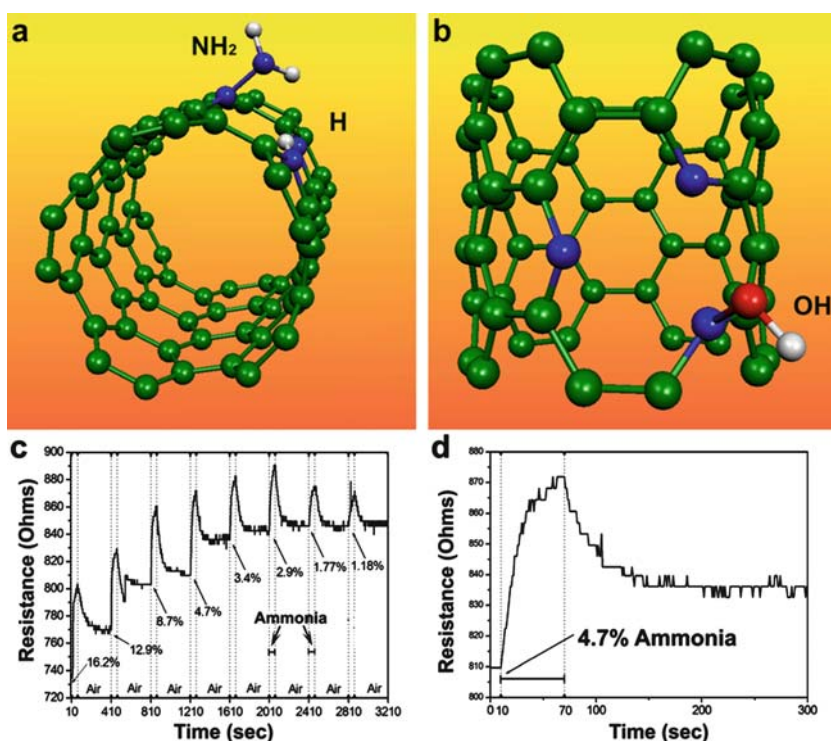


**Fig. 23** Molecular models of a (5,5) carbon nanotube doped with pyridinic sites on their surface and molecules adsorbed on the vicinity of this region for (a) OH groups and (b)  $NH_3$  molecules. (c, d) Plots of resistance vs. time for ammonia for N-doped MWNT sensors: (c) It is clear that the sensor is sensitive to ca. 1% of  $NH_3$ . In this case a clear chemisorption is observed, which can be attributed to the strong interactions between the pyridinic sites of the tube surface with the  $NH_3$  molecule; (d) graph indicating the response time for ammonia gas (4.7%); (adapted from reference 119))

sites on their surface. Therefore, B-doped and other doped CNTs need now to be tested for this particular application.

*Polymer composites with doped nanotubes.* To fabricate nanotube composites exhibiting high performance, the formation of stable tube surface-polymer interfaces is crucial. In this case, the surface of highly crystalline MWNTs tends to be similar to graphite, and chemically “inert.” Therefore, surface modification treatments are required so that efficient tube-matrix interactions need to be established [120]. In this context, the creation of nanotubes containing a few number of foreign atoms in the hexagonal network such as N or B could circumvent this problem. In some cases, the mechanical properties would not be altered significantly because these “doped” structures would preserve their outstanding mechanical properties since the level of doping is low (<1–2%) (see earlier). Preliminary studies on the preparation of epoxy composites using N-doped MWNTs revealed an increase of 20°C in the glass transition temperature with incorporation of 2.5 wt% of CN<sub>x</sub> MWNT using dynamic mechanical thermal analysis (DMTA) [121]. More recently, it has been demonstrated that it is possible to grow polystyrene (PS) on the surface of N-doped MWNTs using atomic transfer radical polymerization (ATRP) [122] and nitroxide-mediated radical polymerization [123] without using any acid treatment. These polymers grown on the doped nanotube surfaces are also known as polymer brushes and could be dissolved in organic solvents (Fig. 24). The latter clearly demonstrates that in-plane doping is important in the establishment of covalent bonds between the nanotube surfaces and polymer chains. Recent mechanical and electrical tests have demonstrated that PS-grafted CN<sub>x</sub> nanotubes exhibit enhanced properties when compared with mixtures of PS and pristine CN<sub>x</sub> tubes (Figs. 25 and 26) [124]. These studies are now motivating further work in the fabrication of robust and conducting composites.

The doped carbon nanotube composites have also been used in energy-related applications. The charge transfer between carbon nanotubes and pendant ferrocene groups is used for converting the solar energy into electric current via photoexcitation process [125].

#### 4.3.4 Efficient Metal Surfaces for Anchoring Molecules

Recently, it has been possible to create active nitrogen-rich sites for the efficient covalent anchoring of proteins [126], Au [127], Ag [128], Fe, and Pt clusters [129] to the surfaces of N-doped MWNTs (Fig. 27). It has been demonstrated that the doped tubes are much more efficient than pure carbon nanotubes. Therefore, novel catalytic applications with these deposited clusters should now be tested.

*Toxicity of doped carbon nanotubes.* The doping effects have dramatic effects on the toxicity of carbon nanotubes to mouse. Comparative toxicological studies of CN<sub>x</sub> MWNTs and pure carbon MWNTs on mice have been carried out [130]. Several routes of administration were tested (nasal, oral, intratracheal, and intraperitoneal). In comparison with previous studies using SWNTs, the new results demonstrated that CN<sub>x</sub> tubes appear to be far less harmful. For example,

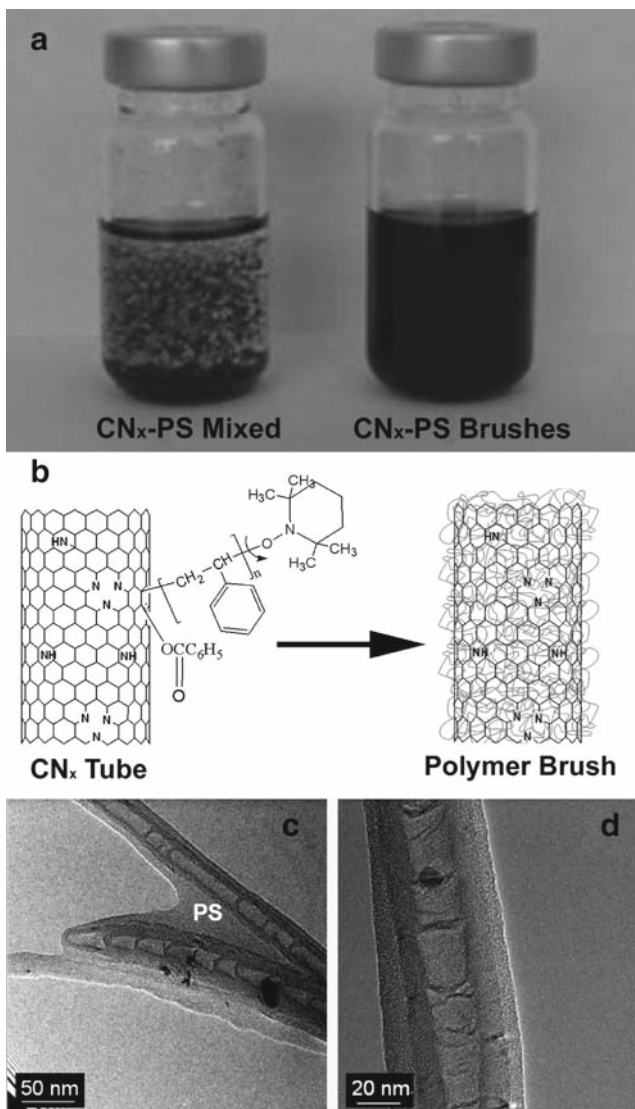


**Fig. 24** (a) Polystyrene-CN<sub>x</sub> Nanotubes suspensions: Solubility differences in toluene between physically mixed PS and CN<sub>x</sub> tubes, and PS-CN<sub>x</sub> brushes obtained via NMRP method; (b) Reaction scheme for the NMRP reaction for producing the PS-CN<sub>x</sub> tubes brushes; (c, d) TEM micrographs showing the PS-CN<sub>x</sub> brushes obtained by the scheme showed in (b); note the uniform coating of PS on the tube surfaces (adapted from reference 122)

using extremely high doses of CN<sub>x</sub> nanotubes (e.g., 5 mg/kg), no lethal effects were observed on the mice, which is in contrast to previous reports using MWNTs or SWNTs [131].

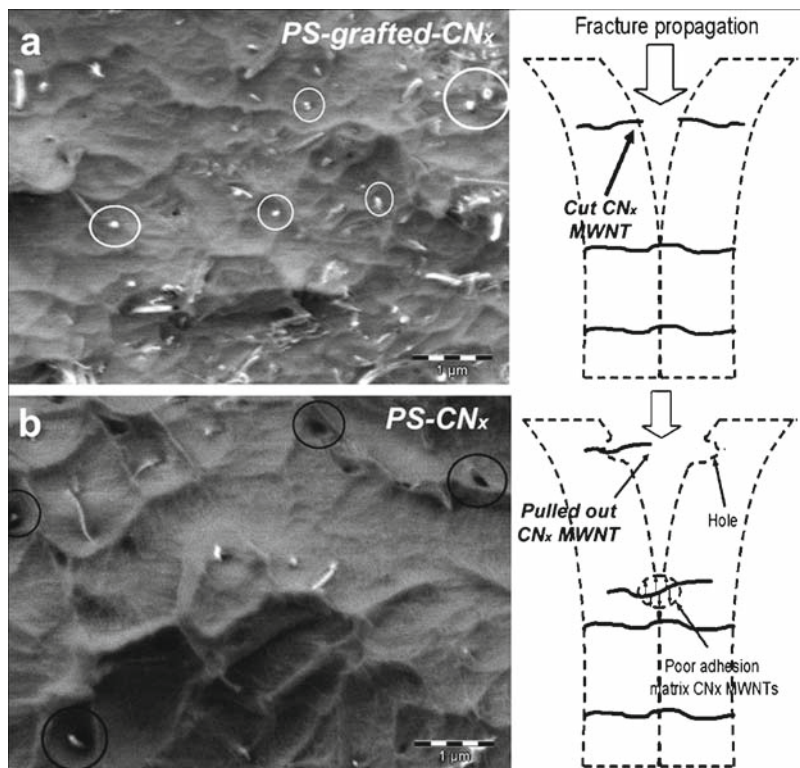


**Fig. 25** SEM micrographs of the CN<sub>x</sub> MWNTs/PS nanocomposites after breaking at ambient temperature; (a) PS-grafted-CN<sub>x</sub>/PS nanocomposite with *white circles* indicating cut tubes, (b) a-CN<sub>x</sub>/PS nanocomposite. The *black circles* indicate holes or pulled out tubes. On the *right side* is represented the proposed mechanisms of fracture (Courtesy of B. Fragneud)

Pure MWNTs appeared to be lethal at all doses tested for intratracheal instillation, whereas CN<sub>x</sub> MWNTs were not. The pathological changes induced by pure MWNTs are more severe than that induced by CN<sub>x</sub> MWNTs; in both, these pathological changes were dose- and time-dependent (Fig. 28). Both types of nanotubes induce erosion and disruption of the bronchi epithelium at different levels, concomitant with a mononuclear inflammatory reaction. Polymorphonuclear cells, when using 5 mg/kg of nanotubes, also induced the arrival of eosinophils. Besides, they induced epithelial hyperplasia; however, the hyperplasia was more frequent in the mice challenged with the MWNTs and at earlier times, even if the bronchioli showed an apparent absence of nanotubes (Fig. 28). Granulomas were seen at late stages with both types of nanotubes (Fig. 28).

The plausible formation of cyanide groups driven by the interaction of CN<sub>x</sub> MWNTs and the mice did not occur. On the contrary, the presence of nitrogen in

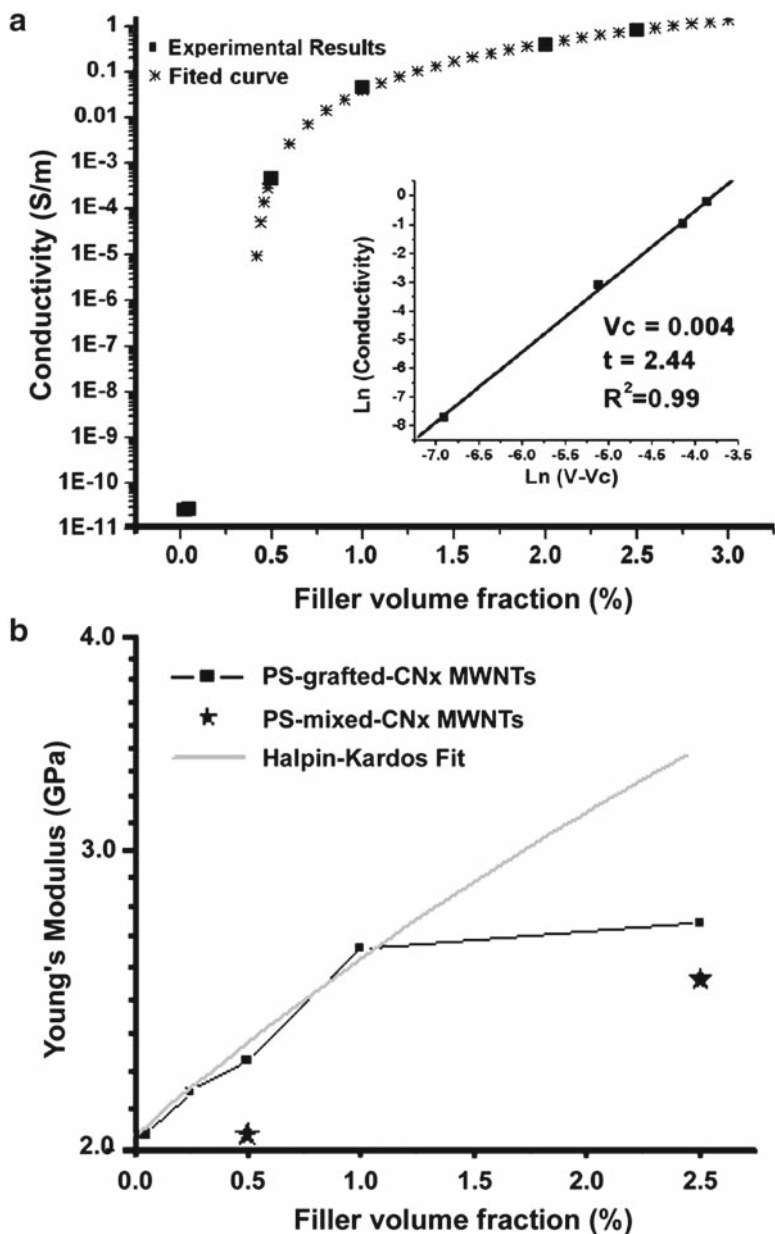


**Fig. 26** (a) Experimental conductivity results and fitted scaling law for a-CN<sub>x</sub> polymer nanocomposite with a PS matrix; (b) Youngs modulus – experimental results for pristine CN<sub>x</sub> PS nanocomposites and PS-grafted CN<sub>x</sub> nanotube composites; also note the theoretical results calculated from Halpin Kardos theory (Courtesy of B. Fragneud)

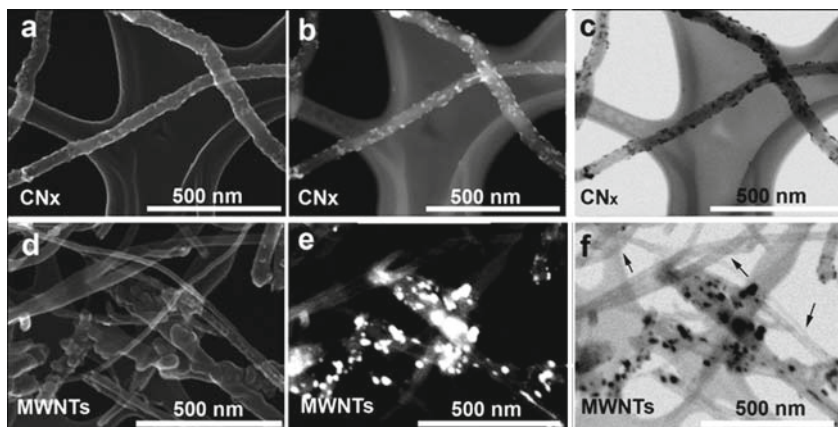


**Fig. 27** SEM and STEM images (bright- and dark field) of carbon nanotubes decorated with Ag Nanoparticles (NPs). The first row (a–c) corresponds to  $\text{CN}_x$  MWNTs and the second row (d–f) depicts MWCNTs. Images (b) and (e) correspond to the dark-field images of (a) and (d), respectively. Bright-field (using the transmission mode) images are depicted in (c) and (f). When comparing the coverage between Ag- $\text{CN}_x$  MWNTs and Ag-MWNTs samples, it is clear that the N-doped tubes exhibit a more uniform coating with more monodisperse Ag NPs (5–10 nm in diameter). Samples using undoped MWNTs resulted in the inhomogeneous coverage of Ag clusters of larger size (10–20 nm in diameter) that tend to agglomerate with other Ag particles and do not cover the tube due to the lack of reactivity. *Arrows* in (f) indicate that various undoped MWNTs do not show any Ag NPs on their surface. This also demonstrates that MWNTs are not capable of uniformly anchoring Ag NPs (adapted from reference 128)

the graphitic network could be the reason for the  $\text{CN}_x$  MWNTs to be less injurious to a living organism such as a mouse. It is possible to have amino groups on the surface of the  $\text{CN}_x$  tubes. It is therefore plausible that these amino groups may be the reason for expecting a better biocompatibility on the  $\text{CN}_x$  tubes when compared with pure carbon MWNTs (undoped). The two types of tubes exhibit clear structural differences. For example, MWNTs display a high degree of crystallinity and therefore are more robust. This crystallinity results in stronger van der Waals interactions and the MWNTs tend to aggregate easily. Therefore, MWNTs will agglomerate faster and would create large clumps that result in the death of the mice by dyspnea. On the contrary,  $\text{CN}_x$  nanotubes possess a bamboo-like structure with a rougher surface, exhibiting weaker van der Waals interactions that result in the formation of less agglomerates causing much less damage to the lungs of mice (e.g., they are definitely better dispersed than pure MWNTs). In addition, MWNTs do not break easily when compared with  $\text{CN}_x$  nanotubes. This mechanical enhancement in MWNTs could also increase the damage in the mice tissue and therefore become more hazardous because they damage the epithelium. Finally, the Fe content within both types of treated tubes is similar (ca. <0.5 wt%), and we could discard the presence of Fe as the trigger for toxicity.



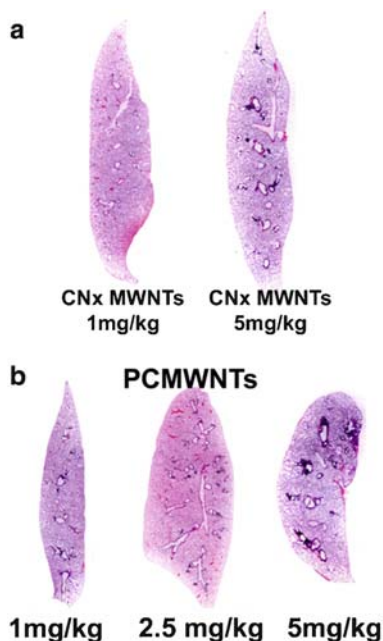


**Fig. 28** Progressive pulmonary lesions caused by intratracheal instillation of (a)  $CN_x$  MWNTs to CD1 mice. The panels show hematoxylin- and eosin-stained lung sections from mice treated with  $CN_x$  MWNTs at 1 mg/kg after 24 h and 5 mg/kg after 24 h (Original magnifications were taken at  $\times 2$ ; (b) pure carbon PCMWNTs (undoped nanotubes) to CD1 mice. The panels show hematoxylin- and eosin-stained lung sections from mice treated with MWNTs at 1 mg/kg after 24 h, 2.5 mg/kg after 24 h, and 5 mg/kg after 24 h. The number of bronchioles of small to large size occupied by MWNTs and the magnitude of the deposition are related to the amount of nanotubes instilled into the lungs. With 5 mg/kg dose, the majority of the bronchioles are involved (adapted from reference 130)

$CN_x$  tubes could be then used in biochemical applications such as agents for drug delivery, supports for enhanced enzyme activities, biofilters, virus inhibitors, gene transfers, etc. However, additional and strict biosafety measures need to be developed for the production and processing of these nanotubes into new materials. In addition, the toxicological effects of other types of doped nanotubes should also be studied in the near future.

A systematic study of cell viability study with ameba and different types of nanotubes (pure carbon MWNTs and N-doped MWNTs) was reported by Elias et al. [132]. They claim that when the cells were incubated with  $CN_x$  MWNTs, they survived and there were no changes in their behavior or morphology at all doses tested, which differs substantially from the incubation with undoped MWCNTs (100  $\mu\text{g}$ ) where the amebas' population died after 8 h. These results suggest that  $CN_x$  MWNTs could be biocompatible and that they could be tested for their usage in various applications, such as cell transporters and drug delivery systems.

## 5 Outlook

Doped nanotubes are attractive for developing both basic science and nanotube-based technology. It was shown that various research groups have worked on N-doped MWNTs; however, further work is needed along for B- and PN-doped nanotube systems. It is noteworthy that to exploit fully these novel properties, low concentrations of dopants (e.g., <0.5%) should be incorporated within these tubes. The illustrated examples and phenomena clearly demonstrate that the science of doping carbon nanotubes should be developed further as this is becoming a real interdisciplinary field. It is easy to realize that physics, chemistry, biochemistry, and materials science are working together to their mutual benefit developing basic science and applying the main properties to technology. We should point out that the physicochemical properties of endohedral and exohedral doped tubes should continue to be studied, as these materials may also show useful applications in various technological arenas.

This chapter was intended to motivate new ways of characterizing these complex systems as the current analytical techniques appear to be limiting the way we could identify low-dopant concentrations within doped tubes. It seems that Raman spectroscopy, TEP studies, and electron transport are very sensitive to low doping concentrations. In addition, reliable methods for producing doped nanotube samples in a reproducible way are required. It is expected that doped nanotubes may replace pure carbon nanotubes for specific applications, but additional and detailed research should continue.

Finally, researchers should be aware that doping of carbon nanotubes may also occur unintentionally, and this will result in significant changes of the electronic, transport, chemical, and vibrational properties. Therefore, one should be careful when carrying synthesis experiments involving noncarbon elements, because these may get embedded into the hexagonal network of nanotubes and would then modify the physicochemical response.

**Acknowledgments** We are indebted to P.M. Ajayan, J.C. Charlier, A. Jorio, V. Meunier, B.G. Sumpter, A.M. Rao, M.S. Dresselhaus, M. Endo, R. Saito, T. Hayashi, Y.A. Kim, H. Muramatsu, H. Terrones, F. López-Urías, E. Muñoz-Sandoval, E. Cruz-Silva, J.M. Romo-Herrera, J.A. Rodríguez-Manzo, A. Zamudio, X. Blase, D. Golberg, R. Kamalakaran, N. Grobert, Ph. Redlich, D.L. Carroll, R. Czerw, A.K. Cheetham, M. Rühle, Y. Bando, K. McGuire, P.L. Gai, A.L. Elías, J.P. Laclette, J.C. Carrero-Sánchez, B. Fragneaud, M. De Honor, A. González-Montiel, J.Y. Cavallié, Karine Masenelli-Varlot, F. Villalpando-Páez, P. Corio, S.B. Fagan, J. Mendes Filho, and L. Noyola-Cherpitel for stimulating discussions and valuable assistance in some of the works reviewed here. MT is grateful to CONACYT-México [45772 (MT), 41464-Inter American Collaboration (MT), 2004-01-013/SALUD-CONACYT (MT), PUE-2004-CO2-9 Fondo Mixto de Puebla (MT), and the MIT-CONACYT collaboration project] for financial support. AGSF acknowledges the support from Brazilian agencies FUNCAP (grant 985/03), CNPq (grants 556549/2005-8, 475329/2006-6, 307417/2004-2), Rede Nacional de Pesquisa em Nanotubos de Carbono, Rede Nacional de Nanobiotecnologia e sistemas nanoestruturados, Instituto do Milênio de Nanotecnologia, and Instituto do Milênio de Materiais Complexos (CNPq/MCT-Brazil). Finally, AGSF and MT acknowledge the bilateral CNPq-CONACYT cooperation funding under grants CNPq 490283/2007-1 and CONACYT entitled "Synthesis and characterization of doped carbon nanotubes: experiments and theory".

## References

1. M. S. Dresselhaus, G. Dresselhaus, P. C. Eklund: *Science of Fullerenes and Carbon Nanotubes* (Academic, New York 1996)
2. M. Terrones: Science and technology of the XXI century: synthesis, properties and applications of carbon nanotubes, *Ann. Rev. Mater. Res.* **33**, 419 (2003)
3. M. R. Pederson, J. Q. Broughton: Nanocapillarity in fullerene tubules, *Phys. Rev. Lett.* **69**, 2689 (1992)
4. P. M. Ajayan, T. W. Ebbesen, T. Ichihashi, S. Iijima, K. Tanigaki, H. Hiura: Opening carbon nanotubes with oxygen and implications for filling, *Nature* **362**, 522 (1993)
5. M. Terrones, N. Grobert, W. K. Hsu, Y. Q. Zhu, W. B. Hu, H. Terrones, J. P. Hare, H. W. Kroto, D. R. M. Walton: Advances in the creation of filled nanotubes and novel nanowires, *Mater. Res. Soc. Bull.* **24**, 43 (1999)
6. J. Sloan, M. Terrones, S. Nufer, S. Friedrichs, S. R. Bailey, H. G. Woo, M. Ruhle, J. L. Hutchison, M. L. H. Green: Metastable one-dimensional  $\text{AgCl}_{1-x}\text{I}_x$  solid-solution wurzite “tunnel” crystals formed within single-walled carbon nanotubes, *J. Am. Chem. Soc.* **124**, 2116 (2002)
7. M. Monthieux: Filling single-wall carbon nanotubes, *Carbon* **40**, 1809 (2002)
8. D. Tasis, N. Tagmatarchis, A. Bianco, M. Prato: Chemistry of carbon nanotubes, *Chem. Rev.* **106**, 1105 (2006)
9. Z. Y. Wang, Z. B. Zhao, J. S. Qiu: Development of filling carbon nanotubes, *Prog. Chem.* **18**, 563 (2006)
10. S. Iijima, T. Ichihashi: Single-shell carbon nanotubes of 1 nm diameter, *Nature* **363**, 603 (1993)
11. D. S. Bethune, C. H. Kiang, M. S. De Vries, G. Gorman, R. Savoy, J. Vazquez, R. Beyers: Cobalt-catalyzed growth of carbon nanotubes with single-atomic-layer walls, *Nature* **363**, 605 (1993)
12. B. W. Smith, M. Monthieux, D. E. Luzzi: Encapsulated C60 in carbon nanotubes, *Nature* **296**, 323 (1998)
13. J. Sloan, J. Hammer, M. Z. Sibley, M. L. H. Green: The opening and filling of single walled carbon nanotubes (SWTs), *Chem. Commun.* **3**, 347 (1998)
14. C. H. Kiang, J. S. Choi, T. T. Tran, A. D. Bacher: Molecular nanowires of 1 nm diameter from capillary filling of single-walled carbon nanotubes, *J. Phys. Chem. B* **103**, 7449 (1999)
15. P. Corio, A. P. Santos, M. L. A. Temperini, V. W. Brar, M. A. Pimenta, and M. S. Dresselhaus: Characterization of single wall carbon nanotubes filled with silver and with chromium compounds, *Chem. Phys. Lett.* **383**, 475 (2004)
16. A. Govindaraj, B. C. Satishkumar, M. Nath, C. N. R. Rao: Metal nanowires and intercalated metal layers in single-walled carbon nanotube bundles, *Chem. Mater.* **12**, 205 (2000)
17. J. Sloan, D. M. Wright, H. G. Woo, S. R. Bailey, G. Brown, A. P. E. York, K. S. Coleman, J. L. Hutchison, M. L. H. Green: Capillarity and silver nanowire formation observed in single walled carbon nanotubes, *Chem. Commun.* **700**, 699 (1999)
18. R. R. Meyer, J. Sloan, R. E. Dunin-Borkowski, A. Kirkland, M. C. Novotny, S. R. Bailey, J. L. Hutchison, M. L. H. Green: Discrete atom imaging of one-dimensional crystals formed within single-walled carbon nanotubes, *Science* **289**, 1324–1326 (2000)
19. D. E. Luzzi, B. W. Smith: Carbon cage structures in single wall carbon nanotubes: A new class of materials, *Carbon* **38**, 1751 (2000)
20. E. Hernández, V. Meunier, B. W. Smith, R. Rurli, H. Terrones, Buongiorno, N. Nardelli, M. Terrones, D. E. Luzzi, J. C. Charlier: Fullerene coalescence in nanopeapods: A path to novel tubular carbon, *Nano Lett.* **3**, 1037 (2003)
21. K. Hirahara, K. Suenaga, S. Bandow, H. Kato, T. Okazaki, H. Shinohara, S. Iijima: One-dimensional metallofullerene crystal generated inside single-walled carbon nanotubes. *Phys. Rev. Lett.* **85**, 5384 (2000)
22. M. S. Dresselhaus, G. Dresselhaus: Intercalation compounds of graphite, *Adv. Phys.* **30**, 139 (1981)

23. A. M. Rao, P. C. Eklund, S. Bandow, A. Thess, R. E. Smalley: Evidence for charge transfer in doped carbon nanotube bundles from Raman scattering, *Nature* **388**, 257 (1997)
24. A. G. Souza Filho, M. Endo, H. Muramatsu, T. Hayashi, Y. A. Kim, E. B. Barros, N. Akuzawa, G. G. Samsonidze, R. Saito, M. S. Dresselhaus: Resonance Raman scattering studies in Br-2-adsorbed double-wall carbon nanotubes, *Phys. Rev. B* **73**, 235413 (2006)
25. M. V. Veloso, A. G. Souza Filho, J. Mendes Filho, S. B. Fagan, R. Mota: Ab initio study of covalently functionalized carbon nanotubes, *Chem. Phys. Lett.* **430**, 71 (2006)
26. T. Ramanathan, F. T. Fischer, R. S. Ruo, L. C. Brinson: Amino-functionalized carbon nanotubes for binding to polymers and biological systems, *Chem. Mater.* **17**, 1290 (2005)
27. S. Kazaoui, N. Minami, R. Jacquemin, H. Kataura, Y. Achiba: Amphoteric doping of single-wall carbon-nanotube thin films as probed by optical absorption spectroscopy, *Phys. Rev. B* **60**, 13339 (1999)
28. C. E. Lowell: Solid solution of boron in graphite, *J. Am. Ceram. Soc.* **50**, 142 (1966)
29. C. T. Hach, L. E. Jones, C. Crossland, P. A. Thrower: An investigation of vapor deposited boron rich carbon - A novel graphite-like material, Part 1: The structure of  $BC_x(C_6B)$  thin films, *Carbon* **37**, 221 (1999)
30. A. Oya, R. Yamashita, S. Otani: Catalytic graphitization of carbons by borons, *Fuel* **58**, 495 (1979)
31. M. Endo, T. Hayashi, S. H. Hong, T. Enoki, M. S. Dresselhaus: Scanning tunneling microscope study of boron-doped highly oriented pyrolytic graphite, *J. Appl. Phys.* **90**, 5670 (2001)
32. M. Endo, C. Kim, T. Karaki, Y. Nishimura, M. J. Matthews, S. D. M. Brown, M. S. Dresselhaus: Anode performance of a Li ion battery based on graphitized and B-doped milled mesophase pitch-based carbon fibers, *Carbon* **37**, 561 (1999)
33. A. Marchand, J. V. Zanchetta: Propriétés électroniques d'un carbone dope à l'azote, *Carbon* **3**, 483 (1966)
34. K. Takeya, K. Yazawa: Unusual galvanomagnetic properties of pyrolytic graphite, *J. Phys. Soc. Jpn* **19**, 138 (1964)
35. K. Takeya, K. Yazawa, N. Okuyama, H. Akutsu: Evidence for existence of extremely light carriers in pyrolytic carbons, *Phys. Rev. Lett.* **15**, 111 (1965)
36. T. Belz, A. Baue, J. Find, M. Günter, D. Herein, H Möckel, N. Pfänder, H. Sauer, G. Schulz, J. Schütze, O. Timpe, U. Wild, R. Schlögi: Structural and chemical characterization of N-doped nanocarbons, *Carbon* **36**, 731 (1998)
37. M. Terrones, N. Grobert, H. Terrones: Synthetic routes to nanoscale  $B_xC_yN_z$  architectures, *Carbon* **40**, 1665 (2002)
38. S. Latil, S. Roche, D. Mayou, J.-C. Charlier: Mesoscopic transport in chemically doped carbon nanotubes, *Phys. Rev. Lett.* **92**, 256805 (2004)
39. S. Azevedo, R. de Paiva: Structural stability and electronic properties of carbon-boron nitride compounds, *Europhys. Lett.* **75**, 126 (2006)
40. E. Hernández, C. Goze, P. Bernier, A. Rubio: Elastic properties of C and  $B_xC_yN_z$  composite nanotubes, *Phys. Rev. Lett.* **80**, 4502 (1999)
41. E. Hernández, C. Goze, P. Bernier, A. Rubio: Elastic properties of single-wall nanotubes, *Appl. Phys. A. Mater. Sci. Process.* **68**, 287 (1999)
42. R. P. Gao, Z. L. Wang, Z. G. Bai, W. A. de Heer, L. M. Dai, M. Gao: Nanomechanics of individual carbon nanotubes from pyrolytically grown arrays, *Phys. Rev. Lett.* **85**, 622 (2000)
43. E. Cruz-Silva, D. A. Cullen, L. Gu, J. M. Romo-Herrera, E. Munoz-Sandoval, F. Lopez-Urias, B. G. Sumpter, V. Meunier, J. C. Charlier, D. J. Smith, H. Terrones, M. Terrones: Heterodoped Nanotubes: Theory, synthesis, and characterization of phosphorus-nitrogen doped multiwalled carbon nanotubes, *ACS Nano* **2**, 441 (2008)
44. O. Stephan, P. M. Ajayan, C. Colliex, P. Redlich, J. M. Lambert, P. Bernier, P. Lefin: Doping graphitic and carbon nanotube structures with boron and nitrogen, *Science* **266**, 1683 (1994)
45. P. Redlich, L. Loeffler, P. M. Ajayan, J. Bill, F. Aldinger, M. Ruhle: B-C-N nanotubes and boron doping of carbon nanotubes, *Chem. Phys. Lett.* **260**, 465 (1996)
46. M. Terrones, W. K. Hsu, S. Ramos, R. Castillo, H. Terrones: The role of boron nitride in graphite plasma arcs, *Fullerene Sci. Technol.* **6**, 787 (1998)

47. W. K. Hsu, M. Terrones: Unpublished results
48. M. Glerup, J. Steinmetz, D. Samaille, O. Stephan, S. Enouz, A. Loiseau, S. Roth, P. Bernier: Synthesis of N-doped SWNT using the arc-discharge procedure, *Chem. Phys. Lett.* **387**, 193 (2004)
49. Y. Zhang, H. Gu, K. Suenaga, S. Iijima: Heterogeneous growth of B–C–N nanotubes by laser ablation, *Chem. Phys. Lett.* **279**, 264 (1997)
50. P.L. Gai, O. Stephan, K. McGuire, A. M. Rao, M. S. Dresselhaus, G. Dresselhaus, C. Colliex: Structural systematics in boron-doped single wall carbon nanotubes, *J. Mater. Chem.* **14**, 669 (2004)
51. M. Terrones, N. Grobert, J. Olivares, J. P. Zhang, H. Terrones, K. Kordatos, W. K. Hsu, J. P. Hare, P. D. Townsend, K. Prassides, A. K. Cheetham, H. W. Kroto, D. R. M. Walton: Controlled production of aligned-nanotube bundles, *Nature* **388**, 52 (1997)
52. M. Terrones, P. Redlich, N. Grobert, S. Trasobares, W. K. Hsu, H. Terrones, Y. Q. Zhu, J. P. Hare, C. L. Reeves, A. K. Cheetham, M. Rühle, H. W. Kroto, D. R. M. Walton: Carbon nitride nanocomposites: Formation of aligned C<sub>x</sub>N<sub>y</sub> nanofibers, *Adv. Mater.* **11**, 655 (1999)
53. R. Sen, B. C. Satishkumar, S. Govindaraj, K. R. Harikumar, M. K. Renganathan, C. N. R. Rao: Nitrogen-containing carbon nanotubes, *J. Mater. Chem.* **7**, 2335 (1997)
54. G. Keskar, R. Rao, J. Luo, J. Hudson, A. M. Rao: Growth, nitrogen doping and characterization of isolated single-wall carbon nanotubes using liquid precursors, *Chem. Phys. Lett.* **412**, 269 (2005)
55. F. Villalpando-Paez, A. Zamudio, A. L. Elias, H. Son, E. B. Barros, S. Chou, Y. A. Kim, H. Muramatsu, T. Hayashi, J. Kong, H. Terrones, G. Dresselhaus, M. Endo, M. Terrones, M. S. Dresselhaus: Synthesis and characterization of long strands of nitrogen-doped single-walled carbon nanotubes, *Chem. Phys. Lett.* **424**, 345 (2006)
56. B.G. Sumpter, V. Meunier, J. M. Romo-Herrera, E. Cruz-Silva, D. A. Cullen, H. Terrones, D. J. Smith, M. Terrones: Nitrogen-mediated carbon nanotube growth: Diameter reduction, metallicity, bundle dispersability, and bamboo-like structure formation, *ACS Nano* **1**, 369 (2007)
57. M. Pinault, M. Mayne-L’Hermitte, C. Reynaud, V. Pichot, P. Launois, D. Ballutaud: Growth of multiwalled carbon nanotubes during the initial stages of aerosol-assisted CCVD, *Carbon* **43**, 2968 (2005)
58. R. Kamalakaran, M. Terrones, T. Seeger, Ph. Kohler-Redlich, M. Rühle, Y. A. Kim, T. Hayashi, M. Endo: Synthesis of thick and crystalline nanotube arrays by spray pyrolysis, *Appl. Phys. Lett.* **77**, 3385–3387 (2000)
59. E. G. Wang, Z. G. Guo, J. Ma, M. M. Zhou, Y. K. Pu, S. Liu, G. Y. Zhang, D. Y. Zhong: Optical emission spectroscopy study of the influence of nitrogen on carbon nanotube growth, *Carbon* **41**, 1827 (2003)
60. K. B. K. Teo, M. Chhowalla, G. A. J. Amaratunga, W. I. Milne, D. G. Hasko, G. Pirio, P. Legagneux, F. Wyczisk, D. Pribat: Uniform patterned growth of carbon nanotubes without surface carbon, *Appl. Phys. Lett.* **79**, 1534 (2001)
61. K. B. K. Teo, D. B. Hash, R. G. Lacerda, N. L. Rupesinghe, M. S. Bell, S. H. Dalal, D. Bose, T. R. Govindan, B. A. Cruden, M. Chhowalla, G. A. J. Amaratunga, J. M. Meyyappan, W. I. Milne: The significance of plasma heating in carbon nanotube and nanofiber growth, *Nano Lett.* **4**, 921 (2004)
62. J. Yu, X. D. Bai, J. Ahn, S. F. Yoon, E. G. Wang: Highly oriented rich boron B–C–N nanotubes by bias-assisted hot filament chemical vapor deposition, *Chem. Phys. Lett.* **323**, 529 (2000)
63. D. Golberg, Y. Bando, L. Bourgeois, K. Kurashima, T. Sato: Large-scale synthesis and HRTEM analysis of single-walled B- and N-doped carbon nanotube bundles, *Carbon* **38**, 2017 (2000)
64. E. Borowiak-Palen, T. Pichler, G. G. Fuentes, A. Graff, R. J. Kalenczuk, M. Knupfer, J. Fink: Efficient production of B-substituted single-wall carbon nanotubes, *Chem. Phys. Lett.* **378**, 516 (2003)
65. M. Endo, H. Muramatsu, T. Hayashi, Y. A. Kim, G. Van Lier, J. C. Charlier, H. Terrones, M. Terrones, M. S. Dresselhaus: Atomic nanotube welders: Boron interstitials triggering connections in double-walled carbon nanotubes, *Nano Lett.* **5**, 1099 (2005)
66. K. Koziol, M. S. Shaffer, A. H. Windle: Three-dimensional internal order in multiwalled carbon nanotubes grown by chemical vapor deposition, *Adv. Mater.* **17**, 760 (2005)

67. C. Ducati, K. Koziol, S. Friedrichs, T. J. V. Yates, M. S. Shaffer, P. A. Midgkey, A. H. Windle: Crystallographic order in multi-walled carbon nanotubes synthesized in the presence of nitrogen, *Small* **2**, 774 (2006)
68. Ph. Kohler-Redlich and M. Terrones, Unpublished results
69. X. Blase, J.-C. Charlier, A. De Vita, R. Car, Ph. Redlich, M. Terrones, W. K. Hsu, H. Terrones, D. L. Carroll, P. M. Ajayan: Boron-mediated growth of long helicity-selected carbon nanotubes, *Phys. Rev. Lett.* **83**, 5078 (1999)
70. W. K. Hsu, S. Firth, P. Redlich, M. Terrones, H. Terrones, Y. Q. Zhu, N. Grobert, A. Schilder, R. J. H. Clark, H. W. Kroto, D. R. M. Walton: Boron doping effects in carbon nanotubes, *J. Mater. Chem.* **10**, 1425 (2000)
71. E. Hernández, P. Ordejón, I. Boustani, A. Rubio, J. A. Alonso: Tight binding molecular dynamics studies of boron assisted nanotube growth, *J. Chem. Phys.* **113**, 3814 (2000)
72. K. McGuire, N. Gothard, P. L. Gai, M. S. Dresselhaus, G. Sumanasekera, A. M. Rao: Synthesis and Raman characterization of boron-doped single-walled carbon nanotubes, *Carbon* **43**, 219 (2005)
73. M. Terrones, W. K. Hsu, A. Schilder, H. Terrones, N. Grobert, J. P. Hare, Y. Q. Zhu, M. Schwoerer, K. Prassides, H. W. Kroto, D. R. M. Walton: Novel nanotubes and encapsulated nanowires, *Appl. Phys. A Mater. Sci. Process* **66**, 307 (1998)
74. D. L. Carroll, P. Redlich, X. Blase, J. C. Charlier, S. Curran, P. M. Ajayan, S. Roth, M. Ruhle: Effects of nanodomain formation on the electronic structure of doped carbon nanotubes, *Phys. Rev. Lett.* **81**, 2332 (1998)
75. R. Czerw, M. Terrones, J. C. Charlier, X. Blase, B. Foley, R. Kamalakaran, N. Grobert, H. Terrones, D. Tekleab, P. M. Ajayan, W. Blau, M. Ruhle, D. L. Carroll: Identification of electron donor states in N-doped carbon nanotubes, *Nano Lett.* **1**, 457 (2001)
76. D. Golberg, P. S. Dorozhkin, Y. Bando, Z. C. Dong, C. C. Tang, Y. Uemura, N. Grobert, M. Reyes-Reyes, H. Terrones, M. Terrones: Structure, transport and field-emission properties of compound nanotubes: CN<sub>x</sub> vs. BNC<sub>x</sub> ( $x < 0.1$ ) *Appl. Phys A Mater. Sci. Process.* **76**, 499 (2003)
77. K. Liu, P. Avouris, R. Martel, W. K. Hsu: Electrical transport in doped multiwalled carbon nanotubes, *Phys. Rev. B* **63**, 161404 (2001)
78. W. K. Hsu, S. Y. Chu, E. Munoz-Picone, J. L. Boldu, S. Firth, P. Franchi, B. P. Roberts, A. Schilder, H. Terrones, N. Grobert, Y. Q. Zhu, M. Terrones, M. E. McHenry, H. W. Kroto, D. R. M. Walton: Metallic behaviour of boron-containing carbon nanotubes, *Chem. Phys. Lett.* **323**, 572 (2000)
79. Y. M. Choi, D. S. Lee, R. Czerw, P. W. Chiu, N. Grobert, M. Terrones, M. Reyes-Reyes, H. Terrones, J. C. Charlier, P. M. Ajayan, S. Roth, D. L. Carroll, Y. W. Park: Nonlinear behavior in the thermopower of doped carbon nanotubes due to strong, localized states, *Nano Lett.* **3**, 839 (2003)
80. L. Grigorian, G. U. Sumanasekera, A. L. Loper, S. Fang, J. L. Allen, P. C. Eklund: Transport properties of alkali-metal-doped single-wall carbon nanotubes, *Phys. Rev. B* **58**, 4195 (1998)
81. K. Bradley, S.H. Jhi, P. G. Collins, J. Hone, M. L. Cohen, S. G. Louie, A. Zettl: Is the intrinsic thermoelectric power of carbon nanotubes positive, *Phys. Rev. Lett.* **85**, 4361 (2000)
82. R. S. Lee, H. J. Kim, J. E. Fischer, A. Thess, R. E. Smalley: Conductivity enhancement in single-walled carbon nanotube bundles doped with K and Br, *Nature* **388**, 255 (1997)
83. A. M. Rao, E. Richter, S. Bandow, B. Chase, P. C. Eklund, K. A. Williams, S. Fang, K. R. Subbaswamy, M. Menon, A. Thes, R. E. Smalley, G. Dresselhaus, M. S. Dresselhaus: Diameter-selective Raman scattering from vibrational modes in carbon nanotubes, *Science* **275**, 187 (1997)
84. S. Bandow, A. M. Rao, G. U. Sumanasekera, P. C. Eklund, F. Kokai, K. Takahashi, S. Iijima: Evidence for anomalously small charge transfer in doped single-wall carbon nanohorn aggregates with Li, K and Br, *Appl. Phys. A Mater. Science Process.* **71**, 561 (2000)
85. M. S. Dresselhaus, P. C. Eklund: Phonons in carbon nanotubes, *Adv Phys.* **40**, 705 (2000)
86. M. S. Dresselhaus, G. Dresselhaus, A. Jorio, A. G. Souza Filho, R. Saito: Raman spectroscopy on isolated single wall carbon nanotubes, *Carbon* **40**, 2043 (2002)
87. A. Kukovecz, T. Pichler, R. Pfeiffer, H. Kuzmany: Diameter selective charge transfer in p- and n-doped single wall carbon nanotubes synthesized by the HiPCO method, *Chem. Commun.* **5**, 1730 (2002)

88. M.S. Dresselhaus, G. Dresselhaus, M. Hofmann: The big picture of Raman scattering in carbon nanotubes, *Vib. Spectrosc.* **45**, 71–81 (2007)
89. M. A. Pimenta, A. Marucci, S. Empedocles, M. Bawendi, E. B. Hanlon, A. M. Rao, P. C. Eklund, R. E. Smalley, G. Dresselhaus, M. S. Dresselhaus: Raman modes of metallic carbon nanotubes, *Phys. Rev. B* **58**, 16016 (1998)
90. A. G. Souza Filho, A. Jorio, G. G. Samsonidze, G. Dresselhaus, R. Saito, M. S. Dresselhaus: Raman spectroscopy for probing chemically/physically induced phenomena in carbon nanotubes, *Nanotechnology* **14**, 1130 (2003)
91. L. Duclaux: Review of the doping of carbon nanotubes (multiwalled and single-walled, *Carbon* **1751**, 717 (2002)
92. J. E. Fischer: Chemical doping of single-wall carbon nanotubes, *Acc. Chem. Res.* **35**, 1079 (2002)
93. S. Banerjee, T. Hemraj-Benny, S. S. Wong: Routes towards separating metallic and semiconducting nanotubes, *J. Nanosci. Nanotechnol.* **5**, 841 (2005)
94. M. Endo, Y. A. Kim, T. Hayashi, H. Muramatsu, M. Terrones, R. Saito, F. Villalpando-Paez, S. G. Chou, M. S. Dresselhaus: Nanotube coalescence-inducing mode: A novel vibrational mode in carbon systems, *Small* **2**, 1031 (2006)
95. C. Fantini, E. Cruz, A. Jorio, M. Terrones, H. Terrones, G. Van Lier, J. C. Charlier, M. S. Dresselhaus, R. Saito, Y. A. Kim, T. Hayashi, H. Muramatsu, M. Endo, M. A. Pimenta: Resonance Raman study of linear carbon chains formed by the heat treatment of double-wall carbon nanotubes, *Phys. Rev. B* **73**, 193408 (2006)
96. S. B. Fagan, A. G. Souza Filho, J. M. Filho, P. Corio, M. S. Dresselhaus: Electronic properties of Ag- and CrO<sub>3</sub>-filled single-wall carbon nanotubes, *Chem. Phys. Lett.* **456**, 54 (2005)
97. P. Corio, A. P. Santos, M. L. A. Temperini, V. W. Brar, M. A. Pimenta, M. S. Dresselhaus: Characterization of single wall carbon nanotubes filled with silver and with chromium compounds, *Chem. Phys. Lett.* **383**, 475 (2004)
98. A. Rakitin, C. Papadopoulos, J. M. Xu: Carbon nanotube self-doping: Calculation of the hole carrier concentration, *Phys. Rev. B* **67**, 033411 (2003)
99. G. Chen, C. A. Furtado, U. J. Kim, P. C. Eklund: Alkali-metal-doping dynamics and anomalous lattice contraction of individual debundled carbon nanotubes, *Phys. Rev. B* **72**, 155406 (2005)
100. G. Chen, C. A. Furtado, S. Bandow, S. Iijima, P. C. Eklund: Anomalous contraction of the C–C bond length in semiconducting carbon nanotubes observed during Cs doping, *Phys. Rev. B* **71**, 045408 (2005)
101. L. Terrazos, R. B. Capaz: Unpublished results
102. A. Das, A. K. Sood, A. Govindaraj, A. M. Saitta, M. Lazzeri, F. Mauri, C. N. R. Rao: Doping in carbon nanotubes probed by Raman and transport measurements, *Phys. Rev. Lett.* **99**, 136803 (2007)
103. N. Caudal, A. M. Saitta, M. Lazzeri, F. Mauri: Kohn anomalies and nonadiabaticity in doped carbon nanotubes, *Phys. Rev. B* **75**, 115423 (2007)
104. A. G. Souza Filho, V. Meunier, M. Terrones, B. G. Sumpter, E. B. Barros, F. Villalpando-Páez, J. Mendes Filho, Y. A. Kim, H. Muramatsu, T. Hayashi, M. Endo, M. S. Dresselhaus: Selective tuning of the electronic properties of co-axial nanocables through exohedral doping, *Nano Lett.* **7**, 2383 (2007)
105. T. Hayashi, D. Shimamoto, Y. A. Kim, H. Muramatsu, F. Okino, H. Touhara, T. Shimada, Y. Miyauchi, S. Maruyama, M. Terrones, M. S. Dresselhaus, M. Endo: Selective optical property modification of double-walled carbon nanotubes by fluorination, *ACS Nano* **2**, 485 (2008)
106. A. Jorio, M. A. Pimenta, A. G. Souza Filho, R. Saito, M. S. Dresselhaus, G. Dresselhaus: Characterizing carbon nanotube samples with resonance Raman scattering, *New J. Phys.* **5**, 137 (2003)
107. E. B. Barros, H. B. Son, G. G. Samsonidze, A. G. Souza Filho, R. Saito, Y. A. Kim, H. Muramatsu, T. Hayashi, M. Endo, M. S. Dresselhaus: Double-wall carbon nanotubes treated with H<sub>2</sub>SO<sub>4</sub>, *Phys. Rev. B* **76**, 045425 (2007)
108. V. Georgakilas, D. Voulgaris, E. Vazquez, M. Prato, D. M. Guldi, A. Kukovec, H. Kuzmany: Purification of HiPCO carbon nanotubes via organic functionalization, *J. Am. Chem. Soc.* **124**, 14318 (2002)

109. M. Zheng, A. Jagota, E. D. Semke, B. A. Diner, R. S. Mclean, S. R. Lustig, R. Richardson, N. G. Tassi: DNA-assisted dispersion and separation of carbon nanotubes, *Nat. Mater.* **2**, 338 (2003)
110. M. Zheng, A. Jagota., M. S. Strano, A. P. Santos, P. Barone, S. G. Chou, B. A. Diner, M. S. Dresselhaus, R. S. Mclean, G. B. Onoa, G. G. Samsonidze, E. D. Semke, M. Ursey, D. J. Walls: Structure-based carbon nanotube sorting by sequence-dependent DNA assembly, *Science* **302**, 1545 (2003)
111. D. A. Heller, E. S. Jeng, T. K. Yeung, B. M. Martinez, A. E. Moll, J. B. Gastala, M. S. Strano: Optical detection of DNA conformational polymorphism on single-walled carbon nanotubes, *Science* **311**, 508 (2006)
112. J.-C. Charlier, M. Terrones, M. Baxendale, V. Meunier, T. Zacharia, N. L. Rupesinghe, W. K. Hsu, N. Grobert, H. Terrones, G. A. J. Amaratunga: Enhanced electron field emission in B-doped carbon nanotubes, *Nano Lett.* **2**, 1191 (2002)
113. M. Doytcheva, M. Kaiser, M. Reyes-Reyes, M. Terrones, N. de Jonge: Electron emission from individual nitrogen-doped multi-walled carbon nanotubes, *Chem. Phys. Lett.* **396**, 126 (2004)
114. M. Endo, Y. A. Kim, T. Hayashi, K. Nishimura, T. Matusita, K. Miyashita, M. S. Dresselhaus: Vapor-grown carbon fibers (VGCFs) – Basic properties and their battery applications, *Carbon* **39**, 1287 (2001)
115. D. Y. Zhang, G. Y. Zhang, S. Liu, E. G. Wang, Q. Wang, H. Li, X. J. Huang: Lithium storage in polymerized carbon nitride nanobells, *Appl. Phys. Lett.* **79**, 3500 (2001)
116. J. Kong, N. R. Franklin, C. W. Zhou, M. G. Chapline, S. Peng, K. J. Cho, H. J. Dai: Nanotube molecular wires as chemical sensors, *Science* **287**, 622 (2000)
117. S. S. Wong, E. Joselevich, A. T. Woolley, C. L. Cheung, C. M. Lieber: Covalently functionalized nanotubes as nanometre-sized probes in chemistry and biology, *Nature* **394**, 52, 1998
118. P.G. Collins, K. Bradley, M. Ishigami, A. Zettl: Extreme oxygen sensitivity of electronic properties of carbon nanotubes, *Science* **287**, 1801 (2000)
119. F. Villalpando-Páez, A. H. Romero, E. Muñoz-Sandoval, L. M. Martínez, H. Terrones, M. Terrones: Fabrication of vapor and gas sensors using films of aligned  $CN_x$  nanotubes, *Chem. Phys. Lett.* **386**, 137 (2004)
120. P. Calvert: Nanotube composites – A recipe for strength, *Nature* **399**, 210 (1999)
121. A. Eitan et al., In *Proceedings of the Tenth US–Japan Conference on Composite Materials*. 634 (2002)
122. B. Fragneaud, K. Masenelli-Varlot, A. González-Montiel, M. Terrones, J. Y. Cavailé: Efficient coating of N-doped carbon nanotubes with polystyrene using atomic transfer radical polymerization, *Chem. Phys. Lett.* **419**, 567 (2005)
123. M. Dehonor, K. Masenelli-Varlot, A. González-Montiel, C. Gauthier, J. Y. Cavailé, H. Terrones, M. Terrones: Nanotube brushes: Polystyrene grafted covalently on  $CN_x$  nanotubes by nitroxide-mediated radical polymerization, *Chem. Commun.* 5349 (2005)
124. Fragneaud, et al.: Unpublished
125. D. M. Guldi, M. Marcaccio, D. Paolucci, F. Paolucci, M. Tagmatarchis, D. Tasis, E. Vasquez, M. Prato, *Angew. Chem. Int. Ed.* **42**, 4206 (2003)
126. K. Y. Jiang, L. S. Schadler, R. W. Siegel, X. J. Zhang, H. F. Zhang, M. Terrones: Protein immobilization on carbon nanotubes via a two-step process of diimide-activated amidation, *J. Mater. Chem.* **14**, 37 (2004)
127. K. Y. Jiang, A. Eitan, L. S. Schadler, P. M. Ajayan, R. W. Siegel, N. Grobert, M. Mayne, M. Reyes-Reyes, H. Terrones, M. Terrones: Selective attachment of gold nanoparticles to nitrogen-doped carbon nanotubes, *Nano Lett.* **3**, 275 (2003)
128. A. Zamudio, A. L. Elfías, J. A. Rodríguez-Manzo, F. López-Urías, G. Rodríguez-Gattorno, F. Lupo, M. Rühle, D. J. Smith, H. Terrones, D. Díaz, M. Terrones: Efficient anchoring of silver nanoparticles on N-doped carbon nanotubes, *Small* **2**, 346 (2005)
129. X. Lepró et al.: Unpublished data



130. J. L. Carrero-Sánchez, A. L. Elías, R. Mancilla, G. Arellín, H. Terrones, J. P. Laclette, M. Terrones: Biocompatibility and toxicological studies of carbon nanotubes doped with Nitrogen, *Nano Lett.* **6**, 1609 (2006)
131. D. B. Warheit, B. R. Laurence, K. L. Reed, D. H. Roach, G. A. M. Reynolds, T. R. Webb: Comparative pulmonary toxicity assessment of single-wall carbon nanotubes in rats, *Toxicol. Sci.* **77**, 117 (2004)
132. A. L. Elías, J. C. Carrero-Sánchez, H. Terrones, M. Endo, J. P. Laclette, M. Terrones: Comparative viability studies of pure carbon and nitrogen-doped multi walled carbon nanotube with amoeba cells: From amoebicidal to biocompatible structures, **3**, 1723–1729 (2007)

# Boron and Boron Carbide Materials: Nanostructures and Crystalline Solids

Kah Chun Lau, Yoke Khin Yap, and Ravindra Pandey

**Abstract** Owing to the rapid developments related to the novel  $B_xC_yN_z$  ternary structures, the pedagogical review chapter has several antecedents as new results have emerged. Specifically, we will focus on the  $B_xC_y$  (with  $x, y = 0-1$ ) hybrid material where the qualitative trend, in general, can be described by the ratio of its constituents. There is, however, a significant asymmetric popularity between the boron and carbon in the scientific literature. Carbon-based structures are well studied compared with boron-based structures. Consequently, understanding of the role played by boron in the formation of the  $B_xC_y$  hybrid structures remains somewhat incomplete. We, therefore, devote a substantial part of discussion on the boron-related structures with an aim to achieve the goal of a complete understanding of the physics and chemistry of the hybrid  $B_xC_y$  material.

## 1 Introduction

Advances in novel experimental techniques for fabrication and measurements together with development of new theoretical methods [1] have resulted, not only knowing the atomistic details of a given structural configuration, but fabrication of artificial structures that required placement of atoms at specified locations for tailor-made properties not exhibited by naturally occurring materials. The arrangements of atoms at nanoscale can now be routinely achieved. Both theoretical and experimental methods have observed a dramatic variation in the physical and chemical properties of a given material with the size at such length scale. For example, carbon exhibits novel properties in the form of clusters, fullerenes, graphene sheet, and carbon nanotubes (CNTs). Likewise, a large diversity in the topological configurations and properties of boron nanostructures has been reported.

---

K.C. Lau, Y.K. Yap, and R. Pandey (✉)

Department of Physics, Michigan Technological University, Houghton, MI 49931, USA  
e-mail: pandey@mtu.edu

A brief yet fully readable account of the evolution of the so-called nanomaterials is beyond the scope of this review due to extraordinary diversity and many interconnections. Here, we restrict ourselves to highlight recent developments in the area pertaining to a hybrid system consisting of both boron and carbon atoms,  $B_xC_y$ . The  $B_xC_y$  hybrid structures can be considered as a subset of novel ternary hybrid structures,  $B_xC_yN_z$  [2]. It is a well-known fact that synthesis of both  $B_xC_y$  and  $B_xC_yN_z$  structures remains a challenge despite the publication of the first report in 1970s [3].

It is expected that the underlying structural and bonding configurations of the hybrid  $B_xC_y$  material will be related to the boron and carbon structures, thereby exhibiting properties generally derived from the constituent elements. It is therefore important to review the structural and bonding configurations of the boron and carbon solids and nanostructures. This is what we propose to do in the following sections summarizing the basic features and structural properties related to structures ranging from clusters to nanotubes to macroscopic crystalline solids. It will be followed by description of the hybrid boron carbide (i.e.,  $B_xC_y$ ). We will give a summary in Sect. 4.

## 2 Boron Allotropes: Solids and Nanostructures

### 2.1 Boron Solids

The understanding of the crystalline phases of the elemental boron solid is not yet fully established. Unlike carbon, bulk boron cannot be found in nature, and all the known boron allotropes were obtained experimentally. Within this context, boron solids can always be considered as fascinating candidates due to their varied polymorphism in the structural arrangements and complex interplay of the chemical bonding due to “electron deficiency” [4, 5]. Electron deficiency is defined as the case where the number of electrons is less than the available atomic orbitals in the valence configuration of an atom. The consequences [4–6] of an electron-deficient bonding in a given material may be summarized as follows: (1) The ligancy (i.e., coordination number) is higher than both the number of valence atoms and the number of valence orbitals. (2) In the lattice, adjacent atoms increase their ligancy to the values larger than the orbital numbers [6, 7]. Therefore, the term “electron deficient” simply suggests that novel structures based on elemental boron are expected to exist in nature. With insufficient electrons to support a structural configuration by conventional “two-electron two-center” bonds, the boron-based compounds generally tend to adopt a novel mechanism to resolve their *electron deficiency* through “two-electron multicenter” bonds, which are topologically connected in a complex networks [4, 5].

Relative to carbon, the crystalline phases of boron are among the most complex structures reported for a pure element [4, 8], which utilize the icosahedral  $B_{12}$  unit as a common structural component in the lattice. As shown in Fig. 1, the  $B_{12}$

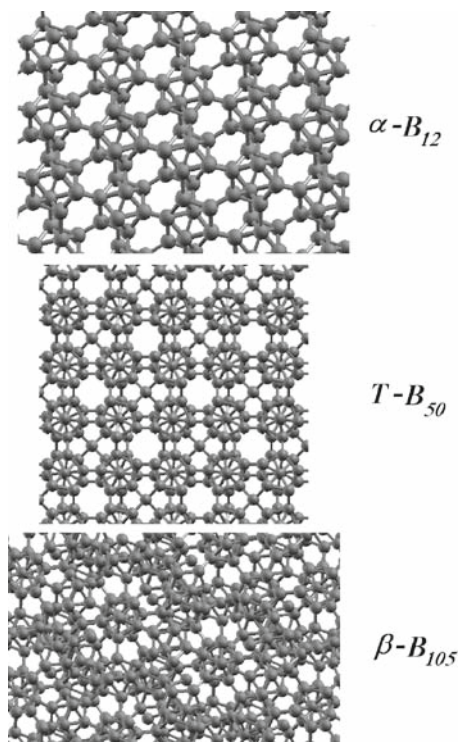


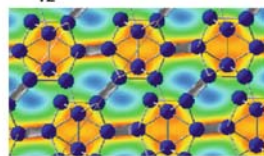
**Fig. 1** Icosahedral unit-based crystalline boron solids: (top)  $\alpha\text{-B}_{12}$ , (center)  $T\text{-B}_{50}$ , and (bottom)  $\beta\text{-B}_{105}$

icosahedron can be interlinked by strong covalent bonds in a variety of ways to form several well-known polymorphs such as  $\alpha$ -rhombohedral  $\text{B}_{12}$  ( $\alpha\text{-B}_{12}$ ) [9–17],  $\alpha$ -tetragonal  $\text{B}_{50}$  ( $T\text{-B}_{50}$ ) [11], or  $\beta$ -rhombohedral  $\text{B}_{105}$  ( $\beta\text{-B}_{105}$ ) [9, 14, 16–19]. In spite of the existence of several crystalline phases, the relative stability between the various polymorphs and the phase diagram of solid boron needs to be studied [20].

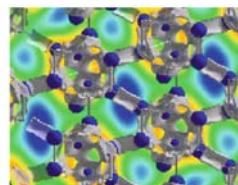
It is interesting to note here that the  $\text{B}_{12}$  unit is a preferred building block satisfying the bonding requirement of boron atoms in a given lattice, though an isolated  $\text{B}_{12}$  cluster itself is not stable [21, 22]. To fulfill the electron deficiency in an isolated  $\text{B}_{12}$  unit [23, 24], boron atoms form triangles or polyhedra to share the electrons among themselves. For example in the  $\alpha\text{-B}_{12}$  phase, a combination of localized covalent (i.e., two-center bonds) and delocalized multicenter bonds (e.g., three-center bonds) appear in the lattice. It can be interpreted as the preservation of the intrinsic stability of each individual icosahedron through the intra- and intericosahedral bonds in the crystalline lattice (Fig. 2). The energetically stable crystalline phases,  $\alpha\text{-B}_{12}$  and  $\beta\text{-B}_{105}$ , are found to be semiconductors while the other metastable solid,  $T\text{-B}_{50}$ , interconnected by interstitial boron atoms (Fig. 1) is found to be a metallic conductor. Although comments have been made about nonmetal to metal

**Fig. 2** The contour maps of the electron density of  $\alpha$ -B<sub>12</sub> (from *top to bottom*: AI, AII, and AIII) showing two-center (2c) and three-center (3c) bonds. The *red* region represents the high electron density contour, while the low electron density contour is shown by the *blue* region. The bonding is represented by the gray isosurface (AI-2c intericosahedral bond at 0.95 e/Å<sup>3</sup>, AII-3c intraicosahedral bond at 0.77 e/Å<sup>3</sup>, and AIII-3c intericosahedral bond at 0.60 e/Å<sup>3</sup>) (reprinted with permission from [25], copyright American Chemical Society)

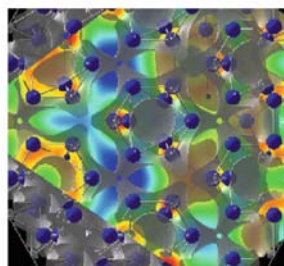
### $\alpha$ -B<sub>12</sub> rhombohedral solid



**A I**



**A II**



**A III**

[14, 15] and nonmetal to superconductor [26–28] transitions, a detailed mechanism of the phase transition is yet to be reported.

## 2.2 Boron Nanostructures

In recent years, a large number of studies on various topological configurations of boron nanostructures, especially boranes [29–33], boron clusters [34–42], nanowires, nanoribbons, nanowhiskers, and nanotubes [43–45] continue to emerge. To understand the properties of boron nanostructures, discussions considering the basic features of distinctly reduced dimensionality and corresponding size-dependent studies are necessary and will be reviewed in the following section.

### 2.2.1 Boron Clusters

Analogous to the 0D carbon fullerenes, a search for the boron fullerene-like cage structures has yielded interesting results. Despite the B<sub>12</sub> unit being the building

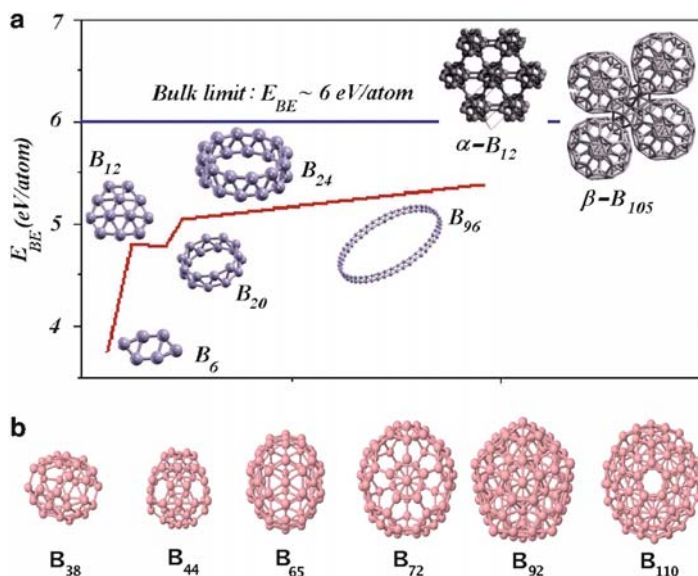


**Fig. 3** (a) The 2D to 3D structural transition in boron clusters [48] (reprinted with permission from [48], copyright Brill Publishing Group), (b) The boron fullerene-like cage structure [49] (reprinted with permission from [49], copyright American Physical Society)

block for the boron solid, the clusters are generally found to prefer the structural motifs different from the  $B_{12}$  unit, such as 2D planar, quasi-1D tubular, or 3D double-ring [7, 42, 46–48] motifs shown in Fig. 3. One of the earliest experimental observation of the cluster [34] was a catalyst for a number of theoretical [38, 39, 46, 50–57] as well as further experimental [35–37, 40] studies on small boron clusters. Based on a series of photoelectron spectra in the small boron clusters regime,  $B_n$  ( $n \leq 5$ ) [41, 58–62], it is now generally accepted that boron and carbon form a set of complimentary chemical systems the bulk carbon is stable in 2D graphitic structure and the carbon clusters are characterized by 3D cages, whereas the bulk boron is characterized by 3D cages and the boron clusters are characterized by the 2D structures. The high stability of the 2D planar structures over the 3D structures is attributed to the presence of the effective electron delocalization on the bonds in the boron lattice [41, 48, 63, 64].

Although the boron clusters in the small clusters regime are well characterized, fewer studies are available for the large boron clusters [48]. To the best of our knowledge, the studies of large boron clusters mostly considered simple geometrical configurations with high symmetries, which do not resemble the fragments of either crystalline or amorphous bulk boron. Overall, the clusters favor the 2D planar structure up to 18 atoms and thereafter prefer the 3D tubular or double-ring structural motifs [42, 48, 65–69]. The 2D–3D structural transition observed at  $B_{20}$ , reminiscent of the ring-to-fullerene transition at  $C_{20}$  [70–72], suggests that  $B_{20}$  may be considered as the embryo of the thinnest single-wall boron nanotube [42].

Besides the 3D tubular or double-ring configuration, the boron cage structure, analogous to carbon fullerenes, has recently been proposed (Fig. 3), opening up the possibility of a completely new family of boron clusters with high stability in the large clusters regime. In spite of the instability of pristine  $B_{12}$  icosahedral cage, the boron fullerenes-like cages would be the second example in nature after the  $C_{60}$ -derived family, with a circular and distinct hollow structure. As has been pointed out earlier [49, 73], the most stable boron cages reach ~91% of the  $\alpha$ -rhombohedral bulk stability. We note that the limit is ~89.9% for the large 3D double-ring isomer (i.e., infinite strip) whose stability tends to increase with the increase of the radius of the ring [48, 49, 68, 69, 73]. Among the boron fullerene-like cage  $B_n$  clusters with  $n = 12$ –300, the  $B_{80}$  fullerene-like cage, therefore, emerges as the most stable cluster with a gap of ~1 eV between the highest occupied and lowest unoccupied orbitals exhibiting an unusual high chemical stability.

The energetic competition among the 2D infinite strip together with the 3D double-ring and fullerene-like cage structures is expected to be reflected in the distinct features of chemical bonding present in the respective configurations. It is essentially an interplay between saturation of dangling bonds and the curvature strain associated with these 2D and 3D configurations. One now needs to address the question of their intrinsic structural stability via both experimental and theoretical studies of the vibrational and thermodynamic stability. Analysis of chemical bonding that governs the *electron-deficient* boron atoms in the large clusters also remains to be considered in future.

### 2.2.2 Boron Sheets

It is well known that CNTs are a structural paradigm for all tubular materials. CNTs can be seen as a cylindrical modification of graphite, which may geometrically be constructed by cutting a rectangular piece out of a single graphene sheet and rolling it up to form a nanotube. However, not a single direct clue can be found for boron nanotubes due to nonexistence of a boron sheet or graphitic-like boron layers in nature. Above all, studies on boron sheet configurations are limited only to theoretical ones that have been focused on the pristine 2D infinite plane and the corresponding finite-size planar structures. The understanding of the physics and chemistry of the layered crystalline condensed phase of boron remains to be an open question.

Assuming that the formation of BNTs can be analogous to CNTs that are formed only under kinetically constrained conditions, one can conjecture that: “*one of the main difficulties in synthesizing boron nanotubes appears to be the instability of a graphene-like boron sheet.*” Thus, while waiting for the empirical evidence, *first-principles* calculations [25, 74–79] have considered the question of the stability of the 2D boron sheets (Fig. 4). Taking the guidance from the finite 2D quasiplanar, convex, and planar boron cluster configurations [7, 48], several types of sheet configurations based on different structural motifs have been proposed. Instead of having the unsaturated dangling bonds as appearing in the finite 2D planar boron clusters, stability of the infinite 2D boron sheet can be attributed to the long-range

Coulomb forces embedded within its unique 2D crystalline lattice. Owing to the curvature strain, a boron sheet appears to be more stable than its curvature-derived nanostructures, namely fullerenes and nanotubes [73–75, 77, 79, 80].

Since the elemental boron solids have neither a purely covalent nor a purely metallic character, one can argue that the three-centered bonds and the electron-deficient features of boron [4, 5] should be energetically more competitive and stable than bonding features with only the  $sp^2$  hybridization as found in the carbon graphitic system. Hence, the competing roles played by the three-centered and two-centered bonding in determining the stability of the 2D boron sheets were investigated [25, 74–79]. Among the possible configurations that have been studied [25, 76, 78], the  $\alpha$ -boron sheet is found to be the most stable 2D planar boron sheet representing a combination of both three-centered and two-centered bondings [78, 79]. It is composed of both hexagonal and triangular motifs (Fig. 4) and the cohesive energy is about  $\sim 93\%$  of the  $\alpha$ -rhombohedral boron solid [78]. Interestingly, the results suggest that the pristine boron sheets should be metallic, irrespective of their different structural motifs [25, 74–79].

Following the  $\alpha$ -boron sheet, the next stable configuration is the buckled triangular sheet [25, 74–77]. It was obtained from the geometry relaxation of a flat

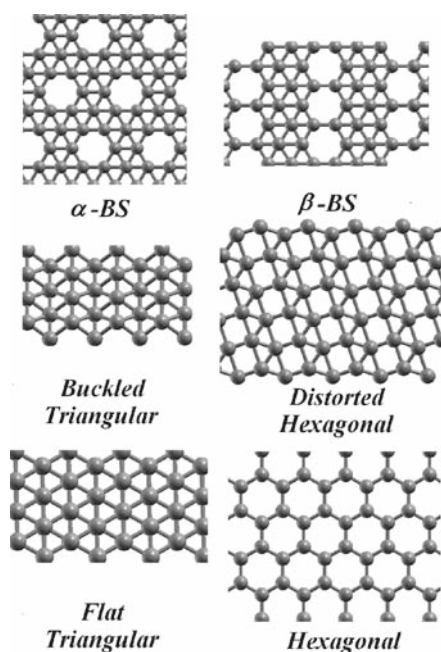


**Fig. 4** The 2D pristine boron sheet configurations [25, 74–78]: (top)  $\alpha$ -sheet and  $\beta$ -sheet (which are hybrid of hexagonal and triangular structural motifs), (center) buckled triangular and distorted hexagonal sheets (i.e., *triangle-square-triangle* {1221} sheet), (bottom) flat triangular and hexagonal sheets (reprinted with permission from [76], copyright American Chemical Society)



triangular sheet through a buckling along the perpendicular direction of the sheet. Subsequently, the buckling mixes in-plane and out-of-plane electronic states and can be thought of as a symmetry reducing distortion that enhances binding. Intuitively, the buckling of boron atoms is a response of the sheet to the internal stress imposed by the arrangement of the atoms in a perfect triangular 2D lattice. In an extensive first-principles study by Lau et al. [25, 76, 80], the results find a stable sheet configuration comprising a network of “triangle–square–triangle” units (i.e., {1221}) in the lattice. It was derived from a distorted hexagonal lattice of boron atoms. Similar to the  $\alpha$ - and buckled triangular sheet configurations, the bonding in the distorted hexagonal sheet is characterized by both two-center and three-center bonds, reminiscent of the electron-deficient features of boron atoms [25, 76, 80]. Above all, the three-centered (i.e., perfect hexagonal sheet) or the two-centered bonded (i.e., flat triangular sheet) configurations [25, 74–77] are found to be energetically less favorable. Unlike carbon, the  $sp^2$  bonding features are not preferred in boron sheets due to the partial occupancy of the in-plane  $sp^2$  bonding states.

### 2.2.3 Boron Nanotubes

The predicted stability of the boron sheet configurations suggests, in principle, the feasibility of synthesis of boron nanotubes. In the scientific literature, there is only a single report [45] of synthesis of BNT showing that the synthesized 1D single-walled boron nanotubes (SWNT) are extremely sensitive to the high-energy electron exposure [45]. Thus, besides offering a new class of 1D nanostructures, the experimental study opened up many unanswered questions on the stability, energetics, and the electronic properties of the tubular boron structures [45]. Inspired by the so-called Aufbau principle proposed by Boustani [46], and partly stimulated by the experimental report, several theoretical studies have carried out the search for the stable tubular configurations of boron. Overall, the results find the stable nanotubes to be composed of different structures due to the several precursive competing boron sheet configurations from which the tubular configurations can be derived. Since the 2D boron sheets are metallic, the simple zone folding scheme suggests that SWBNTs should also be metallic, irrespective of their chiralities. Compared with the other 1D boron nanostructures, e.g., nanowires, nanoribbons, and nanowhiskers [43, 44], BNTs can be categorized as a new class of topological structure in boron [7, 77, 81]. While the boron nanowires, nanoribbons, and nanobelts are all found to be bulk-like (i.e., either in crystalline or amorphous phase) [43, 44, 82], details of the structural morphology of BNTs remain to be verified by experiments, in spite of the theoretical predictions of their stability [74, 75, 77, 79–81, 83–85].

It is interesting to note here that the finite size of boron tubular structures has also been predicted to be stable among other structural motifs [47, 66, 67, 73]. Spanning from  $B_{24}$  to  $B_{240}$ , the quasi-1D boron structures (Fig. 5) have been found to have a finite energy gap between the highest occupied and lowest unoccupied molecular orbitals [47, 66, 67, 73, 85]. As the cluster size and length of the tubular configurations increases, the configurational stability increases, but the energy gap

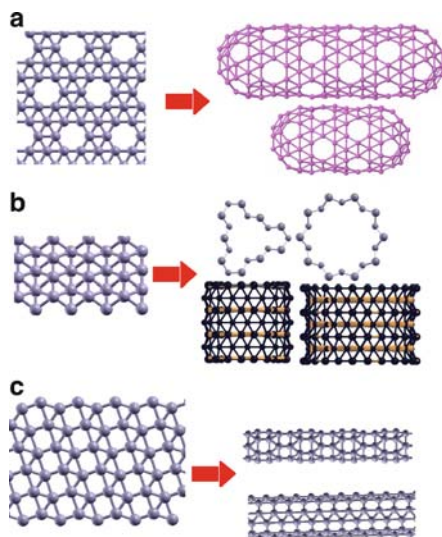


**Fig. 5** The three most stable structural motifs of pristine 2D sheet:  $\alpha$ -sheet, buckled triangular sheet, and distorted hexagonal sheet, and their corresponding pristine single-walled nanotubes with different chiralities [73–75, 77, 79–81]

decreases approaching to be metallic in the limit of infinite length [73, 85]. We note that the electron transport in BNTs is predicted to be ballistic [86].

Analogous to CNTs, details of the construction and classification of pristine infinite SWBNTs derived from the buckled triangular and distorted hexagonal sheets can be found following the scheme suggested by Kunstmann et al. [77, 81]. On the other hand, the construction and classification of the pristine SWBNTs derived from the  $\alpha$ -sheet can be found in the recently published work [79]. The reported tubular configurations derived from energetically preferred  $\alpha$ -, buckled triangular, and distorted hexagonal sheets (Fig. 5) show the stability that is about ~90–93% of the  $\alpha$ -rhombohedral boron solid.

In contrast to the metallic boron nanotubes that derived from the buckled triangular and distorted hexagonal configurations [74, 75, 77, 80, 81, 84], the tubular configuration derived from the  $\alpha$ -sheet shows variation in electronic properties with variation in the structural parameters [79]. For example, the energy gap of a small-diameter semiconducting nanotube decreases as we increase both the diameter and chiral angle of the tube. The nanotubes with diameter larger than 17 Å are predicted to be metallic as is the case with the  $\alpha$ -sheet. Since small-diameter  $\alpha$ -nanotube does not follow the simple zone folding scheme, one needs to examine the variation in the chemical bonding of the  $\alpha$ -nanotube in going from small to large diameter. The diameter-dependent variation in the bonding features is likely to influence the electronic properties of  $\alpha$ -nanotubes.

The crystalline bundles of BNTs have recently been the subject of a theoretical study [81] that found the bundles to be metallic. Considering the semiconducting nature of the boron crystalline solids [14], the metallic BNT crystalline bundles

appear to represent a new condensed phase of boron. For the case of the CNT bundles, the Van der Waals interaction between the pristine CNTs is comparable to that in the graphite layers [87, 88]. On the other hand, the BNTs are covalently bonded in the bundles via two-centered and three-centered bonds [81], reminiscent of the two-centered and three-centered bonds representing the intericosahedral interactions (Fig. 2) in the  $\alpha$ -rhombohedral boron solid [13]. Likewise, one might expect the presence of the covalent bonds in multiwalled BNTs in contrast to the case of multiwalled CNTs where a weak coupling exists among the walls of nanotube formed by carbon. Under ambient condition, one can therefore say that the CNT bundles are sparse in the condensed crystalline phase, while the BNT bundles are expected to be in a close-packed crystalline phase. Hence, substantial differences related to the bulk properties of BNT and CNT bundles will be expected. For example, *first-principles* calculations on the BNT bundles [81] yield the modulus of compressibility (i.e., bulk modulus,  $B_0$ ) to be  $\sim 85$ – $111$  GPa [81], higher than  $\sim 28$ – $39$  GPa of CNT bundles [87] but lower than  $\sim 185$ – $220$  GPa for boron solids [17, 89]. The Debye temperature of BNT bundles is predicted to be  $\sim 700$ – $950$  K at room temperature [81], compared with that of  $\sim 1,219$  K for the  $\beta$ -boron solid [18].

### 3 Boron Carbide Allotropes: Solids and Nanostructures

Carbon and its related allotropes in both solids and nanostructures are generally well studied relative to boron and its compounds. In the synthesis of boron carbide allotropes, the role played by carbon is relatively overwhelming. Therefore, being a fundamental precursor for both solid and nano structures, the importance of carbon in the formation of  $B_xC_y$  allotropes seems to be unquestionable.

#### 3.1 Carbon Solids

The most convenient classification scheme for the carbon polymorphs is based on the type of hybridization of the valence orbitals of carbon [90]. Since the energy differences between the valence orbitals (i.e.,  $2s$ ,  $2p_x$ ,  $2p_y$ , and  $2p_z$ ) are small, the mixing of  $2s$  with  $2p$  bonding determines the structural and bonding properties of carbon solids. Consequently, the diversity of carbon allotropes is associated with the fact that carbon atoms may prefer  $sp^n$  ( $n = 1$ – $3$ ) hybridization [91, 92], rendering  $sp^3$  (tetravalent),  $sp^2$  (trivalent), and  $sp$  (divalent) bonds in a given lattice. Each valence state then corresponds to a certain form of an allotrope, such as (three-dimensional) spatial structure, diamond ( $sp^3$ ), two-dimensional planar structure, graphite ( $sp^2$ ), and the third possible state, one-dimensional chain-like carbyne ( $sp$ ). For diamond, each carbon atom is  $sp^3$  hybridized in the tetrahedral structure, arranged either in the cubic or hexagonal (wurtzite) polymorphs [93, 94].

In graphite, the  $sp^2$  hybridization forms in-plane  $\sigma$  bonds whereas  $C-2p_z$  orbitals prefer the arrangement of the hexagonal crystalline lattice resulting in weak bonding of the graphitic layers via the Van der Waals forces at the interlayer distance of  $\sim 3.5$  Å [95]. Because of the subtle interlayer interaction, the energetic stability of these layered structures essentially depends on the stacking sequences of the individual graphene sheet. Among the four possible types of stacking sequences, namely the *ABAB* (i.e., the Bernal or hexagonal), the *AB'AB'* (i.e., orthorhombic), *ABC ABC* (i.e., rhombohedral), and *AAAA*, the Bernal type is the most commonly found in nature [96, 97]. On the other hand, the *AAAA* stacking has not been observed so far in the natural graphite, but it is very common for graphite intercalation compounds such as  $LiC_6$  and  $KC_8$  [97].

Carbyne is a one-dimensional chain-like molecular structure and is representative of the  $sp$ -hybridization in the lattice. The quasi-crystalline structure consists of carbon chains with double ( $=C=C=$ )<sub>*n*</sub> (i.e., cumulenic) or alternating single/triple ( $C^{\circ}=C$ )<sub>*n*</sub> (i.e., polyynic) covalent bonds. Owing to their relatively high chemical reactivity, solid carbyne typically contains significant concentrations of impurities and amorphous carbon [98, 99].

## 3.2 Hybrid Structures of Boron and Carbon: $B_xC_y$ Solids

The structural and physical properties of the hybrid  $B_xC_y$  can be comprehended as an intermediate between those of the boron and carbon allotropes as the stoichiometry (i.e., the atomic ratio of boron to carbon) varies in the lattice. In the boron-rich structures, the properties are expected to exhibit boron-like features and vice versa. In the following sections, we will review the properties of the hybrid  $B_xC_y$  in either the boron-rich and carbon-rich phases.

### 3.2.1 Boron-Rich $B_xC_y$ Solid

Boron carbide ( $B_4C$ ) is the well-known hybrid solid in which the carbon content can vary from 8 to 20 at.% [100, 101]. It is one of the hardest material after diamond and cubic-BN [102, 103]. In addition to its hardness,  $B_4C$  has a high melting point and high resistance to chemical reagents. Because of these properties, thin films [104, 105] of boron carbide are considered as coating materials for high-temperature applications. On the other hand, by utilizing its unique fivefold symmetry (Fig. 6), which is rare in nature, the icosahedral boron carbide crystals of size ranging from 1 to 10  $\mu m$  have been synthesized [106]. Instead of the amorphous-like boron carbide thin film [105], these  $B_4C$  crystals can be used as a tip of a micro or nanoindenter.

The atomic structure of the icosahedral  $B_4C$  solid is rather unique [108, 109] (Fig. 6). It consists of the distorted  $B_{11}C$  icosahedra located at the corners of a unit cell of rhombohedral Bravais lattice with the space group  $R_3m$ . The icosahedra are

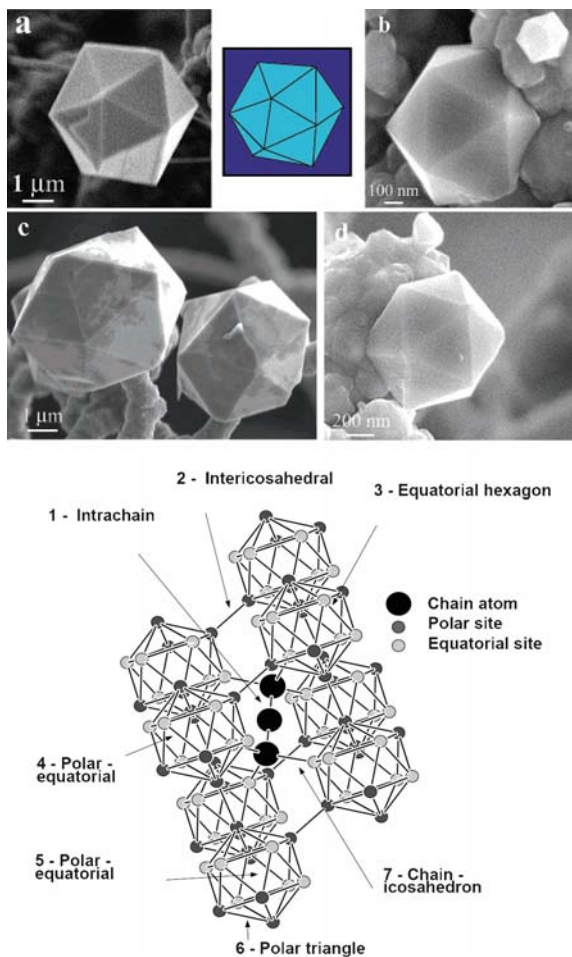


**Fig. 6** *Top:* (a) SEM image of a typical icosahedron crystal of boron carbide. The diagonal across the crystal is about 5  $\mu\text{m}$ . The inset shows an illustrating model of an isolated icosahedron corresponding to the real crystal. (b–d) Icosahedral multiply twinned particles (MTP) crystals observed in the range from 0.5 to 10  $\mu\text{m}$ , with various orientations [106] (reprinted with permission from [106], copyright American Chemical Society). *Bottom:* The atomic structure of  $\text{B}_4\text{C}$  [107] (reprinted with permission from [107], copyright American Physical Society)

connected by the atomic linear chains (e.g., C–B–C) in the lattice [107]. However, the location of the carbon atoms in the  $\text{B}_{12-n}\text{C}_n$  icosahedron and the value of  $n$  are still not exactly known [110–112]. This may be due to some degree of randomness, as the *six* equatorial (chain-connected) and the *six* polar (icosahedron-connected) icosahedral sites are indistinguishable in the lattice. It has recently been suggested that the boron carbide solid could be composed of different polytypes, each corresponding to a given possible configuration of chain and icosahedron determined by the

certain degree of randomness [113] that leads to the fluctuation of its stoichiometry. We note here that the effects of polytypes on the mechanical properties (i.e., Hugoniot elastic limit) of the  $B_4C$  solid were considered in theoretical study [113] without employing an appropriate stochastic model.

To determine the exact sequence of the chain (i.e., C–B–C, C–B–B, or C–C–C) in the  $B_4C$  lattice [114, 115], Raman spectroscopy [116, 117] and FTIR measurements [117] were performed on the amorphous boron carbide ( $a-B_4C$ ). The results find the preference of the C–B–C chain over the C–C–C chain in the lattice. In particular, the signature of decreased intensity of the infrared stretching mode of C–B–C chains shows that the formation of the  $a-B_4C$  lattice may be due to the collapse of  $B_{11}C$ (CBC) unit of the crystalline lattice through the reorganization into the energetically favorite carbon and boron clusters. However, one needs to perform further studies to completely rule out the possibility of C–C–C and C–B–B chains in the crystalline lattice.

### 3.2.2 Carbon-Rich $B_xC_y$ Solid

Considering that the stoichiometry determines the structural and electronic properties of a hybrid solid, we expect the structural features of the carbon-rich  $B_xC_y$  solids to be dominated by either the  $sp^2$  graphitic or the  $sp^3$  diamond configuration. This is indeed the case for the boron-doped  $B_xC_{1-x}$  binary compounds [118–121] having the  $sp^3$  diamond-like tetrahedral networks in the lattice. Diamond, known as the hardest material with the highest atomic density, does not easily incorporate any other dopants in the lattice with exceptions being hydrogen, boron, nitrogen, and silicon. Boron is the only efficient dopant element that can be incorporated with high reproducibility and high enough concentration to be useful for applications of doped diamond in electronic devices [122].

For low-dopant concentrations [118, 119], boron-doped diamond is a p-type semiconductor with carrier concentration of  $\sim 10^{17}$ – $10^{19}$   $cm^{-3}$ . However, the lattice shows metallic-like conductivity [123] for the heavily doped diamond with the dopant concentration of about  $\geq 10^{20}$   $cm^{-3}$ . Furthermore, superconductivity has been seen in the heavily boron-doped diamond solid [124] and thin films [125, 126]. First-principles calculations [127–132] have tried to elucidate the mechanism responsible for superconductivity in the  $B_xC_{1-x}$  compounds. Specifically, the vibrational modes associated with the boron atoms that provide an essential contribution to the *electron–phonon* coupling strength have been identified [132]. The superconducting transition temperature is found to be dependent on the level of the boron doping [127–129]. It has been pointed out that the 3D nature of the network in the boron-doped diamond reduces the density of states at the Fermi level [130] leading to a lower transition temperature as compared to that in  $MgB_2$ . Following this observation, study of the B-doped diamond surfaces is now warranted since the 2D nature of the surface states in the lattice may lead to a higher superconducting transition temperature in the boorn-doped diamond.

The signatures of the  $sp^2$  graphitic structural features have been found in the bulk  $BC_3$  [133–135] (Fig. 7), which was synthesized by the chemical reaction of benzene

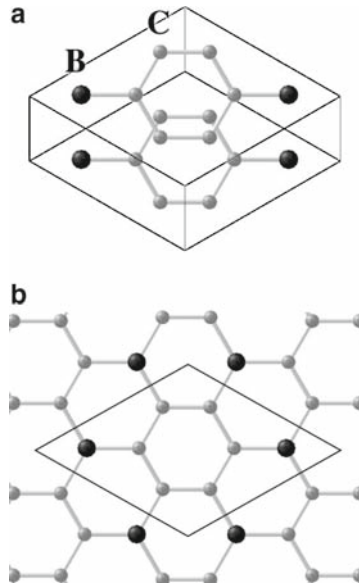


**Fig. 7** Top view of the BC<sub>3</sub> structure with the ABC stacking. In (a) two superimposed unit cells are viewed directly from above and in (b) a single layer of atoms is shown (reprinted with permission from [136], copyright American Physical Society)

and boron trichloride at 800°C [137]. Recent theoretical calculations predict the stacking of the BC<sub>3</sub> layers in a hexagonal lattice to be different from that in graphite. The layers in BC<sub>3</sub> prefer a nondirect stacking instead of direct stacking on top of each other [138] in which *ABAB* and *ABCABC* are predicted to be the energetically stable configurations [138] with real phonon frequencies at  $\Gamma$  *ABAB* being lower in energy by  $\sim 1$  meV/atom.

In BC<sub>3</sub> (Fig. 7), the calculated in-plane bond length ( $\sim 5.11$ – $5.12$  Å) is independent of the stacking sequence leading to the interatomic separation of  $d_{C-C}$  and  $d_{B-C}$  to be  $\sim 1.41$  and  $1.55$  Å, respectively [138]. In contrast to the in-plane configuration, the interlayer distance ( $c/2$  of *ABAB* or  $c/3$  for *ABCABC*) depends strongly on the stacking type ranging from 3.11 to 3.67 Å. Despite the BC<sub>3</sub> monolayer [134] being a semiconductor with an indirect band gap of  $\sim 0.66$  eV, the *ABAB* and *ABCABC* layered bulk are semiconducting with an indirect band gap around 0.5 eV and metallic, respectively. On the other hand, the experimental results [133, 137] find the layered bulk to be metallic. Thus, the layered BC<sub>3</sub> structure, as synthesized experimentally, appears to consist of both stacking configurations. Furthermore, superconductivity in the hole-doped BC<sub>3</sub> was predicted. Because of the strong electron–phonon coupling between the electronic states of the  $\sigma$  band and the phonon modes associated with the bond stretching mode, the superconducting temperature was predicted to increase as a function of the hole doping level in the BC<sub>3</sub> lattice [136].

### 3.3 Hybrid Structures of Boron and Carbon: $B_xC_y$ Nanostructures

Compared to their precursors in the  $B_xC_y$  solid, the properties of the  $B_xC_y$  nanostructures are expected to be different due to their “finiteness” in the physical size together with the large surface area to volume ratio. In terms of the system size, the  $B_xC_y$  nanostructures are intermediate between molecules and solids consisting of up to a few thousand atoms. In these atomic aggregates nanostructures where the surface plays a paramount role, dependence of the material property on the system size becomes non-scalable [139]. Therefore, exploration of the richness of the unique properties of the hybrid  $B_xC_y$  structures in the nanoscale regime will never be a trivial study.

Considering that the research on the novel  $B_xC_y$  nanostructures will largely be driven by that on the carbon-based nanostructures, such as fullerene, graphene, and nanotube, we will highlight some of the recent developments in the areas pertaining to physical and chemical properties of carbon nanostructures in the following section.

#### 3.3.1 Carbon Nanostructures

The carbon-based nanostructures, in general, offer new insight into the low-dimensional physics that has never ceased to surprise and continues to provide a fertile ground for novel technological applications. Accordingly, the rapid progress that stems from the novel carbon nanostructures has been evolved into matured sub-fields of the materials science, such as fullerenes [140–144] and CNTs [91, 92, 141, 145].

Starting from its lowest dimensional case, fullerenes attracted renewed interest owing to the properties of molecular magnets obtained by chemically modifying the structures through the formation of  $X@C_{60}$  (i.e., an endohedral fullerene with a  $X$  atom encapsulation inside a  $C_{60}$  cage). Since the spin of the  $X$  atom in  $X@C_{60}$  exhibits a low interaction with the environment, a very long spin lifetime (i.e., up to  $\sim 0.25$  ms) is observed making  $X@C_{60}$  to be a promising candidate for qubits in the quantum computation [146, 147]. On the other hand, due to its unique and strong 1D configuration, CNTs are promising building blocks for future nanoscale devices. Single-walled CNTs (SWCNTs) can be metallic or semiconducting depending on the tube diameter and chirality (i.e., the way the graphene sheet rolls up as a seamless hollow cylinder) [91, 92]. Both semiconducting and metallic SWCNTs have been used in advanced electronic devices for single-electron transport [148, 149], spin transport [150], rectification [151, 152], and switching [153].

The role played by graphene, composed of a carbon atomic layer extended in a perfect 2D crystalline lattice, is also becoming remarkably important. Acting as a basic building block for all  $sp^2$  graphitic carbon materials [154], graphene has led to the emergence of a new paradigm of “relativistic” condensed matter physics and “quantum electrodynamics” effects, which can now be tested in the tabletop experiments [154, 155]. In addition to the unusual electronic properties, the thermal conductivity



and mechanical stiffness of graphene may rival the in-plane values for graphite, i.e.,  $\sim 3,000 \text{ W m}^{-1} \text{ K}^{-1}$  and 1,060 GPa, respectively. The fracture strength should also be comparable to that of CNTs [156–158]. As a next step toward the potential applications, a general approach for the preparation of a graphene in a polymer matrix with intriguing properties has been found via complete exfoliation of graphite and molecular-level dispersion of individual, chemically modified graphene sheets [159].

Graphene has an exceptional advantage that can complement  $\text{C}_{60}$ , CNTs, and their derivatives.  $\text{C}_{60}$  is a fascinating molecule, but useful material tends to be extended in at least one dimension. For CNTs, working as long, thin, good molecular transistor is adequate, but microelectronics design is inherently the case of 2D. Yet, issues such as diameter, chirality control, and cost of production pose severe challenges for the commercial applications of CNTs. Graphene appears to be the material that we wished all along for novel technological applications.

### 3.3.2 $\text{B}_x\text{C}_y$ Hybrid Nanostructures

The study of the  $\text{B}_x\text{C}_y$  hybrid nanostructures has been driven largely by both scientific curiosity and technological applications. Synthesis of both 0D and 1D  $\text{B}_x\text{C}_y$  nanostructures can be found in the scientific literature. On the other hand, the 2D  $\text{B}_x\text{C}_y$  hybrid nanostructures, such as the semiconducting  $\text{BC}_3$  monolayer, remain merely a focus of theoretical studies [134].

Stimulated by the discovery of carbon fullerenes, the so-called heterofullerenes [160–162], where a few C atoms are substituted by hetero atoms, have become of focus of recent research activities. Substitution of dopant atoms such as B, Si, and N into fullerenes is expected to produce significant variation in the electronic structure of fullerene with the possibility of the new type of physical properties, just like the case of doped diamond. Using the method of the laser-vaporization of a graphite/boron nitride composite disk, the first report of the existence of  $\text{B}_x\text{C}_{60-x}$  fullerene-like cage clusters in gas phase was made [160]. Henceforth, the *B-doped* fullerenes have been studied extensively [163–165], either in the forms of films [165], or through in situ electron irradiation of chemical vapor deposition on  $\text{B}_x\text{C}_{1-x}$  ( $x \leq 0.2$ ) [164].

On the other hand, 1D “bulk-like”  $\text{B}_x\text{C}_y$  nanowires have been synthesized due to their attractive properties for high-temperature applications. Besides the formation of amorphous helical boron carbide nanowires [166], the formation of crystalline  $\text{B}_4\text{C}$  nanowires was also reported [167]. Grown by the plasma-enhanced chemical vapor deposition on the (100)-oriented silicon substrates within the range of 1,100–1,200°C, the crystallinity of the  $\text{B}_4\text{C}$  nanowire has been proven by the Raman and near-edge X-ray absorption fine structure spectroscopy. The predominant  $sp^3$  character suggests that the nanowires are extremely hard. We note that the  $\text{B}_4\text{C}$  nanowires (or nanorods) can also be synthesized directly from CNTs at around 1,200°C [168, 169]. The 1D  $\text{B}_x\text{C}_y$  hybrid nanostructures can also be formed via boron doping of CNTs [164, 170–172]. For example, synthesis of multiwalled  $\text{B}_x\text{C}_{1-x}$  ( $x \sim 0.1$ ) nanotubules [164] and the  $\text{BC}_{35}$  B-doped CNTs [170] has been

reported. A method involving the partial substitution of the carbon atoms on CNTs with  $B_2O_3$  was also proposed [171].

The B-doped CNTs are found to be metallic with no apparent band gap [172]. In the measurements of the resistivity of pristine and B-doped CNTs, it has been shown that the B-doped nanotubes have a reduced room-temperature resistivity with  $\sim 7.4 \times 10^7$  to  $7.7 \times 10^6 \Omega m$ , as compared to that of the pristine nanotubes in the range of  $5.3 \times 10^6$  to  $1.9 \times 10^5 \Omega m$  [173]. Thus, it appears that the metallicity of CNTs can be enhanced by increasing the doping concentration of boron. Consequently, as the ratio of boron is comparable to carbon approaching  $B/C = 1$ , the possibility of the existence of the hybrid BC nanotube has recently been supported by a theoretical study [174]. We expect the experimental verification of the BC hybrid tubular configuration in near future, thus expanding the current list of known  $B_xC_y$  hybrid nanostructures.

## 4 Summary

The present research status of the  $B_xC_y$  hybrid structures has been reviewed in this chapter. We find that the  $B_xC_y$  hybrid structures in either the bulk phase or the nanoscale regime are unique in many aspects. There is also a strong evidence to show that the synthesis of  $B_xC_y$  hybrid structures requires an ability to control the bonding between boron and carbon in the lattice. A detailed and systematic understanding of the elemental boron and its derivatives is also warranted.

Owing to its unique features of electron-deficient bonding, both boron solids and nanostructures seem to generally favor a mixture of localized (i.e., two-center) and delocalized (i.e., three-center or multicenter bonds) bonds in the bonding topology. In contrast to carbon, several metastable competing structural motifs can be found in boron nanostructures (e.g., nanotubes and boron sheets), reminiscent of its polymorphism in the solid state. Hence, polymorphism appears to be one of the stumbling blocks associated with synthesis of boron nanostructures. There is an acute need for more systematic and detailed studies on the elemental boron spanning dimensionality from 0D to 3D. With the help of such theoretical and experimental studies, our goal of a complete understanding of the  $B_xC_y$  system can be achieved.

## References

1. W. Kohn, *Rev. Mod. Phys.* **71**, S59 (1999).
2. Y.K. Yap, Boron-carbon nitride nanohybrids, In: H.S. Nalwa (Ed.) *Encyclopedia of Nanoscience and Nanotechnology*, **1**, 383–394 (American Scientific, New York, 2004).
3. A.R. Badzian, T. Niemyski, S. Appenheimer, and E. Olkusnik, In: F.A. Claski (Ed.) *Proceedings of the Third International Conference on Chemical Vapor Deposition* (Edited by F.A. Claski), 747 (1972).
4. E.L. Muetterties (Ed.), *The Chemistry of Boron and Its Compounds* (John Wiley, New York, 1967).
5. E.L. Muetterties (Ed.), *Boron Hydride Chemistry* (Academic, New York, 1975).

6. L. Pauling, *Nature of Chemical Bond and the Structure of Molecules and Crystals*, 3rd Edition (Cornell University Press, Itacha, NY, 1960).
7. A. Quandt and I. Boustani, *ChemPhysChem* **6**, 2001 (2005).
8. K.C. Buschbeck, *Boron Compounds, Elemental Boron, and Boron Carbides*, *Gmelin Handbook of Inorganic Chemistry*, Vol. 13 (Springer, Berlin, 1981).
9. D.W. Bullett, *J. Phys. C Solid State Phys.* **15**, 415 (1982).
10. C. Mailhot, J.B. Grant, and A.K. McMahan, *Phys. Rev. B* **42**, 9033 (1990).
11. D. Li, Y. Xu, and W.Y. Ching, *Phys. Rev. B* **45**, 5895 (1992).
12. N. Vast, S. Baroni, G. Zerah, J.M. Besson, A. Polian, J.C. Chervin, and T. Grimsditch, *Phys. Rev. Lett.* **78**, 693 (1997).
13. M. Fujimori, T. Tanaka, T. Nakayama, E. Nishibori, K. Kimura, M. Takata, and M. Sakata, *Phys. Rev. Lett.* **82**, 4452 (1999).
14. J. Zhao and J.P. Lu, *Phys. Rev. B* **66**, 092101 (2002).
15. U. Häussermann, S.I. Simak, R. Ahuja, and B. Johansson, *Phys. Rev. Lett* **90**, 065701 (2003).
16. A. Masago, K. Shirai, and H. Katayama-Yoshida, *Phys. Rev. B* **73**, 104102 (2006).
17. R.J. Nelmes, J.S. Loveday, D.R. Allan, J.M. Besson, G. Hamel, P. Grima, and S. Hull, *Phys. Rev. B* **47**, 7668 (1993).
18. J.C. Thompson and W.J. McDonald, *Phys. Rev.* **132**, 82 (1963).
19. D.N. Sanz, P. Loubeyre, and M. Mezouar, *Phys. Rev. Lett.* **89**, 245501 (2002).
20. D.A. Young, *Phase Diagrams of the Elements* (University of California Press, Berkeley, CA, 1991).
21. R. Kawai and J.H. Weare, *J. Chem. Phys.* **95**, 1151 (1991).
22. R. Kawai and J.H. Weare, *Chem. Phys. Lett.* **191**, 311 (1992).
23. H.C. Longuet-Higgins and M. de V. Roberts, *Proc. R. Soc. Lond. Ser. A* **A224**, 336 (1955).
24. H.C. Longuet-Higgins, *Q. Rev. Chem. Soc.* **11**, 121 (1957).
25. K.C. Lau and R. Pandey, *J. Phys. Chem. C*, **111**, 2906 (2007).
26. M.I. Eremets, V.V. Struzhkin, H.K. Mao, and R.J. Hemley, *Science* **293**, 272 (2001).
27. T.H. Geballe, *Science* **293**, 223 (2001).
28. D.A. Papaconstantopoulos and M.J. Mehl, *Phys. Rev. B* **65**, 172510 (2002).
29. W.N. Lipscomb, *Boron Hydrides* (Benjamin, New York, 1963).
30. W.N. Lipscomb, *J. Less Common Met.* **82**, 1 (1981).
31. E.D. Jemmis, M.M. Balakrishnarajan, and P.D. Pancharatna, *J. Am. Chem. Soc.* **123**, 4313 (2001).
32. E.D. Jemmis, M.M. Balakrishnarajan, and P.D. Pancharatna, *Chem. Rev.* **102**, 93 (2002).
33. E.D. Jemmis and E.G. Jayasree, *Acc. Chem. Res.* **36**, 816 (2003).
34. L. Hanley and S.L. Anderson, *J. Phys. Chem.* **91**, 5161 (1987).
35. L. Hanley, J.L. Whittena, and S.L. Anderson, *J. Phys. Chem.* **92**, 5803 (1988).
36. S.J. La Placa, P.A. Roland, and J.J. Wynne, *Chem. Phys. Lett.* **190**, 163 (1992).
37. P.A. Hintz, M.B. Sowa, S.A. Ruatta, and S.L. Anderson, *J. Chem. Phys.* **94**, 6446 (1991).
38. R. Kawai and J.H. Weare, *J. Chem. Phys.* **95**, 1151 (1991).
39. R. Kawai and J.H. Weare, *Chem. Phys. Lett.* **191**, 311 (1992).
40. M.B. Sowa, A.L. Snolanoff, A. Lapicki, and S.L. Anderson, *J. Chem. Phys.* **106**, 9511 (1997).
41. H.J. Zhai, B. Kiran, J. Li, and L.S. Wang, *Nat. Mater.* **2**, 827 (2003).
42. B. Kiran, S. Bulusu, H. Zhai, S. Yoo, X.C. Zeng, and L.S. Wang, *Proc. Natl Acad. Sci. USA* **102**, 961 (2005).
43. C.J. Otten, O.R. Lourie, M. Yu, J.M. Cowley, M.J. Dyer, R.S. Ruoff, and W.E. Buhro, *J. Am. Chem. Soc.* **124**, 4564 (2002).
44. T.T. Xu, J. Zheng, N. Wu, A.W. Nichollas, J.R. Roth, D.A. Dikin, and R.S. Ruoff, *Nano Lett.* **4**, 963 (2004).
45. D. Ciuparu, R.F. Klie, Y. Zhu, and L. Pfefferle, *J. Phys. Chem. B* **108**, 3967 (2004).
46. I. Boustani, *Phys. Rev. B* **55**, 16426 (1997).
47. I. Boustani and A. Quandt, *Europhys. Lett.* **39**, 527 (1997).
48. K.C. Lau and R. Pandey, *Comput. Lett. (Special Issue: Clusters: From a few atoms to nanoparticles)* **1**, 259 (2005).
49. N.G. Szwacki, A. Sadzadeh, and B.I. Yakobson, *Phys. Rev. Lett.* **98**, 166804 (2007).
50. A.K. Ray, I.A. Howard, and K.M. Kanal, *Phys. Rev. B* **45**, 14247 (1992).

51. V. Bonacic-Koutecky, P. Fantucci, and J. Koutecky, *Chem. Rev.* **91**, 1035 (1991).
52. H. Kato, K. Yamashita, and K. Morokuma, *Chem. Phys. Lett.* **190**, 361 (1992).
53. I. Boustani, *Int. J. Quant. Chem.* **52**, 1081 (1994).
54. I. Boustani, *Chem. Phys. Lett.* **240**, 135 (1995).
55. A. Ricca and C.W. Bauschlicher, *Chem. Phys.* **208**, 233 (1996).
56. F.L. Gu, X. Yang, A.C. Tang, H. Jiao, and P.V.R. Schleyer, *J. Comput. Chem.* **19**, 203 (1998).
57. J.E. Fowler and J.M. Ugalde, *J. Phys. Chem. A* **104**, 397 (2000).
58. H.J. Zhai, L.S. Wang, A.N. Alexandrova, A.I. Boldyrev, and V.G. Zakrzewski, *J. Phys. Chem. A* **107**, 9313 (2003).
59. H.J. Zhai, L.S. Wang, A.N. Alexandrova, and A.I. Boldyrev, *J. Chem. Phys.* **117**, 7917 (2002).
60. A.N. Alexandrova, A.I. Boldyrev, H.J. Zhai, L.S. Wang, E. Steiner, and P.W. Fowler, *J. Phys. Chem. A* **107**, 1359 (2003).
61. A.N. Alexandrova, A.I. Boldyrev, H.J. Zhai, and L.S. Wang, *J. Phys. Chem. A* **108**, 3509 (2004).
62. H.J. Zhai, A.N. Alexandrova, K.A. Birch, A.I. Boldyrev, and L.S. Wang, *Angew. Chem. Int. Ed.* **42**, 6004 (2003).
63. J.E. Fowler and J.M. Ugalde, *J. Phys. Chem. A* **104**, 397 (2000).
64. J. Aihara, *J. Phys. Chem. A* **105**, 5486 (2001).
65. M.A.L. Marques and S. Botti, *J. Chem. Phys.* **123**, 014310 (2005).
66. K.C. Lau, M.D. Deshpande, R. Pati, and R. Pandey, *Int. J. Quant. Chem.* **103**, 866 (2005).
67. S. Chacko, D.G. Kanhere, and I. Boustani, *Phys. Rev. B* **68**, 035414 (2003).
68. I. Boustani, A. Rubio, and J.A. Alonso, *Chem. Phys. Lett.* **311**, 21 (1999).
69. I. Boustani, A. Quandt, and A. Rubio, *J. Solid State Chem.* **154**, 269 (2000).
70. R.O. Jones and G. Seifert, *Phys. Rev. Lett.* **79**, 443 (1997).
71. R.O. Jones, *J. Chem. Phys.* **110**, 5189 (1999).
72. H. Prinzbach, A. Weiler, P. Landenberger, F. Wahl, J. Worth, L.T. Scott, M. Gelmont, D. Olevano, and B. Issendorff, *Nature* **407**, 60 (2000).
73. N.G. Szwacki, *Nanoscale Res. Lett.* **3**, 49 (2008).
74. M.H. Evans, J.D. Joannopoulos, and S.T. Pantelides, *Phys. Rev. B* **72**, 045434 (2005).
75. I. Cabria, M.J. López, and J.A. Alonso, *Nanotechnology* **17**, 778 (2006).
76. K.C. Lau and R. Pandey, *J. Phys. Chem. B*, **112**, 10217 (2008).
77. J. Kunstmann and A. Quandt, *Phys. Rev. B* **74**, 035413 (2006).
78. H. Tang and S. Ismail-Beigi, *Phys. Rev. Lett.* **99**, 115501 (2007).
79. X. Yang, Y. Ding, and J. Ni, *Phys. Rev. B* **77**, 041402(R) (2008).
80. K.C. Lau, R. Pati, A.C. Pineda, and R. Pandey, *Chem. Phys. Lett.* **418**, 549 (2006).
81. K.C. Lau, R. Orlando, and R. Pandey, *J. Phys. Condens. Matter* **20**, 125202 (2008).
82. K. Kirihara, Z. Wang, K. Kawaguchi, Y. Shimizu, T. Sasaki, N. Koshizaki, K. Soga, and K. Kimura, *Appl. Phys. Lett.* **86**, 212101 (2005).
83. I. Boustani, A. Quandt, E. Hernández, and A. Rubio, *J. Chem. Phys.* **110**, 3176 (1999).
84. J. Kunstmann and A. Quandt, *Chem. Phys. Lett.* **402**, 21 (2005).
85. D. Zhang, R. Zhu, and C. Liu, *J. Mater. Chem.* **16**, 2429 (2006).
86. K.C. Lau, R. Pandey, R. Pati, and S.P. Karna, *Appl. Phys. Lett.* **88**, 212111 (2006).
87. S. Reich, C. Thomsen, and P. Ordejon, *Phys. Rev. B* **65**, 153407 (2002).
88. J. Tang, L. Qin, T. Sasaki, M. Yudasaka, A. Matsushita, and S. Iijima, *Phys. Rev. Lett.* **85**, 1887 (2000).
89. C. Kittel, *Introduction to Solid State Physics*, 7th Edition (Wiley, New York, 1996).
90. R.B. Heimann, S.E. Evsyukov and Y. Kocack, *Proc. Fifth London Int. Carbon Graphite Conf.* **3**, 104 (1979).
91. R. Saito, G. Dresselhaus, and M.S. Dresselhaus, *Physical Properties of Carbon Nanotubes* (Imperial College Press, London, 2003).
92. M.S. Dresselhaus, G. Dresselhaus, and P. Avouris (Eds.) *Carbon Nanotubes: Synthesis, Structure, Properties, and Applications* (Springer, Berlin, 2001).
93. F.P. Bundy and J.S. Kasper, *J. Chem. Phys.* **46**, 3437 (1967).
94. T. Yagi, W. Utsumi, M. Yamakata, T. Kikegawa, and O. Shimomura, *Phys. Rev. B* **46**, 6031 (1992).
95. H. Rydberg, M. Dion, N. Jacobson, E. Schröder, P. Hyldegaard, S.I. Simak, D.C. Langreth, and B.L. Lundqvist, *Phys. Rev. Lett.* **91**, 126402 (2003).

96. K. Yoshizawa, T. Yumura, T. Yamabe, and S. Bandow, *J. Am. Chem. Soc.* **122**, 11871 (2000).
97. M.S. Dresselhaus and G. Dresselhaus, *Adv. Phys.* **51**, 1 (2002).
98. Y.P. Kudryavtsev, S.E. Evsyukov, M.B. Guseva, V.G. Babaev, and V.V. Khvostov, *Russ. Chem. Bull.* **42**, 399 (1993).
99. B.V. Lebedev, *Russ. Chem. Bull.* **49**, 965 (2000).
100. C.X. Shi and J. Ke (Eds.) *Structure and Properties of Ceramics, Materials Science and Technology*, Vol. 11 (Science Press, Beijing, 1998).
101. G.V. Tsagareishvili and F.N. Tavatzze, *Prog. Cryst. Growth Char.* **16**, 341 (1988).
102. H.T. Hall and L.A. Compton, *Inorg. Chem.* **4**, 1213 (1965).
103. S. Han, J. Ihm, S.G. Louie, and M.L. Cohen, *Phys. Rev. Lett.* **80**, 997 (1998).
104. K.L. Saenger, Angular distribution of ablated material, In: D.B. Chrisey and G.K. Hubler (Eds.) *Pulsed Laser Deposition of Thin Films* (Wiley, New York, 1994).
105. F. Kokai, M. Taniwaki, T. Takahashi, A. Goto, M. Ishihara, K. Yamamoto, and Y. Koga, *Diamond Relat. Mater.* **10**, 1412 (2001).
106. B. Wei, R. Vajtai, Y.J. Jung, F. Banhart, G. Ramanath, and P.M. Ajayan, *J. Phys. Chem. B* **106**, 5807 (2002).
107. R. Lazzari, N. Vast, J.M. Besson, S. Baroni, and A.D. Corso, *Phys. Rev. Lett.* **83**, 3230 (1999).
108. J. Donohue, *The Structure of the Elements* (Wiley, New York, 1974).
109. H.L. Yakel, *Acta Crystallogr. B* **31**, 1797 (1975).
110. F. Mauri et al., *Phys. Rev. Lett.* **87**, 085506 (2001).
111. Y. Feng et al., *Phys. Rev. B* **69**, 125402 (2004).
112. P. Lunca-Popa et al., *J. Phys. D* **38**, 1248 (2005).
113. G. Fanchini, J.W. McCauley, and M. Chhowalla, *Phys. Rev. Lett.* **97**, 035502 (2006).
114. T.M. Duncan, *J. Am. Chem. Soc.* **106**, 2270 (1984).
115. D.M. Bylander et al., *Phys. Rev. B* **42**, 1394 (1990).
116. X.Q. Yan, W.J. Li, T. Goto, and M.W. Chen, *Appl. Phys. Lett.* **88**, 131905 (2006).
117. D. Ghosh, G. Subhash, C.H. Lee, and Y.K. Yap, *Appl. Phys. Lett.* **91**, 061910 (2007).
118. R.M. Chrenko, *Phys. Rev. B* **7**, 4560 (1970).
119. R. Kalish, *Diamond Relat. Mater.* **10**, 1749 (2001).
120. J.E. Butler, M.W. Geis, K.E. Krohn, J. Lawless Jr., S. Deneault, T.M. Lyszczarz, D. Flechtner, and R. Wright, *Semicond. Sci. Technol.* **18**, S67 (2003).
121. J. Robertson, *Semicond. Sci. Technol.* **18**, S12 (2003).
122. K. Thonke, *Semicond. Sci. Technol.* **18**, S20 (2003).
123. M. Werner, O. Dorsch, H.U. Baerwind, E. Obermeier, L. Haase, W. Seifert, A. Ringhandt, C. Johnston, S. Romani, H. Bishop, and R.P. Chalker, *Appl. Phys. Lett.* **64**, 595 (1994).
124. E.A. Ekimov, V.A. Sidorov, E.D. Bauer, N.N. Mel'nik, N.J. Curro, J.D. Thompson, and S.M. Stishov, *Nature* **428**, 542 (2004).
125. Y. Takano, M. Nagao, I. Sakaguchi, M. Tachiki, T. Hatano, K. Kobayashi, H. Umezawa, and H.H. Kwarada, *Appl. Phys. Lett.* **85**, 2851 (2004).
126. Z.L. Wang, Q. Luo, L.W. Liu, C.Y. Li, H.X. Yang, H.F. Yang, J.J. Li, X.Y. Lu, Z.S. Jin, L. Lu, and C.Z. Gu, *Diamond Relat. Mater.* **15**, 659 (2006).
127. L. Boeri, J. Kortus, and O.K. Anderson, *Phys. Rev. Lett.* **93**, 237002 (2004).
128. K.W. Lee and W.E. Pickett, *Phys. Rev. Lett.* **93**, 237003 (2004).
129. E. Bustrarret, J. Kacmarcik, C. Marcenat, E. Gheeraert, C. Cytemann, J. Marcus, and T. Klein, *Phys. Rev. Lett.* **93**, 237005 (2004).
130. X. Blase, Ch. Adessi, and D. Connetable, *Phys. Rev. Lett.* **93**, 237004 (2004).
131. H.J. Xiang, Z. Li, J. Yang, J.G. Hou, and Q. Zhu, *Phys. Rev. B* **70**, 212504 (2004).
132. F. Giustino, J.R. Yates, I. Souza, M.L. Cohen, and S.G. Louie, *Phys. Rev. Lett.* **98**, 047005 (2007).
133. K.M. Krishnan, *Appl. Phys. Lett.* **58**, 1857 (1991).
134. D. Tomanek, R.M. Wentzcovitch, S.G. Louie, and M.L. Cohen, *Phys. Rev. B* **37**, 3134 (1988).
135. Q. Wang, L. Chen, and J.F. Annett, *Phys. Rev. B* **54**, R2271 (1996).
136. F.J. Ribeiro and M.L. Cohen, *Phys. Rev. B* **69**, 212507 (2004).
137. J. Kouvetakis, R.B. Kaner, M.L. Sattler, and N. Bartlett, *J. Chem. Soc. Chem. Commun.* **1758** (1986).

138. H. Sun, F.J. Ribeiro, J. Li, D. Roundy, M.L. Cohen, and S.G. Louie, *Phys. Rev. B* **69**, 024110 (2004).
139. U. Landman and W.D. Luedtke, *Faraday Discuss. Chem. Soc.* **125**, 1 (2004).
140. H.W. Kroto, J.R. Heath, S.C. O'Brien, R.F. Curl, and R.E. Smalley, *Nature* **318**, 162 (1985).
141. M.S. Dresselhaus, G. Dresselhaus, and P.C. Ecklund, *Science of Fullerenes and Carbon Nanotubes* (Academic, San Diego, 1996).
142. H.W. Kroto, J.E. Fischer, and D.E. Cox (Eds.) *The Fullerenes* (Pergamon, Oxford, 1993).
143. H.W. Kroto and D.R.M. Walton (Eds.), *The Fullerenes, New Horizons for the Chemistry, Physics, and Astrophysics of Carbon* (Cambridge University Press, Cambridge, 1993).
144. L. Forro and L. Mihaly, *Rep. Prog. Phys.* **64**, 649 (2001).
145. S. Iijima, *Nature* **354**, 56 (1991).
146. J.J.L. Morton, A.M. Tyryshkin, A. Ardavan, K. Porfyrakis, S.A. Lyon, and G.A.D. Briggs, *Nat. Phys.* **2**, 40 (2006).
147. S.C. Benjamin, A. Ardavan, G.A.D. Briggs, D.A. Britz, D. Gunlycke, J. Jefferson, M.A.G. Jones, D.F. Leigh, B.W. Lovett, A.N. Khlobystov, S.A. Lyon, J.J.L. Morton, K. Porfyrakis, M.R. Sambrook, and A.M. Tyryshkin, *J. Phys. Condens. Matter.* **18**, S867 (2006).
148. S.J. Tan, M.H. Devoret, H. Dai, A. Thess, R.E. Smalley, L.J. Geerligs, and C. Dekker, *Nature* **386**, 474 (1997).
149. M.E. Bockrath, D.H. Cobden, P.L. McEuen, N.G. Nasreen, G. Chopra, A. Zettl, A. Thess, and R.E. Smalley, *Science* **275**, 1992 (1997).
150. K. Tsukagoshi, B.W. Alphenaar, and H. Ago, *Nature* **401**, 572 (1999).
151. Z. Yao, H.W.Ch. Postma, L. Balents, and C. Dekker, *Nature* **402**, 273 (1999).
152. R.D. Antonov and A.T. Johnson, *Phys. Rev. Lett.* **83**, 3274 (1999).
153. S.J. Tan, A.R.M. Verschueren, and C. Dekker, *Nature* **393**, 49 (1998).
154. A.K. Geim and K.S. Novoselov, *Nat. Mater.* **6**, 183 (2007).
155. M.I. Katsnelson and K.S. Novoselov, *Solid State Commun.* **143**, 3 (2007).
156. M.S. Dresselhaus and G. Dresselhaus, *Adv. Phys.* **51**, 1 (2002).
157. M. Hirata, T. Gotou, S. Horiuchi, M. Fujiwara, and M. Ohba, *Carbon* **42**, 2929 (2004).
158. M.F. Yu, O. Lourie, K. Moloni, T.F. Kelly, and R.S. Ruoff, *Science* **287**, 637 (2000).
159. S. Stankovich, D.A. Dikin, G.H.B. Dommett, K.M. Kohlhaas, E.J. Zimney, E.A. Stach, R.D. Piner, S.T. Nguyen, and R.S. Ruoff, *Nature* **442**, 282 (2006).
160. T. Guo, C. Jin, and R.E. Smalley, *J. Phys. Chem.* **95**, 4948 (1991).
161. R. Yu, M. Zhan, D. Cheng, S. Yang, Z. Liu, and L. Zheng, *J. Phys. Chem.* **99**, 1818 (1995).
162. J.C. Hummelen, B. Knight, J. Pavlovich, R. Gonzalez, and F. Wudl, *Science*, **269**, 1554 (1995).
163. T. Kimura, T. Sugai, and H. Shinohara, *Chem. Phys. Lett.* **256**, 269 (1996).
164. D. Golberg, Y. Bando, K. Kurashima, and T. Sasaki, *Chem. Phys. Lett.* **72**, 2108 (1998).
165. Y.J. Zou, X.W. Zhang, Y.L. Li, B. Wang, H. Yan, J.Z. Cui, L.M. Liu, and D.A. Da, *J. Mater. Sci.* **37**, 1043 (2002).
166. D.N. McIlroy, D. Zhang, Y. Kranov, H. Han, A. Alkhateeb, and M.G. Norton, *Mater. Res. Soc. Symp. Proc.* **739**, H5.2 (2003).
167. D.N. McIlroy, D. Zhang, R.M. Cohen, J. Wharton, Y. Geng, M.G. Norton, G. De Stasio, B. Gilbert, L. Perfetti, J.H. Streiff, B. Broocks, and J.L. McHale, *Phys. Rev. B* **60**, 4874 (1999).
168. H.J. Dai, E.W. Wong, Y.Z. Lu, S.S. Fan, and C.M. Lieber, *Nature* **375**, 769 (1995).
169. J. Wei, B. Jiang, Y. Li, C. Xu, D. Wu, and B. Wei, *J. Mater. Chem.* **12**, 3121 (2002).
170. B.C. Satishkumar, A. Govindaraj, K.R. Harikumar, J.P. Zhang, A.K. Cheetham, and C.N.R. Rao, *Chem. Phys. Lett.* **300**, 473 (1999).
171. W.Q. Han, Y. Bando, K. Kurashima, and T. Sato, *Chem. Phys. Lett.* **299**, 368 (1999).
172. D.L. Carroll, Ph. Redlich, X. Blase, J.C. Charlier, S. Curran, P.M. Ajayan, S. Roth, and M. Rühle, *Phys. Rev. Lett.* **81**, 2332 (1998).
173. B.Q. Wei, R. Spolenak, P. Redlich, M. Rühle, and E. Arzt, *Appl. Phys. Lett.* **74**, 3149 (1999).
174. O. Ponomarenko, M.W. Radny, and P.V. Smith, *Phys. Rev. B* **74**, 125421 (2006).

# Index

## A

- Ab-initio calculations, 83, 86, 92, 95, 118, 127–129, 132, 136, 142, 143
  - B and N-doped C-NT, 65
  - dielectric function, 67
  - dislocations, 74
  - hydrogen adsorption, 75–76
  - phonon dispersion relation, 72
- Arc discharge technique, 47–48
- Arc jet technique, 48
- Armchair nanotubes, 6
- Atomic transfer radical polymerization (ATRP), 256

## B

- Bader analysis, 87
- B-C-N materials
  - bond hybridization and molecular packing, 1–3
  - boron, 13–14
  - boron carbide, 13
  - boron carbon-nitride (BCN)
    - cubic phase hybrid, 16–17
    - hexagonal phase hybrid, 15–16
    - nanostuctures, 17–18
  - boron nitride
    - electronic configuration, 9
    - nanotubes, 11–12
    - phases, 9–11
  - carbon
    - carbon nanotubes, 5–9
    - C<sub>60</sub> fullerene, 5
    - diamond, 4
    - graphite and graphene, 3–4
  - carbon nitride, 14–15
  - doped CNTs, 18
- B–C–N ternary material system, 2
- Bethe–Salpeter equation, 67, 112, 115, 118

Bond lengths,  $sp^2$  and  $sp^3$  hybridization, 2

## Boron allotropes

- nanostuctures
  - clusters, 274–276
  - nanotubes, 278–280
  - sheets, 276–278
- solids
  - $\alpha$ - $\beta_{12}$  electron density, 274
  - electron-deficiency, 272
  - icosahedral boron solids, 273

## Boron carbide allotropes

- carbon solids, 280–281
- hybrid structures
  - B<sub>x</sub>C<sub>y</sub> nanostructures, 285–287
  - B<sub>x</sub>C<sub>y</sub> solids, 281–284

## Boron carbonitride nanostructures

- photoluminescence and electron field property, 207
- properties and applications
  - field emission, 214–216
  - semiconducting property and photoluminescence, 213–214
- structure and composition
  - bamboo like structure, 207–209
  - cactus like structure, 209
  - heterojunction, 210
  - phase separation, 209–210
  - single walled BCN
    - nanotubes, 210–213

## Boron carbon-nitride (BCN)

- cubic phase hybrid, 16–17
- hexagonal phase hybrid, 15–16
- nanostuctures, 17–18

## Boron clusters, 274–276

## Boron nanotubes (BNT)

- crystalline bundles, 279
- single-walled boron nanotubes (SWNT), 278
- structural motifs, 278, 279

- Boron nitride(BN)
- clusters
    - arc-melting method, 151
    - atomic structure model, 153
    - discrete variational (DV)-X  $\alpha$  method, 155
    - heat formation, 156
    - highest and lowest occupied molecular orbital, 155
    - high performance liquid chromatography, 157
    - isolated pentagon rule, 153
    - laser desorption time-of-flight (LD-TOF) mass spectra, 151
    - MacTempas software, 155
    - scherrer defocus, 155
  - cup-stacked structures, nanotubes
    - atomic structure model, 164
    - electron diffraction pattern, 164, 165
    - enlarged STM image, 168, 169
    - highly oriented, pyrolytic graphite (HOPG), 168
    - solublyzation, 163
    - TEM image, 164
    - X-ray diffraction patterns, 164, 165
  - electronic configuration, 9
  - encaging Fe nanowires
    - EDX spectrum, 169, 170
    - Fourier transform, 170
    - gibb's energy, 172
    - HREM image, Fe-filled, 171
  - nanocapsules
    - electronic transport properties, 182
    - ellingham diagram, 183, 184
    - magnetic hysteresis loop, 184
    - Scherrer equation, 183
    - TEM images, 186
    - thermal annealing method, 183
    - X-ray diffraction patterns, 183
  - nanohorns
    - atomic structure model, 174
    - composition ratio, 173
    - energy level diagram, 175
    - formation enthalpy, 178
    - HREM images, 174, 176
  - nanoparticles
    - atomic structure model, 181
    - Debye-Scherrer rings, 179
    - electron diffraction pattern, 179, 180
    - filtered HREM image, 179, 181
    - role of van der Waal bondings, 181
    - TEM images, CVD-BN, 180
    - twin boundaries, 179
  - nanotubes, 11–12
    - armchair-type structure, 159
    - Fourier noise filtering, 158
    - HREM image, 159
    - inverse Fourier transform, 159
    - quadruple-walled, structure model, 162
  - phases, 9–11
  - Boron nitride nanotubes (BNNTs), 11–12
    - electronic properties
      - buckling distance, 86
      - chiral vector, 85, 86
    - electron energy loss spectroscopy analysis, 84
    - excitonic binding energy, 91, 92, 94
    - excitonic wavefunction, 94
    - fullerenes physics, 95–96
    - h-BN quasiparticle band structure, 88–89
    - interlayer state, 90–91
    - large ionicity band gap insulator, 87–88
    - optical properties, 91–94
    - polarization effects, 95
    - structure and stability, 85–87
    - total energy, eV/atom, 84
  - Boron sheets
    - buckled triangular sheet, 277
    - carbon nanotubes (CNT), 276
    - 2D pristine configurations, 277
  - Buckling effect, 86
  - Buckminsterfullerene, 5
  - $B_xC_y$  hybrid nanostructures, 286–287
  - $B_xC_y$  solids
    - amorphous boron carbide (a- $B_4C$ ), 283
    - $BC_3$  structure, 284
    - boron carbide ( $B_4C$ ), 281
    - $B_xC_{1-x}$  binary compounds, 283
    - electron-phonon coupling, 283
    - icosahedral  $B_4C$  atomic structure, 281, 282
- C**
- Carbon nanostructures, 285–286
  - Carbon nanotubes (CNTs), 5–9
  - Carbon nanotubes (CNTs), doped, 18
    - boron and nitrogen
      - Fermi level, 229, 230
      - Young's modulus, 230
    - covalent or non-covalent functionalization, 224, 228
    - doping types
      - arc discharge technique, 225
      - EDX elemental mapping, 231
      - electron-donating, 225
      - endohedral doping, 225
      - exohedral doping, 226
      - fullerene peapods, 225
      - structural configurations, 228



- electronic and transport characterization
    - densities of states (DOS), 242
    - electron spin resonance (ESR), 243
  - phosphorous and nitrogen
    - heterodoping process, 230
    - high resolution electron microscopy and microanalysis techniques, 231
  - plasma assisted CVD, 237
  - preparation of substitutional, 231–238
    - direct synthesis, 232
    - postsynthesis methods, 237–238
    - spray-pyrolysis technique, 236
    - transmission electron micrographs, 233
  - structural properties
    - atomic structure of b-doped mwnts, 240
    - electron energy loss spectroscopy (EELS), 239
    - scanning electron microscopy (SEM), 239
    - X-ray powder diffraction (XRD), 239
  - types, 225–228
  - vibrational properties, 244–245
    - B and N doping, 246–248
    - efficient metal surfaces, anchoring molecules, 256–262
    - nonsubstitutional doping, 248–252
    - wider applications, 252–256
  - Carbon nitride nanostructures
    - arc-discharge process, 7
    - chemical vapor deposition (CVD), 197
    - electron-conducting properties, 196
    - physical vapor deposition (PVD), 197
    - properties and application
      - conductance and field emission, 204–205
      - hydrogen storage, 205–206
      - lithium storage, 206
    - structure and composition
      - bamboo-like and polymerized nanobell, 197–198
      - formation mechanism, 200–201
      - heterojunction, 200
      - nitrogen concentration and chemical bonding, 202–203
      - separation, 198–200
  - Carbon nitride system, 14–15
  - Carbothermal synthesis approach, 51–52
  - Carbothermic reduction, 51
  - C<sub>60</sub> fullerene system, 5
  - Chemical reactivity, 74–75
  - Chemical vapor deposition (CVD), 7, 50–51, 197
  - Chirality, 56
  - Chiral nanotubes, 6
  - Composite boron-carbonitride nanotubes
    - C/BN hetero-junction properties, 98–99
  - h-BC<sub>2</sub>N phase
    - electronic properties, 98
    - non-stoichiometric h-B<sub>x</sub>C<sub>y</sub>N<sub>z</sub> structures, 99–100
    - structure and properties, 97–98
  - Coulomb electron-hole interactions, 67, 69
  - Coulomb interaction, 92, 93
  - CVD. *See* Chemical vapor deposition
- D**
- Densities of states (DOS), 155, 157, 175
  - Density-functional perturbation theory, 140
  - Density functional theory (DFT), 89, 98, 112
    - band structure, 66
    - dislocations, 74
    - hydrogen adsorption, 76
  - Density of states (DOS), 9, 65
  - Diamond system, 4
  - Doped carbon nanotubes. *See* Carbon nanotubes, doped
  - DOS. *See* Densities of states
- E**
- EELS. *See* Electron-energy loss spectroscopy (EELS)
  - Electro-mechanical properties, 74
  - Electron-deficiency, 272
  - Electron diffraction (ED), 239–241
  - Electron diffraction pattern (EDP), 56–57
  - Electron energy loss spectroscopy (EELS), 33, 202
    - chemical maps, 61–62
    - core loss region, 57–58
    - doping element composition, 60–61
    - elemental maps, 58, 63
    - spectrum-line (SPLI), 58–59
  - Electron-energy loss spectroscopy (EELS), 107, 116, 124, 125, 129
  - Electronic properties and transport, 64–66
  - Energy-filtered transmission electron microscopy (EFTEM), 58
  - Excimer laser, 28
  - Excitonic effects, 67
- F**
- Ferrocene:etabnol:bencylamine (FEB), 233, 234
  - Filtered Fourier transform, 158–161, 170
  - Fourier transformed infra-red (FTIR) spectroscopy, 33, 34
  - Fowler–Nordheim (FN) mechanism, 204

Fowler-Nordheim plot, 27  
 Frenkel excitons, 91  
 Fringe spacing, 53

## G

Generalized-gradient approximation (GGA), 112  
 GGA. *See* Generalized-gradient approximation  
 Giant dc Stark effect, 95  
 Graphite and graphene system, 3–4

## H

HAADF-STEM. *See* High-angle annular dark-field scanning transmission electron microscopy (HAADF-STEM)  
 Hartree-Fock approximation (HFA), 112, 113  
 h-BN. *See* Hexagonal boron-nitride  
 Heteroatomic single-wall nanotubes, 45–46  
   nano-electro-mechanical systems (NEMS), 76–77  
   physical and chemical properties  
     chemical reactivity, 74–75  
     electro-mechanical properties, 74  
     electronic properties and transport, 64–66  
     hydrogen storage, 75–76  
     mechanical properties, 73–74  
     optical properties, 66–69  
     vibrational properties, 69–73  
   structural and composition analysis, TEM  
     electron energy loss spectroscopy, 57–63  
     growth mechanism, 63–64  
     HRTEM and electron diffraction, 52–57  
   synthesis methods  
     arc discharge, 47–48  
     carbothermal synthesis approach, 51–52  
     chemical vapor deposition, 50–51  
     laser vaporization, 48–50  
 Hexagonal boron-nitride  
   ab initio calculations, 89  
   contour plots, 90  
   crystallographic structure, 85–87  
   optical absorption spectra, 93  
   quasiparticle band structure, 88–89  
   sheet lattice structure, 85  
   symbolic representation, 99  
 HFA. *See* Hartree-Fock approximation  
 High-angle annular dark-field scanning transmission electron microscopy (HAADF-STEM), 169  
 Highest occupied molecular orbital (HOMO), 112, 117

High-resolution transmission electron (HRTEM), 106  
 High resolution transmission electron microscopy (HRTEM), 209, 232, 234, 237, 239  
   laser vaporization, 49  
   structural and composition analysis  
     B- and N-doped C-SWNT, 53–54  
     BN-SWNT, 54–55  
     boron nitride nanotubes, irradiation, 55–56  
 HOMO. *See* Highest occupied molecular orbital  
 Hot filament CVD method, 50, 51  
 HRTEM. *See* High-resolution transmission electron microscopy  
 HRTEM. *See* High-resolution transmission electron  
 Hugoniot elastic limit, 283  
 Hydrogen storage, 75–76  
 Hydrothermal method, 202

## I

Induction-heating furnace, 28  
 Infrared (IR) absorption spectroscopy, 105  
 Inverse Fourier transform, 159–161, 170, 171

## K

Kramers-Kronig analysis, 125

## L

Laser vaporization technique, 48–50  
 Lattice dynamics. *See* Vibrational properties  
 LDA. *See* Local-density approximation  
 LD-TOF mass spectrometry, 151, 155  
 Local-density approximation (LDA), 109, 112–114, 118, 124, 127, 130  
 Local density of electronic states (LDOS), 31  
 Lowest unoccupied molecular orbital, 112, 117  
 Luminescence, 67–69  
 Luminescence spectroscopy  
   bound and free exciton, 122  
   cathodoluminescence spectrum, h-BN  
     crystallite, 122  
   electron-phonon coupling, 123  
   photo-luminescence excitation (PLE), 122  
   stark effect, 123  
 LUMO. *See* Lowest unoccupied molecular orbital  
 Lyddanne-Sachs Teller relation, 22

**M**

- Many-body perturbation theory, 112, 113
- Mechanical properties, 73–74
- Meissner effect, 65
- Molecular dynamics simulations, 63, 74
- Mott–Wannier excitons, 91
- Multiwalled boron nitride nanotubes
  - applications
    - electronic and chemical applications, 37–39
    - hydrogen storage, 35–36
    - mechanical applications, 36–37
    - molecular biological applications, 39–41
  - bank structure, 39
  - CL and UV-vis absorption spectra, 37
  - DNA-BNNT fabrication, 40
  - FTIR spectra, 34
  - functionlization
    - bandgap tuning, 37–39
    - biomaterials, 40
    - noncovalent interactions, 36
  - optimized structure, 38
  - properties
    - electron field emission properties, 26–27
    - electronic properties, 25–26
    - mechanical properties, 24
    - piezoelectric properties, 26
    - thermal properties, 24–25
  - Raman spectra, 34
  - SEM image, 33
  - synthesis
    - arc discharge method, 27–28
    - ball-milling technique, 29
    - catalytic chemical vapor deposition (CCVD), 29–30
    - electron beam in-situ deposition, 30–31
    - experimental setup, 33
    - FeB nanoparticles liquid flow, 30
    - horizontal tube furnace growth, 32–35
    - laser-based method, 28
    - low temperature growth, 31–32
    - phase selective growth, 32
    - plasma jet method, 31
    - substitution reaction, 28–29
  - TEM image, 41
  - thermogravimetric analysis curves, 25
- Multiwalled carbon nanotubes (MWCNTs), 5, 7
- MW-BNNT. *See* Multiwalled boron nitride nanotubes

**N**

- Nanobeam electron diffraction (NB-ED), 56
- Nano-electro-mechanical systems (NEMS), 76–77
- Nanotube helicity, 53–55, 57

**O**

- Optical absorption spectra
  - absorption spectrum, BN tubes
    - dimensionality effects, 121
    - exciton, wavefunction, 120
    - SWBNNT, 119
  - absorption spectrum, bulk h-BN
    - electron probability density, 117
    - GW + BS calculation, 116
    - phonon renormalization, 118
  - band gap problem
    - calculation, 113–114
    - definition, 112
    - density functional theory (DFT), 112, 113
    - electron–electron interaction, 114
    - generalized-gradient approximation (GGA), 112
    - GW approximation, 113, 114
    - Hartree–Fock approximation (HFA), 112
  - excitonic effects, 114–115
  - independent-particle picture
    - band structure comparison, 108, 109
    - depolarization effect, 110
    - Lorentzian broadening, 111
    - random-phase approximation (RPA), 108
    - RPA absorption spectrum, 108, 110
    - zone-folding procedure, 108
  - luminescence in BN tubes, 5
- Optical and vibrational properties
  - luminescence spectroscopy, 122–124
  - optical absorption spectra, 107–122
  - phonons and vibrational spectroscopy, 125–143
  - plasmons and electron-energy loss spectroscopy, 124–125
- Optical properties
  - dielectric properties, 67–68
  - emission properties, 66
  - excitonic effects, 66–67
  - optical excitations, 68–69
  - saturable absorption effect, 66
- Oven-laser ablation method, 28

**P**

- PE-PLD. *See* Plasma-enhanced pulsed-laser deposition

- Phonons and vibrational spectroscopy
- diameter dependence, Raman and IR active modes
    - frequency types, 136–137
    - radial phonon modes, 138
    - scaling constants, determination, 138–139
  - equilibrium geometry, 127–128
  - experimental IR spectra, 143
  - experimental Raman spectra, 141–143
  - phonon calculations, 126–127
  - phonon dispersion relations, bulk h-BN
    - longitudinal and transverse optical, 128
    - Lyddanne–Sachs–Teller relation, 129
    - single sheet, h-BN, 130–131
    - tubes, 131
  - Raman intensities
    - cartesian component, 140
    - density-functional perturbation theory, 140
    - single sheet, h-BN, 130–131
    - symmetry analysis, 131–133
    - zone-folding method, 133–136
  - Photoemission and inverse photoemission spectroscopy, 112, 121
  - Photo luminescence excitation (PLE), 122
  - Physical vapor deposition (PVD), 197
  - Plasma enhanced CVD (PECVD), 15
  - Plasma-enhanced pulsed-laser deposition (PE-PLD), 31
  - Plasma torch. *See* Arc jet technique
  - Plasmons and electron-energy loss spectroscopy
    - continuum dielectric theory, 125
    - dielectric constant, 125
    - Kramers–Kronig analysis, 125
    - phonon dispersion relations, 125, 129
  - PLE. *See* Photo luminescence excitation
  - Point defects, 55
  - $\pi$ - $\pi$  tight-binding model, 88
- R**
- Radial breathing mode (RBM), 8, 107, 126, 132, 136–141, 144
  - Random-phase approximation (RPA), 109
  - Redox reaction, 29–30
  - Resonant raman spectroscopy, vibrational properties
    - B and N doping, 245
    - endohedral sites, 245
    - in-plane Raman-active mode, 244
    - non-substitutional doping
      - hybridization breaking, 248
      - resonant raman scattering data, 249
      - radial breathing mode (RBM), 244
  - Rydberg series, 92, 114
- S**
- Scanning electron micrographs, 233, 236
  - Scanning electron microscopy (SEM), 31, 32, 179, 180
  - Scanning transmission electron microscopy (STEM), 58
  - Scanning tunneling microscopy (STM), 168, 239
  - Scanning tunneling microscopy/spectroscopy (STM/STS), 106
  - Schottky junction, 200
  - Selected area electron diffraction (SAED), 56
  - SEM. *See* Scanning electron microscopy
  - Single-wall carbon nanotubes (SWCNTs)
    - density of electronic states, 8–9
    - structure, 5–7
    - synthesis techniques, 7
  - Single-walled boron nanotubes (SWBNTs), 278
  - Single-walled carbon nanotubes (SWCNTs), 285
  - Sommerfeld factors, 92
  - Spatially resolved electron energy loss spectroscopy (SR-EELS), 47, 58
  - Spectrum-imaging (SPIM), 58–59
  - Stark effects, 66
  - STM. *See* Scanning tunneling microscopy
  - SWBNTs. *See* Single-walled boron nanotubes
  - SWCNTs. *See* Single-walled carbon nanotubes
- T**
- TEM. *See* Transmission electron microscopy
  - TEP. *See* Thermoelectric power measurements
  - Thermoelectric power measurements (TEP), 243
  - Thermogravimetric analysis (TGA), 205
  - Tight-binding calculations, 65, 70, 74
  - Tight binding method, 24
  - Time-dependent density functional theory (TD-DFT), 91
  - Transmission electron microscopy (TEM), 24, 31
    - electron diffraction pattern (EDP), 56–57
    - electron energy loss spectroscopy (EELS)
      - chemical maps, 61–62
      - core loss region, 57–58
      - doping element composition, 60–61
      - elemental maps, 58, 63
      - spectrum-line (SPLI), 58–59
    - growth mechanism, nanotubes, 63–64

**HRTEM**

- B- and N-doped C-SWNT, 53–54
- BN-SWNT, 54–55
- boron nitride nanotubes, irradiation, 55–56

**U**

- UV-visible absorption spectroscopy, 34–35

**V**

- Van-der-Waals interactions, 143
- Vibrational properties
  - infrared spectrum, 70, 72
  - Raman spectra, 69–71
  - UV Raman spectra, 71–72

**X**

- X-ray photoelectron spectroscopy (XPS), 202, 239

**Y**

- Young's modulus, 24, 74

**Z**

- Zero-loss image, 63
- Zigzag nanotubes, 6
  - growth mechanism, 63–64
  - HRTEM imaging, 54–55, 57
  - hydrogen storage, 76
  - vibrational properties, 70